europhysics
conference
abstracts

18th European Conference on

Controlled Fusion and Plasma Physics

Berlin, 3-7 June 1991
Editors: P. Bachmann, D.C. Robinson

Contributed Papers
Part IV

Published by: European Physical Society

Editor: Prof. K. Bethge, Frankfurt/M.

ging Editor: G. Thomas, Geneva

VOLUME
15 C
Part IV

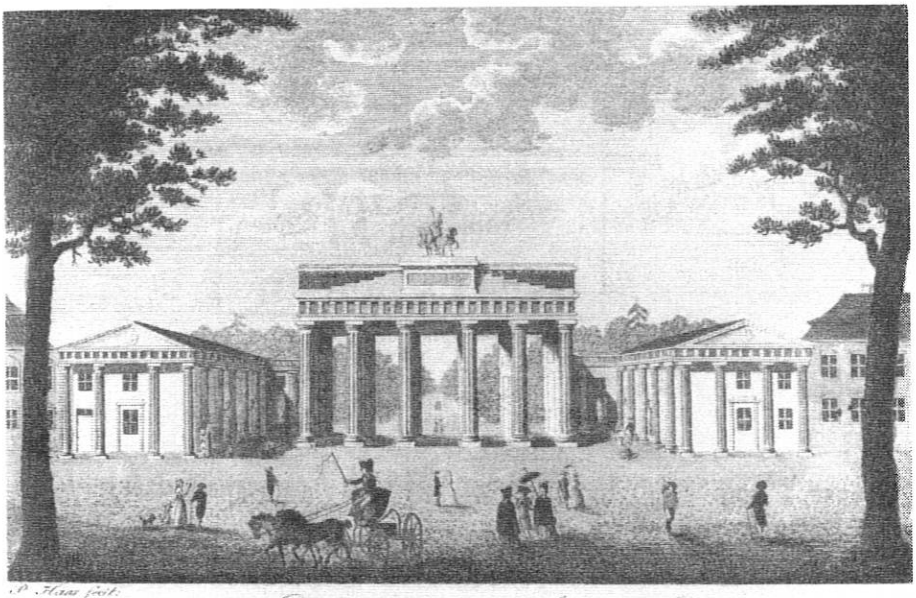

P. Haas fec.

Das Brandenburger Thor zu Berlin.

F
G

18th European Conference on

Controlled Fusion and Plasma Physics

Berlin, 3-7 June 1991
Editors: P. Bachmann, D.C. Robinson

Contributed Papers
Part IV

PREFACE

The 18th European Conference on Controlled Fusion and Plasma Physics was held in Berlin, Germany, from 3th to 7th June 1991. The Conference has been organized by the Central Institute of Electron Physics (ZIE) on behalf of the Plasma Physics Division of the European Physical Society.

The programme, format and schedule of the Conference were determined by the International Programme Committee appointed by the Plasma Physics Division of the EPS. The programme included 14 invited lectures and 388 contributed papers from which 27 were selected for oral presentation.

This 4-volume publication is published in the European Conference Abstract Series and contains all accepted contributed papers received in due time by the organizers. The 4-page extended abstracts were reproduced photographically using the manuscript submitted by the authors. The invited papers will be published in a special issue of the journal "Plasma Physics and Controlled Fusion" and sent free of charge to each registered participant.

The editors would like to acknowledge the skilful and dedicated support given by colleagues in the Department of Plasma Wall Interactions of the ZIE, in preparing the manuscript for reproduction in these four volumes.

May 1991

The Editors

INTERNATIONAL PROGRAMME COMMITTEE

D. Robinson (Chairman), Culham Lab., UK
K. Appert, CRPP/EPFL, Switzerland
G. Briffod, CEN, France
M. Chatelier, CEN, France
V.A. Chuyanov, Kurchatov Institute, USSR
M. Keilhacker, JET, EC
U. Samm, KFA, Germany
F. Santini, EURATOM-ENEA, Italy
F.W. Sluijter, Tech.Univ.Eindhoven, NL
J. Lingertat, ZIE, Germany

LOCAL ORGANIZING COMMITTEE

J. Lingertat, Chairman
P. Bachmann, Scientific Secretary
M. Blaschke, Conference Secretary
D. Amonath
H. Gunkel
W. König
P. Pech
M. Wirsig

CONTENTS

PAPER IDENTIFICATION

All contributed papers are listed with their title and the name of the first authors. Each paper may be identified by its classification symbol which starts with a letter that indicates to which topic it belongs followed by a number.

TITLE LIST

A TOKAMAKS

A1 Tokamaks, General

A2 Transport and Modelling

A3 Turbulence, Waves

A4 Pellet Injection

A5 Improved Confinement

A6 MHD Phenomena, Sawteeth

B STELLARATORS

C ALTERNATIVE CONFINEMENT SCHEMES

D PLASMA EDGE PHYSICS

E PLASMA HEATING AND CURRENT DRIVE

F GENERAL PLASMA THEORY

G DIAGNOSTICS

EXTRACTION OF ENERGY FROM INTENSE ELECTRON BEAM IN HOT PLASMAS BY ELECTRON CYCLOTRON WAVES

C. Maroli, V.Petrillo, G. Lampis+, F. Basilico+
Dipartimento di Fisica dell'Università di Milano
Via Celoria,16 Milano (Italy)
+ Istituto di Fisica del Plasma CNR-EURATOM-ENEA
Via Bassini,15 Milano (Italy)

In this work, a system composed by a maxwellian magnetized plasma base, plus an electron beam streaming through the bulk is studied. It can be described by an electron distribution given by the sum of two maxwellian functions: one relevant to the plasma base, the other, shifted in the momentum space, describing the stream. This system admits instabilities in dependence on the value of its basic parameters,i.e., the densities and the temperatures of both plasma and beam, and the mean velocity of the electrons of the stream. All the quantities describing plasma and beam are varying functions of the slab coordinate x. A wave in the range of the electron cyclotron frequency is injected onto this system, perpendicularly to Bo.The cold dispersion relation of these waves is

$$A\, n^4 + B\, n^2 + C = 0$$

with n normal refractive index and:

$A = \varepsilon_{11}(1 - \eta^2\varepsilon_{13}) + \eta^2\varepsilon_{13}^2 \qquad C = \alpha(\varepsilon_{11}^2 - \varepsilon_{12}^2).$

$B = (1 - \eta^2\varepsilon_{13})(\varepsilon_{12}^2 - \varepsilon_{11}^2) - \alpha\varepsilon_{11} - \varepsilon_{13}^2\eta^2(1+\gamma^2 Y^2) + 2\varepsilon_{12} Y\gamma)$

$\varepsilon_{11} = 1 - X_p/(1-Y^2) + \varepsilon_{13}, \qquad \varepsilon_{12} = X_p Y/(1-Y^2) - \gamma Y \varepsilon_{13}$

$\alpha = 1 - X_p - \gamma X_b, \qquad \varepsilon_{13} = -\gamma X_b/(1-Y^2\gamma^2). \qquad \gamma = (1-\eta^2)^{1/2}$

$X_p = 0.1, X_b = 0.05$ and $\eta = v_o/c = 0.6$ (v_o is the mean velocity of the beam).

In Fig. 1, a typical dispersion plot, n^2 versus x is shown. The

peculiarity due to the presence of the beam is an anomalous dispersion region on the high field side with respect to the EC resonance, constituted by a resonance, a conversion layer and a cut-off. The position of this layer is given by $Y=1/\gamma$, namely $x=R(Y(0)\gamma -1)$. Other cut off layers, relevant to the properties of the bulk, may also be present inside the plasma. Moreover, together with the EC and the usual upper-hybrid(UH) resonances a second resonance (UH2) appears due to the presence of the beam. The conversion layer near to UH2 changes the polarization of an ordinary wave(OW) incoming fron the HFS, transforming it into an extraordinary wave (XW). In this way, the properties usually attributed to the XW, for instance, the resonance on the UH layer, and,the conversion into Bernstein waves, are,here, enjoied by the O mode. The XW propagating toward the core from the HFS does not, in turn, reach the EC and the UH layers, being stopped on the UH2.

A more detailed description of the system is provided by the hot dispersion relation, where both temperatures of plasma and beam are retained as well as mildly relativistic corrections. Figure 2 and 3 show respectively the index of refraction of the O and X branches and that of the Bernstein wave for $X_p=0.2$, $X_b=0.02$, $T_p=$ 1KeV, $T_b=20$ eV and $\eta=0.25$. Thermal effect correct the anomaly region, eliminating both cut-off and resonance, transforming the cold succession of resonance, conversion and cut-off, into a structure of double conversion. Here, the X and the O modes interchange their polarizations. In fig. 3, the refractive index of the B mode is presented. This wave is generated via mode conversion near to the UH layer, where its refractive index assumes values very close to those of one of the e.m. modes. Furthermore,Ren also presents an anomalous dispersion feature in correspondence to UH2, showing there a tendency to the coupling with the e.m. branches.Appreciable values of Im n appear for all modes near to the EC layer, leading to the usual cyclotron absorption. Another absorption or emission layer develops near to UH2. The B wave is characterised there by very large positive values

of Imn, corresponding, due to its backward nature, to strong emission. In comparison with Im n for B waves, the corresponding imaginary part of n of both e.m. waves is negligible.

By varying X_b, the connection between the modes changes, and a double O-X conversion, or a direct O-B conversion occurs.The path of the wave depends on what happens near to each anomalous layer, and only a global approach is able to provide the total reflection R, transmission T, and absorption A coefficients.A set of differential equations is deduced from the relativistic Maxwell-Vlasov system. The electric field obtained injecting an O mode from the HFS shows short wavelength oscillations also on the left of the EC layer,due to the anomaly induced by the beam. The absorption coefficient versus X_b with X_p=0.2,T_b=1KeV,T_p=50eV, η =0.25 is presented in Fig. 4. Strong amplification of the wave (A < 0)is associated to intense production of B waves in the region of the UH2. The e.s. modes interacts strongly with the electrons of the beam, subtracting them energy, amplifying the wave.

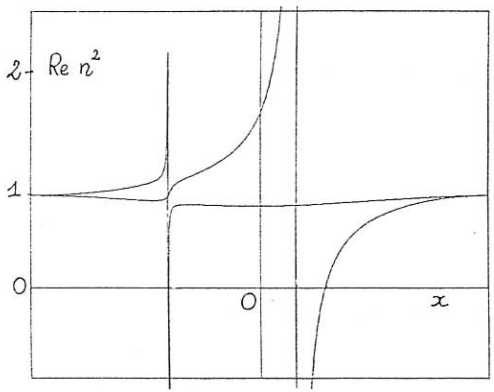

Fig. 1

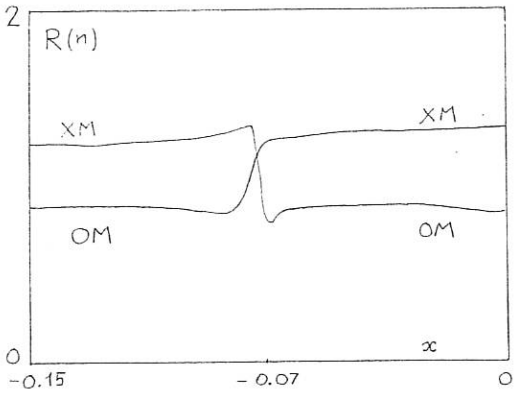

Fig. 2

Fig. 3

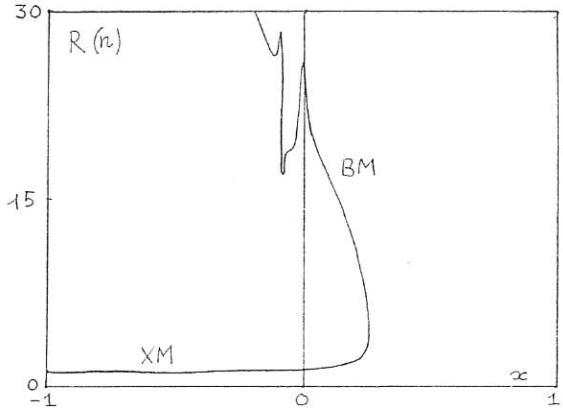

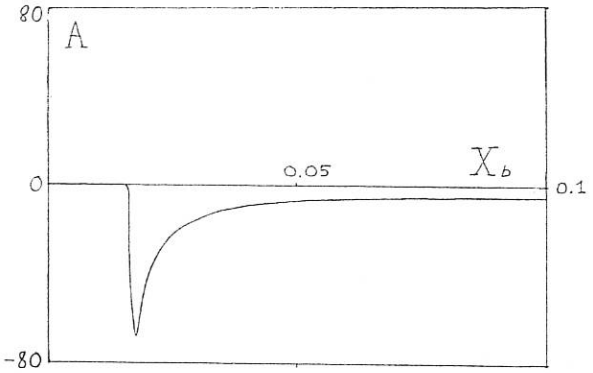

Fig. 4

MODELLING OF INDUCTIVELY COUPLED DISCHARGES EXCITED BY INTERNAL COILS

G.G. Lister† and M. Cox‡

†THORN EMI Central Research Laboratories, Hayes, Mddx., UK
‡AEA Technology, Culham Laboratory, Abingdon, Oxon., UK

Modelling of inductively coupled (ICD) discharges provides a method for computing parameters such as current, electrical conductivity and electromagnetic field strengths which are difficult to measure experimentally. The models reported in the literature to date deal with discharges which are surrounded by an induction coil ([1], [2]) where the plasma is considered as a one-turn secondary winding of a transformer. Eckert [1] derived expressions for electromagnetic fields and impedance in discharges assuming Bessel function solutions to the wave and electron density equations, while more recently Denneman [2] solved the non-linear problem, including the effects of a radial conductivity profile on the electromagnetic fields in a Ar-Hg discharge. Modelling of an ICD in which the coil is in the centre of the discharge presents an additional difficulty, since the coil does not provide a natural external boundary condition. In this paper, we compare numerical results from the approaches of [1] and [2] applied to discharges with internal coils, with a view to identifying relevant parameters applicable to interpretation of experiments.

A coil in the centre of an infinitely long cylindrical discharge, situated between confining walls at inner and outer radii a and b m., respectively, is assumed to induce a poloidal electric field E_θ and axial magnetic field H_z, with time dependence $\exp(j\omega t)$, where ω sec.$^{-1}$ is the applied angular frequency. For all ranges of electron density n_e considered here, the displacement current can be neglected in Maxwell's equations, which may thus be written (in MKS units)

$$\frac{dH_z}{dr} = \sigma E_\theta \quad , \tag{1}$$

$$\frac{1}{r}\frac{d}{dr}\{rE_\theta\} = -j\omega\mu_0 H_z \quad , \tag{2}$$

where μ_0 is the permeability of free space and $\sigma(r)$, the plasma conductivity,

$$\sigma(r) = n_e(r)e^2/m_e(\nu - j\omega) \quad , \tag{3}$$

where e and m_e are the electron charge and mass respectively and ν is the electron-atom collision frequency. In most cases considered below, $\nu/\omega >> 1$ and the influence of ω on σ is small. Equations (1) and (2) reduce to the wave equation

$$\frac{1}{r}\frac{d}{dr}\left\{r\frac{dE_\theta}{dr}\right\} + \left(j\mu_0\omega\sigma - \frac{1}{r^2}\right)E_\theta = 0 \quad . \tag{4}$$

Equation (4) cannot, in general, be solved analytically. However, if we replace $\sigma(r)$ by it's *line averaged* value $<\sigma>$, then (4) has the solution (cf. [1])

$$E_\theta(r) = A_1 H_1^{(1)}(\Gamma r) + A_2 H_1^{(2)}(\Gamma r) \quad , \tag{5}$$

where $\Gamma^2 = j\mu_0\omega < \sigma >$, $H_1^{(1)}$ and $H_1^{(2)}$ are first order Hankel functions and A_1 and A_2 are constants. E_θ and H_z may be obtained in terms of a single constant A, which is a function of the current in the coil, by applying appropriate boundary conditions. We consider two conditions at $r=b$:

a) conducting boundary, $E_\theta(b) = 0$, or

b) radiating boundary, where E_θ and H_z are continuous at $r=b$ and in air

$$E_\theta(r) = A_3 H_1^{(2)}(\Gamma_a r) \quad , \quad \Gamma_a = \omega/c \quad . \tag{6}$$

Assuming single step ionisation only, the electron diffusion equation is

$$\frac{1}{r}\frac{d}{dr}\left\{ r D_a \frac{dn_e}{dr} \right\} + \nu_i n_e = 0 \quad , \tag{7}$$

where D_a is the ambi-polar diffusion coefficient and ν_i is the ionisation rate. For zero electron density at $r=a,b$ and T_e independent of r ,

$$n_e(r) = C\{Y_0(\alpha b)J_0(\alpha r) - J_0(\alpha b)Y_0(\alpha r)\} \quad , \tag{8}$$

where J_0 and Y_0 are zero order Bessel functions and $\alpha^2 = D_a/\nu_i$ is an eigenvalue.

For discharges considered here, a=0.75 cm., b=3.0 cm., and we assume an average electron density $< n_e >$= 5x10^{17} m^{-3} and collision frequency $\nu = 10^9$ sec.$^{-1}$ (corresponding to 1 Torr Ar-Hg in a tube of radius 3 cm.). Two methods were used to obtain solutions, the first using the approximation in equation (5) and the second by integrating (1) and (2) directly. Fig. 1 shows the effect of varying applied frequency on the absolute value of the electric field $E_0(r) = |E_\theta(r)|$, where a conducting boundary is assumed at $r=b$. The results at 13.56 MHz are essentially the vacuum solutions, with a small effect at 41.68 MHz, and a more substantial variation at 200 MHz. This result may be understood in terms of the skin depth δ, including the effect of collisions (for $\nu/\omega \gg 1$) is

$$\delta \approx \frac{c}{\omega_p}\left\{\frac{\nu}{\omega}\right\}^{1/2} \quad , \tag{9}$$

where $\omega_p = 56.4 n_e^{1/2}$ sec^{-1} is the electron plasma frequency. In the cases considered, $c/\omega_p \cong 0.75$ cm., and δ may be of the order of the plasma dimensions, in which case the plasma modifies the phase but not the magnitude of the fields.

Fig. 2 shows the respective profiles of $n_e(r)$ and power per unit volume $W(r) = \sigma(r)E_\theta E_\theta^*$, where both have been normalised according to

$$\frac{2}{b^2 - a^2}\int_a^b F(r) r\, dr = 1 \quad .$$

Figs. 2(a) and 2(b) show *W(r)* profiles at 13.56 MHz for conducting and radiating boundaries respectively, indicating that in the latter case, total power deposition is shifted radially outward. Figs. 2 (c) and 2(d) show results at 200 MHz with conducting boundary, using the full Maxwell's equations and Bessel function approximation, respectively, the major difference being a slightly more peaked profile for *W(r)* in the former case - for lower frequencies the methods give almost identical results. The maximum of $n_e(r)$ is seen to occur at a significantly larger radius than that for *W(r)*, which we believe would be inherently unstable. We would expect the density to peak where the power density is highest, which would require a varying electron temperature.

Finally we consider the impedance at the coil (cf. [1]) defined through

$$Z(a) = \frac{E_\theta(a)}{H_z(a)} = Z_R \exp(j\phi(a)) \quad . \tag{10}$$

Table 1 lists values obtained for $Z_R(a)$ and $\varphi(a)$ for different values of ω, for conducting and radiating boundaries. At higher frequencies (> 100 MHz), results are virtually identical in both cases. With a conducting boundary, we a observe a shift in $\varphi(a)$ from $-\pi/2$ in the low frequency (vacuum) case through a *minimum* at $\phi(a) \sim -\pi/3$ as ω increases (in contrast to the outside coil, where $\varphi(a)$ has a maximum $\sim -3\pi/4$ (cf [1])). For a radiating boundary, the fields are almost in phase at low frequencies, and steadily increasing negatively with frequency. In both cases $Z_R(a)$ increases with frequency.

Table 1
Plasma Impedance
((1) conducting boundary (2) radiating boundary)

$f = \omega/2\pi$ (MHz)	$Z_R(a)^{(1)}$	$\varphi(a)^{(1)}$	$Z_R(a)^{(2)}$	$\varphi(a)^{(2)}$
3.0	1.39	-1.46	6.71	-.053
13.56	5.11	-1.15	6.92	-0.24
27.12	7.72	-0.96	7.54	-0.44
41.68	9.26	-0.98	8.50	-0.61
100.0	13.9	-1.03	13.4	-0.96
200.0	22.6	-1.22	22.6	-1.20

In conclusion, for the parameters considered and frequencies less than ~20 MHz, the absolute values of electric fields are independent of the plasma, but effects on plasma impedance and phase are more marked. Modelling can be a useful tool in interpreting experimental results, but detailed information on plasma parameters such as plasma conductivity and power deposition require more sophisticated models, allowing for, *inter alia,* varying electron temperatures and possible two dimensional effects.

References

[1] Eckert H U, 1961, J. Appl. Phys., **33**, 2780
[2] Denneman J, 1990, J. Phys. D: Appl. Phys., **23**, 293

Figure 1

Effect of applied frequency on $E_o(r)$

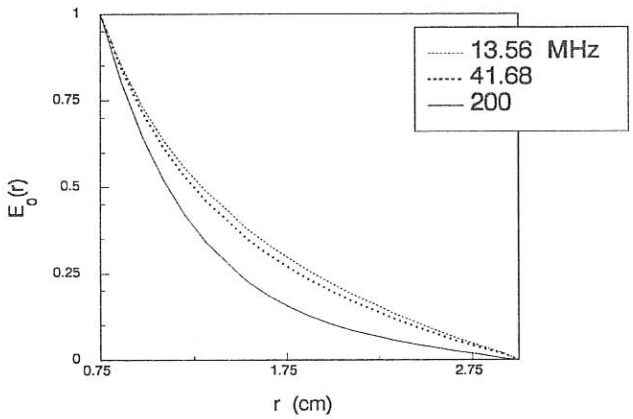

Figure 2

Normalised Power (W) and Electron Density Profiles

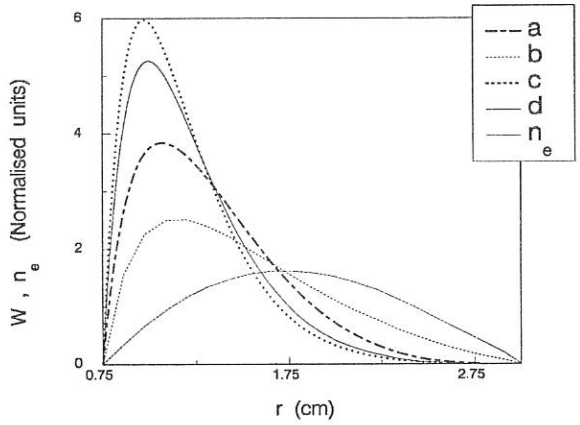

a) conducting boundary b) radiating boundary (13.56 MHz)
c) full Maxwell's equations d) Bessel function (200 MHz)

COLLECTIVE THOMSON SCATTERING IN A RELATIVISTIC MAGNETIZED PLASMA

H. Bindslev

JET Joint Undertaking, Abingdon, Oxon, OX14 3EA, UK.
Permanent address: Risø National Laboratory, DK–4000 Roskilde, Denmark.

Introduction The effects which the dielectric properties of a relativistic magnetized plasma have on the scattering of electromagnetic radiation, are investigated. The scattering is caused by fluctuations in the dielectric properties, which are assumed to derive from fluctuations in the electron density. The origin of the density fluctuations is not considered. Expressions for the scattering cross section and the scattered power accepted by the receiving antenna are derived for a plasma with spatial dispersion. The resulting expressions allow thermal motion to be included in the description of the plasma and remain valid for frequencies of the probing radiation in the region of ω_{pe} and ω_{ce}, provided the absorption is small. Symmetry between variables relating to incident and scattered fields is found and can be shown to be in agreement with the reciprocity relation [1]. Dielectric effects in a cold plasma have been investigated by a number of authors, most recently by Bretz [2] and Hughes and Smith [3]. The present work extends the theory of dielectric effects to hot and relativistic plasmas. Earlier results are confirmed in the cold plasma limit. Significant relativistic effects, of practical importance to the scattering of millimeter waves in large tokamaks, are predicted.

A major motivation for the present work is the fact that collective Thomson scattering diagnostics, intended to measure alpha particle and other fast ion velocity distributions in tokamak plasmas, are presently under development [6,7,8]. In these diagnostics the frequency of the probing radiation is not large relative to the electron plasma and cyclotron frequencies. This means that a number of simplifying assumptions, which are well satisfied for the majority of laser scattering experiments, are not valid. Most notably, vacuum propagation cannot be assumed. In the work by Hughes and Smith [3], the Thomson scattering cross section and the scattered power accepted by the receiving antenna were investigated for a cold plasma. It was shown that, in the parameter ranges relevant for the planned alpha and fast ion Thomson scattering diagnostic at JET, it is necessary to take the dielectric properties of the plasma into account. The dielectric effects manifest themselves in the term referred to as the *geometrical factor*, G. Relative to predictions based on vacuum propagation, large increases in the scattered power were found for X to X mode scattering, with a singularity at the R-cutoff (ordinary and extraordinary mode are referred to as O and X mode respectively). X to X scattering may therefore be an attractive option. At the high temperatures found in large tokamaks, the scattering theory based on the cold plasma model is, however, not reliable in this regime: relativistic effects must be taken into account.

Theory A detailed derivation of the equation of transfer for a scattering system is given in [1]. The derivation consists in the following steps: (a) The field resulting from a point source in a homogeneous plasma is found by solving for the field in the Fourier–Laplace transform of the inhomogeneous wave equation. (b) The far–field is identified with the propagating modes which manifest themselves as singularities in the transform of the field. When evaluating the residue resulting from such a singularity a new term, caused by the spatial dispersion,

is found. Mathematically the term arises because the dielectric tensor depends on the wave vector. (c) The energy flux, associated with the far–field in a homogeneous plasma, is found. The flux includes the electromagnetic flux and the kinetic flux, where the latter is due to the spatial dispersion. (d) The conservation of flux inside a ray tube (WKB approximation) and the equation of transfer for radiation in an anisotropic inhomogeneous medium [4] are used to find the energy flux outside the plasma. From this and the relation for the étendue of a receiver in vacuum, the power accepted by a coherent detector is found. This gives the field at the detector resulting from a point source, which we will call the *detector response*. (e) The currents resulting from the action of the incident field on fluctuations in the dielectric properties of the plasma are the sources of the scattered field. To find the scattered power accepted by a receiving antenna the currents are convoluted with the *detector response* giving the scattered field at the detector and hence the accepted power. (f) The fluctuations in the dielectric properties are expanded to first order in the electron density fluctuations. Care is taken to preserve symmetry under time reversal in this step. As a result the last asymmetry, between incident and scattered fields in the equation of transfer for a scattering system, disappears. The symmetry can be shown to be in agreement with the reciprocity relation [1].

The equation of transfer resulting from the derivation outlined above is

$$\frac{\partial P^{\mathrm{s}}}{\partial \omega} = P^{\mathrm{i}}\, O_b\, \lambda_0^{\mathrm{i}} \lambda_0^{\mathrm{s}} r_e^2\, n_e\, \frac{S(\mathbf{k},\omega)}{2\pi}\, G \quad , \tag{1}$$

where P^{s} is the accepted power, P^{i} is the incident power, O_b is the beam overlap [5], λ_0 is the vacuum wave length, r_e is the classical electron radius, n_e is the electron density, $S(\mathbf{k},\omega)$ is the spectral density function and G is the geometrical factor which contains the new results. Superscripts i and s refer to incident and scattered fields respectively. In the limit where the anti–Hermitian part of the dielectric tensor can be ignored G takes the form

$$G = \frac{\mathcal{C}}{\mathcal{F}^{\mathrm{i}} \mathcal{F}^{\mathrm{s}}} \tag{2}$$

where the *coupling term*, $\mathcal{C}$, is given by

$$\mathcal{C} = \frac{\omega^{\mathrm{i}} \omega^{\mathrm{s}}}{\omega_p^2} \left| (\hat{\mathbf{e}}^*)^{\mathrm{s}} \cdot \left(\frac{\omega^{\mathrm{i}} \mathbf{Q}^{\mathrm{i}} + \omega^{\mathrm{s}} \mathbf{Q}^{\mathrm{s}}}{2\omega_p} \right) \cdot \hat{\mathbf{e}}^{\mathrm{i}} \right|^2 \tag{3}$$

and $\mathcal{F}$, the *normalized flux*, is the energy flux, associated with a field in the plasma, normalized by the flux of a vacuum field with identical amplitude:

$$\mathcal{F} = \frac{1}{\varepsilon_0 c} \left| \left(\mathbf{S}_{ij} - \left(\frac{\omega \varepsilon_0}{2} \right) \left\{ \frac{\partial K_{ij}}{\partial \mathbf{k}} \right\}^h \right) e_i^* e_j \right| \quad . \tag{4}$$

$\mathbf{S}_{ij}$, is the *Poynting tensor*, $\mathbf{S}_{ij} E_i^* E_j = \mathrm{Re}\{\mathbf{E} \times \mathbf{H}\}$, $\mathbf{K}$ the dielectric tensor, $\mathbf{Q} = \mathbf{K} - \mathbf{I}$ the susceptibility tensor, $\hat{\mathbf{e}}$ the unit electric field vector and ω_p the plasma frequency.

A more general form of G is given in [1] but numerical investigations indicate that the anti–Hermitian part of the dielectric tensor can safely be ignored in most cases of practical interest.

The differential scattering cross section takes the form

$$\frac{\partial^3 \Sigma}{\partial \hat{\mathbf{k}}\, \partial \omega} = \frac{\lambda_0^{\mathrm{i}}}{\lambda_0^{\mathrm{s}}} r_e^2 \frac{S(\mathbf{k},\omega)}{2\pi} \frac{\mu^{\mathrm{s}2}}{|\hat{\mathbf{k}}^{\mathrm{s}} \cdot \hat{\mathbf{v}}_g^{\mathrm{s}}|} G \quad , \tag{5}$$

where μ is the refractive index and $\hat{\mathbf{v}}_g$ is a unit vector in the direction of the group velocity.

Results Computer codes have been developed, as part of this work, to evaluate G with dielectric tensors and their derivatives derived from four magnetized plasma models: (a) cold, (b) hot equilibrium, (c) and (d) weakly relativistic equilibria based on Shkarofsky [10] and Yoon and Krauss–Varban [11] respectively. With a number of corrections to Yoon and Kraus–Varban's work [1], the two relativistic codes give identical results.

The plots presented here are calculated with parameters relevant for X to X scattering in JET with the following scattering geometry: $\hat{\mathbf{k}}^i \cdot \hat{\mathbf{B}} = -\hat{\mathbf{k}}^s \cdot \hat{\mathbf{B}}$, θ =Arccos$(\hat{\mathbf{k}}^i \cdot \hat{\mathbf{k}}^s) = 30°$ and ϕ =Arccos$(\hat{\mathbf{k}} \cdot \mathbf{B}) = 30°$ where $\mathbf{k} = \mathbf{k}^s - \mathbf{k}^i$. The curves show the geometrical factor, the coupling term (equation 3), the normalized flux (equation 4) and the refractive index as functions of electron density. $\mathcal{F}$ and μ are identical for incident and scattered fields due to the symmetry in the direction of propagation relative to the magnetic field. The frequency of the radiation is higher than the cyclotron frequency. This implies that the R–cutoff determines the maximum density to which the radiation can propagate. The effect of the R–cutoff is clearly visible in the plots. While the hot plasma predictions tend toward the cold plasma predictions at the R–cutoff, the relativistic plasma model produces a shift in the R–cutoff toward higher densities. This shift can be attributed to the relativistic mass increase of the electrons. The relativistic shifts of the R–cutoff and upper–hybrid resonance were noted by Batchelor, Goldfinger and Weitzner [9]. Although the hot plasma model does produce a change in predictions relative to the cold model, in this regime much more substantial effects are found with the relativistic model. It is noteworthy that a nonvanishing imaginary part to the refractive index is found with the relativistic model and not with the hot model. This absorption is attributable to the relativistic smearing of the cyclotron absorption.

The reliability of the analysis of light scattered for diagnostic purposes depends, among many factors, on the accuracy of the model. The plots clearly illustrate the need for a relativistic model. Another factor of importance to the reliability of the analysis is the sensitivity of the spectrum of scattered light to various plasma parameters. Sensitivity to quantities which the diagnostic seeks to measure is beneficial while sensitivity to other quantities like the electron density reduces the reliability of the analysis. As the R–cutoff is approached the geometrical factor and hence the spectrum of scattered light for X to X scattering becomes increasingly sensitive to the electron density and other parameters, making reliable analysis impossible in the vicinity of the R–cutoff. The practical consequence of the relativistic shift of the R–cutoff is therefore to increase the upper limit on the density range in which reliable measurements can be made with X to X scattering. For O to O scattering the relativistic effects appear to be of no importance to the JET collective scattering diagnostic. When making use of O to O scattering it is, however, important to stay clear of the R–cutoff in order to minimize spurious signals from X to X scattering. This requirement accentuates the importance of an accurate knowledge of the location of the R–cutoff.

References

[1] Bindslev H., to be published.
[2] Bretz N., *J. Plasma Physics*, **38**, 79. (1986)
[3] Hughes T. P. and Smith S. R. P., *J. Plasma Physics*, **42**, 215. (1989)
[4] Bekefi G., *Radiation Processes in Plasmas.* John Wiley & Sons, N. Y. (1966)
[5] Bindslev H. M.Sc. Thesis, Technical University of Denmark (1989).
[6] Costley A. E. *et al.*, JET Reports, JET–R(88)08 (1988), JET–P(89)53 (1989)

[7] Woskov P. P. *et al.*, *Rev. Sci. Instrum.*, **59**, 1565. (1988)
[8] Machuzak J. S., *et al.*, *Rev. Sci. Instrum.*, **61**, 3544. (1990)
[9] Batchelor D. B., Goldfinger R. C. and Weitzner H., *Phys. Fluids*, **27**, 2835. (1984)
[10] Shkarofsky I. P., *J. Plasma Physics*, **35**, 319. (1985)
[11] Yoon P. H. and Krauss-Varban D., *Phys. Fluids B*, **2**, 1918. (1990)

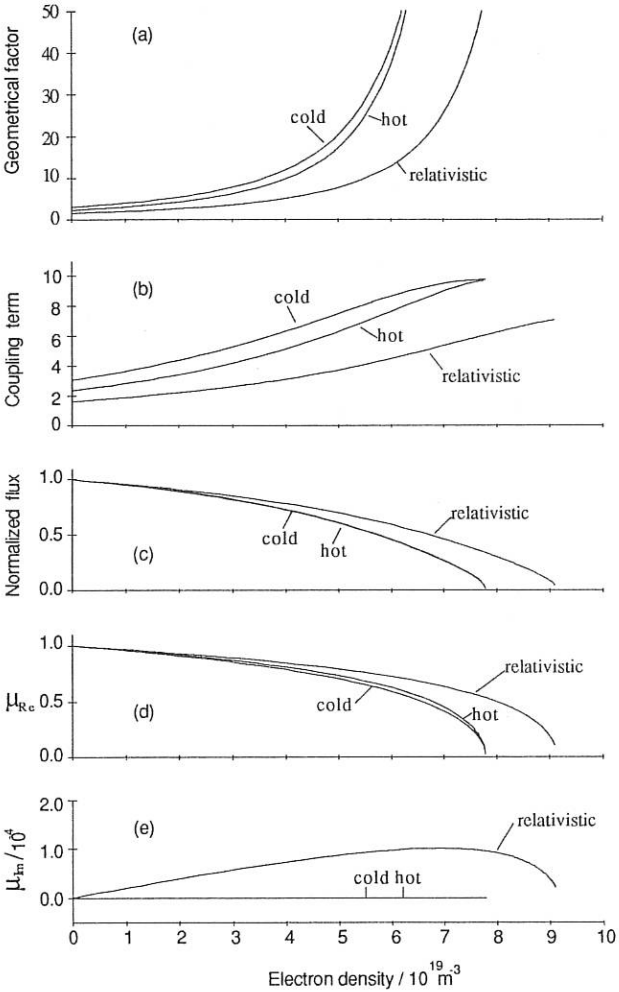

(a) Geometrical factor,
(b) coupling term,
(c) normalized flux,
(d) real part and
(e) imaginary part of refractive index, as functions of electron density.
Parameters:
X to X scattering,
$\omega^i = \omega^s = 2\pi \cdot 140$ GHz,
$\theta = \phi = 30^\circ$,
B = 3.4 T, T_e = 12 keV.

ELECTRIC FIELD EFFECTS ON THE RESISTIVE PRESSURE-GRADIENT-DRIVEN TURBULENCE

L. Garcia
Universidad Complutense and Asociación EURATOM-CIEMAT. Madrid. Spain.

B.A. Carreras, V.E. Lynch
Oak Ridge National Laboratory. Oak Ridge, Tennessee, USA.*

Resistive pressure-gradient-driven turbulence has been studied in detail [1-3] for the case with no diamagnetic effects, and in the low-ω^* regime in which the linear growth rate dominates over the real frequency [4]. Here, we include an external radial electric field in order to study its effect on the turbulence levels.

The equations describing the resistive interchange mode used in this paper are based on a two-fluid model for a configuration with average bad curvature and large aspect-ratio [4]. The geometry is a periodic cylinder of length $L = 2\pi R_0$ and radius a. The model consists of three equations:

$$\frac{\partial \Psi}{\partial t} = -\frac{R_0}{B_0}\nabla_\parallel \Phi + R_0 \eta \tilde{J}_z - \frac{R_0 T_e}{e n_0 B_0}\nabla_\parallel n$$

$$\frac{\rho_m}{B_0}\frac{\partial U}{\partial t} = -\frac{\rho_m}{B_0}\vec{V}\cdot\vec{\nabla}U - \nabla_\parallel J_z + T_e \frac{d\Omega_0}{dr}\frac{1}{r}\frac{\partial n}{\partial \theta} + \frac{\rho_m}{B_0}\mu\nabla_\perp^2 \tilde{U}$$

$$\frac{\partial n}{\partial t} = -\vec{V}\cdot\vec{\nabla}\tilde{n} - \frac{dn_0}{dr}V_r + \frac{1}{eB_0}\nabla_\parallel J_z + \chi_\perp \nabla_\perp^2 \tilde{n}$$

Here, Ψ is the poloidal flux function, n is the electron density, $\vec{V}$ is the fluid velocity, U and J_z are the z-component of the vorticity and current density, respectively, and ρ_m is the mass density. The velocity is expressed in terms of a streamfunction Φ/B_0, $\vec{V} = \left(\vec{\nabla}\Phi \times \hat{z}\right)/B_0$. The velocity streamfunction is trivially related to the electrostatic potential $-\Phi$. The term $d\Omega_0/dr$ is the toroidally averaged curvature. The symbol $\nabla_\parallel$ denotes derivative parallel to the magnetic field, $\nabla_\parallel = \vec{B}\cdot\vec{\nabla}$. Each equation has a dissipative term, corresponding to resistivity, viscosity, and cross-field transport, respectively. The inclusion of an equilibrium radial electric field E_r induces a poloidal flow with velocity $V_E = -E_r/B_0$.

* Operated by Martin Marietta Energy Systems, Inc., under contract DE-AC05-84OR21400 with the U.S. Department of Energy.

This model can be regarded as the reduced magnetohydrodinamic equations based on a two-fluid model for a stellarator configuration with no ion heating and constant electron temperature.

In the absence of diamagnetic terms and density and vorticity dissipation terms, the linear eigenvalue problem can be written using the electrostatic and slab approximation as

$$\frac{d}{dx}\left[(\omega - k_\theta V_E)\frac{d\Phi}{dx} + k_\theta V_E' \Phi\right] = \left[k_\theta^2(\omega - k_\theta V_E) + \frac{V_s^2 k_\theta^2}{r_c L_n}\frac{1}{\omega - k_\theta V_E} + i\frac{S}{a^2\tau_{hp}}\frac{m^2}{q^2}\frac{x^2}{L_q^2}\right]\Phi$$

Here, V_s is the sound velocity, $V_s = (T_e / m_i)^{1/2}$; r_c is the radius of curvature of the magnetic field line, $r_c = (d\Omega_0 / dr)^{-1}$; L_n is the characteristic density scale length, and L_q is the scale length of the safety factor. The Lundquist number $S = \tau_R / \tau_{hp}$ is the ratio of the resistive time, $\tau_R = a^2\mu_0 / \eta$, and the poloidal Alfvén time, $\tau_{hp} = R_0\sqrt{\mu_0\rho_m} / B_0$.

Linearly, the main effect of a sheared radial electric field is the coupling to the Kelvin-Helmholtz (K-H) instability. In hydrodynamics, the K-H instability arises in a stratified heterogeneous fluid when the different layers are in relative motion [5], and the shear in the flow is the source of free energy. In the presence of a magnetic field, the magnetic shear has a strong stabilizing effect for the K-H instability [6].

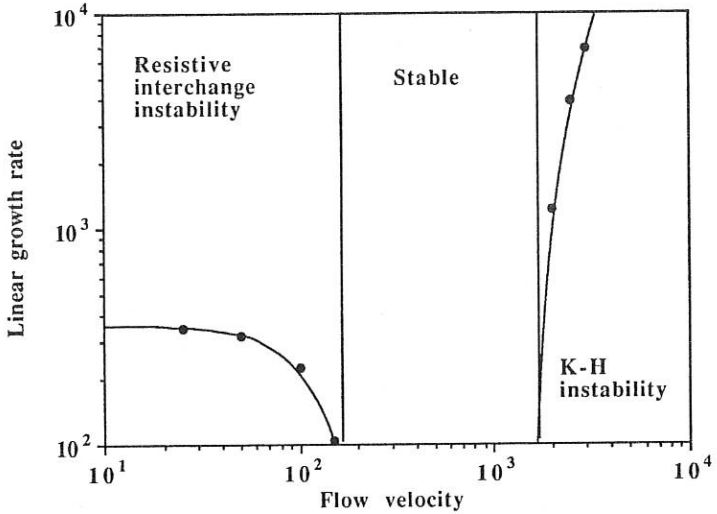

Fig. 1: Linear growth rate as a function of the flow velocity for $L_E = 0.01$. The growth rate and the velocity are normalized to τ_R^{-1} and $a\tau_R^{-1}$, respectively.

In configurations with unfavorable curvature and with magnetic shear, the interchange mode is unstable for low values of the velocity V_0 and sheared flow length L_E. As the sheared flow increases, the growth rate of the mode is reduced until it is totally stabilized. As the flow increases further, the K-H instability can be triggered and the growth rate becomes proportional to the flow rate jump. The dependence of the linear growth rate of the resistive interchange on the flow velocity is shown in Fig. 1. An analytic solution can be found in the limit $L_E \gg W_0$, where W_0 is the width of the linear mode in the absence of flow. The corresponding dispersion relation is

$$\gamma = \frac{\pi}{2} k_\theta V_0 \frac{W_0}{L_E} \cot\left[\frac{\ell\pi}{\sqrt{1+4Ri}}\right] \cong k_\theta V_0 \frac{W_0}{L_E} \frac{\sqrt{Ri}}{\ell}\left(1 - \frac{\pi^2}{12}\frac{\ell^2}{Ri}\right)$$

Here, Ri is the Richardson number, $Ri = (V_s^2 / r_c L_n) / (V_0 / L_E)^2$, which represents the ratio of the buoyancy effects and the shear flow effects.

The nonlinear equations are solved numerically as an initial value problem, using a Fourier expansion in the angles θ and $\zeta = z/R_0$ and finite differences in the radial variable [7]. The nonlinear calculations have been done for values of beta below the ideal MHD stability limit, and we have used the same parameters as those given in Ref. 1: $\beta_0 / 2\varepsilon^2 = 1.25 \times 10^{-2}$, $S = 10^5$. The q, n, and Ω_0 profiles are also the same, with $L_q = 1.275a$, $L_n = 0.685a$, and $r_c = 2.29a$ at the $q = 3/2$ resonant surface. The value of $\omega_e^* (= k_\theta \rho_s V_s / L_n)$ has been chosen to modify the linear growth rate of the instability without changing its nature [4]: $\overline{\omega}_e^* \equiv \tau_R \rho_s V_s / a^2 = 25$, where $\rho_s = V_s / \Omega_i$, and Ω_i is the ion cyclotron frequency. For the (m=3; n=2) mode, the lowest m mode included in the calculation, this choice implies that $\left|\omega_e^* / \gamma\right| \approx 0.5$. The coefficients for the dissipative terms are such as to have stable modes for m > 60 in the absence of an external electric field.

In order to study the effects of the electron diamagnetic terms, we consider first the case with no external electric field [4]. As a result of the nonlinear evolution, a relatively large (m=0; n=0) component of the streamfunction Φ is generated. The resulting poloidal velocity (radial electric field) is strongly sheared. The reduction in the saturation level is about 40%, significantly stronger than what we expected on the basis of mixing length results. However, when the (m=0; n=0) component of the velocity streamfunction is kept equal to zero during the nonlinear calculation, the saturation level of the turbulence is similar to the one for the case with $\omega_e^* = 0$. This results suggest that the self-generated electric field can play an important role in the saturation of the turbulence. The reduction in the turbulence level can be explained by the coupling between poloidal and radial decorrelation [8].

Next, we consider the case of a constant electric field. The numerical results show that the addition of an external constant electric field of the order $\pm T_e/er$ does not affect the electrostatic potential fluctuation level at saturation.

To study the effect of a sheared electric field, we use, in the numerical calculations, an external sheared poloidal flow parameterized as $V_E = V_0 \tanh\left[(r - r_s)/L_E\right]$, where r_s is the position of the q = 3/2 rational surface.The values of the parameters are $L_E = 0.1a$, $V_0 = \pm 500a/\tau_R$, which correspond to a Richardson number of about 5. The time evolution of the fluctuations is slowed down by the sheared poloidal flow, and the saturation level is slightly reduced.

The condition for turbulence reduction of the density by shearing is $\tau_S^{-1} \gg \tau_D^{-1}$, where τ_S is the sheared flow decorrelation time ($\tau_S^{-1} = k_\theta W d V_E / dr$), and τ_D is the density fluctuation turbulence decorrelation time. This condition implies

$$k_\theta \left(W_0 \Lambda^{7/6}\right) \frac{V_0}{L_E} \gg \frac{\gamma_0}{\Lambda^{1/3}} \Rightarrow Ri = \frac{\gamma_0^2}{W_0^2} \frac{L_E^2}{k_\theta^2 V_0^2} \ll \Lambda^3$$

The parameter Λ is the nonlinear enhancement factor defined in Ref. 1. The condition for turbulence reduction by shearing implies, for low Λ values, stabilization of low-m modes by coupling to K-H effects. For the parameters of the present calculations, $\Lambda \approx 3.55$, so this condition is only marginally satisfied. Consequently, it would be necessary to reach high values of the sheared flow in order to get any appreciable turbulence reduction. For those values of the flow, many of the modes included in the calculation become linearly stable, and it is very difficult to distinguish between linear stabilization and turbulence reduction.

REFERENCES

[1] B.A. Carreras, L. Garcia, P.H. Diamond, *Phys. Fluids* **30** (1987) 1388.

[2] G.S. Lee, B.A. Carreras, L. Garcia, *Phys. Fluids B* **1** (1989) 119.

[3] B.A. Carreras, P.H. Diamond, *Phys. Fluids B* **1** (1989) 1011.

[4] B.A. Carreras, V.E. Lynch, L. Garcia, ORNL/P-90/4305, October 1990.

[5] S. Chandrasekhar, "Hydrodynamic and Hydromagnetic Stability", Oxford University Press, Oxford, 1961.

[6] T. Chiueh, P.W. Terry, P.H. Diamond, J.E. Sedlak, *Phys. Fluids* **29** (1986) 231.

[7] L.Garcia et al., *J. Comput. Phys.* **65** (1986) 253.

[8] H. Biglari, P.H. Diamond, P.W. Terry, *Phys. Fluids B* **2** (1990) 1.

The Mechanism of Self-sustainment in Collisional Drift-wave Turbulence

Bruce D. Scott
Max Planck Institut für Plasmaphysik
W8046 Garching, Germany

Self-organised collisional drift wave turbulence is seen to self-sustain in the absence of linear instabilities under a wide range of parameters. Investigations into the initial amplitude threshhold help to establish the mechanism. They also show that the turbulence is non-diffusive in character, since the important assumptions behind turbulence-as-diffusion are all violated. Many important features of experimentally observed tokamak edge fluctuations are reproduced. Additionally, the competition between the gradients to drive the turbulence gives rise to inward-pinch dynamics if there is a large disparity in background scale lengths. If these results are relevant, then turbulent transport in tokamaks is nothing like heretofore existing models of it.

The conventional wisdom on anomalous transport in tokamaks is beset with perplexity. It has usually assumed that there is some sort of instability, usually linear, which is the "mode" responsible for feeding the free energy in the temperature and/or density gradients into a mixing-length/random walk diffusion model. Even the nonlinear closure schemes tend to "renormalise" the advective nonlinearity into a diffusivity and so fall back on this same physical picture. Conventional diffusivity models are also at a loss to explain known cases of up-gradient heat ("profile consistency") or particle ("inward pinch") transport, unless the up-gradient transported quantity is introduced non-self-consistently.

The approach taken here is different. Let it be that the basic sheared-slab drift wave equations admit no linear instabilities. The hypothesis is made that sufficiently strong turbulence ought to find a suitably efficient free energy-tapping structure and thereby sustain itself. The well-known noisy start phase of a tokamak discharge can take care of the initialisation. The computational basis is the simplest set of equations which contain the dynamics which absolutely cannot be avoided, namely, complete fluid electron dynamics and shear. Ions are kept only to provide inertia, and trapped electrons are ignored (anomalous transport is still observed in cases for which exotic effects from these sources should be absent). As to the physical picture of the dynamics, it is left to the equations to determine that, *self consistently*, *i. e.*, no further assumptions into which process or correlation may be dominant or negligible. Since the high resolution demands are entirely beyond the hopes of a multi rational surface (3D) simulation, the simulations in this work are confined to a single surface (2D), since that case, and only that case, can be adequately resolved.[1]

The system of equations used is that of collisional electron fluid dynamics in slab geometry, in which x is down-gradient, z is along the field at $x = 0$ (the resonant surface), and y is along the wave(s).[2] Parallel dynamics enter through the shear: $\mathbf{B} = B(\hat{\mathbf{z}} + x\hat{\mathbf{y}}/L_s)$. For a wavenumber k_y, the parallel gradient is $k_\parallel = k_y x/L_s$. Independent

fields are $\widetilde{n}$, $\widetilde{T}$, $\widetilde{\phi}$, and $\widetilde{u}_\parallel$. The first three are all mutually coupled through resistive dissipation, most strongly where $k_\parallel^2 V_e^2/\nu_e$ is equal to turbulent advection rates ($\omega_t \equiv \widetilde{\mathbf{v}} \cdot \nabla$): parallel dissipation tends to restore electron adiabaticity against the disruptive effect of the turbulent fluctuations. This process is collisional in the edge, since arising from slowing of the electron/ion drift it depends only on time scales: the electrons are collisional whenever linear wave frequencies (near $\omega_* = k_y \rho_s c_s / L_n$, the diamagnetic frequency) and ω_t are slower than ν_e. Resonance with the ions occurs at larger x, when $k_\parallel c_s \sim \omega_t$. Some of the energy in $\widetilde{u}_\parallel$ is dumped into "ion Landau damping", but most is recycled back into $\widetilde{\phi}$, which is how the turbulence is localised.[3]

The dynamics of the system are diagnosed not through the fluctuation amplitudes or spectra, but through the amplitudes, spectra, and spatial (in x) profiles of the source/sink terms. These latter arise from the conservation equation for the fluctuation energy (sum of normalised mean square fluctuations).[2,3] They are: Γ_t, rate of energy fed to the fluctuations by the temperature gradient; Γ_n, same for the density gradient; Γ_c, resistive dissipation of the parallel current fluctuations; Γ_k, dissipation by parallel thermal conduction; Γ_s, dissipation through parallel ion motion. Spectral, and spatial, directions of energy transfer are quickly revealed, as well as dominant processes.

Amplitude threshhold – mechanism for self-sustainment

To allow the Γ's to emerge and evolve self-consistently, the turbulence is initialised adiabatic, $\widetilde{n}/n = e\widetilde{\phi}/T$, with $\widetilde{T} = \widetilde{u}_\parallel = 0$. The $\widetilde{\phi}$ are initialised in a broad-band random-phase distribution localised within about $5\rho_s$ of $x = 0$. The initial amplitude is set to $e\widetilde{\phi}/T = a_0 \rho_s / L_n$.

The nominal run, discussed in Ref. 2, had $a_0 = 1.5$. Run long enough for good statistical saturation, it serves as the benchmark. Others were started, with $a_0 = 0.2$, 0.3, 0.5, 0.7, and 1.0, and run long enough to see whether they achieved self-sustainment or continuously decayed. The nominal run showed all of the Γ's to be strongly peaked at an intermediate scale ("mid-k_y", $k_y \rho_s \sim 0.7$), but with the net source high above the sink. Both low- and high-k_y (about 0.1 and 2) were net sinks. Mid-k_y modes were more or less homogeneous, but low-k_y modes were very narrow in x. Measurements of the power spectrum distribution, $S(k_y, \omega)$ indicated the mid-k_y modes to lie on the linear dispersion curve, but the low-k_y modes to lie well below it. Previous work with a density-only model system had identified this low-k_y part as self-organised: several phase-locked modes propagating at the same speed, essentially that of the mid-k_y part.[3]

The amplitude threshhold search for nonlinear self-sustainment further revealed the mechanism. The cases $a_0 \geq 0.5$ grew to saturation, while those with 0.2 and 0.3 decayed. The 0.5 case in particular spent a well-resolvable time decaying. At a very definite time, however, the energy source feed rate sharply increased; following the detailed structure near this time revealed the establishement of the self-organised structure investigated in Refs. 2 and 3. This structure can be so characterised: The source-tapping mid-k_y modes preferentially transfer energy to low-k_y $\widetilde{\phi}$ and high-k_y $\widetilde{n}$ and $\widetilde{T}$ because of their cascade tendencies.[3] Down- and up-gradient flows from the thin, localised low-k_y $\widetilde{\phi}$ modes produce mid-k_y $\widetilde{n}$ and $\widetilde{T}$ because of the finite mode width and small-scale isotropisation. Through the shear, which couples all three of these fields, low-k_y $\widetilde{n}$, $\widetilde{T}$,

and mid- and high-k_y $\widetilde{\phi}$ are formed, completing the circle. The weakly dispersive low-k_y modes readily phase-lock at a propagation speed near that of the mid-k_y modes (less than the low-k_y linear speed). This structure is self-sustaining, but only if the nonlinear couplings are as strong as the linear ones, which produces the amplitude threshhold near $0.3\rho_s/L_n$. Runs at other parameters exhibited several cases which drop below 1.0 and then recover to saturation. It is therefore safe to say that the amplitude threshhold is somewhat less than ρ_s/L_n, weakly dependent on parameters.

The turbulence is not diffusive

The mixing length, turbulence-as-diffusion physical picture depends on three main assumptions: (1) the important range of scales has its amplitude determined by a balance between source input and nonlinear decorrelation: cascading to larger or smaller scales where the sinks lie, *with negligible energy return to the driven region*, (2) spectral (homogeneous) transfer dominates spatial transfer, so that all scales are equally space-filling, and (3) turbulent thermal and particle fluxes result from a random walk process with a diffusivity given by a mixing length squared times an eddy turnover rate: there must be up- and down-gradient walking, *quasi-Gaussian*, i. e. *random*, which partially cancel to give a net down-gradient flux. The computations, by contrast, show that the net source and sink regions of k_y-space result from partial cancellations, while all Γ's peak at mid-k_y; but the sources, peaking at $x = 0$, and sinks, peaking at $|x| \sim \Delta_D$, are spatially better separated. Assumptions (1) and (2) are therefore reversed, with shear-induced coupling at all scales wiping out simple balances. Assumption (3) fails, since the flux contributions are all coherent flows which result from the self-organisation. Indeed, in the nominal case the thermal flux is almost entirely down-gradient. Finally, if the turbulence is diffusive, then a (stable) $\mathbf{E} \times \mathbf{B}$ shear flow placed across it should suppress it by increasing the decorrelation rates.[4] This is *not* observed: shear flows up to $\partial V/\partial x = 0.3C_s/L_n$ had no effect, and one of $1.0c_s/L_n$ actually drove an instability (not Kelvin-Helmholz, but a "shear-flow induced" drift wave). One can therefore say with great confidence, that fluid electron turbulence is definitively non-diffusive at its most fundamental basis, and that *all* heretofore existing models of turbulence–linear or nonlinear mixing length, weak turbulence, strong turbulence closure models–as well as quasilinear models (which need linear instability) fail to have relevance to it.

Toroidal coupling and mode overlap

Effects of neigboring rational surfaces are judged through the mode overlap criterion. Each mode (m, n) is linearly coupled to modes $(m \pm 1, n)$, so these neighbors act as a competing localisation mechanism.[5] Overlap occurs if $k_y \Delta_{(k_y)} > 1/\hat{s}$, where $\hat{s} = rq'/q$ is the tokamak shear parameter. The single-surface simulations do not consider dynamically the effects of overlap, but the criterion can be used to judge whether it is important in the multi-surface situation. The results indicate that (1) low-k_y modes do not (2) mid-k_y modes marginally (3) high-k_y strongly overlap. Implications for the multi-surface situation are, respectively, (1) the self-organised structure in the long wavelengths should survive, (2) the energy-tapping modes are able to restore the temperature and density profiles for their neighbors, and (3) the small-scale side of the

net sink should be sharply reduced. Therefore, not only should turbulence of this character be present in the real system, it should be even stronger than the single-surface results suggest.

Pinch dynamics

In the 2D slab, increasingly dominant temperature gradient (high-η_e) exacerbates Γ_k to such an extent that a nonlinear stability boundary is introduced. Because of toroidal overlap (above) this should not be expected to carry over into the multi surface situation. (Nearly 50% of all dissipation, which depends on $k_\parallel$, *i. e.*, mode-width, occurs at high-k_y modes with widths much larger than overlap values.)

What was most interesting is that extreme values of η_e yielded pinch dynamics. Two gradients drive the turbulence. When they are equal, both temperature and density fluxes are positive. However, when one is weak (*e. g.*, density), its associated fluctuation finds a more favourable role in acting to cancel out much of the resistive dissipation, which is proportional to the square of $\nabla_\parallel(\tilde{n}+\tilde{T}-\tilde{\phi})$ in normalised units. So if the density gradient is weak, a down-gradient temperature flux (for driving) is compensated by an *up-gradient density (particle) flux*, to make Γ_c smaller. One can propose that a gas-puffed tokamak plasma might self-adjust its density gradient interior to the particle source to yield zero total flux. That is, the density profile would not be maintained by outward diffusion and inward flow, but by cancelling up- and down-gradient flows. Since the positions of those flows is observed in the simulations to be phase coherent, yet another piece of evidence for non-diffusive transport emerges. And nothing more exotic than sheared-slab fluid electron dynamics is needed to explain the particle pinch.

Conclusion

These results reproduce a large number of known *processes*: amplitude ordering $e\tilde{\phi}/T > \tilde{n}/n > \tilde{T}/T$, bidirectional net spectral transfer, thermal flux larger than density flux (except in particle source regions), and fluctuation activity mostly well to the low-k_y side of ρ_s.[2] In addition, this model has at least for some cases reproduced up-gradient pinch dynamics. Electron fluid turbulence is so universal as to expect it to stand as a foundation for turbulent transport in tokamaks: other mechanisms may be present but should be merely additive. Yet this physics requires no instabilities, and is of an entirely non-diffusive character. If these results are at all relevant, then anomalous transport in tokamaks is nothing like any heretofore existing models of it.

References

1. B. D. Scott, *J. Comput. Phys.* **78**, 114 (1988).
2. B. D. Scott, *Phys. Rev. Lett.* **65**, 3289 (1990).
3. B. D. Scott, H. Biglari, P. W. Terry, and P. H. Diamond, *Phys. Fluids B* **3**, 51 (1991).
4. H. Biglari, P. H. Diamond, and P. W. Terry, *Phys. Fluids B* **2**, 1 (1990).
5. L. Chen and C. Z. Cheng, *Phys. Fluids* **23**, 2242 (1980).

THRESHOLD OF ION TURBULENCE IN TOKAMAKS

X.Garbet, L.Laurent, F.Mourgues-Millot, J.P. Roubin, A.Samain, X.L. Zou, J. Chinardet (1)

Association Euratom CEA DRFC/ SPPF
(1) CISI Ingéniérie
CEN Cadarache 13108 St Paul lez Durance France

I) Introduction:

Models of ion mode instability relevant for toroidal geometry were first discussed within the fluid approximation [1] and then using various expansions of the full kinetic response [2,3,4]. More recently, numerical codes based on a full kinetic response have been built [5,6]. According to these models ionic modes are found to be unstable when a critical temperature gradient is reached even in the flat density regime [4,6]. Nevertheless it seems that this threshold is lower than observed in experiments [7,8]. In this paper a numerical investigation of the ion mode stability is proposed. In section II the numerical model is briefly presented and the results are discussed. In contrast of [6], the Landau resonance is found to have a strong stabilizing effect and the most dangerous mode appears to be the trapped ion mode occuring at a threshold compatible with experiments. The properties of this mode are described in section III.

II) Stability threshold

The ion mode stability has been studied using the TORRID code [9]. It computes the eigenfunction U (perturbed potential) within the ballooning non collisional approximation using the exact trajectories. The dispersion relation can be symbolized as:

$$\left\langle \frac{\omega-\omega^*}{\omega-n\omega_g} J_0^2(k_\perp\delta_b)J_0^2(k_{//}/\lambda)U\right\rangle_{trap.} + \left\langle \frac{\omega-\omega^*}{\omega-\omega_d-k_{//}v_{//}} J_0^2(k_\perp\rho)\,U\right\rangle_{circ.} - (1+\frac{1}{\tau})\,U = 0 \quad (1)$$

The brackets are averages in the velocity space respectively in the trapped (trap.) and circulating (circ.) domains. The frequencies ω and ω^* are the mode and ion diamagnetic frequencies, the operators $n\omega_g$, ω_d and $k_{//}$ account for the banana precession resonance, interchange resonance and Landau resonance. The J_0 operators symbolize trajectory averaging respectively on banana width δ_b, bounce motion (extension λ) , Larmor radius ρ. τ is the the ratio of electron to ion temperature. The results are summarized in figure 1. It represents the marginal curve in the plane L_N/R , L_T/R (density and temperature scale lengthes divided by major radius) which links modes obtained for given n,δ (defined in eq.5) and various real frequencies (The numbers written in the small rectangles are $\omega/n\omega_{gth}$ where ω_{gth} is the precession frequency of thermal deeply trapped ions). The plasma parameters (typical JET eqilibrium) are given in the figure caption. The marginal curve can be divided into three zones:

starting from this region going to $\eta_i = \infty$, appearing back at $\eta_i = -\infty$ and ending on the $\eta_i<0$ marginal branch at zero growth rate.

III) Trapped ion modes

In section II it has been shown that above a critical temperature gradient trapped ion modes are found. Numerically it appears that these mode are large scale modes and hence they may affect dramatically the transport if they can grow to the amplitude given by the mixing length rule. To check analytically their properties it is necessary to write explicitely the average in equation (3). The mode is expressed as a function of a generalised minor radius r and θ (ϕ) which are the poloidal (toroidal) angle in the ballooning form:

$$U(r,\theta,\phi) = \sum_m U(r-r_{mn})\, e^{i(m(\theta-\delta)+n\phi-\omega t)} \qquad (5)$$

The radius of the resonant surface q=m/n is r_{mn} and δ is a constant. For large scale modes finite banana effects can be neglected. The trapped particles distribution is expressed as a function of particle energy E and bounce angle θ_o. The plasma dispersion relation writes:

$$0= (1+\frac{1}{\tau})U(x) - \sqrt{\frac{8r}{\pi R}} \int_0^{\theta_m} \frac{\theta_o d\theta_o}{2} \int \frac{dE}{T_i} \sqrt{\frac{E}{T_i}}\, e^{-\frac{E}{T_i}} \frac{\omega-\omega^*(E)}{\omega-n\omega_{gthi}\frac{E}{T_i}} J_o(\frac{\theta_o x}{d}) \int \frac{dx'}{|d|} U(x') J_o(\frac{\theta_o x'}{d}) \qquad (6)$$

The real part of (6) cancels only if $U(x) \approx J_o(x/d)$. The new scale length is the distance between two neighbouring resonant surfaces: $d=1/k_\theta s$ where s is the shear parameter and k_θ the poloidal wavenumber. This scale length is compatible with the assumptions about negligible banana width effects if $k_\theta \rho_{thi} < \sqrt{2r/R}\ 1/qs$ In conclusion, at the threshold large scale modes may appear of which radial extension is only limited by interference effects between adjacent resonant surfaces. These modes exihibit another interesting property: The radial group velocity [11] is of order $\omega_g \delta_b^2/d$, i.e. nearly zero when $d >> \delta_b$. This vanishing group velocity leads to an indetermination on the radial profile of the mode.

IV) Conclusion

The stability of ion modes has been numerically investigated. The main conclusions are:

- The standard modes in litterature (fluid, slab) are found but they do not play a role in determining the plasma stability for relevant tokamak parameters.
- The circulating particle response is damped by Landau resonance and play no role for marginal mode except in plasmas with hollow density profiles.
- The threshold of temperature gradients (twice higher as usually quoted) is determined by stability of trapped ion modes.
- These modes exhibit such large radial scales that they probably clamp the profile at the threshold unless they saturate at low level by non linear effects or velocity shear.

→ Open circles in the low L_T/R zone are marginal modes with $\omega >> \omega_d$ so that the interchange resonance can be neglected. They are slablike modes energized by Landau damping. These modes can be investigated using the following plasma response:

$$- < \frac{\omega-\omega^*}{\omega-k_{//}v_{//}} J_o^2(k_\perp\rho)U >_{circ.} + (1+\frac{1}{\tau})U = 0 \qquad (2)$$

→ The marginal modes at the stability boundary in fig.1 for $\eta_i = L_N/L_T > 0$ are due to trapped ions. They occur at a threshold of $\eta_i \simeq 2/3$, or $L_T/R \simeq 0.15$ in the flat density limit. These modes can be described using the trapped particle response of (1) which is:

$$<- \frac{\omega-\omega^*_{Ti}(1/\eta_i-3/2+E/T)}{\omega-n\omega_{gth}E/T} J_o^2(k_\perp\delta_b)J_o^2(k_{//}\lambda)U >_{trap.} + (1+\frac{1}{\tau})U = 0 \qquad (3)$$

The energy (E) dependence of diamagnetic velocity and precession frequency (approximatively) have been indicated. The imaginary part of the plasma response vanishes only if $\omega/n\omega_{gth} \simeq 3/2 - 1/\eta_i > 0$. The values of $\omega/n\omega_{gth}$ indicated in figure (1) are consistent with that condition along the marginal boundary for $\eta_i > 0$, confirming that this boundary correspond to trapped ions.

→ The marginal branch at $\eta_i < 0$ (hollow density profiles) contains also trapped ion modes at large $|\eta_i|$. However as $|\eta_i|$ decreases the frequency increases and the circulating particle contribution through interchange resonance has to be considered.

A numerical experiment has been done by switching off the trapped particle contribution. This allows to look for marginal "resonant interchange" modes [3,4,6]. Their dispersion relation corresponds to the following approximation of (1) :

$$- < \frac{\omega-\omega^*}{\omega-\omega_d} \sum_{p=0}^{2} \left(\frac{k_{//}v_{//}}{\omega-\omega_d}\right)^p J_o^2(k_\perp\rho)U > + (1+\frac{1}{\tau})U = 0 \qquad (4)$$

It is found that ion Landau damping has a strong stabilizing effect as already suggested by Hirose [10]. Such modes are found marginally unstable only around $L_T/R < 0.06$ in the flat density limit (instead of ≈0.3 as previously quoted [4,6]). The first modes appearing when the temperature gradient steepens are trapped ion modes which set the critical temperature gradient for a possible anomalous ion transport at $L_T/R \simeq 0.15$ for a typical JET or TORE SUPRA plasma.

Non marginal modes have also been investigated. In the low L_T/R, high η_i region growing modes which localized eigenfunction are found which can be described by the fluid theory [1,2] i.e. an expansion of eq.(1) in ω_g/ω and $k_{//}v_{//}/\omega$. When the growth rate is decreased the existence point of the eigenfunction in the L_T/R, L_N/R space describes a curve

References

[1] W.Horton,Duk-In-Choi,W.M.Tang, Phys. Fluids 14,1077, (1981)

[2] P.N.Guzdar, L.Chen, W.M.Tang and P.H. Rutherford, Phys. Fluids 26,673, (1983)

[3] P.Terry,W.Anderson,W.Horton Nuclear fusion Vol 22 N°4 (1982)

[4] H.Biglari,P.H. Diamond et M.N. Rosenbluth , Phys.fluids B1,109, (1989)

[5] W.M. Tang, G. Rewoldt and Liu Chen , Phys.fluids 29, 3715,(1986)

[6] F. Romanelli Phys. Fluids B1,1018,(1989)

[7] F.Tibone, G.Corrigan and T.E. Stringer in controlled Fusion and Plasma heating (Proc. 17th European Conf. Amsterdam 1990, edited by G.Briffod, Adri Nijsen-Vis, F.C. Schüller)

[8] K.H. Burrell et al. 13th International Conference on Plasma physics and Controlled Nuclear Fusion Research, Washington 1990, IAEA-CN-53/A-2-3

[9] X.Garbet, L.Laurent, F.Mourgues, J.P. Roubin, A.Samain J.Comp. Phys. 87,249 (1990)

[10] A.Hirose Phys.Fluids B2 (5) 1990

[11] X. Garbet, L.Laurent, F.Mourgues, A.Samain, J.P. Roubin (Proc. 16th European Conference. Venice 1989, edited by S.Segre, H.Knœpfel, E.Sindoni Vol I p 299)

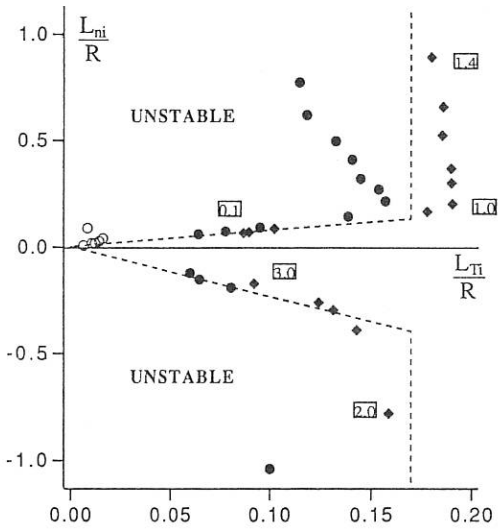

FIGURE 1

Marginal stability diagram for a typical JET equilibrium. The parameters at the considered magnetic surface are Te=Ti=1750 eV, B=2.75T at the low field side, safety factor =1.5, shear parameter = 0.5. The mode parameters are δ=0, n=30 (diamonds) and n=150 (dots).

RADIATIVE INSTABILITY IN A DIVERTED PLASMA

H. Capes, Ph. Ghendrih, A. Samain

Association EURATOM-CEA sur la Fusion Contrôlée
CEN Cadarache F-13108 Saint Paul Lez Durance, Cedex, France

I - INTRODUCTION

This paper deals with the thermal stability of a slab radiating plasma, using the relevant sheath boundary conditions and assuming the pressure perturbation to be negligible as in the radiative condensation instability [1]. We consider a plasma layer with a length L, where the flux lines are diverted from the last closed magnetic surface (LCMS) at $\rho = 1.$, to the wall at $\rho = 0.$, and where the temperature obeys the following equations :

$$\frac{3}{2} n \frac{\partial T}{\partial t} + \frac{1}{L} \frac{\partial}{\partial \rho} Q(\rho) = S(\rho, T) \quad ; \quad nT = cst \qquad (1)$$

where $S(\rho, T), = n n_z F_z(T)$ is the radiated power by impurities, n_z the impurity density, F_z the cooling rate function and n and T the plasma density and temperature. The heat flux is expressed as $Q(\rho) = (K(T)/L)(\partial T/\partial \rho)$ where K (T) is the Spitzer-Härm parallel conductivity ($K(T) \sim T^{5/2}$). The boundary conditions consist of a given heat flux at the plasma core $Q(\rho = 1) = Q_1$, and of the Bohm conditions at the wall ($Q(\rho = 0) = \gamma \Gamma_0 T_0$, $\Gamma_0 = M n_0 v_0$ where T_0, n_0 and v_0 are respectively the plasma temperature density and ion sound wave velocity at the wall ; γ and M are the sheath potential and the Mach number.

We are concerned by the stability on time scales longer than the ion sound wave propagation time, for which the pressure may be assumed to be constant along field lines. In that case the relevant equilibria needed for our stability analysis must be labelled by the edge pressure P_0.

2 - EQUILIBRIUM AND STABILITY

The steady state solutions of Eqs (1) have been previously investigated [2]. It has been shown that for vanishing T_0, no equilibria can be sustained if

$$Q_1^2 < 2 P_0 L \int_0^1 d\rho \, n_z Q(\rho) F_z(T)/T$$

Generally for a given value of P_0, three steady solutions can occur depending on the shape of K (T) and S (ρ, T). Bifurcations between equilibria corresponding to a transition

between a cold and a hot plasma can be triggered either by increasing Q_1 or by decreasing P_0. Such transitions are experimentally observed, as detached-attached edge plasma transitions.

Let us consider the stability of the previous equilibria when S (ρ, T) is an arbitrarily function of T and ρ. By linearizing Eq (1) around a steady solution, we get the following equation for $y = K(T)\,\delta T$:

$$L(y) + \frac{3}{2}\frac{L^2 P_0}{T K(T)}\,\omega\, y = 0 \qquad (2)$$

with $\partial/\partial t = -\omega$ and $L(y) = d^2y/d\rho^2 - \left(L^2 P_0^2/K(T)\right)(\partial S/\partial T)\, y$. The following boundary conditions must be used $(dy/d\rho)_{\rho=1} = 0$ and $(dy/d\rho)_{\rho=0} = \left(L\,\gamma\,\Gamma_0/2\,K_0\right) y_0$. As a consequence L (y) is an hermitian operator.

In order to calculate the sign of ω, we express the response of the plasma equilibrium to an external perturbation [3]. Here we investigate the plasma response to a perturbation $d\,Q_1$. We get the equation :

$$L(z) = 0 \qquad (3)$$

for $z = K(\partial T(\rho, Q_1)/\partial Q_1)$, with $(dz/d\rho)_{\rho=1} = L^{-1}$ and $(dz/d\rho)_{\rho=0} = \left(\gamma L\,\Gamma_0/2\,K_0\right) z_0$.

Next combining Eqs (2, 3) we get a relation for ω :

$$\omega = \left[y\frac{dz}{d\rho} - z\frac{dy}{d\rho}\right] \Big/ \frac{3}{2} L^2 P_0 \qquad \int_0^{\rho} \frac{1}{T K}\, y\, z\, d\rho' \qquad (4)$$

Applying (4) for $\rho = \text{Min}(1, \rho_1, \rho_2)$, where ρ_1 and ρ_2 are the smallest zeros for y and z respectively, so that y and z have a given sign in the interval $(0, \rho)$, it can be demonstrated that a necessary and sufficient condition of stability is given by $z > 0$, whatever ρ. In the case where $z < 0$, all eigenvalues are unstable. When z admits zeros, the modes with the largest internodal distances (smallest ω) are unstable.

3 - STABILITY ANALYSIS

In the case where the impurity density does not depend explicitly on space, z can be expressed analytically in term of z_0 by using the first quadrature of Eq (1) at steady state. It can be shown that the stability (or instability) is ensured when dT_0/dQ_1 (i.e. the slope of the bifurcation diagram $T_0(Q_1)$) is positive (or negative).

The situation is different when n_z depends explicitly on space. As we shall see in the next section, the previous condition $(dT_0/dQ_1 > 0)$ is still necessary, but not sufficient to ensure the stability. To go further it is necessary to compute $z(\rho)$. Let $f(\rho) = z(\rho)/z_0$ with

the boundary conditions f ($\rho = 0$) = 1 and $(df/d\rho)_{\rho=0} = \gamma\ L\ \Gamma_0 / 2\ K_0$. The relation $(df/d\rho)_{\rho=1} = 1/(L\ z_0)$ shows that at the bifurcation ($\omega = 0$, $z_0 = \infty$), the function f (ρ) is extremum at $\rho = 1$ and is identical to the eigenmode y (ρ)/y_0.

4 - EFFECT OF THE IMPURITY PROFILE ON THE THERMAL STABILITY

The following applications are devoted to the ergodic divertor of TORE SUPRA with L = 0.1 m, $n_0 = 10^{19}$ m^{-3}, $T_0 = 10_{ev}$. We consider an impurity mixture of C and 0 with a density n_z and $\frac{1}{L\ n_0} \int_0^L n_z\ d\rho = 10$ %. The cooling rate for the mixture is modelled by :

$$F_R\ (T_{ev}) = 0.4\ 10^{-31}\ [\exp - [(T_{ev} - 6.5)/2.5]^2 + \exp - [(T_{ev} - 18)/9]^2\ ]\ \text{Watt m}^3.$$

The calculation shows that for a smooth impurity profile ($n_z \sim (1 - \rho) + (1 - \rho)^2$), the function f ($\rho$) exhibits at most one extremum. Typical f (ρ) are plotted on Fig. 1 for several equilibria shown on Fig. 2. In this case, the stability criterium does not differ from our previous result [4], where n_z is a function of T only : the stability or instability is given by the sign of $(df/d\rho)_{\rho=1}$ (i.e. of dT_0/dQ_1).

When the impurity density is localized (i.e. $(d \log n_z/d\rho) > (d \log F_z/d\rho)$) in a region where $(\partial S/\partial T) < 0$, eigenmodes with two extrema are excited. This is illustrated on Fig. 3 and 4 with an impurity density strongly peaked at the edge ($n_z \sim (\rho + \rho^2) +$ exp - $[(\rho - 10^{-2})/5\ 10^{-3}]^2$) and next increasing slowly toward the LCMS. For $5 < T_0 < 9$, f (ρ) reaches negative values with $(df / d\rho)_{\rho=1} > 0$. Such equilibria are unstable in spite of the positive sign of dT_0 / dQ_1.

5 - CONCLUSION

A stability criterium for the radiative condensation instability has been demonstrated. If the impurity density has a strong spatial variation, unstable localized modes are excited. However when such modes appear, the largest scale modes have already been destabilized and the bifurcation fails to recover the stability. When the impurity density varies slowly in space, unstable large scale modes are excited, and the stability limit is given by the bifurcation points.

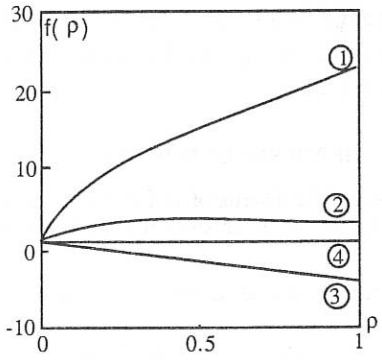

Fig. 1 - Profile of f (ρ) for different edge temperature T_0 (see Fig. 2)

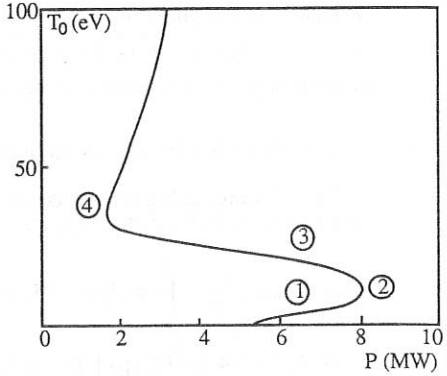

Fig. 2 - S shaped diagram for the steady solutions with $n_z \sim (1 - \rho) + (1 - \rho)^2$

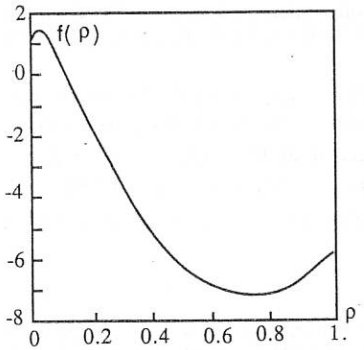

Fig. 3 - Profile of f (ρ) for $dT_0 / dP > 0$ (see Fig. 4)

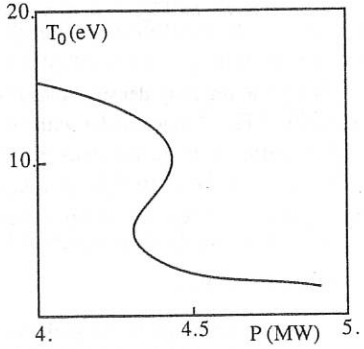

Fig. 4 - Steady solutions with a density profile peaked at the edge

REFERENCES

[1] J.F. Drake (1987) Phys. Fluids 30, 2429.

[2] H. Capes, Ph. Ghendrih, A. Samain, A. Grosman, J.P. Morera (1990) Plasma Phys. and Controlled Fusion, 2, 103.

[3] Y. Kolesnichenko, S. Rezniks, V. Yavorshii (1976) Nuclear Fusion 23, 633.

[4] H. Capes, Ph. Ghendrih, A. Samain, J.P. Morera (1990) Controlled Fusion and Plasma Physics (Proc. 17th European Conference, Amsterdam).

EFFECT OF PARAMAGNETISM ON THE GLOBAL STABILITY OF SCREW PINCHES

C. Wahlberg

Department of Technology, Uppsala University, Box 534, S-751 21 Uppsala, Sweden

Abstract. An analytical expression for the eigenvalue of the global m=1 kink mode in a screw pinch with arbitrary profiles of current density and axial magnetic field is derived in a long wave length approximation of the incompressible, ideal MHD equations. It is shown that the major profile effects can be expressed in terms of the inductance (l_i) and the poloidal beta value (β_p) of the pinch. While the Kruskal-Shafranov (KS) stability condition q(a)>1, not depending on l_i and β_p, is recovered in the Tokamak regime $B_z >> B_\varphi$, another regime of global stability is found for $l_i << 1$ (hollow current distribution), $\beta_p << 1$ (strong paramagnetism) and $B_z(a) << B_\varphi(a)$ [low q(a)]. This result is consistent with recent experimental observations in the so-called ultra low q (ULQ) discharges.

Since the very beginning of fusion research a number of pinch experiments operating with the safety factor q(a) below unity [$q(r) \equiv rB_z(r)/RB_\varphi(r)$ in "straight" approximation and standard notations] and nevertheless being globally stable over a considerable number of Alfvén periods have been performed at various laboratories in the world (e.g. the "stabilized pinches", toroidal screw pinches, Extrap configuration, as well as other configurations described in Ref. [1]). In particular, the ULQ toroidal and linear discharges recently reported by Kamada et.al. and Brunsell et.al. [2] clearly indicate the existence of parameter regions of improved global stability not consistent with the KS condition. In the present work we examine the global m=1 stability of screw pinches with arbitrary equilibrium profiles and no initial assumption about the strength of the applied axial magnetic field. However, it will be assumed that the stability limit, at least for certain profiles, occurs at a relatively long wave length, thus justifying a wave number expansion approach to the problem. It will be shown that a stability region substantially extending the KS stability region is obtained for pinches exhibiting the characteristic signatures of ULQ plasmas, viz.: i) hollow current profile, ii) MHD relaxation activity sustaining a certain paramagnetism of the plasma, and iii) $B_z \lesssim B_\varphi$.

Consider a straight screw pinch plasma with equilibrium profiles $B_\varphi(r)$ and $B_z(r)$ and uniform mass density $\rho(r)=\rho_0$, $0\le r\le a$. Looking at plasma displacements of the form $\xi(r,t)=\xi(r)\exp[i(\omega+\varphi-kz)]$, the linearized, incompressible MHD equations can after a series of manipulations be reduced to a single, second order differential equation in ξ_r of the form $[a(r\xi_r)']' - b\xi_r = 0$, where a and b are functions of r, B_φ, B_z, k and ω^2 [3,4]. A long wave length solution to this equation can be obtained as follows: Assuming that the small k expansion of the eigenvalue ω^2 is given by $\omega^2=\omega^2{}_1\, k + \omega^2{}_2\, k^2 + \ldots$, and that the corresponding expansion of the radial plasma displacement can be written $\xi_r=\xi_r^{(0)} + \xi_r^{(2)} k^2 + \ldots$ where $\xi_r^{(0)}$ is a constant (i.e. a rigid, axisymmetric translation of the pinch), the following will be noticed: The O(1) and O(k) components of the equation vanish identically. Furthermore, the $O(k^2)$ component does not involve ω^2. Then, after some minor algebra, the $O(k^2)$ solution is obtained as

$$\frac{d\xi_r^{(2)}}{dr} = -\frac{\xi_r^{(0)}}{rB_\varphi^2}\left[r^2\left(B_\varphi^2 + B_z^2\right) + \int_0^r r B_\varphi^2\, dr - 2\int_0^r r B_z^2\, dr \right]. \qquad (1)$$

In the expression above B_φ and B_z have been normalized to $B_\varphi(a)$, while r and 1/k are normalized to the plasma radius a. Evaluated at r=1, the first integral is recognized as the (normalized) plasma inductance l_i. Similarly, by using the equilibrium pressure balance equation, the second integral is found to be given by $\beta_p - 1 - B_e^2$, where $B_e \equiv B_z(a)$ denotes the applied axial magnetic field. Then, solving the vacuum problem in the usual manner and applying the MHD boundary conditions (see Ref.[4] for the details), the following long wave length dispersion relation for the global m=1 mode is obtained:

$$\omega^2 = -2kB_e + k^2\left(\ln\frac{|k|}{2} + \gamma_E + 1 + 2B_e^2 - l_i - \beta_p \right), \qquad (2)$$

where $\gamma_E=0.577..$ is Eulers constant, and ω is given in units of the Alfvén frequency $\omega_A \equiv B_\varphi(a)/[a(\mu_0\rho_0)^{1/2}]$.

We now look at the stability limit implied by Eq.(2) at various combinations of B_e, l_i and β_p. In the limit $B_e \gg 1$ (Tokamak case) Eq.(2) simplifies to $\omega^2=-2kB_e(1 - kB_e)$ for l_i and β_p of order one or smaller, and we see that the KS stability condition q(a)>1 [with $k\to a/R$ and $B_e \to B_z(a)/B_\varphi(a)$] is recovered. In the regime $B_e \lesssim 1$, on the other hand, all quantities in Eq.(2) will be of importance for the stability. Since both the l_i

and β_p terms are destabilizing, the optimal profiles with respect to stability are obtained for $l_i<<1$ (i.e. skin-type or hollow current distribution) and $\beta_p<<1$ (i.e. strong paramagnetism). Furthermore, although the term containing B_e^2 is stabilizing, the first term of Eq.(2) is destabilizing (for $kB_e>0$), and it turns out that the most favourable situation occurs for $B_e=0$. The diagram below shows the marginal point $k=k_0$ ($k>k_0$ corresponds to stability) as a function of B_e at various β_p and for $l_i=0$. The solid curves show the exact result for a sharp boundary pinch, while the corresponding result obtained from Eq.(2) is shown for $\beta_p=0$ and $\beta_p=1$ by the dashed curves:

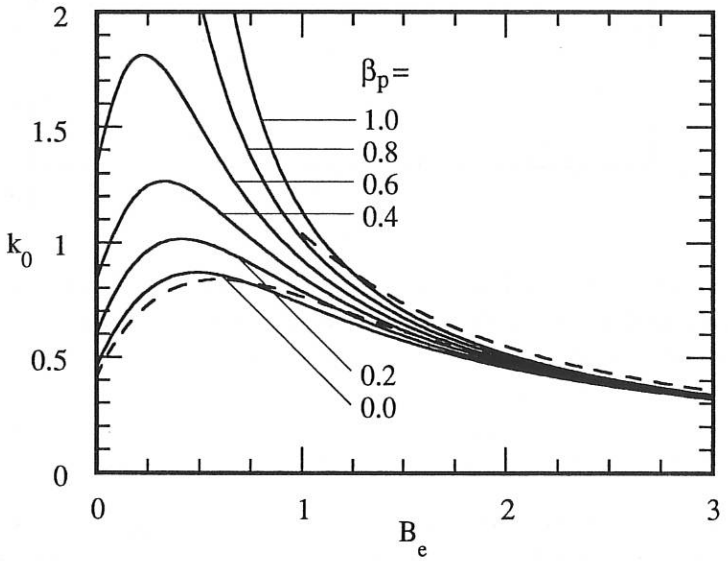

It is seen that all curves approach the q(a)=1 hyperbola ($k_0B_e=1$) for large B_e, whereas for $B_e\lesssim 1$ the stability limit is strongly dependent on β_p. For not too large values of β_p, say $\beta_p\lesssim 0.5$, a region of improved stability is obtained for $B_e\lesssim 0.5$, corresponding to values of q(a) less than 0.5.

In order to study the current profile effect we take a current distribution of the form $j(r)=j_0(1-r^2)^\nu$. With this model hollow ($-1<\nu<0$), flat ($\nu\approx 0$) as well as peaked ($\nu>>1$) current profiles can be simulated. The next figure shows the marginal point k_0 as a function of ν ($-1\leq\nu\leq 3$ corresponds to $0\leq l_i\lesssim 0.72$) at various β_p, and for $B_e=0$:

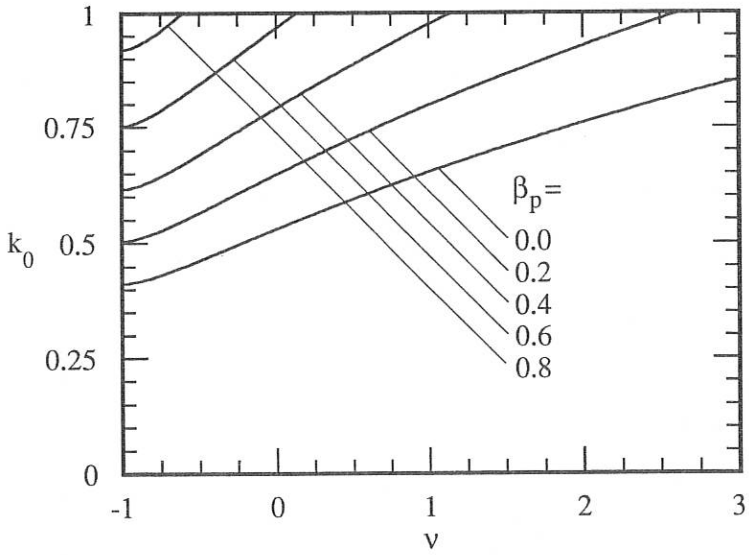

Thus a deterioration of the stability occurs when going from the skin current case to strongly peaked profiles, but the effect is moderate up to relatively flat profiles, provided β_p is not too large.

References

1. Evans, D. E. (Ed.) *Pulsed High Beta Plasmas*, Pergamon, Oxford (1976). Brunelli, B., Leotta, G. G. (Eds.) *Unconventional Approaches to Fusion*, Plenum, New York (1982). Lehnert, B., Fusion Technol. **16** (1989) 7.

2. Kamada, Y.,et.al., Nucl. Fusion **29** (1989) 713. Brunsell, P., et.al., Proc. 17th Eur. Fus. Conf., Amsterdam, 1990, Vol 14 B, Part II, 573, 610.

3. Freidberg, J. P., Phys. Fluids **13** (1970) 1812.

4. Wahlberg, C., Nucl. Fusion (1991), in press. Nycander, J., Wahlberg, C., Nucl. Fusion **24** (1984) 1357.

POSSIBLE NBI-DRIVEN INSTABILITY OF GLOBAL HIGH-FREQUENCY ALFVEN AND FAST MAGNETOSONIC EIGENMODES IN ITER.

Yegorenkov V.D.*), Polevoy A.R.**), Stepanov K.N.*), Sharapov S.E.**)

*) - Kharkov Institute of Physics & Technology, Kharkov, USSR
**) - I.V.Kurchatov Institute of Atomic Energy, Moscow, USSR

In ITER tokamak design it is suggested to sustain the steady current $I \cong 10 - 20$ MA by tangential injection of high energy $E_b \cong 0.7 - 3$ MeV deuterium atoms [1]. The longitudinal velocities of ions formed from the beam exceed the Alfven velocity $C_A \cong (0.3 - 0.6)\ 10^9$ cm/s for typical ITER parameters. The superAlfvenic injection may be considered to be dangerous because of possible beam-type instabilities of Alfven (A) [2-5] and fast magnetosonic (FMS) [3] waves causing anomalous slowing-down of beam ions.

Following [3], in the hollow cylinder model (Fig.1) this paper considers global A- and FMS-modes with frequency $\omega \leq \omega_{Bi}$ localized inside the plasma column in the region limited by two reflection points R_1 and R_2 ($R_1 \leq R \leq R_2$), that are due to radial nonuniformities of the equilibrium density and the magnetic field. These points satisfy the conditions:

$$k_R(R_1) = k_R(R_2) = 0;\ k_R(R) = \left(k_\perp^2(R) - k_z^2 \right)^{1/2} = k_\perp(R),$$

k_z is the wavenumber along z-axis (see Fig.1) (we suppose $k_z=0$ because the instability has the lowest threshold in this case). The quantization conditions are to be fulfilled:

$$\int_{R_1}^{R_2} k_R(R)\,dR = \pi(m+1/2),\ Rk_\parallel = n,$$

where m and n are radial and toroidal numbers.

As was noted earlier [3-5], for ITER parameters the excitation conditions for global modes are very sensitive to density, temperature and beam current profiles and to the beam distribution function form.

In contrast to [3] where the model fast ions distribution function has been used, here this function was computed using a fully linearized ($n_b << n_e$) 2D Fokker - Planck code at each plasma radius. To calculate fast ions' source distribution in ITER geometry, selfconsistent plasma equilibrium, density and temperature profiles the transport code ASTRA - 2 NB [4] has been employed.

The Table gives the ITER operations regimes that are most dangerous for excitation of Global A- and FMS-modes (D^0 beam injection into D^+ plasma). Here P_b is the NBI power, γ_b is the beam ion contribution to the growth rate under the anomalous Doppler (AD) or Cherenkov (Ch) conditions, γ_e is the electron Cherenkov damping rate and γ_i is the bulk ion cyclotron damping rate (normal Doppler effect)

P_b MW	E_b MeV	$n_e(0)$ 10^{20} m^{-3}	$T_e(0)$ keV	Excitation	Wave	n	m	$\frac{\omega}{\omega_{Bi}}$	$\frac{\gamma_b}{\gamma_e + \gamma_i}$
200	3	2.5	17	AD	A	185	3	0.36	0.42
110	1.3	0.94	34	Ch	A	103	0	0.33	0.45
100	3	1.2	34	Ch	FMS	63	4	0.34	1.17
100	3	1.2	34	Ch	FMS	255	0	1.50	0.52

At $E_b \cong 1.0\text{-}1.5$ MeV, $T_e \cong 20$ keV, $n(0) \cong 10^{20}$ m^{-3} cyclotron (AD) excitation is impossible because of strong bulk ion

cyclotron and electron Cherenkov absorbtion, $\gamma_b << \gamma_e \leq \gamma_i$. The γ_b value for AD-instability becomes order of $\gamma_e \geq \gamma_i$ only at larger E_b, P_b and n_e values (see the first line of the Table). But for the values considered this instability is absent ($\gamma_b < \gamma_e + \gamma_i$). The second line of the Table shows the role of Cherenkov excitation of small $k_\perp$ A-waves in the base ITER operation regime. This Ch- instability can be excited by beam ions with $V_\parallel < C_A$. It is also suppressed by bulk plasma absorbtion but the final answer may be acquired only after exact solution of the wave equation (without WKB-approximation).

Cherenkov excitation of FMS-modes for $E_b \cong 1$-2 MeV is suppressed ($\gamma_b << \gamma_e + \gamma_i$) but for higher energies $E_b \cong 3$ MeV the instability occurs for FMS-waves with $\omega < \omega_{Bi}$ (see the third line of the Table).

SUMMARY

1. ITER operation regimes correspond to the absence of the NB-driven beam-type anomalous Doppler and Cherenkov instabilities.

2. In regimes with higher E_b values or reduced tangential beam radius one may expect the instability to appear but the final answer may be obtained after 2D-consideration of global A- and FMS-modes taking into account the poloidal magnetic field.

REFERENCES

1.Gilleland J.R., Sokolov Yu.A., Tomabechi K., Toschi R. Nucl.Fusion, v.15, p.1191, (1989).

2.Leonov V.M., Mukhovatov V.S., Polevoy A.R., Tilinin G.N. Fizika Plasmy, v.15, p.1521, (1989).

3.Yegorenkov V.D., Stepanov K.N. XVII Europ. Conf. Contr. Fus. Plasma Phys., Venice, v.3, p.1207, (1989).

4.Polevoy A.R., Sharapov S.E. ITER Workshop, ITER-IL-Ph-6-9-S-22, (1989), ITER-IL-Ph-6-0-S-7, (1990).

5.Campbell R.B., Kerbel G.D. ITER Workshop, ITER-IL-Ph-6-9-U-6, (1989).

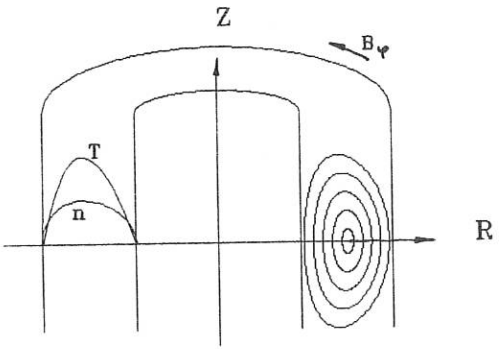

Fig.1. The model geometry and typical ITER density and temperature profiles.

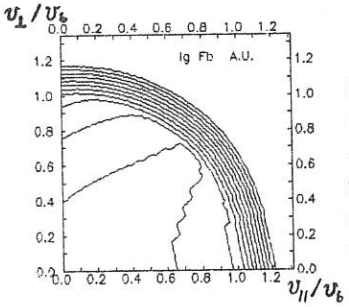

Fig.2. The fast ions' distribution function $F_b(v_\perp, v_\parallel, r)$, calculated by ASTRA-NB code for r = a/2, (a is a minor plasma radius). Parameters correspond to the third line in the Table.

MAGNETIC-DRIFT RESISTIVE BALLOONING MODE IN TOKAMAKS

N.V.Chudin, E.I.Yurchenko

I.V.Kurchatov Institute of Atomic Energy,Moscow, USSR.

1.Introduction. A threshold-free electrostatic resistive mode, strongly-localized along the plasma column radius, with a high growth rate, $\gamma_p \sim \alpha^{2/3} m^{2/3} \tau_s^{-1/3} \tau_\theta^{-2/3}$, was found in [1] in the MHD model. Here α is the relative pressure gradient, m is the poloidal mode number, τ_s is the skin time, τ_θ is the Alfven time with respect to the poloidal magnetic field. The turbulent transport coefficient provided by the resistive ballooning modes is estimated in [2],being of the order of $\chi_p \sim \frac{\alpha}{s} \nu (c/\omega_p)^2$, where s is the shear, ω_p is the plasma frequency, ν is the frequency of electron collisions.

An unexpected result was obtained in [3]. Within the framework of the kinetic theory in the studies on resistive ballooning modes an attention was paid to the importance of successive taking account of the particle drift in an inhomogeneous magnetic field. From analytical and numerical calculations the authors came to the conclusion that there were stable ion diamagnetic modes only, meanwhile the resistive ballooning modes were stabilized. In a given paper it is shown that the MHD branches of resistive modes exist, even when magnetic curvature drift is taken into account.

2. Model equation of resistive ballooning modes. In [3],proceeding from the collisionless kinetic equation for ions and from the collisional kinetic equation for electrons, an equation for perturbation of an electrostatic potential, has been derived. The conclusion is made on its basis that only damping ion diamagnetic modes take place in a tokamak, meanwhile the resistive ballooning modes are stabilized by the shear and toroidicity. In the MHD approximation using the ballooning representation this equation can be reduced to a second order differential equation:

$$\frac{d}{dy}\frac{(1+s^2y^2)}{[1+(1+s^2y^2)/\Gamma]}\frac{d\varphi}{dy} + \alpha(\cos y + sy \sin y) \times$$

$$\times [1-2\varepsilon_n(\cos y + sy \sin y)]\varphi - (\Gamma/N)^2(1+s^2y^2)\varphi = 0, \quad (1)$$

where $\Gamma = \gamma\tau_s/m^2$, $N = \tau_s/\tau_\theta/m^2$, $\varepsilon_n = L_n/R$, $L_n = -n/\nabla n$. Below it is shown that a magnetic-drift branch of resistive ballooning modes can be found from this equation.

3. Analytical study. In case of a resistive plasma ($\Gamma \ll 1+s^2y^2$), Eq.(1) is simplified, and it can be easily solved by the averaging procedure. At $\alpha \ll 1$ and $s \ll 1$, one obtains the expressions for finding the growth rate and the localization zone of eigenfunctions:

$$\Gamma \simeq (\alpha^2/2)/(\alpha\,\varepsilon_n + \Gamma^2/N^2) \quad (2)$$

$$\Delta y^2 \simeq (\alpha/s)^{4/3}/(\alpha\,\varepsilon_n + \Gamma^2/N^2)^{4/3} \quad (3)$$

From (2) one can see that the electrostatic mode with high growth rate $\Gamma \sim \alpha^{2/3} N^{2/3}$, strongly-localized in the real space due to inertia of ions, can be exist at very small $\varepsilon_n \leqslant \alpha^{1/3}/N^{2/3}$ only. At finite ε_n there is a magnetic-drift branch ballooning modes with small growth rate $\Gamma \sim \alpha/\varepsilon_n$, relatively weakly localized in a real space. The growth rate of this branch is proportional to the collision frequency, and the localization zone is related with a magnetic drift. The turbulent transport coefficient $\chi \simeq \gamma/k_\perp^2$, provided by the magnetic-drift branch is equal $\chi \simeq \chi_p(s\,\varepsilon_n)^{1/3}$.

4. Numerical study. Eq.(1) at $\varepsilon_n = 0$ was analyzed in [1], where the existence of two resistive branches (electromagnetic and electrostatic) was shown. A qualitative estimate of the finite ε_n effect on the electrostatic branch is given in Sec.3, where the magnetic-drift branch is found. For a quantitative analysis of both branches the eigenvalue problem is numerically solved for Eq.(1) which is suitably written in following form: $F''_{yy} - U(y)F = 0$, where $F = \varphi[\Gamma(1+s^2y^2)/(\Gamma+1+s^2y^2)]^{1/2}$.

The potential of this equation has a complicated oscillating form. A central well of the potential mainly determines the localization of the electromagnetic branch which, at high conduction, transits into an ideal ballooning mode. The behaviour of the electrostatic branch mainly

depends on the form of a non-central part of the potential.

The results of calculations are given in Figs.1-6. The electromagnetic growth rate dependence on the parameter ε_n, at $\alpha=1$, $N=10^3$ and at two values of of a shear, $s=0.5$ and $s=1$ is shown in Fig.1. At small values of $\varepsilon_n \leq 0.1$ corresponsding to relatively high density gradients the growth rate has a weak dependence on ε_n. The eigenfunction of the electromagnetic branch, localized in the central part of the potential, practically also does not depend on ε_n. For magnetic drift branch of oscilations the growth rate dependence on ε_n, at $\alpha=1$, $N=10^3$, is shown in Fig.2. The growth rate decays with increase in ε_n, according to an analitical estimate. The general view of eigenfunctions at $\varepsilon_n=0$ and $\varepsilon_n=0.1$ is given in Figs.3 and 4. One can see that the localization zone in the y-space is reduced with a rise in ε_n, that corresponds to a broadening of the perturbation localization zone in a real space. A stabilizing effect of the magnetic drift is related with an essential rearangment of the non-central part of the potential, that is shown in Fig.5 and 6, where one can see the potential behaviour at $\varepsilon_n=0$ at $\varepsilon_n=0.1$, respectively.

5.Conclusion. It is shown that two branches of ballooning modes can be developed in resistive tokamak plasma, taking the magnetic curvature drift into account. This drift effect on the electormagnetic branch development is not very essential due to its strong localization in the y-space. At the same time, a relatively fast and weakly localized electrostatic branch transits into a slow magnetic drift one, more localized in the y-space. In this case the turbulent transport coefficient provided by this branch turns out to be of an order of the known coefficient due to an electrostatic resistive ballooning mode.

References.

[1] Pogutse O.P.,Yurchenko E.I., Pis'ma JETP,31,479,1980.

[2] Pogutse O.P.,Yurchenko E.I., 10th Europ. Conf.Contr.Fus. Moscow, B-21,1981

[3] Hirose A.,Kroeker T.L.,Ishihara O.,Can.J.Phys.,66,1069, 1988.

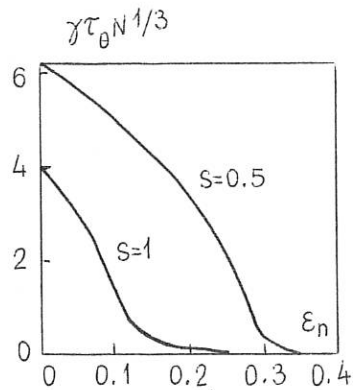

Fig. 1

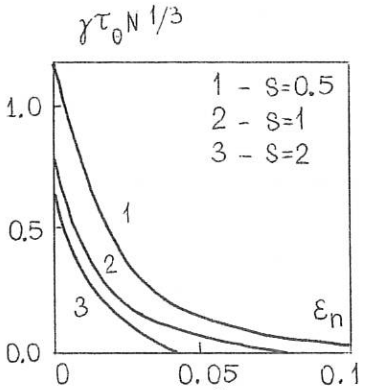

Fig. 2

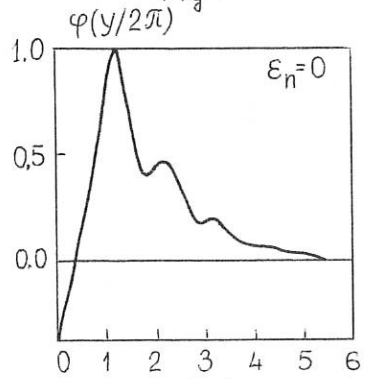

Fig. 3

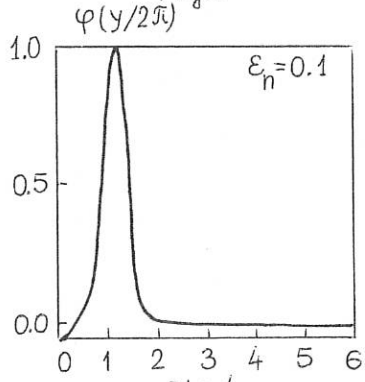

Fig. 4

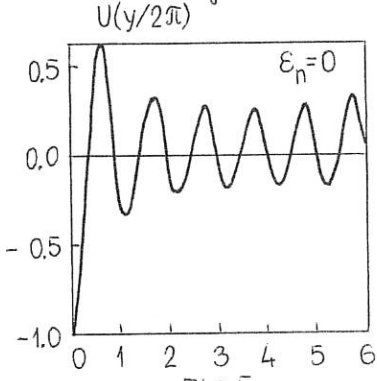

Fig. 5

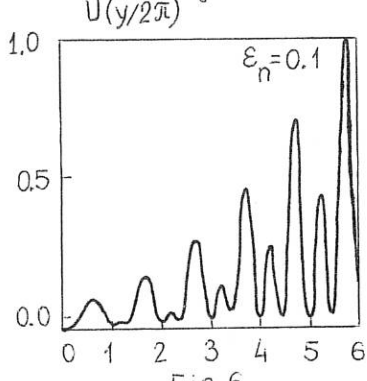

Fig. 6

EFFECT OF AXISYMMETRIC TOROIDAL ROTATION ON BALLOONING MODES IN THE OUTER PLASMA

Sudip Sen*

Dept. of Pure & Applied Physics, UMIST, PO BOX 88, Manchester M60 1QD, U.K.

M.S. Janaki, B. Dasgupta

Saha Institute of Nuclear Physics, AF/1 Bidhannagar, Calcutta 700064, India.

INTRODUCTION :

It is well known that ideal ballooning modes can limit the beta values attainable in a tokamak operation in the usual first stability parameter regime, but the existence of the theoretically predicted second stability regime could give the possibility of high beta operation. In deriving the beta limits, it is generally assumed that the underlying equilibrium state is static. In recent years there has been a growing interest in the behaviour of rotating plasma systems mainly owing to the fact that tokamaks exhibit macroscopic flows after being heated by neutral beams [1-6]. It is generally believed that axisymmetric toroidal rotation has a stabilising influence on ballooning modes on most flux surfaces except in the outer region [6].

While studying the effect of rigid toroidal rotation on ballooning instabilities in the outer plasma we noticed a zone of instability which essentially sets a limit on the second stability region in the rotating plasma. This instable zone however is completely absent in the inner region of the flux surfaces where $r < L_p$ (L_p is the pressure scale length) [7].

LINEAR STABILITY OF EQUILIBRIUM WITH FLOWS :

In a pioneering paper on MHD stability in

* also at Culham Laboratory, U.K.

presence of equilibrium flows, Frieman and Rotenberg [8] showed that the linearised motion of Lagrangian displacement 'ξ 'is described in Eulerian coordinates by

$$\rho_o \frac{\partial^2 \vec{\xi}}{\partial t^2} + 2\rho \vec{V}_o . \nabla . \frac{\partial \vec{\xi}}{\partial t} - F(\vec{\xi}) = 0 \qquad (1)$$

where $F(\vec{\xi}) = \nabla(\gamma p_o . \nabla \vec{\xi} + \vec{\xi} . \nabla p_o - \vec{B}_o . Q) + \vec{B}_o . \nabla Q + Q . \nabla \vec{B}_o$
$+ \nabla . (\rho_o \vec{\xi} \vec{V}_o . \nabla \vec{V}_o - \rho_o \vec{V}_o \vec{V}_o . \nabla \vec{\xi})$

$Q = \nabla \times (\xi \times B_o)$ is the perturbed magnetic field, V_o is the rotational velocity and all other symbols have their usual meaning. For normal mode solutions of the form $\vec{\xi}(r,t) = \vec{\xi}(r)\exp(-i\omega t)$, Eqn(1) becomes

$$-\omega^2 \rho_o \vec{\xi} + 2i\omega_o \rho_o \vec{V}_o . \nabla \vec{\xi} - F(\vec{\xi}) = 0$$

A remarkable feature of Eqn(1) is that the operators $i\rho_o \vec{V}_o . \nabla$ and F are Hermitian, but the total operator is generally non-Hermitian. Thus, unlike the static case, it is not possible to establish a necessary and suffcient condition for stability in a manner analogous to that used in the ideal MHD theories on the energy principle. To cope with the difficulty we follow the prescription of Sen [6] and obtain the ballooning equation for marginal stability in the shifted elliptical model as

$$\frac{d}{d\eta}\left[1+(s\eta-\alpha\sin\eta-\frac{\alpha}{2}\delta\sin 2\eta)^2\right]\frac{dN}{d\eta}$$
$$+ \alpha(1+\delta\cos\eta)\left[\cos\eta + \sin\eta(s\eta-\alpha\sin\eta) - \alpha\,\delta\,\sin 2\eta/2\right]N = 0 \qquad (2)$$

where $\delta = V_o^2(r-L_p) / C_s^2 R_o$, C_s is the sound velocity , L_p is the pressure scale length, $s = (r/q)(dq/dr)$ is the shear parameter, q is the safety factor, $\alpha =$

$-(2R_o q^2/B_o^2)(dp/dr)$, $\eta = s\theta$ is the ballooning coordinate and N is the normalised potential.

DISCUSSION & CONCLUSION :

We have solved eqn(4) numerically to determine the marginal stablity boundaries in the (s-α) parameter space for different positive values of δ. Fig. (1) & (2) show the results for δ=0.05 & 0.2, in each case compared with the static case δ=0. The static result (δ = 0) shows the first and second stability regimes separated by a zone of instability extending all the way to the origin. For δ > 0 the first stability region shrinks and a new zone of instability is found within the second stability region.

Hence the effect of rigid toroidal rotation at the outer region of the flux surfaces is not only to reduce the stability region but it also introduces a new zone of instability. This new zone of instability may be rsponsible for enhanced particle and energy transport at the plasma edge. Recent experiments carried out in ASDEX also confirm that the turbulence in the scrape-off layer is of a flute like nature [9]. The new findings however call for further extensive investigations.

ACKNOWLEDGEMENT:

Useful discussions with Prof. S. K. Mazumdar are gratefully acknowledged. One of us (S.S) is also grateful to Prof. M.G. Rusbridge and Dr. J. Hugill for many stimulating discussions and Culham Laboratory for financial support.

REFERENCES:

[1] A.B. Hassam and R.M. Kulsrud, Phys. of Fluids, 21(1978)2271
[2] T.A.K. Hellsten et al, Phys. of Fluids 22(1979)743
[3] E. Hameri et al, Phys. of Fluids 22(1979)1700
[4] E. Hameri, Math. Phys. 22(1981)2080
[5] A. Bondeson et al, Phys. of Fluids 30(1987)2167
[6] A. Sen et al., Nuc. Fusion 29(1989) 1161
[7] Sudip Sen et al., To be published in Phys. Lett.A
[8] E. Freiman et al., Rev. Mod. Phys. 32(1960)898
[9] A.V. Nedospasov, Sov. J. Plasma Phys.15(1989)659

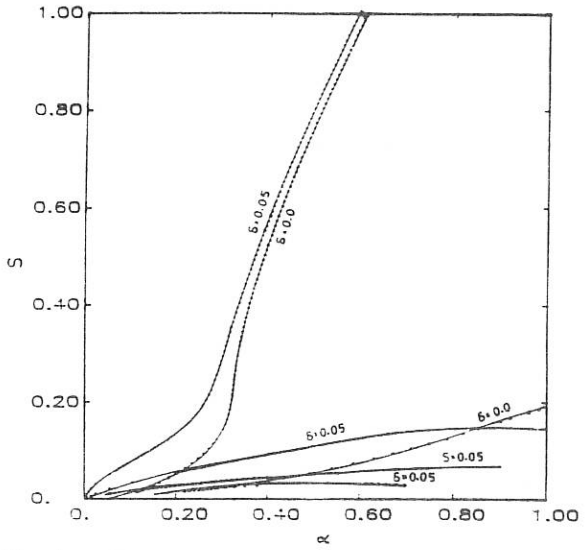

Fig 1. Marginal Stability boundaries with δ = 0.05 and δ = 0.0

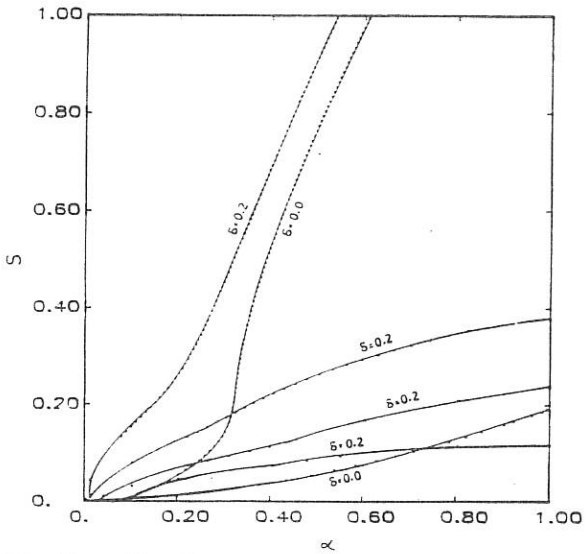

Fig 2. Marginal Stability boundaries with δ = 0.2 and δ = 0.0

TEMPERATURE ANISOTROPY EFFECT ON THE TOROIDAL ION TEMPERATURE GRADIENT MODE

J. Y. Kim, W. Horton, and D. -I. Choi*

The University of Texas at Austin, Austin, Texas 78712

S. Migliuolo and B. Coppi

Research Laboratory of Electronics
Massachusetts Institute of Technology, Cambridge, Massachusetts 02139

ABSTRACT

Using the local-electrostatic kinetic approach, we investigate the effects of the anisotropi -es in the ion temperature and the ion temperature gradient, and the effect of the increasing ion temperature on the toroidal ion temperature gradient driven mode. Comparisons are given between the new toroidal results and the previous slab results.

1 Introduction

In recent tokamak experiments, the use of powerful auxiliary heating schemes such as ion cyclotron heating(ICRF) and neutral beam heating (NBI) can generate a significant magnitude of anisotropy in the velocity distribution of the ions. Thus, it is important to consider the effect of anisotropy on the drift wave instabilities responsible for anomalous transport.

Recently, Migliuolo[1] has investigated the anisotropy effect in the ion temperature (specially due to a $T_\perp$ increase from ICRF) on the ion temperature gradient drift mode in the slab geometry, and found that the anisotropy in the direction of $T_\perp > T_\parallel$ gives an overall stabilizing effect. On the other hand, Mathey and Sen[2] have investigated, in a similar work, the effect of the anisotropy in the ion temperature gradient in the slab geometry, and showed that a finite gradient in the parallel temperature is necessary for the instability, while a gradient in the perpendicular temperature can either enhance or diminish the instability.

*Permanent address : Korea Advanced Institute of Science and Technology, P. O. Box 150, Cheongyangni, Seoul, Korea

In this work, we generalize these studies to the toroidal system, and furthermore investigate the effect of a parallel temperature increase ($T_\parallel > T_\perp$), which can be generated by the neutral beam injection (NBI) heating scheme.

2 Basic Equations

We consider a case when the equilibrium ion velocity distribution function is described by a bi-maxwellian. With a local electrostatic approximation, we obtain the following perturbed ion density from the linearized gyrokinetic equations [3]

$$\tilde{n_i} = -\frac{eN\tilde{\phi}}{T_{\perp i}}\{1+\alpha\Gamma_0(b_i) - \frac{T_{\perp i}}{T_{\parallel i}}\int \frac{(\omega-\omega_{*i}^T)J_0^2(k_\perp v_\perp/\omega_{ci})F_{Mi}(v_\perp,v_\parallel)d^3v}{\omega-\omega_D-k_\parallel v_\parallel}\} \quad (1)$$

where the temperature anisotropy term is $\alpha = T_{\perp i}/T_{\parallel i}-1; \omega_{*i}T = \omega_{*i}[1+\eta_\perp(v_\perp^2/2v_{T\perp}^2 - 1)+\eta_\parallel(v_\perp^2/2v_{T\perp}^2-1/2)]; \omega_D = \epsilon_n\omega_{*i}(v_\perp^2/2+v_\parallel^2)/v_{T\parallel}^2; \eta_{\perp,\parallel} = dlnT_{\perp,\parallel}/dlnN; \Gamma_0(b_i) = I_0(b_i)e^{-b_i}, b_i = k_\perp^2\rho_i^2 = (k_x^2+k_y^2)\rho_i^2; \omega_{*i} = -k_\perp cT_{\parallel i}/eBL_n; v_{T\parallel,\perp} = (T_{\parallel,\perp i}/m_i)^{1/2}, \rho_i^2 = T_{\perp i}/m_i\omega_{ci}^2$ with $\omega_{ci} = eB/m_ic_i; \epsilon_n = L_n/R$ with $L_n = -(dlnN/dr)^{-1}$.

Now, with the adiabatic response of the perturbed electron density $\tilde{n_e} = (eN/T_e)\tilde{\phi}$, the quasi-neutrality condition gives following dispersion relation in dimensionless form

$$1+\tau+\frac{\alpha}{1+\alpha}(\Gamma_0-1) = \int_{-\infty}^{\infty}\frac{dv_\parallel}{\sqrt{2\pi}}\int_0^\infty v_\perp dv_\perp$$

$$\times[\frac{\omega+\tau k_y(1+\eta_\perp(v_\perp^2/2-1)+\eta_\parallel(v_\parallel^2/2-1/2))]J_0(b_i^{1/2}v_\perp)e^{-v^2/2}}{\omega+\tau\epsilon_n k_y((1+\alpha)v_\perp^2/2+v_\parallel^2)-\tau^{1/2}k_\parallel v_\parallel} \quad (2)$$

where $\tau = T_{\parallel i}/T_e, b_i = \tau k_\perp^2(1+\alpha)$, and the wavenumbers $k_\perp$ and $k_\parallel$ have been normalized to $\rho_s = c_s/\omega_{ci}$ and L_n, respectively, and the frequencies ω and ω_{*i} normalized to L_n/c_s with $c_s = (T_e/m_i)^{1/2}$.

It is easy to see that in the slab geometry limit with $\epsilon_n = 0$, Eq.(2) reduces to

$$1+\tau+\frac{\alpha}{(1+\alpha)}(\Gamma_0-1)+\Gamma_0\{[1-\frac{\omega_{*i}}{\omega}(1+\eta_\perp b_i(\frac{I_1}{I_0}-1))]\xi Z(\xi)$$

$$-\frac{\omega_{*i}}{\omega}\eta_\parallel[\xi^2+(\xi^2-1/2)\xi Z(\xi)]\} = 0 \quad (3)$$

where $\omega_{*i} = -\tau k_y, \xi = \frac{\omega}{\sqrt{2\tau}|k_\parallel|}$ and Z is the plasma dispersion function. We find that Eq.(3) is the same dispersion relation as that used previous works[1,2]. From Eq.(3) we can see that the effect of anisotropy effect for the slab mode appears mainly through the finite ion Larmor radius parameter b_i with an additional adiabatic term $\alpha(\Gamma_0-1)/(1+\alpha)$. On the other hand, Eq.(2) for the toroidal mode shows that an additional anisotropy effect comes from the ratio of the toroidal curvature to grad-B drift frequencies.

3 Numerical Results and Discussions

First, we investigate the effect of the anisotropy in the ion temperature. We find that the increasing $T_\perp/T_\parallel$ gives small destabilizing effect on the long-wavelength modes, while giving a significant stabilizing effect on the short-wavelength modes for both of the two cases of slab and toroidal. As a result, the mode with the maximum growth rate shifts to the long-wavelength regime with the significant reduction of its magnitude. On the other hand, the effect of increasing $T_\parallel/T_\perp$ gives a small stabilizing effect (on the long-wavelength modes), or a destabilizing effect (on the short-wavelength modes) for the slab case, while for the toroidal case the effect gives a strong stabilization for the short-wavelength modes, mainly due to the anisotropy effect coming from the toroidal magnetic curvature term in the denominator of Eq.(3).

We also investigate the effect of temperature anisotropy on the marginal temperature gradient value η_c. For the slab case, we find that the increasing $T_\perp/T_\parallel$ shifts the curve of the marginal temperature gradient $\eta_c(k_y)$ to the long-wavelength regime with the increase of the minimum value of η_c in agreement with the result by Migliuolo[1]. The increase of the parallel temperature $T_\parallel$ gives a significant increase of η_c over all k_y, suggesting that the increase of $T_\parallel$ may be favorable for the stability of the η_i mode in the slab limit. On the other hand, for the toroidal case, the marginal stability value of the temperature gradient just shifts to the long-wavelength regime without the notable increase of the minimum value of η_c when $T_\perp/T_\parallel$ increases. The increase of the parallel temperature $T_\parallel$ also shows a similar feature except with a smaller shift of the curve. Thus, even though the growth rate for the short wavelength modes can be reduced significantly, in terms of η_c the temperature anisotropy is not so favorable for the stability of the toroidal mode.

For the effect of an another anisotropy, i.e., the anisotropy in the temperature gradient, we find that there is a remarkable difference between the two cases of slab and toroidal. We find that for the toroidal mode the perpendicular temperature gradient plays a same role as the parallel temperature gradient, and does not give a stabilizing effect, unlike the slab case.

Finally, we investigate the effect of an ion temperature increase relative to the fixed electron temperature, which occurs in the regime such as super shot. With the isotropic ion temperature, we find that even though there is some difference in the quantitative aspects, the $\tau(= T_i/T_e)$ variation gives an effect similar to that of the temperature anisotropy, in that, while the maximum growth rate is reduced by the increasing τ, the minimum value of η_c does not increase and, in fact, shifts to substantially longer wavelength side.

4 Conclusions

The effect of the ion temperature anisotropy gives an overall stabilizing effect in the slab case, but in the toroidal case, the minimum value of the marginal stability value of the temperature gradient η_c does not change appreciably ($\eta_c \approx 2/3$) by the effect,

even though the growth rate of the short-wavelength modes are reduced significantly. The effect of the anisotropy in the temperature gradient ($\eta_{\parallel} \neq \eta_{\perp}$) is also significantly different between the slab and toroidal modes. While the perpendicular temperature can give a significant stabilizing effect for the slab mode, for the toroidal mode it contributes to only the destabilization. Thus, we conclude that for the toroidal mode there is no significant reduction of the ion temperature gradient driven transport from temperature anisotropy.

Acknowledgements

This work is supported by the U. S. Department of Energy under the contact #DE-FG05-80ET-53088, and the Korean Science and Engineering Foundation (KOSEF) for the International Collaborative Research between KOSEF and NSF.

References

1. S. Migliuolo, Phys. Lett. A **29**, 373(1988).

2. O. Mathey and A. K. Sen, Phys. Rev. Lett. **62**, 268(1989).

3. T. M. Antonsen, Jr. and B. Lane, Phys. Fluids **23**, 1205(1980).

EFFECT OF LHCD ON TEARING MODE INSTABILITY

Z.M.SHENG*, N.XIANG, G.Y.YU

Institute of Plasma Physics, Academia Sinica (ASIPP)
Hefei, 230031 The People's Republic of China

Abstract Effect of LHCD on tearing mode instability is investigated through both kinetic and MHD approaches. In linear kinetic theory, the responce of the fast electrons driven by LHCD to tearing mode perpurbations results in reductions of both the growth rate and the width of the perturbative layer of tearing mode in collisional as well as semi-collisional regimes. From MHD theory and LHCD simulation in tokamak geometry, it is shown that LHCD leads to both modification of the current profile and outward shift of the rational surfaces and hence to variation of Δ' of tearing mode. Mostly LHCD plays a stabilizing role against tearing modes. However under some conditions considered in this paper, LHCD can stabilize tearing modes in higher-q(a) plasma while destabilize it in lower-q(a) case, which is in a qualitative agreement with some experimental observations. These studies indicate that the whole scenario of the effect of LHCD on tearing mode instability depends on the combined and/or competitive effects of the two aspects mensioned above.

1. INTRODUCTION

LHCD now is believed to be one of the most promising ways in carrying out the continuous operation of tokamak.[1] It has been studied that LH wave can not only be applied to drive current but also to tailor the current profile of plasma so as to actively control plasma performence, e.g. MHD perturbations, by properly setting both wave and plasma parameters.[2] Experiments showed that the MHD behavior of plasma in case of LHCD is different from those of purely ohmic discharge. Among them, it was reported on Petula-B[3] and HT-6M[4] that the amplitute of Mirnov scillations was significantly reduced in LHCD ramp case. It is interesting to note that on PLT[5] and WT-3[6] LHCD leads to suppression

---

*Present address: Shanghai Institute of Optics and Fine Machinary, Academia Sinica, Shanghai, The People's Republic of China.

of m=2 oscillations in higher-q_a case while it can excit m=2 disturbance in lower-q_a case.

In this paper the effect of LHCD on tearing mode instability is investigated in both kinetic and MHD approaches. The responce of the LH wave-driven fast electrons to the perturbations results in stabilization under some conditions, which will be studied in a frame of linear kinetic theory. From MHD theory and LHCD simulation in tokamak geometry it is expected that both the tailoring of the current profile and the shifting of the rational surfaces by LHCD will vary Δ' of tearing modes. We think that the whole scenario should be the combined and/or the competitive effects of these two aspects.

2. LINEAR KINETIC THEORY

By solving the electron's Fokker-Planck equation with inclusion of both quasilinear diffusion term and perturbative term, the dispersion in collisional regime is deduced to be[7]

$$\omega^4 (\omega - \omega^n_{*i}) \lambda_2^4 / \lambda_1 = i\Gamma_1 \tag{1}$$

where

$$\left.\begin{aligned}
&\Gamma_1 = \left[\Delta' a \Gamma(\tfrac{1}{4})/2\pi\Gamma(\tfrac{3}{4})\right]^4 (k_{\parallel}'^2 a^2)/\tau_S^3 \tau_A^2 \equiv \gamma_c^5, \quad \lambda_1 = \alpha_1(1 - \alpha_3 \omega_{*e}/\omega) + \alpha_4, \\
&\lambda_2 = \alpha_1(1 - \omega_{*e}/\omega - \alpha_2 \omega_{*T}/\omega) + \alpha_4(1 - \omega_{*T}/\omega - \omega_{*J}/\omega), \\
&\tau_S = 4\pi a^2/c^2\eta, \quad \tau_A = a/c_A, \quad \alpha_1 = .98\delta/\hat{\Delta}, \quad \alpha_2 = .8(1 - .56 i \mu_2^2/\mu_1)/\delta, \\
&\alpha_3 = -1.2(1 - .3 i \mu_1)/\delta, \quad \alpha_4 = .13 u_0^2 J_N \Big/ \left[1 + 1.5 u_0 D_0 - .25 i |u_0|^3 (\mu_1 - \mu_2 u_0)\right], \\
&\delta = 1 - .54 i \mu_1 + .45 i \mu_2^2/\mu_1, \quad \mu_1 = \omega/\nu_{ei}, \quad \mu_2 = k_{\parallel} v_{the}/\nu_{ei}, \\
&\hat{\Delta} = 1 - 2.97 i \mu_1 - 1.04 \mu_1^2 + 3.51 i \mu_2/\mu_1 + 1.73 \mu_2^2 - .43 \mu_2^4/\mu_1^2, \\
&u_0 = v/v_{the}, \quad J_N = J_{rf} u_0/e n_e v_{the} |u_0|, \quad \epsilon_J = .13 u_0^2 J_N/(1 + 1.5 u_0 D_0) \sim .18
\end{aligned}\right\} \tag{2}$$

the solution can be written as

$$\gamma = \gamma_c/(.98 + \epsilon_J)^{.6} \tag{3}$$

$$\Delta = \Delta_c/(.98 + \epsilon_J)^{.4}$$

In semi-collisional regime, the dispersion is obtained to be

$$\left\{Re\left[(\omega-\omega_{*i}^{n})\eta k_{Di}^{2}/4\pi i k_{\psi}^{2}\lambda_{1}\right]\right\}^{1/2}=ic^{2}\eta\Delta'/4\pi\lambda_{1}\omega \tag{4}$$

with $k_{Di}^{2}=2\omega_{pi}^{2}/v_{thi}^{2}$, η the resistivity of plasma. A stabilizing effect of LHCD on tearing mode instability is clearly shown. It is noted that Δ' in kinetic theory is assumed to be known and should reflect the modification of current profile by LHCD. This will be obtained from MHD calculation.

3. MHD CALCULATION AND LHCD SIMULATION IN TOKAMAK

The tearing mode equation applied is

$$\frac{\partial}{\partial r}r\frac{\partial}{\partial r}(r\tilde{B}_{r})-\left[m^{2}+\frac{r^{2}\partial j_{to}/\partial r}{B_{po}(1-n^{2}/m)}\right]\tilde{B}_{r}=0 \tag{5}$$

with

$$\Delta'=\left[\left[\frac{\partial\tilde{B}_{r}}{\partial r}\right]\right]_{r_{s}^{-}}^{r_{s}^{+}}/\tilde{B}_{r}(r_{s}) \tag{6}$$

where $j_{to}(r)$, $B_{po}(r)$ and $q(r)$ are unperturbed. In our calculation, 3/1, 2/1 and 3/2 modes are taken into account. LHCD is simulated by calculating wave ray tracing, power spectrum shift, power absorption and driven current profile in tokamak geometry. The total current is assumed to be the sum of the ohmic and LH-driven ones. The results show that in most of the cases considered, LHCD has a stabilizing effect on tearing mode in a sence that Δ' in LHCD ramp case is lower than its value in purely ohmic case. However, as listed in TABLE 1, for plasma with lower q_a value and the chosen wave parameters LHCD leads to an increase in Δ' value, which means that tearing modes are deslabilized due to the existance of LHCD. This result is in a qualitative agreement with experimental observations. The whole scenario of the effect of LHCD on tearing mode instability depends on the combination and/or the competition of both the kinetic and MHD aspects as well as their nonlinear effects.

TABLE 1. EFFECT OF LHCD ON TEARING MODE WITH PLASMA PARAMETERS OF R=.65m, a=.2m, B_t=8KG, $n_{e0}=8*10^{13}cm^{-3}$

q_a	f_{lh}(GHz)	I_{lh}(KA)	3/2 mode	2/1 mode	3/1 mode
8.2	1.5	20	stabilized	stabilized	stabilized
4.1	1.5	4.5	destabilized	destabilized	destabilized

Acknowledgement

Helpful discussion with colleagues in both theory and tokamak divisions in ASIPP is gratefully acknowledged. This work is in part supported by The National Science Foundation of China.

References:

[1] Fisch,N.J., Phys. Rev. Lett. 41(1978)873.
[2] Xiang,N., Master Thesis, ASIPP, Aug. 1989.
[3] Vanhotte,D. et al., Nucl. Fusion 24(1984)1485.
[4] Jiang,T.W. et al., ASIPP/35, Technical Report of ASIPP,1987.
[5] Bernabei,S. et al., in Plasma Physics and Controlled Nuclear Fusion Research, 1987 (Proc. 11th Int. Conf., Kyoto, 1986), vol.1, IAEA, Vienna.
[6] Tanaka,S. et al., in Plasma Physics and Controlled Nuclear Fusion Research, 1989 (Proc. 12th Int. Conf., Nice, 1988), IAEA-CN-50/E-1-5.
[7] Sheng,Z.M., Master Thesis, ASIPP, Aug. 1990.

MAGNETIC RECONNECTION IN COLLISIONLESS PLASMAS

B. Coppi and P. Detragiache

Massachusetts Institute of Technology
Cambridge, MA 02139, U.S.A.
and
Dipartimento di Energetica, Politecnico di Torino
Torino, 10129, Italy

Introduction. We reconsider here the problem of plasma global modes with (principal) poloidal wave number $m = 1$ in the collisionless regime[1-5], since they may be relevant to the crash phase (internal disruption) of sawtooth oscillations in the high temperature, relatively low density regimes characteristic of the JET experiment. In fact, the growth rate γ of the collisionless mode in the relevant regime has the basic scaling $\gamma \propto T^{1/2}/n^{1/2}$, so that $\gamma/\nu_{ei} \propto T^2/n^{3/2}$, where ν_{ei} is the collision frequency.

Mode equations. We refer to a periodic cylindrical plasma configuration (in order to simulate a toroidal one) with magnetic field $\mathbf{B} = B\mathbf{b} = B_z(r)\mathbf{e}_z + B_\theta(r)\mathbf{e}_\theta$ and $B_z \gg B_\theta$. We consider perturbations of the form $\widehat{X} = \widetilde{X}(r)exp(-i\omega t + i\theta - 2\pi iz/L)$, where L is the lenght of the cylinder. The surface $r = r_s$, where $\mathbf{b}\nabla\widehat{X} = 0$ corresponds to $q(r) = B_z r_s/(B_\theta L/2\pi) = 1$, and we introduce the scalar and vector potentials $\widehat{\mathbf{E}} = -\nabla\widehat{\Phi} + i\omega\widehat{\mathbf{A}}/c$, $\widehat{\mathbf{B}} = \nabla \times \widehat{\mathbf{A}}$. In a narrow region of width δ_R about the $r = r_s$ surface, the marginal ideal MHD approximation breaks down, and new equations are needed in order to describe the mode rapid variation inside this region. We assume that this region can be treated as a plane geometry (although we observe that toroidal effects may in fact be important) and take $k_\parallel = -i\mathbf{b}\nabla ln\widehat{X} \simeq x/L_s$, with $x = (r - r_s)/r_s$ and $L_s^{-1} = dq/dr(B_\theta/B_z)\mid_{r=r_s}$. In the region δ_R, $\widehat{E}_\parallel = -ik_\parallel\widehat{\Phi} + i\omega\widehat{A}_\parallel/c \neq 0$ and reconnection is allowed to take place. The relevant equations are quasi-neutrality and the parallel component of Ampère's law, with the perturbed plasma density and current computed from the Vlasov equation for each plasma species. Neglecting the ion current we obtain,

$$P_e(\zeta_e)\left(\frac{\widehat{\omega}}{x}a_\parallel - \phi\right) = \frac{x}{\widehat{\omega}}\widehat{\rho}_s^2\frac{d^2a_\parallel}{dx^2} \tag{1.1}$$

$$P_e(\zeta_e)\left(\frac{\widehat{\omega}}{x}a_\parallel - \phi\right) = \mathcal{F}^{-1}\left(H(\widehat{b}_i)\bar{\phi}(k)\right) \tag{1.2}$$

We have introduced the quantities $\phi \equiv e\widetilde{\Phi}/T_e - \phi_\infty/2$, $a_\parallel \equiv eV_A\widetilde{A}_\parallel/(cT_e) - x\phi_\infty/(2\widehat{\omega})$, $V_A = B/(4\pi n m_i)^{1/2}$, $\widehat{\omega} = \omega/\omega_A$, $\omega_A \equiv V_A/L_s$, $\widehat{\rho}_s^2 \equiv \tau\rho_i^2/(2r_s^2)$, $\tau \equiv T_e/T_i$ and ρ_i is the ion Larmor radius. The quantity $\phi_\infty \equiv e\widetilde{\Phi}_\infty/T_e$ is proportional to $\widetilde{\Phi}_\infty$, the constant potential inside the $q = 1$ surface corresponding to the *outer* ideal MHD solution, and $\widehat{b}_i \equiv k^2\rho_i^2/(2r_s^2)$. Moreover $\bar{\phi}(k) = (2\pi)^{-1/2}\int_{-\infty}^{+\infty} e^{ikx}\phi(x)dx$, $\mathcal{F}^{-1}$ is the Fourier anti-transform, and the two functions $P_e(\zeta_e)$ -proportional to the electron conductivity- and $H(\widehat{b}_i)$ - related to the non-local ion response when the ion Larmor radius is finite-, are defined as,

$$P_e(\zeta_e) = (\eta_e/2)\widehat{\omega}_{*e}/\widehat{\omega} + \left[1 - \widehat{\omega}_{*e}/\widehat{\omega} + \eta_e\widehat{\omega}_{*e}/\widehat{\omega}(1/2 - \zeta_e^2)\right]W(\zeta_e) \tag{2}$$

$$H(\widehat{b}_i) = -\tau - \widehat{\omega}_{*e}/\widehat{\omega} + \left[\tau - \widehat{\omega}_{*e}/\widehat{\omega} - \eta_i(\widehat{\omega}_{*e}/\widehat{\omega})\widehat{b}_i\right]S_0(\widehat{b}_i) + \eta_i(\widehat{\omega}_{*e}/\widehat{\omega})\widehat{b}_i S_1(\widehat{b}_i) \tag{3}$$

where $\zeta_e = (\widehat{d}_e/\sqrt{2}\widehat{\rho}_s)\widehat{\omega}/x$, $\widehat{d}_e \equiv d_e/r_s$ with d_e the plasma skin depth, $\widehat{\omega}_{*e} \equiv \omega_{*e}/\omega_A$ and $\omega_{*e} \equiv cT_e/(eBL_n r_s)$ is the electron drift wave frequency with $L_n^{-1} \equiv (-dlnn/dr)\mid_{r=r_s}$ and $\eta_e \equiv dlnT_e/dlnn\mid_{r=r_s}$. The function $W(\zeta_e) = -1 - \zeta_e Z(\zeta_e)$ is related to the plasma dispersion function $Z(\zeta_e)$ and $S_n(\widehat{b}_i) = exp(-\widehat{b}_i)I_n(\widehat{b}_i)$ where the I_n are modified Bessel functions.

The mode equations (1) have to be solved with the boundary conditions for ϕ to be odd in x (and $a_\parallel$ even), and that, at large x, ϕ and $a_\parallel$ match the *outer* ideal MHD solutions,

$$\phi(x) \sim \phi_\infty\left(\frac{\lambda_H}{\pi x} - \frac{1}{2}sgnx\right) \tag{4-1}$$

$$a_\parallel(x) \sim \frac{\phi_\infty}{\widehat{\omega}}\left(\frac{\lambda_H}{\pi} - \frac{x}{2}sgnx\right) \tag{4-2}$$

where λ_H is the ideal MHD stability parameter[6].

Other dependent variables. The system (1) is invariant under the one-parameter group of transformations Γ_α: $\Gamma_\alpha\phi \to \phi + \alpha$,$\Gamma_\alpha a_\parallel \to a_\parallel - \alpha x/\widehat{\omega}$. We can then expect the system (1) to be *simpler* when written in terms of dependent variables that are Γ_α invariant. There are basically three such variables, $\chi^* = xda_\parallel/dx - a_\parallel$, $e_\parallel = -x\phi + \widehat{\omega}a_\parallel$ and $\Upsilon^* = d\phi/dx$. Whereas (see Eqs.(4)) $\lim_{x\to\infty}(e_\parallel, \Upsilon^*) = 0$, we have $\lim_{x\to\infty}\chi^* = -(\lambda_H/\pi)\phi_\infty/\widehat{\omega} \equiv -\chi_\infty$. It is then convenient to introduce $\chi = \chi^* + \chi_\infty$. In terms of χ and $\Upsilon = \Upsilon^*/\widehat{\omega}$ the system (1) becomes[5],

$$\widehat{\rho}_s^2 \frac{d}{dx}\left(\frac{1}{P_e(\zeta_e)}\frac{d\chi}{dx}\right) - \widehat{\omega}^2\left(\frac{1}{x^2}(\chi-\chi_\infty) - \Upsilon\right) = 0 \qquad (5\text{-}1)$$

$$\bar{\Upsilon}(k) = -\left(\frac{\widehat{\rho}_s k}{\widehat{\omega}}\right)^2 H^{-1}(\widehat{b}_i)\bar{\chi}(k) \qquad (5\text{-}2)$$

i.e. a differential equation in x-space and an algebraic relation in k-space.

Padè approximant. The use of a Padè approximant for the function H^{-1} of the form $H^{-1} \simeq H_P^{-1} = -1/(\widehat{b}_i h_0) - 1/h_\infty$ ($h_0 \equiv \tau + \widehat{\omega}_{*e}(1+\eta_i)/\widehat{\omega}$, $h_\infty \equiv \tau + \widehat{\omega}_{*e}/\widehat{\omega}$), that gives the correct asymptotic form of H^{-1} for both small and large values of $\widehat{b}_i$, was introduced in [7] in the context of a collisional model for the electron dynamics. By using this approximant in (5) we obtain,

$$\widehat{\rho}_s^2 \frac{d}{dx}\left[\left(\frac{1}{P_e(\zeta_e)} - \frac{1}{h_\infty}\right)\frac{d\chi}{dx}\right] - \frac{\widehat{\omega}^2}{x^2}(\chi-\chi_\infty) + \frac{\tau}{h_0}\chi = 0 \qquad (6)$$

i.e. a second order inhomogeneous ordinary differential equation.

Numerical solution. We have solved Eq.(6) numerically for $\chi_\infty = 0$ and $\widehat{\omega}_{*e} = 0$. We notice that these are realistic conditions for JET, since $|\lambda_H| < \widehat{\rho}_s$ and (as can be verified *a posteriori*) $\gamma > \omega_{*e}$. Then the mode is purely growing with a growth rate whose numerical value is well approximated by,

$$\gamma \simeq \omega_A \widehat{d}_e \left(1 + 0.28(1+\frac{1}{\tau})^{1/2}\frac{\widehat{\rho}_s}{\widehat{d}_e}\right) = \frac{1}{L_s}\left(V_A \widehat{d}_e + 0.28 c\widehat{\lambda}_{De}(1+\frac{1}{\tau})^{1/2}\right) \qquad (7)$$

for $\sqrt{2}\widehat{\rho}_s/\widehat{d}_e < 10$ and with $\widehat{\lambda}_{De} = r_s/(4\pi n e^2/T_e)^{1/2}$. Thus in the realistic case of $\sqrt{2}\widehat{\rho}_s/\widehat{d}_e > 1$ ($\widehat{\rho}_s/\widehat{d}_e \simeq 3.5$ for JET) there is an enhancement of the growth rate with respect to the case $\sqrt{2}\widehat{\rho}_s/\widehat{d}_e < 1$ discussed in [2]. However, this enhancement is different from that found in [3,4] by asymptotic methods.

Equation in k-space. In the case $\widehat{\omega}_{*e} = 0$ and, more generally, for aperiodical modes for which $Re(\omega) \gg \gamma$, it is possible to use the following Padè approximant for the function $P_e^{-1}(\zeta_e)$, $P_e^{-1} \simeq P_{e,P}^{-1} \equiv \widehat{\omega}^2\widehat{d}_e^2/(p_0\widehat{\rho}_s^2 x^2) - 1/p_\infty$, where $p_0 = 1 - \widehat{\omega}_{*e}(1+\eta_e)/\widehat{\omega}$ and $p_\infty = 1 - \widehat{\omega}_{*e}/\widehat{\omega}$. We notice that the functional form of $P_{e,P}^{-1}$ is the same as that of H_P^{-1}. Then, substituting $P_{e,P}^{-1}$ in Eq.(5-1) and working in k-space, it is possible to reduce the system (5) to a second order differential equation. The *good* dependent variable is in this case the (normalized) parallel current $J \equiv \widetilde{j}_\parallel/(-enV_A)$, which is related to χ through $J = \widehat{\rho}_s^{-2}(1/x)d\chi/dx$. We obtain,

$$\widehat{\rho}_s^2 \frac{d}{dk}\left[\left(\frac{1}{H(k\widehat{\rho}_i)} - \frac{1}{p_\infty}\right)\frac{d\bar{J}}{dk}\right] - \widehat{\omega}^2\left(\frac{\widehat{d}_e^2}{p_0} + \frac{1}{k^2}\right)\bar{J} = 0 \tag{8}$$

and the boundary condition for $\bar{J}(k)$ for small k is,

$$\bar{J}(k) \sim \left(\frac{1}{2\pi}\right)^{1/2} \frac{\phi_\infty \widehat{\rho}_s^2}{\widehat{\omega}}\left[\frac{\widehat{\omega}^2 h_0}{\tau}\left(\lambda_H \frac{k^3}{3} sgnk - \frac{k^2}{2}\right) - 1\right] \tag{9}$$

We notice that Eq.(8) is similar in form to the equation discussed in [7].

Final remarks. We have shown how the mode equations for collisionless $m = 1$ modes depend upon two functions $P_e(\zeta_e)$ and $H(\widehat{b}_i)$. By using a Padè approximant for either H^{-1} or P_e^{-1}, the mode equations (5) simplify considerably, in x-space in the first case and in k-space in the latter case. This symmetry between x-space and k-space becomes even more pronounced when a Padè approximant is used for both H^{-1}, P_e^{-1}. Then Eq.(6) for $\chi_\infty = 0$ and Eq.(8) can both be solved analytically by means of the double matching procedure outlined in [7].

This work was supported in part by the Air Force Geophysics Laboratory (APL Contract 602220-0) and in part by the Association for the Scientific and Technological Development of Piedmont.

References.

[1] B. Coppi, *Phys. Letters* **11**, 226, (1964).
[2] B. Basu and B. Coppi, *Phys. Fluids* **24**, 465, (1980).
[3] J. F. Drake, *Phys. Fluids* **21**, 1777, (1978).
[4] F. Porcelli, *Phys. Rev. Letters* **66**, 425, (1991).
[5] G. B. Crew and J. J. Ramos *Nucl. Fusion* **26**, 1475, (1986).
[6] G. Ara, B. Basu, B. Coppi, G. Laval, M. N. Rosenbluth, and B. V. Waddell, *Ann. Phys.* **112**, 443, (1978).
[7] F. Pegoraro and T. J. Schep, *Plasma Phys. Controlled Fusion* **28**, 647, (1985).

MATHEMATICAL MODELS DISPLAYING THE GROSS FEATURES OF Sawtooth Oscillations in Tokamaks

F A Haas and A Thyagaraja

AEA Fusion, Culham Laboratory, Abingdon, Oxfordshire, OX14 3DB, UK
(Euratom/UKAEA Fusion Association)

Introduction

There is at present no completely satisfactory theory of sawteeth in tokamaks. Although the simulations of DENTON et al (1986) and AYDEMIR et al (1989) capture some of the periodicity properties, they do not show the partial reconnection currently observed in experiments. In what is a very complicated physical situation it would seem useful, therefore, to investigate the simplest possible model set of equations which illustrate the gross temporal features of sawteeth.

A Nonlinear Dynamical Model

Periodic behaviour of dynamical systems suggests that at most two dynamical variables and an autonomous nonlinear set of equations coupling the time evolution of these variables are involved. We consider the central temperature perturbation $T(0,t)$ suitably normalised and some non-dimensional turbulence amplitude (for example, the magnetic fluctuations) as our basic dynamical variables $y(t)$ and $x(t)$,respectively. Restricting ourselves to an investigation of the time-evolution of sawteeth, we assume $y(t)$ and $x(t)$ to be governed by the pair of nonlinear differential equations

$$\tau_s \frac{dy}{dt} = 1 - \lambda x^2 + f_y(t) \tag{1}$$

$$\tau_s \frac{dx}{dt} = \lambda(y-1)x\phi(x,\lambda) + f_x(t), \tag{2}$$

where τ_s is a time scale characteristic of the equilibrium properties and λ is a non-dimensional constant large compared with unity. Possible physical interpretations of λ and τ_s will shortly be made clear. The quantities $f_y(t)$ and $f_x(t)$ are Langevin-type "noise" functions. The function $\phi(x,\lambda)$ enables us to consider two simple, but different heuristic choices, namely $\phi = 1$ and $\phi = \frac{2\lambda x^2}{1+\lambda x^2}$. The reason for the second more sophisticated choice of ϕ will become apparent later. Equation (1) represents energy balance with confinement degradation in response to turbulence, while equation (2) represents the dynamic relationship between the plasma internal energy (temperature) and magnetic turbulence. Although the equations look rather special and involve a single non-dimensional parameter λ (τ_s can be removed by non-dimensionalising time

using t/τ_s), many other, apparently more general equations can be reduced to this form. The above equations appear to represent a canonical form for a class of equations with very similar dynamical behaviour (ie lead to sawtooth-like periodic time series).

It is immediately clear that for the noise-free case the system has a unique steady solution, $y \equiv 1, x \equiv \frac{1}{\sqrt{\lambda}}$. Furthermore, it is straightforward to show that this solution is a stable centre in the phase plane. A further important property of the above system is that if x is non-negative at $t = 0$, it must remain so for all t. It is also possible to demonstrate that the above equations possess an exact constant of the motion, $I(t)$. For the case $\phi = 1$,

$$I(t) \equiv (y-1)^2 - \frac{2}{\lambda}\ell n x + x^2. \tag{3}$$

The fact that $\frac{dI}{dt} = 0$ for all t, together with the assumed largeness of λ, enables us to integrate equations (1) and (2) in terms of non-elementary integrals and also obtain a complete qualitative description of the motion for initial conditions such that, $y(0) = 0$ and $x(0) =$ any small positive number. This is insightful because it allows us to attach physical interpretations to the parameters λ and τ_s. Thus we find that for $\phi = 1$,

$$\frac{\tau_{\text{crash}}}{\tau_{\text{period}}} = \frac{\ell n \lambda}{\lambda}, \tag{4}$$

and that

$$\tau_{\text{period}} = 2\tau_s \left\{ 1 + \frac{\ell n \lambda}{\lambda} \right\}. \tag{5}$$

The quantity τ_s is typically of the order of the period (and of course to that of the ramp phase); λ is seen to control the ratio $\tau_{\text{crash}}/\tau_{\text{period}}$. As we shall see the estimates obtained for τ_{crash} and τ_{period} from these formulæ agree very well with the subsequent numerical work. Very similar formulæ can be derived for the case $\phi = \frac{2\lambda x^2}{1+\lambda x^2}$. In fact it turns out to be much simpler to proceed numerically.

Numerical Examples

The above equations have been numerically integrated taking the time-step Δt to be 0.1 μs, and with the initial conditions $y(0) = 0$ and $x(0) \sim \exp(-\lambda)$. It has been found that the most significant noise effects arise from f_x, and so in the results presented here, $f_y \equiv 0$. It is convenient to represent f_x by the harmonic form $f \cos \omega t$, where the amplitude f and frequency ω are to be varied. For given ω, we take the ratio $f/\omega\tau_s$ to be a measure of the noise level.

(a) $\phi = 1$

With this form for ϕ we have carried out a wide ranging set of runs with different τ_s, λ and noise levels. Thus, for example, we have investigated the case $\tau_s = 8ms, \lambda = 100, \omega\tau_s = 200$, for the range of noise level $f/\omega\tau_s = 10^{-10}$ (noise free) to 1.0. The

first figure shows the temporal behaviour of $10+y(t)$ (Fig 1a) and $X(t)(\equiv x^2(t))$ (Fig 1b) for $f/\omega\tau_s = 10^{-10}$. We see that the quantity $10 + y(t)$ (normalised so that $y_{max} = 2.0$) shows the characteristic sawtooth waveform, with a period of order 16ms; we note that this is in good agreement with the value given by equation (5). The variable $X(t)$ is seen to be very small during the ramp phase, and to show a δ-function like behaviour during the crash. The crash time, as estimated from equation (4) ($\tau_{\rm crash} \simeq 730\mu s$), is also in good agreement with the calculation. As the noise level is increased the period and amplitude decrease continuously. An abrupt "transition" occurs when $f/\omega\tau_s$ is in the range $10^{-2} - 10^{-1}$. Further increase of $f/\omega\tau_s$ leads to the disappearance of the sawteeth. The variable y is now essentially constant with a superimposed fine scale fast oscillation of frequency ω.

(b) $\phi = \frac{2\lambda x^2}{1+\lambda x^2}$

The simple heuristic model discussed above has two aspects which are unsatisfactory. Firstly, following the crash, the 'turbulence' amplitude in the ensuing ramp phase is at a level which is insignificantly small compared to that expected to occur in an experiment. In other words, $x(t)$ has a magnitude which is insignificant compared to the 'natural' noise/magnetic fluctuation amplitude. Secondly, as constructed, the $\phi = 1$ model is symmetric about $y = 1$. That is, the growth rate for $y > 1$ and the decay rate for $y < 1$, are of the same magnitude. This would seem to be a very implausible property of the model. In order to remove these two aspects of the simple model, we have investigated a second heuristic choice for ϕ, namely, $\phi = \frac{2\lambda x^2}{1+\lambda x^2}$. For conditions identical with the $\phi = 1$ case ($\tau_s = 8.0ms, \lambda = 100, \omega\tau_s = 200$), as $f/\omega\tau_s$ is varied from 10^{-10} to 0.05 there is almost no change in the period or amplitude of the sawtooth. Hence this model is more robust to noise than the previous one. As $f/\omega\tau_s$ is varied from 0.05 to 0.16, however, significant changes in the solution are observed. The period lengthens, the amplitude at the crash falls, and the variable x exhibits the driving noise. Figs 2 and 3 clearly indicate these features. Finally, completely stable behaviour is obtained (see Fig 4) - a result reminiscent of the 'monster' seen in JET. Note that the line plotted in Fig 4b is actually the envelope of very rapid oscillations between 0 and 0.02.

Conclusions

We have established that a very simple pair of non-linear differential equations are able to reproduce the periodic behaviour of sawteeth. The two variables play the role of internal energy (temperature) and magnetic turbulence. If the noise level is increased beyond a sufficiently large value then the period lengthens and the amplitude falls, and eventually a 'monster' - like solution is obtained.

Aydemir, A Y et al Phys. Fluids **B**1, 774 (1989).
Denton, R E et al Phys.Rev. Letts **56**, 2477 (1986)

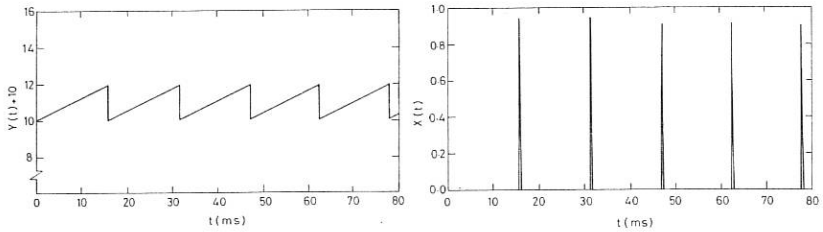

Figs 1a & 1b: $\phi = 1$. Calculated waveforms for $y(t) + 10$ and $X(t)$ with $\frac{f}{\omega\tau_s} = 10^{-10}$. Note that $y_{\max} = 2.0$.

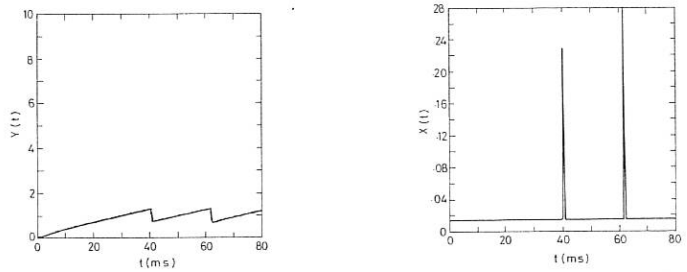

Figs 2a & 2b: $\phi = \frac{2\lambda x^2}{1+\lambda x^2}$. Calculated waveforms for $y(t)$ and $X(t)$ with $\frac{f}{\omega\tau_s} = .125$

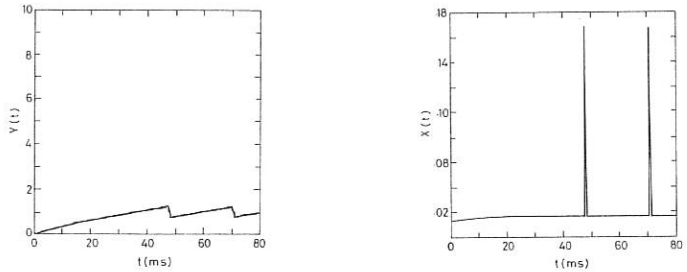

Figs 3a & 3b: $\phi = \frac{2\lambda x^2}{1+\lambda x^2}$. Calculated waveforms for $y(t)$ and $X(t)$ with $\frac{f}{\omega\tau_s} = 0.129$.

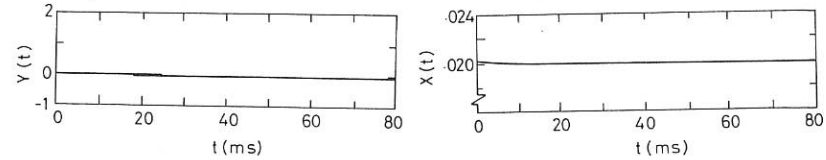

Figs 4a & 4b: $\phi = \frac{2\lambda x^2}{1+\lambda x^2}$. Calculated $y(t)$ and $X(t)$ for $\frac{f}{\omega\tau_s} = 0.167$.

SAWTEETH STABILIZATION BY ENERGETIC TRAPPED IONS

Samain, A., Edery, D., Garbet, X., Roubin, J.-P.

Association EURATOM-CEA sur la Fusion Contrôlée
Centre d'Etudes Nucléaires de Cadarache B.P. n°1
13108 Saint-Paul-lez-Durance, France

ABSTRACT AND INTRODUCTION

The analysis of a possible stabilization of sawteeth by a population of energetic ions is performed by using the Lagrangian of the electromagnetic perturbation. It is shown that the trapped component of such a population has a small influence (of order $(1-q)^2$ in the limit $\omega/\omega_d \to 0$) compared to that of the passing component. The stabilization threshold is calculated assuming a non linear regime in the q=1 resonant layer. The energetic population must create a stable tearing structure ($\Delta'=0$) if the average curvature effect on thermal particles in the layer is small. However, this effect decreases the actual threshold.

I. ELECTROMAGNETIC LAGRANGIAN FOR ENERGETIC PARTICLES

The mode is described by potentials $(\delta U,\delta A) = (U(x),A(x))\exp(-i\omega t) + c.c.$, to which each particle species s responds by the current and charge density $j(x),\rho(x)$. The Maxwell equations are equivalent to state that the gauge invariant functionnal:

$$\mathcal{L}(U^*,A^*;U,A) = \mathcal{L}_{vacuum} + \sum_s \mathcal{L}_s ;$$

$$\mathcal{L}_{vacuum} = -\frac{1}{\mu_0}\int d^3x \left|\vec{rot}\, A\right|^2 + \varepsilon_0 \int d^3x \left|i\omega A - \nabla U\right|^2$$

$$\mathcal{L}_s = \int d^3x \,(jA^* - \rho U^*) \qquad (1)$$

is extremum in U^*,A^*. The functional $\mathcal{L}_s$ is simply related to the integral $\int d^3x\, d^3p\, f\cdot h$ where $f(x,p)$ and $h(x,p) = e(U - Av_{//})$ are the perturbations of the distribution function and of the hamiltonian. A standard expression for $\mathcal{L}_s$ is derived by expressing the Vlasov equation relating f to h in angular action space [1]. This itinerary leads to more flexible and more precise forms of $\mathcal{L}_s$ than the extension of the MHD energy principle [2] using the gauge ($U=0$, $A=\xi\times B_0$), leading to $\mathcal{L}_s = -\int d^3x\, (j\times B_0).\xi^*$ where $j\times B_0$ is related to the pressure tensor perturbation.

We apply the variational principle (1) to the study of the mode triggering the sawteeth, exhibiting $N_{toroidal}=1$ and a MHD structure outside a resonant layer on the surface $r=r_1$, where $q=1$. The stabilization of this mode by a species $s=H$ of hot ions requires that the contribution $\mathcal{L}_H$ balances the destabilizing terms in $\mathcal{L}_{thermal}$, namely the tearing term ($\propto \partial j/\partial r$) and the interchange term ($\propto \partial p/\partial r$) in the MHD region. We dispose of a general expression for $\mathcal{L}_H$ applicable for A parallel to B_0:

$$\mathcal{L}_H = \int d^3x\, d^3p \left\{ -\frac{\partial F}{\partial H} e^2 |U|^2 + \sum_p \frac{\omega \frac{\partial F}{\partial H} + N\frac{\partial F}{\partial \mathcal{M}}}{\omega - p\omega_\theta - N\omega_\varphi} |h_p|^2 \right\} \qquad (2)$$

where $F(\mu,H,\mathcal{M})$ is the unperturbed distribution function ($\mu=mv_\perp^2/2B$, $H=mv^2/2$, $\mathcal{M}=Rp_\varphi$), $\omega_\theta(\mu,H,\mathcal{M})$ and $\omega_\varphi(\mu,H,\mathcal{M})$ are the time average poloidal and toroidal frequencies (for trapped particles ω_θ is the bounce frequency and $\omega_\varphi=\omega_d$ is the banana precession frequency). The subscript p indicates the Fourier component $\exp i(p\theta^*+N\varphi^*)$ along the angular variables for the poloidal and toroidal motion (such that $d(\theta^*,\varphi^*)/dt = \omega_{\theta,\varphi}$; for trapped particles θ^* is the phase of the bounce motion and $\varphi^* \approx \varphi - q\theta$). A more specific expression for $\mathcal{L}_H$ is applicable under the MHD constraint: $i\omega A - \nabla_{//} U = 0$

$$\mathcal{L}_H = \mathcal{L}_{int} + \mathcal{L}_{res}$$

$$\mathcal{L}_{int} = -\mathrm{Re} \int d^3x\, d^3p \frac{e^2}{\omega^2} \frac{\partial F}{\partial \mathcal{M}} \left(\frac{\nabla U \times B_0}{B_0^2} \cdot \nabla \Psi \right) \left(\nabla U \cdot v_{G\perp} \right)^*$$

$$\mathcal{L}_{res} = \sum_p \int d^3x\, d^3p \frac{e^2}{\omega^2} \frac{\omega \frac{\partial F}{\partial H} + N\frac{\partial F}{\partial \mathcal{M}}}{\omega - p\omega_\theta - N\omega_\varphi} \left| (v_{G\perp} \cdot \nabla U)_p \right|^2$$

where $v_{G\perp}$ is the curvature drift velocity and Ψ the poloidal flux. The functional $\mathcal{L}_{int}$ accounts for the traditional interchange MHD effects, while the functional $\mathcal{L}_{res}$ reflects the toroidal magnetic pumping effect by the mode [3]. For ω in the thermal diamagnetic range of frequency, the leading term for trapped particles in $\mathcal{L}_{res}$ is the term p=0, for which the resonant denominator $\omega - p\omega_\theta - N\omega_\varphi$ reduces to the small value $\omega - N\omega_d$. For $\omega - N\omega_d \approx \omega_d$, a stabilizing role may be played by this term if it is dominant compared to $\mathcal{L}_{int}$ [4,5,6]. This is the case if the energetic ion population contains the same number of passing and trapped particles, because the compensation of the unfavorable and favorable curvature then lowers the value of $\mathcal{L}_{int}$. Then, it is very important to notice that we have $\mathcal{L}_H \approx \mathcal{L}_{res}$ proportional to $|U|^2/\omega^2$ quasi independently of the value of (1-q) in the domain $r<r(q=1)$. In view of the MHD constraint $i\omega A = \nabla_{//} U = ((1-q)/R)\, U$, the functional $\mathcal{L}_H$ is proportional to $|A|^2/(1-q)^2$ and dominates the tearing and thermal interchange effects (proportional to $|A|^2$ and $|A|^2/(1-q)$ respectively) at low (1-q). However, in the experimentally important limit $\omega << \omega_d$, if the energetic population

consists of trapped particles only, the value of $\mathcal{L}_H$ may be derived from (2) in the limit ($\nabla_{//}U = i\omega A$, $\omega \to 0$) and therefore

$$\mathcal{L}_H = \int d^3x\, d^3p \sum_p \frac{N\, \partial F/\partial \mathcal{M}}{-p\omega_b - N\omega_d} \left| e^2 (A v_{//})_p \right|^2$$

clearly independent of (1-q) for given A. It may be shown that in this case $\mathcal{L}_H$ is proportional to $|A|^2$ instead of $|A|^2/(1-q)^2$. For $\omega << \omega_d$, the influence of the topology (trapped or passing) of the energetic particles on the stabilization efficiency provides an important experimental check of the model.

II. STABILIZATION THRESHOLDS

By combining $\mathcal{L}_H$ with $\mathcal{L}_{vacuum}$ and $\mathcal{L}_{thermal}$ in the MHD domain, and forming the Euler variational equations, one obtains the mode structure and the contribution $\mathcal{L}_{MHD}$. We essentially assume in what follows a tearing structure, i.e., a non cancelling component A(r)exp i(φ - θ) of the potential A(x). We may then write:

$$\mathcal{L}_{MHD} = \frac{\mathcal{S}}{\mu_0} \Delta' A(r_1) A^*(r_1) \; ; \; \mathcal{S} = 2\pi R \, 2\pi r_1 \qquad (3)$$

where Δ' is the usual jump across the surface $r=r_1$. Neglecting toroidal and thermal pressure effects, we have $\Delta' = +\infty$ in the absence of hot particles, meaning that the mode is strongly unstable as a tearing mode, while it is marginally unstable under the MHD constraint in the layer $A(r_1)=0$. The energetic ions introduce a finite value of $1/\Delta'$, which, in the typical case of an isotropic pressure profile $p_H=p_{H0}$ for $r<r_H<r_1$ and $p_H=0$ for $r>r_H$, is given by [6]:

$$\frac{1}{\Delta'_H} = \frac{r_1}{s_1^2} \frac{\bar{\beta}_H \beta_{crit}}{\beta_{crit} - \bar{\beta}_H}$$

where $\bar{\beta}_H = p_{H0}(2\mu_0/B^2) R^{1/2} r_H^{3/2} / 2 r_1^2$, $s_1 = (\text{dLog } q/\text{dLog } r)$ and $\beta_{crit} \approx (1-q_0)^2/G(r_H)$ with $G(r) = (1 - r^2/r_1^2)^{-1} - \text{Log}\left|1 - r^2/r_1^2\right| - 1/2$. The toroidal and thermal pressure effects in the MHD bulk also play a role in the value of Δ'. For small $1/\Delta'$ ($1/\Delta' << r_1$), one may write:

$$\frac{1}{\Delta'} = \frac{1}{\Delta'_H} + \frac{1}{\Delta'_{thermal}} \qquad (4)$$

where $\Delta'_{thermal}$ is related to the MHD energy $\delta\hat{W}\,\xi^2$ given in [7]:

$$\frac{1}{\Delta'_{thermal}} \approx \frac{\delta\hat{W}\,\mu_0 R^2}{\mathcal{S} r_1^2 s_1^2 B^2} \approx -\frac{3}{2} \frac{r_1}{s_1^2} (1-q_0) \frac{r_1^2}{R^2} (\beta_{pol}^2 - \beta_{cr}^2)$$

where β_{pol} refers to the pressure difference within $r=r_1$ and $\beta_{cr} \approx 0.4$.

The contribution $\mathcal{L}_{layer}$ of the resonant layer to the functional (1), calculated in a non linear island regime, involves the Rutherford currents proportional to the mode growth rate γ and the stabilizing interchange effects due to the average curvature within the layer proportional to $\partial\beta/\partial r$ [8].

$$\mathcal{L}_{layer} = \frac{S}{\mu_0}\left(\frac{-0.8\,\delta_{isl}}{\eta}\gamma + \frac{3}{s_1}\frac{r}{\delta_{isl}}\frac{\partial\beta_{tor}}{\partial r}\left(\beta_{pol} + \frac{l_i}{2}\right)\right) A(r_1)A^*(r_1) \qquad (5)$$

where δ_{isl} is the half island width. Expressing that $\mathcal{L}_{MHD} + \mathcal{L}_{layer}$ derived from (3) (4) (5) is an extremum in $A^*(r_1)$ provides the value of γ. If one neglects the average curvature term ($\propto \partial\beta_{tor}/\partial r$) in (5), one obtains $\gamma = 0$ for $\Delta' = \Delta'_H = 0$, i.e. $\bar{\beta}_H = \beta_{crit}$ [6]. On the other hand, retaining that term in the limit $\delta_{isl} \to 0$, one obtains $\gamma = 0$ for $\Delta'=\infty$. For $1/\Delta'_H << r_1$, i.e. $\bar{\beta}_H << \beta_{crit}$, this means that stabilization is achieved for $1/\Delta'_H \approx r_1\,\bar{\beta}_H / s_1^2 = -1/\Delta'_{thermal}$ which is essentially the condition given in [4],[5]. In fact for small islands, further important effects linked to the transverse diffusion of particles contribute to the value of $\mathcal{L}_{layer}$. These effects first produces an imaginary term proportional to $(\omega-\omega^*)$, whose cancellation imposes that the mode frequency is of order of the thermal diamagnetic frequencies ω^*. On the other hand, if $\delta_{isl} < \delta_{cr} = (D/\omega)^{1/2}$, where D is the transverse particle diffusion coefficient, a large destabilizing term

$$\frac{S}{\mu_0}\left(1.5\,\frac{1}{s_1^2}\frac{1}{\delta_{isl}}\beta_{tor}R^2\left(\frac{\partial T}{T\partial r}\right)^2\right) A(r_1)A^*(r_1) \text{ superimposes in } \mathcal{L}_{layer}\,[9].$$

Therefore, the average curvature effect in the layer can only stabilize the mode for $\delta_{isl} > \delta_{cr}$. In these conditions, the stabilization threshold is given by the expression:

$$\frac{1}{\Delta'_H} + \frac{1}{\Delta'_{thermal}} = \frac{1}{\Delta'_{layer}} \quad \text{where } \Delta'_{layer} = -\frac{3}{s_1}\frac{r_1}{\delta_{cr}}\frac{\partial\beta_{tor}}{\partial r}\left(\beta_{pol} + \frac{l_i}{2}\right)$$

Even for small ratios δ_{cr} / r_1, the stabilization threshold may be determined by Δ'_{layer} rather than by $\Delta'_{thermal}$. The observed stabilization thresholds could in fact give an useful information on the stabilizing or destabilizing effects taking place (with a divergent stucture $\propto 1/\delta_{isl}$) near the resonant layer of the tearing modes.

REFERENCES

[1] A. Samain, Nucl. Fusion **10** (1970) 325.
[2] Liu Chen, R.B. White, M.N. Rosenbluth, Phys. Rev. Lett. **52** (1984) 1122.
[3] F. Koechlin, A. Samain, in Plasma Physics and Controlled Nuclear Fusion Research 1971, IAEA Vienna, 1971 Vol.III, p.505.
[4] R.B. White, M.N. Bussac, F. Romanelli, Phys. Rev. Lett. **62** (1989) 539.
[5] B. Coppi, P. Dedragiache, S. Migliuolo, F. Pegoraro, F. Porcelli, Phys. Rev. Lett. **63** (1989) 2733.
[6] D. Edery, X. Garbet, J-M. Rax, J.-P. Roubin, A. Samain, Proc. 17 th EPS Conf. on Controlled Fusion and Plasma Heating, Amsterdam 1990, Vol.2 p.938.
[7] M.N. Bussac, R. Pellat, D. Edery, et J.L. Soulé, Phys. Rev. Lett. **35** (1975) 1638.
[8] M.Kotschenreuther, R.D.Haseltine, P.J.Morrisson, Phys.Fluids **28** (1985) 294.
[9] A. Samain, Plasma Physics and Controlled Fusion **26** (1984) 731.

THE EFFECT OF THE ION BOUNCE RESONANCE ON IDEAL AND RESISTIVE MHD INSTABILITIES

F. Romanelli, G. Fogaccia+), S. Graziadei+)

Associazione EURATOM-ENEA sulla Fusione,
C.R.E. Frascati, C.P. 65,
00044,Frascati, Rome, Italy

I. Introduction. The effect of parallel compressibility on the stability of resistive ballooning mode and of the m=1 internal kink mode in collisionality regimes appropriate to present day tokamak experiments has been recently investigated[1-3]. As resistive instabilities are described by a two spatial scale structure in toroidal geometry, the effect of compressibility can be defined either with reference to the short scale, of the order of the connection length qR, with q being the safety factor and R being the major radius, or with reference to the long scale associated to the radial localization of the mode. We are interested to the case in which compressibility effects manifest only on the connection length scale, a situation which occurs if the frequency of the mode ω is comparable with the ion transit frequency $\omega_{ti} = v_{ti}/qR$ or with the ion bounce frequency $\omega_{bi}=(\varepsilon/2)^{1/2}\omega_{ti}$, but ω is still larger than the transit frequency over the long scale $\omega >> k_{||} v_{ti}$, with v_{ti} being the ion thermal velocity. In this limit the relevant physical effect is the ion transit and bounce resonances[2].

The effect of the ω_{ti} resonance has been investigated in Refs.[1,3]. The purpose of the present work is twofold: first we want to analyze the effects of ion bounce resonance on resistive ballooning modes in tokamak plasmas; second we want to discuss the effect of the transit resonances on the m=1 internal kink mode with particular regard to the effect of the external region. The effect of the ω_{bi} resonance in the layer has been discussed in Ref.[4].

II. The Resistive Ballooning mode. The optimal ordering scheme is similar to that assumed in Ref.[1]. The first condition to be imposed is the ω_{bi} resonance $\omega \approx \omega_{bi}$. Next we balance inertia and line bending yielding $\omega \approx \omega_A/\chi$ where $\omega_A=v_A/qR$, v_A is the Alfven velocity, and χ is the extended poloidal variable in the ballooning representation. This yields $\chi \approx \delta^{-1}$ with the expansion smallness parameter δ being formally ordered as $\beta^{1/2}$ ($\beta=8\pi nT/B^2$). The ion Larmor radius is ordered according to the requirement that inertia and normal curvature are of the same order $(k_\perp \rho_i)^2 \approx \omega_{Db}/\omega$, or, after using the previous conditions, $k_\theta \rho_i \approx \delta^2$. Therefore, we have $k_\perp \rho_i \approx \delta$, and we can neglect finite ion Larmor radius corrections. Note also that $\omega_{D\psi}/\omega \approx \delta$, with $\omega_{D\psi}$ being the geodesic curvature term. Therefore, at the lowest order, the bounce resonance is

+)ENEA student

not affected by the ω_D term. Within the proposed orderings, the diamagnetic drift effects are important for $L_p/R \approx \delta^2 \approx \beta$, with $L_p^{-1}=|\nabla p/p|$, which is consistent with the choice of a high-β equilibrium. Ion collisionality, meanwhile, is chosen to satisfy the banana condition $\nu_{ii}/\omega_{bi}\approx\delta$. In order to simplify the analysis, we also assume the electrons in the Pfirsch -Schluter collisionality regime $\nu_{ei}/\omega_{te}\approx\delta^{-1}$. The above ordering then allows us to retain the simplest form of Ohm's law. Next we impose the strongly collisional ordering $(k_{||}v_{te})^2/(\omega\nu_{ei}) \approx \delta^2$ or $\omega/\omega_{te}\approx\delta$.

Following Ref.1 the stability of modes driven by free energy in the ideal region is described by the following equation

$$\frac{1}{3}\frac{\Gamma\left[\frac{1}{4}\frac{\left(Q_o^3+L/2\right)}{\left(Q_o^3+L^2/4\right)^{1/2}}-\frac{1}{4}\right]}{\Gamma\left[\frac{1}{4}\frac{\left(Q_o^3+L/2\right)}{\left(Q_o^3+L^2/4\right)^{1/2}}+\frac{5}{4}\right]}\frac{\Gamma\left[\frac{5}{2}\right]Q^{1/2}Q_o^3}{\Gamma\left[-\frac{1}{2}\right]\left(Q_o^3+L^2/4\right)^{3/4}}=\Delta'_B\left(\frac{l^2}{S}\right)^{1/3} \qquad (1)$$

where $Q=-i\omega/\omega_o$, $Q_o^3=Q^2Q_i-QQ_3$, $Q_i=-i(\omega-\omega_{*i})/\omega_o$, $\omega_{*i}=\omega_{*ni}(1+\eta_i)$, $\eta_i=L_n/L_T$, $\omega_{*ni}=cT_i/(eBL_nr_s)$, $L_n^{-1}=\nabla n/n$, $L_T^{-1}=\nabla T/T$, Δ'_B is the ratio between the large and the small solution of the equation in the ideal region and S is the magnetic Reynolds number. The quantity L[5] is related to the long mean free path ordering. In addition, $\omega_o=[(c^2\eta_{||}l^2\langle JB^2\rangle/4\pi\langle JB^2/|\nabla\psi^2|\rangle)/4\pi\eta_{in}\langle JB^2/|\nabla\psi|^2\rangle\langle J|\nabla\psi|^2/B^2\rangle/\langle\nu'\rangle^2]^{1/3}$, where l is the toroidal mode number, $\eta_{||}$ is the parallel resistivity and J, ν' and $|\nabla\psi|^2$ are equilibrium quantities [1]. Kinetic effects are contained in Q_3 which is defined in Ref.1. For a low-β circular flux surface equilibrium the quantity Q_3 is given by

$$Q_3 = -\frac{\omega_{ti}}{\omega_o}4q^2\left[\frac{\omega-\omega_{*ni}}{\omega}G_o\left(\frac{\omega}{\omega_{bi}}\right)-\eta_i\frac{\omega_{*ni}}{\omega}G_1\left(\frac{\omega}{\omega_{bi}}\right)\right] \qquad (2)$$

with $G_o(x)= x^6Z(x)+x(x^4+0.5x^2+3/4)$, $G_1(x)=(x^8-1.5x^6)Z(x)+ x(x^6+0.5x^4+0.75x^2+15/8)$ and $Z(x)$ is the plasma dispersion function. The solution of Eq.(1) are acceptable if $Re\{[L/2+(Q_o^3+L^2/4)^{1/2}]/Q\}>0$.

Looking at the limit $Q_o^3 < L^2/4$, from Eq.(1) we have always three unstable modes with growth rate

$$Q=\left[\frac{3}{4\pi^{1/2}\Gamma\left[\frac{5}{2}\right]}\left|\frac{L}{2}\right|^{3/2}\frac{(\varepsilon/2)^{1/2}}{q^2}\left(\frac{\omega_{bi}}{\omega_o}\right)^5\Delta'_B\left(\frac{l^2}{S}\right)^{1/3}\right]^{2/15}e^{ik\pi/15} \qquad (3)$$

with k=-3,1,7, if $|Q|>>\omega_*/\omega_o$, and five unstable modes with growth rate

$$Q=\left[\frac{3}{4\pi^{1/2}\Gamma\left[\frac{5}{2}\right]}\left|\frac{L}{2}\right|^{3/2}\frac{(\varepsilon/2)^{1/2}}{q^2}\frac{\omega_o}{\omega_{*2}}\left(\frac{\omega_{bi}}{\omega_o}\right)^5\Delta'_B\left(\frac{l^2}{S}\right)^{1/3}\right]^{2/13} e^{i2\pi k/13} \qquad (4)$$

with k=0,8,±6,-4 and $\omega_{*2}=\omega_{*ni}(1-1.5\eta_i)$, in the opposite limit. Note that these modes are very weakly dependent on Δ'_B, $\gamma\simeq\Delta'^{0.1}_B$.

III. The m=1 Internal kink mode. Following Ref.6, the hot ion component is described by the gyrokinetic formalism. The optimal ordering for the hot ion temperature is $T_h/T_i\simeq\varepsilon^{-2}$ and $\beta_h/\beta_i\simeq\varepsilon$, with $\varepsilon=a/R<1$, a being the minor radius and $\beta_j=8\pi n_j T_j/B^2$. Such a choice implies $n_h/n_i\simeq\varepsilon^3$ and overall charge neutrality can be assumed. Therefore, at the lowest order, the plasma is described by the usual one fluid ideal MHD equations.

The compressional effects of the bulk ions are retained through the solution of the drift kinetic equation. Looking for competition between hot magnetic drift resonance and diamagnetic effects, we order the frequencies as $\omega\simeq\omega_{*i}\simeq\omega_{dh}$. This requires $\varepsilon_p=L_p/R\simeq T_i/T_h\simeq\varepsilon^2$. The condition of ω_{bi} resonance yields $\omega\simeq\omega_{bi}$ or $k_\theta\rho_i\simeq\varepsilon^2$. Finally, we balance inertia and line bending on the scale of the layer, which yields $k_\parallel\simeq\beta_i^{1/2}/R$. Note that with the present ordering, $k_\perp\rho_i<1$ on the scale of the layer.

Following the usual variational approach we can derive the following general dispersion relation

$$-is\left\{\omega(\omega-\omega_{*i})/\omega_A^2\right\}^{1/2}+\delta W_c+\delta W_{MHD,h}+\delta W_{kh}+\delta W_{ki}=0 \qquad (5)$$

where $\omega_A=v_A/(3^{1/2}R)$ and $s=rq'/q$ at $r=r_s$ is the shear. Note that the layer physiscs is described by the usual fluid approximation. A slowing down model with a single pitch angle is considered here for the hot ion distribution function. In this case, the hot particle kinetic term δW_{kh} can be modeled as [6] $\delta W_{kh}=(\beta_h/\varepsilon)(\omega/\omega_{dm})\ln(1-\omega_{dm}/\omega)$ with ω_{dm} being the magnetic drift frequency at the maximum energy. The term $\delta W_{MHD,h}$ [7] accounts for the effect of the hot particles on the ideal MHD energy of the bulk plasma δW_c [8] and, for the sake of simplicity, will be neglected in the following. Finally, the term δW_{ki} accounts for the kinetic contribution in the external region. For $\omega_{bi}<\omega<\omega_{ti}$, we have

$$\delta W_{ki}=-\frac{2}{3}\beta_i\int\frac{r}{r_s}d\left(\frac{r}{r_s}\right)\left[\frac{\omega-\omega_{*ni}}{\omega_{ti}}F_o\left(\frac{\omega}{\omega_{ti}}\right)-\frac{\eta_i\omega_{*ni}}{\omega_{ti}}F_1\left(\frac{\omega}{\omega_{ti}}\right)\right] \qquad (6)$$

with $F_o(x)=(x^4+1.5x^2+1)Z(x)+x(x^2+2)$, $F_1(x)=(x^6+x^4+7/4x^2+1.5)Z(x)+x(x^4+$

$1.5x^2+3)$. Upon retaining the contribution of the resonant ions, Eq.(6) yields $\delta W_{ki} \simeq -i\beta_i(4\pi/9)^{1/2}(\omega-\langle\omega^*\rangle)/\omega_{ti}$, with $\langle\omega^*\rangle = 2\int(rdr/r_s^2)\omega^*_i(1+1.5\eta_i)$. The effect of the bulk ion resonances is equivalent to the effect of parallel viscosity and it is stabilizing for $\omega >> \langle\omega^*\rangle$. Such a term is formally similar to the inertia term and smaller by a factor $\beta_i^{1/2}$. For $\omega_{bi} < \omega_{dm} < \omega_{ti}$, the fishbone threshold $\beta_{hc}^{(f)}$ is larger than the internal kink threshold $\beta_{hc}^{(k)} \simeq \varepsilon s\ \omega_{dm}/(\pi\omega_A)$ [6]

$$\beta_{hc}^{(f)} = \beta_{hc}^{(k)}\left(1+\left(4\pi\beta_i / 27s^2\right)^{1/2}\right) \qquad (7)$$

For $\omega \lesssim \omega_{bi}$, the quantity δW_{ki} is associated to the trapped ion response. The resonant ions yield, for $\omega >> \omega^*$, $\delta W_{ki} \simeq -i\beta_i(4\pi/9)^{1/2}\ (\omega/\omega_{ti})(\omega/\omega_{bi})^6$. The effect is again stabilizing and the threshold assumes intermediate values between $\beta_{hc}^{(k)}$ and $\beta_{hc}^{(f)}$.

IV. Conclusions. The stability of resistive ballooning modes has been investigated, in the long mean free path regime, by including the effect of the ω_{bi} resonance. The resulting unstable modes are very weakly dependent on Δ'_B. The effect of the transit and bounce resonance in the external region on the m=1 internal kink mode has been also analyzed. The contribution is stabilizing, yielding an increase of the high frequency fishbone mode threshold by a factor $(1+\beta_i^{1/2})$ for $\omega_{bi} \lesssim \omega_{dm} < \omega_{ti}$. Therefore, under this condition, a stable operating domain exists for $\beta_{hc}^{(k)} \lesssim \beta_h \lesssim \beta_{hc}^{(f)}$.

REFERENCES

[1] F. Romanelli, L. Chen Phys. Fluids B 3, 329 (1991)
[2] Liu Chen in Theory of Fusion Plasmas (Proc. 2nd Int. Workshop Chexbres, 1988), Bologna 1989 p. 327
[3] F. Romanelli, L. Chen and R.B. White to appear on Nucl. Fusion
[4] F. Romanelli in Theory of Fusion Plasmas (Proc. Joint Varenna - Lausanne Workshop Varenna,1990), Bologna 1990, p. 519
[5] J.W. Connor and Liu Chen, Phys. Fluids 28, 2201 (1985)
[6] L.Chen,R.B.White,M.N.Rosenbluth, Phys.Rev.Lett. 52 1122(1984)
[7] R.J. Hastie, L Chen, Bull. Am. Phys. Soc. 30 1422 (1985) and Chinese Phys. Lett. 4 561 (1987)
[8] M.N. Bussac, R. Pellat, D. Edery, and J.L. Soule, Phys. Rev. Lett. 35 1638 (1975)

THEORETICAL CALCULATIONS AND EXPERIMENTAL COMPARISONS FOR HIGH-n TOROIDAL INSTABILITIES AND QUASILINEAR FLUXES*

G. Rewoldt and W. M. Tang

Plasma Physics Laboratory, Princeton University
Princeton, NJ 08543-0451 U.S.A.

Progress in achieving a physics–based understanding of anomalous transport in toroidal systems has come in large part from investigations based on the proposition that low frequency electrostatic microinstabilities are dominant in the bulk ("confinement") region of these plasmas. Although the presence here of drift–type modes dependent on trapped particle and ion temperature gradient driven effects appears to be consistent with a number of important observed confinement trends, conventional estimates for these instabilities cannot account for the strong current (I_p) and /or q-scaling frequently found in empirically deduced global energy confinement times for auxiliary–heated discharges. The present paper deals with linear physics features, ignored in simpler estimates, which could introduce an appreciable local dependence on current. In addition, the dependence of the linear and quasilinear properties of the instability on the electron and ion temperatures is examined.

A comprehensive kinetic code[1] is used to calculate the linear eigenfrequencies and eigenfunctions of high-n tokamak instabilities, such as toroidal drift modes. This analysis is applied to specific cases obtained from TFTR experimental data. An important issue investigated deals with possible current scaling associated with microinstabilities, *i.e.*, dependence on q_a, and thus on plasma current. On a particular magnetic surface, the mode eigenfrequency depends on q and $\hat{s} \equiv (r/q)dq/dr$ partially through the orbit averaged trapped electron magnetic precession frequency given by $\omega_{de}^{(0)} \equiv \omega_{*e}(r_{ne}/R)(E/T_e)G(\kappa)$ and partially through the circulating particle transit frequency, $\bar{\omega}_{tj} \equiv v_j/qR$, and the corresponding trapped particle bounce frequency, $\bar{\omega}_{bj} \equiv (r/R)^{1/2}\bar{\omega}_{tj}$. Here, $\kappa \equiv \left\{\left[1 + \{1 - [(v_\parallel/v)^2]B_0/B(\theta)\}(R/r)\right]/2\right\}^{1/2}$ is a pitch-angle variable that goes from zero for deeply trapped particles to one for barely trapped particles. The variation of $G(\kappa)$ with $q_a \equiv q(a)$, and therefore with the local q and $\hat{s}$, is illustrated in Fig. 1 in various representative equilibrium scenarios where the total plasma current (and therefore, $q_a \equiv a^2B/I_pR$) is changed. It is obvious that the high current (low q_a and corresponding low $\hat{s}$) cases give the smallest values for $G_{\rm ave}$, (the average of $G(\kappa)$ over κ). The strength of the collisionless trapped electron mode (CTEM) depends sensitively on the factor G which in turn can have a significant dependence on current via the local q and $\hat{s}$. With respect to the ion Landau damping, the effect obviously becomes stronger as the ion bounce ($\bar{\omega}_{bi}$) and transit frequencies ($\bar{\omega}_{ti}$) approach the eigenmode frequency (ω). This favorable influence on ω clearly improves as I_p increases since $\bar{\omega}_{ti}$ and $\bar{\omega}_{bi}$ (both $\propto 1/q$) would correspondingly increase toward ω.

Up to this point, the arguments given for the presence of a current dependence in the CTEM have been primarily qualitative. In order to demonstrate this quantitatively, comprehensive linear eigenmode calculations have been carried out numerically.

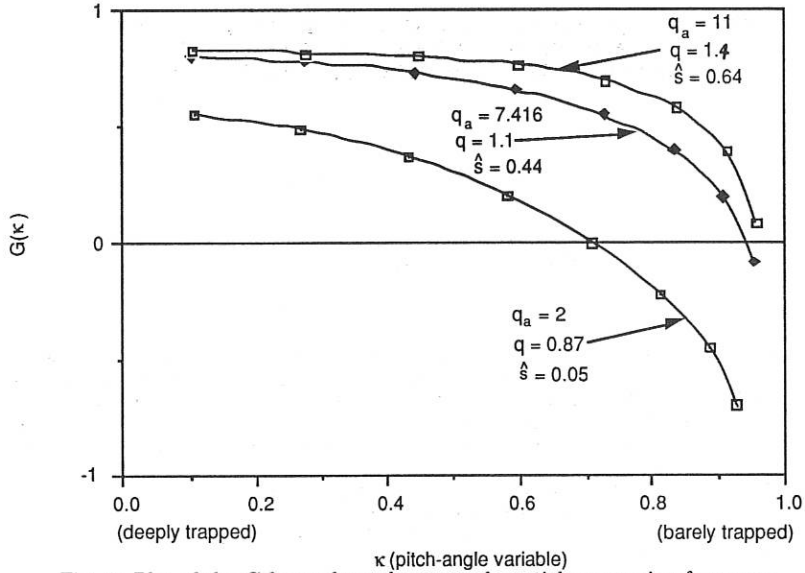

Fig. 1: Plot of the G-factor from the trapped–particle precession frequency as a function of the velocity-space pitch-angle variable κ.

The comprehensive code[1] employed provides solutions to the appropriate toroidal eigenmode equation without any frequency expansions. Thus, the precession resonances as well as the ion bounce and transit resonances are all evaluated without approximations. The usual ballooning formalism is employed, so that the calculations are local to a single, chosen magnetic surface. This stability analysis is interfaced with self–consistent, numerically computed MHD equilibria. In studying the possible dependence on current, the $q(r)$ profile is varied by changing $q(a)$ (i.e. changing the total plasma current) at fixed $q(0)$ with intermediate $q(r)$ values scaling as $q_{\rm new}(r) = \{[q_{\rm new}(a) - q(0)]/[q_{\rm old}(a) - q(0)]\}[q_{\rm old}(r) - q(0)] + q(0)$. A numerical MHD equilibrium is recomputed for each new $q(r)$ profile, and the corresponding growth rate, γ, is then maximized over k_θ.

For the trapped-electron-η_i-type instabilities, the linear growth rate is found to be strongly reduced as q_a is decreased from intermediate ($\sim 6-7$) to low values (~ 2). This dependence is strong enough to account for part, but not all, of the dependence of transport on plasma current observed in most auxiliary-heated tokamak plasmas. As q_a increases from intermediate to high values (~ 11), no single trend is observed. These trends can be understood as coming in large measure from the dependence of the orbit-average magnetic drift frequency for trapped particles on local q and shear values. Dependence of the untrapped ion transit frequency, and thus of the ion Landau damping, on q plays a smaller role in these linear calculations. These trends are illustrated in Fig. 2 for a representative case. Results here are consistent with the preceding qualitative arguments given for the precession drifts and for ion Landau damping.

In addition, for the trapped-electron-η_i-type instabilities, scaling with ion and electron temperature is investigated and compared to transport results from represen-

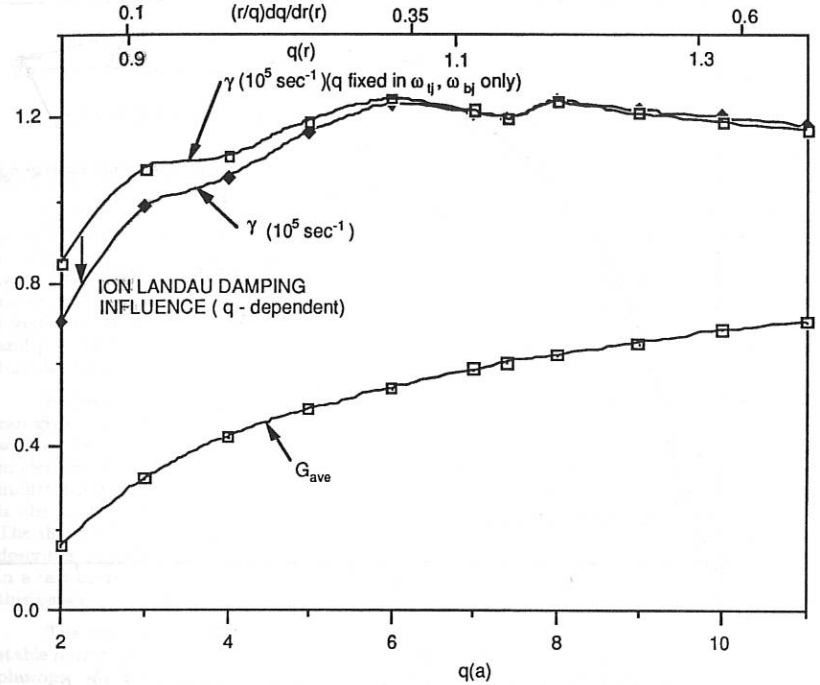

Fig. 2: Plot of linear growth rate (γ) as a function of q_a for representative TFTR parameters in the collisionless electrostatic limit, along with the $G_{\rm ave}$ factor. The lower γ–curve shows the influence of ion Landau damping.

tative TFTR discharges. For a particular supershot case, for $r/a = 0.325$, the linear growth rates are plotted versus $\tau \equiv T_e/T_i$ as T_e or T_i are varied artifically from their respective experimental values in Fig. 3. This is done by multiplying the entire radial profile $T_j(r)$ by a constant, and then recomputing the numerical MHD equilibrium for the modified pressure profile $\propto n_e(T_e + T_i)$. The growth rates are plotted for fixed $k_\theta \rho_i = 0.64$ as T_i is varied at fixed T_e and for fixed toroidal mode number $n = 37$ as T_e is varied at fixed T_i. These are the values of $k_\theta \rho_i$ and n which maximize the growth rate for the local experimental values, $T_e^{\rm exp} = 6.38$ keV and $T_i^{\rm exp} = 16.7$ keV.

As $\tau \equiv T_e/T_i$ varies from its experimental value as either T_e or T_i is varied, the value of the growth rate also varies strongly due to dynamical effects, as various characteristic frequencies such as $\bar{\omega}_{tj}, \bar{\omega}_{bj} \propto T_j^{1/2}$ or $\omega_{dj} \propto T_j$ change. In addition, as either T_e gets large (large τ) or T_i gets large (small τ), the Shafranov shift in the MHD equilibrium increases due to the increase in β, and the amount of "bad" curvature available to destabilize the mode decreases. This accounts for part of the reduction in the growth rate in these limits. The two growth rate curves vary together for moderate τ ($\lesssim 1.5$), but for larger τ this Shafranov shift effect causes a decrease in the growth rate

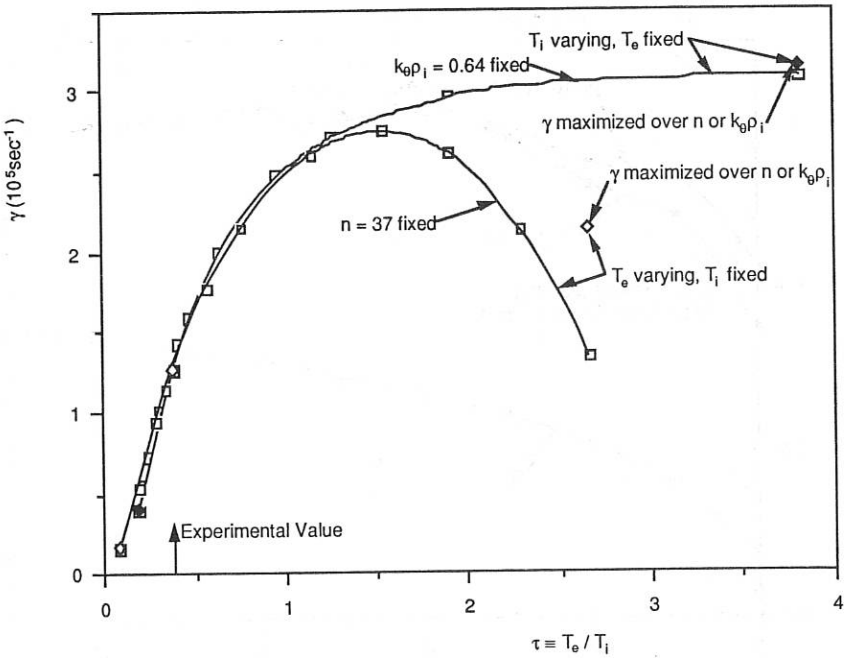

Fig. 3: Plot of linear growth rate (γ) as a function of $\tau \equiv T_e/T_i$ for representative TFTR supershot parameters in the collisionless electrostatic limit.The numerical MHD equilibria are recomputed for the pressure profile $\propto n_e(T_e + T_i)$ for each point plotted.

when T_e increases, while the growth rate only saturates when T_i decreases. This is due to the fact that, for the cases studied here, increasing T_e (from 6.38 keV) significantly changes the MHD equilibrium, while decreasing T_i (for $\tau > 1$) has little influence.

As T_i is varied from its experimental value at fixed T_e, the quasilinear fluxes are calculated for the "mixing-length" saturation level, $e\phi_0/T_e = 1/k_\theta r_p$, which is independent of T_i. With this prescription, the effective ion thermal diffusivity $\chi_i^{\rm eff}(T_i) \equiv -Q_i/[n_i(dT_i/dr)]$ turns out for this case to be nonmonotonic in T_i. In particular, while $\chi_i^{\rm eff}$ increases with T_i for T_i up to about $T_i^{\rm exp} = 16.7$ keV, above that value $\chi_i^{\rm eff}$ starts to decrease. This calculated trend of different low-T_i and high-T_i behavior appears to be consistent with the improvement in ion energy confinement with T_i observed in TFTR supershots[2], opposite to the degradation with T_i observed in TFTR L-mode shots[2].

*Supported by U. S. DoE Contract No. DE-AC02-76-CHO3073.

[1]G. Rewoldt, W.M. Tang, and R.J. Hastie, Phys. Fluids **30**, 807 (1987).
[2]D.M. Meade, *et al.*, in Plasma Physics and Controlled Nuclear Fusion Research 1990 (Proc 13th Int. Conf. Washington, 1990), paper IAEA-CN-53/A-1-1.

EFFECTS OF CURRENT PROFILES ON MHD STABILITY*

L.L. Lao, T.S. Taylor, M.S. Chu, A.D. Turnbull,
E.J. Strait, and J.R. Ferron

General Atomics, San Diego, California

INTRODUCTION AND SUMMARY

The magnetohydrodynamic (MHD) stability of a plasma against the ideal low and high toroidal mode number kink and ballooning modes depends critically on its pressure and current profiles, as well as on the shape of its poloidal cross section, which determines its ability to carry the toroidal current at a given value of edge safety factor q. It has previously been shown that in the absence of finite current density at the edge, the stability of the ideal low toroidal mode number $n = 1$ kink mode can be substantially improved for broad pressure and peaked current density profiles.[1] With these optimized profiles, kink-stable normalized toroidal beta $\beta_N = \beta_T/(I/aB_T)$ near six can be achieved.

In the low plasma collisionality regime, significant bootstrap current can be driven which can give rise to high edge current density. In this paper, the effects of current profiles both with and without finite edge current density on the ideal $n = 1$ kink and infinite n ballooning modes are studied using simulated plasma equilibria with varying β_N, the plasma internal inductance ℓ_i, and different amounts of toroidal current density near the edge J_S. The study is also motivated by the DIII–D experimental results that β_N achieved improves with ℓ_i.[2] The shape of the toroidal current density profiles is varied using the two parameters ℓ_i, which describes its global peakedness, and J_S. The interesting case of negative J_S, which can arise in a fast current-ramped down plasma, will be described separately and is not considered in this paper.

The results of the ballooning mode stability study shows that the critical marginally stable normalized ballooning β limit, β_{NC}, increases approximately linearly with ℓ_i for circular plasmas. As the plasma elongation is increased and becomes more strongly shaped, this dependence on ℓ_i becomes weak because of the change in the topology of the (S, α) diagram introduced by shaping, which reduces the stabilizing effects of the good magnetic field line curvature region. For a divertor plasma, β_{NC} shows essentially no dependence on ℓ_i for the moderate ℓ_i values considered. The results suggest that in the low to moderate ℓ_i operational range in DIII–D, where improvement of β_N with ℓ_i is observed, the plasma beta is limited by kink rather than ballooning modes, which are more sensitive to ℓ_i.

For the intermediate $q_S \simeq 3$ equilibria considered in this paper, the low n kink mode imposes a more stringent limit on the plasma stability than the high n ballooning mode. As J_S increases, the central as well as the edge shear becomes weakened, which makes these equilibria very unstable to the kink mode with a substantial internal as well as an edge peeling external component. Consequently, as J_S increases, the high ℓ_i stable operating space becomes inaccessible and the β_N stable to the $n = 1$ kinks is significantly reduced for all ℓ_i. As has been shown in previous studies,[3,4] the edge peeling component is sensitive to the exact value of q_S and is particularly large when q_S is near below an integer value. For a divertor plasma, the kink modes are mostly internal over quite a range of the accessible ℓ_i space, whereas for a circular plasma they tend to have strong external as well as global characters.

MHD EQUILIBRIUM

The MHD equilibria used in this stability study are computed using the EFIT code[5] running in the fixed boundary equilibrium mode. The two stream functions pressure P and poloidal current F describing the toroidal current density J_T are chosen to have the forms

* Work supported by the U.S. Department of Energy under Contract No. DE-AC03-89ER51114.

$$P'(\psi) = \alpha_0(1 - 5x/8) \quad , \quad FF'(\psi) = \gamma_0 + \gamma_1 x + \gamma_2 x^2 + \gamma_3 x^3 \quad , \tag{1}$$

$$J_T = R\left[P'(\psi) + \frac{\mu_0 FF'(\psi)}{4\pi^2 R^2}\right] \quad . \tag{2}$$

Here, $x = (\psi - \psi_m)/(\psi_b - \psi_m)$ and the flux function ψ is assumed to have a maximum value, ψ_m, at the magnetic axis and decrease to a smaller value, ψ_b, at the plasma boundary.

The parameters α_0, γ_0, γ_1, γ_2, and γ_3 describe respectively β_N, axial safety factor q_0, ℓ_i, the total plasma current I or q_S, and J_S. Here, q_S and J_S are the safety factor and flux surface averaged toroidal current density at a flux surface near the edge $x = x_S$. This particular set of functional forms for P' and FF' provide an adequate description of the DIII–D current and pressure profiles over a wide range of DIII–D operating space. For all equilibria considered here, q_0 is taken to be 1.05 and $x_S = 0.995$.

BALLOONING STABILITY

To study the effects of current profiles on the ideal infinite n ballooning stability, equilibria of varying ℓ_i, J_S, and poloidal cross sections are generated as described in the previous section. The critical normalized beta β_{NC} corresponding to these equilibria are then computed using the MBC[6] and the CAMINO codes.[7] The results are summarized in Fig. 1, where the calculated β_{NC} variation with ℓ_i is shown for three different plasma shapes: a large aspect ratio, A, circle, an ellipse of elongation $\kappa = 1.4$, and a single-null divertor. The plasma parameters for these configurations are given in Table 1. In the numerical stability calculations for the divertor equilibria, the singularity introduced by the separatrix is treated by restricting the computational domain to $x \leq 0.995$. To provide a consistent comparison with limited configurations, their domain of calculations is also restricted to $x \leq 0.995$.

The ellipse and the single-null divertor are typical DIII–D equilibria, whereas the large A circular equilibria are generated by raising the major radii of all DIII–D poloidal shaping coils to large values. All limited equilibria have similar $q_S \simeq 3.2$. For the divertor equilibria, the total plasma current was held fixed at 855 kA, which gives a $q \simeq 3.2$ at $x = 0.95$ when $J_S = 0$. As is shown in Fig. 1, for circular large A equilibria, β_{NC} increases approximately linearly with ℓ_i, as is expected from the well known results on (S, α) diagram, because of the almost linear dependence of α on S. This β_{NC} optimized with respect to the ballooning mode can be approximated by $4\,\ell_i$.

As the plasmas become more shaped in poloidal cross section, this dependence on ℓ_i gradually weakens and for a divertor geometry β_{NC} shows essentially no dependence on ℓ_i over the same range of ℓ_i. This is because of the reduction in the stabilizing effects provided by the good magnetic field line curvature region due to shaping and toroidicity. This is illustrated in Fig. 2, where the (S, α) diagram for a large A circular equilibrium at the flux surface $x = 0.85$ is compared against that at a similar flux surface for a single-null divertor. As is shown, although the increases in the ℓ_i results in a stronger shear S, however, in the divertor case α does not increase linearly with S, as in the circular case. This change in the topology of the (S, α) diagram results in the weak ℓ_i dependence in the divertor case. For the range of ℓ_i considered here, β_{NC} varies only weakly with J_S.

KINK STABILITY

To study the current profile effects on the ideal $n = 1$ kink stability, equilibria of varying β_N, ℓ_i, and J_S are generated for the three different plasma configurations as described above. The stability against the kink modes is then evaluated using the GATO code.[8] The results are summarized in Figs. 3 and 4, where the kink stability boundary is shown in terms of the β_N and ℓ_i space for the circular and the divertor configurations both for $J_{SN} = 0$ and $J_{SN} = 0.5$. Here, $J_{SN} = J_S/(I/\Gamma)$ where Γ is the plasma cross sectional area. With finite J_{SN}, the central as well as the edge shear become weakened, and the high ℓ_i space becomes inaccessible and the β_N stable to the $n = 1$ kinks is significantly reduced for all ℓ_i.

TABLE 1
MAJOR PLASMA PARAMETERS

Plasma Configurations	Large A Circle	Ellipse	Single-null Divertor
Major radius, R_0 (m)	11.668	1.676	1.685
Minor radius, a (m)	0.651	0.659	0.634
Elongation, κ	1.00	1.40	1.89
Upper triangularity, δ_U	0.00	0.00	0.24
Lower triangularity, δ_L	0.00	0.00	0.42
qs	3.20	3.20	–
I (kA)	–	–	855
B_T (T)	0.79	0.79	0.79

As has been noted in Ref. 1, the stability boundary consists of two main branches. The unstable modes in the low ℓ_i branch are external and those in the high ℓ_i branch are internal. For a divertor geometry, the modes are mostly internal over quite a range of accessible ℓ_i, whereas they tend to have a strong external and global appearances in a circular geometry.

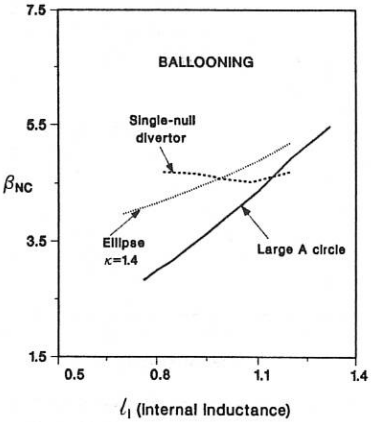

Fig. 1. Comparison of the optimized β_{NC} against the infinite n ballooning mode for three plasma configurations.

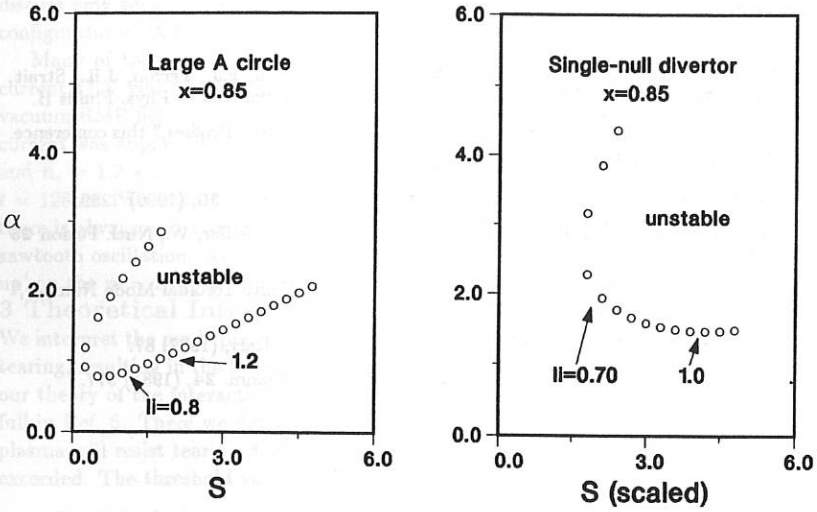

Fig. 2. (S, α) diagrams for a large aspect ratio circle and a single-null divertor at a flux surface $x = 0.85$ near the edge.

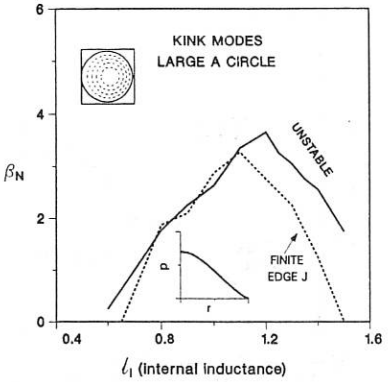

Fig. 3. Comparison of the kink mode stability boundary for the cases when $J_{SN} = 0.0$ and 0.5 for a large aspect ratio circle.

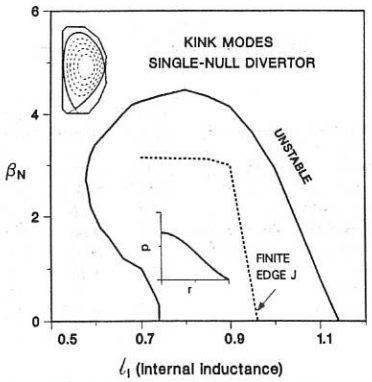

Fig. 4. Comparison of the kink mode stability boundary for the cases when $J_{SN} = 0.0$ and 0.5 for a single-null divertor.

In the presence of finite edge current density, the unstable mode consists of a substantial internal as well as an edge peeling external component which is is sensitive to the exact value of q_S and is particularly large when q_S is near below an integer value.[3,4]

REFERENCES

1. Howl, W., Turnbull, A.D., Taylor, T.S., Lao, L.L., Helton, F.J., Ferron, J.R., Strait, E.J., General Atomics Report GA-A19953, 1990, to be submitted to Phys. Fluids B.
2. Strait, E.J., *et al.*, "Dependence of DIII-D β Limit on Current Profiles," this conference.
3. Manickam, J., Bull. Am. Phys. Soc. **34** (1989) 2049.
4. Schultz, C.G., Bondeson, A., Troyon, F., Roy, A., Nucl. Fusion **30**, (1990) 2259.
5. Lao, L.L., St John, H., Stambaugh, R.D., Kellman, A.G., Pfeiffer, W., Nucl. Fusion **25** (1985) 1611.
6. Moore, R.W., "MBC: A Ballooning Stability Code for Finite Toroidal Mode Number," General Atomics Report GA-A16243 (1981).
7. Chance, M.S., Proc. Theory of Fusion Plasmas, Varenna, Italy, (1987) 87.
8. Bernard, L.C., Helton, F.J., Moore, R.W., Comp. Phys. Comm. **24**, (1981) 377.

INTERPRETATION OF RESONANT MAGNETIC PERTURBATION EXPERIMENTS

T.C.Hender, R.Fitzpatrick, A.W.Morris, P.S.Haynes, I.Jenkins, D.C.Robinson, and T.N.Todd
UKAEA/Euratom Fusion Association, Culham Laboratory, Abingdon, Oxon OX14 3DB, UK.

1 Introduction

Recent experiments on COMPASS-C [1], and previous experiments on other tokamaks (eg [2,3]), have shown a wide variety of effects on MHD activity resulting from the application of externally induced resonant magnetic perturbations (RMP's). These experiments are important since they allow a detailed quantification of the error fields effects in future large devices. The error field implications of the results presented here, are discussed in Ref. [4].

In this paper we first present a brief overview of some of the key COMPASS–C RMP results (further details in [4]) and then discuss a theoretical interpretation of these results, in terms of a resistive MHD theory including RMP's and plasma rotation [5].

2 Experimental Results

In this section we discuss recent results from the COMPASS–C tokamak ($R = 0.56$m, $a_{lim} = 0.2$m). The RMP fields are produced by a saddle coil system consisting of ten 70° long toroidal bars in each quadrant, with poloidal links, which may be changed between discharges. This allows a wide variety of RMP fields to be induced, although here we will discuss only those for which the $m = 2$, $n = 1$ component is dominant. For these RMP configurations, 1kA of RMP coil current gives $b_{r(2,1)} \sim 14$gauss at $r = 20$cm.

Many of the key RMP effects are exhibited in Fig.1 which shows the RMP saddle current (I_c), central soft X-ray (SXR) chord, $n = 1$ plasma radial field (ie with the vacuum RMP field subtracted), and $m = 2$ Mirnov ($\dot{b}_\theta$) trace. In this discharge the RMP current was applied during the current flat-top when $I_p = 98$kA, $q_\psi = 4.25$ ($B_T = 1.1$T), and $\bar{n}_e = 1.2 \times 10^{19}\mathrm{m}^{-3}$. It can be seen from Fig. 1 that a large locked mode grows at $t = 128$ms. We term this event as 'mode penetration'. When mode penetration occurs there is always a strong confinement degradation, leading to complete suppression of the sawtooth oscillation. As the RMP field is switched off, a large mode can be seen to 'spin-up' on the $m = 2$ $\dot{b}_\theta$, and the $n = 1$ radial field, channels.

3 Theoretical Interpretation

We interpret the mode penetration event shown in Fig. 1 as the sudden onset of magnetic tearing, resulting in the formation of a locked (2,1) island. This interpretation arises from our theory of the interaction of RMP fields with rotating plasmas, which is presented in full in Ref. 5. There we demonstrate, both analytically and numerically, that a rotating plasma will resist tearing due to an applied RMP field until a threshold field strength is exceeded. The threshold vacuum field strength at the edge of the plasma is given by

$$\left[\frac{(b_{r\,\mathrm{vac}})_{\mathrm{crit}}}{\epsilon B_\phi}\right]_a = \frac{6.7}{m}\left(\frac{r_s}{a}\right)^{2-m} g^2(\zeta)\mathcal{I}^{2/3}\frac{(f_s\tau_H)^{4/3}}{(ms)^{1/3}}(-\Delta_0' r_s)^{1/3}, \qquad (1)$$

where Δ'_0 is the natural Δ' evaluated at the island separatrix, the shear $s = (rq'/q^2)_{r_s}$, $\epsilon = a/R$, $g^5 - g^2 - \zeta^5 = 0$, with $\zeta = 0.397\left[(\mathcal{I}^{1/3}(-\Delta'_0 r_s)^{2/3}(ms)^{4/3})/(f_s^{7/3}\tau_M\tau_H^{4/3})\right]^{1/5}$, f_s is the mode frequency, and τ_M is a momentum confinement time. If the plasma is free to rotate poloidally then $\mathcal{I} = 1$, if on the other hand poloidal rotation is strongly inhibited (as expected neo-classically) then $\mathcal{I} = q(r_s)R/r_s$. Equation (1) shows the mode penetration threshold is a function of mass density (since the Alfven time $\tau_H = \mu_0 R\sqrt{m_i n_i}/B_T$). To test the experimental dependence of the threshold field on density, a wide scan in density and RMP current was conducted at $I_p \sim 96$kA and $B_T = 1.1$T ($\Rightarrow q_\psi \sim 4.3$); the results are shown in Fig. 2 where the mode penetration threshold is compared with the theoretical expectation for toroidal rotation. In making this theoretical comparison we assumed $\Delta'_0(W) = -\alpha(W/a^2)$ with $\alpha = 3$ chosen to give the 'best fit' results shown in Fig. 2. This expression for $\Delta'_0(W)$ arises from the normal nonlinear approximation, $\Delta'_0(W) = \Delta'_0(0) - \alpha(W/a^2)$ [6], and noting the fact that the driven $m = 2$ islands are much larger than those which occur naturally, so that $\mid \Delta'_0(0) \mid << \mid \alpha W/a^2 \mid$. For typical values of α indicated by Δ' calculations ($\alpha \sim 30$) we find the penetration threshold is reproduced by assuming $\sim 1/5$ of the rotation to be poloidal (and the remainder toroidal). We have also assumed for the theoretical comparison in Fig. 2 that $n_e \propto \sqrt{1 - r^2/a^2}$ and taken the ratio of ion to electron plasma mass as $M_i/M_e = 1.88 m_p/m_e$, which is calculated from measurements, of the Deuterium to Hydrogen ion ratio, and Z_{eff}. Over the range of data shown in Fig. 2, Z_{eff} varies from 2.3 to 4.3 and the D:H ratio varies from 0.73 to 2.13, which gives $M_i/M_e = (1.88 \pm 0.23) m_p/m_e$. This M_i/M_e range represents an effective error bar in theoretical threshold current of $\pm 7\%$. The results in Fig. 2 show both the boundaries for mode penetration and disruptions caused by the (2,1) RMP fields. At high density the disruption and penetration boundaries merge and the distinction becomes ambiguous. The $m = 2$ island widths causing these disruptions are $W/a \sim 20\%$ for $I_c \sim 2$kA. It should be noted that the current profile is expected to vary with $\bar{n}_e$, and so α should vary with $\bar{n}_e$, perhaps accounting for some of the discrepancies in Fig. 2.

We interpret the spin-up event in Fig. 1 as the island driven by the RMP field unlocking as the RMP mode-locking force decreases, and then spinning-up under the influence of the viscous torque exerted by the rotating plasma. Finally, the island decays away on a resistive timescale since it is no longer driven by the RMP. Fourier analysis (in geometric poloidal angle) shows the unlocking mode to be dominantly $m = 2$, with about 30% $m = 3$ and 10% $m = 1$ sidebands. Taken in conjuction with the toroidal mode number measured by the locked-mode coils, shows that the penetrated mode is dominantly $m = 2$, $n = 1$.

According to standard Rutherford island theory [6,7], assuming linear saturation and neglecting wall effects, the island decay after the RMP field is switched off obeys

$$I_1 \tau_R \frac{d}{dt}\left(\frac{W}{a}\right) = a\Delta'_0(0) - \alpha\left(\frac{W}{a}\right), \qquad (2)$$

where $a = 20$ cm is the radius of the plasma edge, $\tau_R = \mu_0 a^2/[\eta_\parallel(r_s)]$ is the resistive timescale, and $I_1 = 2.326$. The solution to Eq. (2) is $W = W_s + (W_0 - W_s)e^{-t/\tau_0}$, where $W_0 = W(t = 0)$, W_s is the final decayed natural island width, and $\tau_0 = I_1\tau_R/\alpha$. In Fig. 3 we plot $\ln[(W - W_s)/W_0]$ as a function of time during a typical spin-up event for a shot with $\bar{n}_e = 1.5 \times 10^{19}\mathrm{m}^{-3}$. It should be noted that the RMP coil current in this case is

switched off rapidly, and that mode rotation does not start until I_c has dropped to $\sim 1/10$ of its value at mode penetration. This means that the $m = 2$ island induced by the RMP decays at a rate governed by the natural $\Delta_0'(W)$ [the RMP plays no direct role]. The fact that a very good straight line is obtained initially in Fig. 2, indicates that the first stages of island decay obey Rutherford's island theory rather well. From Fig. 3, we estimate $\tau_0 \approx 4.6$ ms, which corresponds to $\tau_R \approx 40$ms, a quite resonable value at $q = 2$. It is most important that we have been able to verify Rutherford's island theory, since it is the starting point for our theory of the interaction of RMP fields with rotating plasmas [5].

In order to model the viscous spin-up of the island we use of the following model equation (which neglects wall effects)

$$\frac{d}{dt}\Delta f + \left(\frac{a}{\Delta r}\right)^2 \frac{\Delta f}{\tau_M} = 0. \qquad (3)$$

Here, $\Delta f = f - f_s$ is the mode frequency of the island measured with respect to the natural mode frequency ($f_s \simeq 14.5$ kHz), Δr is the region of the plasma which co-rotates with the island during spin-up, and $\tau_M = a^2/\nu_\perp(r_s)$ is a momentum confinement time. Equation (3) has the solution $\Delta f = (\Delta f)_0 e^{-t/\tau_1}$, where $\tau_1 = (\Delta r/a)^2 \tau_M$, and $(\Delta f)_0 = \Delta f(t = 0)$. The change in mode frequency during the spin–up event in Fig. 1 is well described by this exponential form and implies $\tau_1 \approx 3.8$ms, which implies a momentum confinement time of ~ 5ms. This is to be compared with energy confinement times of ~ 2ms during mode penetration, and ~ 4ms otherwise. To obtain this momentum confinement time we have used $\Delta r/a = 0.8$. This estimate arises from the fact that mode unlocking occurs at $\sim 1/2$ the RMP current required for mode penetration (when the RMP current is reduced slowly). This hysteresis arises because at mode penetration the scale length over which the viscous torque acts is given by the island width, whereas at mode unlock it is given by Δr. Since the ratio of mode locking, to opposing viscous torque is $\propto \Delta r I_c^2$, we obtain $\Delta r/a \sim 0.8$ (using the penetrated $m = 2$ island width $W/a \sim 0.2$).

4 Conclusions

Many of the features of the mode penetration and associated mode spin–up events observed in COMPASS–C are well described by the theory outlined in Ref. [5]. The threshold scaling for mode penetration [Eq(1)] is in good agreement with the experimental results as shown in Fig. 2. The mode spin–up allows a direct confirmation of Rutherford island theory [7] and also allows the viscous momentum confinement time to be estimated.

In conclusion we note that the good agreement of theory and experiment allows the effects of error fields in future devices (particularly next-step tokamaks) to be determined with confidence (eg in ITER the critical error field $\lesssim 0.5$ gauss for penetration, see [4]).

References

[1] A.W.Morris et al, IAEA meeting Washington USA 1990.
[2] F Karger et al, Proc 6th IAEA conf Bertesgaden **1** 274 1976.
[3] J.J.Ellis et al, Proc 10th IAEA conf London **1** 363 1985.
[4] A.W.Morris et al, this conf.
[5] R.Fitzpatrick and T.C.Hender, Phys Fluids **3** 644 1991.
[6] R.B.White et al, Phys Fluids **20** 800 1977.
[7] P.H.Rutherford, Phys Fluids **16** 1903 1973.

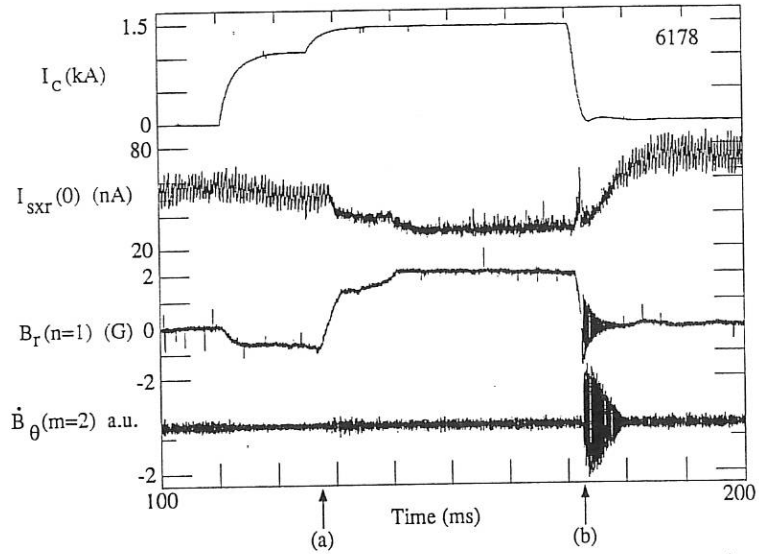

Fig. 1 Effects of applying (2,1) RMP saddle current (I_c). At mode penetration ($t = 128ms$, labeled (a)) the SXR intensity declines, while the $n = 1$ radial field (B_r) shows a growing mode. The large unlocking mode ($t = 173ms$, labeled (b)) is visible on the $m = 2$ $\dot{B}_\theta$.

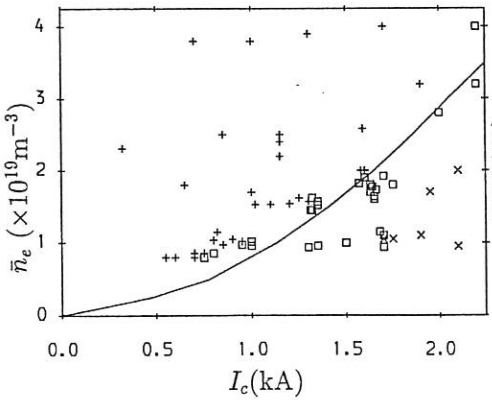

Fig. 2 Dependence of mode penetration on saddle current (I_c) and density ($\bar{n}_e$). The '+' denote no mode penetration, the '□' a penetrated mode and the 'X' a disruption. The solid line is the theoretical expectation for toroidal rotation.

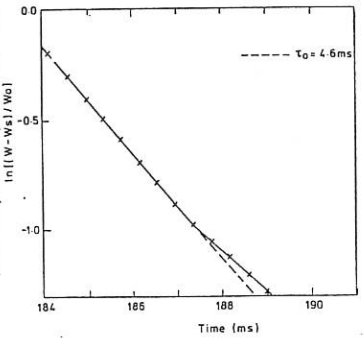

Fig. 3 Decay rate of island width at mode unlocking, showing a decay time of 4.6ms.

MARFE STABILITY

T C Hender* and J A Wesson

JET Joint Undertaking, Abingdon, Oxon, OX14 3EA, UK.
* UKAEA/Euratom Fusion Association, Culham Laboratory, Abingdon, Oxon, OX14 3DB, UK.

1 Introduction

The MARFE has been studied previously by several authors [1,2,3]. These studies show that the MARFE is driven by a radiative coalesence instability, but can be stabilised by sufficiently large parallel and perpendicular thermal conductivities ($\kappa_\parallel$, $\kappa_\perp$). In this paper we present a new analytic formulation which self-consistently treats the axisymmetric thermal equilibrium and the stability of the MARFE perturbation. We also present results from 2-D numerical simulations which are in good agreement with this analytic theory. Finally we will discuss potential implications of our theory in interpreting experimental results.

2 Linear MARFE Stability

Our analysis is based on the heat balance equation

$$\frac{3n}{2}\frac{\partial T}{\partial t} = \nabla.\kappa\nabla T - nn_i R(T) \tag{1}$$

where the thermal conductivity has a value $\kappa_\parallel$ parallel to $\vec{B}$ and $\kappa_\perp$ perpendicular to $\vec{B}$, n and n_i are the electron and impurity densities, and $R(T)$ is the radiation function. To analyse the linear MARFE stability threshold we assume steady state ($\partial/\partial t = 0$) and take the temperature to be $T(r) + \tilde{T}(r)\cos\theta$. For the perturbed temperature the linearised form of Eq. (1) is

$$\kappa_\perp \frac{d^2\tilde{T}}{dr^2} - \kappa_\parallel k_\parallel^2 \tilde{T} = nn_i T^2 \frac{d}{dT}\left(\frac{R(T)}{T^2}\right)\tilde{T} \tag{2}$$

where we have used pressure balance along the magnetic field ($\tilde{n}T + n\tilde{T} = 0$), assumed that $n_i \propto n$ and taken the parallel wavenumber to be $k_\parallel = 1/Rq$. Equation (2) has the awkward property of involving derivatives in r and T. However, we can substitute for the term involving the radial derivatives using

$$\frac{d^2\tilde{T}}{dr^2} = \left(\frac{dT}{dr}\right)^2 \frac{d^2\tilde{T}}{dr^2} + \frac{d^2T}{dr^2}\frac{d\tilde{T}}{dT} \tag{3}$$

where the derivatives dT/dr and d^2T/dr^2 can be determined from the equilibrium relation

$$\kappa_\perp \frac{d^2T}{dr^2} = nn_i R(T) \tag{4}$$

and its integral with respect to T. Substitution of relation (3) into Eq. (2) gives

$$(\Lambda_\perp - 2S(T))\frac{d^2\tilde{T}}{dT^2} = -R\frac{d\tilde{T}}{dT} + (\Lambda_\parallel T^{5/2} - \phi(T))\tilde{T} \tag{5}$$

where we define normalised thermal conductivities

$$\Lambda_\perp = \frac{\kappa_\perp}{nn_i}\left(\frac{dT}{dr}\right)_+^2, \qquad \Lambda_\parallel = \frac{k_\parallel^2}{nn_i}\left(\frac{\kappa_\parallel}{T^{5/2}}\right)$$

and $S(T)$ and ϕ(T) are radiation functions

$$S(T) = \int_T^\infty R(T)dT, \qquad \phi(T) = -T^2\frac{d}{dT}\left(\frac{R}{T^2}\right).$$

Here the notation $(dT/dr)_+$ denotes that it is to be evaluated on the high temperature side of the radiating layer. Equation (5) is the required equation for marginal MARFE stability and may be regarded as an eigenvalue equation for $\Lambda_\perp$, at a given $\Lambda_\parallel$ (or vice-versa).

To illustrate the nature of the solutions, Eq. (5) has been solved numerically, using a coronal carbon model [4] for $R(T)$, to obtain the relationship between the $\Lambda_\perp$ and $\Lambda_\parallel$; the results are shown in Fig. 1, where the units are SI except for T which is in eV. The boundary condition as $T \to \infty$ is $\tilde{T} \to 0$, while at $T = 0$ the boundary condition is less certain, and so results are shown for $\tilde{T}(0) = 0$ and $\tilde{T}'(0) = 0$. The physical significance of the boundary $\Lambda_\perp = 2S(0)$ in Fig. 1 may be seen by deriving the following relation from Eq. (4):-

$$\Lambda_\perp = \frac{S(0)}{\hat{P}(1 - \hat{P}/2)} \tag{6}$$

where $\hat{P} = P_{rad}/P_{in}$ is the radiated power fraction. From Eq. (6) we find at a 100% radiated power ($\hat{P}$=1), that $\Lambda_\perp = 2S(0)$. So the line $\Lambda_\perp = 2S(0)$ represents the limit at which detached non-steady state solutions occur, possibly leading to a disruption.

3 2-D NUMERICAL SIMULATIONS

We have also solved Eq. (1) numerically, to obtain non–linear two–dimensional solutions, $T(r, \theta)$. Again pressure balance along the magnetic field and $n \propto n_i$ are assumed. In the simulations the density is gradually ramped, producing the effect of increasing the radiated power towards, and beyond, the MARFE threshold. Figure 2 shows the development of a MARFE, which is triggered at $P_{rad}/P_{in} = 70\%$ (for the coronal carbon model used), and grows as further increases in density raise P_{rad}/P_{in}. In the absence of further density

increase the final solution shown ($t = 0.14$s) is a non-linearly saturated steady state. Comparisons of the radiated power fraction for MARFE instability show good agreement between the numerical simulations and the linear theory presented in Section 2.
The poloidal extent of the MARFE in Fig. 2 is rather larger than the typically quoted experimental result of $\sim 30°$ [5]. We have found that by introducing a Pfirsch–Schluter like poloidal asymmetry into $\kappa_\perp$ [$\propto (1 + a/R\cos\theta)$], that the poloidal extents found numerically come into much closer agreement with experimental observation. Similar results were obtained using the experimentally verified neoclassical poloidal asymmetry in the density [6].

4 DISCUSSION

We have presented a new formulation for MARFE stability which clarifies the relationship between parallel thermal conductivity, perpendicular thermal conductivity (or equivalently radiated power) and MARFE instability.
To make a detailed comparison of experiment and theory will require careful modelling of the impurity radiation, using for example a non–coronal equilibrium model [7]. However to examine some potential experimental consequences of our theory we employ the transformation $R(T) \rightarrow R(\xi T)$, which allows us to vary the peak radiation temperature (T_{peak}). The results for various values of T_{peak} (coronal carbon model) are shown in Fig. 3, with the MARFE being unstable to the left of each curve. In this case $\Lambda_\parallel$ has been replaced by a more experimentally relevant quantity, under the assumption that $k_\parallel = 0.1m^{-1}$ ($R \sim 3$m and $q \sim 3$) and that $\kappa_\perp = n\chi$ (with $\chi = 3\text{m}^2\text{s}^{-1}$). Likewise $\Lambda_\perp$ has been replaced by the radiated power fraction ($\hat{P}$) using Eq. (6). For given experimental conditions ($P_{in} =$ 10MW and $n = 5 \times 10^{18}\text{m}^{-3}$, say) an operating trajectory is defined as shown in Fig. 3 (broken line). It can be seen that as the peak radiation temperature increases so the radiated power fraction ($\hat{P}$), required to trigger the MARFE also increases (for given P_{in} and n). This rapid change in MARFE stability threshold with T_{peak} may account for the observed differences in MARFE behaviour between Carbon and Beryllium limiter operation in JET [8]. With Beryllium MARFE's typically form at ~40% radiated power in contrast to Carbon for which MARFE's generally occur at ~100% radiated power, just prior to a disruption [9].

References

[1] T Stringer, Proc 12th EPS Budapest 1985, **1** 86.
[2] J Neuhauser et al, Nucl Fusion **26** 1679 1986.
[3] J F Drake, Phys Fluids **30** 2429 1987.
[4] D E Post et al, Atomic Data and Nucl Data Tables **20** 397 1977.
[5] B Lipschultz et al, Nucl Fusion **24** 977 1984.
[6] R D Durst and P S Haynes, this conf.
[7] P G Carolan and V A Piotrowicz, Plasma Phys **25** 1965 1983.
[8] C Lowry and the JET team 1989, Jet preprint JET-P(89)80.
[9] J A Wesson et al. Nucl Fusion **29** 641 1989.

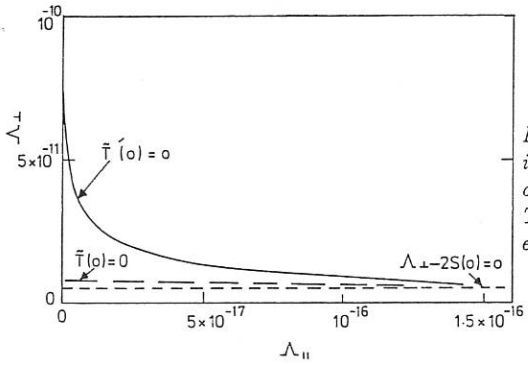

Fig. 1 Marginal MARFE stability threshold for the two choices of boundary condition at $T = 0$. The MARFE's are unstable below each curve.

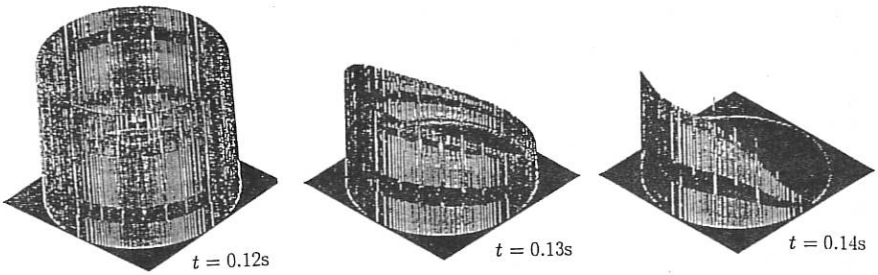

Fig. 2 Plots of equal radiated power showing developement of MARFE in 2-D simulation.

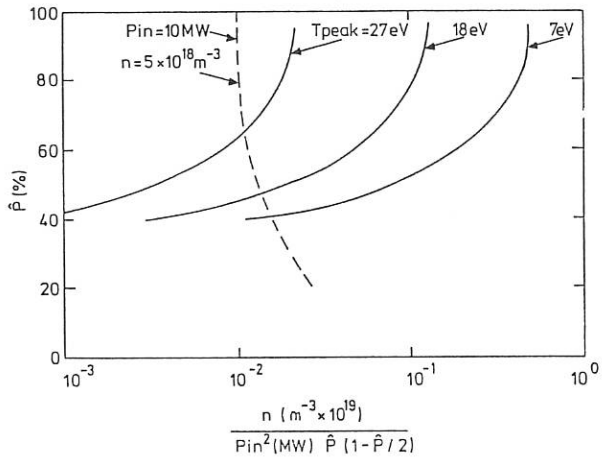

Fig. 3 Marginal MARFE stability threshold (using boundary condition $\tilde{T}(0) = 0$) for various peak radiation temperatures, and a typical operating trajectory ($P_{in} = 10MW$, $n = 5 \times 10^{18}m^{-3}$). MARFE's are unstable above their respective boundaries.

FREE BOUNDARY TOROIDAL STABILITY OF IDEAL AND RESISTIVE INTERNAL KINKS

G. VLAD, Associazione Euratom-ENEA sulla Fusione, C.R.E. Frascati
C.P. 65-00044 -Frascati, Rome, Italy

H. LUTJENS, A. BONDESON, Centre de Recherches en Physique des Plasmas,
Association Euratom - Confédération Suisse, Ecole Polytechnique Fédérale de Lausanne,
21 Av. des Bains, CH-1007 Lausanne, Switzerland

I. INTRODUCTION

Recently, there has been a strong interest in the stability properties of the internal kink mode. This has been spurred mainly by experimental observations of sawtooth oscillations on large tokamaks revealing unexpected features such as double sawteeth with partial reconnection, fast crashes, and central q-values well below unity [1]. These observations are all difficult to reconcile with the conventional Kadomtsev model in which the crash is triggered by the resistive kink mode becoming unstable when the safety factor q falls below unity. The theoretical understanding of the sawtooth activity is made difficult by the sensitivity of the internal kink mode to several factors such as q-profile, pressure, resistivity, aspect ratio, shaping of the cross-section, and even wall position. In addition, the internal kink in a torus (with $q > 1/2$) is a rather weak instability and should therefore be sensitive to kinetic effects.

Here, we present results from a study of the resistive and ideal MHD properties of the internal kink mode. Generally, we have numerically computed growth-rates as functions of various parameters, using the full-resistive-MHD toroidal stability code MARS [2] and the cubic element equilibrium code CHEASE [3].

II. INFLUENCE OF THE CURRENT PROFILE

A major uncertainty for the understanding of the sawteeth is the shape of the current profile. Here, we restrict attention to circular cross-section with an aspect ratio of 4 and choose two types of current profiles. One has uniformly low shear inside a certain radius $r = r_p \approx 0.4a$, outside which the shear increases rapidly. The other has shoulders in the current profile which produce locally low shear near $q = 1$, while the central safety factor q_0 is well below unity. We refer to these as "low-shear" and "TEXTOR" profiles [1], respectively.

Figure 1 shows the low-shear current profile $j = \langle j_\phi \rangle(r)$ (where r is a flux surface label proportional to the square root of the enclosed volume). This current profile is monotone, but the shear $\hat{s} = (r/q)\, dq/dr$ has a slight local minimum at $r = r_p \approx 0.4a$, $\hat{s}(r_p) \approx 0.03$. The shear does not exceed 0.032 in the entire region $r < r_p$. Profiles of this type may arise in sawtoothing discharges if total reconnection occurs within the $q \approx 1$ region, $r < r_p$, followed by neoclassical peaking of the current during the rise phase [4]. We have considered a family of equilibria with self-similar current profiles where we specify the q-value at radius $r = r_p$. For this family, the central safety factor q_0 is related to $q_p \equiv q(r_p)$ by $q_0 \approx 0.948 q_p$. It may be useful to think of these equilibria as an approximation to the sequence in time during the ramp phase of a sawtooth, with q_0 and q_p decreasing functions of time. Figure 2 shows the resulting growth-rates for four different values of poloidal beta at the $q = 1$ surface (0.00, 0.05, 0.10, and 0.15) at Lundquist number $S \equiv \tau_{res}/\tau_A = 10^6$ (Fig 2a), 10^8 (2b) and 10^{10} (2c). For this q-profile, $q_p = 1$ locates the minimum shear ($\hat{s} \approx 0.03$) at the $q = 1$ surface, and when q_p is decreased below unity, the $q = 1$ surface moves out into the region of high shear. For instance, $q_p = 0.98$ gives $\hat{s}(q=1) \approx 0.22$. In all cases shown in Fig. 2, a conducting wall is assumed at $r = b = 1.2a$.

We note from Fig. 2 that *complete* resistive MHD stability is very rarely achieved. However, in many cases, the resistive growth-rates are small, and we are led to the conclusion that a weak internal kink is stabilized for most of the sawtooth cycle by effects not included in the model. A likely candidate for such stabilization is diamagnetic rotation. In present day tokamaks, ω_*/ω_A is typically between 0.5×10^{-3} and 10^{-2}, which is comparable to resistive

MHD growth-rates of the internal kink. It therefore appears plausible that diamagnetic rotation can stabilize the internal kink as long as its resistive-MHD growth-rate is not too large.

By comparing Figs. 2a-c for different values of S, we note a gradual change in the main factor determining the growth-rate. At $S = 10^6$, the growth-rates are mainly dependent on q_p, i.e., on the shear at the q = 1 surface, and are only weakly dependent on the pressure. This is typical of the resistive kink mode. This picture is modified somewhat at $S = 10^8$ which represents an intermediate case. The three lower curves in Fig. 2b ($\beta_{pol} = 0.00, 0.05, 0.10$) still show reasonably high growth-rates (about $2 \times 10^{-3}\ \omega_A$) for a current driven resistive mode, but for $\beta_{pol} \leq 0.1$, the pressure has only a weak influence on the growth-rates. For $\beta_{pol} = 0.15$, destabilization by pressure becomes significant. An interesting aspect of this "pressure driven" instability is that it is clearly sensitive to the q-profile and its growth-rate rises sharply when the q = 1 surface moves out into the region of high shear. Thus, although the instability is *pressure driven*, it can be thought of as being *triggered* by the *current profile*.

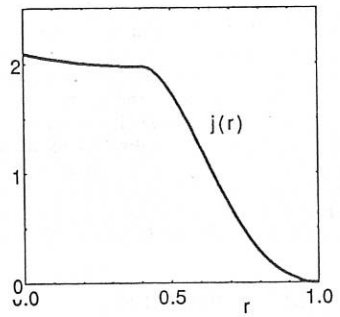

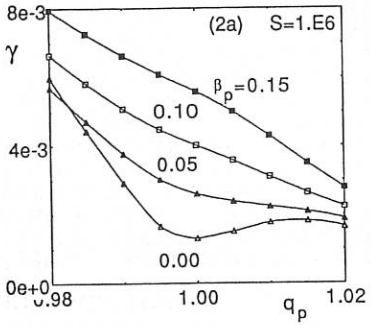

Figure 1. *Low-shear current profile*

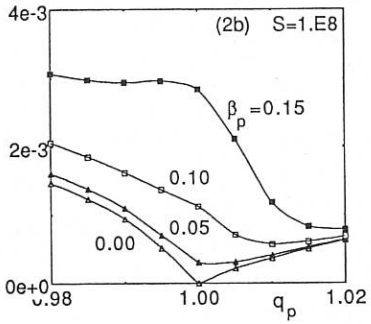

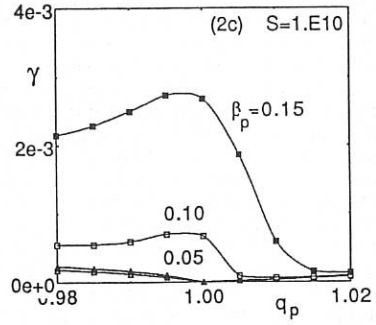

Figure 2. *Resistive growth-rates for low-shear current profile and different β_{pol}*

Much more clear changes from the low-S picture are seen in Fig 2c for $S = 10^{10}$. Here, the resistive growth-rates for $\beta_{pol} = 0.00$, and 0.05 are rather small (a few times $10^{-4}\ \omega_A$) and the pressure driven instability is clearly dominant. Comparing the growth-rates with those for $S = 10^8$, we see that the pressure driven instability is essentially ideal. Thus, it appears that as S is increased, the linear instability leading to the sawtooth crash becomes more and more an ideal, pressure driven instability. However, *this ideal mode is sensitive to details of the current profile and can be triggered by a slight shift in the q-profile.* In fact, the variation of the

growth-rate with q_p at high S and not-too-small β_{pol} is more pronounced than for the resistive kink mode at low S. Figure 2c also shows that the critical β_{pol} for ideal stability is rather low, about 0.1 for this current profile. We have obtained results similar to those in Fig. 2 for a current profile with twice the shear in the central region. In this case, the resistive mode at low pressure gives somewhat higher growth-rates than the low-shear case shown in Fig. 2.

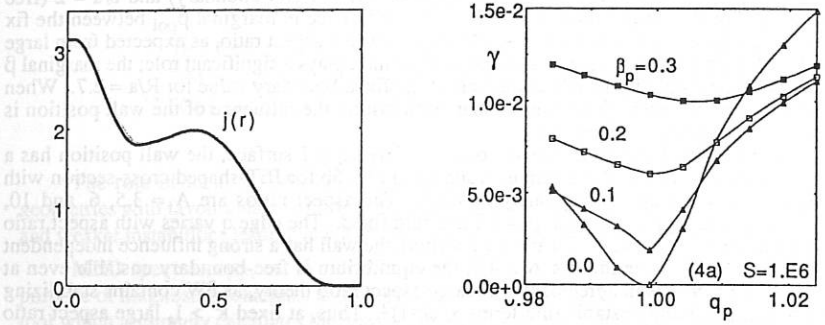

Figure 3. *TEXTOR current profile*

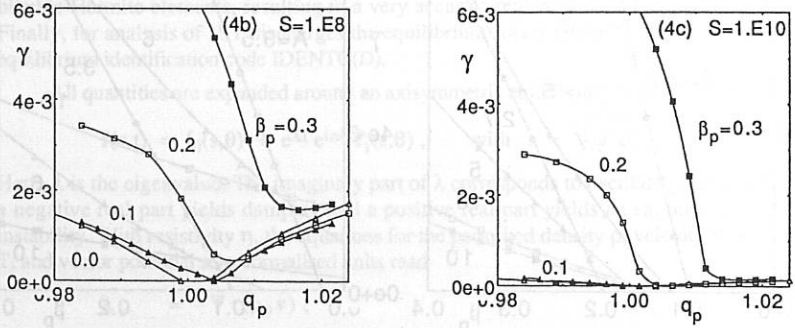

Figure 4. *Resistive growth-rates for TEXTOR current profile and different β_{pol}*

We have also computed resistive growth-rates for a current profile of TEXTOR type, as shown in Fig. 3. The shoulders in the current profile were adjusted so that the shear has a minimum of about 0.034 at $r = r_p \approx 0.44a$. In this case, the global shear in the central region is strong and $q_0 \approx 0.634 q_p$ is well below unity. Figure 4 shows the growth-rates for different S-values and β_{pol} = 0.0, 0.1, 0.2, and 0.3. In general terms, the behavior is similar to that for the low-shear profile, but the TEXTOR profile supports about twice the pressure before becoming ideally unstable.

III. WALL AND SHAPING EFFECTS

Although the displacement of the internal kink mode is mainly localized to the region inside the q = 1 surface, the magnetic perturbation outside q = 1 is not small and it is important for the mode stability [5]. Numerically, we find that the ideal stability boundaries are strongly influenced by wall position when the q = 1 radius is sufficiently large and the aspect ratio is low. As an example, Fig. 5a shows growth-rates for the ideal internal kink as a functions of β_{pol} at q=1 for a sequence of circular equilibria with $r_{q=1}/a \approx 0.6$ and edge q between 2 and 3. Two different wall positions have been considered: b/a = 1 (fix boundary) and b/a = 2 (free boundary). For this equilibrium, we find that the difference in marginal β_{pol} between the fix and free boundary cases scales as the square of the inverse aspect ratio, as expected from large aspect ratio theory. At low aspect ratio, the wall position plays a significant role; the marginal β for free boundary stability is only about half of the fixed boundary value for R/a = 2.7. When the edge q is raised above 3 for the circular equilibrium, the influence of the wall position is weak and not of practical significance.

In the case of shaped cross-section and a large q = 1 surface, the wall position has a more dramatic influence. An example is shown in Fig. 5b for JET-shaped cross-section with elongation κ = 1.7 and triangularity δ = 0.3. The aspect ratios are A = 3.5, 6, and 10, respectively, and $r_{q=1}$ = 0.6a and q_0 = 0.7 are held fixed. The edge q varies with aspect ratio but remains between 3 and 4. For this equilibrium, the wall has a strong influence independent of the aspect ratio. Note that for A > 4.5, the equilibrium is free-boundary unstable even at zero beta. This, too, is in agreement with large aspect ratio theory, as δW contains stabilizing terms $\propto (r_{q=1}/R)^2$ and destabilizing terms $\propto (\kappa\text{-}1)^2$. Thus, at fixed κ > 1, large aspect ratio theory predicts instability even at zero beta when the aspect ratio is sufficiently large. Triangularity has a stabilizing influence, but for JET geometry and the q-profile used here, this stabilization is insufficient to compensate for the destabilization by ellipticity.

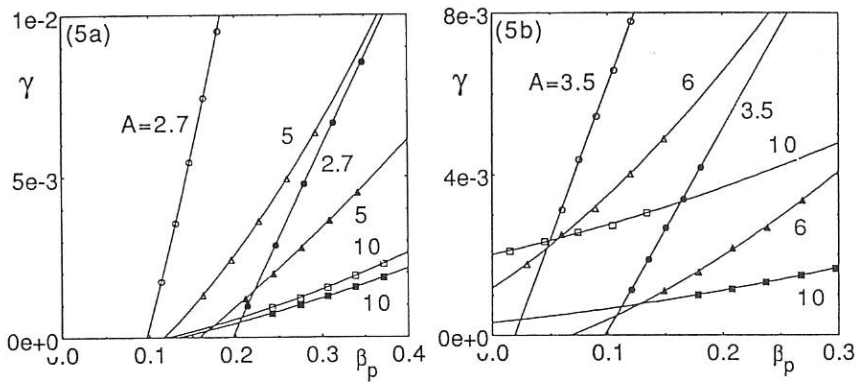

Figure 5. *Ideal growth-rates for free and fixed boundary at different aspect ratios. Free boundary is indicated by open symbols. (a) Circular and (b) JET cross-section*

REFERENCES

1. H. Soltwish, W. Stodiek, J. Manickam, *et al*, IAEA Kyoto (1986), Vol I, p. 263.
2. A. Bondeson, G. Vlad and H. Lütjens, EPS Amsterdam (1990), Vol. II, p.906.
3. H. Lütjens, A. Bondeson, and A. Roy, LRP 405/90, submitted to Comput. Phys. Comm.
4. W. Park and D.A. Monticello, Nucl. Fusion **30**, 2413 (1990).
5. M.N. Bussac, R. Pellat, D. Edery and J.L. Soule, Phys. Rev. Lett. **35**, 1638 (1975).

COMPUTING THE DAMPING AND DESTABILIZATION OF GLOBAL ALFVÉN WAVES IN TOKAMAKS

W. Kerner, S. Poedts*, J.P. Goedbloed**,
G.T.A. Huysmans**, B. Keegan, and E. Schwarz*

JET Joint Undertaking, Abingdon, OXON., OX143EA, UK
* Max-Planck Institut für Plasmaphysik, Garching, Germany
** FOM-Instituut voor Plasmafysica, Nieuwegein, The Netherlands

The role of ideal MHD in magnetic fusion is in the first place to discover magnetic geometries with favourable equilibrium and stability properties. Non-ideal effects cause slower and weaker instabilities leading to enhanced transport and often to violent disruptions.

MHD spectroscopy, i.e. the identification of ideal and dissipative MHD modes for the purpose of diagnosing tokamaks and optimising their stability properties, requires a numerical tool which accurately calculates the dissipative MHD spectra for measured equilibria. The new spectral code CASTOR (**C**omplex **A**lfvén **S**pectrum for **TOR**oidal Plasmas), together with the equilibrium solver HELENA [1], provides such a tool. In CASTOR, the fluid variables ρ, $\mathbf{v}$, T, and $\mathbf{b}$ are discretized by means of a combination of cubic Hermite and quadratic finite elements for the radial direction and Fourier modes for the poloidal coordinate. The equilibrium in non-orthogonal flux coordinates ψ, θ, ϕ with straight field lines is computed using isoparametric bicubic Hermite elements, resulting in a very accurate representation of the metric elements. Finally, for analysis of JET discharges the equilibrium solver HELENA is interfaced with the equilibrium identification code IDENTC(D).

All quantities are expanded around an axisymmetric equilibrium ($\partial/\partial\phi = 0$) in the form

$$f(\mathbf{r},t) = f_0(s,\theta) + e^{\lambda t}\, e^{in\phi}\, f_1(s,\theta)\,, \qquad \text{with} \quad s = \sqrt{\psi/\psi_s}\,. \tag{1}$$

Here, λ is the eigenvalue. The imaginary part of λ corresponds to oscillatory behaviour, while a negative real part yields damping and a positive real part yields an exponentially growing instability. With resistivity η, the equations for the perturbed density ρ, velocity $\mathbf{v}$, temperature T, and vector potential $\mathbf{a}$ in normalised units read

$$\lambda\rho = -\nabla\cdot(\rho_0\mathbf{v})\,, \tag{2a}$$

$$\lambda\rho_0\mathbf{v} = -\nabla(\rho_0 T + T_0\rho) + (\nabla\times\mathbf{B}_0)\times\mathbf{b} + (\nabla\times\mathbf{b})\times\mathbf{B}_0 - \nabla\cdot\Pi\,, \tag{2b}$$

$$\lambda\rho_0 T = -\rho_0\mathbf{v}\cdot\nabla T_0 - (\gamma-1)\,\rho_0 T_0\nabla\cdot\mathbf{v}\,, \tag{2c}$$

$$\lambda\mathbf{a} = \mathbf{v}\times\mathbf{B}_0 - \eta_0\nabla\times\nabla\times\mathbf{a}\,, \qquad \text{where} \quad \mathbf{b} = \nabla\times\mathbf{a}\,. \tag{2d}$$

The pressure tensor Π contains the influence of the anisotropic bulk plasma and of the energetic ions interacting with the fluid. The latter requires the solution of the linearised Vlasov equation for both trapped and passing particles yielding a complicated dependence on λ.

In the absence of particle effects, the resulting generalized non-symmetric eigenvalue problem $\mathbf{A}\,\mathbf{x} = \lambda\,\mathbf{B}\,\mathbf{x}$ with block tridiagonal matrices $\mathbf{A}$ and $\mathbf{B}$ is solved by means of different algorithms (QR, inverse vector iteration, Lanczos) which produce the complete spectrum, single eigenvalues, or branches of the spectrum in the complex λ-plane, respectively. The structure of the code allows for easy extension with other dissipative terms, e.g. viscosity and thermal conductivity.

Resistive spectra for tokamak plasmas with elongated cross-section have been calculated. The central role played by the Alfvén branch is stressed. Global Alfvén modes are closely related to the ideal Alfvén continua. Owing to their global nature these modes can easily be destabilised by energetic particle effects such as fusion-born α-particles. On the other hand, these global Alfvén waves are expected to experience damping by phase mixing through coupling to continuum modes, similar to the quasi-modes discussed in Ref. [2]. This damping is especially pronounced for non-uniform density profiles.

CASTOR is used for studying quantitatively the damping of toroidal Alfvén modes. Since the continuum modes are dominated by their singular behaviour at specific flux surfaces, the corresponding sub-spectra are obtained by solving a reduced eigenvalue problem $\tilde{\mathbf{A}}\,\mathbf{x} = \lambda\,\tilde{\mathbf{B}}\,\mathbf{x}$ on each flux surface. This decoupling with respect to the radial dependence is achieved by taking into account the fact that the tangential components of $\mathbf{v}$ and $\mathbf{b}$ are more singular ($\sim 1/s$) than the normal component ($\sim \ln s$). A circular cross-section equilibrium with aspect ratio A = 2.5, the safety factor increasing from $q_0 = 1.05$ on axis to $q_s = 2.3$ at the plasma surface and with a small pressure, has been analysed. First, we have reproduced the results of Ref. [3] for uniform density. For a toroidal wave number $n = -1$ the $m = 1$ and 2 continua interact thereby producing a gap in the continuum around $s = 0.8$ where $q \approx 1.5$. In the cylindrical limit this coupling vanishes producing two independent continua for $m = 1$ and $m = 2$. In addition, inside the gap a global Alfvén mode exists with large $m = 1$ and $m = 2$ components. Obviously, this mode does not couple to continuum modes and, hence, does not exhibit damping.

Next, cases with a more pronounced mode coupling and exhibiting damping are examined. The density profile is chosen as

$$\rho(s) = 1 - (1 - D)\,s^2 \tag{3a}$$

with $D = 0.05$. The mode numbers are chosen as $n = -3$ and $m = 2$, 3, 4, 5, and 6. The corresponding continua are displayed in Fig. 1a. It is evident that there are gaps in the continua extending from $\mathrm{Im}\,\lambda = 0.40$ to 0.59 near $s = 0.47$ ($m = 3$ and 4), from $\mathrm{Im}\,\lambda = 1.01$ to 1.08 near $s = 0.67$ ($m = 3$ and 5), and from $\mathrm{Im}\,\lambda = 0.35$ to 0.74 near $s = 0.78$ ($m = 4$ and 5), etc. These gaps are due to toroidal effects coupling continuum branches with different poloidal wave numbers m and m' at the surfaces $q = -(m + m')/2n$. In addition, the total ideal MHD spectrum in the range from $0 < \mathrm{Im}\,\lambda < 2$ is shown in Fig. 1b. Due to the finite numerical resolution, continua show up as closely spaced discrete eigenvalues. Two global toroidicity-induced Alfvén eigenmodes[3] are found with a frequency inside the gaps, viz. $\mathrm{Im}\,\lambda = 0.44$ and 0.54, corresponding to the toroidal coupling of $m = 3$ and 4 harmonics dominant around $s = 0.47$ and to the coupling of $m = 4$ and 5 harmonics dominant around $s = 0.78$. The latter one is shown in Fig. 2. Both normal modes experience coupling to a continuum $m = 6$ mode localised near the plasma boundary. The damping of the two global modes inside the large gap is quite small, viz. $\delta = |\mathrm{Re}\,\lambda / \mathrm{Im}\,\lambda| \approx 10^{-3}$. In Fig. 1b the gap just above $\mathrm{Im}\,\lambda = 1$ is also visible with an eigenvalue inside.

In ideal MHD the damping is, of course, zero and the singularity is represented in the limit of increasingly finer mesh as $1/\Delta_s$, where Δ_s is the spatial resolution across the singular surface. The physical significance of this is revealed by introducing the Landau contour in the complex λ-plane for performing the Laplace transform or by introducing damping in the system, e.g. resistivity, as done here. The physically correct damping is found in the limit of asymptotically small η, where δ becomes independent of the resistivity as shown in Ref. [2]. Much stronger damping is found when all Fourier harmonics couple to the singularity, as shown in the eigenfunction of Fig. 3. This corresponds to a global mode inside a small gap due to m = 2 and 3 coupling at the q = 2.5 surface computed for a slightly different equilibrium with larger pressure (β = 1 %). The damping, for n = –1 and m = 1, 2, 3, 4, 5, is found to be $\delta \approx$ 4%. These findings reveal that the damping of the global Alfvén modes can significantly vary according to the weight of the singular part in the overall global eigenfunction.

The damping of the first case is enhanced by slightly changing the density to

$$\rho(s) = [1 - (1 - D)\, s^2]^2 \qquad (3b)$$

with D = 0.01 and the safety factor on axis to $q_0 = 0.8$, so that m = 2 and 3 couple on the q = 5/6 surface and m = 3 and 4 couple on the q = 7/6 surface. The gap structure is displayed in Fig. 4. Two global Alfvén modes are found with Im λ = 0.64 and 0.89, respectively. These modes couple strongly to the continua at positions and with wave numbers being evident from Figs. 4 and 5. For the mode in the m = 3 and 4 gap the m = 3 component is singular at s = 0.78 and the m = 4 and 5 components on the outside of the plasma. In both cases the damping is about $\delta \approx 1 - 2\%$.

Clearly, the analysis can be extended to tokamaks with a non-circular cross-section such as JET. A general result is that the mode coupling is enhanced. For interesting configurations ten and more Fourier harmonics contribute to the eigenfuncion. This leads to a complicated structure of the continua and associated gaps in it. This makes the numerical identification of global modes and their damping with resistivity more elaborate. It is emphasised that this damping is in the order of 1 - 5%.

The effect of energetic fusion-born α-particles on the marginally stable ideal MHD mode is twofold. It can act stabilising and destabilising according to Landau damping or inverse Landau damping [4], [5]. In order for this resonance condition to be satisfied the parallel fast ion velocity has to exceed the Alfvén speed $v_{\parallel} \gtrsim v_A$ ($\approx 10^9$ cm/sec for α-particles with 3.5 MeV) and, secondly, for destabilisation that the diamagnetic frequency exceeds the Alfvén frequency $\omega_{*h} > \omega_A$. In JET, these conditions are met by lowering the magnetic field to about 1 T and by appropriate off-axis heating. In the next step the response of the α-particles on the pressure tensor will be included in CASTOR. This changes the eigenvalue problem to a non-linear one which is solved by a Newton iteration scheme. By incorporating the eigenfunctions from the above normal-mode analysis approximate solutions should become attainable.

[1] G.T.A. Huysmans, J.P. Goedbloed, and W. Kerner, Proc. Europhysics 2nd Intern. Conf. on Computational Physics, Amsterdam (1990) .

[2] S. Poedts and W. Kerner, to appear.

[3] C.Z. Cheng and M.S. Chance, Phys. Fluids **29** (1986) 3695.

[4] G.Y. Fu and J.W. Van Dam, Phys. Fluids **B1** (1989) 1949.

[5] C.Z. Cheng, Princeton Plasma Physics Laboratory Report PPPL - 2717 (1990).

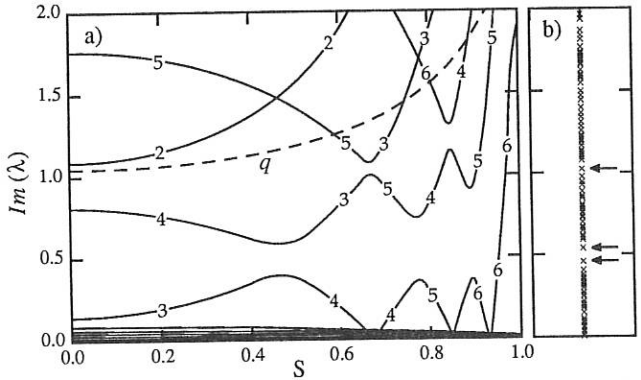

Fig. 1 a) Dependence of continuum frequencies on flux surface label s for n = – 3 and m = 2 - 6 for the density profile of Eq. (3a) with D = 0.05. The dominant Fourier harmonic m is indicated on each curve.
b) Total ideal MHD spectrum obtained with CASTOR.

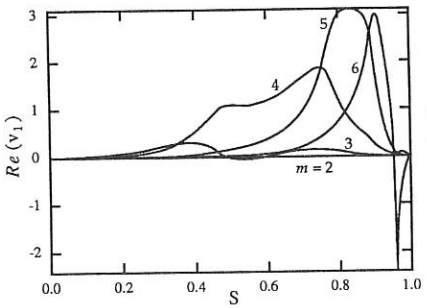

Fig. 2 Radial dependence of the harmonics of the normal component of the eigenfunction of the upper gap mode of Fig. 1b (Im λ = 0.54).

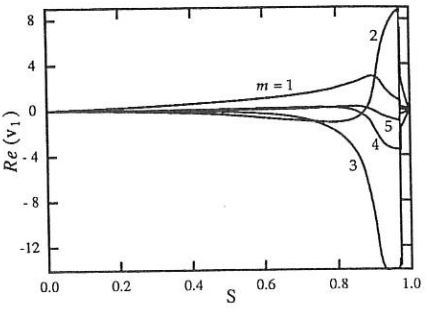

Fig. 3 Radial dependence of the harmonics of the normal component of the eigenfunction of the gap mode for n = - 1 and m = 2 - 6 for equilibrium with β = 1%.

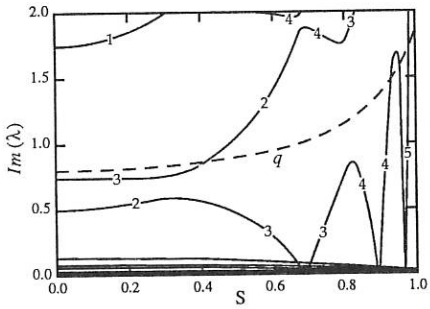

Fig. 4 Dependence of continuum frequencies on flux surface s for n = - 3 and m = 2 - 6 for $q_0 = 0.8$ and the density profile of Eq. (3b) with D = 0.01.

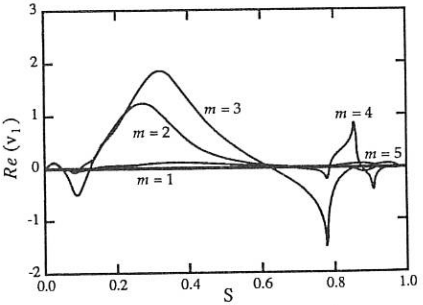

Fig. 5 Radial dependence of the harmonics of the normal component of the eigenfunction of the lower gap mode of Fig. 4 (Im λ = 0.64)

DISPERSION RELATIONS FOR GLOBAL ALFVEN MODES WITH m >>1

O.K.Cheremnykh, S.M.Revenchuk

Institute for Nuclear Research
of the Ukrainian Academy of Sciences, Kiev-28, 252028, USSR

Spectrum of global Alfven modes (GAM) is of great interest in connection with both Alfven wave heating of plasmas in magnetic traps and studying of various instabilities excited by high-energy particles. The present report is devoted to the investigation of spectrum of GAM with large poloidal wavenumbers m >>1. These modes are localized in radial coordinate in a vicinity of the point a_0 where Alfven frequency takes the minimum value:

$$\omega_A'\Big|_{a=a_0} = 0 . \qquad (1)$$

Here $\omega_A = k_\parallel c_A$, $k_\parallel$ is wavenumber in the direction of magnetic field, c_A is Alfven velocity and the prime means the derivative with respect to the radial coordinate a . Small oscillation equation for the GAM under consideration with the frequency ω has the form [1,2],

$$\frac{d}{dy}\left[\left(1+y^2\right)\frac{dX}{dy}\right] + \left[G - \Gamma^2\left(1+y^2\right)\right]X = 0 , \qquad (2)$$

where

$$G = \frac{L^2}{a^2}\frac{2sm}{m-nq}\Big|_{a=a_0} , \quad \Gamma^2 = \frac{m^2\Delta^2}{a^2}\Big|_{a=a_0} , \quad s = \frac{aq'}{q} ,$$
$$\Delta^2 = 2L^2\left[1-\omega^2/\omega_A^2(a_0)\right] , \quad L^2 = \omega_A^2/\omega_A^{2\prime\prime}\Big|_{a=a_0} , \qquad (3)$$

X is radial displacement of plasma column, $y=(a-a_0)/\Delta$, q is

safety factor and n is azimuth wavenumber.

The problem of GAM spectrum determination is reduced to the procedure of finding of eigenvalues G of Eq.(2) supplemented by the following boundary conditions,

$$X\Big|_{y \to \pm\infty} = 0 .$$

Using the change of variables,

$$y = \mathrm{sh}\, z , \quad X = \left(\mathrm{ch}\, z\right)^{-1/2} \Psi(z) , \tag{4}$$

we reduce Eq.(2) to the standard form of Schrödinger equation:

$$\left(d^2\Psi / dz^2\right) + \left[E - U(z)\right]\Psi = 0 \tag{5}$$

with the potential

$$U(z) = \Gamma^2 \left(\mathrm{ch}\, z\right)^2 + \left(2\,\mathrm{ch}\, z\right)^{-2} \tag{6}$$

and energy

$$E = G - 1/4. \tag{7}$$

Now GAM spectrum is determined by energy levels in the potential well (6). Since the potential U(z) is positive always, the energy levels are realized for positive values of energy E only, i.e. if the inequality

$$G > 1/4 \tag{8}$$

is satisfied. It follows from Eq.(8) that considering GAM may exist in presence of magnetic field shear only.

An analysis of Eq.(6) shows that the potential well takes two qualitatively different forms:

(a) If $\Gamma \geq 1/2$, the potential U(z) takes minimum value $U(0) = \Gamma^2 + 1/4$ at the point z=0 and increases monotonically with increasing of $|z|$.

(b) If $0 < \Gamma < 1/2$, the potential U(z) has local maximum at the point z=0 and two minima $U(\pm z_0) = \Gamma$ at the points $\pm z_0 = \mathrm{ch}^{-1}\left(1/\sqrt{2\Gamma}\right)$.

GAM spectra of two types correspond these two forms of the potential well. One of them connected with the potential

well of the form (a) describes the modes with frequencies, which are sufficiently away from Alfven continuum edge. The existence of this spectrum has been predicted by Appert et al. [1] and it has been analized by Mahajan et al. [2]. Near the bottom of the well the shape of the potential (a) only weakly deviates from the parabolic form, which is characteristic for an oscillator. This fact suggests that at least lowest energy level (N=0) differs slightly from the corresponding level of anharmonic oscillator. Expanding the potential (6) into Taylor series in the vicinity of the point z=0 up to the terms of order of z^4, we obtain the following dispersion relation for the mode N=0,

$$\Omega \simeq \Gamma^2 + 3/4 + \left(\Gamma^2 - 1/4\right)^{1/2} - \left(7/24\right)\left(\Gamma^2 - 1/4\right)^{-1/2}, \qquad (9)$$

from the solution of the standard problem. This relation describes correctly the ground level in plasma parameters region $G \gtrsim 1/2$.

We note that the dispersion relation Eq.(21) in Ref. [2] obtained for the lower numbers N may be used in fact for describing the ground state with N=0 and $\Omega > \Gamma^2 \gg 1$ only. For this limit case the dispersion relation by Mahajan et al. coincides with Eq.(9).

Higher energy levels condense due to strong anharmonicity of the potential (6), which has been neglected in analysis of the ground level. Using WKB-approximation, we obtain for the levels $N \gtrsim 1$:

$$\Gamma^2 \simeq \left(\frac{4}{e}\right)^2 \frac{\left(G - 1/4\right)^2}{G - 1/2} \exp\left[-\frac{\left(N + 1/2\right)\pi}{\left(G - 1/4\right)^{1/2}}\right]. \qquad (10)$$

In the limit $G \gg 1$ Eq.(10) coincides with Eq.(23) of Ref. [2].

The potential (b) has a form of two symmetrical wells separated by a barrier. Here GAM spectra of two types may take place. First of them exists, if $\Gamma < 1/2$ and $G < 1/2$, and it is placed near the bottom of both wells. This spectrum

describes GAM with the frequencies lying near the edge of Alfven continuum. In the case of infinitely wide barrier the energy levels for both wells would be the same. The finitness of the barrier leads to a splitting of each level into two ones. These modes are described well in the framework of WKB-approximation and satisfied the following dispersion relation,

$$\Gamma^2 = \frac{64\left(G - 1/4\right)^2}{e^4} \exp\left[-\frac{(2N+1)\pi}{\left(G-1/4\right)^{1/2}} \pm \frac{\exp\left[-\pi\left(1/2 - \sqrt{G-1/4}\right)\right]}{\left(G-1/4\right)^{1/2}}\right]. \qquad (11)$$

The spectrum of the second type for the potential (b) exists, if $G \geq 1/2$ and $\Gamma < 1/2$, and it is placed over the barrier. It coincides with the spectrum for the well (a), which is determined by the formulae (9) and (10).

REFERENCES

1. K.Appert, R.Gruber, F.Troyon, T.Vaclavic, Plasma Phys. 24 (1982) 1147.
2. S.M.Mahajan, D.W.Ross, G.L.Chen, Physics Fluids 26 (1983) 2195.

STABILIZATION EFFECTS ON TOROIDICITY INDUCED SHEAR ALFVÉN WAVES IN TOKAMAKS

H.L. Berk, Z. Guo, D.M. Lindberg, J.W. Van Dam

Institute for Fusion Studies, Austin, TX 78712, U.S.A.

M.N. Rosenbluth

University of California, San Diego, CA 92093, U.S.A.

From results from both theory (1,2) and experiment (3,4) there is concern that the Toroidal Alfvén Eigenmode (TAE) will be excited in an ignited plasma and cause anomalous radial loss of alpha particles. In calculating the TAE frequency, additional Alfvén resonances can arise at a mode's periphery even though a basic gap structure is present, as illustrated in Fig. 1. The resonance at the periphery can be explicitly accounted for using causality arguments which allows an analytic continuation solution that leads to damping. The damping is found to be sensitive to the density profile and detailed parameters. Typical damping rates $-\gamma/w$ found for the $n = 1, m = 1, 2$ modes for the density profile

$$g(r) = \frac{N(r)}{N_0} = \frac{1 + \exp\left(\dfrac{-1 + 2\Delta_1}{2\Delta_2}\right)}{1 + \exp\left[\left(\left(\dfrac{r}{a}\right)^2 - 1 + 2\Delta_1\right)/2\Delta_2\right]}$$

with $\Delta_1 = 0.2$ and $\Delta_2 = 0.05$, and a q-profile $q(r) = 1 + (q(a) - 1)\, r^2/a^2$, is shown in Fig. 2. Typically, $-\gamma/\omega$ varies from 1-3% depending on the details of the profile. This should be compared with the alpha particle drive prediction for the growth rate γ_α (in the absence of other dissipation mechanism). In Fig. 3 γ_α/ω is plotted as a function of $\omega_{*\alpha}/\omega$, based on a formula that accounts for alpha particle banana effects in the equilibrium (5) and uses a slowing-down distribution function. If only alpha particle drag is taken into account in the alpha particle distribution function, one finds for the

$n = 1, m = 1, 2$ mode,

$$\frac{\gamma_\alpha}{\omega} \cong \frac{15\pi}{32}\,\beta_\alpha\, x_A\, H(1-x_A)\left\{\left[1 + x_A^2(6 - 4x_A - 3x_A^2)\right]\,\frac{\omega_{*\alpha}}{\omega} - \frac{18}{5}\,[1 + x_A(1-x_A)]\right\} \quad (1)$$

where

$$\beta_\alpha = \frac{\beta_{\rm pl}}{3}\,\frac{\varepsilon_{\alpha 0}}{(T_e + T_i)}\,\frac{N_d\,N_t}{N_e^2}\,(N_e\,\tau_s)\,\langle\sigma v\rangle_{dt}$$

$$x_A = v_A(r = r_g)/v_{\alpha 0}$$

where $\beta_{\rm pl}$ is the background plasma beta, $\varepsilon_{\alpha 0}$ the birth energy of an alpha particle, $(N_e\,\tau_s)$ the slowing-down parameter that only depends on electron temperature, $\langle\sigma v\rangle_{dt}$ the fusion production rate that only depends on ion temperature, N_d, and N_t and N_e are the deuterium and tritium and electron densities respectively $(N_d\,N_t/N_e^2 \le 1/4)$, $\omega_{*\alpha} = \frac{\varepsilon_{\alpha 0}}{2r_g\,M_\alpha\,\omega_{c\alpha}\,\ell_\alpha}$, $\ell_\alpha^{-1} = \frac{\partial}{\partial r}\,\ln\,\beta_\alpha\Big|_{r=r_g}$ and $H(x)$ a step function. The curve in Fig. 3 explicitly uses $T_e = T_i = T$. At $T = 10\,\mathrm{KeV}$, $\beta_{\rm pl} \approx .03$. Ion scattering is also taken into account in the figure which produces a small correction to Eq. (1). It turns out that Fig. 3 can be used for nominal values of TFTR, CIT, and ITER; the only sensitive parameter is the meaning of ω_α^*/ω which becomes:

$$\frac{\omega_{*\alpha}}{\omega} \approx \frac{16\rho_\alpha}{\ell_\alpha} \equiv \begin{cases} 1.5a/\ell_\alpha & \text{(TFTR)} \\ 0.8a/\ell_\alpha & \text{(CIT)} \\ 0.6a/\ell_\alpha & \text{(ITER)} \end{cases}$$

with ρ_α the alpha particle Larmor radius. Comparing Figs. 2 and 3 we see that a several-percent relative particle growth rate for $n = 1$ will normally be stabilized by dissipation from the Alfvén resonance. Such a dissipation mechanism would also be consistent with the instability threshold observed in experiment (3) which is an order of magnitude higher than the threshold predicted from bulk Landau damping.

In order to obtain analytic insight into the TAE mode, we have developed an asymptotic matching theory that in principle can be applied for arbitrary n-number. For example for $n = 1, m = 2$, the cylindrical eigenfunction satisfies the equation for the mode amplitude $E_2 \exp(in\varphi - im - i\omega t)$

$$\frac{d}{dr}\,r^3\left(g(r)\Omega^2 - k_2^2\right)\,\frac{dE_2}{dr} - r(m^2-1)\left(g(r)\Omega^2 - k_2^2\right)\,\frac{dE_2}{dr} + r^2\,\Omega^2\,\frac{dg}{dr}\,E_2 \qquad (2)$$

with $\Omega^2 = \omega^2\,R_0^2/v_{A0}^2$ with v_{A0} the Alfvén speed on axis, R_0 the major radius, and $k_m^2 = (1 - m/q(r))^2$. For $\Omega^2 = \frac{1}{3}\,\frac{1}{g(r_g)} = \Omega_g^2$ where $k_2^2(r_g) = k_1^2(r_g)$, this equation has a singularity at the gap position $r = r_g$ where $\Omega^2 = k_2^2(r_g)/g(r_g)$. Choosing $\Omega^2 = \Omega_g^2$ the cylindrical equation, given by (2) can be solved for the outer structure of the eigenmode which satisfies the boundary conditions at $r = 0$ and $r = a$. A unique discontinuity $\Delta \equiv (E_2(r_g^-) - E_2(r_g^+))/C_2(r_g)$ must be used at $r = r_g$. This discontinuity can be matched in a continuous way using the toroidal coupling with a slight frequency shift as indicated by the dotted curve in Fig. 4. A global dispersion relation, in terms of the

discontinuity parameter Δ can be obtained, and one observes that the eigenfrequency $(\Omega - \Omega_g)R_0/a$ is a finite number as $a/R_0 \to 0$. The asymptotic nature of this result is confirmed in numerical shooting code results that duplicate the asymptotic method as $a/R_0 \to 0$, as seen in Fig. 5.

This method can be generalized to arbitrary (m, n) coupling. Space limitations here precludes a detailed discussion. Further details are given in the poster.

References

(1) C.Z. Cheng and M.S. Chance, Phys. Fluids **29**, 3695 (1986).
(2) G.Y. Fu and J.W. Van Dam, Phys. Fluids B **1**, 1949 (1989).
(3) K.L. Wong *et al.*, "Excitation of Toroidal Alfvén Eigenmodes in TFTR," submitted to Phys. Rev. Lett.
(4) W.W. Heidbrink, *et al.*, "An Investigation of Beam Driven Alfvén Instabilities in D-III-D Tokamak," submitted to Nucl. Fusion.
(5) H.L. Berk and B.B. Breizman, Phys. Fluids B **2**, 2246 (1990).

Figure Captions

Fig. 1 Example of mode with gap in center of plasma and Alfvén resonance at the edge (the resonance arises because of the intersection of the mode frequency given by horizontal curve with the rising $m = 2$ curve near $r/a = 1$).
Fig. 2 Relative damping rate $-\gamma/\omega$ for a density and q-profile given in the text as a function of the edge q-value, $q(a)$. Multiple roots are found for certain q-waves as indicated on the graph.
Fig. 3 Relative growth rates produced by alpha particles in optimum D-T mixture as a function of $\omega_{*\alpha}$. At 10 KeV for a plasma beta value is 3% at the gap position. At increasing temperature the solid curve is for the same density as the 10 KeV case, while the dashed curve is for the same beta.
Fig. 4 Schematic asymptotic matching of the toroidal eigenmode to cylindrical eigenfunction with a discontinuity at the gap position.
Fig. 5 Comparison of asymptotic prediction of eigenfrequency in limit $a/R \ll 1$, to results of shooting code for a/R finite. Result extrapolates exactly to the $a/R \to 0$ limit.

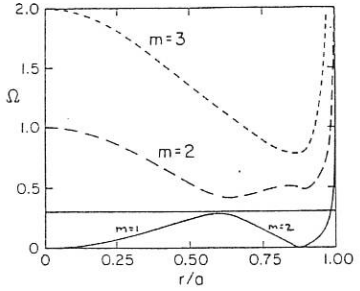

Fig. 1

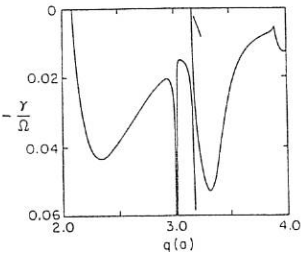

Fig. 2

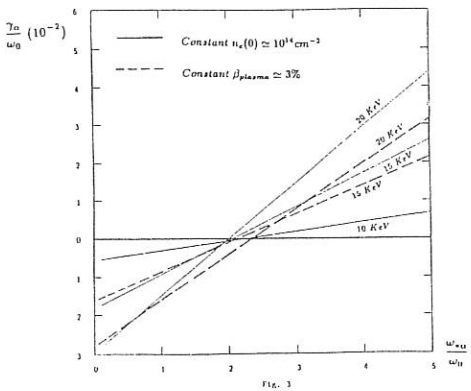

Fig. 3

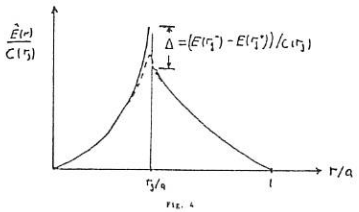

Fig. 4

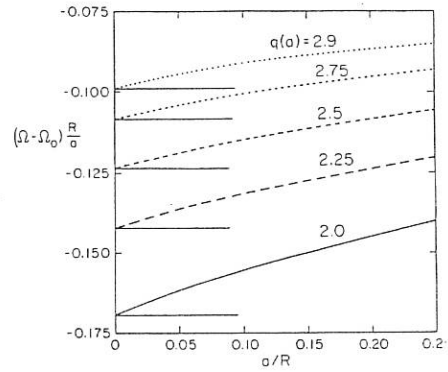

STOCHASTIC NATURE OF ICRF WAVE-PARTICLE INTERACTION

P. Helander, M. Lisak and D. Anderson

Institute for Electromagnetic Field Theory
and Plasma Physics
Chalmers University of Technology
S-412 96 Göteborg, Sweden

ICRF heating of minority ions has proved very successful in Tokamak experiments, but the detailed physics of the heating process is not yet fully understood. As the RF wave and the particles interact, energy is exchanged and the particle orbits are perturbed. As a result, the trajectories may, if the wave amplitude is large, exhibit stochastic behaviour, even when collisions are absent. The ions then diffuse in velocity and coordinate space, giving rise to heating and particle transport. Since the electron temperature usually is very high during high power ICRF heating, ion-electron collisions are relatively infrequent. RF power absorption by energetic ions therefore depends on whether collision-free stochastisation of orbits occurs or not. It is therefore of interest to determine the threshold in wave amplitude for the onset of stochastic motion of the ions. Earlier works treating this problem[1-3] rely on the assumption that the particle orbit width is small in comparison with the distance to the magnetic axis. In present-day experiments particles are heated to energies of several MeV and tend to move along very wide banana orbits. The present work fully incorporates large orbit width effects.

Unperturbed motion

Consider the motion of a charged particle in an axisymmetric, large-aspect-ratio tokamak with concentric flux surfaces. Since the motion is integrable, there exist three constants of motion, e.g.

$$I_1 = 2v^2R_c - v_\perp^2 R$$
$$I_2 = v_\perp^2 R - v^2 R_c$$
$$I_3 = \psi - v_\parallel R \qquad (1)$$

where R_c and R denote the distances from the magnetic axis and the particle to the axis of symmetry, respectively, $v_\parallel$ and are the components of the particle velocity v and ψ is the flux function

$$\psi = \int_0^r \frac{\omega_c r'}{q}\, dr' \cong \frac{\omega_c r^2}{2q}$$

Here r denotes the distance from the particle to the magnetic axis, ω_c is the cyclotron frequency and $q=rB_\psi/RB_\theta$ is the safety factor, here assumed to be roughly constant.

From eqs. (1) we obtain the equation for the guiding centre drift surfaces

$$R = R_c + \frac{I_2 R_c + (\psi - I_3)^2}{I_1} \tag{2}$$

which intersect the equatorial plane of the tokamak whenever

$$R(\psi) = R_c \pm r(\psi) \tag{3}$$

This is a quartic equation in ψ having four roots (ψ_1, ψ_2, ψ_3, ψ_4) of which are always real, the others possible complex.

The solutions to the equations of motion are conveniently expressed in terms of these roots. In the case of two complex roots we find

$$\psi(t) = \frac{(\psi_2 S + \psi_1 T) + (\psi_2 S - \psi_1 T)\, \mathrm{cn}(\omega_o t, \kappa)}{(S+T) + (S-T)\, \mathrm{cn}\, \omega_o t} \tag{4}$$

$$S^2 = (\psi_1 - \psi_3)(\psi_1 - \psi_4)$$

$$T^2 = (\psi_2 - \psi_3)(\psi_2 - \psi_4)$$

$$\omega_o = \frac{\sqrt{ST}}{2qR_c}$$

$$\kappa^2 = \frac{(\psi_1 - \psi_2)^2 - (S-T)^2}{4ST} < 1$$

and in the case of four real roots

$$\psi(t) = \frac{\psi_1(\psi_3 - \psi_2) + \psi_2(\psi_1 - \psi_3)\, \mathrm{sn}^2(\omega_o t, \kappa^{-1})}{(\psi_3 - \psi_2) + (\psi_1 - \psi_3)\, \mathrm{sn}^2(\omega_o t, \kappa^{-1})} \tag{5}$$

$$\omega_o = \frac{1}{4qR_c^2} \sqrt{(\psi_1 - \psi_4)(\psi_3 - \psi_2)}$$

$$\kappa^2 = \frac{(\psi_1 - \psi_4)(\psi_2 - \psi_3)}{(\psi_1 - \psi_3)(\psi_2 - \psi_4)} > 1$$

At sufficiently low energies, the former solution describes the motion of trapped particles, the latter that of circulating ones.

Wave-Particle Interaction

If an elliptically polarised ICRF wave is present, the integrals of motion $\mathbf{I} \equiv (I_1, I_2, I_3)$ are no longer constant bur vary in time. Their time derivatives can be determined by averaging the equations of motion over the unperturbed Larmor rotation. The result is

$$\frac{dI_1}{dt} = \frac{2e\, v_\perp}{m} R_c\left(1 + \frac{k_\parallel v_\parallel}{\omega}\right)[E_+ J_o(k_\perp\rho) + E_- J_2(k_\perp\rho)] \cos\phi = \overline{\Delta I_1} \cos\phi$$

$$\frac{dI_2}{dt} = -\frac{2e\, v_\perp}{m}\left[R\left(1 - \frac{k_\parallel v_\parallel}{\omega}\right) - R_c\right][E_+ J_o(k_\perp\rho) + E_- J_2(k_\perp\rho)] \cos\phi = \overline{\Delta I_2} \cos\phi$$

$$\frac{dI_3}{dt} = -\frac{ek_\parallel R}{m\omega}[E_+ J_o(k_\perp\rho) + E_- J_2(k_\perp\rho)]\,] \cos\phi = \overline{\Delta I_3} \cos\phi$$

where E_+ and E_- denote the amplitudes of the right-hand and left-hand polarised electric field components, respectively, $k_\parallel$ and $k_\perp$ are the parallel and perpendicular wave vectors, ρ is the Larmor radius and ω is the angular frequency of the wave. ϕ denotes the phase difference between the Larmor rotation and the wave

$$\phi = \int (\omega_c - \omega + k_\parallel v_\parallel) dt \qquad (6)$$

Nonadiabatic interaction takes place in a resonance zone, where the ion cyclotron frequency is close to the Doppler shifter angular frequency of the wave so that $\dot{\phi} = 0$. At resonance the invariants I receive nonadiabatic changes computable by means of the stationary phase method

$$\Delta I = \overline{\Delta I} \sqrt{\frac{2\pi}{|\ddot{\phi}|}} \cos\left(\phi \pm \frac{\pi}{4}\right)$$

Between resonances particle motion is essentially unperturbed. The phase ϕ evolves according to eq. (6) where

$$\omega_c(t) = \frac{\omega_c(R_c)\, R_c}{R(\psi(t))} \qquad v_\parallel(t) = \frac{\psi(t) - I_3}{R_c} \qquad (7)$$

with $\psi(t)$ as in eq. (4) or (5), and I is approximately constant. This leads to a set of finite difference equations governing the evolution of **I**

$$\begin{cases} I_{n+1} = I_n\, \overline{\Delta I} \sqrt{\dfrac{2\pi}{|\ddot{\phi}|}} \cos(\phi_n \pm \pi/4) \\ \phi_{n+1} = \phi_n + \int (\omega_c - \omega + k_\parallel v_\parallel) dt \end{cases} \qquad (8)$$

An approximate criterion for the onset of stochasticity in mapping equations like (8) is that the stochasticity parameter

$$K = \left| \frac{\partial \phi_{n+1}}{\partial \phi_n} - 1 \right| \qquad (9)$$

exceed unity[4]. In the present case

$$K = \sqrt{\frac{2\pi}{|\ddot{\phi}|}}\,\overline{\Delta \mathbf{I}} \cdot \left| \int \left(\frac{\partial \omega_c}{\partial I} + k_{\parallel} \frac{\partial v_{\parallel}}{\partial I} \right) dt \right| \qquad (10)$$

where the derivatives with respect to I may be calculated from eqs. (3), (4), (5) and (7) and the integration can be performed numerically.

Conclusions: The requirement that K > 1 far any of the resonance crossings leads to a threshold in the electric field amplitude E_{crit}, which has to be exceeded in order for the ions to move stochastically. In fig. 1 E_{crit} is plotted as a function of $\chi = v_{\parallel}/v$ for a 200 keV H_e-3 ion with r = 30 cm in JET. Trapped particles, which have $-0.36 < \chi < 0.29$ are seen to be much easier stochastisised than circulating ones. At the trapped-passing boundary an arbitrarily weak wave field is needed for orbit stochastisation.

References

1. K.W. Wang and G.J. Morales, Nucl. Fus. 23 (1983) 481.
2. T.H. Stix, Course and Workshop on Applications of RF Waves to Tokamak Plasmas, Varenna, Italy, September 5-14, 1985, Vol. 1.
3. A. Becoulet et al, Phys. of Fluids B3 (1991) 137.
4. R.Z. Sagdeev et al, Nonlinear Physics, Harwood Academic Press 1988.

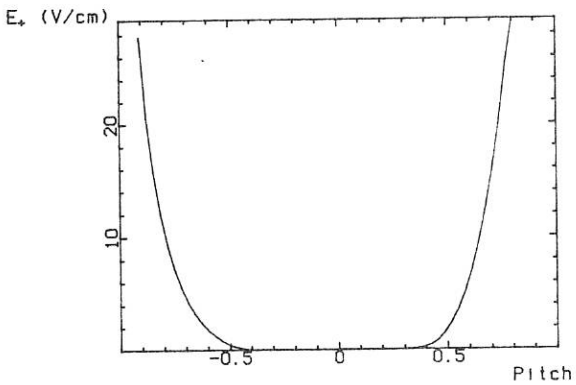

Fig. 1. The critical electric field needed to stochastisise a He-3 ion in JET. Here r=30 cm, $k_{\parallel} = 0.01\ cm^{-1}$, $k_{\perp} = 0.3\ cm^{-1}$ and $E_- = 10\ E_+$.

THE INFLUENCE OF ELECTRONS HEATING ON THE MAGNETOPLASMA SURFACE WAVES PROPAGATION AT THE PLASMA - METAL STRUCTURE

N.A.Azarenkov , K.N.Ostrikov

Kharkov State University , Kharkov ,3I0077,USSR

The study of nonlinear effects in plasma-metal structures nowadays is of considerable fundamental and practical interest.This interest is due to the fact that such structures are often formed in gaseous plasmas and their study is neccesary in connection with the problems of plasma confinement (limiter in tokamak [I]),impurities (divertor [I]) and probe measurements in plasma. They may also occur under plasma or laser prosessing of metals as well as under movement of artificial satellites in ionosphere.In such structures the existence of surface (located near the interface) waves (SW),propagating across the external magnetic field is possible [2] . The phase velocity of the SW is usually much less compared with the light velocity and a behaviour of such waves becomes sufficiently nonlinear under relatively small amplitudes. Note that nonlinear properties of the SW considered may be due to several nonlinear mechanisms. In our previous works [3 , 4] the influence of nonlinearity,which is due to nonlinearity of the basic set of Maxwellian equations and quasihydrodynamic equations , on the SW propagation was studied . The aim of the present report is to study the influence of nonlinearity which is due to electrons heating in the high frequency SW field on magnetoplasma finite amplitude SW propagation at the plasma - metal structure .

Consider semi - infinite plasma occupying the half - space $x > 0$ and bounded at the plane $x = 0$ by an ideally conductive metal surface. The external magnetic field $\vec{H}_0$ is applied parallel to the boundary at z direction. We are interested in study of the SW , propagating across $\vec{H}_0$ (along

Y axis) at the plasma- metal boundary. SW frequency satisfies the following inequality $\omega >> \nu >> \tilde{\nu}$, where ν^{-1} is the characteristic time of collisional electron impulse variation and $\tilde{\nu}^{-1}$ is the characteristic time of collisional electron energy variation . We take into account electrons heating in the SW field , which leads to variation of electron collisional frequency. This results in variations of electromagnetic properties of plasma.

Electrons heating in the SW field is assumed to be weak, so electron temperature can be written as $\Theta = T + \Theta'$, $\Theta' \ll T$, T is the electron temperature in the absence of the SW , Θ' is a variation of electron temperature due to the action of the SW electromagnetic field. Collisional frequency as a function of electron temperature can be presented as follows :

$$\nu(\Theta) = \nu(T) + \delta\nu(x, y, |E|^2), \qquad (I)$$

where $\delta\nu(x,y,|E|^2) = \frac{\partial \nu(\Theta)}{\partial \Theta}\Big|_{\Theta=T} \Theta'(x,y,|E|^2) \ll \nu(T)$. The dependence of collisional frequency ν on x and y coordinates is due to two - dimensional character of the SW field pattern.

To describe an influence of electrons heating on the SW propagation we start from quasihydrodynamic equations for high - frequency electron motions with collisional frequency ν taken in the form (I) and Maxwellian equations for SW electromagnrtic fields . We also used stationary energy balance equation [5] to obtain the electron temperature variation $\Theta'(x,y,|E|^2)$. When calculating $\Theta'(x,y,|E|^2)$ we assumed a temperature dependence on the SW electromagnetic field amplitude to be local. This is valid when the effects of heat conduction may be neglected.

After the solution of the above mentioned equations , using boundary condition $E_y(x=0)=0$, where E_y is the tangential component of the SW electric field , we obtain the following nonlinear dispersion equation :

$$D(\omega, \kappa_2) + i\,\mathrm{Re}\,Q_1 |E|^2 \exp(-2\kappa_2'' y) - \mathrm{Im}\,Q_1 |E|^2 \exp(-2\kappa_2'' y) = 0, \qquad (2)$$

where $D(\omega, \kappa_2)$ is the linear dispersion equation of the SW considered [2], $\kappa_2 = \kappa_2' + i\kappa_2''$ is the SW wavenumber,

$$\mathrm{Re}\,Q_1 = \frac{e^2 \Omega_e^2 (\omega^2+\omega_e^2)^2}{8 m c (\omega^2-\omega_e^2)^4} \frac{(\varepsilon_1')^2 - (\varepsilon_2')^2}{(\varepsilon_1')^{3/2} |\varepsilon_2'|} \frac{\partial \nu(\theta)}{\partial \theta}\Big|_T \frac{\nu(T)}{\tilde{\nu}(T)},$$

$$\mathrm{Im}\,Q_1 = \frac{e^2 \Omega_e^2 (\omega^2+\omega_e^2)}{2 m c (\omega^2-\omega_e^2)^4} \frac{\varepsilon_2'}{|\varepsilon_2'| (\varepsilon_1')^{3/2}} \frac{\partial \nu(\theta)}{\partial \theta}\Big|_T \frac{\nu(T)}{\tilde{\nu}(T)} \left\{ \frac{\omega^2+\omega_e^2}{4\varepsilon_2'} \times \right.$$

$$\times \left[\frac{\varepsilon_1''}{2\varepsilon_1'} \left((\varepsilon_2')^2 - 3(\varepsilon_1')^2 \right) - \frac{\varepsilon_2''}{2\varepsilon_2'} \left(17(\varepsilon_2')^2 - 5(\varepsilon_1')^2 \right) \right] + 2\omega_e \omega \left[\right.$$

$$\left. \left. \varepsilon_1'' - \varepsilon_2'' \left(1 - 9\varepsilon_1'/4\varepsilon_2' \right) \right] \right\},$$

ω_e, Ω_e are electron cyclotron and plasma frequencies, e, m are electron charge and mass, $\varepsilon_1 = \varepsilon_1' + i\varepsilon_1''$, $\varepsilon_2 = \varepsilon_2' + i\varepsilon_2''$ are collisional magnetoactive plasma dielectric tensor components, respectively. Linear dispersion equation $D(\omega, \kappa_2)$ includes linear collisional damping. Terms, proportional to $\mathrm{Re}\,Q_1$ and $\mathrm{Im}\,Q_1$ are due to nonlinear damping and nonlinear frequency shift of the SW considered, respectively. One can see from (2) that nonlinear damping decrement and nonlinear frequency shift decrease with the increase of the distance from the source of SW excitation ($y = 0$).

Numerical estimates show that the condition of a weak electrons heating approximation $\theta' \ll T$ in a dense plasma ($\Omega_e^2/\omega_e^2 \gg 1$) does not give more strict restrictions on the SW amplitude values than the condition of a weak nonlinearity approximation $M \ll 1$, where $M = V_E/V_{ph}$ (V_E is the characteristic electron oscillation velocity in the field of SW, V_{ph} is the SW phase velocity). So, when plasma density $n_0 \sim 10^{12}$ sm^{-3}, $H_0 \sim 1$ kOe, parameter M value 0,1 corresponds to SW amplitude value $E \sim 1$ kV / sm. Such field amplitude values may be produced in experiment.

More detailed investigations were carried out in the

frequency range $\omega_2^2 \ll \omega^2 \ll \omega_e^2$, where ω_2 is the low hybrid frequency. Since wave field amplitude decreases with y , we study nonlinear damping and nonlinear frequency shift near the source of the SW excitation so as to estimate maximally possible effect of electrons heating on the SW propagation. Taking temperature dependence of electron collisional frequency in the form $\nu(\theta) \sim \theta^{-3/2}$, which is appropriate for completely ionized gaseous plasma, we conclude that SW collisional damping decreases in comparison with linear approximation. In this case nonlinear frequency shift is positive in the whole frequency range of our interest and leads to an increase of the SW phase velocity. This result is in contrast with the results of [3], where the influence of nonlinearities which are due to nonlinearity of the basic set of equations was shown to lead to the SW phase velocity decrease. Numerical estimates show that presented nonlinear SW self-interaction mechanism can be predominant only near the source of the SW excitation due to its exponential decay $\exp(-2\kappa_2'' |y|)$.

References

1. Nedospasov A.V., Tokar M.Z. Voprosy teorii plasmy, N 18, Energoatomizdat, Moscow, 1990.
2. Kondratenko A.N. Surface and volume waves in bounded plasma. Energoatomizdat, Moscow, 1990.
3. Azarenkov N.A., Kondratenko A.N., Ostrikov K.N. Int. workshop on nonlinear and turbulent processes in physics. Kiev, USSR , 1989. Proceedings. V. I , p. 30 - 33.
4. Azarenkov N.A., Ostrikov K.N. 17 EPS Conf. on Controlled Fusion and Plasma Heating, Amsterdam, Netherlands, 1990. Contr. Papers. V. 14 B , part 4 , p. 1848 - 1851.
5. Bass F.G., Gurevich U.G. Hot electrons and strong electromagnetic waves in gas discharge and plasma of semiconductors. Nauka, Moscow , 1973.

ON EXISTENCE OF SOLITARY DRIFT WAVES IN THE PRESENCE OF INHOMOGENEOUS ELECTRIC FIELD

Smirnov A.P, Sheina E.A.

Lomonosov Moscow State University, Moscow USSR

1. There are many papers devoted to the question of existence in liquid, atmosphere and plasma localised running vortexes which play important role in the substance and energy transfer. For example, in Ref.1 drift waves described by the equation

$$(u - \Delta u)_t + (u + \eta u^2)_x = J(u, \Delta u), \qquad (1)$$

are considered in magnetized plasma. In Eq.(1) $J(\phi,f) = \phi_x f_y - \phi_y f_x$, $u = u(x,y,t) = e\Phi/T$, Φ - the electric potential, T - the electron temperature, $2\eta = \partial \ln T/\partial \ln n$, n - the plasma density, length is normalized to $r_{L,i}$, time - to $1/\omega_i$, ω_i - ion frequency. Ox axis is perpendicular to the magnetic field and the plasma density gradient. It is shown in [1] that this equation has the solution in the form of solitary wave which moves with constant profile.

In this report we study the question of existence of analogous vortex in the presence of electric field defined by the potential $\phi(y)$. This mathematical model also describes vortexes in the shallow rotating liquid on the background of zonal flow [2]. It is shown on the basis of theorems [3] the existence of exponentially decreasing vortex of monopol type on the background of inhomogeneous electric field satisfying some conditions. These waves move perpendicularly to the plasma density gradient and the magnetic field. The results presented in this report are illustrated by numerical calculations of inhomogeneous field and vortex defined by it.

2. We look for the solution of (1) in the form of solitary wave $\Phi(x - at, y)$ with smooth profile $\Phi(x,y)$ under

condition

$$\Phi \to 0 \text{ as } r \to \infty \qquad (2)$$

on the background of stationary electric field with potential $\Psi(y)$. This solution

$$u(x,y,t) = \breve{u}(x - at, y) = \Psi(y) + \Phi(x - at, y)$$

is stationary solution of Eq.(1) in the coordinate system which moves with velocity a along Ox axis.

From (1) the following condition on $\breve{u}(x,y)$ can be obtained:

$$J(\Delta\breve{u} - A\breve{u} + B\breve{u}^2, \breve{u} + ay) \equiv 0, \qquad (3)$$

$A = (a - 1)/a$, $B = \eta/a$. It holds if

$$\Delta\breve{u} - A\breve{u} + B\breve{u}^2 \equiv R(\breve{u} + ay) \qquad (4)$$

for some function $R(z)$.

Denote $z(y) \equiv \Psi(y) + ay$. As soon as we look for smooth decreasing function Φ using (4) at $|x| \to \infty$ we can get connection between z and R:

$$z'' = \breve{R}(z) + 2Bazy - Aay - Ba^2y^2, \qquad (5)$$

$\breve{R}(t) \equiv R(t) - Bt^2 + At$. From (4) and (5) we obtain the equation

$$\Delta\Phi - 2Bay\Phi = \breve{R}(z(y) + \Phi) - \breve{R}(z(y)) \qquad (6)$$

for profile Φ with condition (2) at infinity. We can write this equation in the form

$$Lu = f(u,x), \qquad (6^*)$$

where $Lu \equiv -\Delta u + \alpha(y)u$,

$$f(t,y) \equiv -\int_{\infty}^{tr}\int \breve{R}''(z(y)+\tau)\, d\tau dr,$$

$$\alpha(x_2) = \breve{R}'(z(x_2)) + 2Bay. \qquad (7)$$

Theorem. Suppose infinitely smooth function $\breve{R}(t)$

satisfies following conditions:

$\breve{R}''(t) \leqslant 0$ in $\mathbb{R}^1$;

either a) $\breve{R}''(t)$ nonincrease in $\mathbb{R}^1$,

or b) $\omega \equiv \sup_{t\in\mathbb{R}^1} (-\breve{R}''(t)) \,/\, \inf_{t\in\mathbb{R}^1} (-\breve{R}''(t)) < 3/2$,

$\breve{R}(z)/|z| = -\infty$ as $|z| \to \infty$;

for some constants C_1 and C_2

($C_2 > 0$ as $a < 0$, $C_2 > B > 0$ as $a > 0$) for all z;

$\breve{R}'(z) \geqslant C_1 - 2C_2 z$;

$\breve{R}(z) \geqslant C_0 + C_1 z - C_2 z^2$;

$$C_0 \geqslant \frac{C_2 B}{4(B-C_2)} \left(\frac{C_1}{C_2} - \frac{A}{B}\right)^2 - \frac{C_1^2}{4C_2}.$$

Then the problem (5), (6), (2) posses' infinitely smooth solution - $z(y)$ and positive exponentially decreasing $\Phi(x,y)$.

The proof of this theorem uses "sub - and supersolution method" ("barrier method") to construct solution of (5) and theorems on existense positive decreasuing solution of quasi-linear equation (6*) [3]. The limit case of our theorem is radially-symmetric vortex with velocity $a > 1$, which was found in [1] without taking into account stationary electric field. This solution corresponds to $\breve{R}(z) \equiv Az - Bz^2$ ($A > 0$, $B > 0$) and $z(y) \equiv ay$.

An example of inhomogeneous field profile $E = \Phi_y(y)$ normalised to $T/(er_{L,i})$ is shown in Fig.1. In this case we take $a = 2$, $\breve{R}(z) \equiv Az - B/2\, z^2$. Level curves of solitary vortex on the background of this field are shown in Fig.2. This vortex moves with velocity a and is anisotropic on the

variables x and y.

Thus we showed that exponentially localised vortex of monopol type moving perpendicularly to the magnetic field and the plasma density gradient might appear on the background of inhomogeneous electric field.

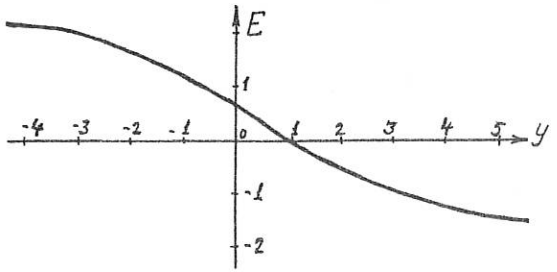

Fig.1. The inhomogeneous electric field profile.

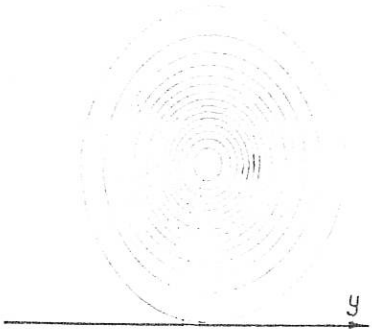

Fig.2. Level curves of solitary vortex.

References

1. Petviashvily V.I. Letters to Journal of Exper. and Theor. Phys. (Soviet), 32 (1980), 632-635.
2. Petviashvily V.I Lett. to Astron. J. (Soviet), 9(1983), 253-256.
3. Smirnov A.P., Sheina E.A. Diff. equat. (Sov.) , 26(1990), 1265-1271

WAVE PROPAGATION IN AN INHOMOGENEOUS RELATIVISTIC MAGNETOPLASMA

Kerkhof, M.J., Kamp, L.P.J., Sluijter, F.W., Weenink, M.P.H.[1]

Eindhoven University of Technology , Dept. of Applied Physics
5600 MB Eindhoven
The Netherlands

1 Introduction

This paper contains two subjects. In the first part a self-consistent description is given of the electron and ion statics in a relativistic inhomogeneous magnetoplasma. In [Mahajan,89] this problem is treated for a non-relativistic plasma with electrons and ions having equal charge.

Furthermore it is shown that there exist equilibrium solutions that simulate the interface of a semi-infinite neutral plasma with a magnetic field.

In the second part the time-dependent Vlasov-Maxwell system is linearized around this equilibrium. The case of a non-relativistic plasma was treated in [Martin,87]. In the present paper a set of fully relativistic differential equations is derived for the first order electric field.

2 Equilibrium in a relativistic two-component plasma

Our starting point is a plasma, that is inhomogeneous in the x-direction and which is contained in a magnetic field $\vec{B}_0$ in the z-direction. The equilibrium

[1] Eindhoven University of Technology , Dept. of Electrical Engineering

electric and magnetic field are described by the potentials Φ and A:

$$\vec{E_0} = -\frac{\partial \Phi}{\partial x}\vec{e_x} \ , \quad \vec{B_0} = \frac{\partial A}{\partial x}\vec{e_z} \ . \tag{1}$$

For the equilibrium distribution functions f_s (s=e,i) that satisfy the time-independent Vlasov equations for the electrons and ions we choose functions that resemble relativistic Maxwellians ([Synge,57], [Mahajan,89],[Clemmow,69]):

$$f_s(x,\rho) = C_s \exp(-\mu_s\sqrt{1+\rho^2} - \frac{q_s\Phi(x)}{\kappa T_s})h_s(\rho_y + \frac{q_s A(x)}{m_s c}) \ , \tag{2}$$

with $\mu_s = (m_s c^2)(\kappa T_s)^{-1}$ and $C_s = \mu_s(4\pi K_2(\mu_s))^{-1}$, where K_2 is the modified Bessel function of the second kind of order two. For convenience we introduce the dimensionless potential $\Psi := eA(x)(m_e c)^{-1}$, the parameters $Z := q_i e^{-1}$, $\alpha := T_i T_e^{-1}$, $\beta := m_i m_e^{-1}$ and the functions g_e and g_i defined by

$$g_e(\Psi) = \frac{N_{e0}}{N_{e0}+N_{i0}}\int_{-\infty}^{\infty} K_e(\rho_y)h_e(\Psi-\rho_y)d\rho_y \ , \tag{3}$$

$$g_i(\Psi) = \frac{ZN_{i0}}{N_{e0}+N_{i0}}\int_{-\infty}^{\infty} K_i(\rho_y)h_i(\frac{Z}{\beta}\Psi-\rho_y)d\rho_y \ , \tag{4}$$

with

$$K_s(\rho_y) = \frac{2\pi\mu_s}{K_2(\mu_s)}\{\frac{1}{\mu_s}(\sqrt{1+\rho_y^2}+\frac{1}{\mu_s})exp(-\mu_s\sqrt{1+\rho_y^2})\} \ . \tag{5}$$

Expressing the particle densities and their current densities in the functions g_s and their derivatives leads after some algebra to the following set of differential equations for the potentials χ ($=e(1+Z\alpha^{-1})\Phi)(2\kappa T_e)^{-1}$) and Ψ:

$$\frac{d^2\chi}{dx^2} = \frac{1+\frac{Z}{\alpha}}{\lambda_{D_B}^2}\exp(-\delta\chi)[\sinh(\chi)\bar{g}(\Psi)+\cosh(\chi)g_d(\Psi)] \ , \tag{6}$$

$$\frac{d^2\Psi}{dx^2} = -\frac{2\sqrt{\frac{\alpha}{Z}}}{\mu_e^2\lambda_{D_B}^2}\exp(-\delta\chi)[\cosh(\chi+\phi_\delta)\bar{g}'(\Psi)+\sinh(\chi+\phi_\delta)g_d'(\Psi)] \tag{7}$$

with

$$\delta = \frac{Z-\alpha}{Z+\alpha}, \quad \phi(\delta) = arctanh(\delta), \quad \bar{g} = \frac{1}{2}(g_e+g_i), \quad g_d = \frac{1}{2}(g_e-g_i) \ . \tag{8}$$

It can be shown that for a suitable choice of $\bar{g}$ (and with g_d taken zero) the solution $n_0(x) \approx \frac{1}{2}N_0(\tanh(xL^{-1})+1)$, $B_0(x) = B_1 - \tilde{B}\tanh(xL^{-1})$, $E_0 = 0$ satisfies the equations (6) and (7).

3 Linearization of the time-dependent Vlasov-Maxwell system

Starting from the presumed equilibrium, the time-dependent Vlasov-equation is linearized with respect to a small deviation. Because we are interested in the high-frequency behaviour of the particles,the ion motion is neglected.

For the first order perturbation of the electron distribution the following equation is obtained

$$(\frac{\partial}{\partial t} + \frac{c\vec{\rho}}{\gamma} \cdot \nabla) f_1 - \frac{e}{m}(\frac{\vec{\rho}}{\gamma} \times B_0 \vec{e_z}) \cdot \nabla_\rho f_1$$
$$= -\frac{e\mu e^{-\mu\gamma}}{4\pi K_2(\mu)}(\frac{\mu}{\gamma} h(\Psi)\vec{\rho} \cdot \vec{E_1} - h'(\Psi)(E_1 + \frac{c\vec{\rho}}{\gamma} \times B_1)_y) \quad . \tag{9}$$

Assuming harmonic time-dependence of f_1, $\vec{E_1}$,and $\vec{B_1}$ according to

$$f_1 \ , \ \vec{E_1} \ , \ \vec{B_1} \propto e^{-i\omega t} \tag{10}$$

and using cilindrical coordinates ($\rho_\perp$, ϕ, $\rho_\parallel$) in momentum space the left-hand side of (9) yields

$$-i\omega f_1 + \frac{c\rho_\perp cos(\phi)}{\gamma} \frac{\partial f_1}{\partial x} + \Omega(x) \frac{\partial f_1}{\partial \phi} \quad . \tag{11}$$

The function f_1 is expanded in a Fourier series

$$f_1 = \sum_{n=-\infty}^{n=+\infty} f^{(n)} e^{in\phi} \quad . \tag{12}$$

This leads to the following equations for $f^{(n)}$:

$$-i(\omega - \frac{n\Omega(x)}{\gamma}) f^{(n)} + \frac{c\rho_\perp}{2\gamma} \frac{\partial}{\partial x}(f^{(n+1)} + f^{(n-1)}) = R^{(n)} \quad , \tag{13}$$

in which R_n is the n-th Fouriercoefficient of (9). Using small gyroradius approximation, the set of equations for $f^{(n)}$ is solved to lowest order. With this result the components of the current density can be calculated. We have

$$\vec{J} = \vec{J_0} + \vec{\vec{\Sigma}} \cdot \vec{E_1} \quad , \tag{14}$$

with

$$\vec{J}_0 = -\frac{1}{\mu_0}\frac{\partial B_0}{\partial x}\vec{e_y} \ , \tag{15}$$

$$\vec{\vec{\Sigma}} = \frac{i\sqrt{\frac{\pi\mu}{2}}e^{-\mu}\omega_p^2}{K_2(\mu)}\vec{\vec{I}} + r_c^2\vec{\vec{T}} \ . \tag{16}$$

Here the tensor operator $\vec{\vec{T}}$ is given by

$$T_{\alpha\beta} = \sum_{i=0}^{2} G_{\alpha\beta}^{(1)}(\mu, \frac{\Omega}{\omega})(\frac{\partial^{(2-i)}\omega_p^2}{\partial x^{(2-i)}})\frac{\partial^{(i)}}{\partial x^{(i)}} + \Omega' \sum_{i=0}^{1} G_{\alpha\beta}^{(2)}(\mu, \frac{\Omega}{\omega})(\frac{\partial^{(1-i)}\omega_p^2}{\partial x^{(1-i)}})\frac{\partial^{(i)}}{\partial x^{(i)}} \tag{17}$$

$$T_{(xz)}, \ T_{(yz)}, \ T_{(zz)}, \ T_{(zy)} = 0 \ . \tag{18}$$

The functions $G_{\alpha\beta}^{(1)}$, $G_{\alpha\beta}^{(2)}$ are linear combinations of the relativistic dispersion functions of the first and second harmonics which are defined by

$$\mathrm{F}_q(\mu, \frac{n\Omega}{\omega}) = \frac{(\frac{\mu}{2})^{(q-1)}e^{\mu}}{\Gamma(q)}\int_1^{\infty}\frac{(\gamma^2-1)^{(q-1)}e^{-\mu\gamma}}{\gamma - \frac{n\Omega}{\omega}}d\gamma \ , \tag{19}$$

([Bornatici,88]) with $q = \frac{5}{2}, \frac{7}{2}$, $n = 0, \pm 1, \pm 2$. The explicit expressions of the elements of the tensor $\vec{\vec{T}}$ will be published later.

References

[Mahajan,89] Mahajan,S.M.,Exact and almost exact solutions to the Vlasov-Maxwell system,Phys.Fluids B1,1,1989

[Clemmow,69] Clemmow,P.C., Dougherty,J.P.,Electrodynamics of Particles and Plasmas, Addison-Wesley Publishing Company,1969

[Synge,57] Synge,J.L., The relativistic gas, North Holland Publishing Company, Amsterdam,1957

[Bornatici,88] Bornatici,M.,Ruffina,U.,Plasma Physics and Controlled Fusion Vol.30,No 2,pp 113-132,1988

[Martin,87] Martin,Th.,Vaclavic,J.:Helvetica Physica Acta, Vol.60(1987),pp.471-479

INFLUENCE OF PLASMA DENSITY INHOMOGENEITIES ON THE EIGENFREQUENCY OF GLOBAL THREEDIMENSIONAL MHD MODES IN TOROIDAL PLASMAS

Ferdinand F. Cap

Institute for Theoretical Physics, University of Innsbruck, Austria

Introduction

The propagation of electromagnetic and of MHD waves in toroidal plasmas is of interest for the heating of fusion plasmas. As long as the wavelength is small in comparison to the length scale of the device the use of geometric optic methods (ray tracing) is suitable. If, however, the wavelength (of low frequency waves) is of the order of the dimensions of the device, global wave solutions are necessary. For toroidal geometry the MHD wave equations are however not separable into ordinary differential equations. Using a collocation method [1], the partial differential equations describing MHD waves are solved for a toroidal and arbitrary meridional cross section of the containment chamber. The influence of various density distributions on the eigenfrequency of the global wave solutions and the satisfaction of the boundary conditions on the metallic vessel wall will be discussed

Starting from the equations of continuity, of motion, Ohm's law and Maxwell's equations we obtained by the usual linearization a set of equations for ρ (density), $\vec{v}$ (particle speed), c_s (adiabatic sonic velocity), c_A (Alfvèn velocity), and the electromagnetic wave fields $\vec{E}, \vec{B}$. Eliminaitiong $\vec{j}$ (current density), $\vec{E}, \vec{B}, \rho$ and v_φ we obtained in circular cylinder coordinates r, φ, z, see Fig. 1, with the assumption $\sim \exp(im\varphi - ikz + i\omega t)$ two ordinary differential equations for $v_r(r)$ and $v_z(r)$ of the MHD waves:

$$i\frac{dv_r}{dr}(c_A^2 + nc_s^2) + kv_z\Big[(c_A^2 + nc_s^2) - \frac{\omega^2}{k^2} + \frac{m^2}{r^2k^2c_A^2}\Big] +$$

$$+\frac{iv_r}{r}\Big[\Big(nc_s^2\Big(r\frac{1}{\rho_0}\frac{d\rho_0}{dr} + 1\Big) - c_A^2\Big)\Big] = 0 \qquad (1)$$

$$\frac{dv_z}{dr}(r^2\omega^2 - m^2c_A^2) + 2i\frac{dv_r}{dr}krc_A^2 + v_z\Big(r^2\omega^2\frac{1}{\rho_0}\frac{d\rho_0}{dr} + 2rk^2c_A^2 + 4m^2\frac{c_A^2}{r}\Big) +$$

$$+ikv_r(r^2\omega^2 - m^2c_A^2 - 2c_A^2) = 0. \qquad (2)$$

Here $\rho_0(r)$ is the assumed plasma density distribution, $\vec{B}_0(r) = B_0(r)\vec{e}_\varphi$ is the toroidal containement field, $B_0(r) = RB_0(R)/r$, R is the major (and later a the minor) toroidal radius, $c_A^2 = B_0^2(r)/\mu_0\rho_0(r)$ and n is an abbreviation for $n = \omega^2r^2/(\omega^2r^2 - m^2c_s^2)$. Due to the gyroscopy of the magnetized plasma the phase factor $i = \exp(i\pi/2)$ appears in (1), (2), so that the MHD waves are prescribed by a time dependent rotating structure. We therefore make a "snap-shot" at time $t = 0$ and consider the two modes type 1 ($v_r \to i\bar{v}_r$) and type 2 ($v_z \to i\bar{v}_z$) whose superposition describes the rotating MHD mode. In order to solve the equations (1), (2) we assumed $T_{ion} = T_{electron} = 10keV$, $B_0(R) = 5T$, $\gamma_{el} = \gamma_{ion} = 2$ and a Gaussian density distribution ($n_0 = 10\text{E}20$ particles m^{-3})

$$\rho_0(r) = n_0A\exp[-\beta(r - R)^2/a^2], \qquad (3)$$

where $A(\beta)$ has been chosen in such a way that the total plasma mass remained constant when β was varied.

Boundary Conditions

The boundary conditions on a containing highly conducting metallic surface are $\vec{v} \cdot \vec{n} = v_n = 0$, $\vec{B} \cdot \vec{n} = B_n = 0$ and $E_t = \vec{E} \times \vec{n} = 0$. If the toroidal containment chamber is situated as Fig. 1 shows, then the normal vector $\vec{n}$ is perpendicular to $\vec{e}_\varphi$ and the boundary conditions for $\vec{B}$ and $\vec{E}$ are automatically satisfied if $v_n = 0$. If the meridional cross-section in the r, z-plane of the containing toroidal surface is described by a curve $z^* = z(r)$ and if $\tan\alpha = dz*/dr$, then $v_n = -v_r \sin\alpha + v_z \cos\alpha = 0$. Inserting the real solutions $\bar{v}_r$ and v_z from (1) and (2) in the form for mode type 1

$$v_z(r,\varphi,z) = \sum_{k,m,s}^{K,M} A_{km}^s v_{zs}^{(k,m)}(r) \cos kz \cdot \cos m\varphi \tag{4}$$

$$\bar{v}_r(r,\varphi,z) = \sum_{k,m,s}^{K,M} A_{km}^s \bar{v}_{rs}^{(k,m)}(r) \sin kz \cdot \cos m\varphi, \tag{5}$$

where $s = 1, 2$ indicates two different but arbitrary initial conditions used in the numerical integration of (1), (2), one obtains for P collocation points r_i, z_i, $i = 1 \ldots P$ a system of P equations for the unknown partial amplitues A_{km}^s. Since the sum over $s = 1, 2$ gives two values and if summation over m gives M values and over k one might have K values, the number N of unknown partial amplitudes A_{km}^s is given by $P = 2(M+1) \cdot K$. The number P of collocation points determines the accuracy of the solution. For fixed P it has been shown [1], that the accuracy of the results is practically independent of the arbitrary choice of the separation constants k. According to our experience with axisymmetric MHD modes [1] we make the choice $k = 1/a,\ 2/a,\ 3/a \ldots K/a$, where a is the "effective" minor torus radius for arbitrary cross section. When the k-values are given, then the condition $v_n = 0$ with $\bar{v}_r, v_z$ inserted from (4), (5) constitutes a system of P linear homogeneous equations for the $2(M+1) \cdot K$ unknowns A_{km}^s. In order that this system can be solved, the determinant D of the coefficients (known at r_i, z_i) must vanish. This condition determines the global eigenfrequency ω. In order to be able to integrate (1), (2), the density distribution of the plasma and the frequency ω have to be known. We thus integrate the differential equations (which deliver the elements of the determinant) with an initial guess for ω and calculate $D(\omega)$. Looking for a root of the function $D(\omega)$ we obtain an improved value for ω and a new integration yields improved coefficients and an improved ω etc.

Results

As soon as the solutions (4), (5) are known it is possible to calculate the electric field $E_r(r,z,\varphi)$ and $E_z(r,z,\varphi)$ being known, the differential equations for the electric field lines $dz/E_z(r,z) = dr/E_r(r,z)$ have to be integrated numerically. The results obtained are summarized in Table 1 and in Fig. 2 – 12.

Curve	b	m	β	A	type 1	type 2	Figs.
circle	a	0	0.4	3.	1.559	1.451	5, 6
circle	a	0	1.4	3.	1.764	1.557	5, 6
circle	a	0	0.2	3.	1.522	1.433	5, 6
circle	a	1	0.2	3.	1.804	1.456	–
circle	a	2	0.2	3.	1.646	1.432	–
circle	a	0	1.2	2.	1.771	1.489	8, 9
circle	a	0	1.2	20.	1.674	1.539	8, 9
circle	a	1	1.2	2.8	1.774	1.541	11, 12
circle	a	1	1.2	20.	1.675	1.540	11, 12
circle	a	2	1.2	4.	1.778	–	10
circle	a	2	1.2	20.	1.677	–	10
ellipse	2.	0	0.	3.	1.701	–	–
ellipse	2.	0	1.2	3.	2.002	–	–
ellipse	2.	0	3.2	3.	2.556	–	–
ellipse	2.	1	0.	3.	1.763	–	7
ellipse	2.	1	1.2	3.	2.026	–	–
ellipse	2.	1	1.6	3.	2.127	–	–

Table 1. Angular eigenfrequencies ω in E7 as dependent from inhomogeneity parameter β, aspect ratio $A = R(a = 1)$ and geometry.

We see that the frequency increases practically linearly with increasing inhomogeneity parameter β. The dependence from the aspect ratio is discussed in Figs. 8 - 12. Also D-shaped cross sections have been calculated.

References

[1] F. Cap, N. Schupfer, Axisymmetric MHD modes in an inhomogeneous toroidal plasma of arbitrary meridional cross section and arbitrary aspect ratio, Nuclear Fusion 29, Nr 9 (1989), 1469 - 1478

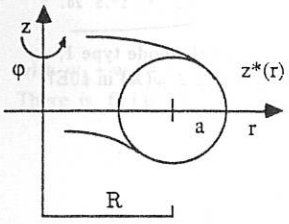

Fig. 1. Coordinate system

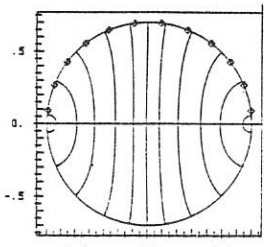

Fig. 2. Field in circle, mode type 2, $m = 0$, $\beta = 2.8$

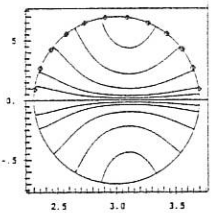

Fig. 3. Field in circle,
mode type 1, $m = 0$, $\beta = 2.8$.

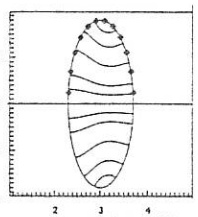

Fig. 4. Field in ellipse,
mode type 1, $m = 0$, $\beta = 2.4$, $b = 1.8$.

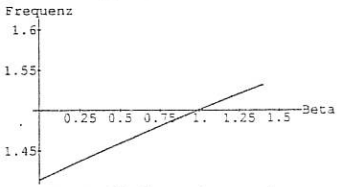

Fig. 5. Circle mode type 2,
$m = 0$, $R = 3.$, $\omega(\beta)$ in 10E7.

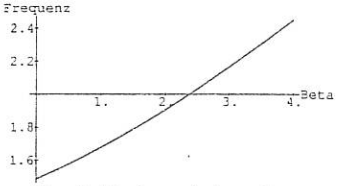

Fig. 6. Circle mode type 1,
$m = 0$, $R = 3.$, $\omega(\beta)$ in 10E7.

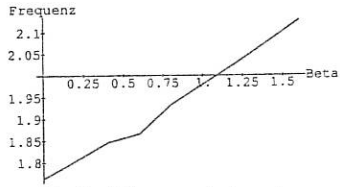

Fig. 7. Ellipse mode type 1,
$m = 1$, $R = 3.$, $\omega(\beta)$ in 10E7.

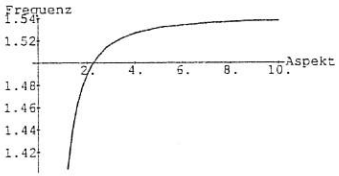

Fig. 8. Circle mode type 2,
$m = 0$, $\beta = 1.2$, $\omega(A)$ in 10E7.

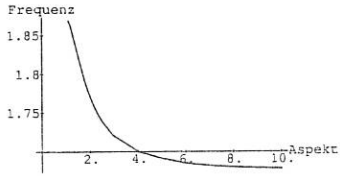

Fig. 9. Circle mode type 1,
$m = 0$, $\beta = 1.2$, $\omega(A)$ in 10E7.

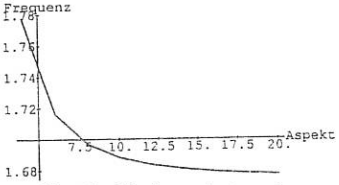

Fig. 10. Circle mode type 1,
$m = 2$, $\beta = 1.2$, $\omega(A)$ in 10E7.

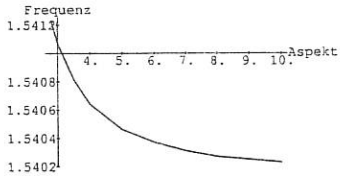

Fig. 11. Circle mode type 2,
$m = 1$, $\beta = 1.2$, $\omega(A)$ in 10E7.

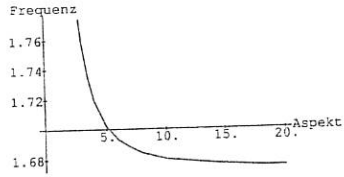

Fig. 12. Circle mode type 1,
$m = 1$, $\beta = 1.2$, $\omega(A)$ in 10E7.

ANOMALOUS DISPERSION OF ELECTRON-CYCLOTRON-WAVES IN NON-MAXWELLIAN, RELATIVISTIC PLASMAS

F.Moser, E.Räuchle, Institut für Plasmaforschung der Universität Stuttgart
7000 Stuttgart 80, Pfaffenwaldring 31, Fed. Rep. Germany

Abstract:

The dielectric tensor due to Orefice (1) is used to investigate the dispersion and absorption of electromagnetic and electrostatic waves propagating obliquely to a constant magnetic field in a weakly relativistic plasma. For the fast and slow ordinary wave propagating perpendicularly to the magnetic field anomalous dispersion is obtained in a small range around the electron cyclotron resonance. The influence of the electron distribution (Maxwellian -, drifting Maxwellian -, Loss - Cone - distribution functions) on the propagation of the electron - cyclotron waves is investigated numerically.

Deviations from thermal equilibrium lead to maser - instability.

The dielectric tensor:

Electromagnetic and electrostatic waves are investigated in the frequency range of the electron - cyclotron resonance. The plasma is assumed to be homogeneous with a constant magnetic field $\vec{B}_0$. Due to Orefice (1) and Moser et al. (2) the dielectric tensor for a weakly relativistic plasma is given by:

$$\varepsilon_{ij} = \delta_{ij} + \left(\frac{\omega_{pe}}{\omega}\right)^2 \left\{ \tilde{H}_{ij}\left[\frac{L_1(f)}{p_\perp}\right] - \Gamma_{ij}(w_1 - w_2\mu_2 p_o^2) \right\} \qquad (1)$$

for an electron distribution function f:

$$f(p_\perp, p_\parallel) = w_1 f_1(p_\perp, p_\parallel) + w_2 f_2(p_\perp, p_\parallel) \qquad (2)$$

with $w_1 + w_2 = 1$.

There is $f_1(p_\perp, p_\parallel)$ a Loss - Cone distribution function given by:

$$f_1(p_\perp, p_\parallel) = n_0 p_\parallel^{2m_\parallel} p_\perp^{2m_\perp} \exp\left[-\tfrac{1}{2}\mu_1(p_\perp^2 + p_\parallel^2)\right]. \qquad (3)$$

Topic: General Plasma Theory (G)

Responsible author: Dr. Fritz Moser

Address: Institut für Plasmaforschung der Universität Stuttgart
7000 Stuttgart 80, Pfaffenwaldring 31, Fed. Rep. Germany

n_0 is the normalization factor given by:

$$n_0 = \frac{1}{m_\perp!}\left(\frac{\mu_1}{2\pi}\right)^{\frac{3}{2}}\left(\frac{\mu_1}{2}\right)^{m_\parallel + m_\perp}\frac{\sqrt{\pi}}{\Gamma(m_\parallel + \frac{1}{2})} \quad . \tag{4}$$

$f_2(p_\perp, p_\parallel)$ is a Maxwellian electron distribution function with an electron drift velocity $\vec{p}_0 \parallel \vec{B}_0$:

$$f_2(p_\perp, p_\parallel) = \left(\frac{\mu_2}{2\pi}\right)^{\frac{3}{2}} \exp\left[-\tfrac{1}{2}\mu_2\left(p_\perp^2 + (p_\parallel - p_0)^2\right)\right]. \tag{5}$$

$\vec{p} = p_\parallel \hat{e}_\parallel + p_\perp \hat{e}_\perp$ is the electron momentum in units of $m_{eo} \cdot c$. m_{eo} is the electron rest mass, Γ is the Gammafunction. w_1 and w_2 are the weights of the drifting Maxwellian - and the Loss - Cone - Anti - Loss - Cone distribution functions, $m_\perp$ is the Loss - Cone index and $m_\parallel$ the Anti - Loss - Cone index. The operator H_{ij} and further details are discribed in (1) and (2), $\Gamma_{ij} = \sigma_{i3}\sigma_{3j}$. The indices $\perp$ and $\parallel$ refer to the directions perpendicular and parallel to the magnetic field.
The plasma is described by the following parameters:

$\omega_{pe} = \left(\frac{4\pi n_e e^2}{m_{eo}}\right)^{\frac{1}{2}}$: the electron plasma frequency,

$\mu_{1/2} = \frac{c^2}{v_{th_{1,2}}^2} = \frac{m_{eo}c^2}{kT_{e_{1,2}}}$: the relativistic parameters with $T_{e_{1,2}}$ the electron temperatures,

$\omega_{ce} = \frac{eB_0}{cm_{eo}}$: the electron cyclotron frequency.

The wave equation and the dispersion relation:

If the dielectric tensor $\varepsilon(\omega, \vec{k})$ is known, the wave equation for the electric wave field $\sim\vec{E}$ is given by:

$$\vec{k} \times \vec{k} \times \sim\vec{E} + \left(\frac{\omega}{c}\right)^2 \varepsilon(\omega, \vec{k}) \sim\vec{E} = 0 \tag{6a}$$

or with $\vec{n} = \frac{c}{\omega}\vec{k}$ the equation of polarization:

$$\vec{n} \times \vec{n} \times \sim\vec{E} + \varepsilon(\omega, \vec{k}) \sim\vec{E} = 0. \tag{6b}$$

From (6a) or (6b) there results the dispersion equation:

$$\text{Det}\,|\Lambda_{ij}| = 0 \qquad (7a)$$

with $$\Lambda_{ij} = n^2(\bar{k}_i\bar{k}_j - \delta_{ij}) + \varepsilon_{ij}(\omega,\vec{k}), \quad \bar{k}_i = \frac{k_i}{|\vec{k}|}. \qquad (7b)$$

Numerical results:

The dispersion relation (7a) is solved numerically using a method of complex residual calculation in the root finding code. If the complex roots for the index of refraction are determined there results the wave field $\delta\vec{E}$, $\delta\vec{B}$ by solving equation (6b). In the numerical calculation of the tensor elements ε_{ij} the recursion formulae for the generalized relativistic dispersion functions due to Shkarofsky (3) and Robinson (4) are used.

Two characteristic examples for the dispersion of the fast ordinary wave are shown in the figures 1) and 2). In Fig.1) the anomalous dispersion considering relativistic effects is compared with the result of nonrelativistic hot theory. Relativistic effects result in smearing out the nonrelativistic singularity at the electron cyclotron resonance. In the nonrelativistic result of hot theory there is no damping of the wave in the frequency range around ω_{ce} ($n_i = 0$), but considering relativistic effects there is a strongly marked damping for $\bar{\omega}_{ce} > 1$ or for $\omega < \omega_{ce}$ with $\bar{\omega}_{ce} = \omega_{ce}/\omega$.

In Fig. 2) the anomalous dispersion of the fast ordinary wave is shown for the propagation in a weakly relativistic, low density plasma with a Loss-Cone distribution function with the Loss-Cone indices $m_\perp = 2$, $m_\parallel = 0$. It is shown that such deviations from thermal equilibrium lead to an instability, the maser-instability.

An analogous anomalous behaviour has been found also for the slow ordinary wave in the frequency range around ω_{ce}, whereas for the extra ordinary wave (X.W.) no anomalous behaviour cut be found neither in low density plasmas ($\bar{\omega}^2_{pe} < 1$) nor in high density plasmas ($\bar{\omega}^2_{pe} \gg 1$). There is $\bar{\omega}_{pe} = \omega_{pe}/\omega$.

For the ordinary wave no anomalous dispersion could be found in the case of propagation in high density plasmas. The anomalous behaviour could only be determined for the case of low density plasmas.

The form of the electron distribution function has a large influence on the absorption of the waves. Therefore the knowledge of the distribution function is necessary to obtain a good theoretical understanding and description of experimental results.

References:

(1) A. Orefice, J. Plasma Physics 39, (1988) 61.

(2) F. Moser et al., Proc. 17th Europ. Conf. on Controlled Fusion and Plasma Heating, Amsterdam, 1990, Vol. IV. 1803.

(3) I. P. Shkarofsky, J. Plasma Physics 35, (1986) 319.

(4) P. A. Robinson, J. Math. Phys. 27, (1986) 1206.

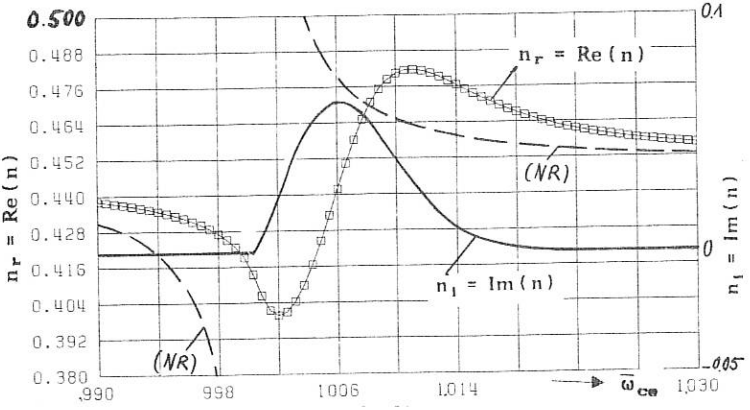

Fig. 1) Anomalous dispersion of the fast ordinary wave in the frequency range $\omega \approx \omega_{ce}$, ($\bar{\omega}_{ce} \approx 1$). Real and imaginary parts of the index of refraction, n_r, n_i, versus the frequency $\bar{\omega}_{ce} = \omega_{ce} / \omega$ compared with the nonrelativistic result of hot theory (NR).
(plasma parameters : $\bar{\omega}_{pe}^2 = 0.8$, $\Theta = 90^0$, $T_e = 1$ KeV, Maxwell distribution, $p_o = 0$)

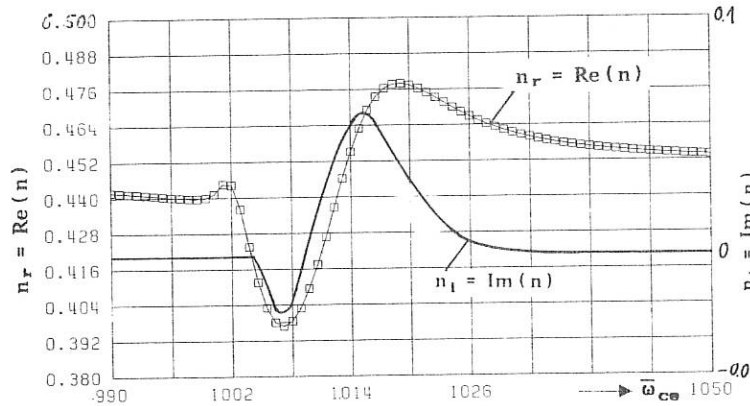

Fig. 2) Anomalous dispersion of the fast ordinary wave in the frequency range $\omega \approx \omega_{ce}$, ($\bar{\omega}_{ce} \approx 1$). Real and imaginary parts of the index of refraction, n_r, n_i, versus the frequency $\bar{\omega}_{ce} = \omega_{ce} / \omega$ for a Loss-Cone distribution function with a Loss-Cone index $m_\perp = 2$.
(plasma parameters : $\bar{\omega}_{pe}^2 = 0.8$, $\Theta = 90^0$, $T_e = 1$ KeV, $p_o = 0$)

A MULTIPLE TIMESCALE EXPANSION AND ANOMALOUS PLASMA TRANSPORT

J.W. Edenstrasser

Institute for Theoretical Physics, University of Innsbruck, Austria

ABSTRACT

At the last meeting we had presented the application of a multiple timescale derivative expansion to the dimensionless Fokker–Planck equation. In continuation of this work, the zero order Fokker–Planck collision operator appearing in the second–order equation is integrated and the first three velocity moments are performed leading to the transport equations on the collision timescale. The transport processes resulting from the finite zero–order fluid velocities and from the MHD fluctuation spectrum turn out to be one order larger than those of classical or neoclassical transport.

INTRODUCTION

To make progress in understanding and describing processes like plasma relaxation, profile consistency and anomalous (turbulent) transport occuring on intermediate timescales between the two limiting scales of ideal MHD and resistive diffusion, we had initiated a multiple timescale approach at the last meeting of this conference series /1/. The expansion was based on a small gyroradius assumption and the four timescales considered were those of particle gyration, particle transit, collisions, and classical transport. The solution of the resulting zero and first–order Fokker–Planck equations has led, depending on the assumption of vanishing or non–vanishing zero–order fluid velocities to the static Stellarator and the stationary Tokamak (RFP) equilibria.

For easier reading and convenient reference we write down once more the Fokker–Planck equation in dimensionless form applying the normalization

$$t = \tilde{t}/\Omega^{-1},\quad f = \tilde{f}_\alpha v_{th}^{o3}/\bar{n}_\alpha,\quad \vec{B} = \tilde{\vec{B}}/\bar{B},\quad \vec{E} = \tilde{\vec{E}}c/v_a\bar{B},\quad \vec{v} = \tilde{\vec{v}}/v_{th}^{o},\quad \vec{\nabla} = l\tilde{\vec{\nabla}},\quad C = \tilde{C}_\alpha/\bar{C}_\alpha. \qquad (1)$$

Ω_α is the gyrofrequency, v_a is the Alfvén velocity, $\bar{n}_\alpha$ is the particle density, $\bar{B}$ is the magnetic field, and v_{th}^{o} the thermal velocity, all five values taken at the magnetic axis for a characteristic instant. l is the characteristic length over which the macroscopic quantities change and which we take as the plasma radius a.

$$\partial f_\alpha/\partial t + \delta_\alpha \vec{v}\cdot\vec{\nabla} f_\alpha + \sigma(q_\alpha)\,(a_\alpha\vec{E} + \vec{v}\times\vec{B})\cdot\partial f_\alpha/\partial\vec{v} = \Gamma_\alpha C_\alpha \qquad \text{with} \qquad (2)$$

$$C_i(f,f) = \frac{\sqrt{\pi}}{2}\sum_{j,k}\frac{\partial}{\partial v_j}\int d^3v\cdot\Big\{f_i(\vec{v})\,\partial f_i(\vec{v}')/\partial v_k' - f_i(\vec{v}')\,\partial f_i(\vec{v})/\partial v_k +$$

$$\frac{A\sqrt{\gamma A}}{Z}\Big[f_i(\vec{v})\,\partial f_e(\vec{v}'\sqrt{\gamma A})/\partial v_k' - \gamma f_e(\vec{v}'\sqrt{\gamma A})\,\partial f_i(\vec{v})/\partial v_k\Big]\Big\}\,U_{jk}(\vec{v}-\vec{v}') \qquad \text{and} \qquad (2.a)$$

$$C_e(f,f) = \frac{\sqrt{\pi}}{2}\sum_{j,k}\frac{\partial}{\partial v_j}\int d^3v\cdot\Big\{\frac{1}{Z}\Big[f_e(\vec{v})\,\partial f_e(\vec{v}')/\partial v_k' - f_e(\vec{v}')\,\partial f_e(\vec{v})/\partial v_k +$$

$$(\gamma A)^{-3/2}\Big[\gamma f_e(\vec{v})\,\partial f_i(\vec{v}'/\sqrt{\gamma A})/\partial v_k' - f_i(\vec{v}'/\sqrt{\gamma A})\,\partial f_e(\vec{v})/\partial v_k\Big]\Big\}U_{jk}(\vec{v}-\vec{v}'), \qquad (2.b)$$

where the dimensionless factors Γ_α in front of the collision operators are given by

$$\Gamma_i := -\frac{3}{2\sqrt{2}}\left[\frac{\nu_i\Omega_i}{\omega_i\omega_i}\right]\delta_i^2 \qquad (2.c) \qquad \Gamma_e := -\frac{3}{4}\left[\frac{\nu_e\Omega_e}{\omega_e\omega_e}\right]\delta_e^2 \qquad (2.d)$$

and the tensor U_{jk} is defined by $\qquad U_{jk}(\vec{x}) = (\delta_{jk}\vec{x}^2 - x_j x_k)\,|\vec{x}|^{-3} \qquad (2.e)$

$$a_\alpha := \frac{v_a}{v_{th}^\alpha},\ \delta_\alpha := \frac{\omega_\alpha}{\Omega_\alpha} = \frac{r_{l\alpha}}{l},\ \sigma(q_\alpha) := \mathrm{sign}(q_\alpha),\ A := \frac{\bar{T}_i}{\bar{T}_e},\ \gamma := \frac{m_e}{m_i} \qquad (2.f)$$

Z is the charge number of the ions, ν_α are the collision rates, ω_α are the transit frequencies $\omega_\alpha = v_{th}^\alpha/l$, $r_{l\alpha}$ are the Larmor radii.

It turns out that for a fusion plasma in a present–day large fusion experiment the four timescales considered obey in a standardized form the relation

$$\tau_{\alpha n} = \tau_{\alpha 0}\delta_\alpha^{-n} \quad \text{with} \quad \tau_{\alpha 0} = \Omega_\alpha^{-1} \quad \text{and} \quad n = 0,1,2,3 \qquad (3)$$

The multiple timescale derivative expansion approach then reads in a standardized form

$$f_\alpha = \sum_{n=0} \delta_\alpha^n f_{\alpha n}(\vec{x},\vec{v};t_0,t_1,t_2,t_3) \text{ and } \frac{\partial}{\partial t} = \sum_{n=0}\delta_\alpha^n \frac{\partial}{\partial t_n}. \qquad (4)$$

This formalism is now applied to the dimensionless Fokker–Planck equation leading for each order of δ_α to a separate equation. The zero and first–order equations have been treated in /1/, leading to the static Stellarator and stationary Tokamak (RFP) equilibria. In this paper we will discuss the second order equation (5).

$$\delta_\alpha^2:\ \frac{\partial f_{\alpha 0}}{\partial t_2} + \frac{\partial f_{\alpha 1}}{\partial t_1} + \frac{\partial f_{\alpha 2}}{\partial t_0} + \vec{v}\cdot\nabla f_{\alpha 1} + \sigma(q_\alpha)\left\{\frac{\delta_i^2}{\delta_\alpha^2}[a_\alpha\vec{E}_2 + \vec{v}\times\vec{B}_2]\cdot\frac{\partial f_{\alpha 0}}{\partial\vec{v}} + \right.$$

$$\left.\frac{\delta_i}{\delta_\alpha}[a_\alpha\vec{E}_1 + \vec{v}\times\vec{B}_1]\cdot\frac{\partial f_{\alpha 1}}{\partial\vec{v}} + [a_\alpha\vec{E}_0 + \vec{v}\times\vec{B}_0]\cdot\frac{\partial f_{\alpha 2}}{\partial\vec{v}}\right\} = \Gamma_\alpha C_{\alpha 0}(f_{\alpha 0}, f_{\beta 0}) \qquad (5)$$

INTEGRATION OF THE ZERO–ORDER COLLISION OPERATOR $C_{\alpha 0}(f_{\alpha 0}, f_{\beta 0})$

The zero order collision operators are obtained from Eqs. (2.a) and (2.b) by inserting for $f_{\alpha 0}$ the drifted normalized Maxwellian distribution functions. According to the different velocity normalization, we have in C_{i0} and C_{e0} to insert $f_{e0}(\vec{v}'\sqrt{\gamma A})$ and $f_{i0}(\vec{v}'/\sqrt{\gamma A})$ respectively, with $\hat{\vec{u}}_{e0} = \vec{u}_{e0}/\sqrt{\gamma A}$ and $\hat{\vec{u}}_{i0} = \vec{u}_{i0}\sqrt{\gamma A}$.

The collision operators can now be integrated leading after some tedious manipulations to the simple form

$$C_{\alpha 0}(\vec{x},\vec{v},t_2,t_3) = B_\alpha\nabla_{\vec{v}}\left\{\exp\left[-\frac{(\vec{\omega}_\alpha + \vec{b}_\alpha)^2}{\lambda_\alpha^2\tau_{\alpha 0}}\right]\mathbb{W}\cdot\vec{z}_\alpha\right\} \qquad \text{with} \qquad (6)$$

$$B_\alpha = \frac{n_{i0}n_{e0}}{\pi^{3/2}T_{\alpha 0}^{3/2}},\quad \vec{\omega}_\alpha = \lambda_\alpha(\vec{v} - \hat{\vec{u}}_{\beta 0}),\quad \vec{b}_\alpha = \lambda_\alpha(\hat{\vec{u}}_{\beta 0} - \vec{u}_{\alpha 0}),\quad \vec{z}_\alpha = c_\alpha\vec{\omega}_\alpha + \vec{b}_\alpha \qquad (6.a)$$

$$\lambda_i = \sqrt{\frac{\gamma A}{\tau\omega}},\quad \lambda_e = \frac{1}{\sqrt{\gamma A T_{i0}}},\quad C_i = \left(1 - \frac{AT_{i0}}{T_{e0}}\right),\quad C_e = \left(1 - \frac{T_{e0}}{AT_{i0}}\right). \qquad (6.b)$$

With the aid of the perpendicular and parallel projection operators $P_\perp$ and $P_\parallel$ the tensor $\mathbb{W}$ can be written as

$$W = (g-h)P_{\perp}(\frac{\vec{\omega}}{\omega}) + 2hP_{\parallel}(\frac{\vec{\omega}}{\omega}),\ g(\omega) = \sqrt{\pi}\frac{\mathrm{erf}(\omega)}{\omega},\quad h(\omega) = \frac{1}{\omega^3}\left\{\frac{\sqrt{\pi}}{2}\mathrm{erf}(\omega) - \omega e^{-\omega^2}\right\} \qquad (6.c)$$

From the above equations we infer that the collision operators $C_{\alpha 0}$ vanishes for $\vec{z}_\alpha = 0$, i.e., for equal zero–order drift velocities and temperature profiles.

VELOCITY MOMENTS OF THE COLLISION OPERATORS $C_{\alpha 0}$

The zero–order moment, defined by $\langle 1\rangle := \int C_{\alpha 0} d^3v$ vanishes on account of the velocity divergence of $C_{\alpha 0}$, thus expressing particle conservation.

After performing the integration of the first–order moment $\langle\vec{v}\rangle := \int\vec{v}C_{\alpha 0}d^3v$ we obtain

$$\langle\vec{v}\rangle_\alpha = \frac{\vec{b}_\alpha}{b_\alpha^2}\frac{2\kappa_\alpha\lambda_\alpha^2 n_{i0}n_{\alpha 0}}{\sqrt{1+\lambda_\alpha^2T_{\alpha 0}}}\left\{\exp\left[-\frac{b_\alpha^2}{1+\lambda_\alpha^2T_{\alpha 0}}\right] - S(\lambda_\alpha^2T_{\alpha 0}, b_\alpha)\right\},\quad \text{with} \qquad (7)$$

$$S(\lambda^2T,b) = \sqrt{1+\lambda_\alpha^2T_{\alpha 0}}\,\lambda_\alpha^2T_{\alpha 0}\exp\left[-\frac{b_\alpha^2}{\lambda_\alpha^2T_{\alpha 0}}\right]\sum_{n=0}^{\infty}\frac{(-1)^n}{n!(2n+1)}\frac{d^{2n}}{d\beta^{2n}}\left[\beta\exp\left[\frac{\beta^2\lambda^2T}{4}\right]\right] \qquad (8)$$

and $\kappa_i = 1 + 1/\gamma$, $\kappa_e = 1+\gamma$, $\beta = \frac{2b}{\lambda^2T}$.

Neglecting terms of the order $0(\gamma)$ we finally obtain

$$\langle\vec{v}\rangle_i = (\vec{u}_{i0} - \hat{\vec{u}}_{e0})\frac{4}{3}\frac{A\sqrt{\gamma A}\ n_{i0}^2}{T_{e0}^{3/2}},\qquad \langle\vec{v}\rangle_e = (\vec{u}_{e0} - \hat{\vec{u}}_{i0})\frac{4}{3}\frac{n_{i0}n_{e0}}{T_{e0}^{3/2}} \qquad (9)$$

The friction forces $\tilde{\vec{R}}_\alpha$ are then simply written in dimensional form

$$\tilde{\vec{R}}_\alpha = m_\alpha\bar{n}_\alpha\Gamma_\alpha\Omega_\alpha v_{th}^{\alpha}\langle\vec{v}\rangle_\alpha \qquad (10)$$

It can be easily shown that the sum of the friction forces vanishes just as it should be.

For the second–order velocity moment defined by $\langle v^2/2\rangle = \int (v^2/2)C_{\alpha 0}\,d^3v$ we analogously obtain

$$\left\langle\frac{v^2}{2}\right\rangle_\alpha = \frac{2n_{i0}n_{\alpha 0}}{b_\alpha\lambda_\alpha T_{\alpha 0}\sqrt{1+\lambda_\alpha^2T_{\alpha 0}}}\left\{\left[k_\alpha + \frac{c_\alpha b_\alpha}{1+\lambda_\alpha^2T_{\alpha 0}}\right]\exp\left[-\frac{b_\alpha^2}{1+\lambda_\alpha^2T_{\alpha 0}}\right] -\right.$$

$$\left. - [c_\alpha b_\alpha + k_\alpha]\ S(\lambda_\alpha^2T_{\alpha 0}, b_\alpha)\right\} \qquad \text{with} \qquad (11)$$

$$k_i = d_i\frac{AT_{i0}}{T_{e0}}(1+\gamma) - b_i,\quad k_e = \frac{d_e}{\gamma}\frac{T_{e0}}{AT_{i0}}(1+\gamma) - b_e,\quad d_\alpha = \pm\lambda_\alpha|\hat{\vec{u}}_{\beta 0}|$$

Again neglecting terms of the order $0(\gamma)$ we finally obtain

$$\left\langle\frac{v^2}{2}\right\rangle_i = \frac{2n_{i0}n_{i0}A\sqrt{\gamma A}}{T_{e0}^{3/2}}\left\{(AT_{i0} - T_{e0}) - \frac{2}{3}\vec{u}_{i0}(\hat{\vec{u}}_{e0} - \vec{u}_{i0})\right\}\quad \text{and}$$

$$\left\langle\frac{v^2}{2}\right\rangle_e = \frac{2n_{i0}n_{e0}}{T_{e0}^{3/2}}\left\{(T_{e0} - AT_{i0}) - \frac{2}{3}\vec{u}_{e0}(\hat{\vec{u}}_{i0} - \vec{u}_{e0})\right\} \qquad (12)$$

The expression for particle heating is in dimensional form then simply given by

$$Q_\alpha = \int m_\alpha \frac{\tilde{v}^2}{2} \tilde{C}_{\alpha 0}\, d^3\tilde{v} = m_\alpha \bar{n}_\alpha v_{ti}^2 \Omega_\alpha \Gamma_\alpha \left\langle \frac{v^2}{2} \right\rangle_\alpha \tag{13}$$

We now conclude that the zero–order fluid velocity crucially enters into the velocity moments of the zero–order collision operator and thus contributes to the corresponding transport on the collision timescale. Since in a present–day large Tokamak or RFP rotation velocities are observed close to the ion thermal velocity, finite zero–order fluid velocities have to be taken into account.

TRANSPORT EQUATIONS ON THE COLLISION TIMESCALE

We now calculate the velocity moment of the second–order Fokker–Planck equation (5) and perform the time average over the first two timescales $\tau_{\alpha 0}$ and $\tau_{\alpha 1}$

$$\frac{\partial n_{\alpha 0}}{\partial t_2} + \nabla (n\vec{u})_{\alpha 1} = 0 \tag{14.a}$$

$$\frac{\partial}{\partial t_2}(n\vec{u})_{\alpha 0} + \nabla \cdot (n\vec{u}\otimes\vec{u})_{\alpha 1} + \frac{1}{2}\nabla (nT)_{\alpha 1} - \sigma(q_\alpha)\left[(n\vec{u})_{\alpha 2}\times\vec{B}_0 - \frac{\delta_i^2}{\delta_\alpha^2}\left[a_\alpha n_{\alpha 0}\vec{E}_2 + (n\vec{u})_{\alpha 0}\times\vec{B}_2\right]\right] =$$

$$= \Gamma_\alpha \delta_\alpha^{-2} \langle v \rangle_\alpha - \sigma(q_\alpha)\frac{\delta_i}{\delta_\alpha}\langle a_\alpha n_{\alpha 1}\vec{E}_1 + (n\vec{u})_{\alpha 1}\times\vec{B}_1\rangle_{\tau_{\alpha 0},\tau_{\alpha 1}} \tag{14.b}$$

$$\frac{\partial}{\partial t_2}\left\{\frac{3}{4}nT + \frac{n\vec{u}^2}{2}\right\}_{\alpha 0} + \nabla\cdot\left\{\left[\frac{5}{4}nT + \frac{n\vec{u}^2}{2}\right]\vec{u}\right\}_{\alpha 1} - \sigma(q_\alpha)\frac{\delta_i^2}{\delta_\alpha^2} a_\alpha (n\vec{u})_{\alpha 0}\vec{E}_2 =$$

$$= \Gamma_\alpha \delta_\alpha^{-2}\left\langle \frac{v^2}{2}\right\rangle_\alpha + \sigma(q_\alpha)\frac{\delta_i}{\delta_\alpha} a_\alpha \langle (n\vec{u})_{\alpha 1}\cdot\vec{E}_1\rangle_{\tau_{\alpha 0},\tau_{\alpha 1}} \tag{14.c}$$

Assuming for the first order quantities $q_{\alpha 1}$ a harmonic time dependence, the time average of the quadratic $q_{\alpha 1}$ quantities on the right–hand side of Eqs. (14.b) and (14.c) will lead to an additional transport on the collision timescale. This will essentially be the turbulent transport arising from the MHD fluctuation spectrum. Moreover, in these terms there may be also included the effects of wave heating or current drive. Note that the transport coefficients arising from these equations are by a factor δ_α^{-1} larger than those of classical or neoclassical transport described by the velocity moments of the third–order Fokker–Planck equation.

The solution for the $q_{\alpha 1}$ quantities and the actual calculation of transport coefficients is the subject of future work.

/1/ J.W. Edenstrasser, Proceedings 17th EPS Conf. on Controlled Fusion and Plasma Heating, Amsterdam, 1990, Vol. II, p. 881.

Work supported by the Austrian Research Funds, contract P 8405.

ELECTRON HEAT CONDUCTION AND SUPRATHERMAL PARTICLES.

O.G. Bakunin, S.I. Krasheninnikov

I.V.Kurchatov Institute, Moscow, USSR.

As recognized at present, the applicability of Spitzer-Harm's theory on electron heat conduction along the magnetic field is limited by comparatively small values of the thermal electron mean free path ratio, λ to the characteristic length of changes in plasma parameters, L: $\gamma=\lambda/L \le 10^{-2}$ [1-6]. As shown in [7], the stationary kinetic equation for the electron distribution function inhomogeneous along the x-axis $f_e(\vec{v},x)$ allows one to have solutions in the self-similar variables. The objective of a given study is to generalize the solutions [7] for the case of arbitrary Z_{eff}, that will allow one to compare approximate solutions to the kinetic equation with the precise ones in a wide range of parameters.

The electron distribution function may be represented in the self-similar variables [7]:

$$f_e(\vec{v},x)= N\ F(\vec{V})/[T_e(x)]^{\alpha},\quad \vec{V}= \vec{v}(m/2T_e(x))^{1/2}, \qquad (1)$$

where N is the normalization factor; $\int F(\vec{v})d\vec{v} =1$; α is the free parameter; the function $T_e(x)$ plays the role of a characteristic average electron energy. In this case kinetic equation for $f_e(\vec{v},x)$ is converted in the following way:

$$\gamma V\mu\left(\alpha F+\frac{V}{2}\frac{\partial F}{\partial V}\right)-\frac{\gamma_E}{2m}\left(\mu\frac{\partial F}{\partial V}+\frac{1-\mu^2}{V}\frac{\partial F}{\partial \mu}\right)=\frac{1}{4}\left(St(\vec{V},F)+Z_I\nu^{-3\partial}_{I}\frac{\partial}{\partial\mu}(1-\mu^2)\frac{\partial F}{\partial\mu}\right), \qquad (2)$$

where the parameter $\gamma_E= eET_e/(2\pi e^4\Lambda n_e)$ is found from the particle flux ambipolarity condition $J= \int F(\vec{V})V\mu\ d\vec{V}=0$; $St(\vec{V},F)$ is the collisional Colombian operator; $E(x)$ is the ambipolar electric field; $\mu= cos(\vec{v}\,\vec{x})$.

The solution of Eq.(2) corresponds to the constant ratio of the mean free path for electrons with the energy of about $T_e(x)$ to the characteristic length of a change in $T_e(x)$:

$$\gamma = - T_e^2(dlnT_e/dx)/(2\pi e^4\Lambda n_e) = const. \qquad (3)$$

Taking account of Eq.(1), the relationship Eq.(3) results in the following dependencies $T_e(x)$, $n_e(x)$ and for the energy flux density $q(x)$:

$$T_e^{(\alpha-1/2)}(dT_e/dx) = const,\qquad n_e \propto T_e^{(3/2-\alpha)}\ ; \qquad (4)$$

$$q(x) = QT_e(x)^{(3-\alpha)}N(2/m)^2, \quad Q = \int F(\vec{V})V^3\mu d\vec{V} . \qquad (5)$$

In the limit of interest, $V >> 1$, Eq.(2) is transformed into the form:

$$\gamma\mu\left(\alpha F+\xi\frac{\partial F}{\partial\xi}\right)-\gamma_E\left(\mu\frac{\partial F}{\partial\xi}+\frac{1-\mu^2}{2\xi}\frac{\partial F}{\partial\mu}\right)=\frac{1}{\xi}\frac{\partial}{\partial\xi}\left(F+\frac{\partial F}{\partial\xi}\right)+\frac{\beta}{2}\xi^{-2}\frac{\partial}{\partial\mu}(1-\mu^2)\frac{\partial F}{\partial\mu}, \quad (6)$$

where $\xi = V^2$, $\beta=(1+Z_I)/2$.

Further simplifications of the kinetic equation can be related with a fast symmetrization of the electron distribution function at high β, when $F(\vec{V})$ can be represented in the form: $F(\vec{V}) = F_0(V) + \mu F_1(V)$; where $F_0 > F_1$:

$$\frac{\gamma^2}{\beta}\left(\xi^{(1-\alpha)}\frac{d}{d\xi}\left(\xi^{\alpha}\hat{F}_0\right) - \frac{\delta}{\xi}\frac{d}{d\xi}\left(\xi\hat{F}_0\right)\right) = \frac{3}{\xi}\frac{d}{d\xi}\left(F_0 + \frac{dF_0}{d\xi}\right), \qquad (7)$$

where $\delta=\gamma_E/\gamma \simeq 1$, $\hat{F}_0=-\xi^{(3-\alpha)}d(\xi^{\alpha}F_0)/d\xi+\delta\xi^2 dF_0/d\xi$.

Now let us consider when such an approach is justified from the viewpoint of a research in an effect of suprathermal particles on electron heat conduction. Let us assume the electron temperature profile to be characterized by the magnitude of $\gamma<<1$. Analyzing Eq.(7), one can show that a distortion in the Maxwellian distribution function and, as a result, an essential effect of suprathermal electrons on heat conduction, provided by the suprathermal particle transport, starts to be manifested at the energies $\xi^5 \geq \beta/\gamma^2$. On the other hand, in order the condition $F_0(v) >> F_1(v)$, to be true, it is necessary, as seen from Eq.(7), to have the electron energy to be rather small $\xi^3 \leq \beta/\gamma$. Hence, it follows that an analysis of the suprathermal particle effect on electron heat condition at the plasma parameter profiles characterized by can be based on a symmetrized kinetic equation of the type [6] or Eq.(7) under condition $\beta \geq \gamma^{-1/2}$ only. Then, at the energies $\xi^4 \geq \beta/\gamma^2$, i.e. when electrons have time to diffuse for a distance (in the free mean paths) of about γ^{-1} distortion in the Maxwellian function becomes very strong ,and $f_e(\vec{v},x)$ is determined by the integral $T_e(x)$ profile. A strong anisotropy in $f_e(\vec{v},x)$ and violation of the applicability conditions Eq.(7) can be expected to approach at $\xi^2 \geq \beta/\gamma$, when the mean free path becomes greater than the characteristic inhomogeneity size in $T_e(x)$. (Fig.1).

In the apposite case ($\beta \leq \gamma^{-1/2}$), a distortion in the Maxwellian distribution function is accompanied by a strong anisotropization even at rather low energies, not mentioning energies of the order of $\xi^2 \geq \beta/\gamma$. Therefore here one should consider the complete equation Eq.(6). (Fig.2).

We omit here the exact solutions of Eqs.(6),(7) since they rather cumbersome [8]. However, the presence of a strongly-anisotropic tail in terms of power law to the distribution function at the energies $\xi \geq (\beta/\gamma)^{1/2}$ should be, first

of all, emphasized in the solutions of the above-derived equations. This result is quite natural, if one takes account of the fact that electrons are collectivized at such energies and their spectrum should be determined by global characteristics of the temperature and density particles, $T_e(x)$, $n_e(x)$, not by their local values. Since we consider the distribution function $f_e(\vec{v},x)$ in the dimensionless variable "energies" ξ, Eq.(1), the only dependence f_e on v, satisfying this conduction, will be $f_e \propto 1/v^{2\alpha}$ [7].

Formally , such a power-law dependence, $f_e(v)$ results in a divergence of the dimensionless heat flux, Q in the expression Eq.(5), at $\alpha \leq 3$, provided by the contribution of suprathermal particles that corresponds to a rather steep dependence $T_e(x)$: $dlnT_e/dlnx \geq 2/7$; the quantity γ in this case can anywhere pear to be negligible. At $\alpha=3$ the divergence has a logarithmic nature, at $\alpha<3$ it obeys the power law. One should note that the Luciani like expression for the heat flux, for the electron temperature and density profilesunder consideration does not discern the cases when $\alpha > 3$ and $\alpha < 3$: $q_L = q_{SH}(x)/[1-\gamma^2(3-\alpha)^2]$.

However, the emergence of a great amount of suprathermal, electrons is related with their transport from some hotter zones. Therefore in the real limited systems, the effect of tail electrons on the heat flux becomes essential at a rather great temperature difference:

$$\frac{T_{max}}{T_{min}} > \left(\gamma\left(\frac{\gamma}{\beta}\right)^{\alpha/2}\right)^{1/(3-\alpha)} \times exp\begin{cases} C_1/\gamma^{1/2}, & \beta<\gamma^{-1/2} \\ C_2(\beta/\gamma^2)^{1/5}, & \beta>\gamma^{-1/2} \end{cases} \quad (\alpha<3), \quad (8)$$

here $C_1 = 2/[3(3-\alpha)]$, $C_2 = 3^{1/5}\Gamma(1/5)\Gamma(4/5)/[5(3-\alpha)]$.

Note, however, that the estimate Eq.(8) and other generalizations made in a given paper are based on self-similar solutions to the collisional kinetic equation, obtained for the electron temperature and density profiles characterized by γ. It in natural that they are not spread to the zones with uniform electron temperature at the steep-wise temperature profile. Moreover, a definite effect on the heat flux production is done by some boundary effect too (e.g. integration between the plasma and divertor plates of the tokamak). Their study is beyond the framework of a given paper.

REFERENCES

1. Gurevich A.V., Istomin Ya.N.,JETP. 77(1977)933.
2. Bell A.R. et al., Phys.Rev.Lett. 46(1981)243.
3. Mason R.J., Phys.Rev.Lett. 47(1981)652.
4. Luciani J.F. et al., Phys.Rev.Lett. 51(1983)1664.
5. Belyi V.V. et al. Phys.Fluids B1(1989)305.
6. Albritton J.R. et al., Phys.Rev.Lett. 57(1986)1887.
7. Krasheninnikov S.I., JETP 94(1988)166.
8. Bakunin O.G., Krasheninnikov S.I.; Preprint IAE-5291/6, 1991.

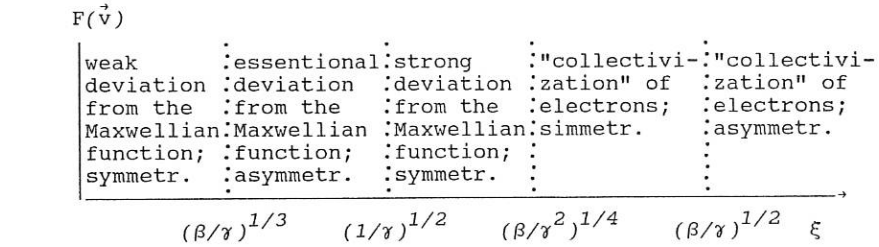

Fig.1. Characteristic zones of electron distribution function change at moderate Z_{eff}: $\beta \leq 1/\gamma^{1/2}$.

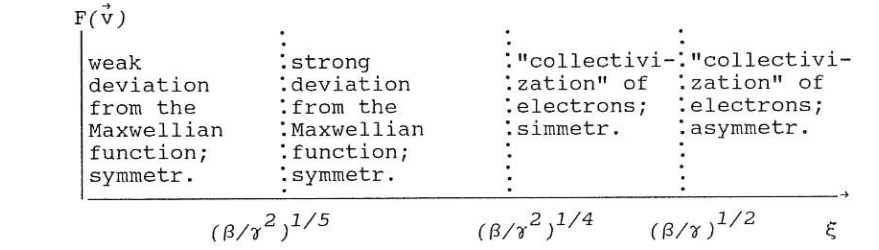

Fig.2. Characteristic zones of electron distribution function change at high Z_{eff}: $\beta \geq 1/\gamma^{1/2}$.

FAST POLOIDAL ROTATION AND IMPROVED CONFINEMENT.

V,Rozhansky*, A.Samain**, and M.Tendler

Royal Institute of Technology, Fusion Research, Stockholm 70, S-10044 Sweden
*Technical University, Leningrad, USSR
**Association Euratom-CEA, DRFC, CEN Cadarache, St Paul lez Durance, France

1.INTRODUCTION.

Recently it has been shown on many tokamaks that a transition into regimes with improved confinement is accompanied by an increase in the poloidal rotation velocity V_p at the edge of a tokamak[1].This is also borne out by experiments on the tokamak " TUMAN 3",where large poloidal rotation velocities much in excess of the poloidal sound speed $\Theta C_s(\Theta=B_p/B$ and $C_s=(T/m_i)^{1/2}$) were induced by means of the externally biased electrode[1].

Here,the temporal and the spatial relaxation of an arbitrary poloidal rotation velocity is considered.It is shown that extending the neoclassical expressions for the parallel viscosity and the inertia for the plateau regime into $V_p>\Theta C_s$ yields qualitatively different results compared to $V_p<<\Theta C_s$[2].The parallel viscosity and the inertia turn out to be the grossly nonlinear functions of the V_p.Moreover for $V_p\geq\Theta C_s$, the time scale for the relaxation of V_p is strongly enhanced versus $V_p<<\Theta C_s$.Furthermore the quasi-stationary state does not emerge at all (the torque provided by the inertia can not be damped by viscosity) within the framework of the neoclassical theory provided that $V_p>>\Theta C_S$.Therefore the inertia and the viscosity driven by the turbulence are invoked resulting in the quasi-stationary profile of the poloidal rotation velocity.Thus our model accounts for fluxes driven by a turbulence and therefore is more general than the neoclassical theory.Resulting profiles of V_p acquire the large flow shear,beneficial for suppresion of edge turbulence by decorrelation[3].

2.KINETIC MODEL.

Because the typical timescale is much longer than the gyroperiod,a drift kinetic equation is employed in the plateau regime.In the circular cross section approximation with coordinates r,υ and z,which will frequently be used for simplicity,the magnetic field is given by

$$\mathbf{B}=B_0(\mathbf{e}_z+\Theta\mathbf{e}_\upsilon)/(1+\varepsilon\cos\upsilon);\ \varepsilon=r/R$$

The drift kinetic equation can be written for the ion distribution function f_i as [4]

$$\partial f_i/\partial t+\mathbf{V}_{ci}\cdot\nabla f_i+\dot{V}_{||i}(\partial f_i/\partial V_{||i})+\dot{V}_{\perp i}(\partial f_i/\partial V_{\perp i})=St\,f_i \qquad (1)$$

where $\mathbf{V}_{ci}$ is the guiding center velocity and $\dot{V}_{||i},\dot{V}_{\perp i}$ are rates of change of the parallel and the perpendicular velocities.They are given respectively by

$$\mathbf{V}_{ci}=-cm_i(V_{\perp i}^2/2+V_{||i}^2)(\mathbf{e}_\upsilon\cos\upsilon+\mathbf{e}_r\sin\upsilon)/eBR+c[\mathbf{B}\times\nabla\Phi]/B^2+V_{||i}\mathbf{e}_z+u_r\mathbf{e}_r \qquad (2)$$

$$\dot{V}_{||i}=-e\Theta\partial\Phi/m_ir\partial\upsilon-V_{\perp i}^2\Theta\varepsilon\sin\upsilon/2r+V_0V_{||i}\,\varepsilon\sin\upsilon/r \qquad (3)$$

$$\dot{V}_{\perp i}=V_{||i}V_{\perp i}\Theta\varepsilon\sin\upsilon/2r+V_0V_{\perp i}\,\varepsilon\sin\upsilon/2r \qquad (4)$$

where u_r is the velocity of anomalous transport and $V_0=c\Phi_0/Bdr$ is the rotation speed in the radial electric field.

The first term in Eq.(4) and the second in Eq.(3) arise due to the conservation of the magnetic moment $\mu=m_iV_{\perp i}^2/2B$ at the trajectory.The last terms in Eqs.(3&4) result from the

inhomogeneity of the electric drift in the nonuniform magnetic field.The solution is sought in the form

$$f_i=f_{0i}(r)+f_{1i}(r,\upsilon),\quad \Phi=\Phi_0(r)+\Phi_1(r,\upsilon) \tag{5}$$

where f_{0i} is the angle-average distribution function,close to Maxwellian and $f_{1i},\Phi_1\sim\exp(i\upsilon)$ are the first order perturbations determined by Eq.(1).In the plateau regime,the conventional approach $\nu_i\to 0$ yields[5]

$$f_{1i}=[P.V.\{(V_0+\Theta V_{||i})^{-1}\}+\pi\delta(V_0+\Theta V_{||i})\partial/\partial\upsilon]\hat{A}_i f_{0i}$$

$$\hat{A}_i=\{e\Phi_1/m_i\,[\Theta\partial/\partial V_{||i}+cm_i\partial/(e_iB)\partial r]-cm_i(V_{\perp i}^2/2+V_{||i}^2)\,\varepsilon\cos\upsilon\partial/(e_iB)\partial r+m_i(V_{||i}^2+V_{\perp i}^2/2)\,\varepsilon\cos\upsilon/T\} \tag{6}$$

where P.V. is the principal value integral.Integrating Eq.(6) over the velocity space and employing the quasi-neutrality,the variations of density $n_1(\upsilon)$ and $u_{||i}(\upsilon)$ are obtained in a simple and compact form for $|V_0|>>\Theta C_s$.

$$n_1(\upsilon)/n_0=-2\varepsilon\cos\upsilon[1+(1+T_e/2T_i)/V_0'^2] \tag{7}$$

$$u_{||i}=2\varepsilon C_s\cos\upsilon\,(1+T_e/2T_i)/V_0' \tag{8}$$

where $V_0'=V_0/\Theta C_s$, $u_{||i}$ is the poloidaly varying flow velocity.The flux surface average $\langle u_{||i}\rangle$ has been assumed to be smaller than V_0/Θ in accordance with experimental results.Thus Eqs.(7 & 8) are highly nonlinear functions of V_0.The dependence given by Eq.(8) differs significantly from the linear function for $|V_0|<<\Theta C_s^2$, given by the well-known Pfirsch-Schluter formula

$$u_{||i}(\upsilon)=-2\varepsilon V_p\cos\upsilon/\Theta \tag{9}$$

where $V_p=V_0+u_{pi}$ is the speed of poloidal rotation and $u_{pi}=c(eBn_0)^{-1}dp_i/dr$ is the diamagnetic drift velocity.Note that the expression for $u_{||i}(\upsilon)$ has the opposite signs in Eqs.(8 & 9) and is much smaller in the case given by Eq.(8) than by Eq.(9).Moreover the variation of density is of the higher order in $\rho/\Theta r$ if $|V_0|<<\Theta C_s^2$.Thence the variation of density contributes much more significantly to the flux surface average flows in the case of $|V_0|>>\Theta C_s$ than for $|V_0|<<\Theta C_s$. Furthermore the variation of density peaks at the inner half of a tokamak.This is reminiscent of the MARFE phenomenon[6].

The flux surface average flow reads

$$\Gamma_i=\langle\int dV_i(V_{ci})_r(f_{0i}+f_{1i})\rangle \tag{10}$$

where V_{ci} is given by Eq.(2).Thus the surface average of the parallel viscous flux is

$$\Gamma_i=\langle\mathbf{B}\cdot\nabla\overleftrightarrow{\pi}\rangle^{(NEO)}=-\sqrt{\pi}n_0cT_i\varepsilon^2(eB_0r)^{-1}V_0'(2V_0'^4+2V_0'^2+1)\exp(-V_0'^2) \tag{11}$$

The particle flux given by Eq.(11) is the $(m_i/m_e)^{1/2}$ times larger for ions than for electrons regardless the value of V_0.Therefore the ambipolarity requires $\Gamma_i\approx 0$ and Eq.(11) yields $V_0'\approx 0$. However,it is important to keep in mind that Eq.(11) has been derived under the assumption that $u_{pi}<<\Theta C_s$.More accurately the relation $V_0=0(\Theta C_s)$ has been obtained.Accounting for the higher order terms in $u_{pi}/\Theta C_s$ (this procedure corresponds to the next order expansion in the parameter $\rho_i/\Theta r$) the well-known expression from the neoclassical theory for the poloidal rotation velocity is obtained

$$V_p=kc(eB)^{-1}dT_i/dr \tag{12}$$

where k is a coefficient.However,although this result remains unchanged,the relaxation process from an arbitrary V_0 to the value given by (12) undergoes the drastic changes when the parameter V_0' ranges from zero to infinity

In order to emphasize the difference we list cases a). $V_0' \ll 1$ [2] and b). $V_0' \gg 1$ below. The flux surface averaged parallel momentum balance governs the process of relaxation showing that the parallel viscous force damps the poloidal flow according to

$$mnd\langle u_{||i}B\rangle/dt=-\langle \mathbf{B}\cdot\nabla \overleftrightarrow{\pi}_{||}\rangle^{(NEO)} \qquad (13)$$

Thus within the framework of neoclassical theory(neglecting terms originating from turbulence)the time dependent inertia proportional to $\partial V_0/\partial t$ cancels the viscous force.The term at the left hand side of Eq.(13) may be described as damping due to the transit time magnetic pumping in the wave field of the 1/R modulation of the toroidal magnetic field[7].In case a).using Eq.(9) and performing the averaging we obtain [2]

$$\tau_a \cong 2(2/\pi)^{1/2} qR/C_s \qquad (14)$$

where $q=\varepsilon/\Theta$ is the safety factor.In deriving Eq.(14) we have used the expression derived in [2]

$$mnd\langle u_{||i}B\rangle/dt= - (1+2q^2)cm_in_0(eB_0)^{-1}\,\partial V_0/\partial t \qquad (15)$$

In contrast to the case a),the typical time scale is grossly enhanced for the case b) in accordance with

$$\tau_b \cong qR/C_s \exp[(V_0')^2]/V_0'^2 \qquad (16)$$

Thence $\tau_b \to \infty$ when $V_0' \to \infty$ and the rotational quasi-steady state does not emerge.We emphasize again that this rather unexpected result originates from the significant accumulation of density at the inner half of a tokamak due to a fast rotation (thereby almost canceling the effect of the increase of the magnetic surface at the outer half) and the sign reversal of $u_{||i}$ for the case b) versus case a).The latter effect is manifested in the expression for the transit time magnetic pumping term

$$mnd\langle u_{||i}B\rangle/dt= 2q^2cm_in_0(eB_0)^{-1}\,(\partial V_0/\partial t)\times(V_0')^{-2}(1+T_e/2T_i) \qquad (17)$$

Thence an arbitrary poloidal rotation velocity increases on the time scale given by Eq.(16) for $|V_0| \gg \Theta C_s$ and the quasi-stationary state described by Eq.(12) does not exist within the framework of the neoclassical theory.

In order to alleviate the difficulty we modify the neoclassical theory incorporating the effect of anomalous transport on convective inertia and viscosity.The corresponding terms are added to the Eq.(13) yielding in the steady-state

$$mnu_r d\langle u_{||i}B\rangle/dr = - \langle \mathbf{B}\cdot\nabla \overleftrightarrow{\pi}_{||}\rangle^{(NEO)} - \langle \mathbf{B}\cdot\nabla \overleftrightarrow{\pi}_{||}\rangle^{(A)} \qquad (18)$$

where $nu_r = -D^{(A)}dn/dr$ is the anomalous flux,which is also assumed to be ambipolar.The anomalous viscosity is determined by the dependence of $u_{||i}$ on the minor radius component r and may be reduced to [8]

$$\langle \mathbf{B}\cdot\nabla \overleftrightarrow{\pi}_{||}\rangle=\langle (B/r)d[rn\eta(du_{||i}/dr)]/dr\rangle \qquad (19)$$

where $\eta/m_i \approx D^{(A)}$ is the anomalous viscosity.If $|V_0| \ll \Theta C_s$ (the case a)) Eq.(18) yields [2]

$$dV_0/dr+\alpha(r)(V_0-V_0^{(NEO)})=(m_in\, r\, u_r^{(A)})^{-1}d[rn\eta(dV_0/dr)]/dr \qquad (20)$$

where $\alpha(r)=(u_r^{(A)}\tau_a)^{-1}$, $V_0^{(NEO)}$ is the neoclassical profile of the rotation velocity.Eq.(20) governs the spatial relaxation of the V_0 profile for the case a).The resulting profile crucially depends on the ratio of the third and the first terms in Eq.(20).If $\eta/m_i \approx D^{(A)}$,then the third term due to anomalous viscosity is of the order L_η/L_{V_0} the first term arising due to the inertia

enhanced by a turbulence.Here,L_n and L_{V0} are the spatial scales of the density and the rotation speed profiles,respectively.

When $|V_0| \geq \Theta C_s$,Eq.(18) represents the strongly nonlinear equation with respect to V_0.The analysis of this complex equation is postponed to subsequent publications.However,for the case b),when $|V_0| >> \Theta C_s$,the simple solution may be obtained because then the effect of the neoclassical viscosity is weak due to the exponentialy small amount of trapped particles. Thus,the second term in Eqs.(18 & 20) can be neglected and the obvious solution is obtained reading $u_{||i}$ is a constant independent of r.Thence substituting Eq.(8) we obtain for $|V_0| >> \Theta C_s$

$$V_0(r)=A\, q\, \Theta^2\, T_i\, (1+T_e/2T_i) \qquad (21)$$

where A is a dimensional coefficient,governed by boundary conditions[2].

In summary, the profile of the velocity of the poloidal rotation is determined by profiles of q,Θ,T_i and T_e if $|V_0| >> \Theta C_s$.

3.CONCLUSIONS.

1. It is shown that the quasi-stationary profile of the poloidal rotation velocity does not emerge within the framework of the neoclassical theory in the plateau regime if the imposed poloidal rotation velocity significantly exceeds the poloidal sound speed.
2. In order to obtain the equilibrium profile the neoclassical theory has been extended by incorporating both the anomalous inertia and viscosity.Thence,the resulting profile for the poloidal rotation velocity is shown to be governed by both of these effects.
3. This profile is characterized by the enhanced flow shear,beneficial for suppresion of edge turbulence by decorrelation.
4. The significant peaking of the plasma density is found at the inner half of a tokamak resulting from the fast plasma rotation.

REFERENCES.

1. Groebner R.J. et al.,in Proceedings of the 16th European Conference on Controlled Fusion & Plasma Physics,Venice,**13B**,245,1989
Taylor R.J.et al.Phys.Rev.Lett.**63**,2365,1989
"TUMAN 3" these Proceedings.
2. Tendler M.& V.Rozhansky Bull.Am.Phys.Soc.**34**,2162,paper 9E4,1989; Comments on Plasma Physics & Controlled Fusion **13**,191,1990; Proceedings of the 17th European Conference on Controlled Fusion & Plasma Physics,Amsterdam,**14B2**,287,1990 and Sov.Phys.-JETP Lett.in press (Pisma v Zh.E.T.F. **53**,80,1991 in Russian)
3. Biglari H.,Diamond P.,Terry P.Phys.Fl.**B2**,1,1990
4. Sivukhin D.V. in Reviews of Plasma Physics,edited by M.Leontovich, Consultants Bureau ,New York v.**1**,p.1.1963
5. Galeev A.A. & Sagdeev R.Z. in Reviews of Plasma Physics,edited by M.Leontovich, Consultants Bureau, New York,v.**7**,p.257,1979
6. Lipschultz B.J.Nuc.Mat.145-147,15,1987
7. Hazeltine R.D.,Lee E.P.,Rosenbluth M.N. Phys.Fluids **14**,361,1971
Hirschman S.P.Nuc.Fus.**18**,917,1978
Hassam A.B.& Kulsrud R.M.,Phys.Fluids **21**,2271,1978
Shaing K.C.& Crume E,C. Phys.Rev.Lett.**63**,2369,1989
8. Garbet X, Laurent L,Mourgues F,Roubin J.P.,& Samain A,in Proceedings of the 12 th International Conference on Plasma Physics and Controlled Fusion,IAEA,Nice,v.**2**,163,1988

Net Transport Equations For A Tokamak Plasma*

J.D. Callen and J.B. Hollenberg
University of Wisconsin, Madison, WI 53706-1687 USA

Introduction. Tokamak plasmas seem to exhibit a combination of classical /neoclassical (Coulomb-collision-induced) and anomalous (turbulence induced?) transport mechanisms — Spitzer electrical conductivity plus bootstrap,[1] trapped-particle[2] and poloidal flow damping[3] effects along the magnetic field $\mathbf{B}$, but mostly anomalous transport perpendicular to $\mathbf{B}$ (except at low plasma current where ion neoclassical heat conduction can become dominant[4]). Thus it is of interest to develop a plasma transport model that includes, simultaneously, both collision- and turbulence-induced processes in a tokamak plasma. In calculating the plasma-turbulence-induced transport it is important to eliminate the components of the fluctuations that cause no net transport (e.g., those that satisfy $\mathbf{E}+\mathbf{V}\times\mathbf{B}=0$). In order to begin such a development we consider a fluid moment $(n,\mathbf{V})$ description of a tokamak plasma that allows for a kinetically and nonlinearly determined stress tensor ($\underline{\Pi}$) closure relation. These extended fluid moment equations are the result of fluid/kinetic hybrid descriptions of plasmas based upon a Chapman-Enskog-like approach that have been developed recently.[5,6]

Time-Scales. Presuming the tokamak plasma is stable to ideal MHD instabilities, on the relatively short Alfvén time scale ($t_A \sim R_o q/V_A \sim 0.1-1\mu sec$) it comes into local MHD equilibrium and the poloidal magnetic flux surfaces are governed by the Grad-Shafranov equation. Collisionless free-streaming ($t_{fs} \sim R_o q/v_T \sim \mu sec$) of electrons and ions cause the density and temperature to be constant (and governed by an ideal equation of state) along magnetic field lines and hence flux surfaces on approximately this same time scale. On the slightly longer time scale of electron collisions ($t_{\nu_e} \sim 1/\nu_e \gtrsim 10\mu sec$) electron inertia effects become negligible and the classical/neoclassical Ohm's law becomes established. On the even longer time scale of diamagnetic flow effects ($t_* \sim 1/\omega_* \sim 10-1000\mu sec$) and resistive reconnection of magnetic field lines ($1/\gamma_R \sim t_A S^{3/5}/m^{2/5} \sim msec$) one can have various types of microinstabilities in a tokamak plasma. On roughly this same time scale ion collisions ($t_{\nu_i} \sim 1/\nu_i \sim msec$) damp the poloidal ion flow[3] and lead to purely toroidal net plasma flows within a magnetic flux surface and ambipolar cross-field transport.[3,7] Finally, on the transport time scale ($\tau_E \sim \Delta t(a/\Delta x)^2 \gtrsim a^2/\nu_i\rho_{\theta i}^2 \sim 100msec$) there are small net cross-field plasma particle and heat flows due to classical ($\Delta x \sim \rho_i, \Delta t \sim 1/\nu_i$), neoclassical ($\Delta x \sim \sqrt{\epsilon}\rho_{\theta i}, \Delta t \sim \epsilon/\nu_i, f_T \sim \sqrt{\epsilon}$) collisional effects and the turbulent fluctuations ($\Delta x \gtrsim cm, \Delta t \lesssim msec$?) in the plasma. A comprehensive theory of plasma transport must properly take into account all these effects to obtain the correct net transport.

Generalized "Frozen Flux" Theorem. In plasma physics textbooks[8] it is usually shown that in the ideal MHD model $[\mathbf{E}+\mathbf{V}\times\mathbf{B}=0]$ the magnetic field moves with the plasma fluid and hence that there is no net transport of the plasma relative to the magnetic field. Kadomtsev and Pogutse[7] have extended these notions by showing that for isothermal electrons and an Ohm's law given by $\mathbf{E}+\mathbf{V}\times\mathbf{B}-(1/nq)\nabla p=0$ there

is still no net transport of plasma relative to an extended magnetic flux function—diamagnetic flows alone induce no net transport. We generalize these concepts still further by calculating the net change in a generalized flux function for the complete momentum balance equation of a given plasma species:

$$mn\frac{d\mathbf{V}}{dt} = nq(\mathbf{E} + \mathbf{V} \times \mathbf{B}) - \nabla p - \nabla \cdot \underline{\underline{\Pi}} + \mathbf{F} \tag{1}$$

in which $\nabla \cdot \underline{\underline{\Pi}}$ is the viscous force and $\mathbf{F} = -nq\mathbf{J}/\sigma$ is the frictional force — both dissipative effects. Motivated by the form of the canonical momentum $\mathbf{p} = m\mathbf{v} + q\mathbf{A}$ and its velocity space moment $\mathbf{P}/n = m\mathbf{V} + q\mathbf{A}$, we generalize the usual magnetic flux $\psi = \int\int d\mathbf{S} \cdot \mathbf{B} = \int\int d\mathbf{S} \cdot \nabla \times \mathbf{A}$ to a surface function $\psi_{\#}$ that is a combination of the magnetic and vorticity flux:

$$\psi_{\#} = \int\int_F d\mathbf{S} \cdot \nabla \times (\mathbf{A} + \frac{m}{q}\mathbf{V}) = \int\int_F d\mathbf{S} \cdot (\mathbf{B} + \frac{m}{q}\nabla \times \mathbf{V}). \tag{2}$$

Then, taking the total time derivative of $\psi_{\#}$ for an arbitrary surface F that moves with the species flow velocity $\mathbf{V}$, we find [after using Eq. (1), Faraday's induction law ($\nabla \times \mathbf{E} = -\partial\mathbf{B}/\partial t$), and the identity[10] $d\mathbf{S} = (\nabla \cdot \mathbf{V})d\mathbf{S} - \nabla\mathbf{V} \cdot dS$]:

$$\frac{d\psi_{\#}}{dt} = -\int\int_F d\mathbf{S} \cdot \nabla \times [\frac{\nabla p + \nabla \cdot \underline{\underline{\Pi}} - \mathbf{F}}{nq}] = -\int_C d\ell \cdot [\frac{\nabla p + \nabla \cdot \underline{\underline{\Pi}} - \mathbf{F}}{nq}]. \tag{3}$$

The first term in the surface-integral expression can be written as $\nabla \times (1/nq)\nabla p = (1/q)\nabla(1/n) \times \nabla p = (1/nq)\nabla T \times \nabla n$. For an ideal (i.e., non-entropy-producing) equation of state $(d/dt)(p/n^{\Gamma}) = 0$, we have $n \propto p$ and hence this first term vanishes. Thus, we find that the only processes which cause $d\psi_{\#}/dt$ to be nonzero (net motion of the plasma species relative to the surface $\psi_{\#}$) are dissipative effects—the viscous and frictional forces in Eq. (1) and the "small" entropy-producing effects that cause deviations from the ideal equation of state. The fact that other, reversible motions of the plasma give rise to no net transport must be taken into account in calculations of net "radial" transport of plasma in a tokamak.

Net Parallel Transport. The parallel (to $\mathbf{B}$) transport (Ohm's law) processes in a tokamak are developed as follows. For times long compared to the electron collision time ($t > 1/\nu_e$) the electron inertia term in Eq. (1) becomes negligible and the equilibrium parallel ($\mathbf{B}\cdot$) electron momentum balance yields the Ohm's law. From the charge continuity equation ($\nabla\cdot\mathbf{J} = 0$) in the presence of diamagnetic flows induced by the gradient of an isotropic pressure (to lowest order), we have

$$J_{\parallel}B = -I\frac{dP}{d\psi}(1 - \frac{B^2}{< B^2 >}) + \frac{< J_{\parallel}B > B^2}{< B^2 >} \tag{4}$$

in which $I(\psi) = RB_T$ is the poloidal current function and $<>$ represents a flux-surface average. Here, the first term represents the Pfirsch-Schlüter current[11] and $< J_{\parallel}B >$ is determined from flux-surface-averaging the Ohm's law to yield ($< \mathbf{B} \cdot \nabla p_e >= < \mathbf{B} \cdot \nabla\phi >= 0$):

$$< J_\parallel B >= \sigma_\parallel < E_\parallel^A B > + \frac{1}{n_e e} < \mathbf{B} \cdot \nabla \cdot \underline{\underline{\Pi}}_e > \tag{5}$$

in which $\sigma_\parallel$ is the Spitzer electrical conductivity, $< E_\parallel^A B >$ represents the inductive electric field drive, and the parallel viscous force causes the neoclassical trapped-particle and bootstrap contributions[3] to Ohm's law in a tokamak. In view of Eqs. (2) and (3), we should really take the $\mathbf{B}_\# = \mathbf{B} + (m_e/q_e)\nabla \times \mathbf{V}_e$ component of Ohm's law and average over the $\psi_\#$ surfaces — instead of just the ψ or magnetic flux surfaces. However, since the electron vorticity correction to the flux function is of order $m_e(\nabla \times \mathbf{V}_e)/q_e B \sim (k_\perp \rho_e)(V_e/v_{Te}) \sim (k_\perp \rho_e)(\rho_e/\ell)$, it is second order in the gyroradius and hence negligibly small for this calculation. Phys. Fluids **31**, 8 (1988); **31**, 2249.

Net Cross-Field Transport. For perpendicular transport we take $\mathbf{B}\times$ (or $\mathbf{B}_\#\times$) the momentum balance equation to determine the perpendicular components of the flow:

$$\mathbf{V}_\perp = \frac{1}{nqB^2}\mathbf{B} \times (-nq\mathbf{E} + \nabla p + \underline{\underline{\Pi}} - nq\mathbf{J}/\sigma - mnd\mathbf{V}/dt \tag{6}$$

which indicates, respectively, the $\mathbf{E} \times \mathbf{B}$, diamagnetic, viscous and frictional force induced, and inertial flows. Taking the flux-surface (or really $\psi_\#$) average of the density balance equation we obtain

$$\frac{\partial < n >}{\partial t} + \frac{\partial}{\partial V_\#} < n\mathbf{V}_\perp \cdot \nabla V_\# >= 0 \tag{7}$$

in which $V_\#$ is the volume of the $\psi_\#$ flux surface. The net "radial" particle flux, after eliminating the non-dissipative flow effects since they apparently, from Eq. (3), do not contribute to net plasma transport, is (after using the vector identity $\nabla\psi \times \mathbf{B}/B^2 = -I\mathbf{B}/B^2 + R^2\nabla\zeta$)

$$\begin{aligned}
\Gamma \equiv & < n\mathbf{V}_\perp \cdot \nabla V_\# > \\
= & < \frac{\nabla\psi \times \mathbf{B}}{B^2} \cdot \frac{nq\mathbf{J}}{\sigma} > + \frac{I}{q} < (\frac{1}{B^2} - \frac{1}{< B^2 >})(\frac{J_\parallel B}{\sigma_\parallel} - E_\parallel^A B) > \\
& - \frac{I}{q < B^2 >} < \mathbf{B} \cdot \nabla \cdot \underline{\underline{\Pi}} > + \frac{I}{q} < R^2 \nabla\zeta \cdot \nabla \cdot \underline{\underline{\Pi}} > .
\end{aligned} \tag{8}$$

Here, the first term indicates both classical transport (due to the equilibrium diamagnetic current) and resistive instability effects (due to fluctuating currents), the second term indicates the Pfirsch-Schlüter transport, the third term indicates neoclassical perpendicular transport[3,12] (note that it depends on the same component of the parallel viscous force[13] as appears in the average Ohm's law [Eq. (5)], and the last term apparently indicates the dominant effects of kinetic plasma instabilities since it is negligible for Coulomb-collision-induced processes.[12] Thus, anomalous transport is represented here by the toroidal viscous force that the plasma turbulence

produces. In obtaining this equation we have neglected the difference between $\psi_{\#}$ and ψ, which, as noted above, seems to be second order in the gyroradius expansion and hence negligible. Also, we have neglected $\nabla n \times \nabla T$ effects due to the "small" departures of the equation of state from its ideal non-entropy-producing form. We are currently developing a more complete approach based upon a formal small gyroradius expansion. We should also note that the present analysis does not allow for "magnetic islands" which would change the topology of the $\psi_{\#}$ surfaces. While the present development of an expression for the net particle flux is somewhat phenomenological, it does indicate that the net transport is due to dissipative effects (friction and viscosity) and how the classical, Pfirsch-Schlüter, neoclassical and turbulence-induced transport fluxes should be added to obtain the complete, net particle flux.

* Research supported by the U.S. DOE under grant DE-FG02-86ER53218.

1. M.C. Zarnstorff et al., Phys. Rev. Letters **60**, 1306 (1988).
2. M.C. Zarnstorff et al., "Parallel Electric Resistivity in the TFTR Tokamak," PPPL-2675 (May, 1990).
3. See for example: J.D. Callen et al., in *Plasma Physics and Controlled Nuclear Fusion Research 1986* (IAEA, Vienna, 1987), Vol. II, p. 157 and references cited therein.
4. M. Murakami et al., Phys. Rev. Letters **42**, 655 (1979).
5. J.P. Wang and J.D. Callen, "Fluid/Kinetic Hybrid Moment Description of Plasmas Via A Chapman-Enskog-like Approach," Report UW CPTC 90-8, November, 1990 (to be published).
6. Z. Chang, "Unified Plasma Fluid/Kinetic Equations for Tokamak Microinstability and Turbulence Studies," Ph.D. Thesis, UW-Madison, March 1991 (available as Report UW CPTC 91-2).
7. T.E. Stringer, J. Plasma Phys. **10**, 433 (1973); S.P. Hirshman, Nuclear Fusion **18**, 917 (1978).
8. See for example: G. Schmidt, *Physics of High Temperature Plasmas* (Academic Press, NY, 1979), 2nd Ed., p. 87 et seq.
9. B.B. Kadomtsev and O.P. Pogutse, in *Plasma Physics and Controlled Nuclear Fusion Research 1984* (IAEA, Vienna, 1985), Vol. II, p. 69.
10. H.K. Wimmel, Eur. J. Phys. **3**, 223 (1982).
11. D. Pfirsch and A. Schlüter, Max Planck Institut Report MPI/PA/7/62(1962).
12. S.P. Hirshman and D.J. Sigmar, Nuclear Fusion **21**, 1079 (1981).
13. K.C. Shaing, Phys. Fluids **31**, 8 (1988); **31**, 2249.

FLUID-KINETIC MODEL OF TOKAMAK TRANSPORT

W. Feneberg

Max-Planck-Institut für Plasmaphysik, EURATOM Association,
D-8046 Garching, Fed. Rep. Germany

W. Kerner

JET Joint Undertaking, Abingdon, Oxfordshire OX14 3EA, United Kingdom

Introduction:

It is well known, that neoclassical transport based on collisions between trapped and transient particles, scales like the collisionality ν^* in the banana region and is far away to explain experiments. ($\nu*$ is of order 0,05 under reactor conditions). For this reason we have started a knew approach for solving the kinetic equation which studies the effect of the transient particles on transport in the region of long mean free path. The losses due to transient particles are based on the drift terms arising from the fast gyromotion in conjunction with poloidal variations of temperature, flow velocity and density on a magnetic surface. In analogy to the collisional regime, the driving term is the diamagnetic poloidal heat flow, which is in toroidal geometry not divergence free.

Complementary to the usual neoclassical ordering scheme a kinetic model is set up by extending the Chapman-Enskog procedure into the long mean free path regime. For the distribution function the ansatz $f = f_M + f_1$ is appropriate, where f_M is a local Maxwellian with two temperatures T_{II} and $T_\perp$. So we preserve the basic idea of Grad's 13-moment method, but intend to solve the kinetic equation directly in order to find a closed system of moment equations. The collision term of Clemmow and Dougherty $\frac{\partial f}{\partial t}|_c = \nu \frac{\partial}{\partial v_{II}} \left[v_{II} f + \frac{T_{II}}{m_e} \frac{\partial f}{\partial v_{II}} \right]$, which is consistent with particle, momentum and energy conservation, is applied enabling an analytic treatment. The basic result obtained for the electrons in this model is the electron parallel heat flux to be independent from the mean free path and thus from the collisionality. This exhibits similarity with the case of a Knudsen gas. As an immediate consequence the radial heat transport is in agreement with plateau scaling and widely exceeds the trapped particles contribution.

A. Parallel heat conductivity derived from a 1-d kinetic equation:

Taking into account the motion of the charged particles along the magnetic field the simplified $1-d$ Fokker-Planck equation for the distribution function f for the electrons reads in the steady state case:

$$v_{II} \frac{\partial f}{\partial x} + V_e \frac{\partial f}{\partial x} - \frac{e}{m_e} E_{II} \frac{\partial f}{\partial v_{II}} - \frac{\partial V_e}{\partial x} v_{II} \frac{\partial f}{\partial v_{II}} = I_e$$

Here v_{II} denotes the random velocity $v_{II} = v - V_e$,V_e the mean velocity and E_{II} the parallel electric field.

We look for a periodic solution with periodicity length $L = 2\pi\ Rq$ which is the closing length of a field line and introduce a periodic coordinate $\theta = x/Rq$.

With the ansatz $f = f_M + f_1$ the first part f_M is given by a local Maxwellian with inhomogeneous density $n_e(x)$, temperatur $T_{II}(x)$ and flow velocity $V_e(x)$

$$f_M = n_e(x) \left(\frac{m_e}{2\pi T_{II(x)}}\right)^{1/2} exp\ (-m_e v_{II}^2/2T_{II}(x)).$$

f_1 is chosen to staisfy the conditions $\int f_1 \delta v_{II} = \int v_{II} f_1 \delta v_{II} = \int v_{II}^2 f_1 \delta v = 0$, therefore it does not contribute to the moments of density, flow and temperature.

For the ordering we introduce two small parameters, namely $\delta = \frac{1}{T_e}\ \delta T_e/\delta\theta$ and $\alpha = V_e/v_{the}$. Here v_{the} denotes the thermal velocity. The moment equations determine n_e, V_e, T_e and E_{II} with the heat flux determined by the kinetic equation. This allows the electric field to be given in terms of appropriate source terms. Here instead of E_{II} the temperature variation is prescribed. Non trivial solutions with finite surface variations for n_e, T_{II}, V_e and the electric potential $E_{II} = -\partial\phi/Rq\partial\theta$, are derived.The heat flux in the energy equ. is assumed to scale like δ inplying the density variation to be of the order $\frac{1}{n_e}\delta n_e/\delta\theta \approx \delta\alpha^{-1}$.

This large density variation is a disatvantage of the 1-d kinetic equation and due to the fact that the collision term I_e of Clemmow and Dougherty does not contain a non symmetric source capable of driving a surface variation. Retaining terms of order δ and $\delta\alpha^{-1}$ the kinetic equation becomes

$$v_{II}\ \frac{\delta f_1}{\delta x} + v_{II}\ \frac{\delta f_M}{\delta x} + V_e \frac{\delta f_M}{\delta x} - \frac{e}{m_e}\ E_{II}\ \frac{\delta f_M}{\delta v_{II}} - \frac{\delta V_e}{\delta x}\ v_{II}\ \frac{\delta f_M}{\delta v_{II}} = I_e$$

Expanding f_1 in Hermite polynomials

$$f_1 = f_M \sum_{n=3}^{N} a_n(\theta)\ H_n(\tilde{x}),\ (\tilde{x} = v_{II}/v_{the}, N = \text{truncation number})$$

the Fourier transformed moment equations for the different orders H_n yield a recursive system. This tridiagonal system is solved nummerically. For the third order moment a_3, which describes the heat flux, we find the very interesting result

$$a_3 \ = \ \mp\, i\ 0.27\ \tilde{T}_{II,m} \left.\begin{matrix} \\ \\ \end{matrix}\right\} \begin{matrix} m > 0 \\ m < 0 \end{matrix}$$

This expression holds for every ratio λ/Rq of the meanfree path $\lambda = v_{the}/\nu$ to the connection length Rq. It is emphasized that collisions are necessary to get a solution. The case without collisions yields only the trivial solution $f_1 = 0$ and

vanshing surface variation of the macroscopic quantities. Even for reactor relevant plasmas the electron collision time is in the order of $30\mu s$. In the special case of $m = 1$,*i.e.* $T_{II} = T_{II,o}\ (\tilde{T}_s sin\theta + \tilde{T}_c cos\theta)$ the heat flux S_{II} reads

$$S_{II} = 0.78\ n_e\ T_{II}\ v_{the}\ (\tilde{T}_c sin\theta - \tilde{T}_s cos\theta)$$

In order to find sufficient convergence we need $N \approx \lambda/Rq$(*i.e.* $N \approx 100$) polynomials! Therefore the standard thirteen-moments approximation yields accurate results only in the collisional regime in difference to the result achieved on the basis of the Krook collision term /1/.

B. The physical model of transport:

The explanation of perpendicular tranport is based on the drift term in the heat flux, whose poloidal component

$$S_{\perp,\theta} = -\frac{5n_e\ T_e}{2eB}\ dT_e/dr$$

is not devergence free in toroidal geometry (here we take circular magnetic surfaces, B the magnetic field). Therefore a return flow S_{II} is set up such that $\nabla \cdot (\vec{S}_{II} + \vec{S}_{\perp}) = O$. This causes a variation of $T_e = T_{e,0}\ (1 + \tilde{T}_s sin\theta + \tilde{T}_c cos\theta)$ in a way where $\tilde{T}_s$ is of order $\epsilon = r/R$ (ϵ the inverse aspect ratio) and $\tilde{T}_c$ of order ϵ^2. With S_{II} from the foregoing chapter we found

$$\tilde{T}_s = -6.4\ \epsilon \varrho_{e,\theta}/L_T.$$

(here $\varrho_{e,\theta}$ is the poloidal gyroraduis, L_T the radial temperature decay length).
To estimate the effect on the radial transport we will use the radial component of the drift term and average over a magnetic surface. This gives a heat diffusivety for the electrons of

$$X_e = 6.4\ (T_{e,o}/eB_o\ R_o)^2\ \frac{R_o q}{v_{the}}(m^2 s^{-1}) \approx T_{e,o}^{3/2} q/B_o^2 R_o$$

For JET values ($T_e = 4keV, q = 2, B_0 = 2,5T$) we find $X_e = 0.4 m^2 s^{-1}$ not far from the observed values!

C. The treatment of the complete kinetic equation:

As described in an earlier paper /2/ the distribution function $f = f_o + f_1$ is based on a two temperature local Maxwellian f_o and for f_1 the ansatz is made

$$f_1 = f_o(\vec{w}) \sum_{n=3}^{\infty} \frac{1}{n!}\ a_i^{(n)}\ H_i^{(n)}\ (\vec{w}),$$

where $H_i^{(n)}$ are Hermitian polynomials of order n. (for definition of $\vec{w}$ see /2/). The equation for f_1 is derived such, that the lower moment equations (zero, first, second order) are satisfied automatically.

f_1 is separated in $f_1 = f_o(\varphi_1 + \varphi_2)$ with $\varphi_1 = \varphi_1(w_{\shortparallel}, w^2)$ a quantity independent from gyrophase. φ_1 is of first order in the smallness parameter δ.

After some algebra we obtain for φ_1 the equ:

$$f_o v_{the}/2T_\perp(b_i\delta T_\perp/\delta x_i)w_{\shortparallel}(w_\perp^2 - 2) + f_o v_{the}/2T_{\shortparallel}(b_i\delta T_{\shortparallel}/\delta x_i)w_{\shortparallel}(w_{\shortparallel}^2 - 3)$$

$$+H_{kl}^{(2)} f_o/\alpha \int H_{k,l}^{(2)} I_e(f_o\varphi_1)\delta^3 w + H_l^{(1)} f_o/\alpha_o \int H_l^{(1)} I_e(f_o\varphi_1)\delta^3 w$$

$$-v_{the} H_{kl}^{(2)} f_0/\alpha \int H_{kl}^{(2)} w_{\shortparallel} f_o b_i \delta'\varphi_1/\delta x_i \delta^3 w + v_{the} w_{\shortparallel} f_o b_i \delta'\varphi_1/\delta x_i = I_\epsilon(f_0\varphi_1)$$

δ' means derivation at fixed velocity variable $\vec{w}$.

$$v_{the} = (T_{\shortparallel}/m_e)^{1/2}, \alpha_o = v_{the}^{-1} m_e/T_\perp \text{ and } \alpha = 2\alpha_o$$

$\vec{b}$ is the unit vector of the magnetic field. Contributions to polynomials of first ($H_l^{(1)}$) and second order ($H_{lk}^{(2)}$) will cancel automatically. To solve this equation we work with an ansatz for $a_i^{(n)}$ which contracts $a_i^{(n)}$ $H_i^{(n)}$ to polynomials of $w_{\shortparallel}, w^2$ only /3/.

The equation for φ_2 depends from the gyrophase. Here we work with the usual gyroradius parameter $\hat{\delta}$ and expand δ_2 up to second order. This work is still progressing.

(1) W. Kerner, D. Pfirsch and H. Weitzner,
Zeitschrift für Naturforsch. 44a (1989) pp.1029 - 1040

(2) V. Oraevskii, R. Chodura, W. Feneberg,
Plasma Physics Vol. 10 (1968) pp.819

(3) H. Weitzner, private communication.

3D MODELLING OF RADIAL DIFFUSION OF HIGH ENERGY IONS IN TOKAMAKS

F.S. Zaitsev ‡†[1], A.P. Smirnov‡[1]. M.R. O'Brien†[2], M. Cox†[2].
[1]Moscow State University, USSR.
[2]UKAEA/Euratom Fusion Association, Culham Laboratory, UK.
‡part 1, †part 2.

Part 1. Neoclassical diffusion.

We solve the 3D Fokker-Planck equation for the hot ion distribution function in a tokamak allowing for neoclassical diffusion [1,2]. The equation for the distribution, which is a function of speed v, dimensionless magnetic moment $s = v_\perp^2 B_o/(v^2 B)$ and a magnetic surface label γ, takes the form [2]:

$$\frac{\partial f}{\partial t} = \frac{v_o^3}{\tau_c}\left\{\frac{1}{v^2}\frac{\partial}{\partial v}\left[a(\gamma,v)\frac{\partial f}{\partial v} + b(\gamma,v)f\right] + \frac{1}{J_1(\gamma,s)}\frac{\partial}{\partial s}\left[c^{(1)}(\gamma,v)sJ_2(\gamma,s)\frac{\partial f}{\partial s}\right] + \right.$$
$$\left.\frac{1}{\lambda(\gamma)J_1(\gamma,s)\gamma}\frac{\partial}{\partial \gamma}\left[\gamma\lambda(\gamma)c^{(2)}(\gamma,v)\frac{s}{\omega_I^2(\gamma)} \times \left(J_1(\gamma,s) - \frac{J_3^2(\gamma,s)}{J_2(\gamma,s)}\frac{\partial f}{\partial \gamma}\right)\right]\right\} \qquad (1)$$

where

$$a(\gamma,v) = \sum_\beta z_\beta^2 \frac{n_\beta(\gamma)}{n_e^o}\frac{m}{m_\beta}\frac{T_\beta(\gamma)}{mv}a_\beta(\gamma,v), \quad b(\gamma,v) = \sum_\beta z_\beta^2 \frac{n_\beta(\gamma)}{n_e^o}\frac{m}{m_\beta}b_\beta(\gamma,v),$$

$$c^{(1)}(\gamma,v) = 4\sum_\beta z_\beta^2 \frac{n_\beta(\gamma)}{n_e^o}c_\beta(\gamma,v)/v^3, \quad c^{(2)}(\gamma,v) = \sum_\beta z_\beta^2 \frac{n_\beta(\gamma)}{n_e^o}c_\beta(\gamma,v)/v,$$

$$\tau_c = \left[\frac{m}{2}\right]^{1/2}\frac{E_o^{3/2}}{\pi n_e^o e^4 z^2 ln\Lambda}$$

Here $\omega_I(\gamma)$ is the poloidal field cyclotron frequency. The last term in (1) describes neoclassical diffusion. For high energy particles some negligibily small terms in the radial flux term were omitted [1,2]. The coefficients a_β, b_β, c_β have the same form as in [3]. The following system of real-space coordinates was used [4]:

$$\begin{aligned} x &= (R - \Delta(\gamma) + \gamma\cos\theta - \delta(\gamma)\sin^2\theta)\cos\phi \\ y &= (R - \Delta(\gamma) + \gamma\cos\theta - \delta(\gamma)\sin^2\theta)\sin\phi \\ z &= \lambda(\gamma)\gamma\sin\theta \end{aligned} \qquad (2)$$

with $0 \leq \gamma \leq \gamma_a$, $-\pi < \theta \leq \pi$, $0 \leq \phi < 2\pi$, γ_a the label of the limiting magnetic surface, θ the 'poloidal' angle and ϕ the toroidal angle. For the flux surface labelled γ, λ, Δ and δ are the ellipticity, shift and triangularity. The coefficients J_i arise from the surface averaging of the equation and take into account the magnetic field geometry.

At the trapped/passing boundary ($s = 1 - (\gamma + \Delta(\gamma))/R$) we assume continuity of the distribution function and of the flux in phase space. The equation for the continuity of the flux is put in more convenient form by changing from s to the variable $\xi = s + (\gamma + \Delta(\gamma) - \Delta(0))/R$. This leads to the appearance of additional terms in the radial flux, however they are of the order γ/R and should not play a substantial role. The boundary conditions at $s = 0$, $s = 1 + (\gamma - \Delta)/R$ and $\gamma = 0$ are the boundedness of f. At $\gamma = \gamma_a$ and at $v \to \infty$, $f = 0$. Eq (1) is solved for $v > v_{min}$: for $v \leq v_{min} = (2T_d/m_d)^{1/2}$ the distribution is Maxwellian.

Calculations were performed with the code VSG developed by F S Zaitsev for T-10 parameters: R = 150cm; γ_a = 29cm; B = 2T; $T_\beta = T_0\ (0.9(1 - \gamma^2/\gamma_a^2) + 0.1)$; $n_\beta = n_e^0$ $(0.9(1 - \gamma^2/\gamma_a^2) + 0.1)$; T_0 = 1keV; $n_e^0 = 10^{13}$ cm^{-3}; β=d(euterons), e(lectrons); current density $j(\gamma) = j_o(1 - \gamma^2/\gamma_a^2)$, $j_o = 212A/cm^2$; $\lambda = 1, \Delta = \delta = 0$. The effects of neoclassical diffusion for devices of the size of T-10 are more important than for larger devices [3]. The grid (v,ξ,γ)=(100,96,32) was used for the numerical solution.

Fig.1 shows the dependence of the steady state distribution f on energy w for s=1 and different γ. The dashed line shows the Maxwellian function, the dot-dashed line the results obtained from analytic formulae [5] and the solid line f^{3D}, the solution of eq. (1). It can be seen that analytic formulae and f^{3D} give very similar results for the middle range of γ. Differences occur for small and large γ. Apparently the reason for this is the assumption in [5] of local Maxwellians for f which give sharper radial dependence.

In order to compare f^{3D} and f^{2D} [3] we have averaged f^{3D} over s. Fig. 2 shows $< f^{3D} >_s$ (solid line) and f^{2D} (dot-dashed line). There is good agreement between these functions for small and middle γ. However for large γ the results differ significantly. This can be explained as follows: $< f^{3D} >_s$ and f^{2D} are comparable in the range of γ where f^{3D} depends on s weakly. The increase in $< f^{3D} >_s$ for large γ is due to the fact that $D_{neo}^{3D}/D_{neo}^{2D} \leq s/\epsilon^{1/2}$ is greater than unity for $\gamma \sim 0$.

Our investigations show that simplified models [5,3] give a good description of the region of detachment from the Maxwellian distribution and the dependence on energy for the middle range of γ. However in the peripheral regions substantial differences occur (2-50 times) arising from the strong dependence of f on D_{neo}.

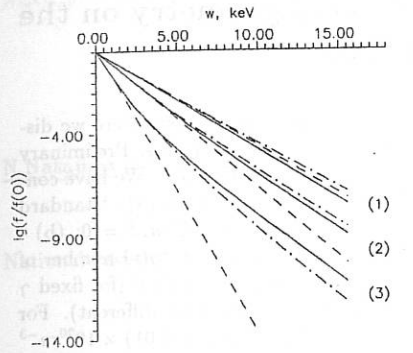

Figure 1 Hot ion distributions for (1) $\gamma = 7.25$cm, (2) $\gamma = 18.13$cm and $\gamma = 25.38$cm. The solid lines are solutions of the 3D equation, the dashed lines are Maxwellians and the dot-dash lines from the analytic expression.

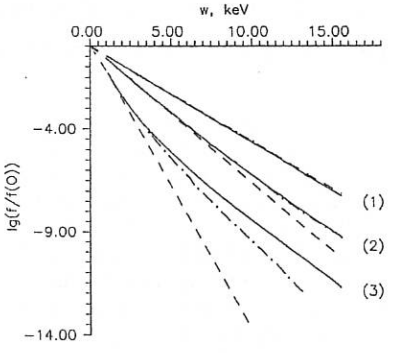

Figure 2 As Figure 1 but distributions are averaged over s. The dot-dashed line is the solution of the 2D equation.

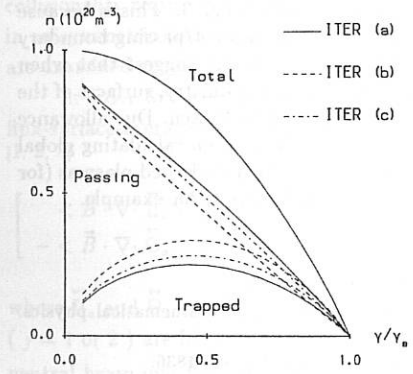

Figure 3 Trapped and passing density profiles for Maxwellian distributions for the 3 models of ITER discussed in the text.

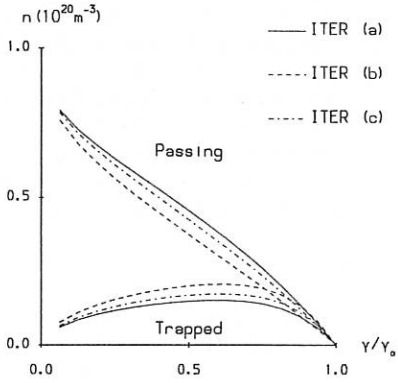

Figure 4 As Figure 3 for distributions with large radial diffusivity.

Part 2. Influence of magnetic field geometry on the distribution function of hot ions.

Many working and planned tokamaks have non-circular cross-section. Here we discuss the influence of deviations from circular geometry on kinetic processes. Preliminary conclusions can be drawn from analyses using Maxwellian distributions. We have considered the $(\lambda, \Delta, \delta)$ model of the magnetic field (2) and studied 3 cases: (a) - 'standard ITER', R=6 m, $\gamma_a = 2m, \lambda = 1.7 + 0.3\gamma^2/\gamma_a^2, \Delta = -0.6(1 - \gamma^2/\gamma_a^2)m, \delta = 0$; (b) - 'circular ITER with the same volume' R=6, $\gamma_a = 2.83, \lambda = 1, \Delta = 0$ (total number of particles is close to (a)); (c) - 'circular ITER with the same minor radius' (for fixed γ the density is the same as in (a), but the total number of particles is different). For (a)-(c) we consider the same profiles: density n = $(0.99(1 - \gamma^2/\gamma_a^2) + 0.01) \times 10^{20} m^{-3}$ and temperature T = 30 $(0.9(1 - \gamma^2/\gamma_a^2) + 0.1)$ keV. Fig. 3 shows density profiles of passing and trapped particles. Cases (a)-(c) differ by 10-30%. The differences arise because cases (b) and (c) have higher 'effective inverse aspect ratios' γ/R_{eff} than (a). Thus geometry can have a strong influence on kinetic processes in which the fraction of trapped particles is important.

To illustrate the influence of geometry we consider the extreme case in which the radial diffisivity of trapped fast ions is very large (D $\approx 100\gamma_a^2/\tau_c$(400keV)) and zero for passing ions. The solution of eq. (1) was performed using two independent codes: VSG and BANDIT-3D [6]. This gave the density profiles shown in fig. 4. Note that the differences between (a), (b) and (c) are similar to those in fig. 3. This is because the maximum losses depend strongly on the position of the trapped/passing boundary in phase space, which differs for (a), (b) and (c). These results suggest that when simulating experiments with a code which treats only circular geometry, surfaces of the correct aspect ratio (and preferably the correct shift) should be chosen. Due allowance should be made for the different areas and volumes of surfaces when calculating global quantities such as current, as well as for the higher poloidal field in shaped plasmas (for the same safety factor) which will give lower neoclassical transport for example.

References

[1] Irisov G.S., Yushmanov P.N., Sov. J. Plasma Phys. 12(1986)387.
[2] Zaitsev F.S., Smirnov A.P. In the book: Numerical methods in mathematical physics. Moscow University (1988)209.
[3] Zaitsev F.S., Smirnov A.P., Yushmanov P.N., Nucl. Fusion. 29(1989)1836.
[4] Zakharov L.E. Preprint IAE N 4115/6 (1985).
[5] Gott Yu. V., Yurchenko Eh.N., Sov. Phy. - Docl. 26(1981)995.
[6] McKenzie J.S., O'Brien M.R., Cox M. To be published in Comp. Phys. Commun.

NEOCLASSICAL CURRENT AND PLASMA ROTATION IN HELICAL SYSTEMS

N.Nakajima and M.Okamoto

National Institute for Fusion Science, Nagoya 464-01, Japan

In order to clarify geometrical effects of the magnetic field on the neoclassical theory in general toroidal systems, the neoclassical parallel particle flow, heat flux, current and plasma rotation of a multispecies plasma are examined using the moment approach on the basis of the original papers [1, 2, 3] under the assumptions of no fluctuations, no external sources and losses except for a fast ion beam and an external inductive electric field, steady state, and $| \vec{u}_a | \ll v_{Ta}$ where $\vec{u}_a$ and v_{Ta} are the macro and thermal velocity of species a, respectively. Hence, we might have a point of view of unifying understanding the neoclassical theory in general toroidal systems. Three collisionality regimes, i.e., the $1/\nu$ (in non-axisymmetric toroidal systems) or banana (in axisymmetric toroidal systems), plateau, and Pfirsh-Schlüter collisionality regimes are examined separately.

In order to obtain the flux-surface-averaged parallel particle flow and heat flux, the flux-surface-averaged parallel momentum and heat flux balance equations are used: [1, 2, 3]

$$\begin{bmatrix} < \vec{B} \cdot \nabla \cdot \overleftrightarrow{\Pi}_a > \\ - < \vec{B} \cdot \nabla \cdot \overleftrightarrow{\Theta}_a > \end{bmatrix} = \begin{bmatrix} < \vec{B} \cdot \vec{F}_{a1} > \\ - < \vec{B} \cdot \vec{F}_{a2} > \end{bmatrix} + \begin{bmatrix} < \vec{B} \cdot \vec{F}_{af1} > \\ - < \vec{B} \cdot \vec{F}_{af2} > \end{bmatrix} + \begin{bmatrix} n_a e_a < \vec{B} \cdot \vec{E}^{(A)} > \\ 0 \end{bmatrix}, \tag{1}$$

where $\overleftrightarrow{\Pi}_a$ and $\overleftrightarrow{\Theta}_a$ are the viscosity and heat viscosity tensor, respectively. $\vec{F}_{aj}$ and $\vec{F}_{afj}$ ($j = 1$ or 2) are frictions of a species a with thermal species and fast ions due to the neutral beam injection, respectively. And $\vec{E}^{(A)}$ is an external inductive electric field. The friction coeffecients are classical quantities in the sense that they are independent of the magnetic field $\vec{B}$ and reflect the self adjointness and momentum conservation of the Coulomb collision operator. The geometrical effects of the magnetic field come from the viscosity terms. In axisymmetric toroidal systems the magnetic field strength B is a function with respect to the flux label and the poloidal angle, so that there is only one type of trapped particles and the geometrical effects of the magnetic field structure in

the flux-surface-averaged parallel viscosity appear through the connection length and the fraction of trapped particles except for some magnetic-surface quantities. In contrast to the axisymmetric toroidal systems, in non-axisymmetric toroidal systems the strength of the magnetic field B also depends on the toroidal angle, thus there are many types of trapped particles and another type of factor reflecting the magnetic field structure appears in the parallel viscosity, which is called the flux-surface-averaged "geometrical factor" $< G_{BS} >$. [2, 4, 5] The flux-surface-averaged parallel viscosity and heat viscosity have the following general form:

$$\begin{bmatrix} < \vec{B} \cdot \nabla \cdot \overleftrightarrow{\Pi}_a > \\ - < \vec{B} \cdot \nabla \cdot \overleftrightarrow{\Theta}_a > \end{bmatrix} = \frac{n_a m_a}{\tau_{aa}} \begin{bmatrix} \mu_{a1} & \mu_{a2} \\ \mu_{a2} & \mu_{a3} \end{bmatrix} \begin{bmatrix} < B u_{\parallel a} > \\ -\frac{2}{5} \frac{< B q_{\parallel a} >}{P_a} \end{bmatrix}$$
$$+ \frac{n_a m_a}{\tau_{aa}} < G_{BS} > \begin{bmatrix} \mu_{a1} & \mu_{a2} \\ \mu_{a2} & \mu_{a3} \end{bmatrix} \begin{bmatrix} \frac{T_a}{e_a}(\frac{P_a'}{P_a} + \frac{e_a \phi'}{T_a}) \\ -\frac{T_a'}{e_a} \end{bmatrix}, \quad (2)$$

where μ_{aj} $(j = 1 \sim 3)$ are the non-dimensional viscosity coefficients which reflect the self adjointness of the Coulomb collision operator. The above general form is obtained by modifying the original results. [1, 2, 3] The geometrical factor prescribes the parallel particle flow and heat flux due to the gradients of the density, temparature, and electrostatic potential. In the $1/\nu$ or banana collisionality regime, the viscosity coefficients are $(j = 1 \sim 3)$ [1, 2]

$$\mu_{aj} = \frac{f_t}{f_c} \bar{\mu}_{aj}, f_t = 1 - \frac{3}{4} \frac{\langle B^2 \rangle}{B_{max}^2} \int_0^1 \frac{1}{\langle g_1 \rangle} \lambda \, d\lambda, g_1 = \sqrt{1 - \lambda \frac{B}{B_{max}}}, \quad (3)$$

where f_t are the fraction of trapped particles and $f_c = 1 - f_t$. The coefficients $\bar{\mu}_{aj}$ $(j = 1 \sim 3)$ are not dependent on the magnetic field but dependent on the particle constitution. The flux-surface-averaged geometrical factor $< G_{BS} >$ is given by the following equations: [2]

$$< G_{BS} > = \frac{1}{f_t} \left\{ \langle g_2 \rangle - \frac{3}{4} \frac{\langle B^2 \rangle}{B_{max}^2} \int_0^1 \frac{\langle g_4 \rangle}{\langle g_1 \rangle} \lambda \, d\lambda \right\}, \quad (4)$$

$$\vec{B} \cdot \nabla \left(\frac{g_2}{B^2} \right) = \vec{B} \times \nabla V \cdot \nabla \left(\frac{1}{B^2} \right), \quad g_2(B_{max}) = 0, \quad (5)$$

$$\vec{B} \cdot \nabla \left(\frac{g_4}{g_1} \right) = \vec{B} \times \nabla V \cdot \nabla \left(\frac{1}{g_1} \right), \quad g_4(B_{max}) = 0. \quad (6)$$

In the plateau collisionality regime, the viscosity coefficients μ_{aj} $(j = 1 \sim 3)$ are expressed as follows : [1, 3, 6]

$$\mu_{aj} = \frac{\lambda_a}{\lambda_{PL}} \bar{\mu}_{aj}, \frac{1}{\lambda_{PL}} \equiv \frac{\Phi_T'(t\mu_p + \mu_t)}{< B^2 >}, \quad (7)$$

where $\lambda_a = \tau_{aa} v_{ta}$ is the mean free path of species a, $\bar{\mu}_{a1} = 2$, $\bar{\mu}_{a2} = -1$, $\bar{\mu}_{a3} = 13/2$, and λ_{PL} is a characteristic length of the magnetic field in the plateau collisionality regime.

Note that $\bar{\mu}_{aj}$ $(j = 1 \sim 3)$ is independent of the particle constitution. μ_p and μ_t are given by

$$\mu_p = \frac{\sqrt{\pi}}{2}\langle\frac{\hat{n}\cdot\nabla B}{\Phi_T'}\sum_{m\neq 0, n\neq 0}\frac{\partial B_{mn}(\theta,\zeta)/\partial\theta}{2\pi \mid tm+n \mid}\rangle, \tag{8}$$

$$\mu_t = \frac{\sqrt{\pi}}{2}\langle\frac{\hat{n}\cdot\nabla B}{\Phi_T'}\sum_{m\neq 0, n\neq 0}\frac{\partial B_{mn}(\theta,\zeta)/\partial\zeta}{2\pi \mid tm+n \mid}\rangle, \tag{9}$$

where $\hat{n} = \vec{B}/B$ and $B = \sum_{m,n} B_{mn}(\theta,\zeta) = \sum_{m,n} B_{mn} cos(2\pi m\theta + 2\pi n\zeta + \varphi_{mn})$ is assumed. The flux-surface-averaged geometrical factor $< G_{BS} >$ is given by

$$< G_{BS} >= \frac{dV}{d\psi}\frac{J\mu_p - I\mu_t}{t\mu_p + \mu_t}. \tag{10}$$

In the Pfirsh-Schlüter collisionality regime, the viscosity coefficients are [1, 2]

$$\mu_{aj} = (\frac{\lambda_a}{\lambda_{PS}})^2\bar{\mu}_{aj}, \frac{1}{{\lambda_{PS}}^2} \equiv \frac{3}{2}\frac{< (\hat{n}\cdot\nabla B)^2 >}{< B^2 >}, \tag{11}$$

where $\bar{\mu}_{aj}$ $(j = 1 \sim 3)$ are not dependent on the magnetic field but dependent on the particle constitution as well as in the $1/\nu$ collisionality regime. λ_{PS} is the characteristic length in the Pfirsh-Schlüter collisionality regime. The flux-surface-averaged geometrical factor is given by

$$< G_{BS} >= 2\pi\frac{< \frac{1}{B}(J\frac{\partial B}{\partial\theta} - I\frac{\partial B}{\partial\zeta})(\hat{n}\cdot\nabla B) >}{< (\hat{n}\cdot\nabla B)^2 >}. \tag{12}$$

In axisymmetric toroidal systems, the geometrical factor reduces to the same expression in all collisionality regimes. In contrast with it, in non-axisymmetric toroidal systems, the expression of the geometrical factor changes according to the collisionality regime as well as the viscosity coefficients, i.e., it has the dependence of the fraction of trapped particles in the $1/\nu$ collisionality regime, and the connection length dependence in the plateau and Pfirsh-Schlüter collisionality regimes. The normalized geometrical factor $< G_{BS} >_N$, which is defined as $< G_{BS} > / < G_{BS} >_T$ and generally smaller than unity, may indicate the deviation of the general toroidal system from axisymmetric toroidal system. The normalized geometrical factor changes drastically according to the magnetic field structure in the $1/\nu$ collisionality regime and it becomes very small and even negative. [2, 4, 5, 7] In the plateau and Pfirsh-Schüter collisionality regimes, it is considerably small. Thus, this geometrical factor mainly makes differences to neoclassical results between axisymmetric and non-axisymmetric toroidal systems.

Solution of Eq.(1) gives some general results. The self adjointness and the momentum conservation of the Coulomb collision operator give common properties to the multispecies plasma in general toroidal systems in spite of the geometrical effects of the magnetic field. The parallel particle flow due to the radial electric field is independent of the particle species and the parallel heat flux is independent of the radial

electric field, if there are no other external sources and losses without the momentum conservation, for example, the charge exchange loss. Consequently, the charge neutrality guarantees the neoclassical current (the bootstrap curent) be independent of the radial electric field. Quantitative changes, however, appear in the neoclassical current mainly through the geometrical factor. [2, 4, 5, 7] The magnitude of the bootstrap current, which is proportional to the flux-surface-averaged geometrical factor, changes considerably in the non-axisymmetric systems according to the magnetic field structure. Moreover, the poloidal and toroidal rotations change both qualitatively and quantitatively. In the axisymmetric toroidal systems, the poloidal rotation in the multispecies plasma is independent of the radial electric field. [8] In non-axisymmetric toroidal systems, however, the poloidal rotation has the radial electric field dependence. The radial electric field dependence becomes larger as the geometrical factor decreases. Consequently, if interactions between thermal ions and fast ions are negligible, then the ion parallel flow almost disappears in non-axisymmetric toroidal systems with a sufficiently small geometrical factor, which contrasts with the fact that the ion parallel flow streams to cancel the ion poloidal flow in axisymmetric toroidal systems.

References

1. S.P.Hirshman and D.J.Sigmar, Nucl.Fusion **21**, 1079 (1981)
2. K.C.Shaing and J.D.Callen, Phys.Fluid **26**, 3315 (1983)
3. K.C.Shaing, S.P.Hirshman, and J.D.Callen, Phys.Fluid **29**, 521 (1986)
4. K.C.Shaing, E.C.Crume Jr., J.S.Tolliver, S.P.Hirshman, and W.I.van Rij, Phys.Fluids B **1**, 148 (1989)
5. K.C.Shaing, B.A.Carreras, N.Dominguez, V.E.Lynch, and J.S.Tolliver, Phys.Fluids B **1**, 1663 (1989)
6. M.Coronado and H.Wobig, Phys.Fluid **29**, 527 (1986)
7. N.Nakajima, M.Okamoto, J.Todoroki, Y.Nakamura, and M.Wakatani, Nucl.Fusion **29**, 605 (1989)
8. R.D.Hazeltine and A.A.Ware, Nucl.Fusion **16**, 538 (1976)

NUMERICAL SOLUTION OF THE DRIFT-KINETIC VLASOV EQUATION

A. Ghizzo*, M. Shoucri, P. Bertrand*, M. Feix†, E. Fijalkow†

Centre Canadien de Fusion Magnétique, Varennes, J3X 1S1, P.Q., Canada

The problem of $\vec{E} \times \vec{B}$ drift at a tokamak edge is of great importance in tokamak physics. It is now generally believed that the anomalous particle and energy transport in tokamaks is caused by turbulent fluctuations generated by instabilities due to the $\vec{E} \times \vec{B}$ drift in the plasma edge. (See recent results from the Tokamak de Varennes [1], [2]). Also, $\vec{E} \times \vec{B}$ rotation associated with a radial electric field in tokamaks edge have been associated with improved confinement performance of the tokamaks known as H-mode [3].

It is the purpose of the present report to present some results in studying the solutions of an important equation pertinent to this problem, the drift-kinetic Vlasov equation or guiding center equation. The advantage of the Vlasov codes over particle-in-cell codes for such a problem is obvious. Given the low noise level of these codes, they provide a powerful tool to study low frequency oscillations.

The Drift-kinetic Equation

This equation couples the motion along a magnetic field with the $\vec{E} \times \vec{B}$ motion normal to the magnetic field (Eqs. 1, 2). We solve these equations for the case of a slab model, periodic in the x-direction, finite in the y-direction, and allows the total magnetic field $\vec{B}$ (in the $x - z$ plane) to have an angle θ with the x direction. In this system of coordinates, the electron distribution function $f\ (x, y, v_{\|e})$ for the electrons obey the following equation:

$$\frac{\partial f_e}{\partial t} + \left(v_{\|e} \cos\theta + E_y \frac{\sin\theta}{\omega_c}\right) \frac{\partial f_e}{\partial x} - E_x \frac{\sin\theta}{\omega_c} \frac{\partial f_e}{\partial y} - E_x \cos\theta \frac{\partial f_e}{\partial v_{\|e}} = 0 \tag{1}$$

and the ions distribution function $f\ (x, y, v_{\|i})$ obey the following equation:

$$\frac{\partial f_i}{\partial t} + \left(v_{\|i} \left(\frac{m_e Ti}{m_i Te}\right)^{1/2} \cos\theta + E_y \frac{\sin\theta}{\omega_c}\right) \frac{\partial f_i}{\partial x} - E_x \frac{\sin\theta}{\omega_c} \frac{\partial f_i}{\partial y} + \left(\frac{m_e}{m_i} \frac{Te}{Ti}\right)^{1/2} E_x \cos\theta \frac{\partial f_i}{\partial v_{\|i}} = 0 \tag{2}$$

*Physique Théorique Univ. de Nancy, Nancy, France
†PMMS/CNRS-Université d'Orléans, Orléans, France

$v_{\|e}$ is normalized to the electrons thermal speed $v_{Te} = (Te/me)^{1/2}$, $v_{\|i}$ is normalized to the ions thermal speed $v_{Ti} = (Ti/mi)^{1/2}$, x and y are normalized to the electrons Debye length λ_{De}, and the time t is normalized to ω_{pe}^{-1}. ω_c is the electron cyclotron frequency normalized to ω_{pe}. The subscript (11) refer to the direction of the total magnetic field.
We solve the Poisson equation:

$$\Delta\varphi = n_i - n_e \tag{3}$$

and

$$E_x = -\frac{\partial\varphi}{\partial x}, E_y = -\frac{\partial\varphi}{\partial y} \tag{4}$$

The numerical code developed applies a method of fractional steps associated with a cubic spline interpolation technique [4].

Solution of the 2D equation.

For $\theta = \frac{\pi}{2}$, Eqs (1-4) reduce to the well-known vorticity equation

$$\frac{\partial\rho}{\partial t} + \vec{\alpha} \cdot \Delta\rho = 0 \tag{5}$$

$$\nabla^2\varphi = -\rho = (n_e(x,y) - n_i(x,y)) \tag{6}$$

where ρ is the electric charge, φ the potential and

$$\vec{\alpha} = \frac{\vec{E} \times \vec{e}_z}{\omega_c} \tag{7}$$

where $\vec{e}_z$ is the unit vector in the direction of the magnetic field.

The linear perturbation of Equations (5)-(7) around a velocity profile of the form

$$\alpha = \sin k_o y \qquad k_o = 2\pi/L \tag{8}$$

leads to an equation well-known in hydrodynamic as the Raleigh stability equation [4]. For L = 2π, the linear growth rate predicted from this equation for the profile in Eq. (8) is 0.122, while the numerical value calculated in Fig. 1 is given by 0.125 [5]. Fig. (2) shows contour plots of the nonlinearly saturated potential.

Solution of the Drift-kinetic Equation ($\theta \neq \frac{\pi}{2}$).

We have studied the solution of Eqs (1-4) for $\theta \neq \frac{\pi}{2}$ using an equilibrium calculated in [6], which consists of a flat density profile in the center decaying to zero at the boundary. The growth rate of the unstable fundamental mode which is maximum at $\theta = \frac{\pi}{2}$, decreases when θ gets less than $\pi/2$.

Calculations are done for $m_e/m_i = 1/100$, $T_e = T_i$ and a time step $\Delta\ t\ \omega_p = 0.05$. The number of grid points used in the simulations is $Nx\ Ny\ Nv_{\|} = 64 \times 80 \times 32$.

The growth rate of the instability at $\theta = \frac{\pi}{2}$, calculated in [6] using a water-bag model, is $I_m\ \omega = 0.138$. The corresponding value calculated numerically is $I_m = 0.13$. Fig. 3 shows the time evolution of $|\ \varphi_k\ |^2$ for the fundamental mode, whose growth rate is decreasing with decreasing

θ value, while in Fig. 4 the time evolution of the first harmonic shows this mode becoming dominant for decreasing value of θ. This behavior is confirmed by examining the contour plots of the potential.

Work is in progress to apply this code to study the $\vec{E} \times \vec{B}$ instabilities at the plasma edge of a tokamak.

References

[1] P. Couture et al "Divertor Plate Biasing Experiments on the Tokamaks de Varennes" (this Conference)

[2] A. Boileau, J.L. Lachambre, Phys. Letters 148, 341 (1990)

[3] R. Weynants, in Plasma Physics and Controlled Fusion Proceeding of the IAEA Conference (Washington, Octobre 1990) to be published.

[4] A. Ghizzo, P. Bertrand, M. Shoucri, T. Johnston, M. Feix, E. Fijalkow, J. Comp. Phys. 90, 43 (1990)

[5] M. Shoucri and G. Knorr, Plasma Phys. 18, 204 (1976); M. Shoucri Int. J. Num. Methods Eng. 17, 1525 (1981).

[6] M. Feix, Proc. 2nd Int. Congress on Waves and Instabilities in Plasma, (Ed. Institute of Theor. Phys. Insbruck University (1975)) p. 51

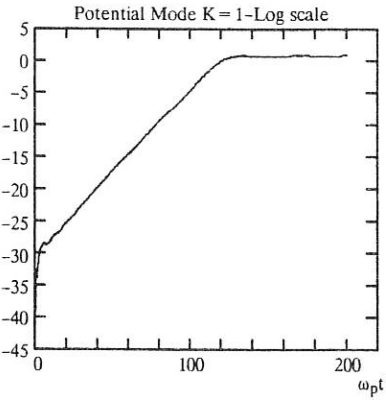

Fig. 1 Growth and saturation of the potential (log scale) as a function of time for the 2D problem

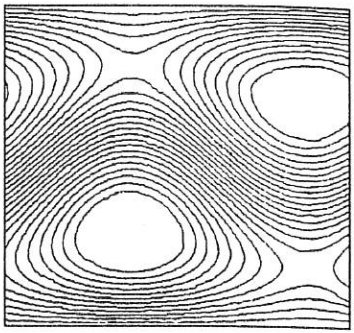

Fig. 2 Contours plot of the potential at saturation ($\omega_p t$ = 200) for the 2D problem

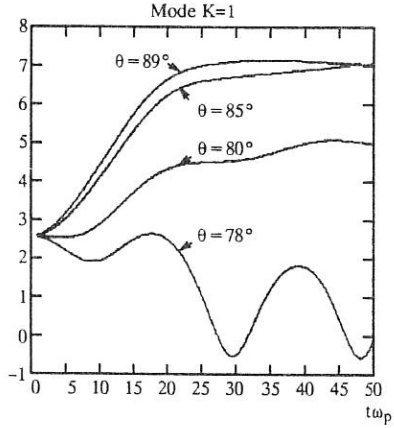

Fig. 3 Time evolution of the fundamental mode of the potential at different angles

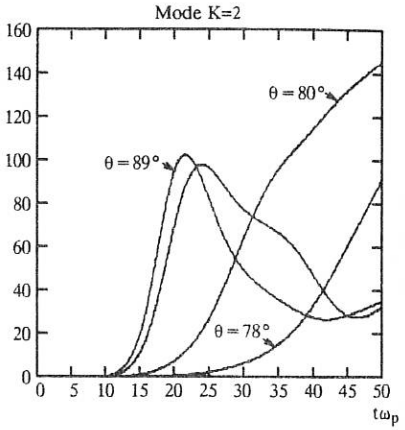

Fig. 4 Time evolution of the first harmonic for the potential at different angles.

THE INTEGRALS OF DRIFT PARTICLES MOTION WITH FINITE LARMOR RADIUS

V.I.Ilgisonis
I.V.Kurchatov Institute of Atomic Energy, Moscow 123182,USSR

A large number of cosmic and laboratory plasma objects is often described with help of collisionless magnetized plasma approximation. The object considered is assumed to vary its state with time and spatial scales which are more great than cyclotron period ($\sim 1/\Omega = mc/eB$) and Larmor radius ($\sim v_T/\Omega$) but less than path and time between collisions. The particle motion consists of fast cyclotron rotation, drift across magnetic field lines and longitudinal moving. The dynamics of slow drift and longitudinal motions of particle ensemble could be described by Rudakov-Sagdeev drift-kinetic equation (DKE) [I] derived from collisionless Vlasov equation by cyclotron rotation averaging. The importance of finite Larmor radius (FLR) effects for plasma equilibrium and stability problems [2] has stimulated the various attempts to modify DKE for non zero value of $1/\Omega$. Contrary to previous papers [2,3,4] concerned to 2D-geometry there was obtained the generalization of DKE [5], including entirely the all FLR-corrections at first order of $1/\Omega$ for arbitrary 3D-case. Using this equation the problem of particle motion integral existence is here investigated taking into account a macroscopic plasma flow and FLR-corrections to drift motion.

The generalized DKE (gDKE) has been obtained from Vlasov kinetic equation by means of expansion procedure in powers of $1/\Omega$ and Larmor rotation phase averaging. The magnetic moment of charged particle $\mu \approx mv_\perp^2/2B$ is well known to be conserved in any order of an expansion in powers of $1/\Omega$ [6]. Being influenced this fact let's attempt to build the analogous integral of DKE. As can be easy seen at zero order of $1/\Omega$ the value

$$\mu_o = mu_\perp^2/2B \qquad (1)$$

is an integral of traditional DKE [I] if the magnetic field is frozen in plasma moving with mass velocity **V**, i.e.

$$\partial_t \mathbf{B} = \mathrm{rot}[\mathbf{V}\times\mathbf{B}] \ . \qquad (2)$$

Here **u** is an ion random velocity and subscripts "$\perp,\parallel$" corresponds everywhere to the direction of vector $\mathbf{b}=\mathbf{B}/B$. If $1/\Omega \neq 0$ the equation (2) should be modified as

$$\partial_t \mathbf{B}/B = \mathrm{rot}[\mathbf{V}\times\mathbf{B}]/B - \mathrm{rot}(\mathbf{F}/mn)/\Omega \ , \qquad (3)$$

where $\mathbf{F} = mnd_t\mathbf{V} + \nabla\cdot\mathbf{P}$, **P** - pressure tensor, n - plasma density, and $d_t = \partial_t + \mathbf{V}\cdot\nabla$. At zero order of $1/\Omega$ the pressure tensor is orthogonal one: $P_{ij} = p_\perp\delta_{ij} + (p_\parallel - p_\perp)b_ib_j$. Taking into account (3) and terms $\sim 1/\Omega$ in gDKE, it's possible to find the FLR-correction to (1):

$$\mu_1^o = -\frac{\mu_o}{\Omega}\,\mathbf{b}\cdot\mathrm{rot}(u_\parallel\mathbf{b}+\mathbf{V}). \qquad (4)$$

So the sum $\mu_o+\mu_1^o$ is the gDKE-integral taking into account the main FLR-terms. The magnetic moment itself is known to contain some more phase angle oscillating additions:

$$\mu_1^1+\mu_1^2 = \frac{\mu_o}{\Omega}\Big(\mathbf{e}_\varphi\cdot\Big(u_\perp\frac{\nabla B}{B}+\frac{2}{u_\perp}\Big((u_\parallel^2+\frac{p_\perp-p_\parallel}{mn})\mathbf{b}\nabla\mathbf{b}-\frac{\nabla p_\perp}{mn}+ \\ +2u_\parallel\mathbf{b}\nabla\mathbf{V}\Big)\Big)+\hat{e}_{\varphi\rho}[u_\parallel\mathbf{b}+\mathbf{V}]\Big), \qquad (5)$$

where $\hat{e}_{\varphi\rho}[\mathbf{V}] = (\mathbf{e}_\varphi\cdot(\mathbf{e}_\rho\cdot\nabla)\mathbf{V}-\frac{1}{2}\,\mathbf{b}\cdot\mathrm{rot}\mathbf{V})$, $\mathbf{e}_\rho$ and $\mathbf{e}_\varphi$ are the orthogonal to $\mathbf{b}$ unit vectors in velocity space:

$$\mathbf{e}_\rho = (\mathbf{u}-(\mathbf{u}\cdot\mathbf{b})\mathbf{b})/u_\perp, \quad \mathbf{e}_\varphi = [\mathbf{b}\times\mathbf{e}_\rho].$$

Thus $\mu_o+\mu_1^o$ is the integral of gDKE and $\mu \approx \mu_o+\mu_1^o+\mu_1^1+\mu_1^2$ is the solution of kinetic equation at first expansion order. The expressions (4,5) generalize the known magnetic moment formulas [6] for plasmas with non-zero mass velocity $\mathbf{V}$.

If a particle moves in a stationary electric potential ($\mathbf{E} = -\nabla\Phi$, $\partial_t\Phi = 0$), its total energy $\varepsilon = e\Phi + mv^2/2$ is very well known to conserve (the presence of slowly varying magnetic field is also permitted). In this case ε is the integral of kinetic equation as follows from direct substitution. However the same substitution of ε into DKE [I] doesn't transfer the equation in an identity. The appearance of this paradox is connected with a breach in the logic of an expansion procedure in powers of $1/\Omega$. So the paradox elimination is possible only on the base of generalized DKE [5]. Actually unlike the function $\mathbf{F}$ the electric field at $\mathbf{V}_\perp \neq 0$ contains the value of order $\sim\Omega$ which should be taken into consideration at main order of expansion. Formally the stationary function $\Phi(r)$ satisfies DKE in case when $\mathbf{V}\nabla\Phi + u_\parallel\mathbf{b}\nabla\Phi = 0$, whence it follows $\nabla\Phi \approx [\mathbf{V}\times\mathbf{B}]/c$ (the multiplier B/c provides to Φ an electric potential dimension). This expression should be substituted into the first order ($\sim 1/\Omega$) terms of gDKE [5], whence we'll obtain that the value

$$\varepsilon_{DKE} = e\Phi + (u_\perp^2+V^2+2u_\parallel V_\parallel+u_\parallel^2)m/2 \qquad (6)$$

is also the integral of the equation considered as a magnetic moment is.

There is the important property of gDKE that the value (6) seems to be the approximate integral of gDKE also in case of variable fields with frequencies $\omega \ll \Omega$. For this the scalar electric potential in (6) should be specially calibrated in accordance with following formula:

$$\partial_t\Phi - \mathbf{V}\cdot\partial_t\mathbf{A}/c \approx 0. \qquad (7)$$

Here $\mathbf{A}$ is a vector potential: $\mathrm{rot}\mathbf{A} = \mathbf{B}$, and the electric

field is given by usual general expression $\mathbf{E} = -\nabla\Phi - \partial_t\mathbf{A}/c$. By the way the scalar potential is defined with appropriate function ξ moving with plasma together (i.e. $\partial_t\xi + \mathbf{V}\cdot\nabla\xi = 0$). In other words the replacement $\Phi \to \Phi + \xi$ (and $\mathbf{A} \to \mathbf{A} + \nabla a$ at the same time where $\partial_t a/c = -\xi$) conserves both the electromagnetic field and the calibration (7). For the stationary plasma flow ($\partial_t\mathbf{V}=0$) the calibration (7) turns into Petviashvili-Gordin one [7].

Now let's consider the macroscopic conservation lows of magnetized plasma dynamics. The equations of continuity and motion are formally identical to corresponding MHD-equations, therefore the total particles number and plasma momentum conservation is obvious in case of essential FLR-effects too. It's natural to expect that the total plasma energy should be conserved without a dissipation as well as it takes place in magnetohydrodynamics. Nevertheless for this time there is no general expression for energy density variation were obtained in frames of drift theory [8]. The such expression can be derived from gDKE in first order of $1/\Omega$. Firstly let's comment this derivation for the usual DKE in zero order.

The space energy density of particle heat motion is simply $\frac{mn}{2}(u_\perp^2 + u_\parallel^2) = p_\perp + p_\parallel/2$. Taking DKE-integral with weights $u_\perp^2$, $u_\parallel^2$ and summing the equations obtained we'll have

$$d_t(p_\perp + p_\parallel/2) = -(2p_\perp + p_\parallel/2)\mathrm{div}\mathbf{V} - \mathrm{div}((q_\perp+q_\parallel/2)\mathbf{b}) +$$

$$+ (p_\perp - p_\parallel)\mathbf{b}(\mathbf{b}\nabla)\mathbf{V} .$$

The non-divergent items in right side are removing by taking into account both magnetic energy and plasma flow kinetic energy. So

$$\partial_t\left(mn\frac{V^2}{2} + p_\perp + \frac{p_\parallel}{2} + \frac{B^2}{8\pi}\right) = -\mathrm{div}\left[\mathbf{V}\left(mn\frac{V^2}{2} + 2p_\perp + \frac{p_\parallel}{2} + \frac{B^2}{4\pi}\right) + \right.$$

$$\left. + \left(q_\perp + \frac{q_\parallel}{2} + \left(p_\parallel - p_\perp - \frac{B^2}{4\pi}\right)\mathbf{V}\cdot\mathbf{b}\right)\mathbf{b}\right] + \mathbf{V}\left(\mathbf{F} + \frac{1}{4\pi}[\mathbf{B}\times\mathrm{rot}\mathbf{B}]\right). \qquad (8)$$

The energy density variation is connected with convective energy transport (first divergent item), longitudinal heat flows (items with $q_{\perp,\parallel}$), energy convection along magnetic field lines (with magnetic energy) and a work of electromagnetic forces too (final item in (8)). For example, if the electric current is conditioned only by plasma component considered then the final item is disappeared precisely what is equivalent to a zero electric field in co-ordinate frame frozen in this component.

Having performed the same procedure for the gDKE we obtain the expression of energy density variation including

FLR-terms:

$$\partial_t\left(mn\frac{V^2}{2} + p_\perp + \frac{p_\parallel}{2} + \frac{B^2}{8\pi}\right) = -\operatorname{div}\left\{\mathbf{V}\left(mn\frac{V^2}{2} + 2p_\perp + \frac{p_\parallel}{2} + \frac{B^2}{4\pi}\right) + \right.$$

$$+ \mathbf{b}\left(q_\perp + \frac{q_\parallel}{2} + (p_\parallel - p_\perp - \frac{B^2}{4\pi})V_\parallel\right) + \frac{1}{\Omega}\left\{\left(2R_\perp + \frac{R_\#}{2}\right)[\mathbf{b}\times\frac{\nabla B}{B}] + (2R_\perp - \right.$$

$$- \frac{R_\parallel + R_\#}{2})(\mathbf{brotb})\mathbf{b} + \mathbf{rotb}\,(R_\# + \frac{R_\parallel}{2}) + (q_\parallel + 4q_\perp)[\mathbf{b}\times\mathbf{b}\nabla V] +$$

$$+ q_\perp\mathbf{b}(\mathbf{brotV}) + B[\nabla\frac{q_\perp}{B}\times V] + \mathbf{b}(\mathbf{brotb})\frac{p_\parallel - p_\perp}{mn}\left(2p_\perp + \frac{p_\parallel}{2}\right) +$$

$$+ \left[\mathbf{B}\times\left(\nabla\left(\frac{p_\perp - p_\parallel}{mnB}\left(2p_\perp + \frac{p_\parallel}{2}\right)\right) - \frac{\nabla p_\perp}{mnB}\left(2p_\perp + \frac{p_\parallel}{2}\right)\right)\right] + \frac{B^2}{4\pi}\left[\frac{\mathbf{F}}{mn}\times\mathbf{b}\right] -$$

$$\left. - \Omega\,\mathbf{P}^1\cdot\mathbf{V}\right)\Big\} + \mathbf{F}\left(\mathbf{V} - \frac{B}{4\pi mn\Omega}\,\mathbf{rotB}\right) + \frac{V}{4\pi}\,[\mathbf{B}\times\mathbf{rotB}]. \qquad (9)$$

Here $R_\parallel = mn\overline{u_\parallel^4}$, $R_\# = mn\overline{u_\parallel^2 u_\perp^2}/2$, $R_\perp = mn\overline{u_\perp^4}/8$ are the fourth moments have been calculated by isotropic part of distribution f_o, and the expression for pressure tensor $\mathbf{P}^i \sim 1/\Omega$ has been given in [5].

For an one-component (e.g. hydrogen) plasma formula (9) describes the energy variation of ions and magnetic field. In quasineutrality $\mathbf{F}+\mathbf{F}_e \approx -\frac{1}{4\pi}\,[\mathbf{B}\times\mathbf{rotB}]$ and $\mathbf{V}_e \approx \mathbf{V} - \frac{B}{4\pi mn\Omega}\,\mathbf{rotB}$ (the subscript "e" marks electron component) and we've the removal of final (nondivergent) term in (9) when pressure in left side denotes the sum of electron and ion pressures.

Finally the total volume energy integral conserves with FLR-corrections similar to ideal MHD:

$$\partial_t\int d^3r\,\left(mn\frac{V^2}{2} + p_\perp + \frac{p_\parallel}{2} + \frac{B^2}{8\pi}\right) = 0.$$

The simple consequences of FLR-generalized DKE given in this paper expand the convenient notions of charged magnetized particles drift motions for a case of final Larmor radius.

REFERENCES

1. Rudakov L., Sagdeev R. In: "Plasma Phys. and Controlled Fusion Reactions Problem", v.3, AN USSR Publ., 1958
2. Rosenbluth M.,Krall A.,Rostoker N. Nuc.Fus.Sup.1962,p.143
3. Rosenbluth M.,Simon A. Phys.Fluids, 1965, v.8, p.1300
4. Lakhin V., Makurin S., Mikhailovskii A., Onishchenko O. J.Plasma Phys., 1987, v.38, p.387
5. Ilgisonis V.I. Sov.Journ.Plasma Phys.,1990,v.15,p.1046
6. Northrop T. "The Adiabatic Motion of Charged Particles", Intersci.Publ. J.Wiley and Sons, N.Y.-London-Sydney,1963
7. Gordin V., Petviashvili V. JETP Letters,1987,v.45,p.215
8. Kulsrud R. In:"Plasma Phys.Foundation",v.I,N.Holland,1983

DRIFT EFFECTS IN THE THEORY OF MAGNETIC ISLANDS

A.I.Smolyakov

I.V.Kurchatov Institute of Atomic Energy, Moscow, USSR

1. Introduction

Destruction of magnetic surfaces is one of the possible reasons for anomalous electron heat transport in tokamaks. Several models for electron heat conduction emerging in overlapping chains small-scale magnetic islands has been proposed recently [1,2]. The problem of magnetic islands emergence and stabilization mechanism is a basic one for such models. It is known [3], that in nonlinear regime magnetic islands grow when Δ' is positive. Magnetic islands pass into the nonlinear regime when their width exceeds the linear tearing layer width [3]. The linear tearing layer is very thin for the present day tokamaks parameter so the typical resonant magnetic perturbations from external sources (e.g. field errors or another instabilities) are large enough to produce magnetic islands in nonlinear regime. Recently it was noted that the magnetic islands dynamics can be essentially modified when plasma inhomogeneities are taken into account [4-6]. This modifications result in a conclusion about possibility of magnetic islands grow when Δ' is negative [5,6]. Here we examine this new driving mechanism which arise from drift effects as well as FLR effects for ions. Besides we investigate the role of radial electric field in the magnetic islands dynamics.

Perturbation in a magnetic field is described by the potential

$$\psi = -\frac{x^2}{2L_s} B_s + \psi \cos \xi \qquad (1)$$

Here $\xi = (m\hat{\theta} - \int^t \omega(t')dt')$, $\hat{\theta} = \theta - \zeta/q$, $x = \alpha - a_s$ -is a distance from the corresponding magnetic surface, $L_s = qR/S$, $S = rq'/q$. Dependence ψ and ω on time is caused by the dissipation. Here we suppose that this dissipation is sufficiently small $(\partial\psi/\partial t)/\psi \cong (\partial\omega/\partial t)/\omega \ll \omega$, so we can apply the method of successive approximations including dissipative effects only in the first order equations and neglecting ones in zero order.

2. Short-wave ($w/\rho_i << 1$) magnetic islands in inhomogeneous plasma

At first let us consider the magnetic islands with width less than ion Larmor radius. For the electrons we adopt the standard MHD by Braginskii, which includes thermoelectrical effects. The ion density response in the short-wave regime is adiabatic. The longitudinal electron heat conduction and longitudinal plasma conductivity are taken into account as a dissipative effects. The initial equations are

$$\frac{d_0}{dt} n - \frac{1}{e} \nabla_\parallel J = 0, \qquad (2)$$

$$E_\parallel + \frac{T_0}{e n_0} \nabla_\parallel n = \frac{1}{\sigma} J - (1 + \alpha) \frac{1}{e} \nabla_\parallel T = 0, \qquad (3)$$

$$\frac{3}{2} \frac{d_0}{dt} T = \nabla_\parallel (\kappa_\parallel \nabla_\parallel T) + (1 + \alpha) \frac{T}{e} \nabla_\parallel J. \qquad (4)$$

Here $E_\parallel = -\nabla_\parallel \phi + \frac{1}{c} \frac{\partial \psi}{\partial t}$, $\frac{d_0}{dt} = \frac{\partial}{\partial t} + V_E \nabla$.

These equations can be integrated in stationary case [5]. Using standard matching procedure for the solutions in nonlinear and linear regions [3] we obtain

$$G_1 \frac{\partial w}{\partial t} = D_R \left(\frac{\Delta'}{4} + \frac{2 G_2}{w} \frac{\omega_{pe}^2}{k_\theta^2 v_{te}^2} \frac{L_s^2}{c^2} (\omega^2 - \omega_*^2) \right). \qquad (5)$$

The second evolution equation is obtained from the energy conservation equation

$$\frac{1}{w} \frac{\partial w}{\partial t} (\alpha_1 \omega - \omega_*) + \alpha_2 \frac{\partial \omega}{\partial t} = \qquad (6)$$

$$-D_R \frac{\alpha_3}{w^2} \frac{\omega_{pe}^2}{k_\theta^2 v_{te}^2} \frac{L_s^2}{c^2} \omega_* (\omega + \omega_*)^2 f \qquad (7)$$

Где $f = C_2 \eta_e + C_1 (\omega/\omega_* - 1)$, $D_R = c^2/4\pi\sigma$, w - islands width, $C_1 = 1 + (1+\alpha)^2 \sigma T/e^2 \kappa$, $C_2 = 3(1+\alpha)\sigma T/2e^2\kappa$. numerical values are $\alpha_1 \cong 2$, $\alpha_2 \cong 1$, $\alpha_3 \cong 0.3$, $G_1 \cong G_2 \cong 0.4$. The steady-state islands with $\Delta' < 0$ are possible when $\omega^2 > \omega_*^2$ and $f = 0$ [5]. The condition for the formation of short-wave

magnetic islands (under the assumption $\Delta'<0$) are $\eta_e > 2\eta_{cr}$ and $\eta_e < 0$, $\eta_{cr}=C_1/C_2$. The width of such islands is of the order of

$$k_\theta w \cong \beta' L_s^2/L_n^2,$$

where $\beta =4\pi n_0 T/B_s^2$, $L_n = n_0/n_0'$, and frequency is defined by equation

$$\omega = \omega_*(1 - \eta_e/\eta_{cr}).$$

For the $\eta_e>0$ these islands move in the direction of the diamagnetic ion drift. We have found that such steady-state islands are stable.

3. Long-wave ($w >> \rho_i$) magnetic islands

In the long-wave regime the effects of the finite Larmor radius are important. Here instead of adiabaticity relation for ions we use the current closure equation div J =0 taking into account the gyroviscosity in the equation of the ion motion. For the electrons equations (2-4) are used. As in a short-wave regime we can integrate initial equations [5] and then we find equations determining evolution of ω and w for the long-wave magnetic islands

$$G_1 \frac{\partial w}{\partial t} = D_R \left(\frac{\Delta'}{4} - \frac{16G_2}{w^3} \frac{L_s^2}{k_\theta^2 c_a^2}\right) \omega(\omega - \omega_{*_i}), \qquad (8)$$

$$\frac{\partial w}{\partial t} (-I_1 \omega_*^2 w^2/\rho_s^2 + I_2\omega^2 + I_3\omega\omega_*) + I_4 w \frac{\partial}{\partial t}\omega^2 =$$

$$-D_R \frac{1}{w^3} \frac{f}{\omega - \omega_*} \frac{L_s^2}{k_\theta^2 c_a^2} \omega^2 (\omega - \omega_{*_i})^2. \qquad (9)$$

Here numerical values $I_1 \cong 0.3$, $I_2 \cong 0.5$, $I_3 \cong 1.4$, $I_4 \cong 1.4$, $16G_3 \cong 1$. From (8) we can find that in the case $\Delta' < 0$ the long-wave magnetic islands can grow when $0 < \omega < \omega_{*_i}$ [5]. The steady-state islands width is of the order of

$$(k_\theta w)^2 \cong (k_\theta \rho_i)^2 \beta' L_s^2/L_n^2.$$

The rotation frequency is determined from the same equation as in a short-wave regime.

4. Magnetic islands in a plasma with radial electric field

In the case of magnetic islands in a homogeneous plasma with radial electric field the first evolution equation is readily derived from (8) by substitution $\omega \to \omega - \omega_E$, where

$\omega_E = k_\theta c\phi'/B_s$, so we can obtain

$$G_1 \frac{\partial w}{\partial t} = D_R \left(\frac{\Delta'}{4} - \frac{16 G_2}{w^3} \frac{L_s^2}{k_\theta^2 c_a^2} (\omega - \omega_E)^2 \right). \qquad (10)$$

Similar equation was derived in [7]. The second equation for the w and ω which is followed from the energy conservation has the form

$$\frac{\partial w}{\partial t} (K_1 \omega^2 + K_2 \omega \omega_E - K_3 \omega_E^2) + w \frac{\partial}{\partial t} (K_4 \omega^2 + K_5 \omega \omega_E) =$$

$$-D_R \frac{1}{w^3} \frac{L_s^2}{k_\theta^2 c_a^2} (\omega - \omega_E)^4. \qquad (11)$$

Here $K_1 \cong 0.9$, $K_2 \cong 1.2$, $K_3 \cong 2$, $K_4 \cong 1.4$, $K_5 \cong 0.1$. The second term in equation (10) associated with plasma inertia is always stabilizing, so the islands grow when $\Delta' > 0$. Recently the stabilization of magnetic islands by radial electric field was investigated numerically in [8].

5. Conclusions

We have obtained the equations for the evolution of the magnetic islands width and rotation frequency in the short-wave and long-wave regimes. We have shown that the nonlinear exciting of magnetic islands with finite threshold can occur when $\Delta' < 0$. The possibility of existence of the steady-state islands in inhomogeneous plasmas is demonstrated. The stability of such steady-state islands is studied. It is found that the radial electric field can stabilize the magnetic islands growth.

References

1. Rebut P.H., Brusati M., Hugon M., Lallia P., Plasma Phys.Cont.Nucl.Fusion Res.(Proceedings of the 11-th Intern.Conf., Kyoto, 1986) v.2, p.187.
2. White R.B., Romanelli F., Phys. Fluids **B1** (1989) 977.
3. Rutherford P.H., Phys. Fluids **18** (1973) 1903.
4. Scott B.D., Hassam A.B., Phys. Fluids **30** (1987) 90.
5. Smolyakov A.I., Sov.J.of Plasma Phys. **15** (1989) 120.
6. Kotschenreuther M., *Initial evolution of nonlinear magnetic islands in high temperature plasmas.* Univ. of Texas (1988) IFSR #319.
7. Fitzpatrick R., Haynes P.S., Hender T.C. et al., 13-th Intern. Conf. on Plasma Phys. and Contr. Nucl. Fus. Res., Washington (1990), report D-2-6-1(C).
8. Persson M., Bondeson A., Phys. Fluids **B2** (1990) 2315.

INFUENCE OF MAGNETIC ISLANDS ON MAGNETIC FIELD LINE DIFFUSION

A. M. Martins and J. T. Mendonça

Centro de Fusão Nuclear, Associação Euratom/IST

Instituto Superior Tecnico, 1096 Lisboa Codex, Portugal.

1. Introduction

One of the proposed mechanisms to explain the observed anomalous transport in Tokamak discharges is the ergodization of magnetic field lines due to the interaction of small magnetic islands, excited by microtearing instabilities in adjacent rational surfaces[1]. Such an interaction does not necessarily lead to a complete ergodization of the field lines and it is perhaps more likely to assume that a number of periodically distributed magnetic islands still remains, surrounded by a stochastic sea. The change in size of these islands will eventually serve as a self-regulatory mechanism for temperature profile consistency.

Apart from the purely stochastic situation, for which analytical expressions for the diffusion coefficient can be derived, the influence of the magnetic island size and spacing has only been studied by numerical methods.

In the present work we study, on purely analytical grounds, the changes occurring when the quasi-linear diffusion process for the stochastic field lines is perturbed by small size magnetic islands. First, we derive our model equation, which is a diffusion equation with a locally perturbed diffusion coefficient. We then solve this equation using an iterative method which leads to a renormalization of the dominant diffusion process. Our final result will depend, in a simple way, on the islands size and spacing.

2. Model equation

In a toroidal configuration, the magnetic field line equations can be written in canonical form as[2]:

$$\frac{d\theta}{d\zeta} = \frac{\partial \psi_p}{\partial \psi} \qquad \frac{d\psi}{d\zeta} = -\frac{\partial \psi_p}{\partial \theta} \tag{1}$$

where ψ and ψ_p are the toroidal and poloidal flux functions and ς an θ are the toroidal and poloidal angles. The general form for the Hamiltonian ψ_p is:

$$\psi_p(\psi,\theta,\varsigma) = \psi_{po}(\psi) + \tilde{\psi}_p(\psi,\theta,\varsigma) \qquad (2)$$

where the first term describes the current profile and the second term is associated with the magnetic field fluctuations:

$$\tilde{\psi}_p(\psi,\theta,\varsigma) = \sum_m A_m(\psi,\varsigma)\, e^{im\theta} \qquad (3)$$

Let us first consider the case where the field lines described by eq. (1) are completely stochastic in some domain of the phase space (ψ,θ). We can assume a statistical ensemble of trajectories in such a domain, described by a given distribution function $f(\psi,\theta,\varsigma)$. We know that, due to the hamiltonian nature of the field line trajectories, the kinetic equation for $f(\psi,\theta,\varsigma)$ reduces to a diffusion equation:

$$\frac{\partial f}{\partial \varsigma} = \frac{\partial}{\partial x_i} D_{ij} \frac{\partial}{\partial x_j} f \qquad (4)$$

where $x_1=\psi$, $x_2=\theta$ and:

$$D_{ij} = \lim_{\varsigma\to\infty} \frac{1}{2\varsigma} \int_0^{\varsigma} d\varsigma' \int_0^{\varsigma} d\varsigma'' < \left(\frac{dx_i}{d\varsigma}\right)_{\varsigma'} \left(\frac{dx_j}{d\varsigma}\right)_{\varsigma''} > \qquad (5)$$

Using the quasi-linear approximation, we can write $D_{11}\equiv D_{\psi\psi}$ as simply proportional to the energy of the magnetic field fluctuations[3,4]:

$$D_{11} = L_o \sum_m m^2 <|A_m(\varsigma=0)|^2> \qquad (6)$$

where L_o is the correlation length in the toroidal direction. We can also write[4] $D_{22}\equiv D_{\theta\theta}\simeq(k_o/m_o)^2 D_{11}$, where k_o and m_o are typical (radial and poloidal) wavenumbers of the magnetic fluctuations. We can further assume that the off-diagonal terms D_{12} and D_{21} are equal to zero, if the radial variation of the coefficients A_m is uncorrelated with their absolute value: $<A_m(\partial A_m/\partial\psi)>=0$. Using these assumptions eq.(4) is reduced to:

$$\frac{\partial f}{\partial \varsigma} = D_o \left\{\frac{\partial^2}{\partial x^2} + \frac{\partial^2}{\partial y^2}\right\} f \equiv D_o \nabla^2 f \qquad (7)$$

where $D_o=D_{11}$, $x=\psi$ and $y=(m_o/k_o)\theta$.

Now assume that this purely diffusion process is locally perturbed by small magnetic islands with area a, where the field lines are regular and not stochastic, localized at given positions $\vec{r}_{ij}=(x_{ij}\,\hat{x} + y_{ij}\,\hat{y})$. The perturbations introduced by these islands on the diffusion process can be easily described by the following

equation:

$$\frac{\partial f}{\partial \zeta} = [\, D_o - D' \sum_{i,j} g\,(\vec{r} - \vec{r}_{i,j})] \nabla^2 f \qquad (8)$$

where $g\,(\vec{r} - \vec{r}_{i,j})$ is strongly peaked arround $\vec{r}_{i,j}$. This simply means that, arround these points, the diffusion coefficient is reduced to a value $(D_o - D')$, which is equal to zero inside the islands. An appropriate cloice is:

$$g\,(\vec{r} - \vec{r}_{i,j}) = a\,\delta(\vec{r} - \vec{r}_{i,j}) \qquad (9)$$

3. Iterative solution

Following a well known iterative method, the solution of eq.(8) can be written as:

$$f(\vec{r},\zeta) = \sum_{n=o}^{\infty} f^{(n)}(\vec{r},\zeta) \qquad (10)$$

where:

$$f^{(o)}(\vec{r},\zeta) = U_o(\zeta,\zeta_o)\, f(\vec{r},\zeta_o) \qquad (11)$$

and:

$$f^{(n)}(\vec{r},\zeta) = \int_{\zeta_o}^{\zeta} U_o(\zeta,\zeta_o)\, \mathcal{L}'\, f^{(n-1)}(\vec{r},\zeta')\, d\zeta' \qquad (12)$$

In these equations the free propagator U_o is the integral operator:

$$U_o(\zeta,\zeta_o) = \frac{1}{4(\zeta-\zeta_o)D_o} \int d\vec{r}'\, \exp\left[- \frac{(\vec{r} - \vec{r}')^2}{4(\zeta-\zeta_o)D_o} \right] \qquad (13)$$

and $\mathcal{L}'$ is the perturbed differential operator:

$$\mathcal{L}' = - a\, D' \sum_{i,j} \delta(\vec{r} - \vec{r}_{i,j})\, \nabla^2 \qquad (14)$$

Let us assume the following initial condition $f(\vec{r},\, \zeta=\zeta_o) = \delta(\vec{r} - \vec{r}_o)$. We know that the Fourier transform of the zeroth order solution (11) is simply given by:

$$f^{(o)}(\vec{k},\omega) = [k^2 D_o - i\omega]^{-1} \exp(i\omega\zeta_o - i\vec{k}\cdot\vec{r}_o) \qquad (15)$$

In order to calculate the following order solutions we assume a periodic distribution for the small magnetic islands: $\vec{r}_{i,j} = iL_x\hat{x} + (jL_y + i\delta)y$, where L_x and L_y are the periodicities and δ a phase shift between adjacent chains of islands. After some calculations, we obtain:

$$f^{(n)}(\vec{k},\omega) = 2\pi \frac{aD'}{L_x L_y} \sum_{i,j} \frac{|\vec{k} - \vec{k}_{i,j}|^2}{k^2 D_o - i\omega} f^{(n-1)}(\vec{k} - \vec{k}_{i,j},\omega) \qquad (16)$$

where:

$$\vec{k}_{i,j} = \frac{2\pi}{L_x}(i - \frac{\delta}{L_y}j)\,\vec{x} + \frac{2\pi}{L_y}j\,\vec{y} \qquad (17)$$

In order to get a simple but still meaningfull solution, we assume that the dominant terms in the summations implicit in eq.(16) are those proportional to $(k^2D_0 - i\omega)^{-1}$, because these terms contribute to the dominant diffusion process described by eq.(15). Neglecting the other terms we obtain, after inverse Fourier transformation:

$$f(\vec{r},\zeta) = \frac{1}{2}\left[\pi(\zeta-\zeta_0)D_{eq.}\right]^{-1/2} \exp\left[-\frac{(\vec{r}-\vec{r}_0)^2}{4(\zeta-\zeta_0)D_{eq.}}\right] \qquad (18)$$

where:

$$D_{eq.} = D_0 - (2\pi)^2 D' \frac{a}{L_x L_y} \qquad (19)$$

4. Conclusions

This result shows that the diffusion process D_0 perturbed by a(n infinite) number of periodically distributed small magnetic islands, is equivalent to a diffusion process $D_{eq.}$, which depends on a small adimensional parameter $(2\pi)^2 a/L_xL_y$ (the area of the islands normalized to the area of the elementary net). When this parameter is close to unity and $D_0=D'$, we will have no diffusion, because the regular islands will dominate over the stochastic region. This means that eq.(18) remains at least qualitatively valid for finite size islands, even if its derivation is limited to infinitesimal islands. This also means that the decrease of the diffusion coefficient with respect to D_0, observed in numerical experiments, can be largely explained by the increase in size of the regular islands. Another interesting feature of eq.(18) is that it is insensitive to the phase shift δ, which only contributes to higher order terms. Finaly, we note that our model equation can also be used to modelize the heat propagation in a hot plasma containing colder islands.

References

1 - P. Rebut and M. Brusati, Plasma Phys Controlled Fusion 28, 113 (1986).

2 - A.H. Boozer, Phys. Fluids 26, 1288 (1983).

3 - B.B. Kadomtsev and O.P. Pogutse, in "Plasma Physics and Controlled Nuclear Fusion Research (IAEA, Vienna,1979), Vol.I, p.649.

4 - I.T. Mendonça, Phys. Fluids 3, 94 (1991).

Computation of Plasma Equilibria with Semifree and Free Boundary

A. Nicolai
Forschungszentrum Jülich GmbH, Association EURATOM-KFA

1. Introduction

Besides the solution of the GRAD-SHAFRANOV equation for the fixed and semifree boundary value problem /1/ the solution of the free boundary value problem is of particular interest because it provides the possibility to account for the passive conductors and the driving voltages. These voltages are in general composed of two parts, one with prescribed time dependence and the other used as feedback part. Hence the performance properties of the feedback control of the plasma position and the shape parameters can be assessed. The solution of the semifree boundary value problem can be used for comparison.
Combining the approach of SHAFRANOV concerning the time evolution of equilibria with the circuit equations, the transport equations for the particle and energy inventory and the equilibrium constraint, the time evolution of the discharge can be tracked during the current rise and the flat top phase.

2. Solution of the semifree boundary value problem /1/

Instead of choosing the driving voltages as an input, the inverse problem might be envisaged. The coil currents maintaining certain prescribed positions of the plasma boundary are computed iteratively. Since either the current in the primary solenoid or the value of the poloidal flux function at the plasma boundary is known from the poloidal flux balance a regularization of the semifree boundary value problem is not needed.The prescribed positions at the plasma boundary are those at the outboard side, at the inboard side, at the upper edge and the lower edge. This means that the plasma elongation and the plasma volume (or the effective plasma radius) can be adjusted. However, it is impossible to adjust the triangularity. This would require more coil groups than envisaged here.

3. Solution of the free boundary value problem

Although the numerical approach in solving the free boundary value problem is quite different from that for the semifree boundary value problem, the computed time evolution of the discharge is similar to the simulation results obtained in treating the semifree boundary value problem. The reason is the feedback control of the shape and position parameters. Since in this paper the aforementioned positions of the plasma boundary are used as designed positions for the feedback control, similar results in solving the free boundary value problem can be expected.
By applying Faraday's law at the coil positions and at the plasma boundary the following equation connecting the driving voltages with the coil currents and the current

density in a virtual casing /2/ replacing the plasma can be obtained:

$$\frac{\partial}{\partial t}\left(\vec{\vec{P}}\vec{J}\right) = \left\{\begin{array}{c}\vec{V} - \vec{\vec{R}}\vec{J} \\ -\vec{U}_p\end{array}\right\} \qquad (1)$$

Here $\vec{\vec{P}}$ is the inductivity matrix accounting for the mutual interaction between the coils and the plasma and among the coils themselves. $\vec{V}$ is the voltage vector, $\vec{\vec{R}}$ the (diagonal) resistance matrix, $\vec{J}$ the current vector and $\vec{U}_p$ stands for the plasma loop voltage.
We note that equation (1) originates from a rigorous approach /2/ and that the numerical errors enter through discretization only. The voltage vector may be composed by a feed forward and a feedback part. Here the feedback part is assumed to be proportional to the deviations between the actual and the designed position and shape parameters. The feedforward part is assumed to be constant.

4. Treatment of the transformer iron

Employing the discontinuity relation for the tangential component of the magnetic inductance an integral equation of Fredholm's second kind was derived for a surface current density, simulating the magnetic action of the iron as described in reference/1/.

5. Evolution of the plasma parameter

The time evolution of the electron and ion temperatures depends essentially on the distribution of the power sources, as Ohmic, neutral injection or high frequency heating, and on the distribution of power losses effected by conduction, convection, line radiation, charge exchange, ionization, and recombination.The particle source and loss mechanisms which determine the particle inventory, are the diffusion perpendicular to the magnetic field, the inward flow, deposition by neutral injection and the recycling processes.
Accounting for these processes and for an evolving flux surface geometry one arrives at the transport equations /1/ for the particle densities the electron and ion temperatures of a multispecies plasma.
These evolution equations are completed by equations for either the poloidal or the toroidal flux function which account for the resistive effects within the frame of a one dimensional approach. The mutual impact of changes in the toroidal flux on the poloidal flux function and vice versa is included also as proposed by SHAFRANOV /3/.

6. Results

The calculations are based on parameters recently analysed for a pulse length prolongation of the TEXTOR device. Here besides the primary solenoid covering the total iron core and the vertical field coils, shaping coils had been assumed to be available where the yokes merge into the iron core (Fig.1). The minor radius is a = 50 cm,

major radius R = 175 cm and the toroidal field B_t = 2.25 T. Fig.2 shows the dependence of the current in the shaping coils and of the magnetic flux on the current in the primary solenoid I_{pr}. Concerning the modelling of the yokes,two cases had been envisaged: firstly the averaged permeability according to ref /1/ and secondly the local iron permeability. In the first case I_{S_1} saturates at -1.3 MA,and in the second case at -1.1 MA, thus showing that the modelling of the yokes has a considerable impact on the shaping current. The Fig. further shows that the flux swing available for the flat top phase is 4.7 Vsec.

A contour plot of the poloidal flux function is displayed in Fig.3. The plot belongs to the flat top phase (I_{pr} = -4 MA) The currents in the shaping coils (I_{S_1} = -1.3 MA) enforce that no primary flux is released between the primary solenoid and the plasma. In this way it is avoided that the plasma is squeezed between the primary solenoid and the vertical field coils, and the cross-section stays almost circular. The triangularity is δ = -3.5 %.

During the current rise phase a positive triangularity δ = 1.5 % occurs because of the attraction by the shaping coil currents (I_{S_1} = 400 kA) which have to elongate the otherwise prolate plasma cross-section. Without the action of the shaping coils this prolate cross-section is due to the attraction by the (positive) primary current I_{pr} = 4.6 MA.

Similar results are obtained in solving the free boundary value problem as outlined above.The time evolution of the designed and computed plasma current (I_p and I_d respectively) shows that in the envisaged time interval ($0 \leq t \leq 400$ msec) the maximum deviation I_p and I_d is around 10 %. However, after the transition to the flat top phase oscillations in I_{S_1} and I_{pr} occur showing that improvements of the equations for feed back parts of the voltages are needed.

7. Conclusions

The calculations show that by means of the shaping coils the circular cross section can be maintained rather accurately although their radii differ considerably from the major plasma radius. Since the maxima of the plasma boundary in the R,z plane are flat, the aforementioned values of the triangularity mean only slight deviations of the computed plasma shape from the designed circular shape. The solution of the free boundary value problem indicates that the aforementioned numerical procedure for the proportional control of the plasma position and shape parameters should be supplemented by terms describing the respective differential or integral control.In this way the accuracy can be improved, the oscillations may be damped and the optimum control can be reached.

/1/ A. Nicolai, P. Börner, J. Comput. Phys., 90 (1989) 98
/2/ K. M. Link, S. C. Jardin, Fusion Technology 12 (1987) 22
/3/ V. O. Shafranov, G. V. Pereversev, L. E. Zakharov in Proceedings of the 3rd. Int. Conf. Plasma Theory, Kiev, Trieste, 1977, p.469

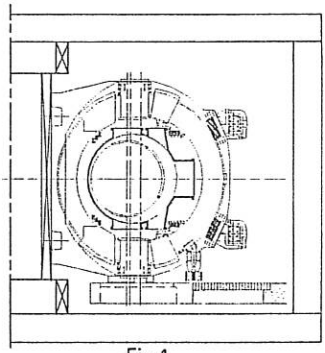

Fig.1

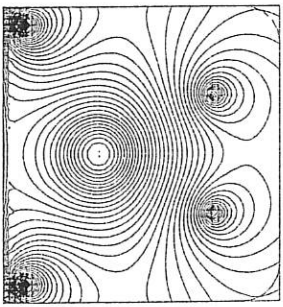

Fig.2

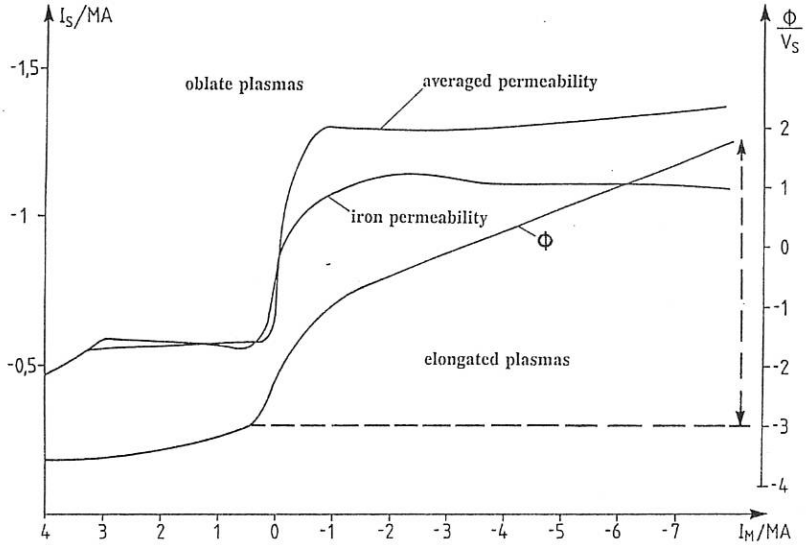

Fig.3

STUDY OF DENSITY AND TEMPERATURE PROFILE ACROSS THE MAGNETIC ISLAND

Qingquan Yu and Yuping Huo

(Institute of Plasma Physics, Hefei, 230031, P.R.China)

I Introduction

It is well known that the magnetic island develops near the rational surface in Tokamak due to the tearing mode instability.[1-3] In the magnetic island region the energy and particle diffusivity are much larger than those outside the magnetic island due to the magnetic field fluctuations and the reconnection of the magnetic field lines of force. It is therefore considered previously that the plasma density and temperature profile are flattened there.[4]

In this paper it is found that the following question exists in the previous theories. That is whether the equilibrium condition

$$\nabla p = \mathbf{j} \times \mathbf{B}/c \qquad (1)$$

can be satisfied if the plasma density and temperature profile are flattened across the magnetic island. Here p is plasma pressure, p=nT, n and $\mathbf{j}$ are plasma and current density, T is plasma temperature, $\mathbf{B}$ is the equilibrium magnetic field.

If the plasma density and temperature profile are flattened across the magnetic island, the equilibrium condition will not be satisfied unless the plasma current density $\mathbf{j}$ and the equilibrium magnetic field $\mathbf{B}$ become much less inside the magnetic island than those in the case of no magnetic island.

In practical case however the magnitude of $\mathbf{j}$ and $\mathbf{B}$ is not much decreased inside the magnetic island,[3] so that the magnetic force is larger than the thermal pressure force in radial direction when plasma density and temperature profile are flattened. The net force exerts on plasma inside the magnetic island is inward which pinches the plasma towards the center of the plasma column.

The resulting inward motion of plasma thus appears which plays the role in increasing the density gradient across the magnetic island and making the thermal pressure force larger.

This pinch process will continue until the density gradient across the magnetic island becomes large enough so that the net driving force approaches zero. More steep density profile is needed to achieve a new equilibrum.

II plasma density and temperature profile inside the magnetic island

Here the consideration is concentrated inside the magnetic island region and a huristic analysis is carried out.

we first consider the plasma temperature profile. The temperature evolution is described by the energy transport equation. Since the thermal diffusivity is much larger inside the magnetic island than that outside, the plasma temperature profile should be flattened inside the magnetic island as that pointed out in previous theories,[5,6] $\partial T/\partial r \cong 0$.

The plasma density n is determined by the continuous equation

$$\partial n/\partial t + \nabla\cdot\Gamma = 0 \qquad (2)$$

Where Γ is the particle flux. Outside the magnetic island Γ can be given by $\Gamma = -D\nabla n$, where D is the particle diffusivity. From the discussions in above section it is found that the thermal pressure force will be smaller than the magnetic force once the plasma temperature profile is flattened inside the magnetic island while the magnitude of $\mathbf{j}$ and $\mathbf{B}$ is not much decreased, a net inward force exists which pinches the plasma inward. Therefore an inward plasma pinch velocity v_p appears in addition to the diffusion flux which also exists outside the magnetic island. The total radial flux inside the magnetic island is now given by

$$\Gamma = -D\nabla n + nv_p \qquad (3)$$

The pinch velocity v_p is determined by the equation of motion in radial direction in cylinder geometry

$$\rho dv_p/dt = -j_z B_\theta/c - T\partial n/\partial r \qquad (4)$$

Where $\partial T/\partial r=0$ is used inside the magnetic island. ρ is plasms mass density.

A simple estimation about the magnitude of v_p can be made here. when the width of the magnetic island is much less than the Tokamak small radius, $w/a<<1$, in lowest order j_z, B_θ and n can be approximated to have the same values as those before the onset of the magnetic island (of course their gradient is changed). Before the onset of the magnetic island the equilibrium condition is satisfied and the plasma temperature is T_a, therefore

$$\rho dv_p/dt = -n\partial T_a/\partial r \qquad (5)$$

v_p is found to be $v_p \sim (v_{ta})^2 t/L_T$ from above equation, where $v_{ta}=(2T_a/M)^{1/2}$, $L_T=T_a(\partial T_a/\partial r)^{-1}$ and M is the ion mass.

From eq.(3) it is found that at the time $t\sim t_s\sim DL_T/(v_{ta})^2 L_n$ the diffusion flux is canceled out by the pinch effect and the total particle flux decrease to zero. Where $L_n=n(\partial n/\partial r)^{-1}$.

Since the particle diffusivity D is much less than the ion parallel diffusivity $D = (v_{ti})^2 \tau_{ii}$ and $L_T/L_n\sim 1$, so that $t_s \ll \tau_{ii}$, τ_{ii} is the ion-ion collision time.

Just at the beginning of onset of the magnetic island the density gradient in it is decreased because of the large particle diffusivity. In a very short time $t\sim t_s$ the pinch flux becomes large enough to cancel out the diffusion flux and lead Γ to approach zero. At $t>t_s$ the pinch flux exceed the diffusion flux, the total flux inside the magnetic island is inward, so that the density gradient is increased there.

The increasing in the density gradient leads ∇p larger, the net driving force is therefore decreased. The acceleration process will not be stoped until the density gradient is large enough so as to achieve a new equilibrium

$$T\,\partial n/\partial r = -j_z B_\theta/c \qquad (6)$$

The density difference across the magnetic island is

$$\Delta n = \int (-j_z B_\theta/cT)\,dr \qquad (7)$$

The integration is carried out across the magnetic island.

If $w/a\ll 1$, in lowest order $\Delta n \cong w j_z B_\theta/cT$, where T, j_z and B_θ take values inside the magnetic island.

Because the temperature gradient is very small inside the magnetic island,[5,6] the density gradient inside the magnetic island will be larger than that in the case of no magnetic island when the magnitude of $j_z B_\theta$ is approximately the same.

So we see that althouth the particle diffusion flux is very large inside the magnetic island, an large inward plasma pinch flux develops due to the force unbalance which cancels out the diffusion effect. At final stage a larger density gradient results from the requirement of equilibrium.

The detailed form of the particle diffusivity is not important in determining the final density gradient inside the magnetic island, the density gradient there is determined by the force balance of eq.(6).

III Conclusions

From the analysis made in former sections we finally reach at the following conclusions:

1. There is a plasma pinch process inside the magnetic island due to the force unbalance resulting from the flattening of plasma temperature profile.

2. The pinch flux becomes large enough in a very short time to cancel out the diffusion flux.

3.The plasma density profile are more steep rather than flattened across the magnetic island due the requirement of equilibrium.

Further numerical study is needed to treat the full transport equations to give the detailed plasma density profile with practical Tokamak and plasma parameters.

In previous tearing mode theory it is considered that the plasma density and temperature profile are flattened across the magnetic island and the diamagnetic frequency is quenched in the nonlinear stage, the nonlinear growth and saturation of the magnetic island and the Mirnov oscillations observed in Tokamak experiments are independent of the diamagnetic effect.[4]

The result that a larger density gradient exists inside the magnetic island found here will change previous conclusions and lead to different results. The nonlinear evolution of tearing mode had already been showed to be dependent on the density and temperature profile theoretically.[7]

ACKNOWLEDGEMENT--The authors would like to acknowledge useful discussions with Prof. G. Y. Yu.

REFERENCES

[1] H. P. Furth, J. Killen, and M. N. Rosenbluth, Phys. Fluids **6**, 459(1963).
[2] P. H. Rutherford, Phys. Fluids **16**, 1903(1973).
[3] R. B. White, D. A. Monticello, M. N. Rosenbluth and B. V. Waddell, Phys. Fluids **20**, 800(1977).
[4] D. Biskamp, Nucl. Fusion **19**, 777(1979).
[5] M. F. Turner and J. A. Wesson, Nucl. Fusion **22**, 1609(1982).
[6] Zhang Chang et al., 13th International Conf. on Plasma Phys. and Controll.Nucl. Fusion, Washington,IAEA-CN-53/D-1-5(1990)
[7] Bruce D. Scott and A. B. Hassam, Phys. Fluids **30**, 90 (1987).

TWO-FLUID THEORY OF PRESHEATH AND SHEATH INCLUDING MAGNETIC FIELDS

H.-B. Valentini

Physico-Technical Institute, Helmholtzweg 4, D/O-6900 Jena

Abstract: The transition between presheath and sheath is taken into account by means of a two-fluid model of the whole plasma. Sheath criteria are investigated. The sheath is defined as region where the influence of the space charge dominates. A magnetic field parallel to the wall can reduce the voltage drop across the sheath and can increase the thickness of the sheath.

1. Introduction

It is customary in the theory of low pressure plasmas to treat the bulk plasma and the space charge sheath at the wall separately (e.g. /1/, /2/). A criterion for the sheath edge and a procedure to match the solutions for the bulk, the presheath and the sheath are necessary (e.g. /3/, /4/). The well known Bohm criterion is relevant for collisionless plasmas only /3/-/5/. Using a two-fluid model for the whole plasma the transition between presheath and sheath including magnetic fields are calculated. Restrictions are eliminated which otherwise would be occur by use of a sheath criterion or a multi-scale theory.

2. Basic equations

The plasma is considered to consist of electrons and of single charged positive ions in a motionless neutral gas. Charged particles are generated within the plasma, flow to the walls, recombine there and re-enter as neutral atoms.

A plane, one-dimensional and steady-state model with insulating walls at $x=\pm d$ is considered. The well known basic equations for the ions (s=i), the electrons (s=e), the neutral atoms (s=n), the electric field intensity E_x and the potential Φ read

$$N_s v'_{sx} + v_{sx} N'_s = Q_s \tag{1}$$

$$N_s M_s v_{sx} v'_{sx} + kT_s N'_s = Z_s e(E_x + v_{sy} B_z) - P_{sx} \tag{2}$$

$$M_s v_{sx} v'_{sy} = -Z_s e\, v_{sx} B_z - P_{sy}/N_s \tag{3}$$

$$E_x' = (e/\varepsilon_0)(N_i - N_e) \qquad (4), \qquad \Phi' = -E_x \qquad (5)$$

where $'=d/dx$ and k, e, ε_0 and later μ_0 are used as usual. Constant temperatures T_s and the magnetic induction B_z directed parallel to the walls are supposed. M_s is the mass, N_s is the particle density, v_s is the drift velocity, $Z_i=-Z_e=1$,

$$Q_e=Q_i=-Q_n=\nu_{ni}N_e\ , \quad P_e = (\nu_{ni} + \nu_{en})N_eM_ev_e\ , \quad P_i = (N_e\nu_{ni} + N_i\nu_k)M_iv_i\ , \quad \nu_k = \nu_c + \nu_i/2 \qquad (6)$$

with the frequencies of ionization ν_{ni}, elastic electron-atom collision ν_{en}, charge exchange ν_c and elastic impacts between ions and atoms ν_i. ν_{ni}, ν_{en} are taken as constant. $\nu_k(x) = q_k(v_{ix}^2 + 8kT_n/\pi M_n)^{1/2}$ holds as approximation with the effective cross section q_k.

The set of the seven differential equations (1)-(4) is nonlinear and involves isolated singular points at the sound speeds $v_{sx}=v_{sc}$ where $v_{sc} = (kT_s/M_s)^{1/2}$. (7)

Six boundary conditions are given by

$$v_{sx}=v_{sy}=0\ , \quad E_x=0 \quad \text{if } x=0 \qquad (8)$$

and from a simplified electron kinetics /2/, /6/, /7/

$$v_{ex} = (kT_e/2\pi M_e)^{1/2} \quad \text{if} \quad x=d\ . \qquad (9)$$

In addition, it is necessary to remove the singularity at $v_{ix}=v_{ic}$ by the condition $v_{ix}M_iQ_i = Z_ie(E_x+v_{iy}B_z)-P_{ix}$. (10)

One can derive the particle balance $N_iv_{ix} = N_ev_{ex}$ (11) and the pressure balance

$$\sum_s N_s(kT_s + M_sv_{sx}^2) + B_z^2/2\mu_0 - E_x^2/2\varepsilon_0 = \text{const} \qquad (12)$$

as integrals of (1)-(3) where s=i, e, n /5/, /8/.

It can be easily seen that

$$T_1 = T_e + T_i\ , \quad v_0 = (kT_1/M_i)^{1/2}, \quad \Theta_s = T_s/T_e\ , \quad l_i = v_0/\nu_{ni}$$
$$\omega_s = eB_z|Z_s|/M_s, \quad E_0 = kT_e/el_i, \quad l_D = (\varepsilon_0kT_e/e^2N_e(0))^{1/2} \qquad (13)$$
$$a_0 = (l_D/l_i)^2\ , \quad K = N_nq_kv_0/\nu_{ni}\ , \quad A_{eo} = \nu_{en}/\nu_{ni}$$

are characteristic parameters, where a_0 describes the influence of space charge and K that of ion-atom collisions.

3. Solution methods

The set (1)-(4) can be solved by an expansion in powers of $x-x_c$ or $v_{ix}-v_{ic}$ near the singular point of the ion gas. A numerical integration is performed in the remaining parts of the relevant interval, where in the subsonic region, i.e.

$v_{ix}<v_{ic}$, the numerical methods tend to be instable if K is large, but they are stable in the hypersonic region, i.e. $v_{ix}>v_{ic}$. If $T_i<<T_e$ an expansion into power series of θ_i is useful /3/, /9/. If $a_0K<<1$ an expansion into power series of a_0 can be used /3/, /7/, /10/. Restricting to cold ions, i.e. $T_i=0$, leads to a hypersonic ion flow in the whole interval.

4. Space charge sheath

It is physically reasonable to define the sheath as region with dominating action of the electric field caused by the space charge density. From (12) follows

$$N_e kT_e + N_i kT_i = E_x^2/2\varepsilon_0 \qquad (14)$$

as the condition for the sheath edge, relevant for all values of K. The quasineutral approximation leads to a sheath edge at $v_{ix}=v_0$ with an infinite electric field intensity.
Another definition of the sheath edge could be

$$(d/d(x/d))(N_i - N_e)/N_e(0) = 1 \ . \qquad (15)$$

5. Results

Results are given in the dimensionless variables

$$s=x/l_i, \quad v_s=v_s/v_0, \quad w_s=N_s/N_e(0), \quad f=E_x/E_0, \quad \eta=-e\Phi/kT_e \qquad (16)$$

for an argon plasma. The sheath criterion (14) becomes

$$w_e = (a_0/2)f^2 \quad \text{if} \quad \theta_i=0 \quad \text{and} \quad \theta_e=1 \ .$$

The fig. 1 shows v_i at the wall, i.e. $v_i=v_{iw}$, where $B_z=0$. If $v_{iw}<1$ the Bohm criterion cannot be satisfied.
In fig. 2 the profiles of the ion and electron densities w, w_e and of the Maxwellian tension $(a_0/2)f^2$ are plotted.
The fig. 3 shows the ratio of the sheath thickness l_b to the mean free path of the ions l_{in} and of l_b to the Debye length l_{Db} at the sheath edge.
In the fig. 4-6 the influence of a magnetic field is represented where only the electron gas is taken to be magnetized. The figures show w, w_e and $(a_0/2)f^2$ if $a_0=2.3\ 10^{-6}$, K=1.84, $\omega_e/\nu_{en}=0$, 100, further, the wall potential η_w dependent on ω_e/ν_{en} if $a_0=2.3\ 10^{-6}$, K=1.84 (a); $a_0=1.5\ 10^{-6}$, K=1576 (b).
More details, including the transverse variation of T_e, are given in /7/.

References
/1/ Tonks L., Langmuir I., Phys. Rev.34(1929)876
/2/ Chodura R. in "Physics of PLasma Wall Interaction in Controlled Fusion" (edited by D. E. Post and R. Behrisch), Plenum Publishing Comp. 1986
/3/ Franklin R. N., "Plasma Phenomena in Gas Discharges" Clarendon, Oxford, 1976
/4/ Riemann K.-U., J. Phys.D: Appl. Phys.(1991)(is printing)
/5/ Valentini H.-B., Beitr. Plasmaphys. 19(1979)221
/6/ Gerhauser H., Claassen H. A., Berichte KFA Juelich Nr. 2125 May 1987
/7/ Valentini H.-B., Contrib. Plasma Phys. 31(1991)No.4
/8/ Valentini H.-B., Beitr. Plasmaphys. 16(1976)181
/9/ Valentini H.-B., J. Phys. D: Appl. Phys. 21(1988)311
/10/ Franklin R. N., Ockendon J. R., J.Plasma Phys.4(1970)371

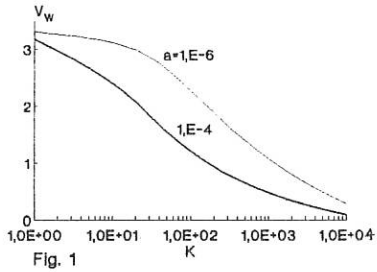

Fig. 1

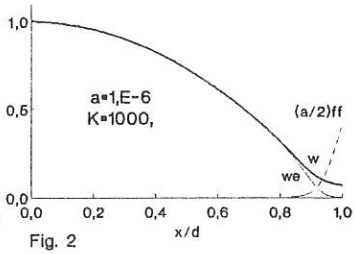

Fig. 2

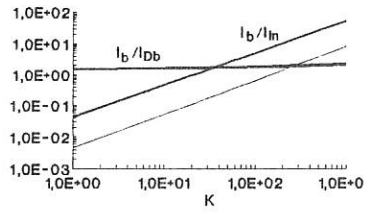

Fig. 3 — a=1,E-4 — 1,E-6

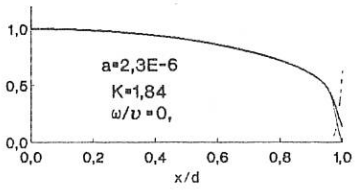

— w — we ····· (a/2)ff

Fig. 4

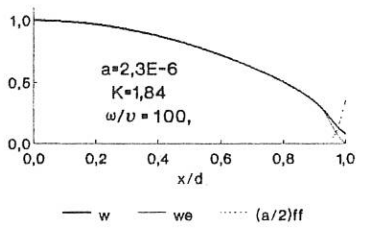

— w — we ····· (a/2)ff

Fig. 5

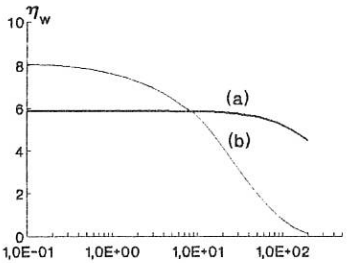

Fig. 6

THE GRAD-SHAFRANOV SHIFT CALCULATED ON THE BASIS OF MAGNETIC COMPRESSIVE AND TENSILE STRESSES

V.O. Jensen

Association Euratom-Risø National Laboratory
Optics and Fluid Dynamics Department
Risø National Laboratory
DK-4000 Roskilde, Denmark

Introduction

A magnetic field can be conceived as a medium where an isotropic compressive stress, $B^2/2\mu_o$, is superimposed on a tensile stress, B^2/μ_o, parallel to the field lines. When an ideal MHD plasma is present in the field, the particle pressure adds to the magnetic stresses to form a combined stress tensor. Based on this tensor it is easy to calculate plasma equilibria and to interpret the results. An extended analysis of magnetic stresses is presented and the equilibrium conditions for the screw pinch and the tokamak plasma are calculated. For the tokamak plasma with circular cross-sections the Grad-Shafranov shift is rederived.

The magnetic stress tensor

The magnetic stress tensor, T_m, is usually derived from the time independent equations of ideal MHD [1].

$$\mathbf{j}\times\mathbf{B} = \nabla p \tag{1}$$

and

$$\nabla\times\mathbf{B} = \mu_o\mathbf{j} \tag{2}$$

which together with $\nabla\cdot\mathbf{B} = 0$ can be written

$$\nabla p = -\nabla\frac{B^2}{2\mu_o} + \nabla\cdot\frac{\mathbf{BB}}{\mu_o} \equiv \nabla\cdot T_m \ . \tag{3}$$

The physical interpretation of Eq. (3) is that a differential volume element, dV, in a region with plasma and/or magnetic field is acted upon by a resulting force $d\mathbf{K} = (\nabla\cdot T_m - \nabla p)dV$. Therefore, Eq. (3) also shows that the ∇p-force in a magnetized plasma in equilibrium is balanced by an isotropic magnetic pressure, $B^2/2\mu_o$, and a tensile stress, B^2/μ_o, acting only along the lines of force.

For further examination of the tensile part of the magnetic stress tensor, $T_{m,t} = \mathbf{BB}/\mu_o$, we introduce a local system of coordinates with the $\hat{z}$-axis pointing along the line of force through the origin and with the yz-plane coinciding with the plane of osculation for this line. In this system we get for the tensile force on an element, dV, centred at the origin

$$d\mathbf{K}_{m,t} = \frac{dV}{\mu_o}\left(B_z\frac{\partial B_y}{\partial z}\hat{y} + B_z\frac{\partial B_z}{\partial z}\hat{z}\right). \tag{4}$$

The $\hat{y}$-component of Eq. (4) describes the force caused by the curvature of the field lines, while the $\hat{z}$-component represents the force resulting from a change of field

strength along the lines of force. The ŷ-component being perpendicular to the B-lines can also be written

$$d\mathbf{K}_{m,t,\perp} = -\frac{dV}{\mu_o}\frac{B^2}{R}\hat{\mathbf{R}}, \qquad (5)$$

where R is the radius of curvature of the field line, and $\hat{\mathbf{R}}$ a unit vector in the **R** direction. It is easy to show and useful to know that Eq. (5) is more generally valid, namely also in situations where B is the projection of the B-field line on any plane containing the radius of curvature and R is the radius of curvature of the field line projection on this plane.

To calculate the resulting force on a finite volume element, V, it is necessary to integrate the particle pressure p, the isotropic magnetic pressure, $B^2/2\mu_o$, and the magnetic tensile stress over the entire surface. Being isotropic p and $B^2/2\mu_o$ are easy, they both act perpendicularly to the surface. The magnetic tension acts with a tensile stress $B_\perp{}^2/\mu_o$ perpendicularly to the surface and with a magnetic shear stress $B_\parallel B_\perp/\mu_o$ parallel to the surface and in the $B_\parallel$-direction.

Remarks on the current-free vacuum field, the virial theorem

It is interesting to note that Eqs. (3)-(5) hold good also for cases without plasma, i.e. for $p = 0$. In this case the field is Laplacian, as also $\nabla \times B = 0$. For any volume element, differential or finite, in such a field the forces caused by the isotropic magnetic pressure $B^2/2\mu_o$ cancel those caused by the tensile stress BB/μ_o. As the sum of all the magnetic forces acting on any volume element is zero, such an element cannot absorb any forces. It can only transmit them and only to regions where $\mathbf{j} \neq 0$. This is another way to show the virial theorem which states that a plasma cannot be confined by the magnetic field generated by currents flowing only in the plasma region. Confinement can only be established when there are regions with currents outside the plasma to which the field can transmit the forces tending to expand the plasma.

Balance equation for linear pinches

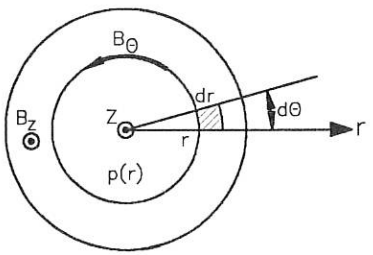

Fig. 1. Linear pinch

The balance equation relating p(r), $B_\Theta(r)$, and $B_z(r)$ for the linear pinches (Z-, Θ-, and screw pinches) is easily derived by using the concept of magnetic stresses. Using Eqs. (3), (4), and (5) on the element $rd\theta\, dr\, dz$ in Fig. 1 leads directly to the well-known equilibrium equation

$$\frac{d}{dr}p(r) + \frac{d}{dr}\left\{\frac{B_\theta(r)^2 + B_z(r)^2}{2\mu_o}\right\} + \frac{B_\theta(r)^2}{\mu_o r} = 0 \,. \qquad (6)$$

Based on the concept the interpretation is simple: the two first terms in Eq. (6) describe the outwards directed particle pressure and the magnetic pressure, respectively. The last term is caused by the tensile force of the bending B_Θ-lines.

The Grad-Shafranov shift in circular tokamak plasmas

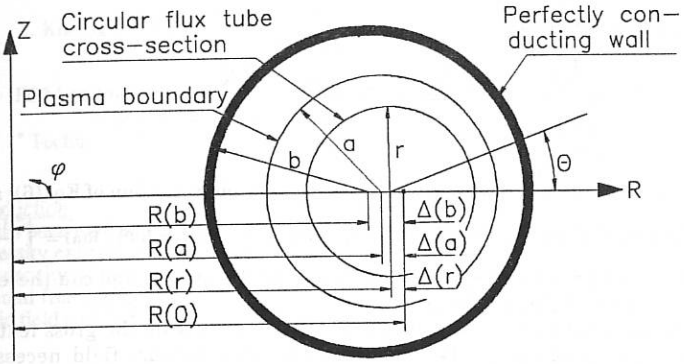

Fig. 2. Tokamak flux tubes with circular cross-sections

Consider a tokamak plasma with circular cross-sections of all flux tubes as shown in Fig. 2. The conducting wall has the minor radius b and the major radius R(b). The plasma minor radius is a and its major radius is R(a). r is the minor radius of a flux tube with the major radius R(r) where $0 \le r \le b$. R(0) is the major radius of the magnetic axis. The Grad-Shafranov shift $\Delta(r) = R(0) - R(r)$ is indicated for the three r-values b, a, and r. The three quantities varying with r and θ are designated $\tilde{p}(r)$, $\tilde{B}_t(r)$, and $\tilde{B}_p(r)$ for $\theta = \pm \pi/2$. Using $\nabla \cdot \mathbf{B} = 0$ and simple geometry (see Fig. 2) leads to

$$B_t(r,\theta) = \tilde{B}_t(r) \frac{R(r)}{R(r) + r\cos\theta} \tag{7}$$

$$B_p(r,\theta) = \tilde{B}_p(r) \frac{R(r)}{\left[R(r) + r\cos\theta\right]\left[1 - \frac{d\Delta(r)}{dr}\cos\theta\right]} \tag{8}$$

while

$$p(r,\theta) = \tilde{p}(r). \tag{9}$$

We consider a flux tube segment with minor radius r and expanding from $-\pi/2$ to $+\pi/2$ in the ϕ-direction. We introduce an $\hat{x}$-axis parallel to the **R**-axis for $\phi = 0$ and calculate the $\hat{x}$-component of all forces acting on the surface of the segment. To the lowest order in the inverse aspect ratio r/R(r) and in $d\Delta(r)/dr$ we find for the forces caused by the particle pressure

$$F_{p.p.}(r) = -2\pi \int_0^r \frac{dp(r')}{dr'} r'^2 dr' \, \hat{x}, \tag{10}$$

by the toroidal field

$$F_{B_t}(r) = \frac{\pi}{\mu_o}\int_o^r \frac{dB_t^2(r')}{dr'} r'^2 dr' \,\hat{x}\,, \tag{11}$$

and by the poloidal field

$$F_{B_p}(r) = \frac{\pi}{\mu_o}\left\{2B_p^2(r)r\left(r - R_o\frac{d\Delta(r)}{dr}\right) - \int_o^r \frac{dB_p^2(r')}{dr'} r'^2 dr'\right\}\hat{x}. \tag{12}$$

The balance condition

$$F_{pp} + F_{B_t} + F_{B_p} = 0 \tag{13}$$

combined with Eq. (6) (or what would be better a toroidal version of Eq. (6)) allow calculations of $d\Delta(r)/dr$ for all r. The internal shift, $\Delta_{int} = R(0) - R(a) = \int_o^a \frac{d\Delta(r)}{dr} dr$, depends on the profiles of p(r), $B_p(r)$, and $B_t(r)$ in the plasma and can therefore be calculated when these profiles are known.

The external shift, $\Delta_{ext} = R(a) - R(b)$, depends only on the gross features of the plasma as it describes the change in the outer vacuum field necessary to transmit the outward forces from the plasma to the wall. By introducing the standard quantities: the poloidal β

$$\beta_p = \frac{4\mu_o}{B_p(a)a^2}\int_o^a p(r')\, r'\, dr' \tag{14}$$

and the normalized internal inductance per unit length

$$l_i = \frac{2}{B_p(a)a^2}\int_o^a B_p^2(r')r'\, dr' \tag{15}$$

we find for the external Grad-Shafranov shift

$$\Delta_{ext} = \frac{b^2}{2R(0)}\left\{\left(\beta_p + \frac{l_i - 1}{2}\right)\left(1 - \frac{a^2}{b^2}\right) + \ln\frac{b}{a}\right\}. \tag{16}$$

This expression was first derived by Shafranov [2]. Now the same result or similar ones calculated by solving the Grad-Shafranov equation can be found in many textbooks, see e.g. [1]. The advantages of using the concept of magnetic stress are that it makes the calculations very simple and that the physical interpretation of the various terms is easily obtained by tracing the terms back through the derivations to Eqs. (7)-(9).

The concept of magnetic stress could also be used to calculate corrections to Eq. (16) caused by higher order effect in the inverse aspect ratio r/R(r). Also non-circular cross sections could be considered. They will be topics for future studies.

References

[1] Freidberg, J.P. Ideal Magnetohydrodynamics, Plenum Press, 1987.

[2] Shafranov, V.D. *In Reviews of Plasma Physics, Vol. II*, edited by M.A. Leontovich, Consultants Bureau, New York, 1966.

PROFILE CONSISTENCY AS A RESULT OF COUPLING BETWEEN THE RADIAL PROFILE FUNCTIONS OF PRESSURE AND CURRENT DENSITY

F.C. Schüller, D.C. Schram*,
J. Konings, A.C.A.P. van Lammeren, J.C.M. Timmermans, M. Verreck
and the RTP-team

FOM-Instituut voor Plasmafysica, Rijnhuizen, Association Euratom-FOM,
P.O. Box 1207, 3430 BE Nieuwegein, The Netherlands
* Technische Universiteit Eindhoven, P.O. Box 513, 5600 MB Eindhoven

1. Introduction.

It has been noticed since a long time [1] that in ohmic tokamak discharges a remarkable near-identity exists between the profile functions of the pressure p(r)/p(o) and of the toroidal current density j(r)/j(o). Kadomtsev [2] came to an explanation of this based on the principle of minimal free energy of the sum of plasma kinetic energy and the energy of the poloidal magnetic field and found:

$$\frac{p(r)}{p_o} = \frac{j(r)}{j_o} = \left\{1 + \frac{r^2}{a^2}\left(\frac{q_a}{q_o} - 1\right)\right\}^{-2} . \qquad (1)$$

Recently, Taylor [3] came to the same expression based on the hypothesis that the current is filamented on a fine scale. In this paper we will call this form of profile consistency the K-T model.

In order to test the K-T model, the consequences for the T_e-, n_e-, $p_e(r)$-profiles are compared with the experimental ones obtained from the RTP-tokamak during steady state and transient periods, caused by applying ECRH and ramping of the plasma current. For a general description of the RTP-results, see [4].

2. Steady state ohmic discharges.

In Eq. (1) the value q_o appears, which cannot yet be measured in RTP. However, the q=1 radius is in agreement with the empirical scaling found in nearly every tokamak (Arunasalam [5]):

$$r(q=1) \simeq a/q_a . \qquad (2)$$

Combining this with the K-T model, one finds:

$$q_o \simeq \frac{q_a}{q_a + 1} . \qquad (3)$$

This simplifies the expression (1) even further for stationary states:

$$j(r)/j_o = (1 + q_a r^2/a^2)^{-2} . \qquad (4)$$

Expression (4) is compared to experimental j-profiles found by Soltwisch [6]. The agreement is good (see Fig. 1), except for deviations caused by magnetic islands.

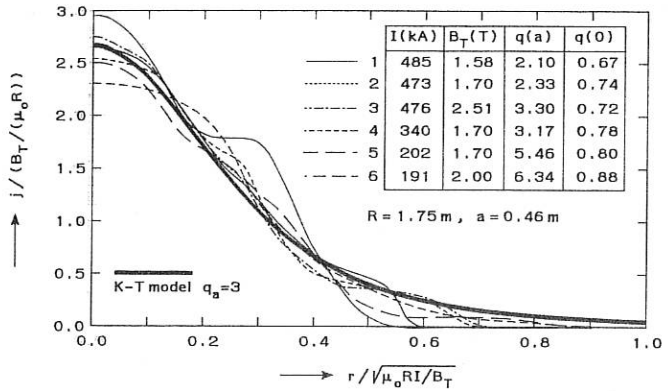

Fig. 1. Soltwisch experimental j-profiles [6], compared to the K-T model prediction.

Under the additional assumptions that corrections to Spitzer-resistivity are constant over the cross-section and that $p_i(r) \propto p_e(r)$, it is easy to predict the n_e-, T_e-, and p_e-profiles and their halfvalue radii

$$n_e(r) = n_{eo}\,(1+ q_a\, r^2/a^2)^{-2/3} \qquad r(n_{eo}/2) = 1.828\; a\; q_a^{-1/2} \tag{5a}$$

$$T_e(r) = T_{eo}\,(1+ q_a\, r^2/a^2)^{-4/3} \qquad r(T_{eo}/2) = 0.825\; a\; q_a^{-1/2} \tag{5b}$$

$$p_e(r) = p_{eo}\,(1+ q_a\, r^2/a^2)^{-2} \qquad r(p_{eo}/2) = 0.643\; a\; q_a^{-1/2}\;. \tag{5c}$$

The experimental halfvalue radii for stationary RTP-plasmas are compared with these predictions (Fig. 2). The agreement is satisfactory.

3. ECRH-heated plasmas at constant current.

RTP-plasmas heated with 180 kW ECRH show a very high and strongly peaked T_e-profile (T_{eo} = 650 → 2600 eV; $r(T_e/2)$ = 0.05 → 0.02 m). Simulation with magnetic diffusion codes indicate that the full re-adaptation of the j-profile to the new resistivity profile takes typically 200 ms i.e. longer than the applied ECRH pulse of 90 ms. Therefore, the stationary relations (4) and (5) are broken since $j(r) \neq T_e^{3/2}$. One has to go back to Eq. (1) and assume $j_{EC}(r) \simeq j_\Omega(r)$. Since, according to the K-T model $n(r) \propto j(r)/T(r)$, one expects a hollow n_{EC}-profile inside r = 3 cm radius and a broadened n_{EC}-profile outside with halfvalue radius increased by 2.5 cm. This is in excellent agreement with experimental $n_e(R)$-profile (Fig. 3).

4. Ohmic discharges with a ramped current.

Experiments were done with ohmic plasmas during which the plasma current was ramped up from 60 kA (q_a = 6.67) to 100 kA (q_a = 4.0) in 50 ms or ramped down from 100 kA to 60 kA (Fig. 4) and compared to a stationary plasma with I = 80 kA (q_a = 5.0). The density halfvalue radius follows the changing q_a-value as predicted by Eq. (5a), but delayed with about 10 ms, due to the finite skin current penetration.

5. EC-heated discharges with a ramped current.

The same current evolution waveforms have been used in these experiments as mentioned under Section 4, but now at elevated electron temperature because of 180 kW ECRH (T_{eo} = 700 → 1800 eV). The averaged skin penetration time increases with about a factor 4. The skin current penetration time at the edge becomes equal to the current ramp time and therefore the j-profile in the centre is nearly unchanged by the current ramps. Accordingly, $r(n_{eo}/2)$

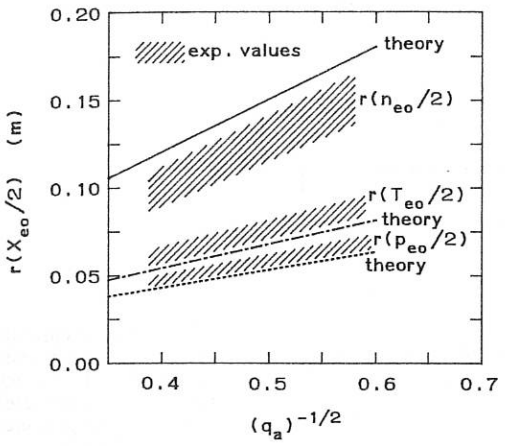

Fig. 2.
Experimental halfvalue radii for n_e-, T_e-, and p_e-profiles compared to the K-T model for a range: $3.0 < q_a < 7.0$ and $2 < n_{eo}$ (10^{19} m^{-3}) < 8.

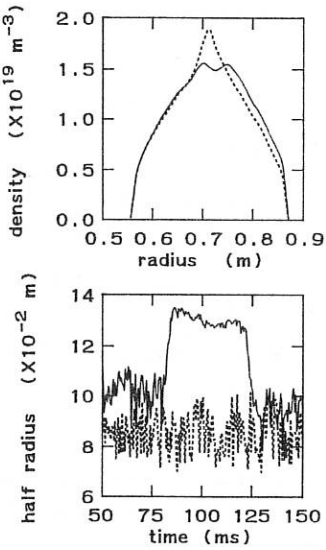

Fig. 3.
a. The density profile with ECRH (full time) and without (dotted line).
b. The density halfvalue radius as a function of time.

does not change very much. In Fig. 4c one can notice that the density halfvalue radius is increased immediately after switch-on of the ECRH, as explained in Section 3, but does not change very much during current ramp.

For these discharges the $T_e(R)$-evolution measured by superheterodyne e.c.e. was available. In Fig. 5, the $p_e(R)$-profiles calculated from measured $n_e(R)$ and $T_e(R)$ are shown for the case of a ramped-up current. The central 2 cm part is omitted since this falls into the EC-deposition profile, which presumably breaks the K-T model validity. Outside this radius the $p_e(r)$ follows the j(r)-profile: immediately after switch-on of the ECRH the pressure increases dramatically (curve 2) over the ohmic case (curve 1). After the current ramp-up (curve 3) the whole $p_e(r)$-profile appears to be lifted with a constant amount. The latter means a larger relative increase at the edge than in the centre as expected from the K-T model.

6. Conclusions.

All experimental observations made in RTP so far are in agreement with the K-T model even in transient situations where skin effects break the proportionality of $j \propto T^{3/2}$. The observed profile consistency, therefore, seems to be related to j- and p-profiles more than to a particular dependence of the transport coefficients on n and T. The density profile appears to be the quantity which adjust to maintain $p \propto j$.

Acknowledgement
This work was performed under the Euratom-FOM association agreement with financial support from NWO and Euratom.

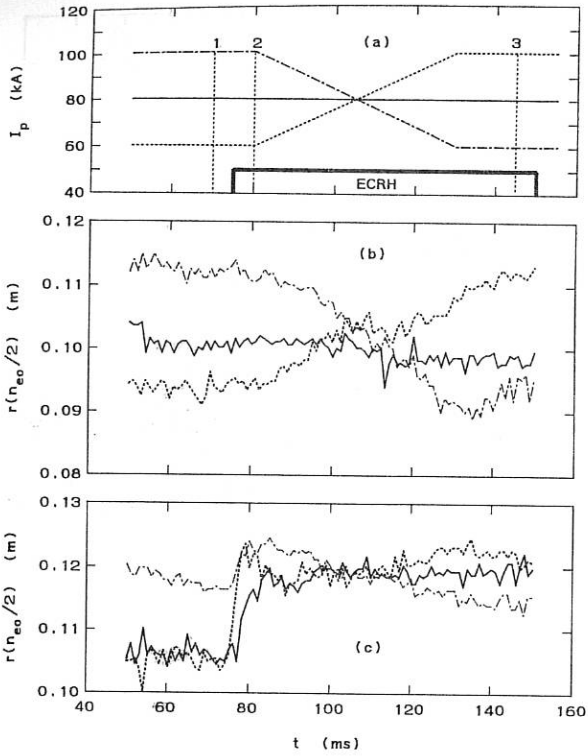

Fig. 4.
a. The plasma current ramps used with and without ECRH;
the vertical lines are referring to the pressure profiles of Fig. 5.
b. The resulting n_e halfvalue radii for ohmic discharges as a function of time. Line indicators are the same as in 4a.
c. As 4b with 180 kW ECRH.

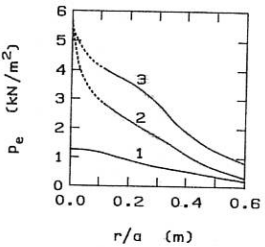

Fig. 5.
The electron pressure profiles obtained from multichannel e.c.e. and interferometry for the 3 time-points indicated in Fig. 4a.

References.
[1] D.C. Schram, F.C. Schüller, Physica **100C** (1980).371
[2] B.B. Kadomtsev, Phil. Trans. R. Soc. Lond. **A322** (1987).125-131
[3] B.J. Taylor, University of Texas, Report IFSR 447 (1990), Austin, Texas, USA.
[4] F.C. Schüller et al., this conference.
[5] V. Arunasalam et al., Nucl. Fusion **30** (1990) 2111.
[6] H. Soltwisch et al., Proc. 11th Conf. on Plasma Phys. and Contr. Nucl. Fusion Res., Kyoto (1986) Vol. 1, p. 263-273.

IMPURITY CONTROL BY THE RADIAL ELECTRIC FIELD IN A STOCHASTIC LAYER

F. Nguyen, A. Samain, Ph. Ghendrih.

Association EURATOM-CEA sur la fusion controlée
CEN Cadarache, F-13108 Saint-Paul-Lez-Durance Cédex, FRANCE.

Abstract

A decontaminating working régime of the ergodic divertor at low collisionality has been studied : the outwards radial electric field which appears in the laboratory frame when the ergodic divertor is energized, in conjunction with the magnetic ripples action on ions, can produce outwards flux of impurity ions $-Dn_Z(\partial n_Z/n_Z\partial r+Z\partial n_e/n_e\partial r)$. This contrasts with the neoclassical flux $-Dn_Z(\partial n_Z/n_Z\partial r-Z\partial n_H/n_H\partial r)$ which produces the deleterious accumulation of impurity ions in the n_H profile.

I Introduction

The ergodic divertor allows to apply resonant magnetic perturbations which destroy the magnetic surfaces at the edge. The magnetic field lines within that stochastic layer connect the confined plasma to the wall [1]. One expects from this arrangement the same basic effects as from the axisymmetric divertors, e.g. frictional decontamination of impurity ions by recycling hydrogen ions and accumulation of a low temperature high density plasma near the wall [2,3]. In this paper, our interest is focused on the possibility of impurity control by the ergodic divertor in a low collisionality régime. The frictional decontamination effects are then very weak. The only possible action on impurity ions is through the radial electric field. A radial electric field E_r appears indeed [4,5,6,7] in the frame where the ergodic perturbation is static, i.e. in the laboratory frame, to ensure the confinement of electrons in the stochastic layer : $E_r = (T_e/e)/(\partial n_e/n_e\partial r)$. This effect takes place as soon as the stochastic flux lines are connected to the wall because of the fast parallel motion of electrons along the field lines, even if the magnetic perturbation has pratically no direct effect on the ion transport. The basis of the effect we consider is that the ions tend to be extracted outwards by the radial electric field E_r.

Effective extraction necessitates however that the average motions of ions along θ, φ are hindered by resonant static electromagnetic perturbations. Then, the balance of the radial force $n_{ion}e_{ion}E_r$ by the Lorentz force due to average θ and φ motions results into θ and φ frictions forces, which in turn produce an outwards radial diffusion. We will study the effect of magnetic ripples $\delta B_{ripple}/B=b.\cos N\varphi$ acting together with the poloidal magnetic modulation $\delta B_{pol}/B=(r/R)\cos\theta$.

II Neoclassical fluxes in presence of the ergodic divertor

A very convenient presentation of the mecanism of ion diffusion is obtained by considering that each ion assembly exhibits average velocities v_θ, v_φ in the poloidal (θ) and toroidal (φ) directions, and that these velocities produce frictions $-f_\varphi v_\varphi$ and $-f_\theta v_\theta$ due to the magnetic pumping effects [9,10]. The calculation of the friction coefficients f_φ and f_θ is based on neoclassical theory. For each type of perturbation, taken alone, the friction force is effective in the kinetic régime : $k_{//}\lambda_{coll} > 1$ where λ_{coll} is the parallel mean free path and $k_{//}=1/qR$ for $\delta B_{pol}/B=(r/R)\cos\theta$ and $k_{//}=N/R$ for $\delta B_{ripple}/B=b\cos N\varphi$. The values of the coefficients k_θ and k_φ depend whether the perturbations $\delta B/B$ produce trapped particles or not [11]. Two different régimes of low collisionality are investigated. In the Landau régime (plateau régime as far as k_θ is concerned), $1<k_{//}\lambda_{coll}<(\delta B/B)^{3/2}$, one has :

$$k_\theta \text{ or } k_\varphi = \frac{n\sqrt{\pi}}{\left(\frac{1}{qR} \text{ or } \frac{N}{R}\right)} \frac{m^2}{4T}\left(\frac{r}{R} \text{ or } b\right)^2 v_{th}^3 \left(\frac{1}{r} \text{ or } \frac{N}{R}\right)^2$$

where m is the particle mass and v_{th} the thermal velocity $(2T/m)^{1/2}$. In the Zakharov-Karpman régime [8] (banana régime for k_θ), $(B/\delta B)^{3/2}< k_{//}\lambda_{coll}$, it comes

$$k_\theta \text{ or } k_\varphi = n\sqrt{\pi}\left(qR \text{ or } \frac{R}{N}\right)^2 \frac{m^2}{4T}\left(\frac{r}{R} \text{ or } b\right)^{\frac{1}{2}} v_{th}^2 \left(\frac{1}{r} \text{ or } \frac{N}{R}\right)^2 \frac{1}{\tau_{coll}}$$

where $1/\tau_{coll}=\langle(\Delta v_\perp)^2\rangle_{th} / v_{th}^2$ and $\langle(\Delta v_\perp)^2\rangle_{th}$ is the Spitzer coefficient for the considered species at the thermal velocity v_{th}. For both species, light ions (H) and impurity ions (Z), in the stochastic layer, the mechanical balance equations yield :

$$(1) \qquad n.e.(E+v\wedge B) - \nabla P + F = 0$$

where F represents the friction forces $-k_\theta v_\theta$, $-k_\varphi v_\varphi$ and the collisional forces along θ, φ between the two ions assemblies proportional to the differences $v_{\varphi,\theta H}-v_{\varphi,\theta Z}$. The radial

particle fluxes $\Gamma=nv_r$ arise to balance these friction forces. The set of equations (1) for H and Z ions along the radial, poloidal and toroidal directions allows to calculate the velocities v_θ, v_φ and the flux Γ for given density gradients $\partial n_{H,Z}/\partial r$ and a given electric field $E_r=(T_e/e)/(\partial n_e/n_e\partial r)$. In the limit of strong magnetic ripple, $k_\varphi(H)>>(B\theta^2/B_\varphi^2)k_\theta(H)$, we find that the static ergodic divertor perturbation leads to a radial impurity flux of the form :

$$(2)\quad \Gamma_Z = -Dn_Z[(\partial n_Z/n_Z\partial r)+Z(\partial n_e/n_e\partial r)] \qquad (D>0)$$

which creates an outwards accumulation of the Z ions outside the n_e profile. This result contrasts with the neoclassical flux :

$$(3)\qquad \Gamma_Z=-Dn_Z[(\partial n_Z/n_Z\partial r)-Z(\partial n_H/n_H\partial r)]$$

which produces the deletetrious concentration of impurities within the n_H profile.

III Discussion

The form (3) is a consequence of the friction effects between light ions and impurity ions which tend to set the two assemblies of ions in thermodynamical equilibrium in the same frame rotating around the major axis, and this, independently of the value of the radial electric field E_r. On the contrary, the form (2) reflects that all assemblies are in thermodynamical equilibrium, locked in the laboratory frame from, the ions by the magnetic ripple and the poloidal modulation, the electrons by the static magnetic perturbation of the ergodic divertor. The desired decontaminating régime (2) applies only at low collisionality. It appears from calculations that both assemblies H and Z must be in the plateau or banana régime. If the Z assembly is in the Pfirsch-Schlüter régime, one recovers the form (3), independently of the E_r value in the laboratory frame and of the magnetic ripples level. At very low collisionality, the Z ions may be trapped in the magnetic ripples and then experience a radial diffusion because of the vertical drift combined to the effect of collisions. In that case, the structure (2) applies.

Numerical application with typical Tore-Supra paramaters $n=10^{18}m^{-3}$, T=1 keV, b=0.1, B=4T shows that a flux of the form (2) occurs with $D\_0.1m^2.s^{-1}$ comparable to neoclassical values. In a steady state where the flux Γ_Z is balanced by a turbulent flux Γ_t of the form $\Gamma_t=-D_t(\partial n_z/\partial r)$, ones finds that $n_z=n_e^{-\alpha}$, $\alpha=Z(D/(D+D_t))$, implying that a significant decontamination effect only occurs across the layer for steep density gradients at the

edge and if $Z(D/(D+D_i)) > 1$. This contrasts of course with the neoclassical case (3) where one would have $n_Z = n_H^{+\alpha}$.

IV Conclusion

We have shown that a decontaminating régime of the ergodic divertor can also be expected at low collisionality. This effect is due to : the stochasticity of the layer and the ergodic connection to the wall create a radial electric field, directed outwards, in the laboratory frame (thermodynamical equilibrium of the electrons), a static resonant perturbation - we have considered the case of magnetic ripple -, by hindering the average ion motions along θ, φ then tends to expell the ions outside the n_e profile. One can expect that the electromagnetic perturbation induced directly by the ergodic divertor has a similar action on impurity transport. The study of this effect and of the corresponding decontamination level is in progress.

References

[1] F. NGUYEN, Ph. GHENDRIH, A. SAMAIN, J. Nucl. Mat. 176&177(1990)499

[2] A. SAMAIN, A. GROSMAN, T. BLENSKI, G. FUCHS, B. STEFFEN, J. Nucl. Mat. 128&129(1984)395.

[3] A. SAMAIN, T. BLENSKI, Ph. GHENDRIH, A. GROSMAN, Contr. Plasma Phys. 30(1990)157.

[4] W. FENEBERG, M.A. HELLBERG, Contr. Plasma Phys. 28(1988)329.

[5] X. GARBET, F. MOURGES, A. SAMAIN, Plasma Physics. and Contr. Fusion 30(1988)343.

[6] P.M. SCHOCH, S.C. McCOOL, A.J. WOOTTON, *et al.*, in Contr. Fus. and Plasma Heating (Proc. 15th EPS, Dubrownik 1988), 12B(1988)191.

[7] TORE-SUPRA Team, private communication.

[8] V.E. ZAKHAROV, V.I. KARPMAN, Sov. Phys. JETP 32(1963)351.

[9] R. DEI-CAS, A. SAMAIN in Plasma Physics and Contr. Nucl. Fus. Res. 1974, (Tokyo Conf.) IAEA, Vienna, 1(1975)563.

[10] E. CANOBBIO in Plasma Physics and Contr. Fusion Res., IAEA, Vienna, 3(1971)491.

[11] R.J. GOLDSTON, H.H. TOWNER, J. Plasma Phys. 26(1981)283.

NONLOCAL DIELECTRIC RESPONSE OF A TOROIDAL PLASMA

P.U. LAMALLE

Laboratoire de Physique des Plasmas - Laboratorium voor Plasmafysica
Association "Euratom-Etat belge" - Associatie "Euratom-Belgische Staat"
Ecole Royale Militaire - B1040 Brussels - Koninklijke Militaire School

Introduction

The high levels of auxiliary heating (RF, NBI or their combination) achieved in today's tokamak experiments and planned for reactor size machines produce distribution functions which are highly anisotropic and far from Maxwellian. Moreover, rotational transform and finite aspect ratio give rise to nonuniform particle guiding center (g.c.) motion and trapped orbits. We present a model of the conductivity tensor describing radio-frequency heating which takes these features into account. Linear wave theory is applied to a banana regime plasma within the drift orbit approximation. Wave frequency is assumed large with respect to the frequency of g.c. poloidal motion. For an initial exploitation, mode conversion physics is excluded with restriction to situations where $\omega \sim \omega_{ci}$ and $k_\perp \rho_L \ll 1$. Our focus is rather on the effects of finite transit time of ions through cyclotron resonance and nonuniform g.c. motion. Trapped particles are fully incorporated in the theory with account for tangent resonance interactions (i.e. Doppler-shifted wave-particle resonance layer quasi-tangent to g.c. trajectory).

The perturbed distribution function

Wherever no confusion arises, particle species index β is omitted. We adopt the ordering $\omega, \omega_c \gg \omega_b \gg 2\pi/\tau_{QL}$ (1), where ω is the RF field angular frequency, ω_c the cyclotron frequency, $\omega_b = 2\pi/\tau_b$ the g.c. poloidal bounce frequency, and τ_{QL} the characteristic evolution time of the equilibrium distribution f_0. In the whole paper, <...> means a trajectory time average over τ_b. All RF quantities are represented by complex amplitudes: $f(\mathbf{r},\mathbf{v})$, the perturbed distribution function; $\mathbf{E}(\mathbf{r})$ and $\mathbf{B}(\mathbf{r})$, the electromagnetic fields. Solving the linearized Vlasov equation by the method of characteristics yields the well known expression

$$f(\mathbf{r},\mathbf{v}) = -\frac{q}{m}\int_{-\infty}^{t} e^{-i\omega(t'-t)}(\mathbf{E}(\mathbf{r}')+\mathbf{v}'\wedge\mathbf{B}(\mathbf{r}')).\frac{\partial f_0}{\partial \mathbf{v}'}\,dt' \qquad (2),$$

where the integral is evaluated along the unperturbed particle orbit passing through $(\mathbf{r},\mathbf{v})$ at t'=t. In axisymmetric toroidal geometry and within the drift approximation, this orbit is best conveniently described by the set $\{P,\theta,v,x,\sigma,\alpha\}$. $P=\Psi - 2\pi R^2 m\,\dot{\varphi}/q_\beta$ is $-(2\pi/q_\beta)$ times the toroidal canonical momentum; it includes g.c.radial motion (e.g.finite banana width). Ψ is the poloidal flux function, θ the g.c. poloidal angle, α the gyrophase, σ the sign of $v_{//}$, all at time t. v is the (invariant) particle velocity , and x the dimensionless adiabatic invariant $x \equiv \mu B_a/(mv^2/2)$ (B_a: equilibrium induction on magnetic axis). G.c. toroidal (φ) motion, including banana drift, is expressed in terms of these variables. Larmor gyration around the g.c. is given by $\dot{\phi} = -\omega_c + v_{//}/\mathcal{T}$, $\phi(t'=t) = \alpha$, where $\mathcal{T}$ is the local torsion radius of the magnetic field line.

Restricting the discussion to equilibria independent of gyrophase $f_o=f_o(v,x,\sigma,P)$ (3) [9], we define a reference magnetic surface $\Psi_*=P+<2\pi m R^2\dot{\varphi}/q_\beta>$ and the equilibrium coefficients

$$Ng_{o\perp}=\frac{1}{v}\frac{\partial f_o}{\partial v}+2x\left(\frac{1}{v_\perp^2}-\frac{1}{v^2}\right)\frac{\partial f_o}{\partial x},\quad Ng_{//}=\frac{1}{v}\frac{\partial f_o}{\partial v}-\frac{2x}{v^2}\frac{\partial f_o}{\partial x}+\frac{\gamma}{v_{//}}\frac{\partial f_o}{\partial P},\quad Ncg_{1\perp}=\frac{2xv_{//}}{v_\perp^2}\frac{\partial f_o}{\partial x}-\gamma\frac{\partial f_o}{\partial P}\qquad (4),$$

$\gamma\equiv\dfrac{\partial P}{\partial v_{//}}$, and $N=N(\Psi_*)$ is the average density on the reference magnetic surface.

Eq.(2)becomes $$f=-\frac{Nq}{m}\int_{-\infty}^{t}e^{-i\omega(t'-t)}\{\frac{v_\perp}{\sqrt{2}}e^{\mp i\phi}(g_{0\perp}E_\pm\pm ig_{1\perp}cB_\pm)+v_{//}g_{//}E_{//}\}\,dt'\qquad (5)$$

The fields have been decomposed in polarized +(left hand),-,// components relative to the local $\mathbf{B}_o$. At this stage, they are still evaluated at particle position, all other quantities being expressed in terms of the g.c. variables (e.g. $v_\perp=v\sqrt{x\,B/B_a}$, $v_{//}=\sigma v\sqrt{1-x\,B/B_a}$, $B=|\mathbf{B}_o|$). Superposed signs are used for conciseness, and mean a sum of the two alternative terms (e.g. $a_\pm b_\mp \equiv a_+b_-+a_-b_+$).

Equation (5) includes 3 sources of spatial nonlocality :

-finite Larmor radius ρ_L effects around g.c., which can be treated by the usual $\perp$ expansion of the fields and operator methods. This is potsponed to future work, and in what follows the RF fields are evaluated at g.c.;

-g.c.radial excursions (for bananas, $\sim\rho_{L\theta}$, the poloidal Larmor radius);

-g.c.poloidal motion due to rotational transform.

The integral extends to time scales $>\tau_{QL}$, where collisions and heating ensure wave-particle phase decorrelation [5,6]. This process can be accounted for by introduction of an attenuation factor $\kappa(t-t')$ in the integrand ($\kappa(o)=1$, $\kappa(\infty)=o$; κ can also depend on constants of the motion).

The simple model $\kappa(\tau)=e^{-\nu(v)\tau}$ (6) is equivalent to the usual handling of causality by inclusion of an imaginary part $i\nu(v)$ in ω. More realistic models as $\kappa(\tau)=e^{-(\tau/t_L)^3}$ (6'), based on results of e.g. ref.[5], improve the theory at lower energies.

Axisymmetry allows to study single toroidal modes $(f,\mathbf{E},\mathbf{B})=(f_n,\mathbf{E}_n,\mathbf{B}_n)e^{in\varphi}$ independently. From here on, we shall omit the mode index n wherever unambiguous. Defining the phase function $$\psi_L(t)\equiv\int_o^t(\omega-L(\omega_c-\frac{v_{//}}{\mathcal{J}})-n\dot{\varphi})dt'\qquad (7),$$ where L is the cyclotron harmonic number,

$H_0(\mathbf{E})\equiv v_{//}g_{//}E_{//}$ and $H_{\pm1}(\mathbf{E})\equiv\frac{v_\perp}{\sqrt{2}}(g_{0\perp}E_\pm\pm i\,g_{1\perp}cB_\pm)$ (8), we take advantage of the g.c. motion periodicity in the poloidal plane: in eq.(5), $\mathbf{E}_n,\mathbf{B}_n$ and equilibrium coefficients vary with the same period τ_b. $\psi_L(t)$, integral of a periodic function, can be split into a periodic and a secular part $<\dot{\psi}_L>t$. The general orbit integral is then reduced to the Fourier series

$$f=-\frac{Nq}{m}\sum_{L=0,\pm1}\sum_{l=-\infty,\infty}\{K(il\omega_b-i<\dot{\psi}_L>)e^{i[\Pi_L(t)+L\alpha]}<H_L(\mathbf{E})e^{-i\Pi_L(t)}>\}\qquad (9),\quad \text{where}$$

$\Pi_L(t)\equiv\psi_L(t)-<\dot{\psi}_L>t+l\omega_b t$ (10) and the integrand of last <...> is periodic.

$$f = -\frac{Nq}{m}\sum_{L=0,\pm1}\sum_{l=-\infty,\infty}\{\ K(il\omega_b - i\langle\dot{\psi}_L\rangle)\, e^{il[\Pi_L(t)+L\alpha]}\langle H_L(E)\, e^{-il\Pi_L(t)}\rangle\ \} \qquad (9),$$ where

$\Pi_L(t) \equiv \psi_L(t) - \langle\dot{\psi}_L\rangle t + l\omega_b t$ (10) and the integrand of last <...> is periodic.

K(s) is the Laplace transform of the attenuation function $\kappa(t)$. In the simple collision model eq.(6), $K(il\omega_b - i\langle\dot{\psi}_L\rangle) = i/(\langle\dot{\psi}_L\rangle - l\omega_b)$ (10) generalizes the usual resonant denominator of homogenous plasma theory; with model eq.(6'), $K(s) = \pi\, 3^{-1/3}\, t_l\, Hi(-3^{-1/3}\, t_l\, s)$ (10').

Eqs.(7-10) express the general RF perturbation of the distribution function in tokamak geometry, including Landau and fundamental cyclotron interactions.

The RF conductivity tensor

Eq.(9) directly yields the R.F. current and conductivity tensor:

$\mathbf{j}\{\mathbf{E}\} \equiv \sigma.\mathbf{E} = \sum_\beta q_\beta \int f_\beta\, \mathbf{v}\, d\mathbf{v}$ (11). However, we rather concentrate on the global quantity

$\mathcal{W}_{FE\beta} = \frac{1}{2}\int_V \mathbf{F}^*.\mathbf{j}_\beta\{\mathbf{E}\}\, d\mathbf{r}$ (12), V being the whole plasma volume, and **F** a general electric-like vector field. Indeed, $\mathcal{W}_{FE\beta}$ includes all information on the plasma R.F. response: $\mathcal{W}_{EE\beta} = P_\beta - iQ_\beta$ is the total (active-i*reactive) power absorbed by species β; choosing suitable δ-functions for **F** yields back $\mathbf{j}\{\mathbf{E}\}$ and power deposition on flux surfaces; finally, once discretized, $\mathcal{W}_{FE}$ is also a direct input to finite element wave codes.

Transforming to g.c. coordinates, integrating over toroidal angle and gyrophase, separating contributions from passing and trapped particles, parametrizing poloidal angle integrals as g.c. time ones, and summing over σ for trapped particles, our main result follows:

$$\mathcal{W}_{FE\beta} = -\frac{i\pi\varepsilon_0}{2}\int_0^{\Psi_e}\frac{dP}{B_a}\,\omega_p^2\int_0^\infty dv\, v^3 \sum_{pass.,tr.}\left\{\begin{array}{l}\sum_{\sigma=\pm1}^{(pass.)}\\ \text{no sum (tr.)}\end{array}\right\}\int_{x_1}^{x_2} dx\,\tau_b \sum_{L=0,\pm1}\sum_{l=-\infty}^{\infty}\{$$

$$-i\,K(il\omega_b - i\langle\dot{\psi}_L\rangle)\ \langle G_L^*(F)e^{il\Pi_L(t)}\rangle\,.\,\langle H_L(E)e^{-il\Pi_L(t')}\rangle\ \} \qquad (13),$$

$G_0(F) \equiv v_{//}F_{//}$ and $G_{\pm1}(F) \equiv \frac{v_\perp}{\sqrt{2}}F_\pm$ (14);

For passing particles, $x_1 = 0$, $x_2 = B_a/B_{max}(P)$; for trapped particles, $x_1 = B_a/B_{max}(P)$, $x_2 = B_a/B_{min}(P)$.

-When f_0 is isotropic and the g.c. radial motion is negligible or the equilibrium homogenous, eq.(13) reduces to

$$\mathcal{W}_{FE\beta} = -\frac{i\pi\varepsilon_0}{2}\int_0^{\Psi_e}\frac{dP}{B_a}\,\omega_p^2\int_0^\infty dv\, v^2\frac{\partial f_0}{\partial v}\sum_{pass.,tr.}\left\{\begin{array}{l}\sum_{\sigma=\pm1}^{(pass.)}\\ \text{no sum (tr.)}\end{array}\right\}\int_{x_1}^{x_2} dx\,\tau_b \sum_{L=0,\pm1}\sum_{l=-\infty}^{\infty}\{$$

$$-i\,K(il\omega_b - i\langle\dot{\psi}_L\rangle)\ \langle G_L^*(F)e^{il\Pi_L(t)}\rangle\,.\,\langle G_L(E)e^{-il\Pi_L(t')}\rangle\ \} \qquad (15)$$

and P_β is positive definite when $\partial f_{0\beta}/\partial v \le 0$ for all v, in agreement with [1].

-In the homogenous limit (uniform g.c. motion: at magnetic axis, or in a cylinder), the series of poloidal bounce harmonics l reduces to a series of independent contributions from field poloidal modes $e^{il\theta}$. Velocity space integration then yields the usual plasma dispersion function [7].
-Global power absorption P= Re $\mathfrak{W}_{EE}$ is in general not positive definite due to equilibrium anisotropy ($g_{1\perp}\neq 0$), tails ($g_{0\perp}>0$), or radial inhomogeneity ($g_{1\perp}\neq 0$, $g_{//}$ may be>0).

The bounce integrals

Eq.(13) requires to evaluate Fourier integrals on one bounce. The arbitrary fields are expanded in poloidal harmonics $e^{im\theta}$, and this dependence included in the phase Π_L. Under the basic ordering (1)(L=±1 terms) or in the case $k_{//}v_{//}\sim\omega$ (L=0 term, significant Cerenkov interaction), $\Delta\Pi>>2\pi$ on one bounce. The remainder of the integrand varies on time scale τ_b, and stationary phase points(s.p.) contributions give highly accurate asymptotic expansions. As third order s.p. are of special interest to the study of tangent resonance ($\ddot{\Pi}=0$: extrema in B, vicinity of banana tip), we use a uniform expansion valid for quadratic+cubic phase [8]:

$$I\sim \sum_j e^{-i\Pi}\,\Lambda(\ddot{\Pi},\dddot{\Pi}\ldots)\Big|_{s.p.j} \qquad (16)$$

All fast variations lie now in the phase factor. Λ is regular at $\ddot{\Pi}=0$ and is simply expressed in terms of the exponentially scaled Airy function and its derivative.

In quasi-homogenous situations (for L=±1, in the tiny region $\rho\leq R_0\,\omega_b/\omega_c$; for L=0, cases where $k_{//}v_{//}\sim$ const.), or for very well trapped orbits, a Bessel expansion of the phase factor is more appropriate than eq.(16).

Conclusions

Under natural assumptions, expressions have been obtained for the R.F. conductivity tensor and power absorption operators of a toroidal plasma with arbitrary poloidal cross section and rotational transform. As these quantities pick up contributions from individual guiding center orbits, they are valid for quite general equilibria (e.g. all solutions of the bounce averaged Fokker-Planck equation). They allow a self-consistent study of wave propagation and absorption in auxiliary heated tokamaks. Striking differences with straight B_0 models are finite ion cyclotron resonance crossing time, trapped particle effects and tangent resonance phenomena. Collision-limited nonlocality is induced by rotational transform over magnetic surfaces, and radially by drift effects.

Asymptotic methods allow practical use of this theory; its quantitative investigation and its implementation in a full wave code are under way.

Acknowledgements

I sincerely thank Drs. D.W.Faulconer and R.Koch for numerous fruitful discussions, and Dr. R.R.Weynants for a stimulating remark.

References

[1] D.N.Smithe, Plasma Phys. Contr. Fusion 31 (7), 1989.
[2] D.W.Faulconer, Plasma Phys. Contr. Fusion 29, p.433, 1987.
[3] V.S.Belikov, Ya.I.Kolesnichenko, Plasma Physics 24 (1), 1982.
[4] N.I. Grishanov, F.N.Nekrasov, Fizika Plasmy 16, 1990.
[5] S.V.Kasilov, A.I.Pyatak, K.N.Stepanov, Nuclear Fusion 30 (12), 1990.
[6] A.Bécoulet, D.J.Gambier, A.Samain, Phys.Fluids 3 (1),1991.
[7] M.Brambilla, Plasma Phys. Contr.Fusion 31 (5), 1989.
[8] R.B.Dingle,"Asymptotic expansions: their derivation and interpretation", Academic Press, 1973.
[9] F.L.Hinton, R.D.Hazeltine, Reviews of Modern Physics, 48 (2), 1976.

STATE DIAGRAMS OF TOKAMAKS AND SCALING LAWS

E. Minardi

Istituto di Fisica del Plasma, Assoc. EUR-ENEA-CNR
Via Bassini 15, 20133 Milano, Italy

Abstract The scaling of the confinement time of auxiliary heated tokamaks with respect to toroidal magnetic field, current and auxiliary power, is derived from the condition of vanishing production of the magnetic entropy.

The axial current density profiles $j(r)$ of a cylindrical tokamak with vanishing entropy production (according to the configurational magnetic entropy introduced in previous work (Minardi, 1990)) satisfy the equation

$$\nabla^2 j + \mu^2 j = - \mu^2 p_A/E \qquad (1)$$

where p_A is the auxiliary power density, E is the axial electric field and μ is a parameter which labels the states with constant entropy. When (1) is solved in the confinement region $\lambda s \leq r \leq s$, taking p_A as uniform for simplicity, and the boundary values $j_s=j(s)$, $\hat{j}=j(\lambda s)$, $q_s=q(s)$, $\hat{q}=(\lambda s)=1$, one finds a relation of the form (see Minardi, 1988, eq. (3.5))

$$L(q_s,\ \lambda,\ p_A/E\hat{j},\ \mu s,\ j_s/\hat{j}) = 0 \qquad (2)$$

between the discharge parameters of the isoentropic states. We shall take a (time averaged) flat profile for $j(r)$ in the sawtooth zone $r \leq \lambda s$ so that $\hat{j}=cB/2\pi R$ (in view of $\hat{q}=1$). Assuming in addition the ohmic relaxation $j \propto ET^{3/2}$, one obtains, from the compatibility of (1) with the energy balance in a one-fluid model, the following conditions

$$n(r)\chi(r) = F\ \hat{T}^m\ (T(r)/\hat{T})^{1/2}, \quad \mu^2 \propto E^{(5+2m)/3}\ B^{(1-2m)/3}\ F^{-1} \qquad (3)$$

where $\hat{T}=T(s\lambda)$; F is assumed as independent of current, temperature and auxiliary power and m is arbitrary at present. Also we have supposed that the losses are due only to the thermal diffusivity χ. Combining the relations above one obtains the following scaling of the confinement time

$$\tau \propto \chi^{-1} \propto B^{-4m/(5+2m)} F^{-5/(5+2m)} \mu^{4m/(5+2m)} \qquad (4)$$

where μ depends on the discharge parameters through the state equation (2). In order to specify further the scaling of τ let us consider a transformation $\vec{B} \to k\vec{B}$ of the magnetic field which implies, through Ampère law, a transformation $j \to kj$ of the current density. We consider that the electric field and the density are invariant with respect to this transformation because E, n and B can be independently controlled externally. Assuming that the parameter μ is also invariant one has from Ohm's law and from (3) that $\mu \propto E^{(5+2m)/6}$, $T \to Tk^{2/3}$ and $F \to Fk^{(1-2m)/3}$. Then μ depends only on E, while χ depends on B through F. One has $F \propto B^{-1}$ for m=2 and $F \propto B^{-2/3}$ for m = 3/2. We note that when the density is forced to transform as $k^{4/3}$ one has the "dimensionally similar" transformation preserving β and collisionality considered recently by Waltz et al. (1990). The symmetry above is broken when the parameters are constrained by the state law (2), that is to say when they are related by isoentropic transformations. It is this symmetry breaking which is the source of the Goldston scaling, as we shall see. Indeed, under the transformation above, τ, according to (4), transforms as follows

$$\tau \to k^{-1/3} \tau \propto B^{-1/3} \mu^{4m/(5+2m)} \qquad (5)$$

but μ is related to the other parameters by the isoentropic law (2). In order to discuss the constraints imposed by this law in physical terms it is convenient to rewrite it in terms of the variable

$X = p_A(\mu s)^{6/(5+2m)}/\hat{j}E$ which is proportional to p_A/B in view of the relation above between μ and E and of $\hat{j} \propto B$. Then (2) can be written as $L(q_s, \lambda, p_A/B, \mu s, j_s/\hat{j}) = 0$. Considering this equation, one should keep in mind that it expresses a relation between externally controllable quantities and the parameters of the plasma. As already observed B and E (or, which is the same, B and μs) are independent variables, as well as B and p_A. The state law establishes, for instance, a relationship between B and λ at constant E or, in a case with constant current I(s), between E (or μs) and p_A (because p_A influences the resistivity and then E through the energy balance and the temperature in a ohmically relaxed plasma). The following cases are physically interesting:

Scaling of τ with B and p_A. (I, $j_s/\hat{j}$ fixed) By changing B with fixed μ (or E) and $p_A = 0$ one follows the trajectories in (q_s, λ) space described in fig. 1. It is a general property of the state law (2) that these trajectories are essentially independent of $X \propto p_A/B$ and hold also for $p_A \neq 0$. Along these trajectories τ varies as $B^{-1/3}$. If then one applies the auxiliary power at a fixed point (q_s, λ, $j_s/\hat{j}$) of a trajectory, one obtains the trajectory of fig. 2 (where m=3/2) in (p_A/B, μs) space. As can be numerically verified this trajectory is practically independent of the

values taken by q_s, λ and $j_s/\hat{j}$ along the trajectories of fig. 1 and can be represented for $X > 0.50$, by the power law

$$(\mu s)^{4m/(5+2m)} \propto (B/p_A)^{\alpha} \qquad (6)$$

where α increases slowly with m. For $3/2 \leq m \leq 2$ one has $0.50 < \alpha < 0.60$. Thus, independently of the point (q_s, λ, $j_s/\hat{j}$), τ scales as follows:

$$\tau = \tau_o \, (B_o/B)^{1/3} \, (\mu/\mu_o)^{4m/(5+2m)} \propto B^{\alpha-1/3} \, p_A^{-\alpha} \qquad (7)$$

For $\alpha = 0.50$ one has $\tau \propto B^{1/6} \, p_A^{-0.50}$, practically independent of B.

Scaling of τ with I and p_A. (B, $j_s/\hat{j}$ fixed) First one changes the current along a trajectory (q_s, μs) with B fixed and $p_A=0$ and then one applies the auxiliary power following a trajectory in (p_A/B, μs) space with q_s fixed. As we know from previuos work (1990) τ scales as follows

$$\tau = \tau_o \, (\mu/\mu_o)^{4m/(5+2m)} \propto I^{\beta} \, p_A^{-\alpha} \qquad (8)$$

where $\beta \sim 1$ and $\alpha \sim 0.5$. Alternatively one can reach the same final state as above by following initially the path (q_s,λ) of fig. 1, with given electric field and $p_A=0$. Along this path τ does not depend on the current because μ is fixed (see (5)). We observe that this path should be favoured in the ohmic case because it can be followed without further consumption of Volt-sec. At the end of the path the auxiliary power is applied in a situation in which q_s is low and λ is large. The system is then susceptible to move along the trajectories of fig. 3 which involve a rapid reduction of the sawtooth zone when p_A increases at low q with constant E. The final point is then reached with a transformation in (p_A/B, μs) space which implies a decreasing electric field when p_A increases.

In conclusion the constraints on the parameters imposed by the isoentropic state law allow the interpretation of the scaling of the confinement time of auxiliary heated tokamaks with respect to B, I and p_A. However, the vanishing of the entropy production is violated in many cases, for instance in the H-transition. In these cases the scaling of the confinement time may be different.

Minardi, E. and Lampis, G. (1990) Plasma Phys. Contr. Fusion 32, 891.
Minardi, E. (1988) Plasma Phys. Contr. Fusion 30, 1701.
Waltz, R.E., De Boo, J.C., Rosenbluth, M.N. (1990) Phys. Rev. Lett. 65, 2390.

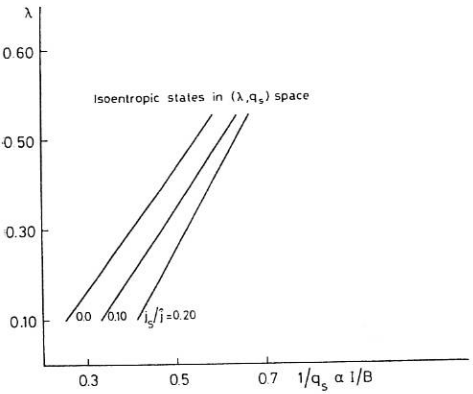

Fig. 1

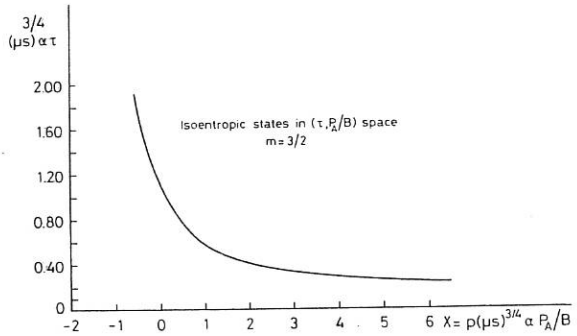

Fig. 2

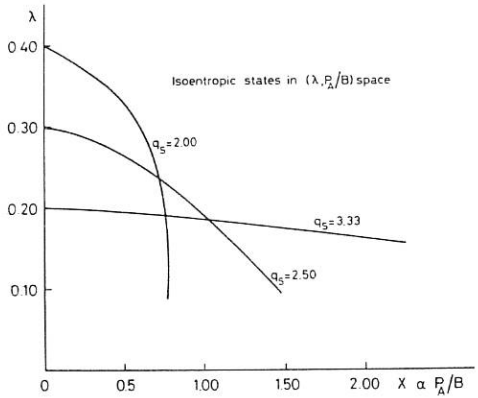

Fig. 3

NEOCLASSICAL POLOIDAL FLOW BIFURCATION IN THE H MODE TRANSITION

E.Lazzaro, F.Lucca,C.Nardone*,A.Tanga*

Istituto di Fisica del Plasma, Associazione EURATOM- ENEA-CNR, via Bassini 15, 20133 Milano, Italy

Introduction

The sudden onset of mass poloidal rotation at the L to H mode transition observed in tokamaks operating with divertor configurations and intense auxiliary heating [1], is a manifestation of nonlinear behaviour in the parallel momentum balance equation. In normal conditions a poloidal rotation of the plasma is inhibited, or damped on an ion-ion collision time, by the parallel viscous force which, according to conventional neoclassical theory depends linearly on the poloidal particles and heat flows [2]. Attempts to account for the observations have relied on particular models for the external torque input, assumed mainly to be due to ion orbit losses, and on the derivation of nonlinear expressions of the parallel viscous stress for high (sonic) poloidal velocities [3]. This and other models tend to predict far too high rotation velocity and cannot relate the transition to a power threshold in agreement with observations.

Given the variety of methods of supply of external power which causes the onset of rotation we reconsider more generally the mechanism of the poloidal spin up of the plasma within the frame of standard neoclassical theory in the moments approach, with an external power and momentum source [2]. The model proposed is based on the coupled set of equations governing the parallel momentum balance and the global power balance, with the generalised neoclassical Ohm's law. We simply assume that in the generality of cases the effective torque driving plasma rotation must be constrained by a relation to the total externally supplied power.

The tenets of the model rely on the neoclassical result stating that the cross field heat flux q^{Ψ} and the particle flux Γ^{Ψ} are linearly related to parallel viscous forces $< \mathbf{B}\cdot\nabla\cdot\Pi >$ and therefore to poloidal flows. We can show that with a power balance constraint the equation for poloidal rotation can have bifurcated solutions, when a power threshold is overcome.The model depends on two control parameters, the total power and the edge pressure gradient, and is applicable to the conditions on these parameters occurring at the L - H transition.

Equations of the model

We adopt substantially the standard notation of [3] and consider a pure (Z=1) plasma of electrons and deuterons. To leading order in the Larmor radius expansion parameter the equation for the surface averaged (ion) mass poloidal rotation velocity in a a narrow layer at the plasma edge is:

$$m_i n \frac{dU_p}{dt} + \frac{B_\theta}{B^2}\langle B \cdot \nabla \cdot \Pi_i \rangle = \frac{B_\theta}{B^2}\langle G_{ext} B \rangle$$

The power balance equation in thermal steady state is:

$$\frac{1}{V'}\frac{\partial}{\partial \psi}\left[V'\left(q^\psi + \frac{5p}{2n}\Gamma^\psi \right)\right] = \langle JE \rangle + P_{abs}$$

And the neoclassical Ohmic power term is :

$$\langle E \cdot J \rangle \cong \sigma_{nc} E_{//}^2 + \frac{3g}{1+3g} c E_{//} R \left| \frac{dp}{d\psi} \right| + \frac{3g}{1+3g} \frac{B}{B_\theta} E_{//} e n U_p$$

where $g \sim (2\varepsilon)^{1/2}/(1-(2\varepsilon)^{1/2})$ is the ratio of trapped and circulating particles. Note that at the edge <EJ> is dominated by the bootstrap term contribution.

Now we use the neoclassical expressions of the cross field fluxes and of the viscous tensor [2] to express, from the LHS side of the power balance equation, an explicit constraint on the absorbed power in terms of the poloidal flow velocity:

$$P_{abs} \cong -\langle EJ \rangle + 0.8 \nu_i m_i n g \frac{cRT}{eB_\theta} \left| \frac{d}{d\psi} \ln\left(\frac{V R B_\varphi T}{\langle B^2 \rangle} \right) \right| U_p$$

Multiplying the momentum equation by Up, passing to the dimensionless variable $x=U_p/c_s$, and combining the expressions for P_{abs}, <EJ>, to express $\langle G_{ext} U_p \rangle = f P_{abs}$, with $f<1$, the following equation for the "poloidal kinetic energy" is obtained:

$$\frac{dx^2}{d\tau} = -[\mu_{i1} + 0.7\mu_{i2}]x^2 + (P - Q_1)x - Q_2$$

$$\text{with} \qquad Px = f\frac{B_\theta}{B}\frac{P_{abs} + \langle EJ \rangle}{\nu_i m_i n c_s^2}$$

$$Q_2 + Q_1 x = f\frac{B_\theta}{B}\frac{\langle EJ \rangle}{\nu_i m_i n c_s^2}.$$

This equation exhibits bifurcations and has the analytic solution:

$$\tau = \frac{2}{\gamma - 1} \ln \frac{|x - x_1|}{|x - x_2|^\gamma} \; ; \; \gamma = x_1/x_2 \; ; \; x_{1,2} \text{ roots of the rhs of the equation .}$$

Considering now for the temporal evolution of the kinetic energy a "potential" function F in the x>0 variable, i.e.

$$F(x) = \frac{T}{3}x^3 - \frac{(P - Q_1)}{2}x^2 + Q_2 x$$

the stationary states are located at the relative minimum and maximum of the function F. This function depends on the two control parameters P (external power), and Q_2 (edge gradient) which at the L-H transition are assumed to be positive and sufficiently large. In normal undriven

conditions Q_2 is zero and the standard neoclassical result is recovered, with a minimum of F at $|x|=0$, as shown in Fig.1. Fig. 2, 3 show the function F versus the dimensionless velocity $|x|$, using data from JET L and H modes. In undercritical driven condition (P>0), with $Q_2=0$ the "L mode" has a stable minimum close to x=0 (Fig.2). When a power threshold is overcome, and the condition $Q_2>0$ is established, the external driving term (linear in x because of the neoclassical transport constraint) overcomes the viscous drag term proportional to x^2 leading to a bifurcation instability. Fig.3, relative to H mode transition, shows that the solution around zero becomes unstable while a stable solution appears at higher velocity. The transition from the lower (unstable) rotation regime to the higher one occurs in a few ion collision times as shown in Fig.4 which gives the time dependence of x. The power threshold is increasing with the magnetic field but only as $B^{1/2}$. For fixed power, the threshold can be expressed as a necessary condition on the temperature edge gradient, which must have a scale length related to the ion banana width:

$$\left|\frac{d\ln T}{dr}\right| \geq \frac{2.7\pi}{f(1+3.02g)} \frac{eV_{loop}}{\nu_i m_i v_{th_i} qR} \left(\frac{\varepsilon}{\rho_{\theta_i}}\right)$$

The bifurcation is indeed due to the bootstrap current contribution to the ohmic power term; if he auxiliary power steepens the edge pressure gradient this term provides an additional drag which tends to limit the poloidal rotation but the lower velocity is unstable and a flip to high rotation occurs. The resulting high shear in rotation contributes to quash microturbulence and therefore enhance by a factor (but not in scaling) the confinement time.

*A.T, C.N. present address : JET joint Undertaking, Abigdon OX143EA, UK

Figure captions:

Fig.1- Unforced case. Potential of viscous and active forces vs poloidal velocity.
$Q_1=0.13$ P=0.13 $Q_2=0.0$ T=5.

Fig.2 -L mode. Potential of viscous and active forces vs poloidal velocity.
$Q_1=-0.15$ P=0.47 $Q_2=0.02$ T=5. Shot 20354.

Fig.3 -H mode. Potential of viscous and active forces vs poloidal velocity.
$Q_1=-0.13$ P=1.49 $Q_2=0.02$ T=5.00

Fig.4 - Normalized poloidal velocity U_p/C_s vs dimensionless time $\tau=\nu_i t$

References

[1]J.L.Luxon et al. Plasma Physics and Contr. Fusion, Nucl.Fus. **32** (1990) 1083.
[2]S.Hirshman,D.J.Sigmar Nucl.Fus. **21** (1981) 1079.
[3]K.Shaing,E.C.Crume,Phys.Rev.Lett. . **63** 1989) 2369.

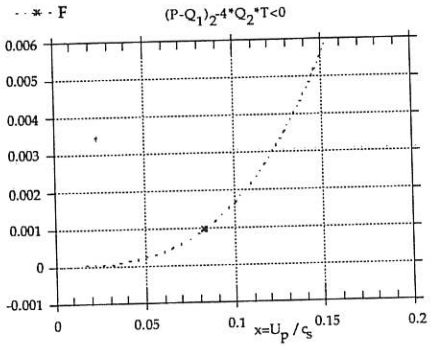

Fig.1

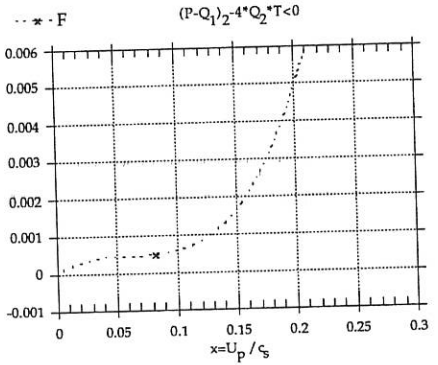

Fig.2 - L mode JET 20354

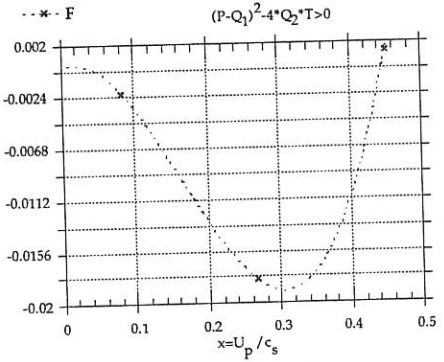

Fig.3 - H mode

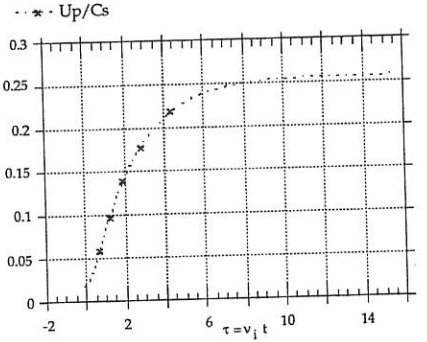

Fig.4 - U_p/C_s vs $\tau=\nu_i t$

ON THE EXISTENCE AND UNIQUENESS OF DISSIPATIVE PLASMA EQUILIBRIA IN A TOROIDAL DOMAIN

M. Spada and H. Wobig

Max-Planck-Institut für Plasmaphysik, IPP-EURATOM Association
D-8046 Garching bei München, Federal Republic of Germany

INTRODUCTION AND OUTLINE OF THE MODEL

The ideal magnetohydrodynamic (MHD) model is often adopted to describe the equilibrium of a confined plasma. Within this model, the pressure gradient is simply balanced by the magnetic force ($\nabla p = \mathbf{j} \times \mathbf{B}$), and one assumes the existence of nested magnetic surfaces which are constrained to have the shape of the plasma ($\mathbf{B} \cdot \nabla p = 0$). In this paper, we consider a one-fluid dissipative MHD model which includes inertial forces, finite resistivity and viscosity, and a particle source which sustains the pressure gradient in the plasma. This dissipative model eliminates the topological constraints of the ideal MHD model, and is also applicable to non-axisymmetric equilibria with magnetic islands and stochastic regions. In particular, the model applies to the boundary regions of stellarators and tokamaks, where the plasma is collision dominated and magnetic surfaces are destroyed.

In the following, we formulate a boundary-value problem on the basis of the above model assumptions and address the question of existence and uniqueness of solutions. Generalizing the techniques used in the mathematical theory of hydrodynamic flow, we rigorously prove that at least one weak solution exists if the plasma β is sufficiently small, or if viscosity and resistivity are sufficiently large; moreover, we prove that, under a condition of the same kind as that for existence, but more stringent, there exists only one solution. We refer to (SPADA and WOBIG, 1991) for all the technical details.

Specifically, we assume that the equilibrium of a plasma, filling a toroidal region Ω of the space $\mathbf{R}^3$, can be described by the following set of one-fluid, dissipative MHD equations: $\rho(\mathbf{v} \cdot \nabla)\mathbf{v} = -\nabla p + \mathbf{j} \times \mathbf{B} + \hat{V}\mathbf{v}$; $\eta \mathbf{j} = \mathbf{E} + \mathbf{v} \times \mathbf{B}$; $\mathbf{j} = \nabla \times \mathbf{B}$; $\nabla \cdot (\rho \mathbf{v}) = S$; $\nabla \cdot \mathbf{B} = 0$. Here, ρ is the plasma density, η the resistivity, $\mathbf{v}$ the flow velocity, $\mathbf{B}$ the magnetic field, $\mathbf{j}$ the current density, p the scalar pressure, $\mathbf{E}$ ($= -\nabla\phi$) the electric field, S a particle source which sustains the pressure gradient in the plasma. Moreover, $\hat{V}\mathbf{v}$ is the Braginskii viscous force field (BRAGINSKII, 1965) given by $(\hat{V}\mathbf{v})_i = -\partial \pi_{ij}/\partial x_j$, $\pi_{ij} = \sum_{\alpha=0}^{4} \gamma_\alpha \eta_\alpha W_{\alpha ij}$ ($\gamma_\alpha \equiv -1$ for $\alpha = 0, 1, 2$ and $\gamma_\alpha \equiv 1$ for $\alpha = 3, 4$) where $W_{\alpha ij} = A_{\alpha ij,kl}(\mathbf{h}) W_{kl}$ (repeated indices are summed); here, $\mathbf{h} \equiv \mathbf{B}/B$ and W_{kl} is the rate-of-strain tensor: $W_{kl} = \partial_l v_k + \partial_k v_l - \frac{2}{3}\delta_{kl} \nabla \cdot \mathbf{v}$ ($= W_{lk}$); the coefficients $A_{\alpha ij,kl}$ are given on p. 250 of (BRAGINSKII, 1965). From now on, we assume that the plasma density, the resistivity, as well as the viscosity coefficients η_α ($\alpha = 0, \ldots, 4$), are uniform.

We proceed reducing the above system to a problem with unknowns $p, \mathbf{v}, \mathbf{B}$; let us use the third equation into the first and the second, and take the curl of the second equation. We assume, for the moment, that there is no loop-voltage; we shall discuss, later on, how our results are modified if it is present. Thus, we obtain: $\rho(\mathbf{v} \cdot \nabla)\mathbf{v} = -\nabla p + (\nabla \times \mathbf{B}) \times \mathbf{B} + \hat{V}\mathbf{v}$; $\eta \nabla \times (\nabla \times \mathbf{B}) = \nabla \times (\mathbf{v} \times \mathbf{B})$; $\rho \nabla \cdot \mathbf{v} = S$; $\nabla \cdot \mathbf{B} = 0$.

We supplement this system with the following boundary conditions: $\mathbf{v} = \mathbf{v}_0$ on Γ, $\mathbf{B} \cdot \mathbf{n} = 0$ and $\eta(\nabla \times \mathbf{B}) \times \mathbf{n} = (\mathbf{v}_0 \cdot \mathbf{n})\mathbf{B}$ on Γ, where $\Gamma = \partial\Omega$ is the boundary of Ω and $\mathbf{n}$ is the unit outward normal on Γ. The last condition expresses the requirement that the tangential component of $\mathbf{E}$ vanishes on Γ.

We assume that Ω is a toroidal domain (viz., an open connected set) of $\mathbf{R}^3$, and that the boundary Γ is a manifold of class $\mathcal{C}^\infty$; moreover, we assume that Ω is Lipschitz. Concerning S and $\mathbf{v}_0$, they are assumed to be smooth ($S \in \mathcal{C}^\infty(\overline{\Omega})$ and $\mathbf{v}_0 \in (\mathcal{C}^\infty(\Gamma))^3$) and to fulfil the compatibility condition $\rho \int_\Gamma d\sigma\, \mathbf{v}_0 \cdot \mathbf{n} = \int_\Omega d^3x\, S(\mathbf{x})$.

The domain Ω is not simply-connected; specifically, it is doubly-connected. The above problem becomes well-posed by prescribing the value of the toroidal flux of $\mathbf{B}$ (SERMANGE and TEMAM, 1983; FOIAS and TEMAM, 1978). Let $\mathbf{B}_0 \in (\mathcal{C}^\infty(\overline{\Omega}))^3$ be the field having the prescribed toroidal flux, and fulfilling the following equations: $\nabla \cdot \mathbf{B}_0 = 0$ and $\nabla \times \mathbf{B}_0 = 0$ in Ω, $\mathbf{B}_0 \cdot \mathbf{n} = 0$ on Γ. Because of the topology of Ω, this problem for $\mathbf{B}_0$ has non-trivial solutions. Now we set $\mathbf{B} = \mathbf{B}_0 + \mathbf{B}_p$, the field $\mathbf{B}_p$ being our new unknown.

As regards the flow velocity field, let $\mathbf{v}_S \in (\mathcal{C}^\infty(\overline{\Omega}))^3$ be one of the solutions of the following problem: $\rho \nabla \cdot \mathbf{v}_S = S$ in Ω, $\mathbf{v}_S = \mathbf{v}_0$ on Γ. In the following we shall consider $\mathbf{v}_S$ as *given* and *fixed*. Setting $\mathbf{v} = \mathbf{v}_S + \mathbf{u}$, the field $\mathbf{u}$ becomes our new unknown.

Using the above split for $\mathbf{B}$ and $\mathbf{v}$ and introducing the approximation $\mathbf{h} \approx \mathbf{B}_0/|\mathbf{B}_0|$, we have the

following problem for the unknowns p, $\mathbf{u}$ and $\mathbf{B}_p$:

$$\rho(\mathbf{u}\cdot\nabla)\mathbf{v}_S+\rho(\mathbf{v}_S\cdot\nabla)\mathbf{u}+\rho(\mathbf{u}\cdot\nabla)\mathbf{u}-(\mathbf{B}_0\cdot\nabla)\mathbf{B}_p-(\mathbf{B}_p\cdot\nabla)\mathbf{B}_0-(\mathbf{B}_p\cdot\nabla)\mathbf{B}_p$$
$$+\nabla\left(p+\frac{1}{2}|\mathbf{B}_0+\mathbf{B}_p|^2\right)-\hat{V}\mathbf{u}=\mathbf{f}_S+(\mathbf{B}_0\cdot\nabla)\mathbf{B}_0 \tag{1}$$

$$\eta\nabla\times(\nabla\times\mathbf{B}_p)+\frac{S}{\rho}(\mathbf{B}_0+\mathbf{B}_p)-(\mathbf{B}_0\cdot\nabla)\mathbf{v}_S-(\mathbf{B}_p\cdot\nabla)\mathbf{v}_S-(\mathbf{B}_0\cdot\nabla)\mathbf{u}$$
$$-(\mathbf{B}_p\cdot\nabla)\mathbf{u}+(\mathbf{v}_S\cdot\nabla)\mathbf{B}_0+(\mathbf{v}_S\cdot\nabla)\mathbf{B}_p+(\mathbf{u}\cdot\nabla)\mathbf{B}_0+(\mathbf{u}\cdot\nabla)\mathbf{B}_p=0 \tag{2}$$

$$\nabla\cdot\mathbf{u}=0,\quad \nabla\cdot\mathbf{B}_p=0. \tag{3}$$

This system is supplemented with the following boundary conditions: $\mathbf{u}=\mathbf{0}$ on Γ, $\mathbf{B}_p\cdot\mathbf{n}=0$ and $\eta(\nabla\times\mathbf{B}_p)\times\mathbf{n}=(\mathbf{v}_S\cdot\mathbf{n})(\mathbf{B}_0+\mathbf{B}_p)$ on Γ. Here, well known identities have been used. Moreover, the field $\mathbf{f}_S$ appearing in equation (1) is defined by $\mathbf{f}_S\equiv-\rho(\mathbf{v}_S\cdot\nabla)\mathbf{v}_S+\hat{V}\mathbf{v}_S$. Note that $\mathbf{f}_S$ is a *given* quantity. It will play the role of an external force field.

FUNCTIONAL SETTING OF THE EQUATIONS

Let $L^2(\Omega)$ be the space of real-valued functions on Ω which are square integrable for the Lebesgue measure $d^3x=dx_1dx_2dx_3$; this is a Hilbert space for the scalar product $(\xi,\xi')=\int_\Omega d^3x\,\xi(\mathbf{x})\xi'(\mathbf{x})$. Let $H^m(\Omega)$ be the Sobolev space of functions which are in $L^2(\Omega)$ together with their weak derivatives of order less than or equal to m (ADAMS, 1975); $H_0^m(\Omega)$ is the Hilbert subspace of $H^m(\Omega)$ made of functions vanishing on Γ. Moreover, we use the notations $\mathbf{L}^2(\Omega)=(L^2(\Omega))^3$, $\mathbf{H}^m(\Omega)=(H^m(\Omega))^3$, $\mathbf{H}_0^m(\Omega)=(H_0^m(\Omega))^3$.

We shall use the following spaces: $\mathcal{V}_1=\{\mathbf{v}\in(\mathcal{C}_c^\infty(\Omega))^3,\nabla\cdot\mathbf{v}=0\}$; V_1 = the closure of $\mathcal{V}_1$ in $\mathbf{H}_0^1(\Omega)$; $\mathcal{V}_2=\{\mathbf{B}\in(\mathcal{C}^\infty(\overline{\Omega}))^3,\nabla\cdot\mathbf{B}=0,\mathbf{B}\cdot\mathbf{n}|_\Gamma=0$ and $\int_\Sigma d\sigma\,\mathbf{B}\cdot\mathbf{n}=0\}$; V_2 = the closure of $\mathcal{V}_2$ in $\mathbf{H}^1(\Omega)$; here, Σ is any smooth manifold of dimension 2 such that the open set $\dot{\Omega}=\Omega\setminus\Sigma$ is simply-connected and Lipschitz (i.e., Σ is not tangent to Γ); roughly speaking, Σ is a poloidal cut.

We equip V_1 with the scalar product $((\mathbf{v},\mathbf{v}'))_1=(\partial_i\mathbf{v},\partial_i\mathbf{v}')$, where $\partial_i=\partial/\partial x_i$ and, as always, repeated indices are summed. This is a scalar product on $\mathbf{H}_0^1(\Omega)$ thanks to the Poincaré inequality, and provides the norm on V_1 given by $\|\mathbf{v}\|_1=\{((\mathbf{v},\mathbf{v}))_1\}^{1/2}$.

We equip V_2 with the scalar product (SERMANGE and TEMAM, 1983) $((\mathbf{B},\mathbf{B}'))_2=(\nabla\times\mathbf{B},\nabla\times\mathbf{B}')$. This scalar product defines a norm on V_2 given by $\|\mathbf{B}\|_2=\{((\mathbf{B},\mathbf{B}))_2\}^{1/2}$, which is equivalent to that induced by $\mathbf{H}^1(\Omega)$ on V_2; see (SERMANGE and TEMAM, 1983).

Finally, we introduce the product space $V=V_1\times V_2$ and equip it with the scalar product $((\Phi,\Phi'))=\eta_*((\mathbf{v},\mathbf{v}'))_1+\eta((\mathbf{B},\mathbf{B}'))_2$ for all $\Phi=(\mathbf{v},\mathbf{B})$, $\Phi'=(\mathbf{v}',\mathbf{B}')\in V$, where $\eta_*\equiv\frac{1}{3}\min_{\alpha=0,1,2}\eta_\alpha$. This scalar product provides the norm on V given by $\|\Phi\|=\{((\Phi,\Phi))\}^{1/2}$.

We proceed now establishing a weak formulation of problem (1)–(3).

Let us assume that p, $\mathbf{u}$, $\mathbf{B}_p$ is a *smooth solution*. The first step is to multiply equation (1) by a test function $\mathbf{w}\in\mathcal{V}_1$ and integrate over Ω. Note that, for all $\zeta\in\mathcal{C}^\infty(\overline{\Omega})$, we have $\int_\Omega d^3x\,(\nabla\zeta)\cdot\mathbf{w}=\int_\Omega d^3x\,[\nabla\cdot(\zeta\mathbf{w})-\zeta\nabla\cdot\mathbf{w}]=\int_\Gamma d\sigma\,\zeta\mathbf{w}\cdot\mathbf{n}=0$, and also $\int_\Omega d^3x\,[(\mathbf{B}_0\cdot\nabla)\mathbf{B}_0]\cdot\mathbf{w}=\int_\Omega d^3x\,[(\nabla\times\mathbf{B}_0)\times\mathbf{B}_0+\nabla(\frac{1}{2}|\mathbf{B}_0|^2)]\cdot\mathbf{w}=0$. Concerning the quantity $(-\hat{V}\mathbf{u},\mathbf{w})$ arising from the l.h.s. of equation (1), we proceed in the following way; let us introduce the bilinear form $\mathcal{E}:V_1\times V_1\to\mathbf{R}$, $(\mathbf{a},\mathbf{b})\mapsto\mathcal{E}(\mathbf{a},\mathbf{b})$, $\mathcal{E}(\mathbf{a},\mathbf{b})\equiv-\sum_{\alpha=0}^4\gamma_\alpha\eta_\alpha\int_\Omega d^3x\,\partial_l a_k(A_{\alpha ij,kl}+A_{\alpha ij,lk})\partial_j b_i$. One can easily check that, since $\mathbf{u}$ is assumed to be a smooth solution and $\mathbf{w}$ to belong to $\mathcal{V}_1$, the identity $(-\hat{V}\mathbf{u},\mathbf{w})=\mathcal{E}(\mathbf{u},\mathbf{w})$ holds. Moreover, by using trivial inequalities as well as the Cauchy–Schwarz inequality for sums and for integrals, we can easily convince ourselves that, $\forall\mathbf{a}\in V_1$ fixed, the mapping $\mathcal{E}(\mathbf{a},\bullet):V_1\to\mathbf{R}$, $\mathbf{b}\mapsto\mathcal{E}(\mathbf{a},\mathbf{b})$, is a *bounded* linear functional. Therefore, by using the Riesz' representation theorem, we see that there exists one and only one $\tilde{\mathbf{a}}\in V_1$ such that $\mathcal{E}(\mathbf{a},\mathbf{b})=((\tilde{\mathbf{a}},\mathbf{b}))_1$ $\forall\mathbf{b}\in V_1$. Since, for $\mathbf{a}\in V_1$ fixed, the element $\tilde{\mathbf{a}}\in V_1$ is unique, we can give the following good definition of the operator $\tilde{E}:V_1\to V_1$, $\mathbf{a}\mapsto\tilde{E}\mathbf{a}\equiv\tilde{\mathbf{a}}$. It is advantageous to introduce also the operator E by setting $\tilde{E}\equiv\eta_*E$ so that, finally, we have $(-\hat{V}\mathbf{u},\mathbf{w})=\eta_*((E\mathbf{u},\mathbf{w}))_1$. Note that the operator $\tilde{E}$ is linear (and, hence, the operator E too), as $\mathcal{E}$ is a bilinear form.

In order to shorten the notation, we introduce a trilinear form on $(\mathbf{H}^1(\Omega))^3$ by setting $b(\xi,\xi',\xi'')=\int_\Omega d^3x\,\xi_i(\partial_i\xi'_j)\xi''_j$. This form is *continuous* (SERMANGE and TEMAM, 1983).

Thus, the above-mentioned projection of equation (1) yields the following (weak) equation:

$$\eta_*((E\mathbf{u},\mathbf{w}))_1 + \rho b(\mathbf{u},\mathbf{v}_S,\mathbf{w}) + \rho b(\mathbf{v}_S,\mathbf{u},\mathbf{w}) + \rho b(\mathbf{u},\mathbf{u},\mathbf{w}) - b(\mathbf{B}_0,\mathbf{B}_p,\mathbf{w}) - b(\mathbf{B}_p,\mathbf{B}_0,\mathbf{w}) - b(\mathbf{B}_p,\mathbf{B}_p,\mathbf{w}) = (\mathbf{f}_S,\mathbf{w}). \tag{4}$$

Next, let us deal with equation (2) and remember we are assuming p, $\mathbf{u}$, $\mathbf{B}_p$ to be a smooth solution. We proceed in the following way (see also (SERMANGE and TEMAM, 1983)): we multiply equation (2) by a test function $\mathbf{C} \in \mathcal{V}_2$ and integrate over Ω. Note that the identity $\int_\Omega d^3x\ [\nabla \times (\nabla \times \mathbf{B}_p)] \cdot \mathbf{C} = \int_\Omega d^3x\ (\nabla \times \mathbf{B}_p) \cdot (\nabla \times \mathbf{C}) - \int_\Gamma d\sigma\,[(\nabla \times \mathbf{B}_p) \times \mathbf{n}] \cdot \mathbf{C}$ holds. A straightforward calculation yields the following (weak) equation:

$$\eta((\mathbf{B}_p,\mathbf{C}))_2 + b(\mathbf{u},\mathbf{B}_0+\mathbf{B}_p,\mathbf{C}) - b(\mathbf{B}_0+\mathbf{B}_p,\mathbf{u},\mathbf{C}) - b(\mathbf{B}_0+\mathbf{B}_p,\mathbf{v}_S,\mathbf{C}) - b(\mathbf{v}_S,\mathbf{C},\mathbf{B}_0+\mathbf{B}_p) = 0. \tag{5}$$

In order to establish a problem for weak solutions in the product space V, we introduce the operator $U: V \to V$, $\Phi = (\mathbf{v},\mathbf{B}) \mapsto U\Phi \equiv (E\mathbf{v},\mathbf{B})$. Note that U is a linear operator as E is linear.

Furthermore, in order to shorten the notation, let us define the mapping $\mathcal{B}: V \times V \to \mathbf{R}$, $(\Phi,\Phi') \mapsto \mathcal{B}(\Phi,\Phi')$, $\mathcal{B}(\Phi,\Phi') \equiv \rho b(\mathbf{v},\mathbf{v}_S,\mathbf{v}') + \rho b(\mathbf{v}_S,\mathbf{v},\mathbf{v}') + \rho b(\mathbf{v},\mathbf{v},\mathbf{v}') - b(\mathbf{B}_0,\mathbf{B},\mathbf{v}') - b(\mathbf{B},\mathbf{B}_0,\mathbf{v}') - b(\mathbf{B},\mathbf{B},\mathbf{v}') + b(\mathbf{v},\mathbf{B}_0+\mathbf{B},\mathbf{B}') - b(\mathbf{B}_0+\mathbf{B},\mathbf{v},\mathbf{B}') - b(\mathbf{B}_0+\mathbf{B},\mathbf{v}_S,\mathbf{B}') - b(\mathbf{v}_S,\mathbf{B}',\mathbf{B}_0+\mathbf{B})$, where $\Phi = (\mathbf{v},\mathbf{B})$ and $\Phi' = (\mathbf{v}',\mathbf{B}')$. Note that the mapping $\mathcal{B}$ is manifestly linear in the second argument but nonlinear in the first one.

Now, we add equations (4) and (5) and obtain the following (weak) equation:

$$((U\Phi,\Psi)) + \mathcal{B}(\Phi,\Psi) = (\mathbf{f}_S,\mathbf{w}) \tag{6}$$

where $\Phi = (\mathbf{u},\mathbf{B}_p)$ and $\Psi = (\mathbf{w},\mathbf{C})$.

We can now establish the following weak formulation of problem (1)–(3):

PROBLEM (*weak solutions*). Under the above hypotheses for Ω, $\mathbf{v}_S$ and $\mathbf{B}_0$, find $\Phi = (\mathbf{u},\mathbf{B}_p) \in V$ such that equation (6) is satisfied for all $\Psi = (\mathbf{w},\mathbf{C}) \in V$.

Note that we do not require that the solution has to be smooth. For a thorough discussion on the weak formulation of problems of this kind see (LADYZHENSKAYA, 1963; TEMAM, 1979; SERMANGE and TEMAM, 1983).

EXISTENCE, UNIQUENESS AND ESTIMATE OF WEAK SOLUTIONS

We proceed considering the question of existence and uniqueness of the above-defined weak solutions. As we shall see, proving existence also yields an estimate of the solution(s). The mathematical techniques we are going to use are classical for problems of this kind (LADYZHENSKAYA, 1963; TEMAM, 1979); nevertheless, since we describe viscosity by the Braginskii operator while in previous work the Laplacian operator was always used, we shall have to carry out a special analysis in relation to this point.

Firstly, we consider the r.h.s. of equation (6). It is easy to show that the mapping $V \to \mathbf{R}$, $\Psi = (\mathbf{w},\mathbf{C}) \mapsto (\mathbf{f}_S,\mathbf{w})$, is a bounded linear functional. According to Riesz' theorem, this functional can be represented in the form $(\mathbf{f}_S,\mathbf{w}) = ((F_S,\Psi))$ for one and only one element $F_S \in V$; obviously, the second component of F_S is equal to zero.

Next, we consider the term $\mathcal{B}(\Phi,\Psi)$ in the l.h.s. of equation (6). It is not difficult to prove that, $\forall \Phi \in V$ fixed, the mapping $\mathcal{B}(\Phi,\bullet): V \to \mathbf{R}$, $\Psi \mapsto \mathcal{B}(\Phi,\Psi)$, is a bounded linear functional, so there exists an operator $\tilde{B}: V \to V$ such that $\mathcal{B}(\Phi,\Psi) = ((\tilde{B}\Phi,\Psi))$. The operator $\tilde{B}$ is clearly nonlinear.

Thus, going back to equation (6), we can write it in the following way: $((U\Phi,\Psi)) + ((\tilde{B}\Phi,\Psi)) = ((F_S,\Psi))$. It is advantageous to introduce the constant operator $C_S: V \to V$ such that $\Phi \mapsto C_S\Phi \equiv F_S$ for all $\Phi \in V$, and also the operator $Z \equiv C_S - \tilde{B}$. The element $\Phi \in V$ is a weak solution of our problem if and only if the above equation is satisfied for all $\Psi \in V$; therefore, the weak problem reduces to solving the nonlinear equation $U\Phi = Z\Phi$ in the space V.

Next, one can prove that the estimate from below $\mathcal{E}(\mathbf{v},\mathbf{v}) \geq \eta_*\|\mathbf{v}\|_1^2$ holds, namely, the form $\mathcal{E}$ is coercive. This means, roughly speaking, that the Braginskii viscosity operator is negative definite; this property has a plain and elegant physical interpretation: the viscous forces do always dissipate energy. It is not difficult to see that, therefore, the operator U is one-to-one and U^{-1} is bounded. Thus, the equation we must solve can be written equivalently as a fixed-point equation:

$$U^{-1}Z\Phi = \Phi. \tag{7}$$

To investigate the solvability of equation (7), we apply the Leray–Schauder principle (LADYZHENSKAYA, 1963). This principle is particularly suitable for problems of this kind since it guarantees existence but not uniqueness.

It is easy to check that V, the space in which equation (7) is defined, is a separable Hilbert space (viz., it has a countable dense subset). Moreover, one can prove that the operator $U^{-1}Z$ is completely continuous in V, i.e., it maps any weakly convergent sequence $\{\Phi_n\}$ in V into a strongly convergent sequence $\{U^{-1}Z\Phi_n\}$ in V. Therefore, the Leray–Schauder principle guarantees that, if all possible solutions of the equation $\lambda U^{-1}Z\Phi = \Phi$ for $\lambda \in [0,1]$ lie within some ball $\|\Phi\| \leq R$, then the equation (7) has at least one solution inside this ball. One can prove that the norms $\|\Phi^{(\lambda)}\|$ are uniformly bounded if

$$G_S \equiv \|\mathbf{v}_S\|_{\mathbf{L}^4(\Omega)} \left(\frac{3\sqrt{3}\rho M_1}{\eta_*} + \frac{M_2}{\eta} \right) < 1. \tag{8}$$

Here, $M_{1,2}$ are the imbedding constants of the compact imbeddings $V_{1,2}(\|\bullet\|_{1,2}) \to \mathbf{L}^4(\Omega)$; note that they depend only on Ω. Therefore, if the condition (8) is satisfied, at least one weak solution of our problem does exist. The requirement is that the source must be sufficiently small, or viscosity and resistivity sufficiently large.

Moreover, for the solution(s) the following estimate holds:

$$\|\Phi\| \leq \frac{\|\mathbf{v}_S\|_{\mathbf{L}^4(\Omega)}\|\mathbf{B}_0\|_{\mathbf{L}^4(\Omega)}/\sqrt{\eta} + \|F_S\|}{1 - G_S}. \tag{9}$$

As one could expect, the above estimate shows that the larger are viscosity and resistivity (or the smaller is the source), the smaller is $\|\Phi\|$: the dissipation quenches the flow velocity and the plasma currents. In particular, if the source vanishes we have that $\Phi = 0$, viz., the plasma is quiescent and no current flows in it. (We recall that we assumed there is no loop-voltage; in the presence of loop-voltage, another positive quantity would appear in the numerator of equation (9) and a nontrivial solution could exist even if the source vanishes.)

Equations (8)–(9), together with the condition for uniqueness we are going to derive and the above study of the Braginskii viscosity operator, are the main results of this analysis.

We conclude this study dealing with uniqueness of the solution. Suppose that condition (8) is satisfied, and that Φ and Φ' are two solutions; let us define $\Lambda \equiv \Phi - \Phi'$ ($\in V$). By using a classical technique (LADYZHENSKAYA, 1963), one can prove that if

$$G_S + \left(\frac{\rho M_1^2}{\eta_*^{3/2}} + \frac{M_1 M_2}{\sqrt{\eta_*}\eta} + \frac{M_2^2}{\sqrt{\eta_*}\eta} \right) \frac{\|\mathbf{v}_S\|_{\mathbf{L}^4(\Omega)}\|\mathbf{B}_0\|_{\mathbf{L}^4(\Omega)}/\sqrt{\eta} + \|F_S\|}{1 - G_S} < 1 \tag{10}$$

then $\Lambda = 0$: there exists only one solution. The requirement for uniqueness expressed by the above formula is of the same kind as that for existence. It is important to remark, however, that condition (10) is more stringent than condition (8).

Finally, we remark that the Navier–Stokes problem can manifestly be studied as a particular case of problem (1)–(3). The important existence and uniqueness results for the Navier–Stokes problem, which are well known (LADYZHENSKAYA, 1963), can be easily recovered from conditions (8) and (10).

REFERENCES

ADAMS R. A. (1975) *Sobolev Spaces.* Academic, New York.

BRAGINSKII S. I. (1965) in *Reviews of Plasma Physics* (edited by M. A. LEONTOVICH), Vol. 1, p. 205. Consultants Bureau, New York.

FOIAS C. and TEMAM R. (1978) *Annali Scu. norm. sup., Pisa* **V, 1**, serie IV, 29.

LADYZHENSKAYA O. A. (1963) *The Mathematical Theory of Viscous Incompressible Flow.* Gordon and Breach, New York.

SERMANGE M. and TEMAM R. (1983) *Communs pure appl. Math.* **36**, 635.

SPADA M. and WOBIG H. (1991) *to appear.*

TEMAM R. (1979) *Navier–Stokes Equations.* North-Holland, Amsterdam.

L-H TRANSITIONS VIA THE MATSUDA ANOMALY

Satish Puri
Max-Planck-Institut für Plasmaphysik, EURATOM Association,
Garching bei München, Germany

1. INTRODUCTION

Electron-ion momentum-transfer collisions parallel to the magnetic-field direction are anomalously enhanced if $r_{ce} < \lambda_D$ for electrons with $v_{\|e} \sim \mathcal{O}(v_{ti})$ [1,2]. Henceforth this anomaly will be referred to as the Matsuda anomaly. As the electrons slow down while approaching the turning point θ_t, the enhancement in the drag force collisionally captures a fraction α_{cap} of the electrons. These electrons couple strongly to the ion component and are prevented from continuing their banana orbits *until* they are able to overcome the drag force. The dwell time, τ_{esc}, of this stagnant population results in a radial displacement $L = v_{\perp d}\tau_{esc}\sin\theta_t$ via the ∇B drift. The electron diffusivity becomes

$$D_e = \frac{< L^2 >}{\tau_{esc} + 0.5\tau_b}\alpha_{cap} \ , \tag{1}$$

where τ_b is the bounce time. The escape time, τ_{esc}, is found to increase approximately exponentially with T_i^{-2}; relatively small changes in T_i at the plasma edge cause disproportionately large variations in D_e, resembling L-H Tokamak transitions [3]. For $T_i \sim \mathcal{O}(100)\,eV$, the step length L becomes comparable to the width of the edge region, signaling the onset of convective transport and the diffusion model ceases to be valid.

2. ELECTRON CAPTURE

Electrons (prior to capture) and ions are assumed to possess Maxwellian velocity distributions (the capture and stagnation processes introduce a pronounced loss cone in electron-velocity distribution). Probability that an electron encounters no collisions is

$$P_{esc}(\lambda) = \exp\left[-\int^{\lambda}\frac{d\lambda'}{\lambda_{mfp}(\lambda')}\right] \ , \tag{2}$$

where $d\lambda = qR_0\,d\theta$, $\lambda_{mfp} = |v_\||/\nu_a$, ν_a is the anomalously enhanced electron-ion collision frequency which for $\lambda_D = (1/\omega_{pe})\sqrt{T_e/m}\sqrt{T_i/(T_i + ZT_e)} > r_{ce}$ or $\eta = (\omega_{ce}/\omega_{pe})\sqrt{.5T_i/(T_i + ZT_e)} > u_{\perp/e}$ is given by [2]

$$\nu_a \approx \frac{Z}{4\pi}\frac{\hat{n}_i}{n_i}\frac{< v_i^2 >}{v_\|^2}\frac{\omega_{pe}^4}{n_e v_\|^3}\ln\left(\frac{\eta}{u_{\perp/e}}\right) \ , \tag{3}$$

$\hat{n}_i$ is the number of ions within the sphere in velocity space with radius $|v_\||$, $< v_i^2 >$ is the average v^2 for these particles, v_{te} and v_{ti} are the electron and ion thermal speeds, $u_{/e,i} = v_e/(\sqrt{2}v_{te,i})$ is the normalized electron velocity, q is the safety factor, Z is the ionic charge, $\rho = r/a$, a is the plasma radius and R_0 is the torus major radius.

The collision probability becomes $P_{coll}(\lambda) = 1 - P_{esc}(\lambda)$ which upon differentiation gives the capture (collision) probability per unit length at position λ as $p_{cap}(\lambda) = P_{esc}(\lambda)/\lambda_{mfp}(\lambda)$. The capture probability per unit radian at θ for an electron of velocity $(u_{\|/e}, u_{\perp/e})$ at $\theta = 0$ becomes

$$p_{cap}(u_{\|/e}, \theta, u_{\perp/e}) = \Theta(\theta) \left[\exp\left(- \int_0^{\theta} \Theta(\theta')\, d\theta' \right) + \kappa(\theta_t) \exp\left(- \int_{\theta}^{\theta_t} \Theta(\theta')\, d\theta' \right) \right] ,$$

where θ is assumed to lie in the range $0 \le \theta \le \pi$,

$$\kappa(\theta_t) = 1 - \int_0^{\theta_t} \Theta(\theta) \exp\left(- \int_0^{\theta} \Theta(\theta')\, d\theta' \right) d\theta ,$$

$$\Theta(\theta) = \frac{q R_0 \nu_a(\theta)}{\sqrt{2} v_{ti} u_{\|/i}(\theta)} , \tag{4}$$

$$u_{\|/e,i}(\theta) = \left[u^2_{\|/e,i}(0) - \frac{\varepsilon(1 - \cos\theta)}{1 + \varepsilon \cos\theta} u^2_{\perp/e,i}(0) \right]^{1/2} ,$$

and θ_t is the turning point for the velocity $(u_{\|/e}, u_{\perp/e})$. The captured fraction becomes

$$\alpha_{cap}(u_{\|/e}, \theta, u_{\perp/e}) = \pi^{-3/2} \exp\left[-u^2_{/e}(0) \right] p_{cap}(u_{\|/e}, \theta, u_{\perp/e}) .$$

Integrating over the parallel velocities gives

$$\alpha_{cap}(\theta, u_{\perp/e}) = \int_{u_{\|a}}^{u_{\|b}} \alpha_{cap}(u_{\|/e}, \theta, u_{\perp/e})\, du_{\|/e} ,$$

where $\varepsilon = r/R_0$, the integration limits $u_{\|a} = \sqrt{\varepsilon(1 - \cos\theta)/(1 + \varepsilon\cos\theta)}\, u_{\perp/e}$ and $u_{\|b} = \sqrt{2\varepsilon/(1 - \varepsilon)}\, u_{\perp/e}$ being set by the trapping condition. The Matsuda anomaly extends to parallel electron velocities of the order of ξv_{ti}, with $\xi \sim \mathcal{O}(1)$, or within an angle

$$\Delta\theta \sim \frac{m}{M} \frac{\xi^2}{u^2_{\perp/e}(0)} \frac{(1 + \varepsilon\cos\theta_t)^2}{\varepsilon(1 + \varepsilon)\sin\theta_t} , \tag{5}$$

from the banana-orbit turning point θ_t. Since $\Delta\theta \ll \theta_t$ (except for an insignificant region $\theta_t \lesssim m/M$), the capture process is concentrated near $\theta \sim \theta_t$.

3. ELECTRON ESCAPE

The escape probability and escape rate out of this *stagnant pool* are given by

$$\begin{aligned} P_{esc}(\theta, u_{\|/e}, u_{\perp/e}) &= \exp\left[- \int_0^{\theta} \Theta(\theta')\, d\theta' \right] \text{ for } v_{\|} < 0 , \\ &= \exp\left[- \int_{\theta}^{\theta_t} \Theta(\theta')\, d\theta' - \int_0^{\theta_t} \Theta(\theta')\, d\theta' \right] \text{ for } v_{\|} > 0 , \end{aligned} \tag{6}$$

and

$$\dot{P}_{esc}(\theta, u_{\parallel/e}, u_{\perp/e}) = \omega_{esc} P_{esc}(\theta, u_{\parallel/e}, u_{\perp/e}) ,$$

respectively, where $v_\parallel > 0$ for electrons moving along increasing θ and $\omega_{esc} = |v_\parallel|/r$ is the angular escape frequency. Integrating over the parallel velocities gives

$$\dot{P}_{esc}(\theta, u_{\perp/e}) = \int_{-\infty}^{\infty} \omega_{esc} f_s(\theta, u_{\parallel/e}, u_{\perp/e}) P_{esc}(\theta, u_{\parallel/e}, u_{\perp/e})\, du_{\parallel/e} , \tag{7}$$

where f_s is the stagnant-population parallel-velocity distribution. The escape rate may be approximately ascertained by replacing $\omega_{esc}(v_\parallel) f_s(\theta, u_{\parallel/e}, u_{\perp/e})$ in (7) by $c_{esc}(v_\parallel)\tilde{f}_s(\theta, u_{\parallel/i}, u_{\perp/e})$, where $\tilde{f}_s$ possesses the Maxwellian parallel-velocity distribution of ions, while $c_{esc} = \omega_{esc}\nu_a/(\omega_{esc} + \nu_a)$ acts to tailor the Maxwellian by concentrating $c_{esc}\tilde{f}_s$ at $v_\parallel \lesssim \xi v_{ti}$. Finally, one obtains

$$\tau_{esc}(\theta, u_{\perp/e}) = \dot{P}_{esc}^{-1}(\theta, u_{\perp/e}) .$$

4. PARTICLE AND ENERGY DIFFUSIVITIES

The stagnant fraction α_s becomes

$$\alpha_s(\theta, u_{\perp/e}) = \frac{\tau_{esc}(\theta, u_{\perp/e})}{\tau_{esc}(\theta, u_{\perp/e}) + .5\tau_b(\theta, u_{\perp/e})}\, \alpha_{cap}(\theta, u_{\perp/e}) .$$

The contribution to the particle diffusivity is

$$D_e(\theta, u_{\perp/e}) = v_d^2(\theta, u_{\perp/e})\tau_{esc}(\theta, u_{\perp/e})\, \alpha_s(\theta, u_{\perp/e}) , \tag{8}$$

where the radial component of the drift velocity is given by

$$v_d(\theta, u_{\perp/e}) = \frac{1}{2}\frac{(1+\varepsilon)\sin\theta}{(1+\varepsilon\cos\theta)}\frac{v_{te}^2 u_{\perp/e}^2}{\omega_{ce} R_0} . \tag{9}$$

Integrating over θ and $u_{\perp/e}$ gives the total diffusivity at r as

$$\hat{D}_e(r) = 4\pi \int_0^\pi d\theta \int_0^\eta D_e(\theta, u_{\perp/e}) u_{\perp/e}\, du_{\perp/e} . \tag{10}$$

Similarly, the contribution of radial electron drift to the electron thermal diffusivity may be expressed in the form

$$\chi_e(\theta, u_{\perp/e}) = \frac{(1+\varepsilon)u_{\perp/e}^2(0)}{(1+\varepsilon\cos\theta)}\, D_e(\theta, u_{\perp/e}) , \tag{11}$$

where the entire kinetic energy of the electron is assumed to be contained in $u_{\perp/e}$ at the trapping location $\theta \approx \theta_t$.

5. COMPUTATIONAL RESULTS

Fig.1 shows the diffusivities as a function of plasma radius for several T_0 in a hydrogen plasma with $n_e = n_{e0}(1-\rho^2)$, $T_e = T_{e0}(1-\rho^2)$, $q = q_0 + (q_a - q_0)\rho^2$, $Z = \exp(\rho \ln Z_a)$, $B_{\varphi 0} = 5\,T$, $n_{e0} = 10^{20}\,m^{-3}$, $q_0 = 1$, $q_a = 3.5$, $Z_a = 3$, $R_0 = 2\,m$, $A = 3$ and $T_{i0} = T_{e0} = T_0$. For normal operating conditions, the diffusivity contributed by the Matsuda anomaly is inconsequential in the plasma interior. However, the relatively large collisionality near the plasma edge triggers an explosive buildup; the diffusivity increases by several orders of magnitude within a span of a few centimeters.

Such violent episodes might have been anticipated from the $\exp(-\int \Theta\, d\theta)$ dependence of capture and escape probabilities. In (6), $P_{esc} \to 0$ as $\int \Theta\, d\theta \approx \Theta\Delta\theta \gg 1$. For a given radius, (3)-(5) yield $\Theta\Delta\theta \sim qR_0 Z T_i^{-2} n_e \ln B_0$. The T_i^{-2} dependence of $\Theta\Delta\theta$ predisposes the particle and thermal fluxes to the sudden onset/extinction of the stagnation catastrophe with decreasing/increasing ion temperature at the plasma edge. The phenomenon, instigated by purely collisional processes, has the appearance of a bifurcation. The poloidal variation of diffusivity (Fig.2) is in agreement with the observed asymmetry of the heat flux to the divertor [4]. Further details are given in Ref.[5].

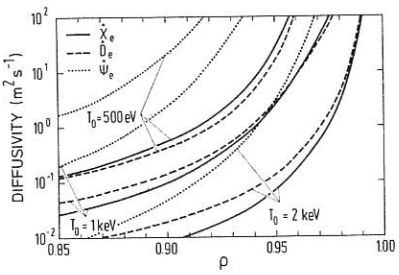

Fig.1 Diffusivity versus ρ

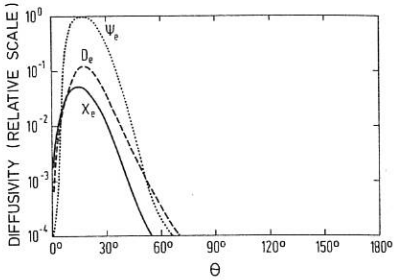

Fig.2 Diffusivity versus θ

6. CONCLUSION

The stagnation catastrophe bears a close resemblence to the L-H mode transition in Tokamaks, satisfying the transition criteria given in Ref.[4]; namely, (i) the theory is capable of bifurcation, (ii) the transition has a threshold involving the edge temperature, (iii) the edge gradients would become steep at the transport barrier, (iv) the asymmetry of the heat flux to the divertor is reduced, and (v) the transition is not critically dependent upon the heating method.

REFERENCES

[1] K. Matsuda, Phys. Rev. Lett. 49 (1982) 1486.
[2] A. A. Ware, Phys. Rev. Lett. 62 (1989) 51.
[3] F. Wagner et al., Phys. Rev. Lett. 49 (1982) 1408.
[4] K. H. Burrell et al., Plasma Phys. and Contr. Fusion 31 (1989) 1649.
[5] S. Puri, Max-Planck-Institut für Plasmaphysik Report No. IPP 4/244, October 1990.

THE ROLE OF PFIRSCH-SCHLÜTER CURRENTS IN PLASMA EQUILIBRIUM, STABILITY AND TRANSPORT

H. WOBIG

Max-Planck-Institut für Plasmaphysik,
EURATOM Association, D-8046 Garching, FRG

In a toroidal equilibrium the plasma current $\mathbf{j}$, which is needed to satisfy the equilibrium condition $\mathbf{j} \times \mathbf{B} = \nabla p$, usually is decomposed as a diamagnetic current $\mathbf{j}_\perp = \mathbf{B} \times \nabla p / B^2$ and a parallel current $\mathbf{j}_\parallel$. The first to compute these currents were D.Pfirsch and A. Schlüter [1] who found the approximation $j_\parallel \approx (j_\perp 2/\iota) \cos\theta$ in an axisymmetric magnetic field $\mathbf{B}$. This approximation has been made for stellarators without net toroidal current and large aspect ratio. In tokamaks, however, with finite toroidal currents the problem arises, how to define the P.S.-currents properly. In the literature often the condition $< \mathbf{j}_{PS} \cdot \mathbf{B} >= 0$ is used which unfortunately leads to a rather inconvenient form of $\mathbf{j}_{PS}$. A more convenient definition starts from the Hamada coordinate system (ζ, θ, s; ζ and θ are toroidal and poloidal coordinates and s is the volume of the magnetic surface) of a general toroidal equilibrium. The magnetic field is given by $\mathbf{B} = \psi'(s)\mathbf{e_t} + \chi'(s)\mathbf{e_p}$ and the current by $\mathbf{j} = I'(s)\mathbf{e_t} + J'(s)\mathbf{e_p}$. $\mathbf{e_p} = \nabla\zeta \times \nabla s$, $\mathbf{e_t} = \nabla s \times \nabla\theta$, $\nabla \cdot \mathbf{e_p} = 0$, $\nabla \cdot \mathbf{e_t} = 0$ are the poloidal and toroidal base vectors on the magnetic surface. Using the equilibrium condition $J'\psi' - I'\chi' = p'$ the current can be written in the form $\psi'(s)\mathbf{j} = p'(s)\mathbf{e_p} + I'(s)\mathbf{B}$. The current $p'(s)\mathbf{e_p}$ flows along the coordinate lines ζ=const. which are poloidally closed and therefore the net toroidal current is zero. $p'(s)\mathbf{e_p}$ is the sum of diamagnetic currents and P.S-currents which are given by

$$\psi'(s)\mathbf{j}_{PS} = p'(s)\frac{(\mathbf{e_p} \cdot \mathbf{B})}{B^2}\mathbf{B} \qquad (1)$$

The toroidal current is then described by the second term $I'(s)\mathbf{B}$. This definition of the P.S.-currents leads to the following definition of the Pfirsch-Schlüter diffusion flux. The radial integrated flux of the flow vector $p\mathbf{u}$ is

$$-(\psi'(s))^2 \Gamma = \eta p \{< \mathbf{e_p} \cdot \mathbf{e_p} > p'(s) + I I'(s)\} \qquad (2)$$

The first term describes the classical diffusion plus the Pfirsch- Schlüter diffusion. The Pfirsch-Schlüter diffusion coefficient is $D_{PS} = \eta p < \mathbf{e_p} \cdot \mathbf{e_p} > /\psi'(s)^2$ and the factor $< \mathbf{e_p} \cdot \mathbf{e_p} >$ is proportional to $1 + 2/\iota^2$ in large aspect ratio configurations. The second term is a classical pinch effect. An extensive discussion of the implications of these two definitions of the P.S.-currents will be published elsewhere [2]. In the following the definition eq.(1) will be used.

Plasma equilibrium. The main effect of P.S.- currents on plasma equilibrium is the Shafranov shift due to the vertical magnetic field. In standard stellarators this shift is $\Delta \approx \beta R/2\iota^2$ which defines an equilibrium β- limit when Δ is equal to 1/2 of the plasma radius. Above this limit the distortion of the configuration is considered as too large. In

the concept of advanced stellarators [3] the P.S-currents are minimized to large extent by shaping the magnetic surfaces properly; in Helias configurations [4](see Fig. 1) the ratio $< j_\parallel^2/j_\perp^2 > \approx 0.5$ was achieved while in standard stellarators this number is $\approx 2/\iota^2$. This reduction leads to a very small Shafranov shift and to a small change of the rotational transform by the finite beta effect. Another effect of the parallel plasma currents is the formations of islands on rational magnetic surfaces [5]. This is a particular problem of non-axisymmetric configurations, since on rational magnetic surfaces islands may arise which are correlated to the magnetic field of the P.S.-currents nearby. If the plasma is stable against resistive interchange modes, these islands saturate at a finite level; in the opposite case they grow with β [6]. However, a self-consistent picture with island overlap and stochasticity is still missing.

Neoclassical transport. Neoclassical transport in toroidal equilibria is the result of radial particle drift $\mathbf{v}_D \cdot \nabla s$ and Coulomb collisions. The ideal case is the isodynamic equilibrium [7] where the radial drift is zero and all neoclassical effects are zero, too. In reality, however, radial losses can only be minimized to a finite limit by reducing the P.S-currents and localizing trapped particles in regions of small radial drift. In terms of P.S.-currents the radial drift velocity is

$$\mathbf{v}_d \cdot \nabla s = \frac{mc}{q\psi'(s)}(v_\parallel^2 + \frac{1}{2}v_\perp^2)\{\mathbf{e_p} \cdot \frac{\nabla B}{B} - \frac{\mathbf{e_p} \cdot \mathbf{B}}{B^2}\mathbf{B} \cdot \frac{\nabla B}{B}\} \tag{3}$$

For stellarators ($I = 0$) one can prove that $\mathbf{e_p} \cdot \mathbf{B} \to 0 \Leftrightarrow \mathbf{e_p} \cdot \nabla B \to 0$. Therefore, it may be expected that small but finite P.S-currents imply small neoclassical effects. Neoclassical losses are driven by the poloidal viscous forces $\mathbf{e_p} \cdot \nabla \cdot \pi$, where $p\delta_{ik} + \pi_{ik}$ is the pressure tensor. Retaining the Chew-Goldberger-Low form of the pressure tensor, the integrated neoclassical particle flux is given by

$$-\psi'(s)q\Gamma_{neo} = < (p_\parallel - p_\perp)\,\mathbf{e_p} \cdot \frac{\nabla B}{B} > \tag{4}$$

Similar expressions can be derived for higher order moments and the related fluxes. In deriving eq. 4 use has to be made from the equilibrium condition $\mathbf{e_p} \times \mathbf{B} = \nabla\psi$. The geometrical factor $\mathbf{e_p} \cdot \nabla B$ clearly shows the correlation between neoclassical losses and P.S-currents. The anisotropic pressure $p_\parallel - p_\perp$ has to be calculated from the kinetic equation. Various approaches using Monte-Carlo techniques [8] and analytic approximations [9] have shown that in Helias configurations with reduced P.S-currents neoclassical losses are also small. This holds for losses by barely trapped particles in the plateau regime and losses by trapped particles in the $1/\nu$-regime. In this regime losses can be characterized by an effective helical ripple of $\epsilon_{h,eff} \approx 0.01 - 0.02$ [9].

Stability. In tokamaks the ohmically driven parallel current is the dominating one and the related instabilities like kink modes and tearing modes are determined by this current rather than the P.S.-currents. In stellarators P.S.-currents are the only parallel currents and therefore they may also contribute to plasma instabilities. The Mercier criterion for localized modes $(H - \iota'(s)/2)^2 - D_R > 0$ with

$$D_R = [\psi']^4 < \frac{B^2}{|\nabla s|^2} > \times\{p'\frac{\psi''(s)}{\psi'(s)} + (p'(s))^2 < \frac{\mathbf{e_p} \cdot \mathbf{e_p}}{|\nabla s|^2} >\} \tag{5}$$

shows the importance of reducing $\mathbf{e_p}\cdot\mathbf{e_p}$ as much as possible, since in configurations with a magnetic well the last term in D_R is the only destabilizing one. $-D_R > 0$ is the resistive interchange criterion which is more stringent than the Mercier criterion. The stability limit in 5-period Helias configurations found from the resistive interchange criterion is $<\beta>= 5-10\%$.

In order to study microinstabiities using linearized kinetic equations the distribution function F of the plasma equilibrium must be specified. Electrostatic drift instabilities are described by the linearized Fokker-Planck equation with the driving term $\delta\mathbf{E}\cdot\nabla_v F$, where $\delta\mathbf{E}$ is the perturbed electric field. A distribution F which is compatible with the ideal equilibrium condition $\nabla p = \mathbf{j}\times\mathbf{B}$ has the form $F = F^s(v^2,s)+F^a$. Pfirsch-Schlüter currents and all equilibrium flows in the magnetic surface are vector moments of the antisymmetric distribution F^a. Expanding F^a in Laguerre polynomials $g_k \propto L_k^{3/2}(v^2)$ [10] yields

$$F^a = \sum_k f_M g_k\, \mathbf{v}\cdot\mathbf{U}_k \quad ; \quad \nabla\cdot\mathbf{U}_k = 0 \tag{6}$$

where f_M is a Maxwellian, $\mathbf{U}_o$ is the particle flow and $\mathbf{U}_1$ is the thermal flow. In stellarators without integral toroidal fluxes these vector moments are given by $A_k'(s)\mathbf{e_p}$; the gradients $A_k'(s)$ are related to the scalar moments of F^s [11](pressure gradients, temperature gradients etc.). These are the driving terms of drift instabilities. $F^s(v^2)$ is only destabilizing if it is non-monotonically decreasing in v^2. The destabilizing term is

$$\delta\mathbf{E}\cdot\nabla_v F^a = \sum f_M g_k \delta\mathbf{E}\cdot\mathbf{e_p}\, A_k'(s) + \frac{2}{v_\alpha^2}(f_M g_k)'\delta\mathbf{E}\cdot\mathbf{v}:\mathbf{v}\cdot\mathbf{e_p}A_k'(s) \tag{7}$$

Since drift waves have a small but finite parallel electric field $\delta\mathbf{E}\cdot\mathbf{B}$ the factor $\mathbf{e_p}\cdot\mathbf{B}$ occurs in the second term of eq.7. Retaining the gyro-angle average of the tensor $\mathbf{v}:\mathbf{v}$ yields

$$\delta\mathbf{E}\cdot\mathbf{v}:\mathbf{v}\cdot\mathbf{e_p} \to \frac{v_\perp^2}{2}\delta\mathbf{E}\cdot\mathbf{e_p} + (v_\parallel^2 - \frac{1}{2}v_\perp^2)\frac{\delta\mathbf{E}\cdot\mathbf{B}}{B^2}(\mathbf{e_p}\cdot\mathbf{B}) \tag{8}$$

Thus, the driving term of drift waves consists of three terms, one of these is proportional to the P.S-current factor $\mathbf{e_p}\cdot\mathbf{B}$. The relevance and importance of this driving term is under study.

Turbulent transport by drift waves depends on the phase relation between fluctuations $\delta\mathbf{E}(t)$ and the plasma response $\delta f(t)$. Let $\delta n_k = \int \delta f g_k\, d^3\mathbf{v}$ be the generalized density fluctuation; then the turbulent flux of the flow $\int f g_k \mathbf{v}\, d^3\mathbf{v}$ through the magnetic surface is given by

$$-\psi'(s)\Gamma_{k,t} \;=\; <\overline{\delta n_k \delta\mathbf{E}}\cdot\mathbf{e_p}> + <\overline{\delta\mathbf{E}\cdot\delta\mathbf{M}_k}\cdot\mathbf{e_p}> \tag{9}$$

where the tensor $\delta\mathbf{M}_k[f^s]$ is defined by $\delta\mathbf{M}_k =: 2/v_\alpha^2\int g_k'\mathbf{v}:\mathbf{v}\delta f\, d^3\mathbf{v}$. The overline denotes the time average. For turbulent particle fluxes ($k=0, g_o'=0$) the second term is zero and the first term is the well-known expression for turbulent losses. In case of energy losses (k=1), however, the thermal flux of the particle species α is

$$\begin{aligned} -\psi'(s)\Gamma_1 =& <\overline{\delta n_1\delta\mathbf{E}}\cdot\mathbf{e_p}> + <\frac{2c_1}{m_\alpha v_\alpha^2}\overline{\delta p_\perp\delta\mathbf{E}}\cdot\mathbf{e_p}> \\ &+ <\frac{2c_1}{m_\alpha v_\alpha^2}\overline{(\delta p_\parallel - \delta p_\perp)(\delta\mathbf{E}\cdot\mathbf{B})}(\frac{\mathbf{e_p}\cdot\mathbf{B}}{B^2})> \end{aligned} \tag{10}$$

with c_1 = const. The third term in the thermal flux contains the parallel electric field, the pressure fluctuations $\delta p_\parallel - \delta p_\perp$ and the P.S-term $\mathbf{e_p} \cdot \mathbf{B}$. This term does not arise if turbulent transport is calculated in slab geometry or cylinder geometry where PS.-currents are zero.

Conclusions Pfirsch-Schlüter currents have various negative effects on plasma confinement in stellarator geometry. The Shafranov shift and the modification of the ι-profile can be minimized to a large extent by reducing the P.S.-currents in the advanced stellarator concept. Since particle orbits and P.S-currents are linked via mod B on magnetic surfaces this reduction has beneficial effects on neoclassical transport and bootstrap effects. MHD-stability does not only depend on P.S-currents, however β-limits set by resistive interchange modes can be increased by reducing the P.S-currents. In the theory of electrostatic drift modes an extra driving term exists caused by finite P.S-currents; its influence on the growth rates needs further study. The extra term in turbulent energy fluxes is of particular interest for drift waves, since the parallel electric field $\delta\mathbf{E} \cdot \mathbf{B}$ is finite and a large anisotropy of the pressure fluctuations $\delta p_\parallel - \delta p_\perp$ has to be expected.

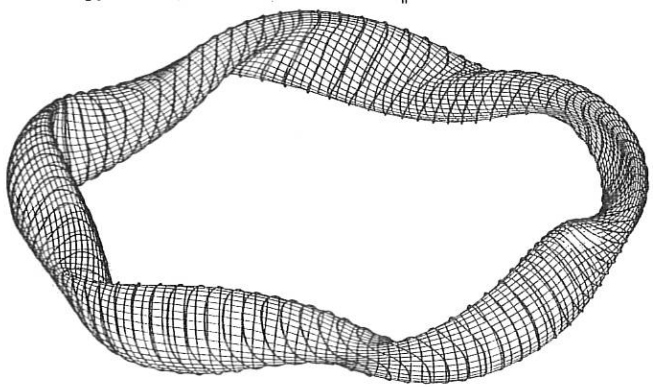

Fig. 1: *Magnetic surface of a 5-period Helias configuration. Thick lines are poloidally closed current lines. The average* $< j_\parallel^2 / j_\perp^2 >$ *is 0.5.*

References

[1] D. Pfirsch, A. Schlüter (MPI/PA/7/1962)
[2] M. Coronado, H. Wobig ,*to be published*
[3] G.Grieger et al. *Proc. 12th Int. Conf. Plasma Phys. and Contr. Fusion Res.* Nice, 1988
[4] J. Nührenberg, R. Zille, *Phys. Letters* A **114** (1986), 129
[5] A.H. Boozer, *Phys. Fluids* **27**, 2116 (1984)
[6] C.C. Hegna, A. Bhattacharjee, *Phys. Fluids* **B1** , 392 (1989)
[7] D. Palumbo, *Il Nuovo Cimento X*, **53B**, 507, (1968)
[8] W. Lotz, J.Nührenberg, *Phys. Fluids* **31**(10) ,2984 (1988)
[9] C. Beidler *this conference*
[10] S.P. Hirshman, D. Sigmar, *Nucl. Fusion*, **21**, 1079 (1981)
[11] H. Wobig, *to be published*

FIRST RESULTS OF ECRH TRANSMITTED POWER MEASUREMENTS ON RTP

F.M.A. Smits, S.L. Bank, W.A. Bongers, A.A.M. Oomens, R.W. Polman, RTP Team

FOM-Instituut voor Plasmafysica 'Rijnhuizen', Association EURATOM-FOM,
P.O. Box 1207, 3430 BE Nieuwegein, The Netherlands.

Introduction

A diagnostic, TraP, has been installed to measure the transmitted power fraction of the 60 GHz, 180 kW ECRH beam, launched in O-mode radially from the low field side into RTP. The RTP tokamak has the parameters: $R = 0.72$ m, $a = 0.17$ m, $n_e = 2 \cdot 10^{18} - 2 \cdot 10^{20}$ m^{-3}, $B \leq 2.4$ T, $I_p \leq 150$ kA and a pulse length of 250 ms. The main purposes of TraP are: (1) check ray tracing and absorption theory at high power in poloidal and toroidal direction up to densities near cut-off, to extend previous work [1,2,3,4]; (2) provide measurements of the power deposition profile as an input for local transport analysis.

Measurement set-up

TraP includes a set of 9 horns placed in an orthogonal cross at the high field side facing the ECRH launcher to determine the beam width and position in both directions (Fig. 1). The horns are embedded in a smooth top-roof mirror which prevents reflections back into the launcher. In combination with a cylindrical mirror on the low field side, it reduces the influence of unabsorbed multiply reflected rays to a negligible level. Low power measurements revealed that open ended wave guides in an oblique mirror have an asymmetric antenna pattern and are sensitive to interference due to diffraction at the mirror edges. These effects are avoided by using horns with a minimum of the antenna pattern in the direction of the diffracting edge and by rounding off the edges. Conical horns and circular fundamental wave guides receive and transmit both polarizations. Polarization scrambling in the guides caused by bends and elliptical deformations has been compensated by squeeze sections. Taking a horizontally polarized input wave and monitoring the polarization ellipse at the end of the guide, the wave guide is squeezed until the incident polarization is restored. If no other irregularities occur in the guide, the vertical polarization is then also restored. At the end of the wave guides, the horizontal polarization component is measured by diode detector units with DC-30 MHz preamplifiers. An ellipsometer [5] has been built which can measure both polarizations and their respective phase simultaneously. It is replaceable with any of the detector units. It consists of an orthomode transducer to separate the field components, and a varactor tuned Gunn oscillator with two mixers for coherent down conversion of both signals. A phase locked loop locks the Gunn within 0.5 μs to the gyrotron frequency. The 10 MHz IF signals are analysed by a vector volt meter to determine both the amplitude and the mutual phase. TraP is absolutely calibrated by in situ measurements of wave guide attenuations and detector (ellipsometer) sensitivities. A separate detection unit, called

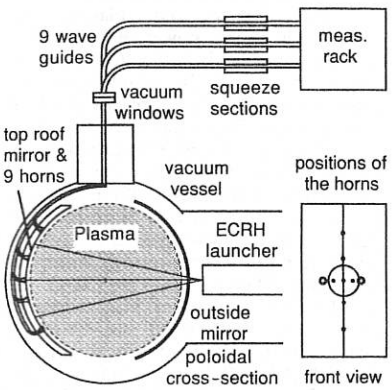

Fig.1. Experimental set-up.

'sniffer probe', has been installed in the equatorial plane at 120° toroidal angle with respect to the ECRH launcher to estimate the global absorption. For full shot recordings, the signals are 20 kHz low pass filtered and sampled at 50 kHz. For fluctuation studies, 20 kHz high pass filters are used and the sampling frequency is set to 8 MHz. A data processing code is written which calculates the main transmitted power parameters such as the horizontal and vertical beam positions and the total transmitted power in between shots.

Refraction

For the calculation of the transmitted power density distribution at the measurement surface as a function of time, and for the simulation of measured power levels, lots of ray tracing is required. Full threedimensional ray tracing is computer time consuming and not practical for the interpretation of large amounts of data. The full toroidal ray tracing code TORAY shows small focussing in toroidal direction which increases with density, and large poloidal refraction which is sensitive to the density profile and the vertical plasma position. Therefore, in toroidal direction, a first order estimate of the beam narrowing is obtained from a dataset calculated for a parabolic density profile as a function of the peak density. For data interpretation in poloidal direction, a fast poloidal ray tracing code with circular symmetry, CRAY, has been developed, based on the analytical solution of the ray equation [6]. It calculates the transmitted power density profile at the measurement surface as a function of the measured electron density profile and the plasma position. A typical output is given in Fig. 2 for the density profile of a high T_e discharge [7]. CRAY is in excellent agreement with TORAY.

The density and plasma position dependence of the power density profile is measured by having the resonance surface outside the plasma. In poloidal direction, the power density profile decreases and broadens with density. This causes the central horn signal to decrease almost linearly with density, while the outer horn signals first increase and then decrease with density. If the plasma centre reaches the cut-off density ($4.46 \cdot 10^{19}$ m^{-3}), the signals vanish. Poloidal power density profiles are given in Fig. 3 for several densities during a single shot. The solid lines are CRAY calculations for which the vertical plasma position and total transmitted power are fitted to the measurements. The total transmitted power is 170 ± 25 kW at all densities, indicating that the scattered power is negligible. The plasma position is slightly below the centre, causing

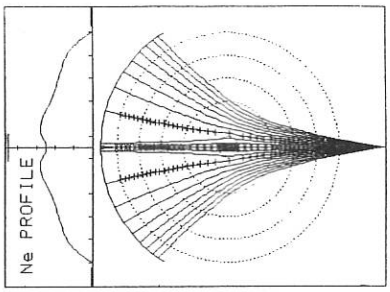

Fig. 2. Typical CRAY output.

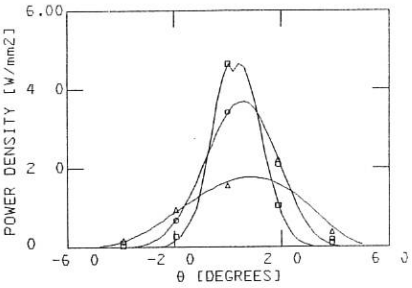

Fig. 3. Poloidal power density profiles. Symbols indicate measurements, lines are CRAY fits

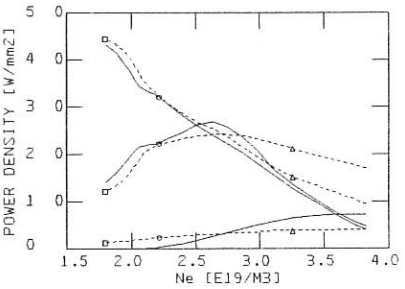

Fig. 4. Measured (dots) and fitted (full) upper horn signals as a function of peak density.

the power density profile to shift upwards with increasing density. The measured and fitted evolution of the upper horn signals as a function of peak density are given in Fig. 4. At higher densities, the fit becomes worse due to the strong dependence on the measured electron density profile. For the same shot, the toroidal beam width as a function of the peak density is determined from a Gaussian fit on the data. Within the error bars, it is in agreement with TORAY calculations for a quadratic density profile with the same peak density.

Absorption

The total absorbed power can be calculated without any ray tracing by subtracting the integrated power density profile from the input power. Assuming the beam refraction is not affected by absorption [8], the absorbed power *profiles* in poloidal and toroidal direction can be determined by calculating the transmitted power density profile at the measurement surface and subtracting the measured power density profile. Assuming localized deposition of the power at the resonance surface, the local power deposition profile can be determined from projection along the rays back to the resonance plane. In poloidal direction, application of this scheme is difficult at high densities because of the sensitivity of the transmitted power profile to small variations in the vertical position of the density maximum. In toroidal direction, projection back on the resonance surface is not possible yet due to a lack of fast ray tracing software.

Absorption experiments are performed by moving the resonance layer through the plasma during the current flat top at constant density. Fast inward and slow outward moving (1.2 m/s and 0.2 m/s), as well as a static scan has been done at several densities and plasma currents. Most of these measurements are in close agreement. The horizontal array signals are given in Fig. 5 as a function of the resonance position. The traces are built up from two different shots with the same peak density (2-2.5·10^{19} m^{-3}). The transmitted power signal decreases strongly (>10% of the input power) in a region around the plasma centre coinciding with effective heating [7]. This region increases with plasma current. The asymmetry around the plasma centre may be explained by the relativistic down shift. The central channel measures other minima at -9 cm possibly related to the q=2 surface. A strong (20% of the O-mode transmitted power) X-mode component in the central channel is observed simultaneously with the mimima. A large toroidal asymmetry is observed, coupled to a pronounced decrease in fluctuation level. Even when modulating ECRH in this region, the modulation has disappeared entirely on the

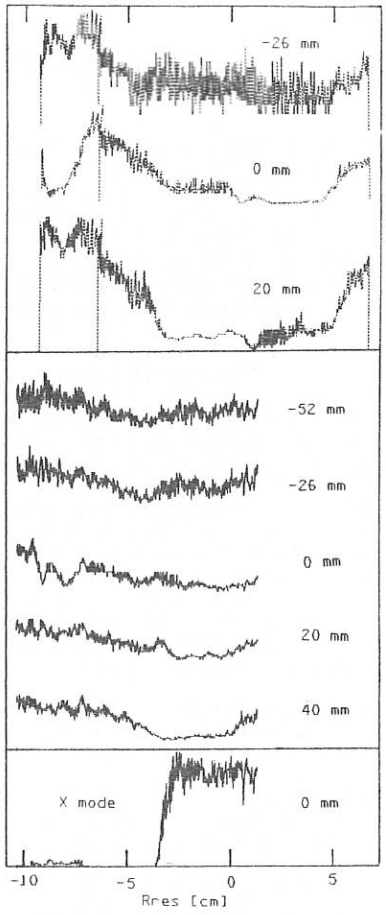

Fig.5. Traces of the horizontal array signals as a function of the resonance position. They are indicated by their position to the central horn. Full lines are for Ip = 60 kA, dotted lines are for Ip = 120 kA.

low signals. A density scan with the resonance in the centre, shows that the asymmetry and the X-mode component disappear with increasing density (Fig. 6). Generally, boronization did not affect the results significantly. At this stage, it is impossible to say whether the asymmetry is due to wave scattering, absorption, or arcing at the mirror surface.

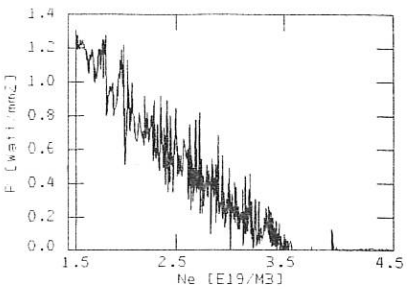

Fig. 6. The X-mode signal of the central horn as a function of the peak density for a single shot.

Sawteeth, MHD oscillations, fluctuations

The signals turn out to be very sensitive to density fluctuations and MHD activity. Small sawteeth, including the usual inversion, and m=2 activity are clearly observed. Correlation analysis of high frequency measurements during 60 kA high T_e-shots showed a strong anticorrelation between the upper and lower horns and correlation between the horizontal horns, suggesting that the observed density fluctuations may have an m=1 character. The frequency spectra show a broad peak from < 20 to 200 kHz followed by an exponential decrease of 1-2 orders of magnitude reaching noise level at 2-4 MHz.

Conclusion and discussion

An ECRH transmitted power measurement set-up has been designed, constructed and put into operation. Uncontrolled wall reflections disturbing the measurements have been prevented. Spatially resolved absorbed power profiles can be deduced from a combination of transmitted power measurements and ray tracing calculations. Refraction is in agreement with ray tracing predictions. Absorption measurements show large toroidal asymmetry accompanied by mode scrambling and a strong decrease in fluctuation level at peak densities below $3.5 \cdot 10^{19}$ m^{-3}. The diagnostic is promising for the observation of small sawteeth and MHD phenomena. Cross correlation of signals yields information on the mode number and rotation frequency. For more detailed studies, a fast toroidal ray tracing code must be developed. For the measurement of poloidal asymmetries, an additional diagnostic to determine the position of the plasma centre accurately is required. The measured signals can furthermore be projected back onto the resonance surface to obtain the local optical depths. The possibility of arcing at the mirror surface explaining the toroidal asymmetry must be checked experimentally. Further investigations at high density and several temperatures are needed to fully check linear theory.

Acknowledgement

This work was performed under the Euratom-FOM association agreement with financial support from NWO and Euratom.

References

[1] P.C. Efthimion et al., Phys. Rev. Lett. **44** (1980) 396.
[2] P.G. Schüller et al., Proc. 4th Int. Workshop on ECE and ECRH, Rome (1984) 95.
[3] H.P.L. De Esch et al., Proc. 6th Joint Workshop on ECE and ECRH, Oxford (1987) 257.
[4] V. Erckmann et al., Proc. 7th Joint Workshop on ECE and ECRH, Hefei (1989) 245.
[5] F.M.A. Smits, Proc. 7th Joint Workshop on ECE and ECRH, Hefei (1989) 389.
[6] J. Shmoys, J. Appl. Phys. **32** (1961) 689.
[7] F.C. Schüller et al., this conference.
[8] H. Weitzner, Phys. Fluids **23** (1980) 1359.

MEASUREMENTS OF PLASMA POTENTIAL IN T-10

Melnikov A.V., Tarasyan K.N., Vershkov V.A., Dreval V.A., Sushkov A.A.
I.V.Kurchatov Atomic Energy Institute, Moscow, USSR,
Krupnik L.I., Nedzelskij I.S.
Kharkov Physical-Technical Institute, Kharkov, USSR,
Kharchev N.K.
Institute of General Physics, Moscow, USSR.

The dynamics of radial electric field in a tokamak plasma affects considerably on the processes of radial particle transport and on the transitions into the improved confinement regimes (L-H, S-B transitions, etc.). To study the plasma electric potential in T-10 a diagnostic system for plasma probing by a beam of Cs^+ ions with the energy up to 160 keV was developed [1]. The schematic location of the elements of the diagnostic complex in a midplane of the facility is given in Fig. 1. A peculiar feature of this complex is the presence of an electrostatic plates P in front of the aperture of the secondary ions analyzer A. The electrostatic plates correct the toroidal displacement of secondary ions which is caused by the magnetic field poloidal components. Fig. 2 shows a calculated detector grid in the midplane of the plasma column with correspond values of beam energies and injection angles. The measurements were carried out in the points of detector line r = 19-31 cm (fat line). Spatial resolution of measurements is 1 cm.

The measurements were performed in the regime with the magnetic field B_T = 1.5 T, I_p = 135 kA and with a sharp turn-off a gas-puffing valve on 265 ms of the discharge. In that moment plasma density reached it's critical value. The time evolution of some discharge parameters are shown in Fig.5. This regime is similar to the one studied earlier (S-B transition at B_T = 3.0 T, I_p = 200 kA [2]).

Radial profiles of plasma potential in the regime to be investigated are shown in Fig.3. Two potential profiles are given for every moment of time (a,b,c): for the regime with a circular graphite limiter r_L = 33 cm (light circle) and for the regime with the rail limiter r_L = 30 cm introduced from the lower port (black stars). The chamber radius is r_W = 38 cm.

Heavy ion beams method's measurements are supplemented with the data of Langmoure probes (black circle) that were set on the top of rail and on

the circular limiters.

The errors in absolute values of plasma potential are determined, mainly, by the accuracy of secondary ions current on the analyzer collector plates measurements . An accelerating and analyzing voltages set up with some uncertainty, which has systematic character. So the absolute referencing in the potential profile (a possible vertical displacement of the curve) equals±150V. Note, that an error in a relative time dependence of the potential is much less, since it can be taken during single discharge (the influence of the variations between the pulses is excluded; the angle of particles entrance into analyzer does not change).

One may clearly distinguish three regions on the potential profile:
I - the internal region of a weak electric field (r = 19 - 24 cm);
II - the region of a strong electric field, that locates closer to limiter (r = 24 - 28 cm);
III - the pre-limiter region with a weak positive or negative electric field (r = 28 - 38 cm).

Mean electric field value in the whole region of measurements is 100 V cm^{-1}, and in the second region up to 200 V cm^{-1}. The potential flattening in the first region may be connected with the development of the magnetic island in the vicinity of a surface q=2. A peculiar electron temperature profile flattening indicates to its presence. The dimension of the second region practically coincides with the characteristic depth of cold neutrals penetration into plasma. From Fig.4 it is seen that in the potential response to gas-puffing turn-off, there is a qualitative difference between the third region where the potential starts to decrease at once and the first and the second regions where potential grows with time-delay. Hence, time evolution of the potential in very external point (r=31cm) correlates well with the time variation of flow from plasma to the circular limiter. The decrease of the flow after the valve's turning-off correlates with the decrease of the electrical field absolute value in the third region, and the successive increase of the flow (325 ms) leads to the field increase. The increasing of plasma flow on the limiter is typical to the regime with the switching off valve and can be explained by the broadening of the plasma column. The potential time evolution in the first region is explained clearly by behaviour of the density integrated along the 20 cm - chord. A considerable growth of the potential in this region occurs after density drop lower than the initial value. Similar dependence of plasma potential on density was observed in TM-4 experiments [3].

The experiments with the disruption regimes showed a sharp growth of plasma potential which observed at 25ms before the disruption that correlates with MHD-activity increase (Fig.5). Here solid lines is disruption, dashed lines - turn-off the gas-puffing regime. The similar effect was seen in ISX-B tokamak [4] as well as in TEXT [5] in the experiments with magnetic surfaces ergodisation by means of special coils.

In conclusion let us note that mean value of the electric field in the external region of the plasma column (r/a = 0.6-1) is 100 V cm^{-1} and it is up to 200 V cm^{-1} in the region of neutrals penetration.

ACKNOWLEDGEMENTS

The authors are grateful to K.A.Razumova and Yu.N.Dnestrovskij for interest to this work and fruitful discussions.

REFERENCES

1. Bondarenko I.S. et al. In: 5-th All Union conference on high temperature plasma diagnostics. USSR. Minsk, 1990, 186.
2. Alikaev V.V. et al. Plasma Phys. and Cont. Fusion., 30, 381 (1988).
3. Bugarya V.S. et al. Nuclear Fusion, 25, 1707 (1985).
4. Schoch P.M. et al. 15-th European Conf. on Contr. Fusion and Plasma Phys., Dubrovnik, 1988, 1, 191.
5. Groebner R.J. et al. 16-th European Conf. on Contr. Fusion and Plasma Phys., Venice, 1989, 1, 245.

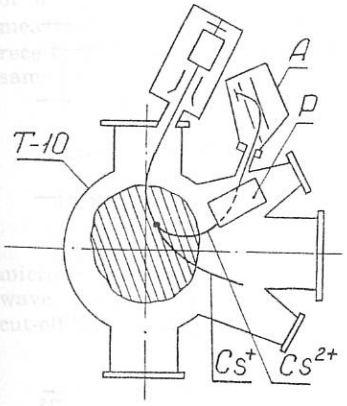

Fig.1

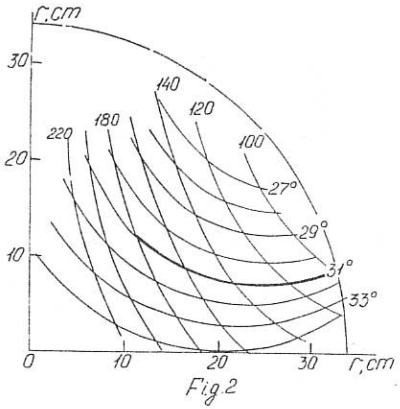

Fig.2

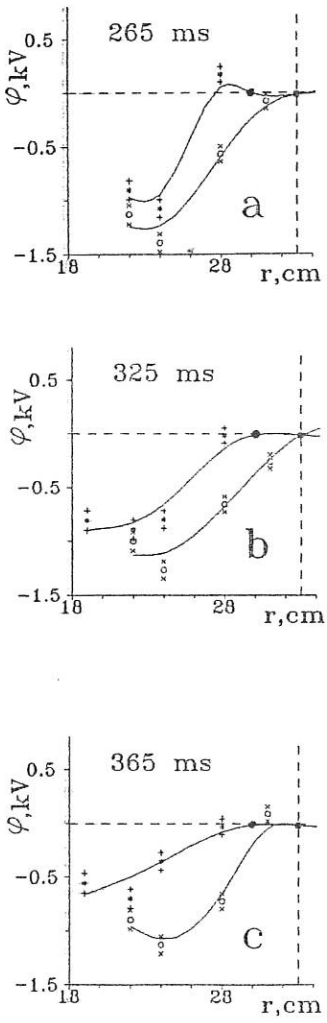

Fig. 3

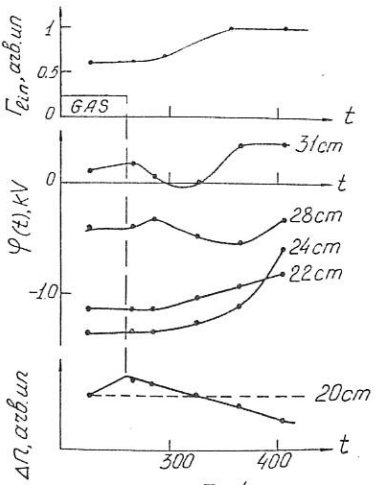

Fig 4

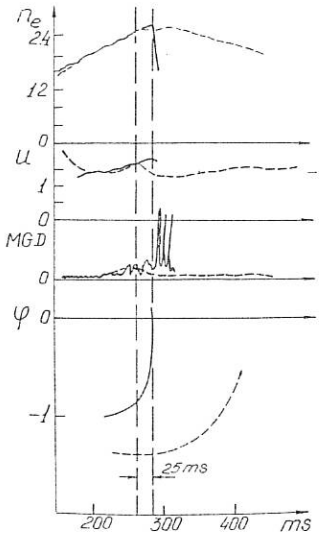

Fig 5

TWIN E-MODE REFLECTOMETRY FOR MAGNETIC FIELD MEASUREMENTS IN TOKAMAKS

E.Lazzaro, G. Ramponi.
Istituto di Fisica del Plasma, Associazione EURATOM- ENEA-CNR, via Bassini 15, 20133 Milano, Italy

Introduction

In recent years microwave reflectometry has been more and more used as a succesful means for diagnosing fusion plasmas/1,2,3/. The method is based on the propagation and reflection of a probing wave in an inhomogeneous plasma. Two modes of operation are possible, depending on the polarization of the injected waves: the ordinary O or Extraordinary E mode. In the O-mode, the reflection condition (cut-off) depends only on the local plasma density, allowing measurements of the density profile in the swept frequency operation, or of movements of the density layers in the fixed frequency operation. For the E-mode there are two possible reflection layers, at the "lower" ω_L and "upper" ω_U cut-off respectively:

1) $\omega_L = -\frac{1}{2}\omega_{ce} + \sqrt{\frac{1}{4}\omega_{ce}^2 + \omega_p^2/(1 - n_{//}^2)}$

2) $\omega_U = +\frac{1}{2}\omega_{ce} + \sqrt{\frac{1}{4}\omega_{ce}^2 + \omega_p^2/(1 - n_{//}^2)}$

Each one of the two cut-off conditions depends both on the density and on the magnetic field. Consequently reflectometry in the E-mode is generally considered suitable to give informations on the density profile when the the magnetic field is known or viceversa. Here we present the principle and give a preliminary assesment of sensibility and applicability of an alternative method of using refllectometry in the E mode. We suggest that simultaneous measurements at ω_U and ω_L in swept frequency operation (by launching and receiving the waves in the equatorial plane from the low-field side, along the same line of sight), could give the "total" magnetic field profile, by noting that:

3) $\omega_U - \omega_L = \omega_{ce}$

4) $\omega_p^2 = (1 - n_{//}^2)\omega_L \omega_U$

Principle of the measurement

The principle of a reflectometer consists in phase measurements of a microwave wave reflected by a cut-off layer in comparison with a reference wave. The phase difference for a wave launched from R_{out} and reflected on a cut-off layer located at a (major) radius $R_c > R_0$ is /4/:

$$5)\quad \Phi(R_c)=\frac{2\omega}{c}\int_{R_c}^{R_{out}} n_\perp(\omega,\omega_L(R),\omega_U(R))dR-\frac{\pi}{2}$$

The R dependence is through the cut-off frequency,therefore it is possible to probe different radial positions by sweeping the frequency . The formal inversion of relation (5) yields:

$$6)\quad R_\omega - R_{out}=-\frac{c}{2\omega}\int_{\omega_{min}}^{\omega}\frac{\frac{d\Phi}{dv}}{n_\perp(\omega,v)}dv$$

The task is to find, for a fixed value of ω_L a value of ω_U such that $R\omega_L=R\omega_U$: in this case relation (3) gives directly $\omega_{ce}(R)$. A numerical iterative technique has been developed to solve this equation in the unknown ω_U, for given tabulated values of the group delay times $d\Phi/dv$, obtained experimentally, and containing the information on the magnetic field . The theoretical expression for the E- mode group delay time is :

$$7)\quad \tau(\omega_{L,U})=\frac{d\Phi}{d\omega}=\frac{2}{c}\int_{R_{L,U}}^{R_{out}}\frac{\omega^4+\omega_{UH}^2(\omega_L^2+\omega_U^2-2\omega^2)-\omega_L^2\omega_U^2}{n_\perp(\omega)(\omega^2-\omega_{UH}^2)^2}dR$$

Preliminary Tests

In order to simulate the "possible" results of such a measurements in a JET-like plasma, we use the following profiles and data:
Density profiles:

$$n=n_0(1-r^2/a^2)^\alpha$$

Magnetic field including poloidal and paramagnetic components:

$$B(r)=B_0\frac{\left[1+\beta e^{-.25r^2}\right]}{1+r/R_0}\sqrt{1+\left(\frac{r}{R_0 q(r)}\right)^2}$$

where:

$$q=q_0+(q_a-q_0)r^{2\gamma}$$

with
a=1m,R_0=3m,B_0=3.4T, n_0=3x10 cm-3, q_0=1, q_a=3, α=1-3, β=0.--.1, γ=1--3.
In Figs.1,2 the "expected" values are shown of the delay time for E-waves propagating perpendicularly to the magnetic field in the equatorial plane from the low field side toward the upper and lower cut-off layers, respectively. Figures 3 and 4 show the positions of the reflection points in the two ranges of frequencies. First we note that the ranges of chosen frequencies cover a sufficiently large portion of the plasma, which width depends obviously on the density profile.

We also note that , for a 10% variation of the paramagnetic field, the typical percent variation of the delay time is 40% for the upper cutoff and 25% for the lower cutoff. Moreover both the cutoff layers are sensitive, as expected, to density profile variation but the E.C. frequency, as difference of the two corresponding cutoff frequencies, is free from all systematic errors and independent on the density. We finally note that a direct deduction of the poloidal field is however impractical because the required accuracy on ω_{ce} should be better than 0.1% to appreciate a variation of 10% in the poloidal field.

Preliminary tests show that twin reflectometry at both the E-mode cutoffs, could provide direct information on the paramagnetic field distribution,free from systematic errors on the density profile.This diagnostic technique can reach the central plasma region if the density profiles are sufficiently peaked. The full reconstruction of the poloidal field profile is then made easier by inserting the explicit information on the paramagnetic field profile in the expression of the toroidal current density used in a Grad-Shafranov equilibrium solver:

$$J_{\varphi}(R,\psi) = R\frac{dp}{d\psi} + \left[\frac{2\pi m}{e}\right]^2 \frac{\omega_{ce}}{\mu_0}\frac{dR\omega_{ce}}{dR} - \frac{\nabla\psi\partial\psi}{\mu_0 R\partial R}$$

The single remaining unknown source function $dp/d\psi$ can be obtained by fitting to other kinetic measurements. Limitations of this diagnostic technique are due to poor spatial resolution in the low frequency range of the lower cutoff, near the plasma edge. The spatial resolution improves moving towards the central region ,and is increasing with the central plasma density, the magnetic field (i.e. for short wavelenghts) and with the density gradient.

REFERENCES

/1/ R. Prentice et al. Proc.17th EPS Conference on Contr. Fusion and Plasma Heating, Amsterdam Vol 14 B part III p. 1500 (1990)
//2/ E .Anabitarte et al. ibid. p.1492
/3/ M.Manso et. al. ibid. p.1552
/4/W.L.Ginzburg,"Propagation of Electromagnetic waves in plasmas",Gordon and Breach Inc. 1961

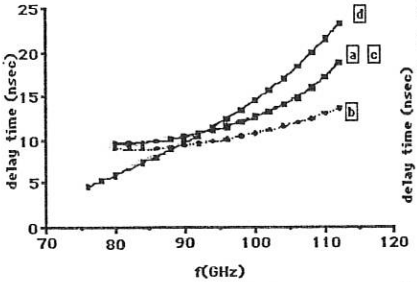

Fig.1-Group delay time for X wave propagating from the low field side toward the upper cutoff layer.
Curve: a) reference case with $\beta=0, \alpha=3, \Upsilon=1$; b) with $\beta=0.1$; c) with $\Upsilon=3$; d) with $\alpha=1$.

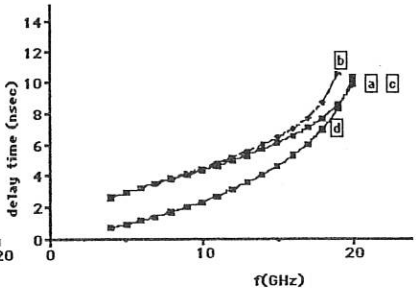

Fig.2-Same as Fig.1, but for the Lower cutoff frequency range.

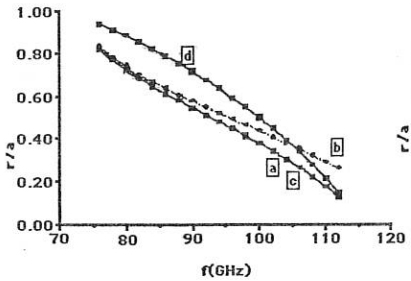

Fig.3-Position of the reflection points for the cases of Fig.1.

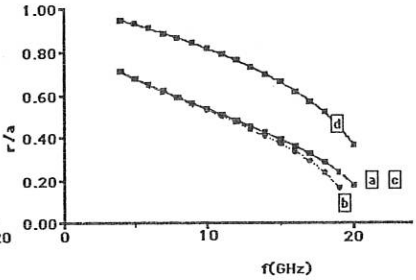

Fig.4-Same as Fig.3, but for the Lower cutoff frequency range.

MAGNETIC FIELD MEASUREMENTS AT JET BASED ON THE FARADAY AND MOTIONAL STARK EFFECTS

C Challis, M von Hellermann, B Keegan, R König, W Mandl, J O'Rourke, R Wolf, W Zwingmann

Jet Joint Undertaking Abingdon, Oxfordshire OX14 3EA, UK

INTRODUCTION

An integrated identification of the plasma equilibrium which makes use of the poloidal flux and the tangential magnetic field at the vacuum vessel, as well as measurements of the Faraday effect along vertically probing chords, has recently been developed and tested at JET /1/. We report on the study with this of the current broadening in a 2.2 T, 3 MA, single-null X-point plasma during 7 MW of neutral beam injection. Details of the measurement of the motional Stark effect, the magnitude of which is given by the Lorentz field experienced by the neutral beam, and its incorporation into the equilibrium identification algorithm are described.

FARADAY EFFECT

The rotation of the polarisation angle of far-infrared radiation provides a line-integrated measurement of $\int B_{||} n_e \, dl$. In JET laser light at 195 μm is used. There are six vertical and one oblique viewing chords. The Faraday angles (typically ~ 0.2 rad) are measured with 1% sensitivity and 5% accuracy with a time resolution of 1-10 ms /3/.

MOTIONAL STARK EFFECT

A local measurement of the toroidal and poloidal magnetic fields is obtained from the Doppler shifted emission from deuterium in the neutral beams due to the Motional Stark electric field $E = v_{beam} \times B$. Both the magnitude and the direction of the electric field vector are measured.

The beam emission spectra are observed via a horizontal fan of eight viewing lines, intersecting the JET neutral heating beams near the midplane of the torus at major radii between R = 305 cm and R = 370 cm. The magnetic axis of JET is in the vicinity of R = 310 cm , the last closed flux surface lies at R = 410 cm. The angles between the viewing lines and the neutral beams are in the range of 120° to 150° causing a Doppler shift of the beam emission spectrum. The observation port consists of a lens system with 1.0 mm optical fibres in the focal plane, each corresponding to a single viewing line. 90 m of fibres relay the collected light to the spectrometer, where the spectra are imaged on a two dimensional CCD detector, which in the present set-up is able to detect up to 12 spectra simultaneously with an integration time in the range of 50 to 100 msec. The neutral beams are viewed indirectly via a nickel mirror, which has a special coating to minimise polarisation effects. The mirror can be folded back to protect itself and the vacuum window behind it from being coated during discharge cleaning or beryllium evaporation. The incoming light is split by means of two polarising beam splitter cubes into two perpendicular polarised components with one fibre for each component. With this technique, giving a full spectrum for each polarisation component, the polarisation direction at three plasma locations could be measured simultaneously.

A typical set of spectra each corresponding to a polarisation component is shown in Fig.1. The radial positions are determined from the Doppler shift between the cold edge feature and the

Stark spectrum. From the intensity ratio of the Stark π-components, which are strictly linearly polarised, the angle of the Stark electric field is calculated. The two detection channels for the perpendicular polarisation directions are calibrated against each other by using the unpolarised bremsstrahlung background. To obtain the full spectral resolution a multi-Gaussian fit is used. Making use of the known symmetries and line ratios of the Stark multiplet /2/ the number of free parameters used is kept to a minimum. It enables the Stark π-components to be separated from the σ-components and the bremsstrahlung background leading to a determination of the Stark splitting from which the magnitude of the local electric field is derived.

At present the magnitude of the electric field can be determined with an uncertainty of less than 1%, the polarisation angle within the range of ±0.5° to ±1.0° depending on the intensities of the spectra. This leads to an error of toroidal magnetic field of less than 2% and an absolute uncertainty of the poloidal magnetic field of 0.03 T to 0.04 T.

EQUILIBRIUM IDENTIFICATION

The equilibrium state is calculated from measurements with a modified version of the code IDENTD /1/. The identification is done by fitting a cost function to the measurements with the constraint of the Grad-Shafranov equation of the flux function Ψ. The control variables are the parameters **a**, **b** and β of the toroidal current density profile, defined by

$$j_{tor} = R\,\beta\,A(\Psi,a) + (1-\beta)\,B(\Psi,b)/R.$$

A and B are chosen to be piecewise linear functions (R: radius). The cost function is formed by the sum of the squares of the differences between numerically obtained and measured quantities and is given by

$$K = \sum_{i=1}^{N} w_i \cdot (f_{i,calculated} - f_{i,measured})^2 + \mu \cdot \Omega[\psi].$$

The w_i are related to the errors of the measurements and must be chosen accordingly. The regularising term Ω controls the smoothness of the current density. Its parameter μ has to be adjusted to fit the measurements within these error bars, but preventing unphysical oscillations of the current. The original version of IDENTD includes magnetic measurements of 14 flux loops and 18 pick-up coil at the vessel contour, the plasma current, the diamagnetic signal, the Faraday rotation values as described above and the total pressure profile. The measurement of the Stark electric field was included recently. The magnetic field cannot be deduced directly from the Stark measurements, because the magnetic field component parallel to the neutral beam velocity v_{beam} is undetermined. Therefore the E values defined by

$$E = v_{beam} \times B = (v_{beam} \cdot e_{tor}\ \nabla\Psi + v_{beam} \times e_{tor} - v_{beam} \cdot \nabla\Psi \cdot e_{tor})/R$$

are fitted (e_{tor} is the unit vector in toroidal direction).

RESULTS

Pulse #21022 is a 2.2 T, 3 MA, single-null X-point discharge in which 7 MW of neutral beam injection (NBI) produced a H-mode lasting some 4.5 sec. No Stark effect data are available for this pulse so that only magnetic and Faraday data are used. Fig. 2 shows the change in the current distribution between the end and the beginning of the H-mode phase. Also shown is the change calculated using neo-classical resistivity (including the bootstrap current). The steep density gradients produced by the H-mode drive a large bootstrap current (~ 0.5 MA) in the outer portion of the discharge, causing a broadening of the current distribution in good agreement with the integrated equilibrium analysis /4/. The discrepancy near the centre can be attributed to the fact that the diffusion calculation does not include any effect of sawteeth on the current distribution.

Incorporating the Stark effect a 2.9 T, 2.1 MA discharge (#22826) with 2.8 MW of NBI has been investigated. The discharge shows sawtoothing behaviour during the investigated time slices. The calculated equilibrium without including Faraday and Stark effects give a q on axis well above 1. The Faraday data lead to a equilibrium with q_o near to 1. Since no Faraday data

were available at the plasma centre, the equilibrium calculations still do not produce a well defined q_0. Although an uncertainty in the alignment of the Stark measurement has not been resolved totally, adding the results from the Stark effect indicates that q_0 is below 1. Fig. 4 shows the obtained q- and current density profiles. In Fig. 3 the measured Faraday and Stark data are compared with the results obtained from the equilibrium calculations. All measurements are fitted within their experimental uncertainties.

SUMMARY

The above results show that both Faraday and Stark data representing measurements from the inner plasma influence the outcome of the calculated equilibrium significantly and can be used to study non inductive currents. The radial variation of the Stark electric field indicates that q_0 in #22826 is below 1 during the time slice considered.

REFERENCES

/1/ J. Blum et al., Nuclear Fusion, 30(1990)1475.
/2/ A. Boileau et al., J. Phys. B, 22(1989)1145.
/3/ G. Braithwaite et al, Rev. Sci. Inst., 60(1989)2825.
/4/ D Pearson et al., "Latest JET experimental results on the sawtooth", this conference.

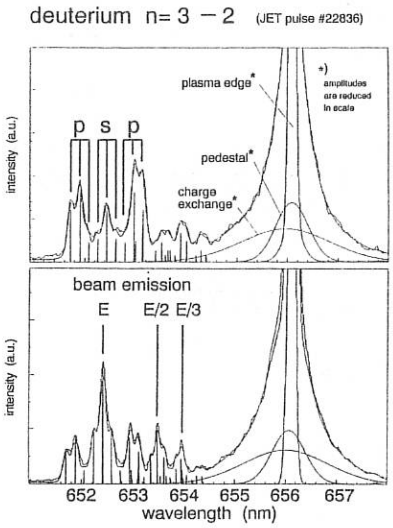

Fig. 1 Spectra of the two perpendicular polarisation components from one plasma location of the deuterium Balmer-α n=3 - 2 transition showing the Stark components with σ (s) and π (p) polarisation. The deuterium emission from the full, half and third energy fraction are marked with E, E/2 and E/3 respectively. Over the measured signal the fitted multi-Gaussian function is plotted. The spectra come from a single 40 keV/amu JET heating beam. The charge exchange part of the spectra is described elsewhere /2/.

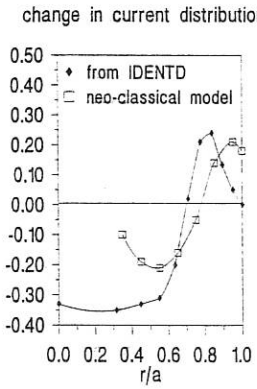

Fig. 2 Change of current distribution during beginning and end of H-mode phase (#21022, r/a: relative minor radius).

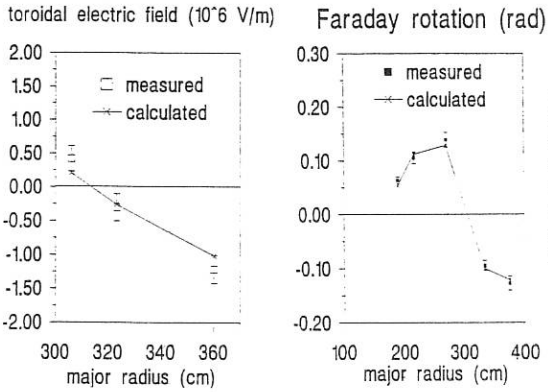

Fig. 3 Measured Faraday rotation angle and toroidal electric field from Stark effect in comparison with the results from the equilibrium calculation. The measurement errors are indicated by vertical bars.

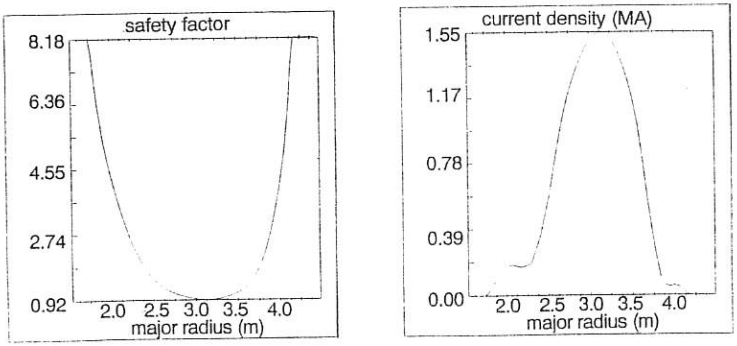

Fig. 4 q- and current density profiles (#22826) from IDENTD calculation with Faraday and motional Stark measurements included.

The Correlation of Magnetic Flux Surfaces With Soft X-Ray Iso-emissivity Surfaces in COMPASS-C

R.D. Durst, P. Haynes

UKAEA Fusion/Euratom Association
Culham Laboratory, Abingdon, Oxon OX14 3DB, UK

1 Introduction

It is often assumed that the surfaces of soft x-ray (SXR) iso-emissivity and magnetic flux surfaces are identical. Indeed, it has been proposed that a knowledge of soft x-ray iso-emissivity surface geometry may be used to determine the details of the interior equilibria in tokamak discharges [1,2,3]. However, the level of correlation of SXR iso-emissivity surfaces with flux surfaces is not well established experimentally. In this work this correlation is studied for a variety of discharge conditions in the tokamak COMPASS-C. It is found that a significant up-down asymmetry can occur (of the order of the inverse aspect ratio, ϵ), principally at high density. Neoclassical theories of impurity distribution on a flux surface [4,5] reproduce both the sign, magnitude and the scaling of the asymmetry.

2 Poloidal Asymmetries in Impurity Density

Poloidal asymmetries in the radiation from the plasma edge have been observed on a number of machines including Alcator [6], PDX [7], TFTR [8] and JET [5]. Poloidal asymmetries at the edge may be caused by localized neutral sources due to plasma-surface interaction or gas refueling. However, there is strong evidence that such asymmetries may often be due to a variation of impurity density around flux surfaces such as predicted by theories based on neoclassical impurity transport [4,5]. Feneberg et al. [5] give this up-down asymmetry (in the absence of poloidal rotation) as

$$\frac{n_Z^{(1)}}{n_Z^{(0)}} = \frac{2\epsilon\Omega}{\Omega^2 + 1} \tag{1}$$

where ϵ is the inverse aspect ratio, a/R, $n_Z^{(0,1)}$ are the symmetric and up-down asymmetric part of the impurity density, i.e.,

$$n_Z = n_Z^{(0)} + n_Z^{(1)} sin(\theta) \tag{2}$$

and Ω is the ion collisionality parameter

$$\Omega = -\frac{\omega_{ci}\tau_{ii}\epsilon^2 P_i}{q^2 Z^2 \rho P_i'}. \tag{3}$$

Here ω_{ci} is the ion cyclotron frequency, τ_{ii} is the ion-ion collision time, P_i is the ion pressure, P_i' is the radial ion pressure gradient, q is the local safety factor, Z is the ionic charge and ρ is the radial flux surface coordinate.

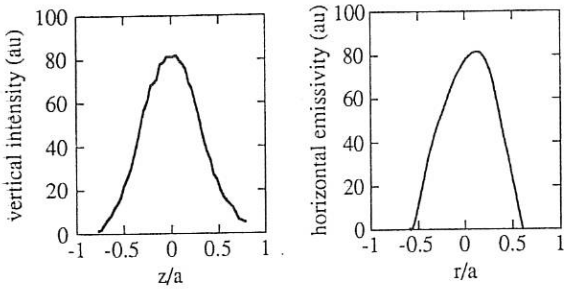

Figure 1: Examples of raw, vertical and Abel inverted, horizontal soft x-ray profiles produced by the tangentially viewing soft x-ray camera.

A smaller, in-out asymmetry is also predicted

$$\frac{n_Z^{(2)}}{n_Z^{(0)}} = \frac{2\epsilon}{\Omega^2 + 1} \tag{4}$$

This theory has been successful in reproducing the poloidal dependance of the edge emissivity in JET. However, note that equations 2 and 4 also imply the existence of significant poloidal asymmetries in the interior impurity densities. This would lead to a decorrelation between the SXR iso-emissivity surfaces and magnetic flux surfaces.

3 Description of the Experiment

COMPASS-C is a compact, circular tokamak (R=0.55 m, a=0.196 m) with a full aperature poloidal limiter (graphite), and a boronized vacuum vessel. The 2-dimensional distribution of soft x-ray intensity is imaged by a tangentially viewing soft x-ray camera [9]. The camera has a resolution of 128x128 pixels which is, in practice, reduced to 64x64 by averaging adjacent pixels. This corresponds to a 5 mm spatial resolution in the plasma. The spectral response is set by a 9 micron aluminium foil filter to the region of 1-10 keV [9]. In this region the spectrum is seen to be dominated by recombination continuum. The temporal resolution of the system is typically 10-16 msec. This means that many sawtooth cycles are averaged. The diagnostic incorporates a microchannel plate intensifier which may be gated so that the sawtooth crash is not integrated.

Figure 1 shows typical vertical and horizontal data from the tangential SXR camera. Note that vertical asymmetries can be detected by direct inspection of the raw data as shown. However, to detect horizontal asymmetries the raw data must be Abel inverted and then compared to the flux surface geometry (which is derived from magnetic diagnostics).

4 Vertical Asymmetries

To characterize vertical asymmetries the asymmetry factor, $\Delta_v = n_Z^{(1)}/n_Z^{(0)}$, or the skewness, ξ, may be used. The skewness is a measure of asymmetry defined by

$$\xi \equiv \frac{\mu - \varpi}{\sigma} \tag{5}$$

where μ is the mean of the distribution, ϖ is the mode (maximal point) of the distribution and σ is the standard deviation. In practice, for experimental data ξ is calculated using Pearson's

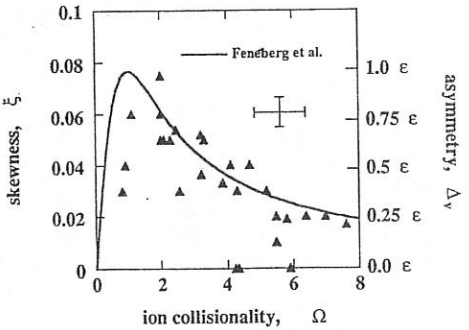

Figure 2: The vertical asymmetry as a function of the ion collisionality parameter, Ω. The range of discharge conditions represented is, $q_a = 2.3 - 6.0, \bar{n}_e = 0.9 - 6.0 \text{x} 10^{19} m^{-3}, T_i(0) = 100 - 160 eV$.

formula for a unimodal distribution which expresses the skewness in terms of the first four moments of the distribution [10].

For small asymmetries ξ and Δ_v are equivalent in that they are proportional to each other. However, ξ has the advantage of relative insensitivity to noise compared to the asymmetry factor. Also, note that ξ is invariant under translation: it only measures changes in shape, not positional shifts. Thus a vertical shift of the plasma can not be misinterpreted as an asymmetry.

The vertical skewnessess for a variety of COMPASS-C discharges are plotted in figure 2 together with equation 1. The right hand scale shows the asymmetry factor (proportional to skewness for small Δ_v) at $\rho = 0.3$. The dimensionless pressure scale lengths, $\partial P_i / \partial \rho \; P_i^{-1}$ are assumed to be in the range 3-4. Because of its boronized vacuum vessel the dominant impurities in COMPASS are boron and carbon and thus Z is taken as 5-6. The data show a fairly clear correlation with the prediction of equation 1.

Equation 1 predicts that the direction of the asymmetry depends on the direction of the toroidal field. Normally the COMPASS-C toroidal field is clockwise which leads to an enhancement in SXR emission from the top of the torus. Reversal of the field direction was found to reverse the sense of the vertical asymmetry in agreement with equation 1.

5 Horizontal Asymmetries

Horizontal asymmetries are more difficult to measure as the SXR data must be Abel inverted, then compared to the Shafranov shifted flux surfaces as reconstructed from magnetic data. As there are appreciable errors associated with both the Abel inversion and the flux surface reconstruction this technique can only hope to identify fairly large in-out asymmetries: asymmetry factors smaller than 0.3 cannot be reliably detected using this procedure. Also, only a small number of discharges have been analysed in this way.

The Abel inversions were performed by assuming toroidal symmetry and using the Bayesian Regularized Algebraic Reconstruction Technique [9]. The errors in the shifts derived from this procedure are estimated to be about 20% near the peak to about 70% near the edge of the profile (because of the smaller signal to noise ratio at the edge).

The flux surfaces were reconstructed from the experimental magnetic coil and flux loop data using a forward modelling technique. A database of 1000 near circular discharges was generated using a free boundary equilibrium code. This data base was then searched to find the best fit between the calculated equilibria and the experimental magnetic measurements.

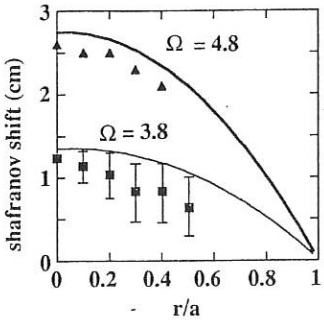

Figure 3: The Shafranov shifts from magnetics and SXR data for two discharges where $\Omega = 4.8$ (upper curve from magnetics, triangles from SXR) and $\Omega = 3.8$ (lower curve with squares).

Two techniques have been used to perform this fitting procedure: a least squares minimization and a novel, neural network approach. In the neural network technique a multi-layer perceptron [11] with 15 hidden neurons was trained using 250 of the model equilibria and tested using the remaining 750. For realistic noise levels both systems perform similarly and can reproduce the Shafranov shifts in the interior ($\rho \leq 0.6$) to within 15-20%.

Figure 3 shows a comparison between the Shafranov shifts calculated from the inverted SXR emissivity profiles (triangles and squares) and the shifts derived from magnetics (solid lines) for two discharges. Any in-out asymmetries of the SXR emissivity would cause a relative distortion between the curves derived from SXR's and magnetics. Though differences are apparent they are within the experimental uncertainties. It thus appears that there are no large ($\Delta_h > 0.3$) in-out asymmetries in the SXR emission. This is consistent with theory as equation 4 predicts that $\Delta_h < 0.1$ for $\Omega = 3 - 5$.

6 Conclusions

It is seen that there can exist significant differences between SXR iso-emissivity surfaces and magnetic flux surfaces in the plasma interior. In COMPASS-C vertical asymmetries are seen which are thought to be due to the variation of impurities along a flux surface. The sign, magnitude and scaling agree with the neoclassical theory of Feneberg et al [5]. In practice this means that the asymmetry scales mainly with the central density and can reach values on the order of the inverse aspect ratio at high density. Within the accuracy of the experiments performed to date no significant in-out asymmetries are seen in the interior of COMPASS-C.

[1] Christiansen, J.P. and Taylor, J.B., Nuclear Fusion 22, 111 (1982).
[2] Christiansen, J.P., Callen, J.D., Ellis, J.J., Granetz, R.S., Nuclear Fusion 29, 703 (1989).
[3] Powell, E.T., Ph.D. Thesis, Princeton University, 1991.
[4] Burrell, K.H. and Wong, S.K., Nuclear Fusion 19 (1979).
[5] Feneberg, W., Mast, F.K., Gottardi, N., Martin, P., JET-R(86)07.
[6] Terry, J.L., Marmar, E.S., Chen, K.I. and Moos, W.H., Phys. Rev. Lett. 39, 1675 (1977).
[7] Brau, K. and Suckewer, S., Nuclear Fusion 23, 12 (1983).
[8] Schivell, J., and Bush, C.E., Rev. Sci. Insrum. 57, 2081 (1985).
[9] Durst, R.D., the COMPASS Group, Rev. Sci. Instrum., 61, 2751 (1990).
[10] Kendal, M. and Stuart, A., The Advanced Theory of Statistics, Charles Griffin, 1977.
[11] Lister, J.B. and Schnurrenberger, H., LRP 397/90, CRPP Lausanne (1990).

IMPURITY ATOMS DIAGNOSTIC BY OBSERVATION OF NEAR-RESONANT RAYLEIGH SCATTERING

A.B. Berlizov, I.V. Moskalenko and D.A. Shcheglov

I.V. Kurchatov Institute, Moscow, USSR

The studies of near-resonant Rayleigh scattering (NRS) of laser light provide data related to interaction light with atoms, but also considered to be useful as preparatory steps for development of NRS-diagnostics for fusion plasmas [1-3].

This paper describes the application of NRS-technique for spatially resolved measurements of atoms density in a plasma. We treat this method to be supplementary to LIF-technique and useful in the cases when: (1) medium under investigation is optically thick in the line center; (2) fluorescence is influenced by collisions in the plasmas; (3) high level of line background radiation is present; (4) lidar scheme of measurement is desirable. We report on our selections of atomic transitions, the development of lasers for NRS method and scattering experiment at barium atoms.

THE SCATTERING CROSS SECTION AND SATURATION OF NRS SIGNALS

The cross section for scattering of laser frequency ω_L is given by [1]:

$$\frac{d^2\sigma_R}{d\Omega_s d\omega_s} = \frac{\omega_L \omega_s^3 |\langle 1|\vec{e}_L\vec{d}|2\rangle|^2 \; |\langle 2|\vec{e}_s\vec{d}|1\rangle|^2}{\hbar^2 c^4 \left[(\omega_L-\omega_0)^2 + \Omega_R^2 + \Gamma^2\right]}, \quad (1)$$

where ω_s and ω_0 are the frequencies of scattered light and atomic transition, respectively, $\vec{e}_L$, $\vec{e}_s$ - the polarization vectors. $\Gamma = \gamma_N + \gamma_E + \gamma_I$, where γ_N - the rate of natural radiative decay of the excited state; γ_E, γ_I - rates of elastic and inelastic collisions; $\langle 1|\vec{e}_L\vec{d}|2\rangle$ - is a matrix element for transition between two relevant states. The Rabi frequency is defined as $\Omega_R = \langle 1|\vec{e}\vec{d}|2\rangle E_0/\hbar$

Laser intensity $I_L \sim \Omega_R^2$ and Rayleigh scattering intensity I_R for collisionless regime is proportional to

$$I_R \sim \Omega_R^2/(\Delta^2 + \Omega_R^2) = x/(1+x), \quad (2)$$

where detuning Δ is equal to $(\omega_L-\omega_0)$ and $x = (\Omega_R/\Delta)^2$. If $x \ll 1$, $I_R \sim x$, but the condition $x \geq 1$ defines the Rayleigh scattering saturation region.

SELECTION OF (ω_L, ω_0) PAIRS FOR NRS-EXPERIMENTS

Our conception of NRS-diagnostic for tokamak plasmas as a "by-product" of LIF and Thomson systems restricts our choice by powerful fixed-frequency lasers (ruby, Nd^{3+}, excimers) in combination with SHG, THG and Stokes Raman shift in H_2, D_2, CH_4 gases. The analysis provided a few tens (λ_L, λ_0)-pairs to be of interest. A number of the cases are listed in Table 1.

Table 1

No	λ (nM)	λ (nM)	Atom	Transition	Source of radiation
1.	1079,4	1083,0	HeI	$2^3S_1 - 2^3P^o_{1,2}$	$AlYO_3:Nd^{3+}$
2.	447,2	447,15	HeI	$2^3P^0 - 4^3D$	THG(Nd^{3+}) - 2S(CH_4)
3.	502,9	501,57	HeI	$2^1S_0 - 3^1P_1^o$	—"— - 2S (H_2)
4.	487,9	486,1	H_β	(n=2) - (n=4)	SHG(ruby) - —"—
5.	435,2	434,05	H_γ	(n=2) - (n=5)	—"— - 2S(CH_4)
6.	248,4	247,9	CI	$2^1S - 3^1P^o$	KrF
7.	313,0	313,1	BeII	$2s^2S - 2p^2P$	KrF - 2S(H_2)
8.	308	307,16	BaI	$6^1S_0 - 7^1P^o$	XeCl

DEVELOPMENT OF LASERS FOR NRS EXPERIMENTS

It was proposed [3] to apply NRS near HeI transition 2^3S-2^3P (Fig.1b). As a part of our NRS-program the $AlYO_3:Nd^{3+}$ laser was developed (λ_L = 1.079 μm, pulse energy 0.8 - 1 J, pulse duration 10-15 nsec, repetition rate up to 20 pulse/sec). The estimate of x-parameter gives the value x = 0.5-1 for laser beam cross section of ~ 1 cm^2. It means that there is no sense in further increas of peak power for this laser.

Another proposal relates to NRS from metastable level of CI atom (see No 6 in Table 1) with help of XeF excimer laser. The idea to realize LIDAR system for ITER divertor plasmas diagnostic with good spatial resolution is now under consideration. It was also proposed to use "hybrid" picosecond system with wide-aperture KrF laser as a final amplifier with output energy at least 1 J.

MODEL SCATTERING EXPERIMENT

We performed the NRS-experiment at barium vapor near the resonance line $6s^2$-6s7p using XeCl laser (λ_L = 308 nm, see Fig. 1a and Table 1). Barium was selected as convenient test atom for model experiments and also as one of candidates for spectroscopic marker elements. (Implanted spectroscopic markers have been proposed as a technique for ITER first wall erosion monitoring [4]).
The experimental setup and the study of Rayleigh component in emission spectra were described in our previous paper [3]. We report on our studies of side emission in scattering experiment using excimer laser light. We observed the fluorescence at the resonance wavelength λ_0 of barium atom (6s-7p at Fig.2). This component was produced by collisions of Ba atom and buffer gas (argon). Intensity I_F was studied as a function of buffer gas pressure - see Fig.3. By measuring the ratio of I_F/I_R one is able to have an information concerning elastic and inelastic events ($I_F/I_R \approx \gamma_E/(\gamma_N+\gamma_I)$ - see [2]), but quantitative analysis needs correction for optical thickness of media and it will be made elsewhere.

The estimate of x value /see [2]/ gave for our experimental condition $x \approx (1\text{-}2)\times10^{-3}$ i.e. the measurements were made in low-intensity region. The same fact explaines the absence of "three-photon" component at $\omega_3 = 2\omega_L - \omega_0$ in emission spectrum of Fig.2. It is due to the dependence of I_3/I_R ratio on the same parameter x: $I_3/I_R \approx x^2/4$ for $x \leq 2$. It means that fluorescence component is of exclusively collisional origin and can be explained as a result of collisional excitation from virtual level. The measuring of I_F intensity could also be used for plasma diagnostic in case of low level of background radiation at λ_0.

REFERENCES

1. W.-G Wrobel, Max-Planck-Institut für Plasmaphysik, Report IPP-1/160, 1976.
2. J.L. Carlsten, A. Szöke and M.G. Raymer. Phys. Rev. A15 (1977) p. 1029.
3. A.B. Berlizov, I.V. Moskalenko, D.A. Shcheglov. Abstracts of V All-Union Topical Conference on high-temperature plasmas diagnostics. Minsk, 1990. Paper 1.4.21. P.142-143 (in Russian)
4. V. Mukhovatov, H. Hopman, S. Yamamoto et al. ITER Diagnostics. ITER Documentation Ser. No. 33. IAEA, Vienna, 1990.

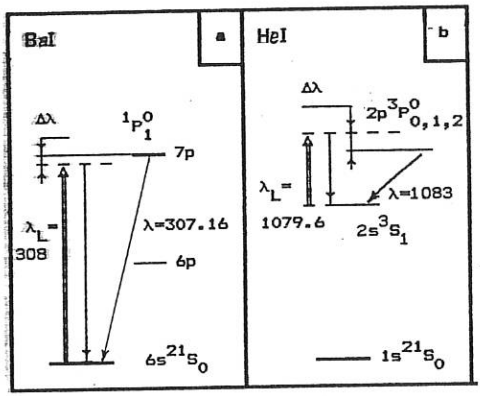

Fig.1. Simplified energy levels for BaI and HeI

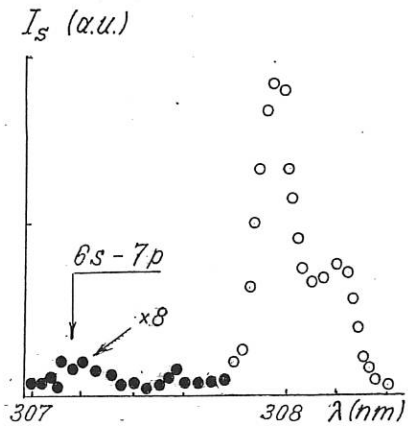

Fig.2. Wavelength dependence of scattering and fluorescence signal

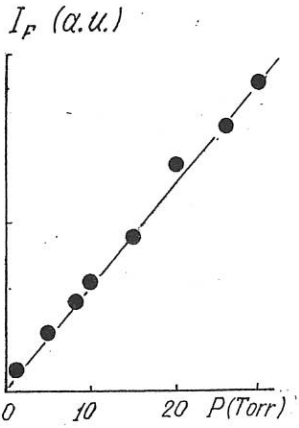

Fig.3 Collision-induced fluorescence as a function of Ar buffer gas pressure

INVESTIGATIONS OF LIGHT IMPURITIES TRANSPORT IN TOKAMAK USING SMALL-VIEW OPTICAL TOMOGRAPHY.

B. V. Kuteev*, M. V. Ovsishcher

Scientific-Industrial Center "INFORMATIKA ", Samara, USSR
*Leningrad State Technical University, USSR

In most problems of optical plasma diagnostics the object of interest, i.e. poloidal local emission distribution $I(r,\theta)$ is supposed to be close to the axial symmetry. Conventionally used Abel inversion generalizations give satisfactory results when reconstructing with a full set of chord signals received from the distributions without peripheral disturbances and strong oscillations in poloidal direction. But the impurity transport phenomena - in particular at the beginning of the shot or just after pellet injection - are to be described by non-axial $I(r,\theta)$ having peripheral maxima according to impurity source localization. Such distributions can't be reconstructed by ordinary Cormack's or similar methods [1] when the number of projections is small. In this paper a tomography method for such a distribution is worked out which consists of the following steps: i)separation of "disturbance" and "background" contributions in projection data; ii) coordinate calculation of a peripheral disturbance center; iii) separate reconstruction of "background" and "disturbance" distributions; iiii) joining the reconstruction results in a single image.

Experimental projection data from FT-2 tokamak concerning optical radiation of low-Z impurities in hydrogenous plasma were obtained by the two-projection spectro-tomographic collection system with an optic-mechanical timed scanning [1]. It was found out that all projections may be divided into two groups: "double- humped" (with two distinct maxima) and "three-humped" (with three maxima ,respectively). In the case when both projections are "double-humped" it may be supposed that the excess of one "hump" over the other is the result of peripheral "disturbance". The appearance of "three-humped" projection may be then caused by the situation when a "disturbance" maps in this view upon the central part of the projection and doesn't coincide with any equal "humps" of non-disturbed state. Then the algorithms of the contribution separation are the following:

Algorithm A1. It is developed for "double-humped" projection processing. Point-to-point subtraction of projections oriented in such a way that contributions from "disturbance" (maximal "humps") are placed in different "halves" of projections:

$$F_r(p) = F_1(p) - F_2(p) \qquad (1)$$

should suppress the background if it is close to axial

symmetry. Considering that the "disturbance" is supposed to be strongly localized, the following functions

$$F^{+}(p) = \begin{cases} F_r(p), p \geq 0 \\ 0, \quad p < 0 \end{cases} \qquad F^{-}(p) = \begin{cases} F_r(p), p \leq 0 \\ 0, \quad p > 0 \end{cases} \qquad (2)$$

give the "disturbance" contribution, and the linear combinations

$$F_1^p(p) = F_1(p) - F^{+}(p) \; ; \; F_2^p(p) = F_2(p) - F^{-}(p) \qquad (3)$$

give the value of "background" contribution in each projection.

Algorithm A2. The following function in A2 is taken as the value of "background" contribution:

$$F^p(p) = \min \{F_1(p), F_2(p), F_1(-p), F_2(-p)\} \qquad (4)$$

Then "disturbance" contribution is determined as

$$F_1^d(p) = F_1(p) - F^p(p); \; F_2^d(p) = F_2(p) - F^p(p) \qquad (5)$$

The advantage of A1 consists in the possibility of taking into account the localization of peripheral "disturbances" and non-axiality of the "background" (the difference between $F_1^p(p)$ and $F_2^p(p)$). Its disadvantage consists in the fact that it does not exclude the existence of small negative values in divided projections when "disturbances" are displaced to the center, although they may be eliminated with the help of algorithm A2 or suppressed artificially. Algorithm A2 does not give negative values in projections, but it assumes the "background" to be axially symmetrical and the asymmetry is considered to be the result of "disturbance" thus limiting the class of reconstructed functions. Algorithms A1 and A2 do not need a "leading" ("basic") projection and may be used in projection data processing having two "double-humped" projections.

Algorithm A3. Algorithm A3 is intended for projection data processing, having "double-humped" and "three-humped" projections and needs the choice of "double-humped" projection as the "basic" one (for definiteness, $F_1(p)$). Then the following function is the value of the "background" projection:

$$F_1^p(p) = \min \{F_1(p), F_1(-p)\} = F^p(p) \qquad (6),$$

and the following function is the value of the "disturbance" projection:

$$F_1^d(p) = F_1(p) - F_1^p(p); \; F_2^d(p) = F_2(p) - F_2^p(p) \qquad (7).$$

Algorithm A3 is similar to algorithm A2, though the value of the "background" is estimated considering only one projection, which may lead to distortions during their division.

After projection division and passing into the "center of gravity" of the corresponding distribution the reconstruction may be performed using any known small-view tomographic algorithm (i.e. tomography with a small number of projections) [2]. The unification of the reconstruction results into one image is fulfilled with account of their mutual localization.

Mathematical simulation of tomographic reconstruction with the use of developed algorithms was performed on model distributions produced when solving the simplest two-dimensional equation of impurity transport with appropriate boundary conditions and realistic transport coefficients typical for small tokamaks like FT-2. The algorithm's work abilities were investigated and proved in many cases.

Tomographical reconstruction of the experimental data obtained from FT-2 tokamak for lines OII - OIV, CIII - CV, H_β with bi-view diagnostics was made with the help of A1 - A3 algorithms. An example of the algorithm A1 when reconstructing OV emission is shown in the figure. Sequential frames are obtained with time interval of 3.6 ms. A comparison between initial and recounted projections let us consider of the satisfactory quality of reconstruction. Impurity source moves at the initial stage and then retains its position during the main part of discharge. It is clear that more anisotropic distributions than treated by Cormack algorithm can be reconstructed by the method proposed.

Conclusions.

Several algorithms for tomographical reconstruction of impurity emission in tokamak are developed and tested via model task and experimental data from FT-2 tokamak. They are suitable for analysis of the strongly asymmetric impurity emission.

References.

1. B.V. Kuteev et.al. Proc of the 15th Europ Conf. on Contr. Fusion and Plasma Heating, part.3, pp.1179-1182, Dubrovnik (1988).
2. G.T. Herman. Image reconstruction from projections. Academic Press, 1980.

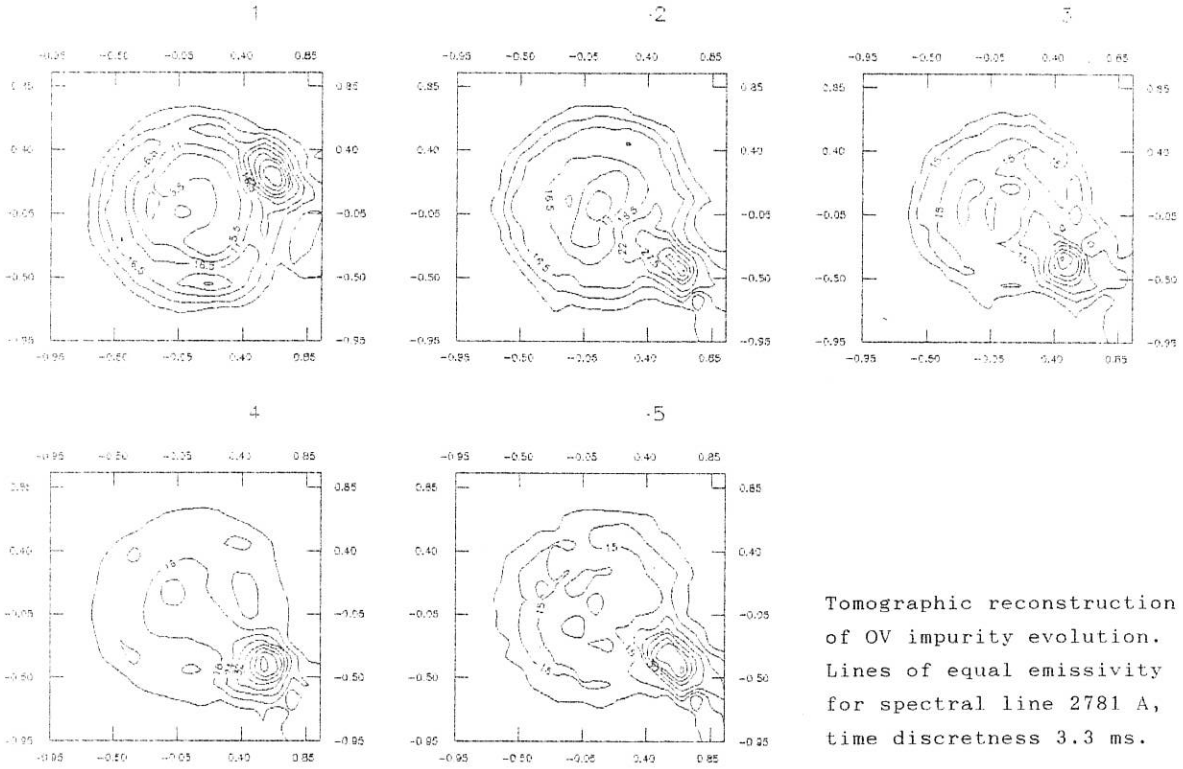

Tomographic reconstruction of OV impurity evolution. Lines of equal emissivity for spectral line 2781 A, time discretness 3.3 ms.

MEASUREMENT OF GAS INJECTION EFFICIENCY FOR HELIUM, NEON AND ARGON IMPURITIES IN TEXTOR

G M McCracken*, U Samm, G Bertschinger, V Philipps, R A Pitts*, D H J Goodall*, A Pospieszczyk, B Schweer, P C Stangeby +, G Waidmann

Institut fur Plasmaphysik, Forschungszentrum Julich, GmbH
Association KFA Euratom KFA, D-5170 Julich, Fed Rep Germany
*AEA Fusion, Culham Laboratory, Abingdon, Oxon, OX14 3DB, UK
(Euratom/UKAEA Fusion Association)
+University of Toronto, Institute for Aerospace Studies, 4925 Dufferin Street, Downsview, Ontario, Canada, M3H 516

Introduction

The impurity concentration in a plasma depends not only on the production rate but also on the probability that the impurities produced actually enter the confined plasma. After entering the plasma and becoming ionised, impurities move parallel and perpendicular to the field lines. If they are ionised near or outside the last closed flux surface they may have a very short lifetime in the plasma, thus making an insignificant contribution to radiation or fuel dilution.

In earlier experiments in TEXTOR, the parallel diffusion and ion heating was studied [1,2]. A series of experiments are reported here in which impurities have been puffed as gases into the plasma boundary and measurements made of the resulting increase in radiation and Z_{eff}. From these measurements a global figure of "gas efficiency" has been calculated. It has been found that this gas efficiency varies with the impurity species.

Experiment

Gas has been introduced into the discharge, both from the wall radius and from a hole in a rail limiter whose radius can be varied. The gas flow from the wall is accurately calibrated and can be preprogrammed. The gas is injected at a constant flow rate for a fixed period, typically 0.5 to 1.0 sec, during the steady state period of the discharge. The plasma density can either have feedback control to maintain the density constant when the impurity is injected, or maintain a constant plasma species fuelling rate and observe the density rise due to the impurity injection.

Measurements are made of the local emission at the limiter using a visible spectrometer, of the recycling rate, the total radiation and of various impurity lines in the plasma. The central value of Z_{eff} is calculated from the loop volts and measurements of $T_e(O)$ using the ECE system. The edge plasma density and temperature profiles are measured.

Results

A comparison has been made of the effects of injecting He, Ne and Ar into a standard ohmic discharge with $I_p = 350$kA, $n_e = 2 \times 10^{19}$ m^{-3}, T_e (a) ~ 1 keV. A typical result for neon injection is shown in fig. 1. Density feedback control was used in these experiments. The recycling of the neon at the limiter increases approximately linearly during the gas injection. The emission from low ionisation states, total radiation, and Z_{eff} all increase similarly, and then decay at the end of the gas injection phase. The hydrogen recycling falls slightly during impurity injection and then recovers. The torus had been boronized a few days before the impurity injection experiments and a typical value of Z_{eff} before impurity injection was 1.3. The increase in Z_{eff} and in radiation as a function of the number of injected atoms is shown in figs. 2 and 3 for helium, neon and argon. As is expected the helium radiation rise is very small, while the rise for neon is significantly greater than that for argon. The Z_{eff} data shows similarly that the rise for neon is greater than for argon; although lower, the helium injection makes a significant contribution to Z_{eff}.

Measurements have also been made of the partial pressure of neutral impurities in the scrape off layer during the discharge with a mass spectrometer. The partial pressure increases and decays proportionally to the spectroscopic signals for all three impurity species, fig.1. At the end of the discharge the impurities are observed to be released from the torus and pumped away by the vacuum system. The integrated gas release shows that $> 70\%$ of the total amount of the injected helium and neon is released after the discharge, if the pumped limiter is closed.

The decay time of the impurity concentration during the discharge also depends on whether the pumped limiter, ALT II, ducts are open or shut. In the case of helium and neon a significantly faster time constant of the decay rate is obtained with the pump duct opened. However, even without the pumped limiter it is observed that argon and to some extent, neon, decays, indicating a net pumping by the walls. In contrast, there is no significant net pumping of helium.

Discussion

The central Z_{eff} is a measure of the impurity concentration. The impurity concentration of the impurity was calculated using a mean charge state of 2, 10 and 18

respectively for helium, neon and argon. From the impurity concentrations, the average number of impurity atoms is calculated assuming a flat impurity concentration profile. It is seen that whereas the gas efficiency for helium is $\sim 100\%$, neon is 40% and argon is only 3%. These results are qualitatively consistent with the power radiated, where the argon radiation is less than the neon despite the higher charge state.

The ionisation rate of 0.05 eV atoms starting at the wall has been calculated as a function of radius using the measured density and temperature profiles in the boundary. The results show that the fraction of helium, neon and argon which reach the last closed flux surface without ionisation is 80%, 31%, and $< 1\%$ respectively. However, ionisation does not in itself produce a net loss of particles. Modelling with LIM [3] shows that they could recycle from the limiter or wall and re-enter the plasma without significant loss. No significant fraction of the inventory was obtained as neutrals, consistent with the mass spectrometric data. It is therefore postulated that those ions produced in the SOL are trapped in the wall or limiter when they are accelerated into the surfaces by the plasma sheath potential.

Earlier measurements with CO, CH_4 and other species also showed very low gas efficiencies consistent with the high molecular ionisation cross sections. [2,4] Further investigation of other impurity species and of the effect of plasma parameters on the gas efficiency is planned.

Conclusion

Measurements of the gas efficiency of a range of impurity gas species introduced into a plasma have been made and it is found that the value varies widely. Low gas efficiency has been attributed to a combination of high ionisation rate coefficient and efficient trapping of the ion species in the surfaces of wall and limiter.

References

1. G M McCracken, U Samm, S J Fielding et al, J Nucl Mat. 176 and 177 (1990) 191.

2. S J Fielding, G M McCracken, R A Pitts et al, in Proc. 17th EPS Conference on Plasma Physics and Controlled Fusion, Amsterdam III (1990) 14 72.

3. P C Stangeby et al, Nucl Fus 28 (1988) 1945.

4. G Bertschinger, Deutsch Physikalische Gesellschaft, 1988 unpublished.

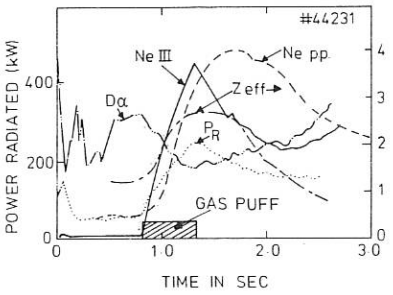

Fig. 1
Time dependence of radiated power, NeIII at limiter, Z_{eff}, D_α recycling at the limiter and neon partial pressure in the torus, during and after a 0.5sec neon gas puff.
Ip = 350kA $n_e = 2 \times 10^{19}$ m^{-3}

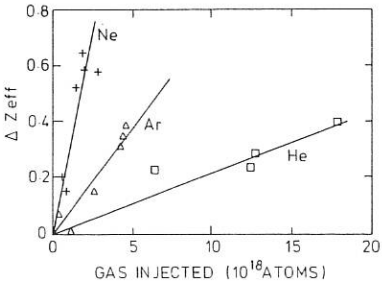

Fig. 2
Maximum incremental Z_{eff} during helium, neon and argon gas puffs into a deuterium discharge.

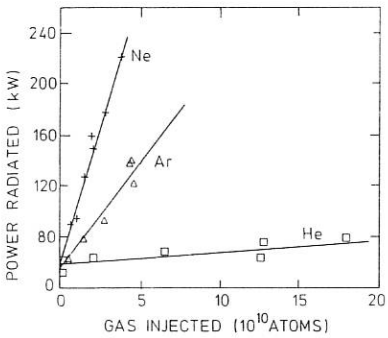

Fig. 3
Peak Power radiated during helium neon and argon gas puffs into a deuterium discharge.

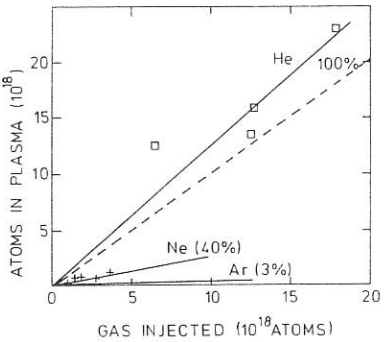

Fig. 4
Fuelling efficiency calculated from central ΔZ_{eff} for helium, neon and argon impurities injected into a deuterium discharge.

NEUTRAL DENSITY IN FT OHMIC PLASMA

G. Bracco, A. Moleti, V. Zanza

Associazione EURATOM-ENEA sulla Fusione, C. R. E. Frascati,
C.P. 65 - 00044 - Frascati, Rome, Italy

In tokamak plasma the information about neutral density in the plasma core is very poor. If the ion temperature profile is known the measurement of the charge exchange neutrals permits to evaluate the neutral density and hence to estimate the particle sources and fluxes which can be compared with the theoretical previsions.

A set of ohmic discharges of deuterium plasma in FT has been selected with a magnetic field of 6 T, a safety factor q between 3 and 4 and line averaged plasma density $\bar{n}$ in the range 0.4 to 2.3×10^{20} m^{-3}. In FT a 7-channels, mass selecting neutral particle analyser (NPA) measures the passive neutral particle flux, observing the plasma perpendicularly to the toroidal magnetic field. The selected energy range has been 1 to 7 keV.

The flux $\Phi(E)$ of the charge exchange neutrals at energy E is given by:

$$\Phi(E) = \int n_i f(E) (n_0 \langle sv \rangle_{cx} + n_e \langle sv \rangle_{rc}) e^{-\int dl'/\lambda} dl \qquad (1)$$

where n_i is the ion density, f(E) is the ion energy distribution function, n_0 is the neutral density, $\langle sv \rangle_{cx}$ is the charge exchange reaction rate, $\langle sv \rangle_{rc}$ is the recombination rate, λ is the neutral mean free path and the integration is performed along the line of sight. In relation (1) f(E) is exponentially decreasing with the distance from the plasma centre (if E is greater than the maximum ion temperature) while n_0 and the transparency factor are exponentially increasing towards the plasma edge. The combination of these dependences provides a rather precise radial localisation of the measured neutral flux at each energy so that even with one line of sight the charge exchange spectra contain informations about the profiles. Unluckily if both ion temperature and neutral density profiles are unknown the unfolding of the equation (1) does not provide an unique solution.

In FT it has been shown [1] that experimental ion temperatures are in good agreement with Chang Hinton neoclassical previsions and so the ion temperature profile obtained as the solution of the ion power balance with neoclassical thermal conductivity has been used to analyse the NPA spectra. The electron temperature profiles have been measured by the Thomson scattering at 7 radial position, $\bar{n}$ values are provided by a single channel HCN interferometer. The Thomson scattering data on electron density profile have suffered from problems in the absolute calibration and so a parabolic density profile has been used as reference. The experimental values have been also used even if uncertain in order to assess the dependence of the results on the assumed density profile. The Z effective has been derived from the plasma resistivity.

The radial profile of the neutral density has been evaluated using a 1-D neutral transport code which solves the continuity equation for neutrals in a similar way of the ANTIC code [2] The reaction rates for charge exchange, electron and proton

ionization have been evaluated from the published cross section data retaining the dependence both from the neutral energy and the plasma temperature. The recombination cross section has been taken from [3]. The code requires as boundary condition the neutral density and temperature at the plasma edge which have been chosen to reproduce the absolute values of the NPA fluxes at the lower energies.

In order to check the accuracy of the neutral density determination by the simulation of the NPA fluxes, for each of the selected plasma discharges several cases have been completed changing the following parameters: the shape and the edge value of the electron density profile, the fitting method of the electron temperature profile, the neoclassical multiplier in the ion temperature computation, the edge value of the neutral density temperature, the Z effective by using Spitzer resistivity with and without neoclassical corrections, the main impurity species (high or low Z). In each case a good agreement between computed and experimental NPA fluxes has been required together with the agreement between the computed and experimental value of the neutron emission. These two requirements limit the possible combinations between the variations of the previous parameters. It can be noted that in the case of the high density plasma ion and electron temperatures are very close, Z effective is close to 1 and so ion dilution is unimportant, and the neutral density in the plasma core is fixed by the recombination. In this case the two constraints on NPA fluxes and neutron emission do not permit a large variation of the electron density profile parameters.

In the following the results are shown together with the error bars obtained with the procedure described previously. In fig. 1 the localization of the NPA fluxes is shown as a function of $\bar{n}$. The radial average position of the 1 keV detected neutrals is typically between 0.13 and 0.16 m (limiter radius is 0.2 m) while the flux at the maximum detected energy varies between 0.04 m at low energy and 0.08 m at high density. At high density the maximum energy with a detectable signal is 5 KeV In fig. 2 the energy at which the NPA flux has a maximum of production at half radius is shown as a function of and it varies between 1.5 and 4 keV. It can be concluded that the experimental NPA fluxes provide information about the neutral density up to about 2/3 of the plasma minor radius in every plasma condition.

In fig. 3 the neutral density at the plasma centre and at half radius is shown as a function of $\bar{n}$. Recombination is the main source of neutrals at $\bar{n}$ greater than 0.9×10^{20} m^{-3} at plasma centre and at $\bar{n}$ greater than 1.4×10^{20} m^{-3} at half radius. Neutral density in the plasma edge region is not under observation of the NPA due to

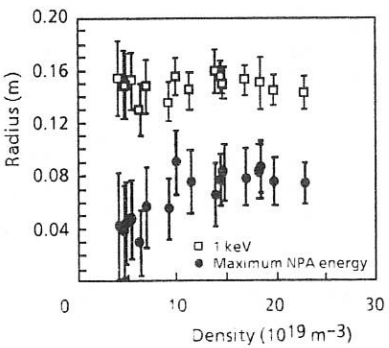

Fig. 1 - NPA flux localization

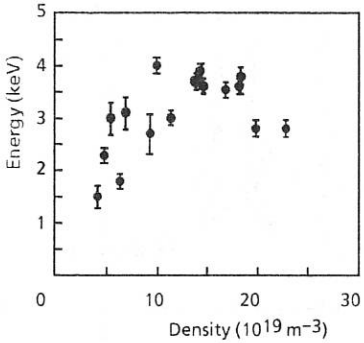

Fig.2 - Energy of the NPA flux produced at half radius

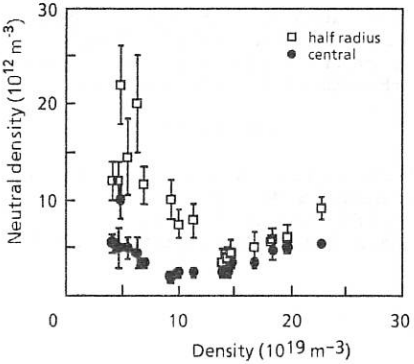

Fig.3 - Experimental neutral density

the chosen energy range. Moreover the neutral density at the edge is affected by strong toroidal and poloidal disomogenities which reflect mildly in the plasma core expecially at high plasma density. For these reasons the global particle confinement which depends strongly from edge conditions, can not be evaluated using these NPA data. On the contrary the steady state particle transport in the plasma core can be quantified as the neutral density values shown previously are known with sufficiently low error bars.

In fig. 4 the particle fluxes at half and 2/3 of the plasma radius, computed using the experimentally deduced neutral density are shown as a function of $\bar{n}$. When the neutral density is due to recombination only the particle fluxes are near to zero. The comparison between experimental and theoretical particle fluxes must take in account that also the theorical previsions are affected by large errors expecially when gradient dependent fluxes are evaluated. The neoclassical particle fluxes [4] in the plasma core are dominated by Ware pinch and so are directed toward plasma

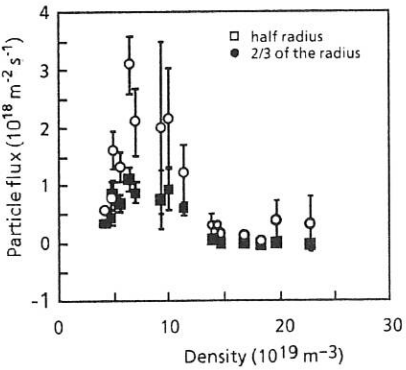

Fig.4 - Experimental particle fluxes

centre and the absolute values are one order of magnitude greater than the experimental values. (-3 to -1x10^{19} m^{-2} s^{-1} at half radius). It can be observed that the experimental fluxes are in the order of magnitude of the Pfirsch-Schluter fluxes (1 to 10x10^{18} m^{-2} s^{-1}) which have the outward direction.

REFERENCES

[1] F. Alladio et al.: (Proc. 13th IAEA Conf. 1990) paper CN-53/A-2-5
[2] S.Tamor: J..Comput.Physics. 40, 104 (1981)
[3] Y.S.Gordeev et al.: JETP Lett. 25, 205 (1977)
[4] F.L.Hinton, R.D.Hazeltine: Rev.Mod.Physics. 48, 239 (1976)

FIRST RESULTS FROM THE JET TIME OF FLIGHT NEUTRAL PARTICLE ANALYSER

S Corti, G Bracco*, A Moleti*, V Zanza*

* *JET Joint Undertaking, Abingdon, UK*
Associazione Euratom-ENEA, Frascati, Italy

1 - Introduction

A Time of Flight (TOF) Neutral Particle Analyser (NPA) has been recently installed at JET. The system consists of a single NPA based on the measurement of the time of flight of the analysed particles /1/, so that a random background can be discriminated by a standard coincidence technique. The analyser energy range is 0.5-200 keV and it has been absolutely calibrated for hydrogen, deuterium and helium neutrals.

The analyser is located at the bottom of the machine and its line of sight follows a vertical chord passing at a major radius R=3.1m on the equatorial plane of the torus. The neutrals coming from the plasma are ionised in a gas stripping cell and energy analysed with a cylindrical electrostatic plate system. The inner cylindrical plate is terminated at both ends by two flat electrodes and is set to a positive potential. This configuration provides the focalization of the ion beam from the stripping cell in both planes parallel and perpendicular to the cylinder axis.

A set of 15 TOF detectors collect the ions with an energy dynamic range 1:25. Each detector is composed by a thin ($1\mu g/cm^2$) carbon foil and two channeltrons. The ions produce secondary electrons in the carbon foil which are detected by the first channeltron (CEM A) thus providing the start trigger for the coincidence. The signal in the second channeltron (CEM B), produced directly by the particles, constitutes the stop trigger.

The start pulse triggers a set of three programmed time delays (in the range 10-400 ns) and at the end of each delay a time gate of pre-programmed length is generated (5-33 ns). A coincidence event is counted if the stop pulse occurs during the gate time. In this way up to three different masses can be counted by each detector.

The analyser uses channeltrons as particle detectors, and channeltrons are sensitive also to neutrons (n), gamma (γ), X and UV radiation. The analyser box and the surrounding materials do not provide any significant attenuation of n and γ, while X and UV radiation enters the analyser through the stripping cell diaphragms and is not fully absorbed by the light trap.

The n induced background has been measured by keeping the valve to the torus closed and a good time correlation has been found with the n production rate. The evaluation of the radiation induced count rate showed a maximum of 1000 counts/s clearly correlated with the detector position in the analyser box. It can therefore be concluded that the only large random noise source is the n induced background and that its intensity requires the shielding of the analyser to prevent the channeltron saturation. A shielding factor of $\simeq$100 would allow the operation of the analyser up to a n production rate of the order of $\simeq 3\ 10^{18}$ n/s.

2 - Experimental Results

In the following some results of the TOF NPA in the last JET campaign will be described. The main objectives of this first operational period of the new NPA, apart the assessment of the random noise rejection capability, has been the initial exploration of the neutral particle spectra in the present, very varied, JET operating scenarios.

It is well known that the neutral flux at energies greater than the peak ion temperature strongly depends on plasma density, as the neutral density and the plasma transparency decrease exponentially with density. This means that a significant high energy neutral flux, able to provide information on the peak ion temperature, can only be detected at low plasma density. For example, in pulse 23003 (deuterium, ohmic, 2.8 T, 3 MA), with a volume averaged density of 10^{19} m^{-3}, neutral fluxes up to 30 keV have been measured. The ion temperature obtained from the slope of the NPA spectra in the energy range 5-15 keV is in good agreement with the peak ion temperature obtained by the neutron flux monitors [fig. 1].

Deuterium (D) Neutral Beam Injection (NBI) in a hydrogen (H) plasma allows the exploration of various aspects of the analyser operation. These include the analysis of the mass rejection capability and some more detailed studies of ion temperature and neutral fluxes in NBI heated discharges, where the main plasma component can be measured separately from the injected particles. The spectra obtained in pulse 22926 (2.8 T,3 MA,2 $10^{19}m^{-3}$,5 MW NBI at 80 keV, single upper null) are shown in fig. 2. The D spectrum shows the standard slowing down features while the H spectrum has a well identified slope, in the energy range 5÷30 keV, which allows to estimate the ion temperature. At higher energies the H spectrum becomes similar in shape to the D one, but with an intensity of a factor 100 lower. This can be attributed to the contamination of the H channels by the D beam.

In pulse 22927 (same as above but with 8 MW NBI) very large sawteeth are observed on the ECE T_e. A clear modulation of the NPA T_i obtained from the H slope is also observed and appears to be well correlated with the T_e sawteeth. From a more detailed examination of the H fluxes at various energies [fig. 3] it can be seen that for energies greater than 20 keV a proper sawtooth is present, while the signal at 17.9 keV shows no sawteeth, suggesting that neutrals at this energy are coming from the region of the inversion radius. At lower energies at each sawtooth crash corresponds a rapid increase of the neutral flux which can be explained with these fluxes originating from the region between inversion and mixing radii, where a widening of the T_i profile produces a flux increase due to higher neutral density and lower neutral attenuation.

In fig. 4 two H spectra, before and after a sawtooth crash, are displayed. The portions below 18 keV remain unchanged, apart for a variation of intensity, while those at higher energies (originating from the central region of plasma) show a definite change in slope. It is well known that passive charge exchange measurements are difficult to interpret because the localization of the observed neutrals is not clear. We want to point out here that, if the interpretation of the previous data is correct, a precise localization of the neutral source zone is available so that the neutral density at the inversion radius can be directly evaluated by taking into account the neutral attenuation. It must also be stressed that the measurements of these details of the H spectra has only been possible by taking advantage of the random noise rejection capability of the analyser. In fact, as shown in fig. 5, in the discharge considered

above the neutron induced count rate is a factor 10 to 50 higher than the count rate due to particles.

In pulse 23034 (deuterium, 3.1 T, 3.5 MA, double null) a 6.3 MW He_4 neutral beam has been injected. The TOF NPA has been tuned to detect D and He_4 particles and in fig. 6 the spectra of the two species during NBI are shown. At high energies (>70 keV) the detection of D particles appears to be contaminated by the He neutrals. The species rejection factor is again typically 100.

From preliminary estimates it appears that the observed He^0 particles are the product of the C-X process between He^+ ions and D neutrals. A more precise description of all processes involved is complicated by the mentioned poor localization of the measured neutrals and needs some more investigations and a careful modeling of the plasma.

In pulse 23100 (3.2 T, 3.6 MA, double null, pellets at 44.7 and 45 s) Ion Cyclotron Resonance Heating on H minority has been performed by injecting 11 MW of RF power. At the same time 2.7 MW of D Neutral Beam have been injected for diagnostic purposes.

In fig. 7 the H fast tail and the D slowing down spectra are shown. If the correction due to the variation of the charge exchange cross section rate with energy is applied to the H spectrum, it appears to be fully saturated at high energy pointing to a very high energetic minority tail. The D spectrum is composed by three distinct portions: a low energy (E<20 keV) part dominated by bulk ions, a slowing down region (20-80 keV) and the region at E>80keV. The slope of the spectrum for energies greater than the injection energy is given by an average of the electron and ion temperatures weighted on the fraction of power deposited on electrons and ions. Being in this pulse $T_e \simeq T_i$, this slope is directly related to the plasma temperature. This is shown in fig. 8 where the slope of the NPA D spectrum at E>80 keV is plotted versus time together with T_i from CXRS and X-ray crystal spectroscopy.

3 - Conclusions

Some results obtained with the new TOF NPA in various JET plasma scenarios have been shown. A series of interesting features of the NPA spectra have been identified which constitute the starting point for a systematic work to be performed with this instrument in the future JET operation campaigns. Some of the results have been obtained in plasmas producing a high neutron induced background, so that the random noise rejection capability of the analyser has been demonstrated.

References

/1/ - G Betello, G Bracco, A Moleti, B Tilia, V Zanza : 17th EPS Conference on Controlled Fusion and Plasma Heating, Amsterdam, 1990

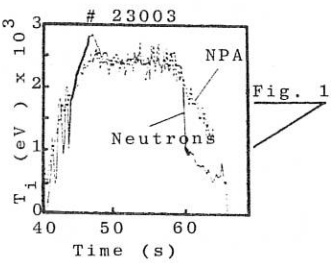

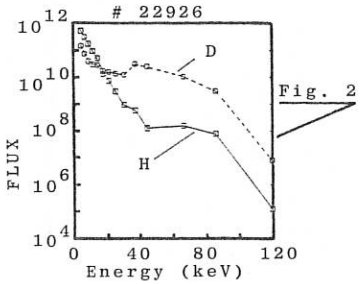

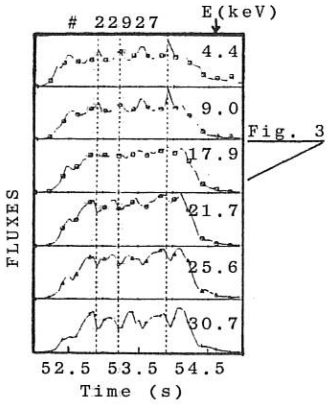

Fig. 3

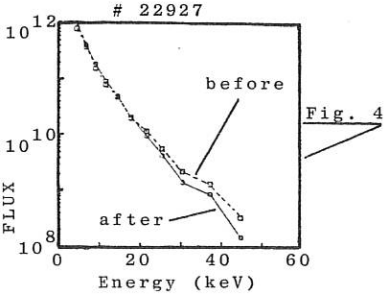

Fig. 4

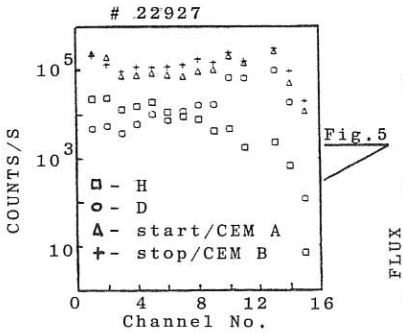

Fig.5

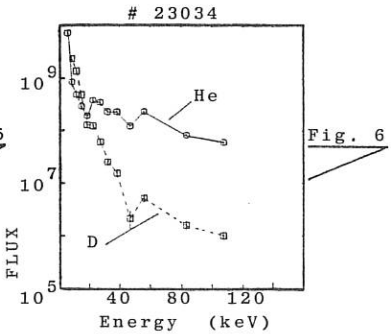

Fig. 6

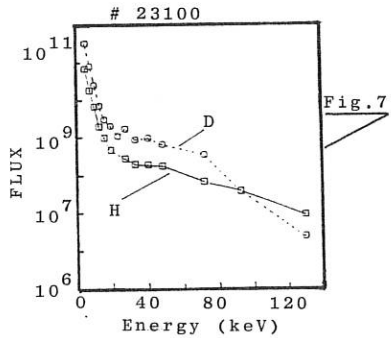

Fig.7

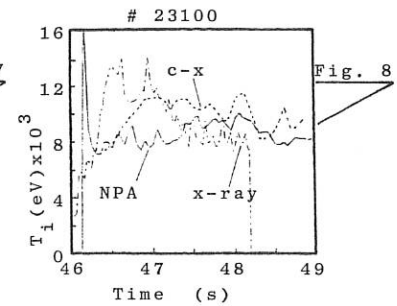

Fig. 8

COMPARISON BETWEEN RUTHERFORD SCATTERING AND NEUTRAL PARTICLE ANALYSIS IN OHMIC DISCHARGES IN TEXTOR

A.A.E. van Blokland, G. Bertschinger*, E.P. Barbian, A.J.H. Donné, T. Oyevaar, D. Reiter*, H.F. Tammen and T.F. Vijverberg

FOM Instituut voor Plasmafysica, Nieuwegein, The Netherlands
* IPP, Forschungszentrum Jülich GmbH, Ass. Euratom/KFA, FRG

Introduction

The diagnostic methods for the determination of the ion temperature in thermonuclear plasmas need further development to reach the same standard available for electron parameter measurements. One technique to improve this situation is the Rutherford scattering diagnostic (RUSC), which has been recently installed at TEXTOR. To evaluate the potential of this method, the ion temperatures in ohmic discharges are compared with the results obtained from passive neutral particle analysis (NPA), which is usually applied as a standard diagnostic for medium sized tokamaks. The results from both independent methods show good agreement for a range of densities (n_e= 1.0 - 4.0$\times 10^{13}$ cm^{-3}) in deuterium plasmas.

The Rutherford scattering diagnostic

The method is based on the elastic scattering of injected mono-energetic He atoms over a small angle by plasma ions. The energy distribution of the scattered atoms is determined by kinematic conservation laws. Therefore, in the case of a Maxwellian ion velocity distribution, the energy distribution of the Rutherford scattered particles is broadened by the thermal movement of the plasma ions. The width of the energy distribution is related to the mass ratio of the beam and plasma particles, m_b / m_p, the scattering angle, θ, the beam energy, E_b, and the ion temperature, T_i,

$$\Delta E_{FWHM} = 4 \sin\theta \sqrt{\frac{m_b}{m_p} E_b T \ln 2}$$

Hence, the T_i-value in the scattering volume can be directly obtained from the observed broadening at a certain scattering angle. The position of the maximum of the energy distribution depends on the mass ratio of the colliding particles.

The experimental set-up of the active beam scattering diagnostic consists of a neutral He beam (30 keV, 5 mA equivalent current), which is vertically injected into the plasma, and a mass-selective time-of-flight (TOF) analyser to detect the scattered atoms. The scattering angle is adjustable between 3° and 8° /1/. For θ = 7°, the vertical length of the scattering volume is 0.25 m. Ion temperature profile measurements can be performed on a shot-to-shot basis by a lateral movement of the beamline in the radial direction.

Figure 1 shows a measured TOF-spectrum of scattered He atoms. The initial beam energy was chosen at 30 keV, $\theta = 7^{\circ}$ and the scattering volume was situated at the centre of the plasma. The solid line in Fig. 1 represents the instrumental broadening of the analyser, determined from scattering on a cold deuterium gas. The circles show the distribution which is additionally broadened due to the interactions with the plasma ions during an ohmic deuterium discharge. In general, also contributions from He particles scattered on minorities of H-, C-, O- and Fe-ions show up in the measured spectra. Since, the differential cross section scales with the square ion charge number, a relatively small impurity concentration can influence the shape of the spectrum /2/. The ion temperature is obtained by using a fitting procedure for the interpretation of the observed spectra. The calculated distributions of the different ion components are compared to the data, leaving the T_i-value and the different ion concentrations as free parameters.

An independent measurement of Z_{eff}, which might be deduced from the different ion concentrations resulting from the best fit, is yet beyond the scope of this work, because of the poor accuracy of the available atomic data for electron loss in combination with the small-angle scattering /3/.

The error in T_i is determined by the instrumental broadening, the finite value of the detector solid angle and, the temperature and density profile in the scattering volume. Furthermore, the finite number of events taken for one single spectrum limits the accuracy. The combination of the above mentioned error sources results in a typical ΔT_i of 12% for 1000 events in a spectrum.

Neutral Particle Analysis

In the plasma core, a small fraction ($\sim 10^{-6}$) of the particles is not ionized and is therefore not confined by the magnetic fields. Neutral particles are created by the recycling of H- or D-ions at the plasma facing components. Most of these atoms recombine to molecules and flow with thermal velocities back into the plasma. These molecules become dissociated or ionized. Some of the atoms undergo charge exchange with the plasma ions. After the collision, both particles keep their initial velocity, since a negligible part of the kinetic energy is exchanged. Information on the ion velocity distribution is thus obtained by measuring the energy spectrum of the neutralized particles, emerging from the plasma.

In TEXTOR the toroidal pumping limiter ALT II is the main source of the neutral particles. Up to 80% of the plasma ions recycle at this limiter, the remaining part at the liner. Consequently, the poloidal distribution of the atoms is strongly asymmetric. For the interpretation of the measured spectra the 3-dimensional Monte Carlo code EIRENE is used /4/. This code models the random walk of the atoms in the plasma.

The calculations show that the slope of the high energy part of the spectrum depends mainly on the maximum temperature along the line of sight of the analyser. For the chosen position of the neutral particle analyser, the correction of the ion temperature is below 20%. A more accurate approximation is obtained by adjusting the local temperature values until the experimental spectra are reproduced.

The neutral particle analyser is an electrostatic device of the Harrower type with 9 energy channels. The energy range is between 0.5 and 55 keV. In order to increase the energy resolution, the deflection voltage of the analyser is ramped up slowly during the stationary phase of the discharge. Ion temperature profiles can be measured by scanning the line of sight of the analyser over the minor radius of the plasma on a shot-to-shot basis. Fig. 2 shows both the measured and simulated energy spectra for the central radial position. The analyser is optimized to handle count rates of detected particles of up to 5 MHz per energy channel. Depending on the particle flux, the time resolution is better than 1 ms. The accuracy in the determination of the ion temperature is approximately 10%. Compared to the error of the calibration, other sources like the statistical errors and the inaccuracy of the profile corrections are negligible. The minimum measurable temperature is 250 eV.

Comparison between both methods

In Fig. 3 the results of both diagnostics for a density scan are shown. The temperatures correspond well within the experimental error of the methods. The NPA diagnostic measures the higher part of the velocity distribution ($2kT<E<5kT$), while RUSC uses the lower part ($E \leq 2kT$), which implies that the diagnostic is insensitive for deviations from a Maxwellian distribution. Furthermore, impurities can obscure the spectrum of the scattered He particles and might thus influence the accuracy of the obtained temperatures for RUSC. However, the interpretation of the spectra is rather straightforward for RUSC, whereas a complicated procedure is needed to interpret the NPA-spectra. The spatial resolution is better defined for RUSC. Both methods might give an underestimation for the central T_i and need therefore to be corrected for the density and temperature profiles. Both methods have the limitation that several shots are needed to measure a T_i profile.

References

/1/ A.A.E. van Blokland, E.P. Barbian, T.W.M. Grimbergen and T. Oyevaar, Proc. 16th Conf. on Plasma Phys. and Contr. Fusion, Amsterdam (1990) 1528,

/2/ E.P. Barbian, A.A.E. van Blokland, A.J.H. Donné and H.W. van der Ven, Proc. 15th Conf. on Plasma Phys. and Contr. Fusion, Dubrovnik (1988) 1159,

/3/ A.J.H. Donné and F.J. de Heer, J. Appl. Phys. **62**, (1987) 780,

/4/ G. Bertschinger, D. Reiter and L. Könen, Proc. 12th Conf. on Plasma Phys. and Contr. Fusion, Budapest, (1985) 251.

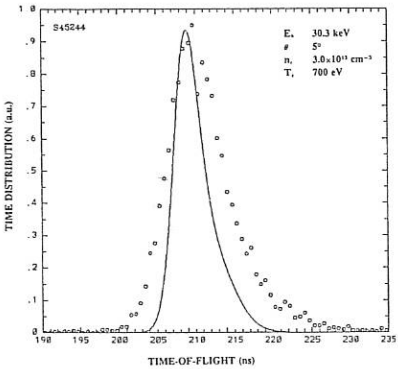

Figure 1 TOF-spectrum of scattered He atoms. The instrumental broadening of the analyser is represented by the solid line. The circles show the spectrum during the flat top of the discharge.

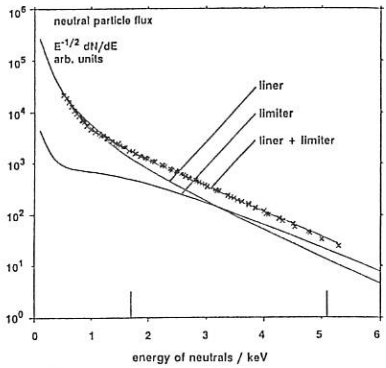

Figure 2 Measured (×) and calculated (solid lines) neutral particle spectrum during the stationary phase of a deuterium discharge.

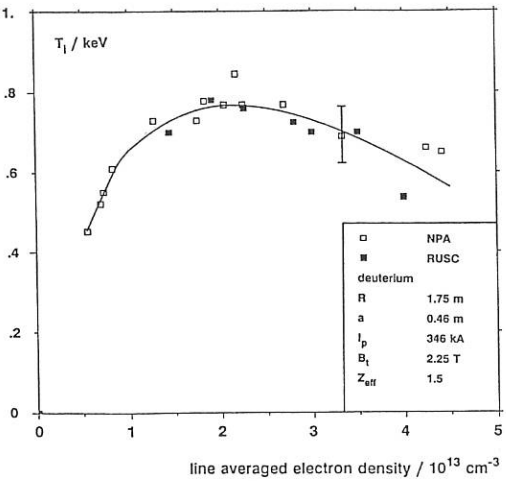

Figure 3 Central ion temperatures for a density scan.

A NEW DIAGNOSTIC FOR THE TRITIUM PHASE OF JET COVERING THE VISIBLE AND UV WAVELENGTH RANGE

H.W.Morsi, R.Hatzky, M.von Hellermann, W.Mandl, R.R.McKillen, M.Mijnarends, P.Millward, P.Nielsen, J.Reid, P.Roberts, J.Ryan, P.Thomas, B.Viaccoz

JET Joint Undertaking, Abingdon, OX14 3EA, UK

Introduction

The objectives of an active-phase direct optical link between the JET tokamak and spectral instruments beyond the biological shield are manifold. The present optical fibre links, which are used as a standard at JET, may be subjected to much enhanced radiation levels in future operations with D-T plasmas, and a direct optical link, based on a system of remotely controllable relay mirrors, will be a vital test for future activated fusion devices.

A further aim is to extend the spectral range of exploitable charge exchange (CX) lines to shorter wavelengths, which is presently limited by the transmission of quartz fibres to CX lines above 4000Å. The latter aspect is particularly relevant in the case of HeII where the sole CX line of HeII (n=4 to 3) in the visible , is superimposed by a BeIV CX line (n=8 to 6) at the same wavelength (4685Å). This fact constraints the present helium analysis to plasma conditions with $n(Be)<0.3 \cdot n(He)$. For future alpha particle studies, especially at low alpha particle densities, this constraint may require either sophisticated analysis procedures or alternatively the use of other less "disturbed" lines, possibly in the UV wavelength range.

Finally the UV link is intended to provide an optical transfer channel for short optical jumpers to other JET observation ports - for example coherent fibre bundles imaging the X-point strike zone - to the diagnostic instruments in the roof laboratory of JET.

Instrumentation

An essential feature of the optical mirror link (Fig.1) with regard to a future fusion device, is the minimisation of the neutron shielding. The optical mirror link consists of 5 mirrors, of which 2 mirror assemblies (A and B) inside the torus hall and a flat mirror (C) at the outer end of the penetration trough the biological shield form a labyrinth like light path to avoid direct neutron fluxes from the torus. The mirror assemblies (A and B) consist each of a spherical inner part for plasma light and flat outer parts used by an automatic mirror alignment laser system. The fourth (spherical) mirror (D) focus' the plasma light via a beam splitter onto 2 Czerny-Turner spectrometers (f=1m) equiped with light intensifiers and linear array detectors (OMA). The laser alignment system is similar to the system used on the LIDAR Thomson scattering diagnostic at JET.

The true imaging capabilities of the optics allow the extension to spatially and spectrally resolved measurements by replacing the linear array detectors with 2-dimensional systems. The critical feature of the system is the alignment stability of its mirrors because of the combination of long light path (30m) with small apertures (biological wall: 95mm, torus

port: 22mm).

The étendue of the spectrometers (f/D=8.7) is matched to the optical mirror link, and ray tracing confirms that over 90% of the rays between entrance slit and its image in the plasma centre are maintained. The mirrors are coated with UV-enhanced aluminum permitting spectroscopic access to the atmospheric cut-off wavelength around 2000Å. All components of the diagnostic are remotely controllable, emphasising its tritium compatibility.

An adapter which accommodates an input and/or output optical head to the light path of the UV optical mirror link is inserted between torus port and mirror A (Fig.1). The input optical head channels light of other measurements (e.g. light emitted from the X-point target strike zone, or from the future JET divertor chamber) to the roof laboratory. The output optical head is presently used for the plasma core CX spectrometers (fibre link).

Data analysis and preliminary results

First measurements with emphasis given to the UV wavelength range were carried out during the last two weeks of 1990 operation. A UV-line survey down to 2070Å revealed several interesting results of which two are presented:

The CX recombination line of carbon CVI (n=7 to 6) at 3435Å (Fig.3) appears to have a reduced passive 'cold' component compared to the active 'hot' CX component form the plasma centre. In addition, there is no evidence of other strong impurity line activity in the spectral neighbourhood. It appears therefore that during neutral beam injection (NBI) the cold component at 3435Å can be neglected, allowing - in principle - a fast automatic analysis of the CX spectrum by a single Gaussian fit. Since the S/N-ratio of the detectors can still be optimized, the time resolution will be eventually limited by the 3ms detector readout time.

By comparison, the equivalent CVI line at 5290Å (n=8 to 7), in the visible spectral range , has usually a more pronounced cold component, and moreover during JET discharges with plasma touching either the Be belt limiter or the Be target plates in lower X-point configuration, a very intense BeII line at 5270Å may be a factor of 10 in intensity above the CVI spectrum. The presence of the BeII line requires therefore a 3 Gaussian fit, which implies more CPU time and larger statistical errors in the analysis procedure.

In Fig.4 central ion temperatures (Ti) for an entire NBI phase are calculated. The comparatively larger noise on the Ti-trace deduced from the visible CX line at 5290Å (fibre link) shows that its sensitivity limit is reached at a carbon concentration level of the order of n_C/n_e=0.2% In contrast to this, the line at 3435Å, with its significantly higher CX cross-section promises detection levels below 0.1 %

The intensity ratio of the two CX lines at 3435 and 5290Å is found to be 2.5, which is in reasonable agreement to the predicted values σ(n=7 to 6)/σ(n=8 to 7)=2.3 [1].

The commonly used HeII (n=4 to 3) CX transition in the visible at 4685Å superimposes on the BeIV (n=8 to 6) CX emission (Fig.5). The extraction of the active CX helium emission (hot component) involves 10 Gaussians, of which 4 are superimposed on the He-line wavelength position alone, thus creating large ambiguities even with interactive fit procedures.

The HeII (n=5 to 3) CX transition in the UV at 3202Å permits an analysis

with 3 Gaussians only. The BeIV (n=10 to 6) CX emission at 3202Å is weaker than expected and needs further investigation.

References

[1] Boileau et al., Plasma Phys. and Contr.Nucl.Fusion **31**, 779 (1989)

Figure captions

Fig.1 Overall schematic view of the new optical mirror link diagnostic at JET. Only mirrors A, B and the relay optics adapter are exposed to direct neutron fluxes. Mirror C is hit by scattered neutrons only. The reduced thickness of mirror C minimizes vertical secondary scatter into the roof laboratory.

Fig.2 Schematic view of diagnostic equipment beyond the biological shield in the roof laboratory.

Fig.3 CX CarbonVI spectrum in the UV, recorded with the optical mirror link. a) Cold component from edge recycling without NBI. b) Hot and cold components during NBI. Hot component from plasma centre fitted. Cold component not fitted, but relative amplitude shown as dashed level.

Fig.4 Comparison of Ti(CVI) deduced from the visible and UV CX lines.

Fig.5 BeIV CX spectra at 4658Å (n=6 to 5) and 4685Å (n=8 to 6) in the visible wavelength range. The 4685Å BeIV line coincides with the only HeII CX line accessible in the visible. The example is for a relatively high Be concentration level n(Be)>>n(He).

Fig.6 HeliumII CX spectrum at 3202Å (n=5 to 3). Similar to the visible spectrum a BeII line is present in the neighbourhood. The corresponding BeIV CX line (n=10 to 6) is supposed to be small but not completely suppressed in comparison with the HeII lines.

Fig.1

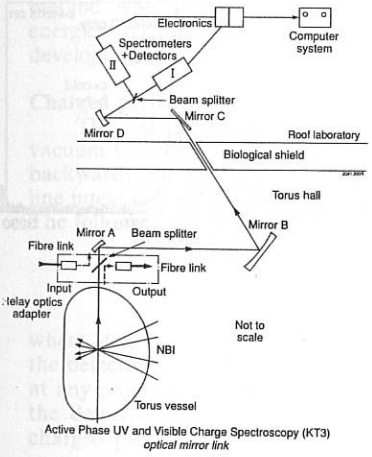

Fig.2

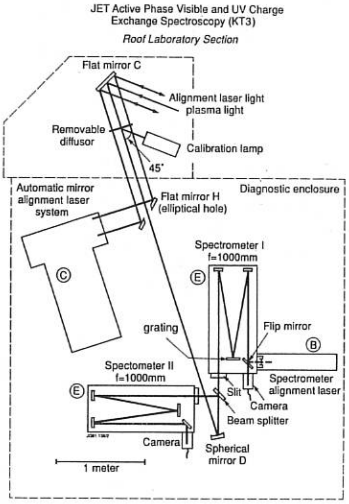

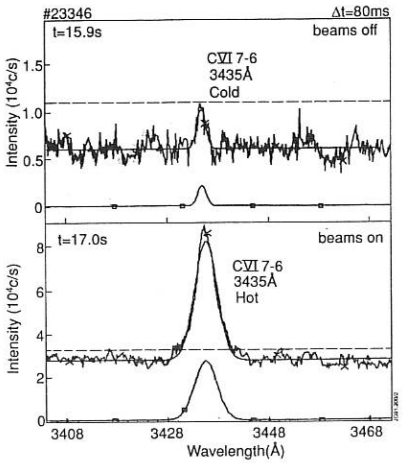

Fig.3

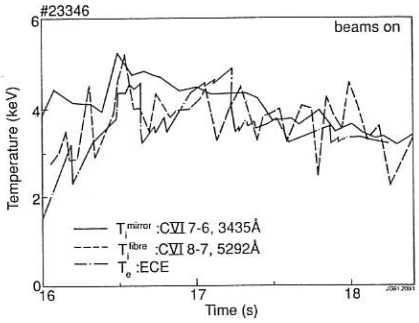

Fig.4

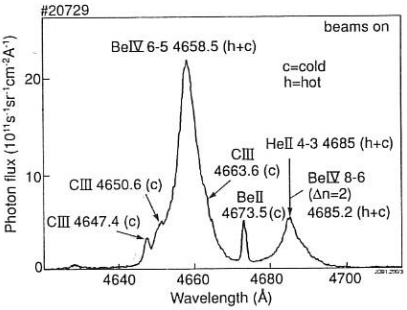

Fig.5

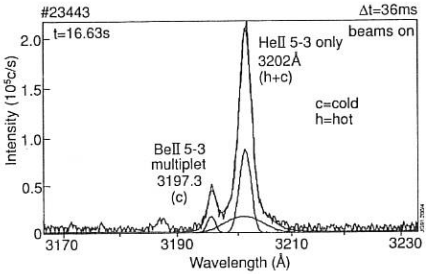

Fig.6

ALPHA-PARTICLE DIAGNOSTICS FOR THE D-T PHASE

S. W. Conroy, H. Bergsaker, J. P. Coad, O. N. Jarvis, F. B. Marcus, G. M. McCracken *, R. A. Pitts *, G. Sadler, P. van Belle, J. Zhu +

JET Joint Undertaking, Abingdon, OX14 3EA, U. K.
+ University of Sussex, Brighton, Sussex, U. K.
* AEA Fusion, Culham Laboratory, UKAEA/Euratom Fusion Association, OXON, U. K.

Abstract

Diagnostics to examine the lost α particle flux at JET during the D-T phase are under development. A passive ^{3}He collector probe has been tested during ^{3}He NBI and RF heated discharges. ^{3}He ions with energies of at least 100 keV have been detected; their source is probably due to the metastable component of the ^{3}He NBI. A code has been developed to model the charged particle fluxes at the wall.

Introduction

3.56 MeV α-particles produced in D-T plasmas in JET are expected to be well confined. However, processes such as sawteeth or α-particle driven instabilities may cause the loss of some of these fast particles to the wall. Detection of these escaping particles would provide useful information on the loss processes from the plasma, but represents a considerable challenge at JET because of the 300°C vessel temperature and the high neutron fluxes. Two approaches to measuring α-particle fluxes at the edge of the plasma are discussed here. The first is a time-resolved method of measuring the prompt loss particles. The second is a time-integrated method which gives the energy spectrum of the escaping alphas down to low energies. To aid in the design and interpretation of these detectors, a code has been developed to calculate the expected particle fluxes during D-T operation.

Charged particle flux calculations

The code calculates the flux of charged particles at a detector inside the JET vacuum vessel. For computational simplicity the particles are calculated travelling backwards in time from the surface of the detector, with the upper bound on the line integral determined by the first intersection of the orbit with a material surface. The following integral is evaluated

$$\text{Flux} = \frac{1}{4\pi} \int_0^A dA \int_0^{4\pi} \cos\theta \, d\Omega \int_0^\infty S \, dl$$

where A is the surface of the detector, θ is the angle to the normal of the plane of the detector made by the incident particle and S is the charged particle emissivity at any point on the orbit [1]. The details of the geometry of the JET vessel and of the detector under test are all explicitly included. The code assumes that the charged particles are not slowed down or scattered between their birth points and

hitting the detector. This assumption is good for prompt loss charged fusion products where the slowing down time is typically several orders of magnitude larger than the time taken to traverse the distance to the detector. However, for lower energy particles, this assumption may become invalid. The code also assumes that the particle source function has toroidal symmetry. The magnetic field geometry is calculated directly from measurements made for a specific JET discharge using the IDENTC code. Toroidal ripple effects are not normally included but a simple ripple model has been used for preliminary investigations. However, the fluxes appear not to be seriously affected unless a ripple much larger than that normally found at JET is used.

Escaping alpha particle detector

The main problem with building a time resolved prompt loss α particle detector at JET is the low flux of α-particles compared with the high flux of neutrons. This requires the use of a detector highly insensitive to neutrons and γ-rays yet still capable of accurately measuring low fluxes of α-particles. The most likely available position for a prompt-loss α-particle detector is in a vertical port, where the maximum detection efficiency for a 3MA, 2.9T plasma is typically $\approx 10^{-8}$ cm^{-2}. For a plasma with 10^{19} s^{-1} D-T reactions, this implies a flux of 10^{11} α-particles cm^{-2} s^{-1}, equivalent to a 32 nA current. This is a lower limit for the current as non-classical particle loss mechanisms may greatly increase it. The current could be measured by use of a Faraday cup detector. This forms the basis of the proposed escaping α-particle detector, shown in figure 1a.

The diagnostic will be mounted inside a vertical port in the shadow of X-point dump plates and should be primarily sensitive to prompt-loss α-particles. A test version is expected to operate in the D-D phase of JET operations in order to show the feasibility of the current detection in the electrically noisy environment of the JET vacuum vessel.

Fast ion probe

Initial measurements of helium ion collection used passive nickel samples distributed poloidally on the vessel wall and exposed to $\approx$5000 discharges [2]. The depth distribution of helium in the samples was obtained by sputter erosion and mass spectrometer detection. A significant population of energetic helium ions with energy > 1 keV was detected. To study the energy distribution under better defined conditions, a series of samples were exposed to one or more discharges in the probe shown in fig. 1b, using the JET Fast Transfer System [3] to position them near the plasma edge. The collectors are distributed in slots at different angles to the magnetic field in order to select ions of different Larmor radius. The energy distribution of the helium ions incident on each sample is derived by a deconvolution of the depth distribution [4].

Three classes of discharge will be discussed in this paper, labelled as types I-III. Type I discharges were primarily heated by D° NBI. The ^{4}He fluence at three different slots is shown in fig. 2a and it can be seen that the fluence at slot 0 is much greater than at slot 1 or 2. The average energy of the ^{4}He has been measured to be less than 2 keV. Type II discharges were heated with ^{3}He NBI (2.5MW at 120 keV), D NBI (3MW at 80 keV) and ^{3}He ICRH (6MW). Figure 2b shows that the measured ^{3}He fluence was much higher for slots ± 2 than for slot 0. The derived energy distribution of the ^{3}He ions in three slots is shown in fig. 3 and a substantial high energy component to the ^{3}He distribution is observed

in slot 2. Type III discharges involved ^{3}He ICRH but not ^{3}He NBI. The fluences are found to be similar to those in type I discharges.

To simulate the results of the Fast Ion Probe (FIP), a detailed model of the probe geometry and of the adjacent ICRH antennas were included in the code. The results from the code are shown in figure 4, where the source function of ^{3}He is assumed to be isotropic with an emissivity of 10^{21}m^{-3}s^{-1} at all radii. The type I discharge can be explained simply as a high density of ^{4}He with low temperature, since low energy ^{4}He ions have a small enough gyroradius that they cannot easily enter slots ±1 or ±2. The magnitude of the signal implies an emissivity of order 10^{20} m^{-3}s^{-1}. The type II discharges cannot be so easily interpreted. The ratio of slots ±2 to slot 0 implies an anisotropic population of ^{3}He, with few particles having a pitch angle less than 45°. This could be generated by the metastable ^{3}He beam ions deposited near the edge on banana orbits [5]. This is supported by the observation in type III discharges, which have no ^{3}He NBI, that slot 2 has a much lower fluence than slot 0. The results are also consistent with the observation that no energetic deuterons have been detected during D° NBI [2]; this is as expected since the metastable component of D° beams is negligibly small.

The flux of energetic ^{3}He detected at the FIP in type II discharges implies an emissivity of $\approx10^{20}$ m^{-3}s^{-1} at the edge. If this were uniformly distributed over the wall it would imply a total energy loss of many MW. Since this is considerably larger than the 0.25 MW expected to be lost by the ^{3}He beams near the plasma edge, we conclude that the ^{3}He flux to the probe is enhanced by a process not included in the model so far. Work is in progress to include large angle scattering by nuclear processes and ripple effects as possible explanations of this effect. The observed low fluence in slot 0 in the type II discharges implies a density of thermal ^{3}He near the edge approximately two orders of magnitude lower than the ^{4}He edge density in the type I discharge. This could be explained by ^{3}He being strongly pumped by the beryllium limiters as the type I discharge was run during the carbon limiter phase of JET, whereas the type II discharge occurred during the beryllium limiter phase.

Conclusions

The development of diagnostics to study the escaping α-particles from the JET plasma during the D-T phase is underway. The prompt loss α-particle detector has been designed and should be constructed and tested in JET soon. The Fast Ion Probe has been used in a number of discharges and has been shown to be effective for detecting high energy particles in the edge region. The results have been explained in a qualitative manner but more work needs to be done on the quantitative comparison. Further measurements on a wider variety of discharges should also be carried out. In particular, observation of discharges with ^{3}He NBI but no ICRH should be carried out in order to confirm that the source of the high energy particles in type II discharges is the metastable component of ^{3}He NBI.

References

[1] W. W. Heidbrink, Ph. D. Thesis, Princeton University, U.S.A. (1984)
[2] E. V. Carruthers et al, J. Nucl. Mat. **176** and **177** (1990) 1027
[3] D. H. J. Goodall et al, J. Nucl. Mat. **93** and **94** (1980) 383
[4] J. Zhu, Ph. D. Thesis, Sussex University, U. K. (1991)
[5] F. B. Marcus et al, this conference

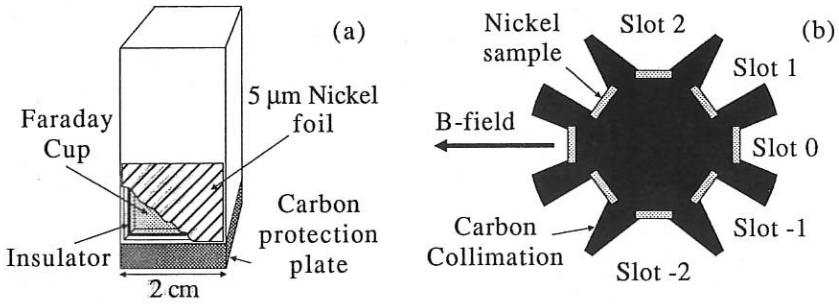

Figure 1: (a) the proposed escaping α-particle detector. (b) a section through the fast ion probe.

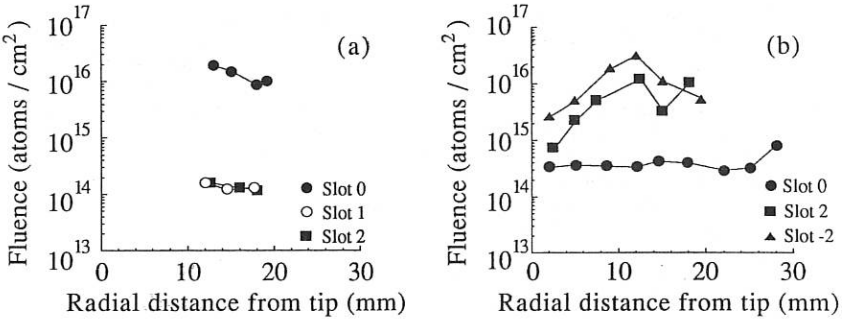

Figure 2: (a) and (b) show the observed Helium fluence as a function of distance along the FIP for type I and type II discharges, respectively.

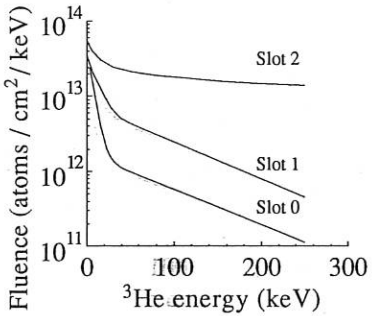

Figure 3: Energy distribution of ^{3}He in type II discharges.

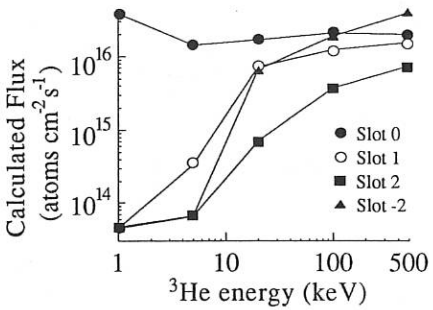

Figure 4: Calculated ^{3}He fluxes as a function of energy for the FIP.

NEUTRON PRODUCTION DURING DEUTERIUM INJECTION INTO ASDEX

B. Bomba, ASDEX Team, NI Team, Max-Planck-Institut für Plasmaphysik, EURATOM Association, D-8046 Garching

Y. Feng, K. Hübner, B. Wolle, Institut für Angewandte Physik, Universität Heidelberg, D-6900 Heidelberg

I. Introduction

In this paper we discuss the behaviour of the neutron rate during deuterium injection into a deuterium plasma for several confinement regimes, namely co-injection, density limit discharges, and discharges with counter-injection. With these results we are able to explain the ion temperature development in these regimes. Finally, we present results from deuterium injection into a helium plasma.

II. Theoretical predictions

During deuterium injection into a deuterium plasma the total neutron rate Q is the sum of the beam-beam neutron rate Q_{bb}, the beam-target neutron rate Q_{bt} and the target-target neutron rate Q_{tt}. Here Q_{bb} consists of neutrons from reactions between the injected deuterons, Q_{bt} is produced by the Maxwellian plasma and the injected particles, and Q_{tt} is the result of reactions between the Maxwellian deuterons.

For the plasma parameters in ASDEX, plasma current $J_{plasma} \leq 460$ kA, toroidal magnetic field $B_{tor} \leq 2.8$ T, injection power ≤ 2.7 MW, injection energy

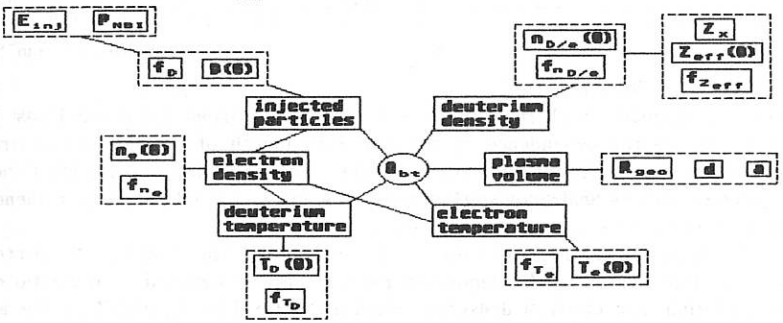

Fig. 1

$E_{inj} \leq 53$ keV, central ion and electron temperatures $T_D(0)$ and $T_e(0) \leq 3$ keV, central electron density $n_e(0) \leq 1.5 \cdot 10^{14}$ cm^{-3}, the total neutron rate is dominated by the beam-target neutron rate ($Q_{bt}/Q_{tot} \geq 0.8$). As illustrated in Fig. 1, Q_{bt} is directly determined by the injection, deuteron temperature T_D and density n_D, electron temperature T_e, and plasma geometry, whereas the electron density n_e has a more indirect effect, influencing the injection and the two temperatures.

To express the radial variation of a plasma parameter g(r), it was defined as the product of its central value g(0) and its profile function $f_g(r)$: $g(r) = g(0) * f_g(r)$. Furthermore, we use the peaking factor $q_g = g(0) \,/\, \langle g(r) \rangle = V_{plasma} \,/\, \int f_q(r)\, dV$, where V_{plasma} is the plasma volume, q_g increases with tapering profiles.

The calculations for this paper were done with our new NRFPS neutron rate interpretation code, which takes a solution of the Fokker-Planck equation to describe the velocity distribution function of the particles /1/. The following discussions are based on a data bank of 246 injection profiles, calculated with the FREYA code, depending on the electron density and injection energy.

Figures 2a and 2b show the influence of the electron density on the beam-target neutron rate. With tapering n_e profiles and $n_e(0)$ kept constant, the deposition profile also tapers, q_D increases, and the central deposition D(0) rises. The rise increases with decreasing central density, and so Q_{bt} increases with rising q_{ne} as shown in Fig. 2a. If we increase the central density for constant profile, the deposition profile f_D broadens and the central value D(0) decreases.

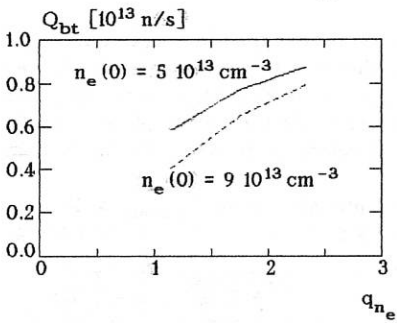

Fig. 2a

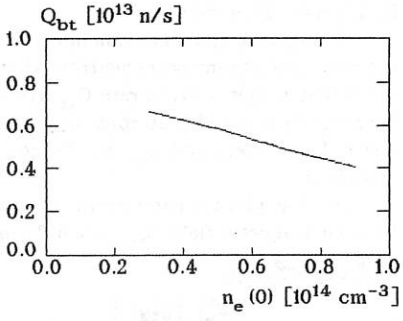

Fig. 2b

Thus Q_{bt} decreases with rising $n_e(0)$ (Fig. 2b). The reasons for these kinds of behaviours are the dependence of the ionisation length of the injected neutral particles on the density and conservation of the number of injected particles. Other parameters such as Shafranov shift, temperature and so on only slightly influence the deposition in the parameter area discussed.

The beam-target neutron rate is proportional to the number of injected particles, represented by the deposition profile, and proportional to the ratio of the deuterium and electron densities, which are defined by Z_x and Z_{eff}. For all our calculations we use $Z_x = 7$ as an average for oxygen and carbon.

The electron density influences the temperatures too; it is $n_e(0) \sim 1 \,/\, T_e(0)$, but the proportionality factor changes with the injection power and depends on the confinement regimes.

Figures 3a and 3b show the influence of the temperature on the beam-target neutron rate. Increasing $T_e(0)$ increases Q_{bt}. The rise depends on the ratio T_D/T_e, the same profile being assumed (Fig. 3a). Of course, Q_{bt} decreases with tapering

profiles if the central value is constant. But the decrease in the case of tapering electron temperature profiles is higher than in the case of tapering ion temperature profiles (Fig. 3b), since the total slowing-down time of the injected particles is more influenced by impact with target-electrons than with target-ions.

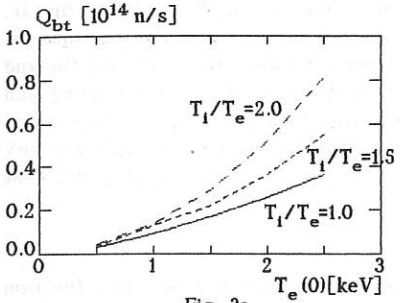

Fig. 3a

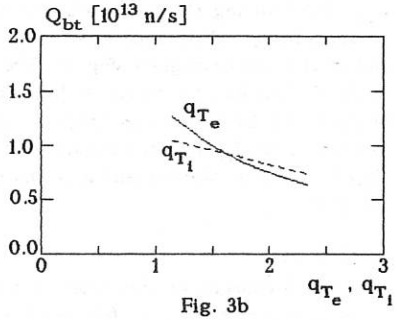

Fig. 3b

III. Density limit

In density limit discharges $n_e(0)$ rises during co-injection, while q_{ne} keeps constant. Consequently, $T_e(0)$ decreases from 1 keV to 0.6 keV and q_{Te} does not change either. If the measured neutron rate Q(t) is plotted versus $P_{NBI}*T_e(0) * n_d/n_e$, it is found that the proportionality factor between Q(t) and this product depends on the time of the density development. In Fig. 4 the squares represent the beginning, the crosses the middle, and the triangles the end of injection, when the density limit is reached. The difference in the measured neutron rate between the beginning and end is 50 %. From our model we get a decrease of 50 % in the neutron rate owing to the rising densities and 25 % owing to the decrease in the electron temperature. Therefore, there must be an increase in the T_D/T_e ratio. With our interpretation code we get T_D = 1.2 keV (T_D/T_e = 1.2) at the beginning of injection and T_D = 0.84 keV (T_D/T_e = 1.4) at the end.

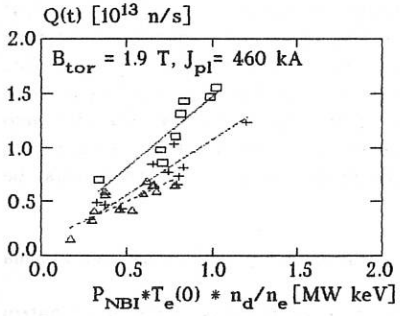

Fig. 4

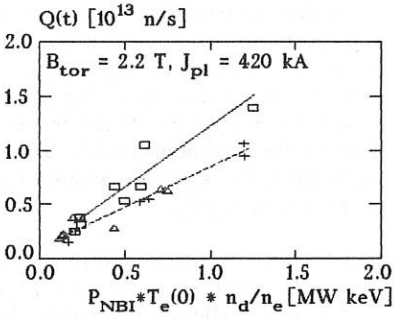

Fig. 5

IV. Counter-injection

As in density limit discharges, $n_e(0)$ rises during discharges with counter-injection, from $6 \cdot 10^{13}$ cm^{-3} to $9 \cdot 10^{13}$ cm^{-3}, and $T_e(0)$ decreases, from 0.9 keV to 0.6 keV. But the density profiles taper during the injection from $q_{ne} \approx 1.6$ to $q_{ne} \approx 2.1$. Plotting the measured neutron rate versus $n_D/n_e * P_{NBI} * T_e(0)$ (Fig. 5), we again found a difference between Q(t) at the beginning of the injection (squares) and at the end (triangles) (Fig. 5). The difference between the start and the end is 30 %. One has to expect a decrease of 30 % due to the density rising and peaking and 25 % due the temperature decrease. Thus, their must again be an increase in the T_D/T_e ratio. Results from the interpretation code give T_D = 1.08 keV (T_D/T_e = 1.2) at the beginning of injection and T_D = 0.78 keV (T_D/T_e = 1.3) at the end.

V. $D^0 \rightarrow {}^4He$

For discharges of this type we cannot show the neutron rate as a function of $P_{NBI} * T_e(0) * n_D/n_e$ as for density limit discharges and counter-injection, because the deuterium density n_D is not known from Z_{eff} measurements. The bremsstrahlung spectrum is disturbed by spectral lines from the helium. So the points will scatter around a rising line as in the Fig. 4 and 5.

On the other hand, this situation allows us to check our results from the NRFPS code for the beam-beam neutron rate. When injection starts, there are only neutrons from d-d reactions until the fast particles are thermalized. This period is characterized by the energy relaxation time τ_w. For the plasma parameters of discharge #32548 ($n_e(0) = 1.1 \cdot 10^{14}$ cm^{-3}, $T_e(0)$ = 0.8 keV, E_{inj} = 50 keV) we get τ_w = 8 ms. There is good agreement between the calculated beam-beam neutron rate from NRFPS ($Q_{bb} = 6.0 \cdot 10^{11}$ n/s) and the measured neutron rate ($Q(t) = 5.2 \cdot 10^{11}$ n/s).

VI. Comparison with H- and L-mode

In /2/ we studied the neutron rate during the H- and L-modes. There Q(t) is proportional to $P_{NBI} * T_e(0) * n_D/n_e$, but this does not depend on whether Q(t) is measured at the beginning or end of injection. The ratio T_D/T_e is thus constant. In density limit discharges with co-injection and discharges with counter-injection $T_e(0)$ decreases because of the rising density. The rise also broadens the deposition profile. But the decrease of the measured neutron rate due to these two effects is smaller than the predicted one. Thus, there must be an increase in T_D/T_e.

/1/ B.Wolle, B.Bomba, K.Hübner, 17th Europ. Conf. on Control Fusion and Plasma Physics, Amsterdam 1990, part IV, p. 1516

/2/ B.Bomba, K.Hübner, J.Kucinski, S.Lutz, et al., 16th Europ. Conf. on Control Fusion and Plasma Physics, Venice 1989, part IV, p. 1457

OBSERVATION OF VELOCITY DEPENDENCE AND LINE-OF-SIGHT EFFECTS IN ION TEMPERATURE AND TOROIDAL ROTATION VELOCITY MEASUREMENTS AT JET.

M.Danielsson, E.Källne, K.-D.Zastrow, M.von Hellerman,+ W.Mandl,+ H.Morsi+ and H.P.Summers+.

Department of Physics I, Royal Institute of Technology, S 10044 Stockholm, Sweden
+ JET Joint Undertaking, Abingdon, OX14 3EA, England

The goal of this work has been to improve the accuracy of the plasma rotation velocity and ion temperature measurements based on spectroscopic techniques. It has been clear from previous comparison of data from different diagnostic systems that the spread in data was too large to be explained by statistics only (see e.g.[1]). In this paper we have studied in detail the different physical aspects of the spectroscopic measurements and as a result achieved a significantly improved accuracy of the measurements for a large range of plasma parameters.

At JET the two spectroscopic techniques used for ion temperature and toroidal velocity measurements are based on high resolution x-ray measurements from intrinsic medium Z impurities (mainly Ni is used) [2] and visible charge exchange spectroscopy using the neutral heating beams and observing emission from low Z impurities in the plasma (e.g., Be, C and O) [3]. Thus, the x-ray spectroscopy method is based on interpreting data along a line-of-sight through the plasma and the visible charge exchange spectroscopy is based on spatially resolved observations along the neutral beam path through the plasma.

The radial dependence of the line-of-sight observations can be extracted through modelling the observed spectrum using observed radial profiles from e.g., electron temperature and density together with the calculation of the x-ray spectrum with proper line profiles taken into account. As a result of this analysis method the central values for ion temperature is obtained from the line width and the central rotation velocity from the line shift in contrast to the average values obtained directly from interpreting the line-of-sight data. The difference between the central and the average values thus depends on several plasma parameters such as electron temperature and density, profile functions for the electron and ion distributions[4]. The dependence on the different factors can only be obtained through a complete modelling of the x-ray spectrum which takes into account all the atomic processes producing the spectral lines and integrating each spectrum along the line-of-sight. The best fit modelled spectrum representing the observation along the line-of-sight is achieved from an iterative procedure comparing with the experimentally observed line-of-sight spectrum. Figs. 1a and 1b show the result of the analysis for a specific JET pulse with a maximum electron temperature of ca 7 keV. It is clear, that the accuracy of the line-of-sight x-ray measurements is considerably improved by the analysis method which can also be extended to other spectroscopic line-of-sight observations. Furthermore, it is interesting to note that the analysis method gives not only consistent and considerably improved ion

temperature and toroidal velocity data but also data on electron temperature[5] and Z_{eff} of the plasma.

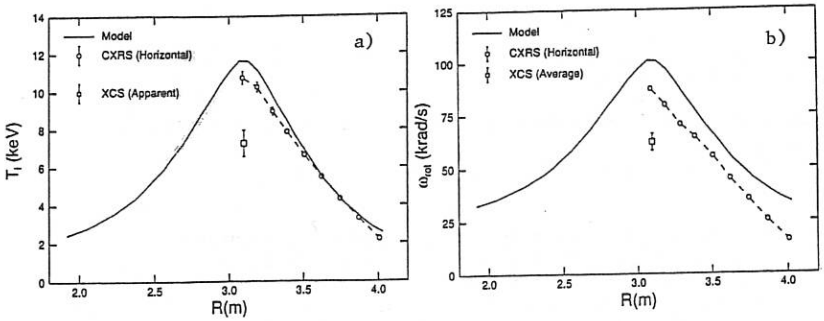

Fig.1 Ion temperature (a) and toroidal velocity(b) profile from the model fit compared to the profile and central chord value from charge exchange recombination spectroscopy (- - -) and the average values from the line-of-sight x-ray spectroscopy ($\overline{\square}$).

For the charge exchange spectroscopy observations the velocity dependence of the reaction cross section gives rise to an apparent rotation velocity depending on the ion temperature. Fig.2 shows the predicted apparent rotation velocity taking into account the geometry of the JET spectroscopy set-up and the different energies in the neutral beam[6]. The predicted apparent rotation velocity has been experimentally verified analysing the spectral data from the charge exchange spectroscopy emission from carbon ions over a wide range of ion temperatures. The agreement with the theoretically predicted dependence is good and shows clearly that the effect will cause a systematic deviation of the toroidal velocity data deduced from charge exchange spectroscopy.

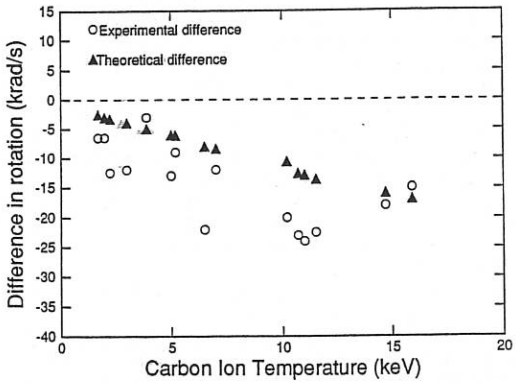

Fig.2 Apparent rotation frequency as a function of ion temperature caused by the energy dependence of the charge exchange cross section(▲) and compared to the experimentally obtained values(o).

Spectroscopic observations from both the helium-like nickel x-ray lines (w from Ni^{26+}, $1s^2\ {}^1S_0$ - $1s2p\ {}^1P_1$, is used since its effective emission is largest for all nickel ionisation stages for electron temperatures up to 11 keV) and for hydrogen-like carbon visible lines (produced by the reaction $D^o + C^{6+} \rightarrow D^+ + C^{5+}(n=8) \rightarrow C^{5+}(n=7) + h\nu$) have been compared for a large number of JET pulses using several time slots for each plasma pulse. The results are presented in Figs. 3 and 4. It is clear that the effects of the improvement in the analysis methods can be quite dramatic. The full analysis of the x-ray measurements has furthermore considerably decreased the scattering of the data and reduced the uncertainty in the central ion temperature values from 60% to 20%.

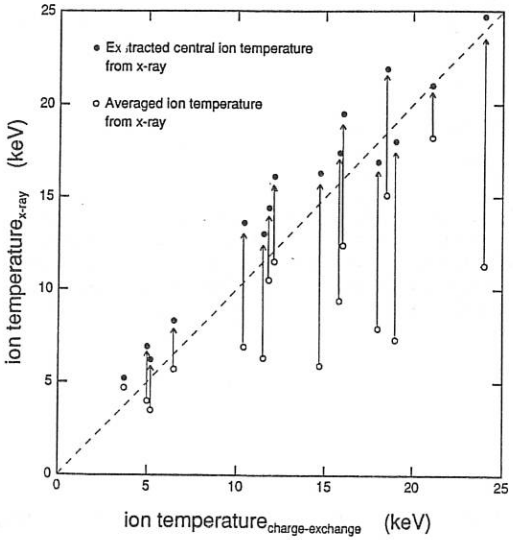

Fig.3 Comparison of ion temperature values from charge exchange and x-ray measurements before (o) and after (●) the full analysis method has been applied to the x-ray data.

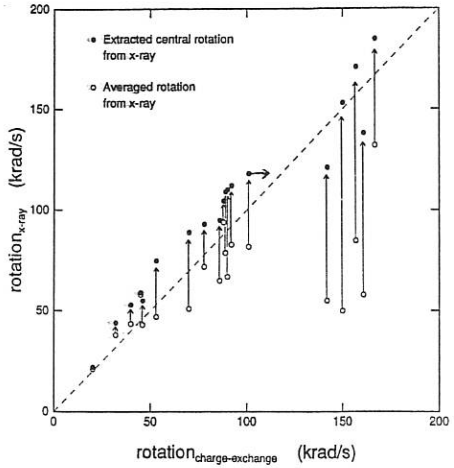

Fig.4 Comparison of toroidal rotation velocity data from charge exchange and x-ray measurements before (o) and after(●) the full analysis method of the x-ray data has been applied. The effect on the charge exchange data from the velocity dependence of the cross section is indicated with a horisontal bar.

References

1. H.W.Morsi et al, in Proc. 17th EPS Conf on Plasma Physics and Controlled Fusion, Amsterdam, 1990
2. R.Giannella, J.de Physique 49,C1-283(1988)
3. M.G. von Hellerman et al, Rev.Sci.Instr.61,3479(1990)
4. K.-D.Zastrow et al, JET report JET-P(90)18
5. K.-D.Zastrow, E.Källne and H.P.Summers, Phys.Rev.A41,504(1988)
6. M.G.von Hellerman et al, to be submitted, and H.P.Summers private communication

$T_i(r)$ PROFILES FROM THE JET NEUTRON PROFILE MONITOR FOR OHMIC DISCHARGES

B Esposito[+], F B Marcus, J M Adams*, S Conroy, O N Jarvis, M J Loughlin, G Sadler, P van Belle, N Watkins*

JET Joint Undertaking, Abingdon, Oxon, OX14 3EA, England [+]Associazione EURATOM-ENEA, CRE Frascati, Italy
*AEA Industrial Technology, Harwell Laboratory, Oxon, OX11 ORA, England

ABSTRACT

A study has been made of the neutron emissivity, using the JET neutron profile monitor, obtained for ohmically heated deuterium discharges. Both one-dimensional (1-D) best-fit inversion procedures and 2-D tomography have been used to deduce the radial profile of the neutron emission from the line-integral data. The profiles of ion temperature and ion thermal conductivity are then derived. The scaling of the ion thermal conductivity with plasma current is found to be opposite to that of neoclassical theory.

INTRODUCTION

The behaviour of the deuterium ions in a thermonuclear deuterium-deuterium (D-D) plasma has been extensively studied at JET by means of the neutron profile monitor [1]. This profile monitor consists of nineteen collimated channels and detectors, ten horizontal and nine vertical (eight are used). The measurement, after corrections for solid angle, detector efficiency, neutron attenuation, neutron backscatter, livetime and collimator scattering, gives the line-integrated neutron emissivities from each channel. These can be inverted to obtain the actual distribution of the neutron emissivity in the plasma.

In ohmic plasmas, the neutrons produced are due only to thermal reactions. The ion temperature profile can then be inferred from the neutron emissivity and deuteron density profiles, the latter obtained separately from electron density and Z_{eff} measurements. Ion temperature profiles of ohmic discharges in JET are particularly useful for transport studies because of the large plasma current range, and they can then be used to deduce the ion thermal conductivity for comparison with neoclassical theory.

DISCHARGE CHARACTERISTICS

The ohmic discharges chosen were deuterium plasmas with high enough neutron yields, for good statistics ($> 10^{13}$ neutrons except for 2 MA plasmas, integrated over time), and $Z_{eff} < 4$, to obtain a good estimate of deuteron density. During each discharge, the integration times were at least one second, with the neutron emissivity and the electron density constant to within 20%, except for sawtooth oscillations. Sawteeth were present in discharges with medium and high currents. Some ^{3}He minority ICRF heated discharges are also investigated, making a total of 30.

NEUTRON EMISSIVITY PROFILES

The neutron profile monitor data are analysed in this paper principally by means of the 1-D ORION code [2], with comparisons made

with the 2-D NEUTOMO tomography code [3]. ORION uses a minimization procedure that fits a neutron emissivity profile represented in a 1-D functional form $S_n(\rho)=S_0(\rho)(1-\rho^2)^{\alpha_n}$, where $\rho=r/a$, to the measured line-integral channel data. Magnetic flux surfaces are assumed to have constant emissivity. Fig. 1 shows the experimental neutron brightness in bar chart form versus channel number in the 4.8 MA ohmic discharge #15119, with data integrated from 9 to 14 s. The best fit from the ORION code, where α_n=4.15 was found, is also plotted as circles. The advantage of the parabolic (to the α_n power) form is that the profile width of a wide range of discharges can be compared with one parameter.

Fits are also obtained with NEUTOMO which does not assume any particular functional form of the emissivity. The 2-D NEUTOMO results are then averaged into 1-D to compare with the ORION 1-D results; they are shown as x's in Fig. 1. Fig. 2 shows the volume neutron emissivity plotted versus normalized radius ρ, for #15119. For $\rho>0.3$, the results are similar but diverge on axis. The discharge has large sawtooth crashes, and the neutron emissivity profile, integrated over these sawteeth, is a superposition of profiles before (peaked) and after (flattened to hollow) the sawtooth crash. Even so, the α_n calculated by ORION gives a good measure of the relative peaking of the discharges. At low plasma current, the two codes give similar results near the axis.

In Fig. 3, the peaking factor α_n is plotted versus plasma current for the ohmic discharges. Sawteeth are present at 3 MA and above. Also shown is the α_n for deuterium plasmas with ICRF ^{3}He minority heating, where the results are somewhat more peaked. The trends clearly show that the profiles broaden as the plasma current increases.

ION TEMPERATURE PROFILES

Once the neutron emissivity is available for a plasma with only thermal D-D reactions, the ion temperature versus radius is determined from $S(\rho)=0.5n^2\langle\sigma v\rangle$, where n is the deuteron density found from the electron density profile and Z_{eff}, and $\langle\sigma v\rangle$ is the thermal D-D fusion reactivity for neutron production. The resultant ion temperature profiles are fairly well fitted by the function $T(\rho)=T(0)(1-\rho^\beta)^\gamma$. In the ohmic discharges analyzed, the central ion temperatures are less than 2.7 keV. The neutron emissivity is proportional to T_i^κ, where $\kappa > 4$ in this range. For ICRF heated plasmas with higher temperatures, κ still exceeds 3. Therefore, even though there is some disagreement in neutron emissivity on axis between the ORION and NEUTOMO calculations, the ion temperature profile is still accurately determined and agrees with independent neutron spectrometer measurements. For (errors) in the neutron emissivity (15%), electron density (10%), and Z_{eff} (30%), the errors in ion temperature are 15% and 30% for Z_{eff} of 2 and 4, respectively. As is shown in Fig. 4, the ratio of central ion to electron temperature is equal to about 2/3 and nearly constant over a wide range of central electron density. ICRF heated plasmas in this data sample reach higher densities than ohmic, and have a slightly higher ratio, around 3/4.

ION THERMAL CONDUCTIVITY

In the central and intermediate regions of an ohmically heated plasma, the ion power balance in steady state should be dominated by heat gain from the electrons and loss from ion thermal conductivity, apart from the effects of sawteeth in the central region. By integrating the electron-ion transfer power up to a radius ρ, and

finding the ion temperature gradient $dT/d\rho$ at each radius, the ion thermal conductivity χ_i is calculated. The ORION and NEUTOMO temperature profiles give similar results for $0.3<\rho<0.5$, where they are most reliable, since sawteeth are important for $\rho<0.3$ and, for $\rho>0.6$, the effects of radiation, convection, and charge exchange may be more important for the power balance. ICRF heating with ^{3}He discharges is not included in this analysis, since there is some direct ion heating from the fast ^{3}He ions.

The ion thermal conductivity χ_i for each discharge is averaged over the range $0.3<\rho<0.5$ and plotted as a function of plasma current in Fig. 5. The range of χ_i is from ~0.5m^2/s to ~2.5m^2/s and χ_i increases with plasma current. The error bars can be as large as 100%. The experimental scaling of χ_i therefore appears to be opposite to that of neoclassical ion thermal conductivity [4] and, for individual discharges, even with large error bars, the neoclassical value is always exceeded. For the χ_i values averaged over $0.3<\rho<0.5$, the ratio to the neoclassical value varies from over 2 at the lowest current to over 30 at the highest current.

DISCUSSION AND CONCLUSIONS

It is shown that neutron profile monitor data, using both 1-D and 2-D analysis methods, provides a measure of the thermal D-D neutron emissivity during ohmic and ICRF ^{3}He minority discharges which, in turn, provides a reliable determination of the radial deuterium temperature profiles. The neutron emissivities and the ion temperatures are found to be much more peaked at the plasma centre for low current discharges than at high current. The ratio of central ion to electron temperatures is nearly constant over a wide range of densities. By means of a simple local transport analysis, the ion thermal conductivity can be derived from the deuterium temperature profile. The inferred χ_i for $0.3<\rho<0.5$, is in the range 0.5 to 2.5 m^2/s and is higher than predicted by neoclassical theory. The wide range of plasma current in JET demonstrates the deviation from theory in ohmic discharges.

REFERENCES

[1] J M Adams et al, Proc. 16th EPS Conf. Venice (1989) 13B I, 63.
[2] S W Conroy, Ph.D Thesis, Imperial College London, (1990)
[3] F B Marcus et al, Plasma Physics and Controlled Fusion 33 (1991) 277
[4] C S Chang and F L Hinton, Phys. Fluids 29 (1986) 3314.

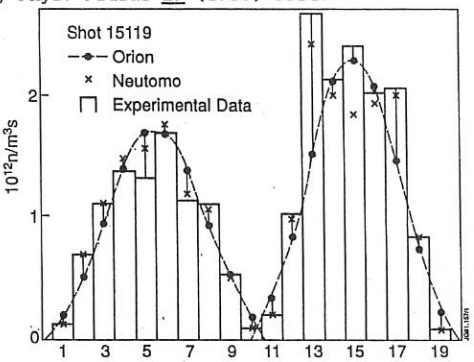

Fig.1. Neutron brightness versus channel number for 5 MA ohmic discharge #15119 showing experimental measurements (bar chart), 1-D ORION fits (circle, dotted line), and the 1-D average of a 2-D NEUTOMO tomography fit (crosses)

Fig.2. Neutron emissivity for 5 MA ohmic discharge #15119 with NEUTOMO and ORION

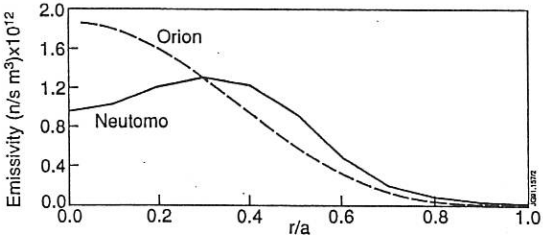

Fig.3. Neutron emissivity parabolic peaking factor α_n versus plasma current Ip, for ohmic and ^{3}He minority ICRF heating

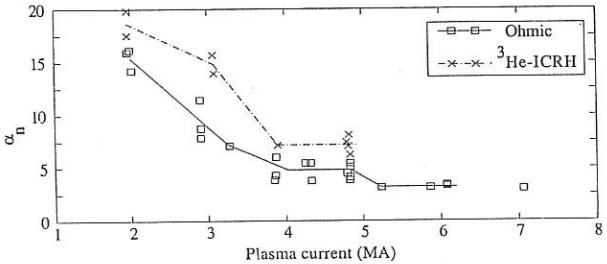

Fig.4. Ratio of central ion temperature from ORION to central electron temperature (ECE) versus electron density, ohmic and ICRF

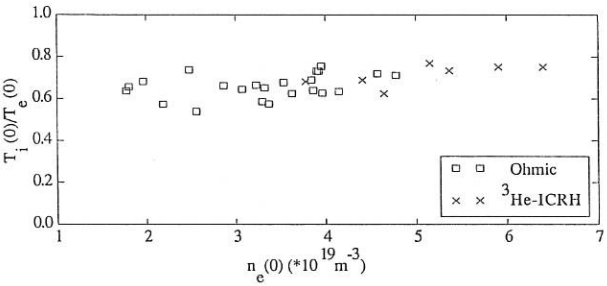

Fig.5. Ion thermal conductivity (averaged over $0.3<\rho<0.5$) versus plasma current Ip.

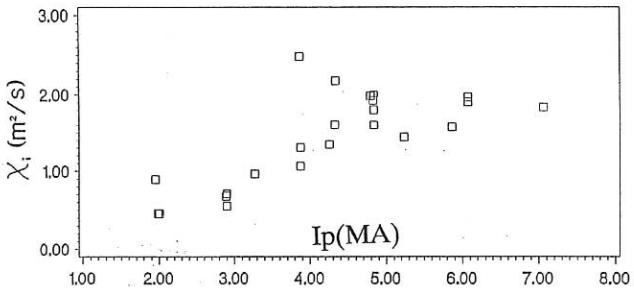

Ion Temperature and Fuel Dilution Measurements using Neutron Spectrometry.

M.J.Loughlin, J.M.Adams[+], S.Conroy, T.Elevant[*], N.Hawkes[+], O.N.Jarvis, F.B.Marcus, H.Morsi, M.Olsson, G.Sadler, P.van Belle, M.von Hellermann.

JET Joint Undertaking, Abingdon, Oxon., OX14 3EA, England.
[+]AEA Industrial Technology, Harwell Laboratory, Oxon., OX11 0RA, England.
* Royal Institute of Technology, Stockholm, Sweden.

Abstract

Ion temperature measurements are routinely made using neutron spectrometry during different forms of additional heating. In this paper the results are compared with those from other diagnostics. Estimates of the deuterium concentration derived from neutron diagnostics are also presented. The advantages of using of helium neutral beams for neutron diagnostics are discussed.

1.Introduction

The neutron energy spectrum from a purely thermonuclear deuterium plasma takes the form of a gaussian centred near 2.45MeV. The width (*fwhm*) of the peak is related to the deuterium temperature (T_i) according to the formula:

$$fwhm = \alpha\ T_i^{1/2}$$

where α is weakly dependent on ion temperature [1] and is approximately equal to 82.5 when the ion temperature and *fwhm* are in keV. This ion temperature measurement, when coupled with measurements of the total neutron yield, can be used to provide an estimate of the deuterium ion concentration.

The use of additional heating can greatly affect the neutron energy spectrum. Deuterium neutral-beam injection leads to predominantly beam-plasma and, to a lesser extent, beam-beam reactions. The former results in a much broader neutron spectrum [1] which limits the ability of neutron spectrometry to determine the ion temperature. The use of an 'inert' beam species, such as helium eliminates beam-plasma reactions. This provides the opportunity to compare temperature measurements from neutron spectrometry and charge exchange spectroscopy, which has not been previously possible. The neutron spectrometers used at JET include a ^{3}He ionisation chamber and a time-of-flight spectrometer [2,3].

A high energy tail in the deuteron energy distribution, which can be generated during RF heating, produces a broad neutron energy distribution which does not obscure the 2.45MeV peak produced by the neutrons generated in thermal fusion reactions, i.e. the *fwhm* is still measurable. On the other hand, the presence of beryllium in the plasma can lead to a gross distortion of the neutron energy spectrum, and the width of the peak can no longer be related to the temperature.

2. Neutron Spectra during NBI.

The neutron energy spectrum recorded during deuterium NBI is made up primarily of two major components, the relatively narrow thermonuclear peak and the broader beam-plasma distribution. The fractional plasma-plasma yield can be determined by fitting the sum of the two calculated spectra to the measured spectrum using the relative areas and the ion temperature (i.e. the width of the gaussian) as fitting parameters [2]. If the ion temperature is already known this can, alternatively, be used as a constraint. With both ion

temperature and the plasma-plasma fraction known, the deuterium concentration can be determined even in the presence of a sizeable beam-plasma component[4].

When helium and deuterium beams are used simultaneously, the thermonuclear fraction can be relatively large, which greatly simplifies the measurement of the ion temperature from the neutron spectrum. Measurements using this technique are compared to those from charge exchange spectroscopy in figure 1 and show good agreement. For all the disharges studied, the plasma-plasma yield represented more than 50% of the total neutron yield.

3.Neutron Spectra during RF and RF/He-beam heating.

In the absence of deuterium NBI and at moderate levels of RF power per particle the neutron spectrum is gaussian and the ion temperature can be determined. At higher RF power levels, reactions between a high energy tail in the ion energy distribution and the bulk plasma result in a low flat continuum in the neutron spectrum; the 2.5MeV thermonuclear peak is superimposed on top of this. A comparison of ion temperature measurements from neutron spectrometry and the x-ray crystal spectrometer [5] (fig. 2) yields good agreement. This demonstrates that the *fwhm* of the gaussian peak can still be accurately determined in the presence of a non-thermonuclear background and remains an accurate measure of the temperature.

Neutron spectrometry has a limited time resolution because of the limited count-rate capability of most spectrometers and the need for a certain minimum number of counts. However, the high levels of thermonuclear emission produced during combined He NBI and RF heating permits a spectrum to be accumulated in 500ms and, when combined with total neutron yield measurements, allows a determination of the deuterium concentration (n_d) as a function of time (fig. 3). This is particularly important during He injection when n_d cannot be determined from Z_{eff} measurements, because the He concentration is not known, or from charge exchange spectroscopy since there is currently no appropriate line-of-sight for the He injection box.

The presence of a high energy tail in the ion energy distribution can lead to a distortion of the neutron spectrum due to neutron producing reactions between the fast ions and beryllium when this is present as an impurity. Reactions involving protons, deuterons, and ^{3}He ions have been identified by analysis of γ-ray spectra collected simultaneously. The effect is most pronounced during 'monster sawteeth'. In figure 4 the electron temperature traces for discharges 23261 and 23285 are shown as a function of time. During discharge 23285 there are rapid sawteeth while in 23261 the sawteeth are stabilised. The neutron spectrum from the first discharge retains the thermonuclear peak while in the second the 2.45MeV peak is obscured almost totally by neutrons produced in reactions with beryllium, although the RF power per particle is the same in both discharges. The impurity accumulation in the absence of sawteeth can be a serious problem.

4.Comparison of heating techniques

Neutron spectrometry has been applied to the regime of neutral beam heating using helium beams. The advantages of this form of heating in terms of neutron economy and reduced machine activation are discussed elsewhere [6] but the relative efficiency of He NBI is demonstrated in figure 5. The ion temperature, obtained from neutron spectrometry is plotted as a function of total additional heating divided by the axial electron density. The temperatures during pure deuterium beam heating, measured using the charge exchange spectroscopy diagnostic since neutron spectrometry measurements are less straight-forward during pure D NBI, are also included. It can be seen

that the ion heating using He beams can be at least as effective as pure deuterium beam heating. The effect of additional RF heating is unpredictable but under optimised conditions substantial ion heating is possible.

5. Conclusions

Neutron spectrometry can be used to obtain a reliable measure of the ion temperature during neutral beam heating provided the thermonuclear fraction is sufficiently high (>50%) and during RF heating if the spectrum is not unduly contaminated by reactions with impurities. These measurements, if combined with the total neutron yield, can yield the deuterium concentration.

Helium NBI is as effective in heating the plasma as deuterium beams while facilitating neutron diagnosis of the plasma by eliminating beam-plasma reactions.

The ion temperature attainable with RF and He NBI are comparable to those obtained with deuterium beam heating alone for similar levels of power per particle.

References

[1] P.van Belle and G.Sadler, 'Basic and Advanced Fusion Plasma Diagnostic Techniques', (Varenna 1986) Vol III, 767, EUR 10797 EN.
[2] M.J.Loughlin *et al.*, Nucl. Instrum & Meth. A281 (1989) 184.
[3] T.Elevant *et al.*, JET-P(89) 76.
[4] O.N.Jarvis *et al.*, Nucl Fusion, 30 (1990) 307.
[5] H.W.Morsi *et al.*, 17th EPS Conf. on Controlled Fusion and Plasma Physics, Amsterdam 1990, Vol IV, 1608.
[6] F.B.Marcus *et al.*, these proceedings.

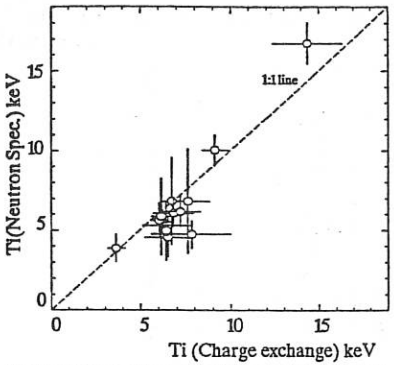

Figure 1: Comparison of ion temperature measurements from the neutron spectrometer and charge exchange diagnostics.

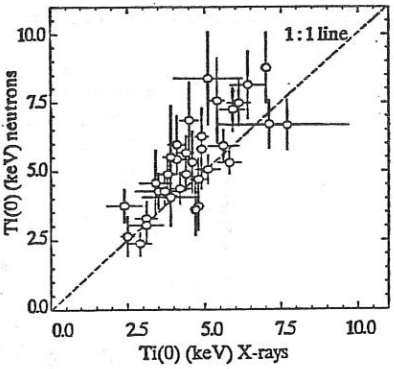

Figure 2: Comparison of central ion temperatures from neutron spectrometry and nickel x-ray measurements. The x-ray results have been fully corrected for electron density and temperature profile effects.

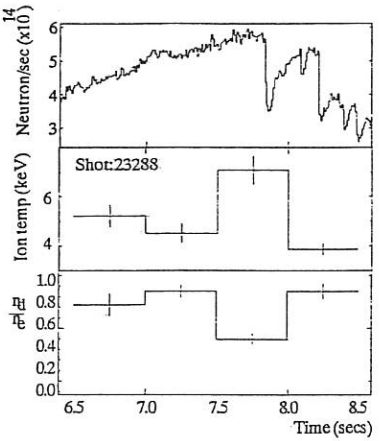

Figure 3: Ion temperature and nd/ne measurements from a neutron spectrometer and neutron emission as a function of time. (Shot 23288 4MW NBI, 6.5MW RF, tuned to H) Typical error bars are shown.

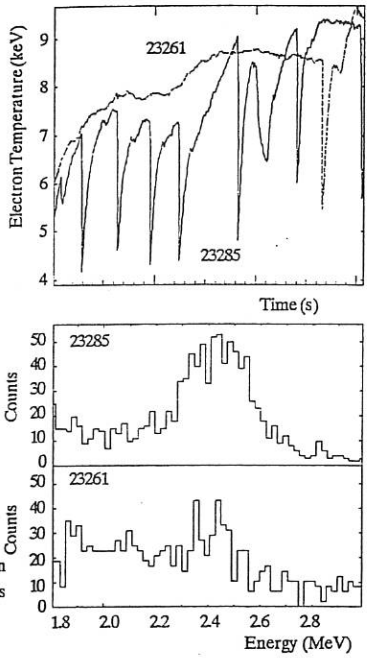

Figure 4: For the shot 23261 and 23285 the RF power per particle is approximately equal but the neutron spectrum in shot 23261 is almost entirely due to neutrons from Be. This effect does not occur when there are rapid sawteeth (see top trace).

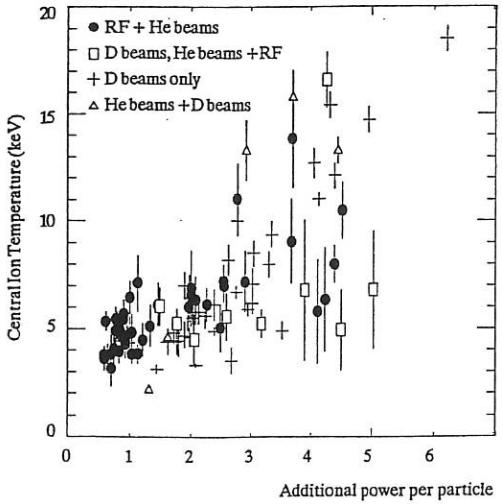

Figure 5: Ion temperatures during various heating scenarios

ON THE OPPORTUNITY TO MEASURE THE PLASMA ION TEMPERATURE BY A PHOTOELECTRON METHOD

Yu.V.Gott, V.A.Shurygin

I.V.Kurchatov Institute of Atomic Energy,

Moscow, USSR

A photoelectron method for measuring the ion temperature, T_i, based on a conversion of X-ray impurity line (its width is determined by the Doppler effect) into a photoelectron one is proposed in a given paper. Such a conversion occurs as a result of the photoeffect in interaction of X-ray radiation quanta with atoms of a target-converter in a photoelectron spectrometer (PES). The energy E_e of photoelectrons , produced in this process is related with the energy E_γ of quanta by the known relationship [1]:

$$E_e = E_\gamma - E_i - \varphi \,, \qquad (1)$$

where E_i is the electron binding energy in the i^{th}-shell of the target atoms, φ is the work function of the substance of which the spectrometer is made. The proper width of a photoelectron line emerging under an effect of monochromatic X-ray radiation and produced by photoelectrons outgoing from a target without energy loss is practically equal to the width of a corresponding atomic level and for the K-shells

with $Z \leq 32$ does not exceed 2 eV. Thus one can see that the X-ray spectrum conversion into a photoelectron one occurs with high precision. Measurement of the photoelectron line broadening related with the Doppler effect is possible only in case, when the proper width of the used atomic target level, ΔE_i, and a full width at half maximum (FWHM) of the response function of the PES energy analyzer, ΔE_A, satisfy the condition

$$\Delta E_i, \Delta E_A \ll \Delta E_\gamma \ , \qquad (2)$$

where

$$\Delta E_\gamma = E_\gamma \ (\ T_i/(1.72 \ 10^5 \ A_j))^{1/2}, \qquad (3)$$

is the Doppler broadening of a plasma impurity line, A_j is the atomic weight of an impurity ion, T_i is expressed in keV. From (2) it follows that the accuracy of T_i-measurement by the photoelectron method will depend not only on the T_i-magnitude and on the option of a suitable plasma impurity line, but on the option of a target and on the resolving power of the PES-energy analyzer.

Let us consider an opportunity to optimize the option of a target and that of an energy analyzer for PES. From (1) one can see that the requirement to the resolving power of an energy analyzer can be essentially reduced, if one chooses the target so that the binding energy in the K^{th}-shell would be close to E_γ in its magnitude. In this case, the energy of the produced photoelectrons is reduced, that results in an increase in relative broadening of a photoelectron line, $\Delta E_e/E_e$. So the necessary resolving power of the PES-analyzer ($R_e=E_e/\Delta E_A$, $\Delta E_A \approx \Delta E_\gamma$, $E_\gamma - E_i >> \varphi$) can be estimated by relationship:

$$R_e = (E_\gamma - E_i - \varphi)/\Delta E_e \approx R_\gamma - E_i/\Delta E_\gamma \ , \qquad (4)$$

where $R_\gamma = E_\gamma/\Delta E_\gamma$ is found from (3).

Let us consider the resonance line Ni XXVIII (E_γ = 7.805 keV), widely used at present for determination of the plasma ion temperature, as an example. The Doppler FWHM of this line exceeds 5 eV at the plasma temperature $T_i \geq 5$ keV. In this case it is suitable to use the target of cobalt, for the atoms for the K^{th}-shell of which E_K=7.709 keV, ΔE_K=1.45 eV [2]. From (2)-(4) one obtains $E_e \approx 100$ eV, $R_e \geq 30$, meanwhile for a traditional crystalline X-ray spectrometer it is necessary to have R_γ exceeding 10^3 in its magnitude.

From (1) one can see that the contribution into the photoelectron spectrum production will be done by all the shells at which $E_i < E_\gamma + \varphi$. As a result, along with the photoelectron line one can expect the emergence of the background related with the photoelectrons knocked-out from the L- and M-atomic shells and loosing a part of their initial energy in the process of their yield from the target. One should reduced the efficiency of L- and M-photoelectron registration to reduce this background, e.g. by reduction of a target thickness to 50-100 Å and/or by using of appropriate filters in front of target.

The PES- registration efficiency with such a target and with an energy analyzer having a rather high transmission ($\sim$ 1%) at the resolving power equal 100 will be about 10^{-6} electrons/quantum. At a high magnitude of the X-ray quanta flux from the plasma of large facilities this deficiency of the technique is not of great importance.

Thus one can use the PES with an energy analyzer operating in the energy range $E_e < 1$ keV with the resolving power equal 100 and with the transmission of about 1% for realization of a photoelectron technique for measuring an ion temperature exceeding 5 keV. The analyzers with such a resolving power are widely used in various

studies at present.

One of the advantages of such a technique for measuring T_i is that it can be used under hard radiation conditions of the reactor plasma, since the PES detector is located outside the diagnostic channel, that allows one to realize its effective radiation shield and to reduce the background provided by neutrons and hard γ-quanta.

REFERENCES

1. Siegbahn K., Nordling C., Fahlman A., et al. (1967) in Electron Spectroscopy for Chemical Analysis - Atomic, Molecular, and Solid State Structure Studies by Means of Electron Spectroscopy (Almqvist and Wiksells, Boktryekeri AB, Stockholm, Sweden, 1967); Nova Acta Regiae Soc. Sci. Upsaliensis, Ser.1V20.
2. Blokhin M.A., Shveicer I.G., (1982) in X-ray spectral handbook, Nauka, Moscow, (in Russian).

MEASUREMENT OF ION TEMPERATURE PROFILES IN THE TCA TOKAMAK BY COLLECTIVE THOMSON SCATTERING

C.Nieswand, R.Behn, M.R.Siegrist, M.Dutch, B.Duval, A.Pietrzyk, A.Pochelon

Centre de Recherches en Physique des Plasmas
Association Euratom - Confédération Suisse
Ecole Polytechnique Fédérale de Lausanne

1. Introduction

After many years of development in the field of plasma diagnostic techniques, local ion temperature measurements in tokamak plasmas are still rather difficult. Neutral particle analysis (NPA), e.g., although it is a line integrated measurement, provides approximately the maximum temperature along the line of sight. But the result is influenced by charge exchange cross-sections, the neutral particle distribution and, with our system at TCA, by the H-D composition of the plasma.

It has been shown, that collective Thomson scattering in the far infrared is capable of measuring ion temperatures in tokamak plasmas with good spatial and temporal resolution [1]. Nevertheless, the result depends on other plasma parameters which must be determined simultaneously.

The collective Thomson scattering system on TCA has been modified to allow measurements of the spatial ion temperature profile in the central part of the plasma. The results are presented and compared with NPA temperature profiles measured in similar TCA plasmas.

2. Experiment

The source for the collective Thomson scattering experiment is an optically pumped D_2O laser with 0.5-1 MW power within 1.5μs at 778.47 GHz. The beam is focussed vertically into the plasma and the scattering volume of 3mm diameter is observed under nearly 90°. The solid angle of observation is about $4.3 \cdot 10^{-3}$ sr. This results in a scattered power of the order of 10^{-19} W/Hz. A heterodyne detection system was developed to obtain spectral resolution at such a low signal level. An optically

pumped CW CD_3Cl laser at 782.17 GHz with 1mW CW power serves as a local oscillator and is focussed together with the scattered light onto a Schottky barrier diode mixer. A 12 channel spectrometer analyzes the difference frequency with 80 MHz resolution.

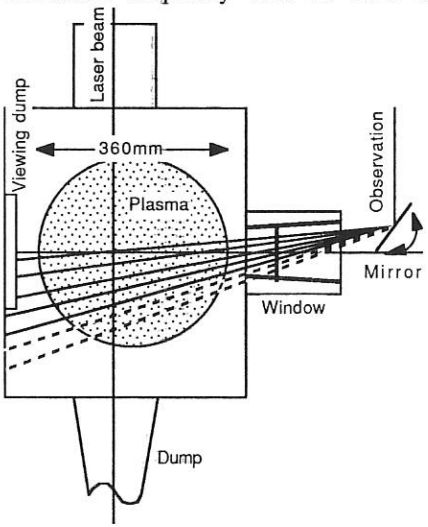

Fig.1: Scattering geometry

The position of the scattering volume could be changed by tilting the first focussing mirror in the detection optics (see fig.1). This allowed observation of the profile from the plasma centre to 2/3 of the plasma radius. Of course the scattering angle and the angle between the scattered wave vector k_s and the magnetic field B are different for each radial position. The influence of the latter can become very important when it approaches 90^o. In this particular case, the spectrum is dominated by structures induced by the magnetic field. It was verified in this experiment, that this angle was always smaller than 87^o so that the influence of the magnetic field was kept small.

A radial profile was built up from a series of reproducible tokamak discharges, and each temperature value in figure 2 is an average over 2 or 3 shots.

The evaluation of the spectra requires the knowledge of additional plasma data. The electron temperature was provided by incoherent Thomson scattering using a ruby laser. A q profile was derived from these data, from which the angle between k_s and B could be determined. The electron density was measured by a 4 channel FIR interferometer. The impurity concentrations were asumed to be uniform over the plasma radius with 2% carbon, 1% oxygen and 0.2% iron, corresponding to a Z_{eff} of 2.5.

All measurements were performed in high density deuterium discharges ($n_e \approx 10^{20} m^{-3}$) to obtain acceptable signal to noise ratios. Such discharges could be produced in TCA with high reproducibility by hard gas puffing. The plasma current was kept constant while the density was in the transient phase.

In a series of comparable discharges the line of sight of the neutral particle analyser was scanned vertically over the plasma minor radius. Thus, we could compare T_i measurements from two different diagnostics methods.

3.Results

T_i profiles measured by collective Thomson scattering and by neutral particle analysis are shown in figure 2. The corresponding T_e profile from ruby Thomson scattering is included. It has a central value of about 750 eV and is clearly peaked. The data from the collective Thomson scattering reveal a flat profile with a nearly constant T_i value of about 400 eV in the observed part of the plasma and crosses the Te profile at one half of the minor plasma radius. In the outer part of the plasma T_i seems to be larger than T_e. This means, together with the facts that the central temperatures are very different and the equipartition time is very short (<10μs), that the radial ion heat transport must be very large. However, the NPA results show a significantly lower value of about 300eV. It indicates, that T_i is not significantly larger than T_e in the outer parts of the plasma, but both temperatures are equal at r=100mm.

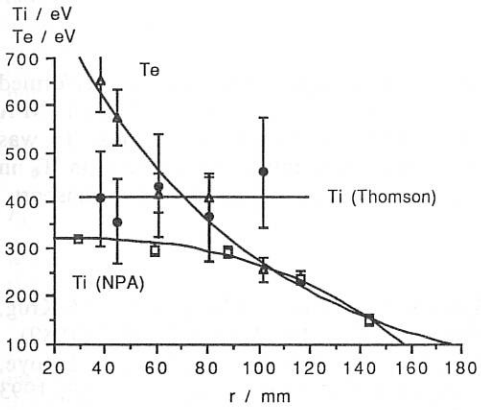

Fig 2: Measured temperature profiles in a high density plasma during hard gas puffing, 130ms after breakdown

The confidence interval for the ion temperature measured by collective Thomson scattering was analyzed with Monte Carlo simulations and can reach about 12% for densities of $10^{20} m^{-3}$ and for a single shot, if the 12 channels of the spectrometer are tuned to the optimum part of the spectrum of the scattered light [2].

For these calculations uncertainties of 5% for n_e, 10% for T_e, 30% for the impurity concentrations and 10% for the magnitude of the magnetic field were assumed.

Unfortunately, the number of spectral channels used had to be reduced because stray light dominated the scattered light in the most central spectral channels. The stray light became large during measurements at outer radial positions, when the detector looked directly on the metal wall of the tokamak vessel and not on the ceramic viewing dump. This increases the uncertainty considerably. With only 11 channels the uncertainty grows up to 25% [2] and even exceeds this value when less channels are used.

The statistical error for the NPA measurements was found to be about 8%. The NPA might give systematically too low temperatures, because the result is a weighted average over all temperatures along the line of sight. The existence of hydrogen released from the wall imposes another systematic error on the NPA measurement, because the system is calibrated to deuterium.

Within these errorbars the results of both diagnostics are comparable. The form of the profile in this region is flat in both cases.

The observation of peaked T_e and flat T_i profiles is consistent with results obtained in other tokamaks with comparable parameters [3,4,5]. It should be noted that our measurements refer to discharges with $n_e \approx 1 \cdot 10^{20} m^{-3}$, whereas most of the results given in [3,4] have been obtained at considerably lower central densities ($2\text{-}5 \cdot 10^{19} m^{-3}$).

4. Conclusion

It was shown that the measurement of T_i profiles can be performed by collective Thomson scattering. The results are consistent with NPA measurements in the range of the errors of these diagnostics. It was found that in high density TCA discharges T_i might be larger than T_e in outer parts of the plasma . This implies a large radial ion heat transport.

References :

[1] R.Behn, D.Dicken, J.Hackmann, S.A.Salito, M.R.Siegrist, P.A.Krug, I.Kjelberg, B.P.Duval, A.Pochelon; Phys.Rev.Lett. 62, 2833 (1989)

[2] M.R.Siegrist, R.Behn, D.Dicken, B.P.Duval, J.Hackmann, B.Joye, J.B.Lister, C.Nieswand, A.Pochelon, D.C.Yuan; J.Appl.Phys. 69, 1993 (1991)

[3] D.Dimock, D.Eckhartt, H.Eubank, E.Hinnov, L.C.Johnson, E.Meservey, E.Tolnas, D.J.Grove ; Proc. 4th conference on Plasma Physics and Controlled Fusion Research in Madison, 451 (1971)

[4] L.A.Berry et al. ; Proc. 6th conference on Plasma Physics and Controlled Fusion Research in Berchtesgaden, Vol.I, 49 (1976)

[5] TFR Group ; Proc. 7th Fusion in Lausanne, Vol.I, 2 (1975)

POTENTIAL OF MILLIMETER-WAVELENGTH COLLECTIVE SCATTERING IN A HIGH FIELD TOKAMAK

U. Tartari and M. Lontano

Istituto di Fisica del Plasma, EURATOM-ENEA-CNR Association
via Bassini 15, 20133 Milano, Italy

Introduction - The availability of high power ($P_o \leq 400\,kW$) mm-wavelength ($\omega_o/2\pi = 140\,GHz$) gyrotrons has given impulse to the development of collective Thomson scattering (CTS) for ion velocity distribution diagnostics in tokamaks /1, 2/. Here the results of a preliminary investigation on the feasibility of ion temperature measurements by CTS in the high magnetic field tokamak FTU ($B_o \leq 8\,T$) are reported.

High signal-to-noise ratios (SNR) and receiver-noise limited performances are more easily approachable in CTS in high field devices due to the high density and to the favourable propagation condition $\omega_{pe} < \omega_o < \omega_{ce}$, which implies that no electron cyclotron radiation is emitted in the CTS bandwidth by a Maxwellian plasma.

In contrast, satisfying a condition which has been considered necessary /3/ for feasibility of CTS, i.e. avoiding the modulations at the ion cyclotron frequency ω_{ci} which occur in the spectrum for fluctuation wavevectors with $k_{//} < \omega_{ci}/v_{Ti}$ ($k_{//} \simeq 0$), v_{Ti} being the ion thermal velocity, can be impratical in a medium temperature, high field device, the angular range in which the modulations occur being wider than that available at the narrow ports where the receiving antenna is to be accomodated.

The possibility of resolving the modulations is considered here, stimulated by the fact that, besides T_i, a high spectral resolution CTS diagnostic would offer the possibility of measuring the total magnetic field internal to the plasma.

SNR analysis - The scattered power and the SNR at the output of the n-th channel of a coherent receiver can be written as

$$P_s^{(n)} = r_e^2\, n_e\, P_o \Gamma_p \Gamma_g\, S_{ch}^{(n)} \qquad SNR^{(n)} = [P_s^{(n)}/(P_s^{(n)} + P_N)](\tau_i \Delta f_{ch})^{1/2} \qquad (1)$$

where P_o is the incident power, Γ_p a polarization factor, Γ_g a geometrical factor, $S_{ch}^{(n)}$ the channel-integrated form factor, $P_N = T_N \Delta f_{ch}$ the total noise power, τ_i the integration time, and Δf_{ch} the bandwidth of the resolution channel.

Neglecting plasma effects, the polarization factor is $\Gamma_p = |\hat{s} \times (\hat{s} \times \hat{e}_o)|^2$, the unit vectors $\hat{s}$ and $\hat{e}_o$ referring to the line of sight and to the polarization direction of the incident electric field, respectively. Independently of the scattering angle θ, Γ_p is maximized ($\Gamma_p = 1$) by taking the incident and the scattered wave both in the ordinary mode and by choosing a scattering geometry such that the scattering plane is parallel to the poloidal plane. For vertical incidence this requires a toroidal angle between the line of sight and the normal to the magnetic field $\psi \simeq 0°$. In FTU the useful angular range at the port is $\psi \simeq \pm 5°$; avoiding the modulations requires a magnetic angle $\phi = \sin^{-1}(\cos\theta/2 \sin\psi) \geq 13°$, i.e. $\psi \geq 18°$ for $\theta = \pi/2$ (see **Fig. 1a**).

The geometrical factor writes $\Gamma_g = V_s\, \Delta\Omega_c / A_i$, V_s being the scattering volume, $\Delta\Omega_c$ the collection solid angle, and A_i the cross-section of the incident beam. Coherent

detection sets an upper limit to $\Delta\Omega_c$ through the limitation to λ_o^2 of the étendue. With 1/e-truncated Gaussian beam profiles, both the geometrical factor and spatial resolution are optimized by taking the waists of the transmitting and the receiving antenna, $(w_T)_{\min} = (w_R)_{\min} = w_o$, to be minima. Preliminary antenna design shows that focusing at $w_o = 2\ cm$ is achievable /4/. The size and shape of V_s, hence spatial resolution, are evaluated in terms of the ellipsoidal interference pattern formed by the incident and the so-called 'antenna' beam /5/. With $w_o = 2\ cm$ and $\theta = \pi/2$, the best spatial resolution achievable in FTU is found to be $\xi_r = \pm\ 6.5\%$; resolution in $\underline{k}$ space is $\xi_k \leq \pm\ 1\%$.

For unmodulated spectra the channel-integrated form factor can be simply written as $S_n = S(\underline{k}, 2\pi f_{no})\,\Delta f_{ch}$, where $S(\underline{k}, 2\pi f)$ is the spectral density function and f_{no} the central frequency of the channel. To represent the average behaviour of the CTS spectrum we refer to a 'standard' channel, still of width Δf_{ch}, centered at a frequency f_{so} such that $S(\underline{k}, f_{so}) = S(\underline{k}, 0)/2 \equiv S_o/2$. From well known CTS formulas and accounting for a scattering parameter $\alpha = 1/k\lambda_{De} \geq 3$, k being the fluctuation wavenumber and λ_{De} the Debye length, one finds $S_o = \pi^{1/2}/(2k\ v_{Ti})$.

In conclusion, for the SNR in the standard channel we find

$$\overline{SNR} = 1.45\text{x}10^{-13} P_o n_e \lambda_o^3 A_m^{1/2} \tau_i^{1/2} w_o^{-1} T_N^{-1} T_i^{-1/2} |\sin\theta|^{-1} (\sin\theta/2)^{-1} \Delta f_{ch}^{1/2} \qquad (2)$$

where A_m is the ion mass ratio and the units are kW, cm^{-3}, sec, keV and MHz. To quantify the SNR margins we also introduce a feasibility parameter given by

$$F = (\overline{SNR})_m / (\overline{SNR})_{mm} \simeq 10^{-1} (\overline{SNR})_m \qquad (3)$$

where $(\overline{SNR})_m$ is the SNR available in the standard channel in the most unfavourable plasma conditions $(n_e = (n_e)_{\min} \equiv n_{em},\ T_i = (T_i)_{\max} \equiv T_{iM},\ A_m = 1)$ and $(\overline{SNR})_{mm}$ the SNR required in the same channel $((\overline{SNR})_{mm} \simeq 10)$ to have just SNR $\simeq 1$ in the last $(f_{last} = 2f_{so})$ channel. The condition $F \geq 1$ must hold for feasibility.

Optimized resolution bandwidth - The spectral resolution required in the measurement, $\xi_s = \Delta f_{ch}/\Delta f_{tot}$, where Δf_{tot} is the total (finite) single-side bandwidth of the spectrum, can be evaluated with reference to the goodness of fit of the analytical spectral function. For smooth (unmodulated) spectra this in turn can be related to the number of degrees of freedom, $\nu = N_d - n_p \geq 1$, N_d being the number of data points and n_p the number of independent parameters in the fitting function. A conservative choice for the minimum number of active channels necessary to achieve the minimum required ξ_s in a single sideband measurement is $N_a^{(m)} \equiv N_d^{(m)} = n_p + 1 \simeq 6$. An optimized channel bandwidth is defined accordingly by taking

$$\Delta f_{ch} = [\Delta f_{tot}(T_{im}) - \Delta f_{for}]/N_a^{(m)} \qquad (4)$$

where $\Delta f_{tot}(T_{im})$ is the total spectral bandwidth associated to T_{im}, the minimum temperature in the range of interest, and Δf_{for} the 'forbidden' bandwidth which has to be excluded from the actual measurement for stray gyrotron-radiation and/or other reasons. With reference to twice the Doppler shift associated to $V_{\max}/2$ of a Maxwellian distribution we take $\Delta f_{tot} = [(\ln 2)^{1/2}/\pi]\,k\ v_{Ti}$. In explicit form

$$\Delta f_{tot}(T_i) = 1.45\text{x}10^2 T_i^{1/2} \lambda_o^{-1} A_m^{-1/2} \sin\theta/2 \qquad (5)$$

(MHz, keV, cm). In FTU we have $T_i = 1 \div 5\ keV$; hence for $\theta = \pi/2$ and $\lambda_o = 0.21\ cm$ ($f_o = 140\ GHz$) we obtain $\Delta f_{tot} = 346 \div 1092\ MHz$ and $\Delta f_{ch} = (4.88\text{x}10^2 - \Delta f_{for})/N_a^{(m)}$, with Δf_{ch} and Δf_{for} in MHz.

Forbidden bandwidth - At the receiver input, stray radiation at the gyrotron frequency must be lower than the local-oscillator (LO) power to avoid mixer damage and/or generation of spurious signals. The total attenuation required therefore is simply $L_{tot} \geq L_o + |L_{LO}|$, where L_o and L_{LO} are the incident and the LO power in dB. With $P_o = 100\ kW$ and assuming $P_{LO} = 1\ mW$ then $L_{tot} \geq 80\ dB$. If, besides external rejection, notch filtering is used then $L_{tot} = L_{rej} + L_{fil}$. Partition is not fully free, however. A minimum level of external rejection will be needed in all cases to ensure proper attenuation of the noise-like out-of-line radiation emitted by the gyrotron due to its limited spectral purity, which cannot be filtered. This minimum level can be shown to be given by $L_{rej}^{(m)} \simeq (28 + L_o - L_{in} + |L_{so}^{(M)}|)\ dB$, where L_{in} expresses the gyrotron spectral purity and $L_{so}^{(M)}$ is the maximum scattered power in dB, at $f = 0$, in the whole plasma parameter range. In the FTU case $L_{so}^{(M)} \simeq (L_o - 141)\ dB$. With the same P_o and P_{LO} as above and assuming $L_{in} \simeq 100\ dB$ we then obtain $L_{rej} \geq 60\ dB$ and $L_{fil} \leq 20\ dB$, which are acceptable performances.

The attenuation bandwidth of the notch filter should cover the whole bandwidth spanned by the gyrotron due to its limited stability in frequency. Unaffected transmission will be possible only outside about twice this bandwidth. Reciprocally, for any acceptable Δf_{for} a gyrotron stability as good as $\Delta f_{gyr}/f_o \leq \pm 0.04\%$ would be required. We then see that using a notch filter in a medium temperature tokamak like FTU will be quite problematic.

Achieving $L_{rej} \geq 80\ dB$ only by external rejection will require installation of very efficient radiation dumps. The required spectral purity, in contrast, will be relaxed below $L_{in} = 100\ dB$. The effects of the jittering of the gyrotron frequency should be minimized in any case by frequency tracking of the LO or by the use of a homodyne receiver. Further, high-frequency chopping of the gyrotron pulse and synchronous detection should be used to avoid noise-like fluctuations in the low-frequency converted signal due to the variations in the amplitude of the gyrotron output.

If no notch filter is used, Δf_{for} will be determined by the complementary requirements of avoiding the narrow spectral regions where: a) the spectral purity of the gyrotron is too low; b) microturbulent scattering from the plasma edge is too strong. On these bases as a conservative choice we take $\Delta f_{for} \simeq 100\ MHz$. In the conditions specified above, with $\Delta f_{for} = 100\ MHz$ and $N_a^{(m)} = 6$ in FTU we get $\Delta f_{ch} = 65\ MHz$. Since with $B_o = 7\ T$ $f_{ci} = 106.4\ MHz$ (53.2 MHz) for a H (D) plasma, Δf_{ch} is seen to be already of the order or below the ion cyclotron frequency.

Estimate of the SNR margins - In FTU we can take $n_{em} = 1\text{x}10^{14}\ cm^{-3}$ and $T_{iM} = 5\ keV$; in the conditions specified above and with $\Delta f_{ch} = 65\ MHz$, therefore, from eqs. (2) and (3) we get $F = 3.43\text{x}10^1 P_o \tau_i^{1/2} T_N^{-1}$ (kW, sec, eV). Further, with $P_o = 100 \div 400\ kW$ and realistically taking $\tau_i = 10^{-1} s$ for the effective (i.e. accounting for the duty cycle of the high-frequency chopping of the gyrotron pulse) integration time, $F = (1.084 \div 4.336)\text{x}10^3\ T_N^{-1}$. Also considering the square-root dependence of the SNR from Δf_{ch}, wide margins are therefore seen to be available for trade-off of SNR with spectral resolution up to total noise temperatures of a few hundreds eV.

While referred to the standard channel and then implicitly to smooth spectra, the results above for the SNR will also hold for modulated spectra ($\psi < 18°$), provided

they are referred to the amplitude of the peaks (spectral envelope). The simple criterium adopted in order to estimate the minimum required number of active channels ($N_o^{(m)} \simeq 6$), and then spectral resolution, however, is readily understood to be inadequate in the case of rapidly varying spectral functions.

High spectral resolution CTS - If $T_N = 50\ eV$ is taken as a conservative estimate for the total noise temperature, and a reduction down to $F = 2$ of the feasibility parameter is considered acceptable, yet with the lowest incident power level, $P_o = 100\ kW$, the channel bandwidth can be narrowed down to $\Delta f_{ch} = 0.5\ MHz$. The use of such a very narrow channel bandwidths should be possible if a homodyne receiver is used. Only m groups of channels of a few units each and centered about $1 \leq m \leq m_M$, with $m_M = int\,(\Delta f_{tot}/\Delta f_{ch})$, would be actually needed for each of the two (H, D) plasma compositions.

In the limiting case $\Delta f_{ch} = 0.5\ MHz$, the spectral resolution achieved with respect to $\omega_{ci} = 2\pi f_{ci}$ would be as good as $\xi_{cycl} = \Delta f_{ch}/f_{ci} \simeq 0.5\%$ ($\simeq 1\%$) for a H (D) plasma. Still lower ξ_{cycl} values would be required to infer the local (off-axis) poloidal field component of the total field from the spacing between the modulation peaks. The ξ_{cycl} estimated above, however, should be good enough to allow a measurement of the paramagnetic component /6/ of the toroidal field.

The detailed shape of the modulated spectra (see **Fig. 1b**) being strongly dependent on the magnetic angle ϕ numerical integration in $k_{//}$ up to the $(\Delta k_{//})_{max}$ associated to $\Delta\Omega_c$ should be performed for reliable fitting of the data. In the T_i measurements $(\Delta k_{//})_{max}$ should be better treated as an additional fitting parameter, its value being not known with the required accuracy. In the total-B measurements, in contrast, this same dependence could provide a means for inferring the direction of the total field and then the amplitude of the (off-axis) poloidal field in the toroidal plane.

References

[1] - A.E.Costley et al., JET Rep. R(88)08, 1988.
[2] - F.Orsitto, Rev. Sci. Instrum., 61, 3093,1990.
[3] - F.Orsitto and P.Buratti, XV-th EPS Conf., p.III, 1183, Dubrovnik, 1988.
[4] - S.Cirant, IFP, private communication.
[5] - E.Holzhauer and J.H.Massig, Plasma Phys., 20, 867, 1978.
[6] - J.D.Callen and R.A.Dory, Phys. Fluids, 15, 1523, 1972.

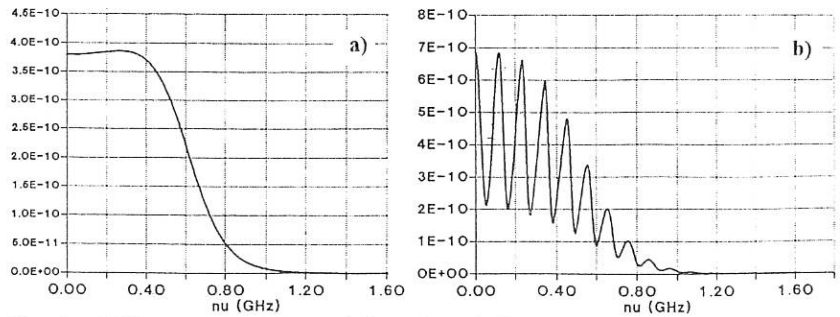

Fig. 1 - *CTS spectra in FTU with $\theta = \pi/2$ and $T_i = 2\ keV$, for magnetic angles:* **a)** $\phi = 15°$; **b)** $\phi = 5°$.

ION TEMPERATURE PROFILES DEDUCED FROM DOPPLER BROADENING OF X-RAY LINES IN ASDEX

C.C. Chu, R. Nolte*, G. Fußmann, H.U. Fahrbach, W. Herrmann, E. Simmet, and ASDEX-Teams

Max-Planck-Institut für Plasmaphysik, EURATOM Association, D-8046 Garching, FRG

Abstract: In the present work, the evaluation of the ion-impurity temperatures T_{Dopp} deduced from the Doppler broadening in the soft X-ray range 1-10 Å will be described. Consistency checks were made by comparing T_{Dopp} obtained from He-like chlorine (Cl XVI) resonance line with those from Ar XVII and Cu XXVIII. The agreement of T_{Dopp} at the plasma centre is within 5~10%. Comprehensive data of T_{Dopp} are compared with those predicted by neoclassical ion-heat-transport calculations ($T_{i,neo}$), as well as those measured by active and passive charge-exchange fluxes ($T_{i,act}$, $T_{i,pass}$). We find good agreement between the radial profiles of T_{Dopp} , $T_{i,neo}$ during the ohmically heated discharges. There is also good agreement between T_{Dopp}, $T_{i,act}$ and $T_{i,pass}$ at the palsma centra during the ohmically, LH- and NI-heated discharges, but T_{Dopp} radial profiles are stronger peaked than those of $T_{i,act}$ and $T_{i,pass}$.

Doppler-Broadening Evaluations: The $1s^2\ ^1S_0$ - $1s\,2p\ ^1P_1{}^0$ He-like chlorine (Cl XVI) resonance-line(w) profile with wavelength $\lambda_0 = 4.4442$ Å is measured by means of a Johann spectrometer equipped with a proportional counter of high spatial resolution. The line of sight of the spectrometer can be inclined over a radial range from r = 0 to 35 cm (plasma radius a = 40 cm) from the plasma geometric axis, where r denotes the shortest radius perpendicular to the line of sight. Since the ion temperature varies slowly in the radiation range of the resonance line along the line of sight, the total Doppler broadening integrated over the line of sight has an effectively Gaussian form. In order to take into account the contributions from natural (Lorentzian), instrumental (quasi-Gaussian) and Doppler (Gaussian) broadening, we apply the procedure suggested in Ref.[1], i.e. fitting a Voigt function after performing a deconvolution of the measured profiles with the instrumental profile. The ion temperature deduced from the Doppler broadening part of the profile is obtained from the usual relation

$$T_{Dopp}\ [keV] = 4.96 \times 10^5\ A_m \left(\frac{\Delta\lambda}{\lambda_0}\right)^2 \qquad (1)$$

where $\Delta\lambda$ is half the 1/e-width and A_m the relative atomic weight of the observed element. Fig. 1 shows a typical fitted w-line (Cl XVI) profile during an ohmically heated discharge. The line profile is fitted over the entire blue wing but only over half of the red wing, in order to exclude asymmetry effects arising from the presence of unresolved dielectronic satellites ($n \geq 3$). When a good signal-to-noise ratio is obtained in the observed line profile, the uncertainty in T_{Dopp} owing to fitting with the Voigt function is less than 3%. A further uncertainty of 5% can be ascribed to a certain arbitrariness in the choice of the fitting range on the red wing. In the off-axis observation region, when the emissivity ε of the resonance line decreases rapidly, the low signal-to-noise ratio results in errors up to ~ 25%.

For evaluating ion temperatures from eq.(1), a proper dispersion relation (Å /channel of the proportional counter) is required. This relation is obtained from suitably spaced Cl XVI spectral lines having well known wavelengths. The deduced dispersion relation is confirmed by wavelength analysis of the He-like Ar XVII and Cu XXVIII spectral lines. An x-ray source with a Pd anode (λ_{Pd} = 4.3767 Å) was used for the determination of the instrumental profile. A slit (120 µm x 12 mm) was positioned on the Rowland circle (R=1.5 m) of the Johann spectrometer, thus providing an X-ray image of the slit with unit magnification onto the detector. Both the slit and proportional counter were carefully aligned so as to produce the narrowest possible instrumental profile. The measured instrumental profile consisted of a Gaussian profile with an additional slight wing superposed [1]. The full half-width of the instrumental profile $\Delta\lambda_{inst}$ was determined to 6.45 x 10^{-4} Å, resulting in an instrumental resolution of $\lambda_0/\Delta\lambda_{inst}$= 6771. It is important to note that over- or under-estimation of the line wing in the convolution procedure could lead to an error of some ± 5% in the determination of temperature.

In the experiments, the brightness is given by the measured line emission integrated over the line of sight. Expressed as an integration over the minor raduus r' it is given as a function of λ and r by [2]

$$B(\lambda, r) = \frac{1}{2\pi} \int_r^a \varepsilon(r') \frac{e^{-\left[\left(\frac{\lambda - \lambda_0}{\Delta\lambda(r')}\right)^2\right]}}{\sqrt{\pi}\,\Delta\lambda(r')} \frac{dr'}{\left[1 - \left(\frac{r}{r'}\right)^2\right]^{1/2}} \qquad (2)$$

From the half 1/e-width of the measured spectrum of B at various radii, one obtains the ion temperature $\overline{T(r)}_{Dopp}$ averaged over the line of sight. The emissivity ε(r') can be calculated using a transport code (Zediff), measured n_e and T_e profiles. We assume that the radial profile of the local ion temperature can be written as :

$$T(r)_{Dopp} = [\, T(0)_{Dopp} - T(a)_{Dopp} \,]\left[1 - \left(\frac{r}{a}\right)^2\right]^{\alpha} + T(a)_{Dopp} \qquad (3)$$

The local ion temperature $T(r)_{Dopp}$ has been obtained from $\overline{T(r)}_{Dopp}$ by optimizing the three parameters $T(0)_{Dopp}$, $T(a)_{Dopp}$ and α, so that there is best agreement between $\overline{T(r)}_{Dopp}$ calculated from eq. (2) and the measured profile $\overline{T(r)}_{Dopp}$. The uncertainty in the evaluation of $T(r)_{Dopp}$ owing to the uncertainty in determining the radial profil of $\overline{T(r)}_{Dopp}$ and the emissivity ε is estimated to be less than ~ 10% at least for the core region ($r \leq a/4$).

Results: In Table 1 we present central ion temperatures deterimned from Doppler-broadening of different elements for ohmically and LH-heated discharges. Note that in the latter case the central electron temperature $T_e(0) \sim 6$ keV exceeds $T_{Dopp}(0)$ by a factor of about 6. The agreement between the Doppler-broadening measurements is better than 5% and thus quite satisfying. Although one must be aware that the temperature of the impurities may principally differ from those of the background ions, it is etimated(using formulare given in Ref [3]) that these differences should be less than ~5% under all conditions discussed in this paper.

Profiles of T_{Dopp} are compared with predictions by neoclassical ion-heat-transport calculations ($T_{i,neo}$, assuming $\chi_i = 1 \times \chi_{i,neocl}$) as well as those measured by active and passive charge-exchange fluxes ($T_{i,act}$, $T_{i,pass}$) in Fig. 2 for an ohmically heated discharge. Generally, good agreement is obtained between the radial profiles of $T(r)_{Dopp}$ and $T(r)_{i,neo}$ during ohmic heating. In Fig. 2 the profiles of $T(r)_{i,act}$ and $T(r)_{i,pass}$ lie below those of $T(r)_{Dopp}$ and $T(r)_{i,neo}$. According to the current calibration of the charge-excharge fluxes, however, the values of $T(r)_{i,act}$ and $T(r)_{i,pass}$ should be increased by at least 5%. Furthermore, there is an effect from halo-particles which increases the neutral flux at low energies and tends to reduce the evaluated $T(r)_{i,act}$ values at the plasma centre. Fig. 2 shows that in the plasma centre, $T(r)_{i,act}$ values (marked with a triangle) using the fluxes at all energies according to their statistical weight, are about 25% lower than those (marked with an asterisk) evaluated at high energies only. Table 2 shows the comparison of the central temperatures during ohmic heating for various values of B_t, I_p, $\overline{n_e}$. In general, $T(0)_{Dopp}$ agrees quite well with $T(0)_{i,neo}$; in the case with $B_t = 2.17$ T, $I_p = 420$ kA, $\overline{n_e} = 1.0 \times 10^{19} m^{-3}$, however, $T(0)_{i,neo}$ is about 30% higher than $T(0)_{Dopp}$ and $T(0)_{i,act}$. The reason for this inconsistency may be due to the fact that neoclassical calculations tend to become more uncertain in the low ion density regime.

There is also good agreement between the central ion temperatures $T(0)_{Dopp}$, $T(0)_{i,act}$ and $T(0)_{i,pass}$ during LH and NI-heated discharges (see Table 3); however, the T_{Dopp} radial profiles show a more pronounced peaking than those of $T_{i,act}$ and $T(r)_{i,pass}$ during the NI-heated discharge. Fig. 3 shows the profiles of $T(r)_{Dopp}$, $\overline{T(r)}_{Dopp}$, $T(r)_{i,act}$ and $T(r)_{i,pass}$ during a NI-heated discharge. The deviations may be attributed to non-Maxwellian tails contributing significantly to the signals in the neutral particle-charge exchange mesasurements.

Summary: The experimental performance was checked by comparing the ion temperature obtained from the resonance lines of different elements under the same operation conditions of ASDEX. The agreement is within 5%. The error sources in the evaluation of T_{Dopp} have been discussed. Generally, $T(r)_{Dopp}$ agrees well with $T(r)_{i,neo}$ during ohmically heated discharges. There is also good agreement between $T(0)_{Dopp}$, $T(0)_{i,act}$ and $T(0)_{i,pass}$ during ohmically, LH- and NI-heated discharges. In general the radial profiles of T_{Dopp} are more peaked than those of $T_{i,act}$ and $T_{i,pass}$. Before interpreting these differences, a more accurate calibrition of the active and passive charge-exchange diagnostic -being currently performed- must be taken into account.

References:

[1] K.D. Lawson and N.J. Peacock, JET-Report (88) 12

[2] F. Bombarda et al, JET-Report(88) 36

[3] G. Fußmann, JET-Report (87) 12

* present address: PTB, Abteilung SE3, Bundesallee 100, D-3300 Braunschweig, FRG

B_t=2.17 T, I_p=320 kA, $\bar{n}_e$=4.2x 10^{19} m^{-3}		
element	λ_0 [Å]	$T(0)_{Dopp}$ [keV]
Cl XVI	4.4442	0.75 ± 0.06
Ar XVII	3.9492	0.78 ± 0.09
B_t=2.79 T, I_p=420 kA, $\bar{n}_e$=1.4x 10^{19} m^{-3} P_{LH} = 1.2 M W		
element	λ_0 [Å]	$T(0)_{Dopp}$ [keV]
Cl XVI	4.4442	1.01 ± 0.11
Cu XXVIII	1.47766	0.98 ± 0.10

Table 1 $T(0)_{Dopp}$ obtained from different elements during ohmic and LH-heating.

LH: B_t=2.78 T, I_p=450 kA; NI: B_t=2.17 T, I_p=320 kA

$\bar{n}_e$ [10^{19} m^{-3}]	P_{LH} [MW]		$T(0)_{Dopp}$ [keV]	$T(0)_{i,act}$ [keV]	$T(0)_{i,pass}$ [keV]
1.4	1.0	ctr.	1.06	1.10	1.14
	1.0	co.	1.04	0.85	0.82
2.8	1.0	ctr.	1.06	1.28	1.30
	1.0	co.	1.02	1.18	1.30
4.2	0.8	ctr.	0.83	1.26	1.25
	0.8	co.	0.88	1.08	1.10
1.4	0.7	ctr.	1.04	1.03	1.05
	0.7	co.	0.87	0.83	0.80
2.8	0.5	ctr.	0.99	1.18	1.25
	0.5	co.	1.25	1.06	1.25
$\bar{n}_e$ [10^{19} m^{-3}]	P_{NI} [MW]		$T(0)_{Dopp}$ [keV]	$T(0)_{i,act}$ [keV]	$T(0)_{i,pass}$ [keV]
1.4	1.7	co.	2.80	2.5	----
2.1	1.7	co.	2.17	2.05	2.0
2.8	1.7	co.	1.91	1.80	----

Table 3 Comparison of $T_i(0)$ for LH- and NI-heated discharges (L-mode).

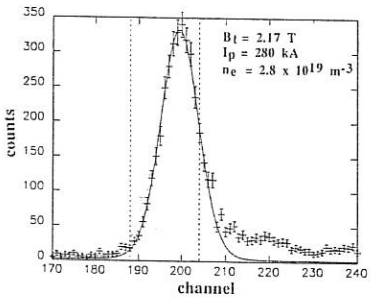

Fig.1 W-line profile of Cl XVI during an ohmically heated discharge (‡: measured, ——: fit).

I_p [kA]	$\bar{n}_e$ [10^{19} m^{-3}]	$T(0)_{Dopp}$ [keV]	$T(0)_{i,neo}$ [keV]	$T(0)_{i,act}$ [keV]	$T(0)_{i,pass}$ [keV]
420	0.98	0.56	0.70(?)	0.54	----
280	2.8	0.78	0.78	0.6–0.72	0.64
380	2.8	0.89	0.885	0.64–0.8	0.70
220	2.94	0.64	0.61	----	0.75
280	2.94	0.65	0.69	----	----
320	2.94	0.76	0.74	----	0.82
420	2.94	0.77	0.84	----	----
320	3.92	0.64	0.66(?)	----	0.75
420	3.92	0.75	0.77	----	0.75
320	4.9	0.58	0.59	0.59	----
420	4.9	0.68	0.67	0.72	----

Table 2 Comparison of $T_i(0)$ for ohmically heated discharges (B_t =2.17 T).

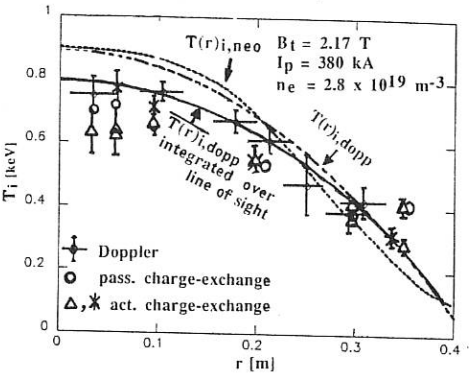

Fig.2 Radial profiles of T_{Dopp}, $T_{i,neo}$, $T_{i,act}$, and $T_{i,pass}$ during ohmic heating.

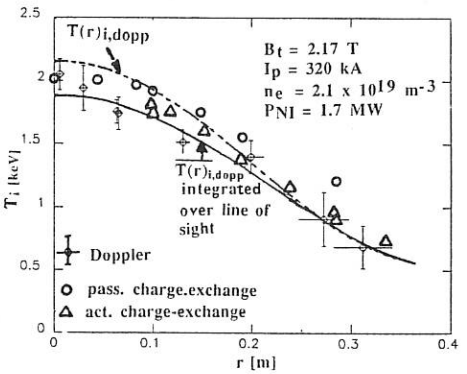

Fig.3 Radial profiles of T_{Dopp}, $T_{i,act}$, and $T_{i,pass}$ during NI-heating(L-mode).

STUDY OF PLASMA TURBULENCE IN THE TJ-I TOKAMAK BY A SPECTROSCOPIC TECHNIQUE

B. Zurro and TJ-I Team. Asociación EURATOM/CIEMAT para Fusión. E-28040 Madrid. Spain

1. Introduction. To study the ion energy transport in tokamaks, reliable ion temperature profiles must be obtained. However, using a passive technique like the energy analysis of charge-exchange neutrals well known difficulties have been encountered in several devices, attributed to convective ripple transport (1), (2) and (3) which deforms the ion energy distribution tail from which the ion temperature is deduced. To avoid this problem in the TJ-I tokamak the impurity and proton temperature profiles have been measured simultaneously by spectroscopic techniques. The results indicate that in addition to the thermal decoupling of central impurity and proton temperatures already reported in Ref. (4), a similar effect is observed at the plasma periphery. This effect, which is analyzed as if due to plasma turbulence, may provide a passive and complementary method to obtain information on the average fluctuating electric field in tokamaks.

In this paper, firstly, the experimental system and results of spatial resolved profiles of impurities and protons temperatures are presented. Second, several plausible broadening mechanisms which might be responsible for the observed effect are discussed, in particular the level of turbulence to account for the difference between impurity and proton temperatures at plasma periphery are deduced. Finally, strong and weak points of the interpretation are discussed.

2. Experimental. This experiment has been carried out with ohmically heated discharges of the TJ-I tokamak (R_0 = 30 cm, a = 10 cm) operated with toroidal fields ranging from 0.8 to 1.5 T and a plasma current between 20 and 45 kA. The line averaged density was varied between 0.5 and $3x10^{13}$ cm^{-3}. Proton and impurity temperature profiles have been measured using a 1 m monochromator with an optical multichannel detector attached in its focal plane. The line of sight can be scanned by a shot to shot technique. The impurity temperatures have been deduced from the full width at half maximum (FWHM) of emission lines belonging to CV (2271 Å), OV (5292 Å) and OV (2781 Å) after being corrected for the instrumental width. The proton temperature has been obtained from H_β emission coming from high energetic neutrals (200-1000 eV), so avoiding the contribution of Frank-Condon neutral emission.

Typical results of CV and OV ion temperature profiles obtained in TJ-I are given in Fig. 1(a) for a low density discharge ($0.75x10^{13}$ cm^{-3}). The flat profiles shown in in this figure, do not seem to be an experimental artifact since, as shown in Fig. 1 (b), the OV temperature measured

along a fixed chord responds to variations in the electron plasma density.
This decreases with density is found for every bulk impurity ion. However, they are much higher than the proton temperature, whose profiles for two densities (0.5 and $2x10^{13}$ cm^{-3}) are shown in Fig. 2. Notice that proton behaviour with density is opposite to that of impurities, as already reported in Ref. (4). CV emission peaks at the plasma center and OV emission at around 5 cm, with both ions radiating in the plasma periphery at an intensity 5-7 times lower than at their maxima.

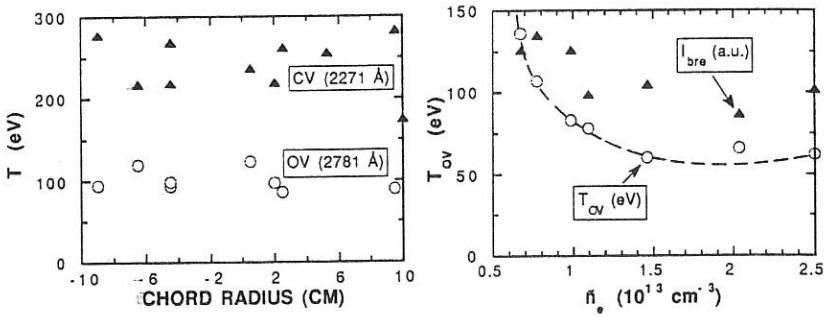

Fig. 1. (a) Typical profiles of CV and OV apparent temperatures deduced from line integrated line shape measurements in a poloidal scan. OV emission peaks in TJ-I at around 5 cm and CV at the plasma center (B_T = 1T, I_p = 38 kA); (b) Plot of OV apparent temperature (r = 6.5 cm) as a function of the line averaged electron density. Notice that this temperature decreases on increasing the plasma density.

Regarding proton temperatures, deduced from spatial-resolved measurements of the H_β line wings, no similar effect to that reported in other tokamaks when measured by the analysis of the energy of charge-exchange neutrals has been observed. Although, we do find slightly different temperatures from the red and blue wings, in Fig. 3 an averaged of both values is plotted.

It must be mentioned that at high densities, not only the gap between proton and impurity temperatures is reduced but also the impurity temperature profile exhibits, in some cases, a "normal" shape but always with a higher temperature than protons at the plasma periphery.

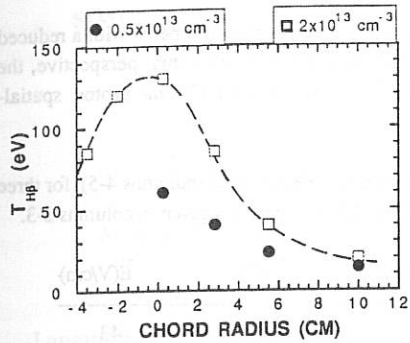

Fig. 2. Plot of proton temperature deduced from H_β line wings at two different plasma densities, $\bar{n}e = 2x10^{13}$ cm^{-3} (upper curve) and $\bar{n}e = 0.5x10^{13}$ cm^{-3} (lower curve). Notice that, in contrast with impurity behaviour, the higher the electron plasma density the higher the proton temperature (central and peripheral).

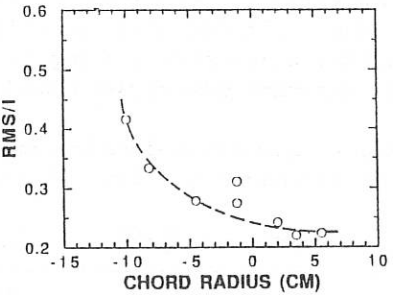

Fig. 3. Plot of relative intensity fluctuations measured by the OV (2781 Å) line.

3. Role of plasma turbulence on line broadening. Let us consider some possible mechanisms contributing to line broadening. It has been shown, by numerical simulation, that the Zeeman effect is not relevant for the transitions used and for the magnetic fields of TJ-I plasmas ($B_T \leq 1.5$ T). The slight additional broadening due to this splitting tends to be counteracted by the chord integration effect which tends to give a lower temperature than the hottest point of the chord. The high neutral concentration at the plasma periphery (10^9 - 10^{10} cm^{-3}) makes it possible that highly ionized drifting particles from the hotter core, undergo charge-exchange recombination with neutrals, producing line radiation in lower ionization stages. This effect does not seem to be relevant due to the quantum numbers of the transitions used in this work, unless cascade population is important.

Microscopic fluctuations in plasma density ($\tilde{n}$) and electric field ($\tilde{E}$) have been observed in tokamak plasmas. These fields impose velocity fluctuations via ExB drifts, $\tilde{v}=\tilde{E}/B$. In connection with Doppler broadening of impurity lines these fluctuating velocities are of particular interest because they are independent on mass and charge. It can be proved (5), that the effect of the turbulence characterized by a temperature $\tilde{T}$, on the actual measured temperature T_{app} is given by, $T_{app} = T_k + m_z/m_p\tilde{T}$. Hence, one would deduce from Doppler measurements a pseudo-temperature (T_{app}) which is larger than the true temperature (T_k), in particular for impurities due to their higher mass.

At least in one tokamak (6) high frequency electric fields of a few kV/cm have been invoked at the plasma edge to explain the structure of hydrogenic lines observed under different polarizations. It is not surprising that smaller fluctuating fields exist at the periphery of the

TJ-I tokamak and even pass unperceived for Langmuir probes measurements with a reduced bandwidth ($\leq$ 100 kHz). If we consider the OV data of Fig. 2 from this perspective, the turbulence temperature and fluctuating electric field deduced from OV and proton spatial-resolved temperature data are given in Table I.

TABLE I. Deduced values of turbulence temperature and electric field (columns 4-5), for three different plasma radii (first column) with proton and OV temperatures given in columns 2-3.

r(cm)	T_p(eV)	T_{OV}(eV)	$\tilde{T}$(eV)	$\tilde{E}$(V/cm)
5	45	95	3.1	43
8	23	90	4.1	50
10	15	85	5.8	59

The critical point to confirm this conjecture is that the values deduced along a peripheral chord from several ions of different mass should give the same result of turbulent temperature. In contrast, it is observed in TJ-I plasmas that for the same peripheral chords the higher the ionization potential the higher the apparent ion temperature. Consequently, there seems to exist a correlation between the maximum temperature reached by a particular ion and that at the plasma periphery, which cannot be accounted for by the turbulence effect alone included in the previous formula. The turbulence at the plasma periphery has been monitored measuring the OV intensity fluctuations, the relative root mean square of these fluctuations is plotted as a function of the chord radius in Fig. 4. Notice that it is higher for outer chords with a variation similar to the electric field deduced from temperature data with the former method.

4. Conclusions. Spatial-resolved measurements of single impurity line broadening in this tokamak are not compatible with an ion temperature profile decreasing towards the plasma edge. Plasma turbulence at the periphery reasonably accounts for the effect, however different electrostatic turbulence levels are deduced with distinct ions, which suggests that either magnetic turbulence cannot be ignored in this analysis, or another unknown effect plays some role. An anomalous ion heating, which was invoked to explain the central ion heating in this tokamak (4), and which cannot be completely ruled out, does not seem effective at the plasma periphery.

REFERENCES

(1) M. Gregoire et al., Report EUR-CEA-FC-873 (1977).
(2) L. M. Kovrizhnykh, Sov. J. Plas. Phys. **8**, 630 (1982).
(3) R. D. Bengtson et al., Bull. Am. Phys. Soc. **34**, 2156 (1989).
(4) B. Zurro et al., Plasma Phys. Contr. Fusion **32**, 565 (1990).
(5) G. Fussmann, Report JET-R(87) 12 (1987).
(6) V. A. Rantsev-Kartinov, Sov. J. PLasma Phys. **13**, 217 (1987).

SIMULTANEOUS MEASUREMENT OF 3 FLUCTUATING PLASMA PARAMETERS

A. Carlson, L. Giannone, and the ASDEX Team

Max Planck Institute for Plasma Physics, Garching, Germany

Langmuir triple probes can provide simultaneous measurements of n_e, T_e, and V_{pl} with good temporal and spatial resolution, and therefore are especially suited to detailed investigations of plasma turbulence in the scrape-off-layer. Unfortunately, the finite tip separation coupled with the fluctuating gradients prevents a simple interpretation of the results. We have developed a method using, essentially, two or more triple probes, which allows a good estimate of the three plasma parameters and their spatial derivatives at each point of time (assuming tip separation is much less than correlation length and dimensionless fluctuation levels are much less than unity). In particular, we can unambiguously measure the temperature fluctuations and the turbulent particle and heat flux.

1. The multiple triple-probe technique

Measurements were made in the ASDEX scrape-off-layer, 2-3 cm outside the separatrix in the mid-plane, using a 16-tip linear array with 0.3 cm tip separation. The portion of the array relevant here is sketched in Fig. 1. The arrangement is essentially four triple probes side by side, with the difference that, for experimental convenience, a single power supply is used for all four biased probe pairs. The quantities measured are the potential V_{fl} on the four floating tips, the ion saturation current I_{sat} on the four negatively biased tips, the current I_+ on the four positively biased tips, and the potential V_+ on these tips. We do not use any of the data from the last four tips because the power spectrum of the signal from tip 12, for unknown reasons, has a different shape than those of the other three positive tips. We use measurements from all the remaining 8 tips, although the same information can in principle be obtained using as few as five tips.

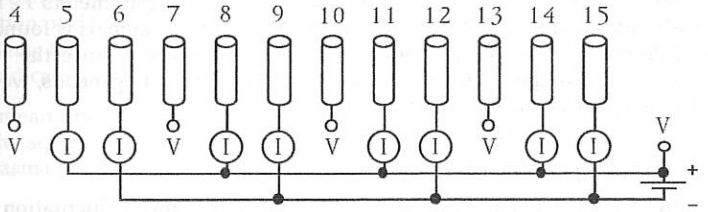

Fig. 1. Schematic circuit of the Langmuir probe array.

To account for small differences in the areas of the tips, the currents are normalized to each other so that the magnitudes of their time averages are all equal:

$$\langle I_{sat}(x_6)\rangle = \langle I_{sat}(x_9)\rangle = \langle I_+(x_5)\rangle = \langle I_+(x_8)\rangle, \quad (1)$$

where $\langle\ \rangle$ represents an average over all time points and we have chosen the senses of the currents so that they are all normally positive.

We need to estimate the values of all three triple probe parameters at a single point. If f_{TP} represents any of V_{fl}, I_{sat}, and I_+, measured at positions x_1 and x_2, then the value at x (with $x_1<x<x_2$) is approximated by linear interpolation to be

$$f_{TP}(x) = \left(\frac{x_2-x}{x_2-x_1}\right) f_{TP}(x_1) + \left(\frac{x-x_1}{x_2-x_1}\right) f_{TP}(x_2). \quad (2)$$

For the results presented here, we reduce all measurements to positions 6 and 9 shown in Fig. 1.

Standard triple probe theory assumes that all three tips see the same plasma, and that the positive tip carries the negative of the ion saturation current. We can make neither assumption, but the formula for the temperature can be modified in a straight-forward way to read

$$T_e = \frac{(V_+ - V_{fl})}{\ln(1 + I_+/I_{sat})}, \quad (3)$$

with temperature measured in volts. Since this function is poorly defined if either I_+ or I_{sat} is too small, we do not calculate the plasma parameters if either current differs from the mean by more than 1.5 standard deviations. This criterion eliminates about 35-40% of the time points. The density and plasma potential are calculated using the usual formulas:

$$n_e = \left[\frac{2\sqrt{m_i}}{e^{3/2}\,\mathrm{A}}\right] \frac{I_{sat}}{\sqrt{T_e}}, \quad (4)$$

$$V_{pl} = V_{fl} + \left[0.5 \ln\left(\frac{m_i}{\pi\, m_e}\right)\right] T_e\,. \quad (5)$$

There is a good deal of controversy over the exact values to be used for the constants in (4) and (5). A different choice should not affect our qualitative conclusions, but the quantitative results, e.g. the magnitude of the turbulent particle flux, could be significantly changed. To avoid biasing the statistics with even a small number of unrealistically large values of the density, we also institute a lower bound of 3 eV on the temperature (the mean is 12 eV), but this needs to be applied to very few points.

We use formulas (3) through (5) to calculate the plasma parameters T_e, n_e, and V_{pl}, at positions 6 and 9. The fluctuation amplitudes of these signals is found to be slightly different for the two positions (20% for the density). Since the present analysis is only meaningful if the fluctuations are spatially homogeneous, we adjust the amplitudes to be equal at positions 6 and 9:

$$\langle f_{pl}(x_6)^2\rangle = \langle f_{pl}(x_9)^2\rangle, \quad (8)$$

where f_{pl} is any of $(T_e-\langle T_e\rangle)$, $(n_e-\langle n_e\rangle)$, and $(V_{pl}-\langle V_{pl}\rangle)$.

Finally, for each plasma parameter f_{pl}, we define a mean fluctuation and a fluctuation gradient at $x=(x_6+x_9)/2$:

$$\overline{f_{pl}} = \frac{f_{pl}(x_6) + f_{pl}(x_9)}{2}, \tag{9}$$

$$f_{pl}' = \frac{f_{pl}(x_9) - f_{pl}(x_6)}{x_9 - x_6}. \tag{10}$$

We have now calculated six fluctuating plasma quantities (counting the gradients) at a single position. Any of these quantities can be meaningfully multiplied with any other and the time average considered, resulting in 21 quadratic mean products. We consider in turn the products of two spatially-constant terms, the products of two gradient terms, and finally mixed products, using data from ASDEX discharge 33473.

2. The mean products of the spatially constant terms

The first three products are just the rms fluctuation levels, which can be normalized as appropriate to the mean density or the mean temperature:

$$\sqrt{\langle \overline{n_e}^2 \rangle} \,/\, \langle n_e \rangle = 0.27, \tag{11}$$

$$\sqrt{\langle \overline{T_e}^2 \rangle} \,/\, \langle T_e \rangle = 0.48, \tag{12}$$

$$\sqrt{\langle \overline{V_{pl}}^2 \rangle} \,/\, \langle T_e \rangle = 1.34. \tag{13}$$

The density fluctuation level is similar to that calculated using less elaborate methods. The level of temperature fluctuations is seen to be fairly large, which invalidates the many methods that neglect them. The normalized potential fluctuation level is even greater than unity. This is a consequence of the large temperature and moderate *floating* potential fluctuation levels. Since the scrape-off-layer is in contact with a material surface, it is reasonable to expect that the physics of the turbulence limits the floating potential, rather than the plasma potential. However, it is still the plasma potential that drives turbulent transport.

There are three mean cross products:

$$\langle \overline{n_e}\ \overline{T_e} \rangle \,/\, \sqrt{\langle \overline{n_e}^2 \rangle \langle \overline{T_e}^2 \rangle} = -0.66, \tag{14}$$

$$\langle \overline{T_e}\ \overline{V_{pl}} \rangle \,/\, \sqrt{\langle \overline{T_e}^2 \rangle \langle \overline{V_{pl}}^2 \rangle} = 0.99, \tag{15}$$

$$\langle \overline{V_{pl}}\ \overline{n_e} \rangle \,/\, \sqrt{\langle \overline{V_{pl}}^2 \rangle \langle \overline{n_e}^2 \rangle} = -0.63. \tag{16}$$

We see that temperature and plasma potential are perfectly correlated, and that the correlation of density with temperature equals that of density with potential, again suggesting that the temperature drives the potential. The values -0.66 and -0.63 could indicate a lack of coherence or simply a phase shift.

3. The mean products of the gradient terms

The squares of the gradients can be used to define a mean wavenumber for each plasma parameter:

$$k_n = \sqrt{\langle n_e'^2 \rangle / \langle \overline{n_e}^2 \rangle} = 1.14\ \mathrm{cm}^{-1}, \tag{17}$$

$$k_T = \sqrt{\langle T_e'^2 \rangle / \langle \overline{T_e}^2 \rangle} = 0.68\ \mathrm{cm}^{-1}, \tag{18}$$

$$k_V = \sqrt{\langle V_{pl}'^2 \rangle / \langle \overline{V_{pl}}^2 \rangle} = 0.68 \text{ cm}^{-1} . \quad (19)$$

We see that the density fluctuations have more power at shorter wavelengths.

The gradient cross terms indicate the mean wavenumber of the parts of the spectrum which overlap and are coherent:

$$k_{nT} = \sqrt{\langle n_e' T_e' \rangle / \langle \overline{n_e}\ \overline{T_e} \rangle} = 0.52 \text{ cm-1} , \quad (20)$$

$$k_{TV} = \sqrt{\langle T_e' V_{pl}' \rangle / \langle \overline{T_e}\ \overline{V_{pl}} \rangle} = 0.67 \text{ cm}^{-1} , \quad (21)$$

$$k_{Vn} = \sqrt{\langle V_{pl}' n_e' \rangle / \langle \overline{V_{pl}}\ \overline{n_e} \rangle} = 0.43 \text{ cm-1} . \quad (22)$$

The fact that these wavenumbers are smaller than those for the self products suggests a greater coherence between density and temperature/potential for long wavelengths.

4. The mean products of one gradient and one constant term

Of the quadratic mean products with exactly one gradient, three will vanish because of the normalization (8):

$$\langle \overline{n_e}\, n_e' \rangle = \langle \overline{T_e}\, T_e' \rangle = \langle \overline{V_{pl}}\, V_{pl}' \rangle = 0 . \quad (23)$$

The remaining six products can be grouped into pairs which should be equal and opposite if the turbulence is homogeneous. We give the results (without normalization, in units of 10^{19} m^{-3} V/m and V^2/m) here:

$$\langle \overline{n_e}\, T_e' \rangle = -0.58 \qquad \langle n_e' \overline{T_e} \rangle = 3.52 \quad (24)$$

$$\langle \overline{T_e}\, V_{pl}' \rangle = 32.6 \qquad \langle T_e' \overline{V_{pl}} \rangle = -27.1 \quad (25)$$

$$\langle \overline{V_{pl}}\, n_e' \rangle = 6.81 \qquad \langle V_{pl}' \overline{n_e} \rangle = -0.01 \quad (26)$$

The two members of each pair indeed have opposite signs but not nearly equal magnitudes. This can be traced back to the fact that $\langle \tilde{n}\, \tilde{T} \rangle$ is not equal at x_6 and x_9, even though $\langle \tilde{n}^2 \rangle$ and $\langle \tilde{T}^2 \rangle$ are. This may be a problem related to violation of the assumptions of small separation ($k_n(x_9-x_6)=1.0$) and small fluctuation levels ($\delta T_e/T_e=0.5$), or to our method of dealing with small currents (eliminating a third of the measurements). On the other hand, the probe head may actually be perturbing the turbulence in a way that is different for different regions of the array.

In conclusion, the additional information available from many tips can be self-consistently used to determine the levels and correlations of density, temperature, and potential fluctuations. The temperature fluctuations are found to be large enough to dominate the potential fluctuations. The redundancy of information provides a means of cross checking the measured particle and energy fluxes.

PULSED RADAR; A PROMISE FOR FUTURE DENSITY PROFILE MEASUREMENTS ON THERMONUCLEAR PLASMAS

S.H. Heijnen, C.A.J. Hugenholtz, and P. Pavlo*

FOM-Instituut voor Plasmafysica "RIJNHUIZEN", Nieuwegein, The Netherlands
* CSAV Institute of Plasma Physics, Prague, Czechoslovakia

Introduction

The usage of pulsed radar techniques for density measurements has become possible due to the progress in technology that enabled the transmission of very short ($\leq$ 1 ns) pulses and accurate enough measurements of the time of flight in the ns range. There are some striking advantages of pulsed radar [1,2] above the "classical" swept frequency reflectometry:

- the movement of the plasma position can be neglected during the flight time of the pulse in the plasma,
- the influence of false reflections will not effect the measurement in pulsed radar because the echoes fall in non-interesting time windows,
- the frequency accuracy and stability of the source is not important.

The difficulty of pulsed radar is the very fast time measurement needed to obtain the desired accuracy.

A first attempt of pulsed radar, at a frequency of 34 GHz, has been performed at the RTP tokamak. The measured time delays, using a Gaussian shaped pulse of 1.5 ns width, are in good agreement with expected values.

A numerical analysis is performed to study which additional information can be obtained when besides the time-of-flight, the modification of the rf pulse shape by the plasma is recorded. Calculations are made for the RTP-tokamak with Gaussian shaped pulses and in WKB approximation.

Pulsed radar set-up at the RTP tokamak

A block diagram of the preliminary pulsed radar set-up is given in Fig. 1. About 100 mW of microwave power, at a frequency of 34 GHz, is supplied to an amplitude modulator which is pulsed by a pulse generator with 1 ns rise and fall times. The modulator consists of a hybrid Tee, two attenuators for balancing, and two detectors (1N53). The generated microwave pulses are about 1.5 ns wide, measured at half height, with a repetition time of 20 ns. The microwave pulses are fed through a low-pass filter (Flann waffle iron) to protect the modulator and the Gunn-oscillator for the gyratron power (200 kW at 60 GHz) used for ECRH experiments at RTP. The power of the gyratron measured at the radar antenna is about 50 W if no plasma is present and falls to less than a Watt with plasma. The pulse reflected from the plasma is coupled out with a directional coupler, passed through a second low-pass filter, and fed to a biased detector (1N26). The amplified detector signal is recorded with a 20 GHz sampling oscilloscope (Tektronix CSA 803).

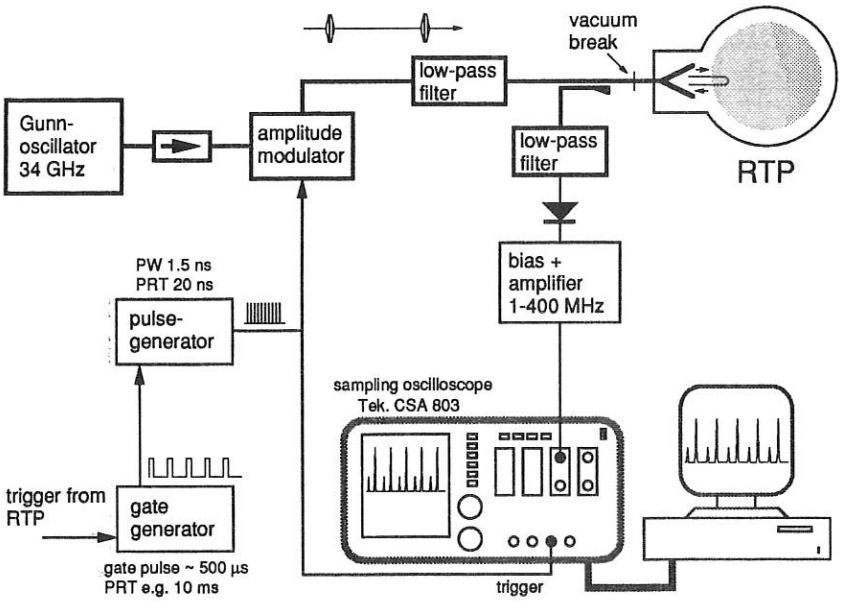

Fig. 1. Pulsed radar set-up at the RTP tokamak.

Measurements at the RTP tokamak

A gate generator (Fig. 1), with a tuneable pulse width, selectable pulse repetition time and number of pulses, controls the measurement. This generator gates a second pulse generator which makes the modulation pulses. The synchronous output triggers the sampling oscilloscope which samples with a frequency of 200 kHz in sequential equivalent time. This means that for each trigger one data point is recorded and that each data point is delayed a few ps more in regard to the trigger time than the foregoing data point. During each gate pulse of 500 µs, 100 data points are recorded. This gives a wide enough time window for one pulse delay measurement. Figure 2 shows nine successive measurements, which are performed at a repetition time of 10 ms. The density of the RTP plasma increases from zero to flat top ($n_e \sim 6.10^{19}$ m^{-3}) in about 50 ms. The first echo in each time window originates from the vacuum window. In the first time window (0 ms) a echo from the far wall of the torus can be seen. This echo disappears in the second and third window due to refraction. Echoes from the plasma appear in the following time windows. The recorded data is filtered with a time response of 1.10^{-9} ns because of the rather high noise (~ 2 mV) of the 20 GHz sampling oscilloscope.

An improved waveguide system will give a better S/N ratio. A major improvement would be a heterodyne detection system. As the amplitude modulation is not 100% there is still some background power which gives some interference as can be seen in Fig. 2. This can be improved when an up-convertor is used. The up-convertor makes it also possible to produce shorter pulses (e.g. 500 ps). An other solution for the interference is the use of two antennae.

The reflected radar pulse is recorder in ~50 μs with the present sampling oscilloscope. For more accurate measurements the sampling oscilloscope should be replaced by a real-time data recording system.

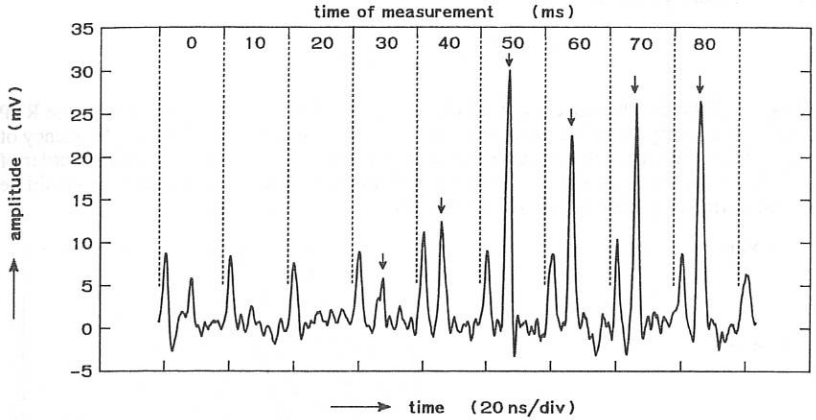

Fig. 2. Pulsed radar measurement at RTP. Arrows indicate the pulse reflected by the plasma.

Numerical analysis

For waves emitted perpendicular to the toroidal magnetic field lines and with the electric field vector parallel to the magnetic field (O-mode), the phase shift at the point of reflection is given by [3] :

$$\phi(f) = \frac{4\pi f}{c} \int_{a}^{r_c(f)} \sqrt{1 - \left(f_p^2/f^2\right)}\, dr - \frac{\pi}{2} .$$

Here, f_p is the plasma frequency ($f_p \approx 8.979 \sqrt{n_e(r)}$), c is the speed of light, and r_c is the point of reflection where f_p equals f. Already in 1961, Budden [3] showed that the time-of-flight for a pulse reflecting at a plasma density layer is given by :

$$t_0 = \frac{1}{2\pi} \phi'(F) ,$$

where $\phi'(F)$ is the first derivative of the phase change taken at the operating frequency. For the pulsed radar experiment we use Gaussian shaped pulses. When third and higher order derivatives of the phase change are neglected, it can be proven that the pulse remains Gaussian shaped after reflection, but now with a width given by:

$$W_r = W_t \sqrt{1 + \left(\frac{2 \ln 2\, \phi''(F)}{\pi^2 W_t}\right)^2} ,$$

where W_t is the pulse width of the transmitted pulse, W_r is the pulse width of the reflected pulse and $\phi''(F)$ is the second derivative of the phase change taken at the operating frequency. Taking the density profile as:

$$n_e\left(\frac{r}{a}\right) = n_e(0)\left(1 - \left(\frac{r}{a}\right)^{\alpha}\right)^{\beta} \quad ,$$

the time-of-flight and the pulse width can be calculated. In Fig. 3 this is shown for the RTP tokamak for a variety of profile parameters (α,β), a pulse width W_t of 0.3 ns, at a frequency of 34 GHz. When the same calculations are done for pulses of 1 ns, broadening is in the order of only 0.5%. It is clear from Fig. 3 that the time-of-flight as well as the broadening should be measured to find the position of the reflecting layer.

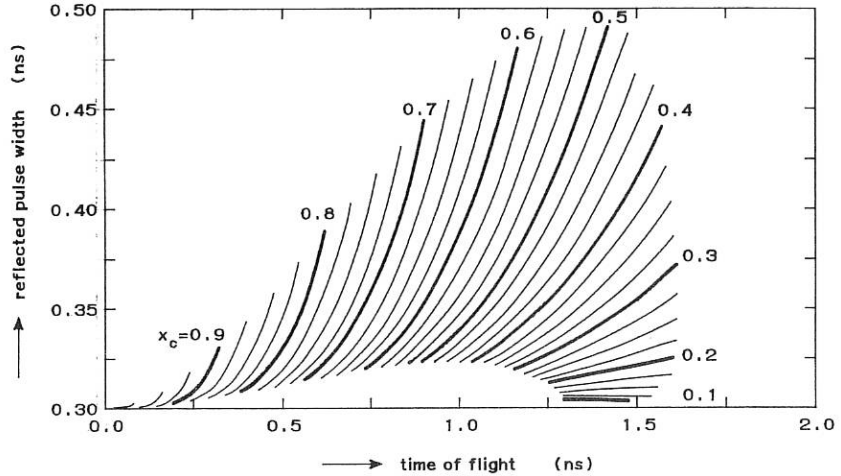

Fig. 3. Time-of-flight and pulse width calculations for the RTP tokamak ($x_c = r_c / a$). Parameters: pulse width 0.3 ns, central density 3.10^{19} m^{-3}, radar frequency 34 GHz.

Conclusion

It is proven that pulsed radar can work even at a small (minor radius 0.17 m) tokamak. The system must be improved for more accurate measurements. This is possible by increasing the S/N ratio, shorten the pulse length, and improving the data recording system. It has been shown that even on a small tokamak like RTP, pulse width broadening can be observed when a pulse width of $\leq$ 500 ps is used.

References

[1] C.A.J. Hugenholtz and S.H. Heijnen, Rev. Sci. Instrum. **62** April (1991)
[2] O.S. Pavlichenko, A.I. Skibenko, and I.V. Yasin, ITER Diagnostic Workshop, Garching, Germany, ITER-IL-Ph-07-0-15, Feb. 12-23 (1990)
[3] K.G. Budden, *Radio waves in the ionosphere*, University Press, Cambridge (1961)

CORRELATION REFLECTOMETRY TECHNIQUES FOR TJ-I AND ATF

J. Sánchez, B . Brañas, T. Estrada, E. De La Luna, A.P. Navarro, E. Anabitarte*
J.M. Senties*
ASOCIACION EURATOM/CIEMAT 28040 Madrid Spain
* Univ. Cantabria 39005 Santander Spain

G. R. Hanson, J.H. Harris, J.D. Bell, J.B. Wilgen
Oak Ridge National Laboratory, Oak Ridge TN 37831 USA

Two point radial correlation reflectometry has been used on TJ-I Tokamak and ATF Stellarator, to extend deeper in the plasma bulk the successful studies on electrostatic edge turbulence already performed by Langmuir probes (1, 2).

The use of broadband homodyne systems allows access to a larger range of radial positions but imposes some constraints on the ability of reflectometry to determine correlation lengths and the k-spectrum of the density fluctuations: $\cos\phi$ and not directly the phase delay ϕ is measured.

Different techniques are used to overcome the ambiguities introduced by the homodyne measurement: slow frequency sweeping for TJ-I and dual sine/cosine detection with fringe counting algorithms for ATF.

Coherence measurements on TJ-I

A broadband reflectometer (33-50 GHz X and O mode) is in operation in TJ-I (R=.3m, a=.1m, B_0<1.5 T). For radial coherence studies the system uses two oscillators feeding a common launching-receiving antenna. Homodyne detection is used in both channels.

The method of slow frequency sweeping for coherence studies has been already introduced (3) : one oscillator remains at fixed frequency f1 and the second one makes a slow frequency sweeping around f1. The coherence is then evaluated in a dynamic process. Simulations showed how the coherence measured by this method had maximum and minimum values as the differential phase delay between both reflectometers increased, the maxima being the best approach to the real coherence values for the density perturbation.

In this paper first plasma experiments using the method in TJ-I are reported: Fig 1 shows the coherence between the direct signals from both detectors obtained with X-mode operation of the reflectometer.The coherence shows well defined maxima and minima as the frequency difference Δf between both oscillators increases. The apparent coherence for $\Delta f=0$ is not close to 1 in this experiment , this is because the coherence for $\Delta f=0$ depends on the difference between the phase delays of both reflectometers.

The coherence length can be extracted by extrapolating the trend shown by the maxima in fig 1. For this experiment, assuming parabolic profile for the density ($n_0=1.5\times10^{13}$ cm^{-3}), the coherence length is about 2 mm for the radial position r/a=0.8.

One of the main concerns in this experiment was the short density plateau in TJ-I (typically <10ms) which leads to a relatively fast sweeping rate. This makes the statistics to become poorer. As the experimental results show, a suitable choice of the delay paths and the extension of the frequency sweeping (which determine the number of fringes in the phase) can bring a good enough statistics to determine the correlation lengths.

That analysis can be performed for different frequency windows , leading to a determination of the $\sigma_{kr}(\omega)$ function, as the inverse of the radial correlation length for the given frequency interval, studies in this direction are in progress.

The determination of the $S(k_r,\omega)$ function, on the other hand, seems to be difficult due to the short statistics, this should not be a problem in larger machines with a longer density plateau (>50 ms).

An interesting additional result is the information on the differential phase delay: $d\phi/df$ during the frequency sweeping: the number of "coherence fringes" per frequency interval in fig 1 must be twice that of the "profile fringes" which determine $d\phi/df$. Thus the density profile information, which is in many cases disturbed by the density fluctuations, can be obtained trough coherence measurements. Also the effect of parasitic references in single antenna reflectometers is removed since the correlation between both channels is not affected by fixed additional references as far as they are well below the main one.

All those possibilities make the method strongly attractive for self-consistent coherence studies, taking in a single shot the complete coherence information and that of the local density gradient, which is necessary for the estimation of the distance between the reflecting points. Studies are on the way to confirm those applications under different plasma conditions.

Following the same pattern, fixed frequency experiments can be performed by taking for the analysis the points for which the coherence is maximum. Then with a better statistics the spectral density $S(k_r,\omega)$ (see fig. 2) and the spectral width $\sigma_{kr}(\omega)$ functions for radial k can be obtained (4).

Coherence measurements on ATF

The ATF (l=2, 12-field-period torsatron, R=2.1m, a= 0.27 m B_0< 2 T) reflectometer operates two frequencies simultaneously with the same antenna system. Two tunable microwave sources allow continuous operation between 30 and 40 GHz. Different antennas are used to launch and receive the beam (5).

The receiving system uses a dual sine-cosine homodyne detection for each channel. A fringe counting algorithm has been developed for extracting the phase delays from the sine-cosine signals. This fringe counting procedure has some noise at low frequencies (<15 kHz) due to phase jumps.

The radial correlation analysis is performed with the temporal phase evolution from both channels, by using the two point correlation technique (6). The spectral density function $S(k_r,\omega)$ obtained with this method is presented in fig.3. As we can see the mean k_r is close to zero, having the spectral density also a maximum for the low k values.

From the spectral density function the radial k-width: $\sigma_{kr}(\omega)$ can be determined. Fig. 4 shows σ_{kr} and the power spectra for a typical ECH discharge on ATF, the reflecting point position being r/a = 0.8. The data below 15 kHz are removed due to the difficulties in the fringe counting. An increase in σ_{kr} (decrease of the correlation length) is observed when ω increases, in agreement with the typical trend for edge turbulence obtained from Langmuir probes measurements. In addition, a peak in the spectrum with a larger correlation length appears around 40 kHz (5).

The value of the mean radial-k is usually close to zero, fig.5 shows its evolution when the distance between reflecting points Δr increases. As expected, the values of k_r are independent on the distance and only in the vicinity of Δr=0 an increase in k appears due probably to

the indetermination introduced by the short Δr, also for those values the separation between reflecting points gets smaller than the theoretical width of the reflecting layer and the k interpretation becomes difficult.

When regarding the coherent mode at 40 kHz the low radial k value the existence of a pressure-gradient-driven interchange mode in the density gradient region of the plasma. This mode should have a long toroidal extension, as deduced from the high coherence between the reflectometer and the Fast Reciprocating Langmuir Probe. Also the spectra of density fluctuations obtained with the Heavy Ion Beam Probe shows the mode.

The mode has no contribution to the ExB transport, following Langmuir Probes results (6), but the heat transport could be large through the interchange of hotter and cooler particles.

An additional analysis was performed to search for a possible dependence of this mode with the magnetic configuration (rational surfaces). The method used on the shearless W7AS stellarator (7) was applied: the RMS of the reflectometer signal is in good correlation with the temporal ripple in the poloidal field (360 Hz on ATF) when the reflecting point approaches the location of the mode peak activity. The effect was clearly shown, indicating a dependence of the mode peak location with the magnetic configuration.

Conclusions

Two different methods have been proposed for coherence studies by reflectometry.

The slow sweeping applied to TJ-I allows the determination of the correlation length in a single shot, with the possibility of giving additional information on the local density gradient.

The sine-cosine detection on ATF is able to decouple phase and amplitude effects in the reflected signal. Coherence lengths have been determined and very low k are observed for radial propagation of the fluctuations. The ATF reflectometer has also showed the existence of coherent structures in the gradient region which are attached to the magnetic configuration.

References

1.- C. Hidalgo, M.A. Pedrosa, A.P. Navarro, F.L. Tabares et al." Electrostatic turbulence in the TJ-I tokamak". Nucl .Fusion 30, 4, 717-21 (1990)
2.- C. Hidalgo, J.H. Harris, T.Uckan, J.D. Bell et al. " Plasma fluctuations near the shear layer in the ATF torsatron", submitted to Nucl. Fusion (1990)
3.- T. Estrada, J. Sanchez, B. Brañas, A.P. Navarro. "Broadband Homodyne Reflectometer Devoted to Density Fluctuations Measurements". Rev. Sci. Instrum., 61, 3034, (1990).
4.- C. Hidalgo, M.A. Pedrosa, I. Garcia, E. De La Luna et al. "Turbulence studies in the proximity of the velocity shear layer in the TJ-I tokamak", This conference.
5.- G.R. Hanson, J.B. Wilgen, E. Anabitarte et al. "ATF Two-Frequency Correlation Reflectometer". Rev. Sci. Instrum, 61, 3049 (1990).
6.- J.M. Bell, Y.C. Kim, E.J. Powers. J. Appl. Phys. 53, 3933 (1982)
7.-J.H. Harris , L. A. Charlton , E. Anabitarte, C. Hidalgo et al. " Fluctuations and Stability in the ATF Torsatron". 30th IAEA Conference (Washington, 1990), paper IAEA-CN-33, C-4-7
8.- J. Sanchez, H.J.Hartfuss, E. Anabitarte, A.P. Navarro et al. Reflectometry Observations of Density Fluctuations in Wendelstein VII-AS Stellarator. Nucl. Fusion 30, 2383 (1990).

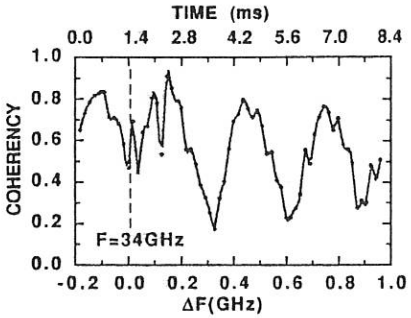

Fig.1.-Coherence between the reflectometer signals as a function of the frequency difference during the slow sweeping experiment on TJ-I.

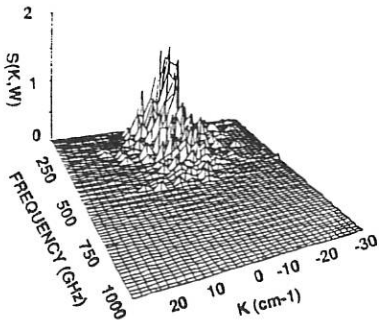

Fig.2.-Typical spectral density function for TJ-I at r/a=0.8.

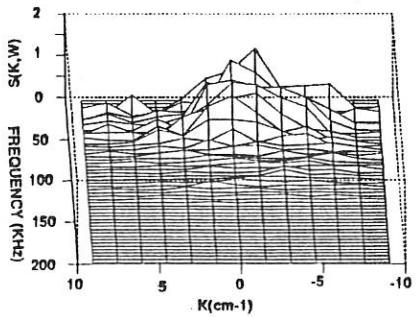

Fig.3.- Typical spectral density function for ATF at r/a=0.8, in ECH discharges.

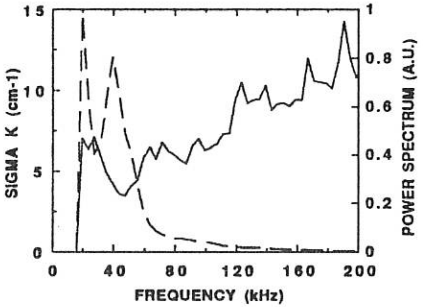

Fig.4.- Radial k and power spectra for density turbulence on ATF.

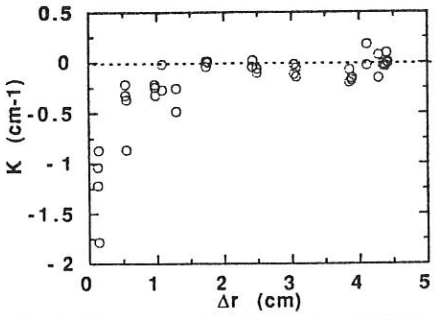

Fig.5.- Mean value of the turbulence radial k on ATF at different probing point separations.

MEASUREMENT OF FAST CHANGES OF THE EDGE DENSITY PROFILE IN TEXTOR

H. GUNKEL*, J.O. KUSZYNSKI*, A. POSPIESZCZYK, B. SCHWEER

Institut für Plasmaphysik, Forschungszentrum Jülich GmbH, Association EURATOM-KFA, P.O. Box 1913, W - 5170 Jülich, Fed. Rep. Germany

*) Zentralinstitut für Elektronenphysik (ZIE), P.O. Box 1250, O - 1086 Berlin, Fed. Rep. Germany

1. Introduction

The determination of the spatial distribution of the electron density in the boundary layer of a plasma is of importance for the investigation of plasma-wall interactions in plasma devices. Atom beam techniques are suitable diagnostics to determine electron density profiles in the edge plasma of a tokamak. Spatial observation of the visible light emitted by excited atoms due to electron collision allows the determination of the electron density profile as an absolute quantity if the light emission is recorded up to the total absorption (ionization) of the beam/1/.

At TEXTOR the emitted spatial density profile is usually recorded by photosensitive linear arrays, having an integration time of $\tau \geq 0.5$ ms. Fast changes of the edge density profile whose observation is of importance, e.g. for fluctuations, disruptions or investigations of H-mode transitions, cannot be measured with such an integration time. Moreover, in the case of atom beams which are generated by the laser blow off technique only one density profile per laser shot can be obtained. In order to improve the time resolution and to increase the number of measured profiles with the laser blow off equipment of TEXTOR a CCD-camera with high frame rate (36.8 kHz, $\tau_{int} = 27.2$ μs) has been designed. First measurements with this diagnostic on TEXTOR will be reported.

2. Principles of the method

A description of the principles of the method and of the procedure for the evaluation of the measurements is already outlined in Refs. 1 and 2.

The local electron density $n_e(r)$ can be obtained from the recorded light intensity profile $I_A(r)$ by

$$n_e(r) = \bar{v}_A I_A(r) \; / \; \langle \sigma_I v_e \rangle \int_r^0 I_A(r')dr'$$

where $\langle \sigma_i v_e \rangle$ is the ionization function (rate coefficient), averaged over a Maxwellian distribution of electron velocities v_e, and $\bar{v}_A$ is the mean velocity of the injected atoms.

The equation is based on the condition that the ratio of the rate coefficients for ionization and excitation is only a weak

function of the radial distance r, i.e. of $T_e(r)$. In our case of a Li-atom beam this prerequisite is fulfilled. Density-dependent rate coefficients for ionization have been taken into account.

3. Experimental setup

Fig. 1 displays the general scheme of the diagnostic system. It is identical with the system fully described in Ref. /1/, except the camera system used here. The focussed light of a ruby laser (1 J output energy) ablates small portions (ϕ = 1-4 mm) from the rear side of a glass substrate with a LiF layer of 500 Å thickness. The ablated Li atoms travel 110 cm to the plasma boundary with a velocity of $\bar{v}_A$ = 1.1 x 10^6 cm/s, and the emitted light is recorded temporally by a photomultiplier and spatially by a CCD camera, both in combination with an interference filter at λ = 6708 Å ($2p^2P^0$ - $2s^22S$).

By taking into account the selected imaging optics (F/0,95) and the CCD-pixel geometry, each pixel observes a volume in TEXTOR of 1.6 x 16 x 130 mm (radial, toroidal, line of sight). Especially the depth of focus corresponds to the width of the atom beam. This is the prerequisite for a high contrast of the image of beam.

The essential parts of the camera system are shown in fig. 1 and tab. 1. Because of the high sampling rate of the CCD camera an auxiliary transient recorder was necessary as an intermediate storage. The input channels A and B of the recorder have different amplification (ratio 1 : 5). In this way weak signals can also be converted with high resolution, although the transient recorder has a resolution of 8 bit only.

4. Results

Ordinary line cameras with a low frame rate necessitate the density profile to be calculated on the basis of the above mentioned average velocity because the integration time of the camera is longer than the lifetime of the atom beam. By contrast, our camera with high frame rate yields 3-5 frames per laser shot in dependence on the intensity of the emission and the lifetime of the atom beam. Therefore we are able to derive the density profile from each frame on the basis of the correct velocity v_A of the corresponding group of atoms (0.8 x 10^6 cm/s $\leq v_A \leq$ 1.6 x 10^6 cm/s). This becomes apparent from fig. 2, where the time-dependent spatial emission profiles of the atom beam are shown. At increasing time the lower velocity of the atoms leads to a shift of the spatial emission profile towards the plasma boundary (lower penetration depth). Simultaneously, the height of the emission profiles changes according to the temporal variation of the lithium atom density in the beam. This is demonstrated by the signal of the photomultiplier, which records the temporal distribution of the number of injected atoms without spatial resolution.

In figs. 3 and 4 emission profiles and the corresponding

electron density profiles obtained under different discharge conditions are shown. Fig. 3 refers to a purely ohmic discharge, while fig. 4 shows results with additional neutral beam heating. In the latter case significant temporal variations of the density profile can be seen. This demonstrates that a camera with sufficiently high frame rate is suitable to observe the time dependence of the density profiles within short time intervals.

References

/1/ A. Pospieszczyk and G.G. Ross, Rev.Sci.Instr. 59 (1988) 605
/2/ E. Hintz, P. Bogen, J. Nucl. Mater. 128&129 (1984) 229

Table 1: CCD DATA AQUISATION SYSTEM

CCD line scan camera L115/10 (ZIE)
line scan sensor L115 (WF*); 256 pixels;
pixel size: 13x350 μm; responsivity: -5,7 Vcm/μJ
satur. exposure: $\leq$70 nJ/cm^2; video sampling rate: up to 10 MHz
exposure time: 27,6 μs ... 450 μs
* WF - Werk für Fernsehelektronik Berlin

Transient recorder TM1009 (René Maurer)
video sampling rate: 5 MHz; 128 pixels/line
memory: 2 x 2 kByte, i.e. 2 x 16 line scans
2 x 8 bit ADC; 2 x 8 bit DAC

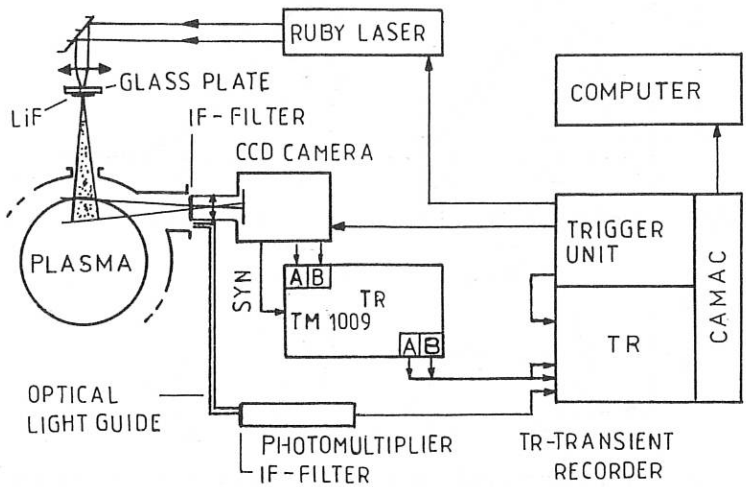

FIG. 1: EXPERIMENTAL SETUP

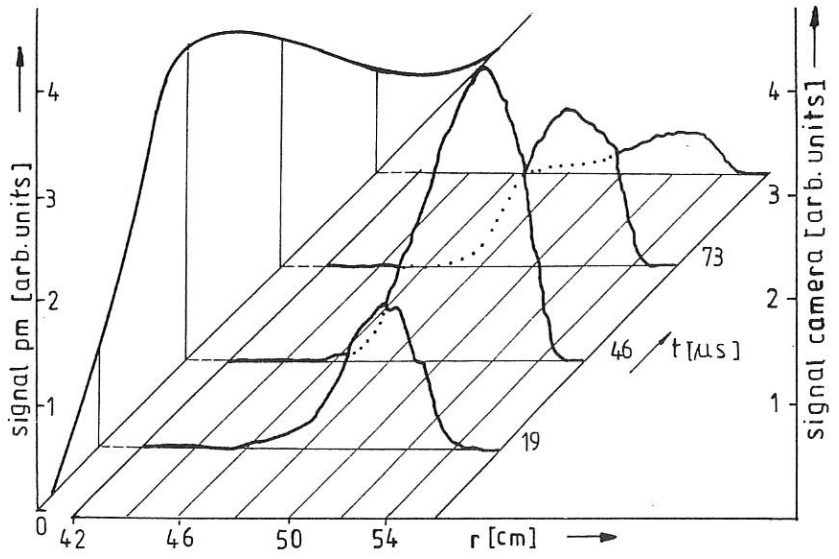

FIG:2 Emission signals as a function of radius and time

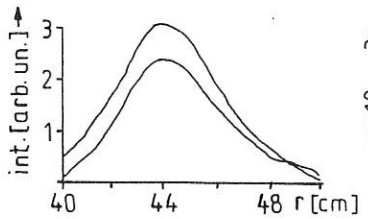

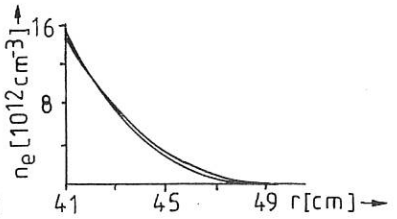

FIG:3 Emission profiles (*) Density profiles shot 43131

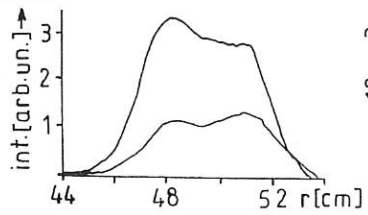

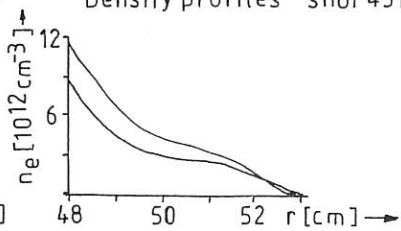

FIG:4 Emission profiles (*) Density profiles shot 43188

(*) $\Delta t = 27.2\,\mu s$

REFLECTOMETRIC DIAGNOSTICS OF PLASMA DENSITY FLUCTUATIONS IN TUMAN-3 TOKAMAK.

Bulanin V.V., Grinshtain Y.M., Korneev D.O.
State Technical University, Leningrad, USSR

Its E.R.,Rozhdestvensky V.V., Stepanov A.Yu.
Ioffe Physical-Technical Institute, Leningrad, USSR

The reflectometer diagnostics has been recently used on the DIII-D tokamak for studying the evolution of density fluctuations in the plasma under the L-H transition /1/. For the same purpose the simple homodyne reflectometer with a single antenna /2/ was applied in the Tuman-3 tokamak with the ohmically H-mode regime initiated by means of gas puffing or radial electric field switching on /3/ and with the 2-fold fast current rampdown regime /4/. The diagnostic scheme is shown in Fig.1. The oversized circular waveguide of 60 mm in diameter placed at the low magnetic field side was used to probe the plasma along the torus major radius by the O- or X-mode microwaves at frequencies 16,5-26 GHz and to receive the reflected wave. For the O-mode the cut off appears to be at densities $n_e=(0.3-0.8)\ 10^{13}\ cm^{-3}$, and for the X-mode $-(0.1-0.5)\ 10^{13}\ cm^{-3}$. The detected signal includes the information on amplitude and phase fluctuations of the reflected wave. The signal was amplified at frequency band f=(0.1-500) kHz and memorized in the digital form with the sampling step of 1 μs. After processing one can obtain data on the evolution of following values: the RMS amplitude averaged inside the different frequency bands $\langle \upsilon^2 \rangle^{1/2}$, frequency spectrum S(f), spectral density isolines of the reflectometer output oscillations.

Fig.2 shows the typical oscillograms of $\langle n_e \rangle$ and $\langle \upsilon^2 \rangle^{1/2}$ corresponding to the O-mode (1) and X-mode (2) probing at F=26 GHz , which were taken without the H-mode transition. One can see that the $\langle \upsilon^2 \rangle^{1/2}$ value starts to increase at 10 ms and changes insignificantly after 15 ms for the O-mode case. This time interval shifts to the beginning of the discharge with the

frequency F being decreased. For the X-mode case $\langle v^2 \rangle^{1/2}$ starts to increase at once with the plasma appearance. This proves apparently that the probing wave cut off layer moves towards the antenna with the density rise. At the same time the low frequency component to be appeared with such displacement has not been detected. The spectrum S(f) for the quasi stationary discharge stage is shown in Fig.2(c). The sampling time of analysis is 512 μs. The spectrum is presented by the wide frequency band component which falls down by the factor of 2-3 with the frequency increasing up to 500 kHz. The peak amplitude and frequency are changing during the discharge.

As it follows from Fig.3 the ohmically H-mode transition is accompanied by the fast decrease both of D_α (a) and reflectometer output oscillations for the X-mode probing at F=16,5 GHz (b). In this case the reflectometer signal decreases over all frequency bands. Fig.4a shows that high frequency f>200 kHz oscillations are suppressed in a greater extent than the low frequency ones. The H-mode spectrum transformation is changing with the probing frequency being increased when the cut off layer shifts into the plasma. At F=20 GHz (Fig.4b) the amplitude of low frequency f<100 kHz oscillations grows, whereas the amplitude of high frequency ones falls down. At F=23 GHz the falling of $\langle v^2 \rangle^{1/2}$ can disappear (Fig.3c). At F=26 GHz all spectrum components are growing up (Fig.3d). This phenomenon may be connected with the shifting of the cut off layer towards the antenna because the density gradient after the H-mode transition becomes larger than before /1,5/. It is necessary to note that H-mode transition does not produce any remarkable spectrum S(f) changes under the O-mode probing. Some increase of $\langle v^2 \rangle^{1/2}$ is observed just like as under the X-mode probing at F>24 GHz. In both cases it means that the cut off layer is localized in the region where plasma oscillations are not suppressed during the transition.

Fig.5 shows that periodical (T<1 ms) oscillations of the soft X-ray intensity can arise during the H-mode (b). The I_{SXR} peaks coincide in time with the drops of high frequency f>200

kHz oscillations under the X-mode probing.

The experimental results on the H-mode transition stimulated by the radial electric field are exhibited in Fig.6. One can see the same oscillation behaviour as under the gas puffing stimulation: the fast D_α decrease (c) is accompanied by the falling of the high frequency f>200 kHz oscillation $\langle \upsilon^2 \rangle^{1/2}$ for the X-mode probing (d).

In the experiments with the fast I_p rampdown, /4/, no significant spectrum S(f) changes were observed (Fig.6). The current rampdown produces the fast D_α decrease (a) whereas the high frequency f>200 kHz oscillation $\langle \upsilon^2 \rangle^{1/2}$ changes have not been observed. This fact is in accordance with probe measurement data which proves that $n_e(r)$ at the periphery is kept constant /4/.

Thus the results obtained show that under the ohmically H-mode transition initiated with the both methods mentioned above the oscillation amplitude of the reflectometer signal falls down quickly when the cut off region is localized in the plasma periphery. This falling down is connected with the most preferential suppression of high frequency oscillations. In the current rampdown experiments such effect has not been observed. Our results are in accordance with the reflectometer measurement data obtained in divertor discharges under additional powerful plasma heating /1,5/. They support the idea of the suppressing of plasma oscillations by the radial electric field shear /6/.

1.Doyle E.J., et al., Proc. 17th EPS Conf.,Amsterdam,v.14B,1, p 203,(1990); ibid v.14B,4,p 1596

2.T.Estrada,A.P.Novarro, et al.,17th EPS Conf.,Amsterdam,v.14B,4,p1592-1595

3.Askinasi L.G., Lebedev S.V., et al., this conference.

4.Askinasi L.G., Sakharov N.V., et al., this conference.

5.Tsuji S., at al.,"The Limiter H Mode With Lower Hybrid Current Drive", 30th Inter., Conf., Washington,CN-53/E-1-4

6.Biglari, H., Diamond, P.H., and Terry, P.W., Physics of Fluids B2, 1 (1990).

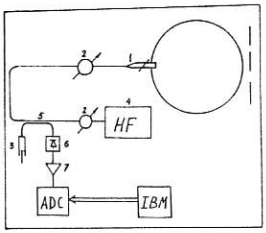

Fig. 1 1-antenna,2-attenuator,3-reflector, 4-oscilator,5-directional coupler, 6-detector,7-amplifier

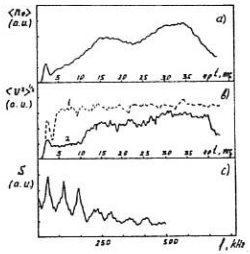

Fig. 2 a) chord averaged density, b) $\langle U^2 \rangle^{1/2}$ for X-mode (1) and O-mode (2), c) reflectometer signal spectrum

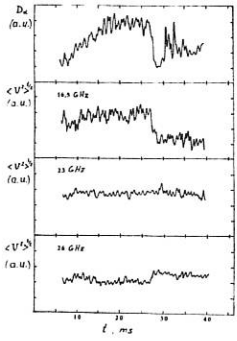

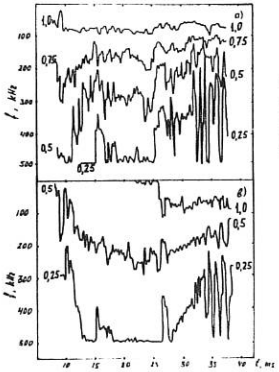

Fig. 3 D_α (a), and $\langle U^2 \rangle^{1/2}$ evolutions for diferent probing frequencies (b,c,d)

Fig. 4 The spectral density isolines in temporal and frequency frame

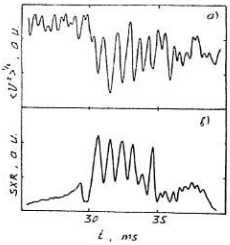

Fig. 5

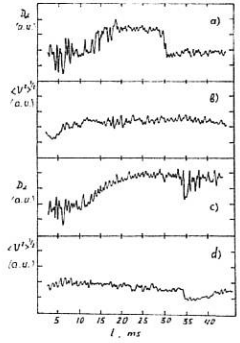

Fig. 6 The frame dependence of D_α and $\langle U^2 \rangle^{1/2}$ at the 200-500 kHz frequency band for the current rampdown discharge (a,b) and for induced with redial electric field change H-mode (c,d)

PLASMA TURBULENCE STUDYING ON THE T-10 BY MICROWAVE REFLECTOMETRY

V.A.Zhuravlev, V.V.Dreval

I.V.Kurchatov Institute of Atomic Energy, Moscow, USSR.

Two types of "O"-mode operating reflectometers were developed on the T-10 tokamak for plasma studying. The first one measures the time delay of reflected signal and is intended for studying of density profiles and low-frequency turbulence up to 40 kHz. The second is the heterodyne reflectometer, which is intended for studying plasma oscillations from some kHz to some MHz.

The time-delay reflectometer [1] worked with fixed microwave signal frequencies from 22.6 to 49 GHz (with densities in the reflecting layer from 0.6 to 3×10^{13} cm^{-3}). Sweeping of the microwave frequency is possible too. The time delay is measured independently on the mode of the microwave oscillator operation in this reflectometer. In fig.1a the behavior of the the time delay of 41.8 GHz signal during whole tokamak pulse is shown. Zero time delay corresponds roughly to the tokamak chamber wall. The reflecting layer arises on 100-th ms near the center of the chamber and then moves to the periphery. In fig.1b saw-teeth oscillations on the same stretched out in time signal are shown. Fast oscillations with some kHz frequencies are presented in the signal. In fig.2 the spectrum of fast oscillations in the time-delay signal is shown. The time-delay reflectometer through whole testing period showed good possibilities for studying of low-frequency turbulence simultaneously with measuring of radial position of the reflecting layer.

The second reflectometer is the heterodyne one [1]. Microwave frequency of the reflectometer is fixed during the tokamak pulse. The spectrum of plasma turbulence was received by measuring of fluctuations of the reflected signal frequency. Amplitude modulation of the reflected signal was obliterated by intermediate-frequency amplifier. The input of amplitude modulation to spectra of plasma turbulence didn't exceed 20% for worst conditions. Fluctuations of the reflected signal frequency were analyzed by multichannel analyzer in 5-300 kHz range of frequencies of fluctuations (not the range of reflected signal frequency shifts). The spectrum of $\tilde{n}_e/\nabla n_e$ was computed from the spectrum of frequency oscillations. Three types of turbulence were observed in plasma: MHD oscillations; oscillations with

frequency up to 30 kHz and with fast, in comparison to MHD, amplitude and frequency variations during 3-6 periods; chaotic fluctuations with 50-300 kHz frequencies. Amplitude modulation spectra of the reflected signal shows that low-frequency oscillations (with frequencies below 50 kHz) have long (≥15 cm) poloidal wavelengths. Parameters of high-frequency fluctuations corresponds to the parameters of fluctuations that were studied by scattering in different tokamaks [2]. In [3] the strong dependence of D_e on $\nabla n_e/n_e$ was supposed. That's why the time behavior of high-frequency turbulence during perturbations of the density profile was studied.

The turbulence behavior during ECRH was not quite clear because of different conditions of heating. Database available didn't allow to obtain clear dependence. Nevertheless it is possible to maintain that the turbulence rise after the ECRH start was dependent not on the power of ECRH only, but on radial distribution of power input too.

Results on the dependence of turbulence amplitude on plasma density profiles were more clear. In fig.3 and 4 radial distributions of amplitudes of the turbulence A are shown. A is given in arbitrary units. In fig.3 different density profiles were created by rise and decrease of plasma density in $1.5\text{-}3.5\times10^{13}$ cm^{-3} range during the same tokamak pulse with $q(a)\approx4.5$. In fig.4 turbulence distributions were obtained for stationary stages of tokamak pulses with $q(a)\approx6$ and $q(a)\approx4$. In the plasma periphery ($r\geq22\text{-}24$ cm) turbulence had the same amplitudes for different density profiles. But for smaller radii amplitudes of turbulence for wide profiles (rising n_e for fig.3 and regime with $q(a)\approx4$ for fig.4) were lower than for narrow profiles (decreasing n_e and regime with $q(a)\approx6$). Relative differences of turbulence amplitudes were 2-4 times greater then relative differences of local plasma parameters (n_e, ∇n_e) for different profiles. Equality of turbulence amplitudes in periphery of plasma for different regimes may be caused by either temperature dependence of turbulence or turbulence properties only (saturation for instance).

The turbulence amplitude was measured in regimes with periodic deuterium puffing. In pulses with $\bar{n}_e\leq2.5\times10^{13}$ cm^{-3} and $r_{ref}\leq20\text{-}22$ cm correlation between the pulse valve work and the turbulence amplitude was observed. In pulses with $\bar{n}_e\approx3.5\times10^{13}$ cm^{-3} and $r_{ref}\approx23\text{-}24$ cm the correlation was not found. In this pulses plasma density had ≈6% modulation caused by periodical puffing. The turbulence amplitude had more than 40% modulation for $r_{ref}\leq20\text{-}22$cm. In fig.5 the

behavior of the turbulence amplitude A is shown after the pulse valve switching on. The time behavior of the density gradient ∇n_e in the reflecting layer, which was obtained by the model [3] with the neoclassical pinching velocity V_p and different D_e, is shown in fig.5 too. When D_e in the model was independent on ∇n_e ($D_e \sim const$), the density profile evolution in the model was slow, in comparison to experiment, and correlation between the time evolution of ∇n_e and the turbulence amplitude A wasn't quite correct. When the dependence $\Delta D_e/D_e \sim 4\text{-}6\Delta(\nabla n_e)/\nabla n_e$ was used in the model, the time evolution of the density profile was close to experimental one, and the evolution of ∇n_e was really correlated with the experimental evolution of turbulence amplitude. The relative change of ∇n_e was 4-6 times less than the relative change of turbulence amplitude, i.e. the evolution of D_e in the model was the same as the evolution of turbulence amplitude in experiment. The strong dependence of the turbulence amplitude on the density gradient exists only for region with $r \leq 20\text{-}22$ cm. It is possible that the dependence exists for some tokamak regimes, but not for all regimes. There is no any data on the temperature dependence of the turbulence. Behavior of low-frequency oscillations during puffing was not clear, may be because two different species of the oscillations were not distinguished.

Conclusion: The strong dependence of high-frequency turbulence amplitude A on the shape of density profiles was found for some regimes of T-10 for $r \leq 20\text{-}22$ cm. That may be strong non-linear dependence of A on $\nabla n_e/n_e$. Using of the same dependence for D_e in the model [3] of density profile behavior gives the possibility to describe puffing experiments in the model with the neoclassical V_p and small D_e.

1. Sov. Journal of technical physics, v.57,1987, n.5, p.858
2. Sov. Plasma physics, v.15, 1989, n.4, p.503
3. Sov. Plasma physics, v.15, 1989, n.4, p.387

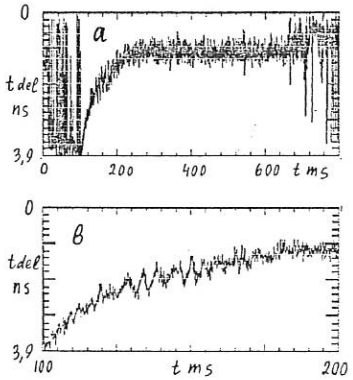

Fig. 1

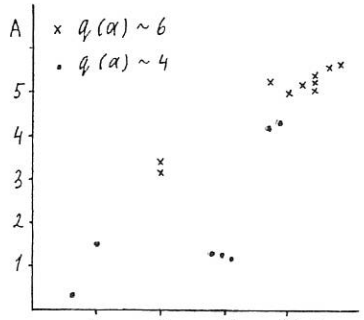

Fig. 4

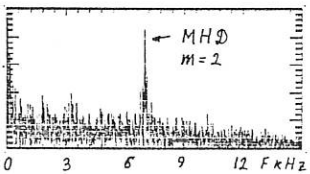

Fig. 2

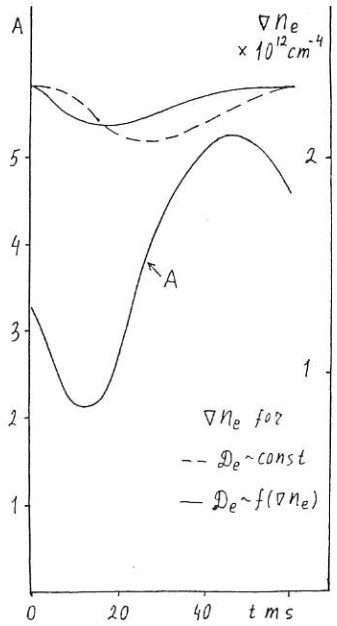

Fig. 5

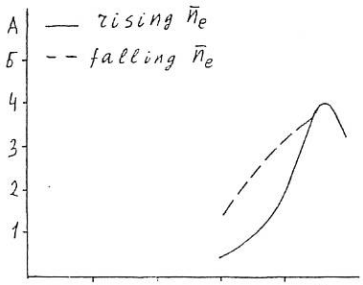

Fig. 3

A FIVE-CAMERA X-RAY TOMOGRAPHY SYSTEM FOR THE RTP TOKAMAK

D.F da Cruz Jr. and A.J.H. Donné

FOM-Instituut voor Plasmafysica "Rijnhuizen", P.O. Box 1207
3430 BE Nieuwegein, The Netherlands

Introduction

In most soft x-ray tomography systems in operation nowadays, the poloidal number of the oscillations that can be reconstructed is limited to m=2. This is due to the small number of cameras used, and their relative positioning around the tokamak. Because of the limited access to the tokamak optimum positioning of the cameras is almost impossible, especially in those cases where cameras have to be mounted outside the vessel. A five-pinhole camera system is in use on Tokamak de Varennes [1], where fluctuations up to m=3 could be resolved [2]. At the RTP-tokamak a similar system is being installed inside the vacuum vessel in order to study plasma oscillations with high poloidal number. With this system one can expect to reconstruct oscillations with poloidal number up to m=4 (and perhaps one component of m=5) without assuming any rotation of the plasma. The instrumental details of the system have been published elsewhere [3]. Below only a short description is given. The research programme of RTP will be described on this conference [9].

Camera Description

The five 'slit-hole' cameras for RTP will be placed inside the tokamak vessel. They are positioned as close as possible to the plasma at 20 cm from the plasma centre (minor radius: $\approx$ 16 cm). This allows us to reach certain angles which cannot be viewed from outside the vacuum vessel. The cameras are positioned at angles of 10°-55°-90°-240° and 290° with respect to the tokamak equatorial plane, to attain the best poloidal resolution for the system.

Each camera has two 16-channel arrays of Si photodiodes. The diodes are sensitive to photons with energies between 1 and 10 keV. One array is exposed to the plasma radiation. The other, which is screened from plasma radiation, works as a reference for the first array. This has been done to subtract by differential amplification any electromagnetic pick-up that could occur inside the tokamak vessel .

The detectors view the plasma through an aperture with dimensions of 1.0 mm in the poloidal direction and 4.0 mm in the toroidal direction. The aperture is vacuum sealed with a 25 μm thick Be-foil to avoid detection of visible light, and to select the spectral region of interest. The first array is positioned 10 mm behind the aperture. The solid angle of the system determines a viewing chord with a radial extension of 10-20 mm, depending on the particular viewing chord. In the toroidal direction this extension is about 16.0 cm (major radius: 72 cm). The detectors observe the plasma along chords with impact parameter p ranging from 1 to 12 cm. The mapping of the chords into the (p,ϕ)-plane is shown in Fig. 1, in which each point represents one viewing chord.

In order to protect the arrays from high temperatures during baking of the vessel, a water cooling system is employed.

Electronic System

The Si photodiodes are of the PNN^+ type normally used for visible light detection [4]. However they are also suitable for detection of x-ray radiation [5]. The total thickness of the diodes is 400 μm, with a 10 μm thick sensitive layer and a 1 μm thick p-layer. The area of each element is 4.0×0.94 mm^2 and the spacing between neighbouring elements is 1.0 mm. The detectors are operated in the current mode with a reverse bias of +12 V.

The first stage of amplification, along with the differential amplifiers, are positioned outside the vacuum system but as close as possible to the cameras, in order to minimize the stray capacitance of the cables. The 32 pre-amplifiers as well as the 16 differential amplifiers for each camera are mounted on 8 separate printed circuit boards. Since the circuits are very close to the magnetic field coils, the prints are positioned inside a box with double walls of Cu and μ-metal to avoid any electromagnetic disturbances.

The electronic system has been designed to have a total bandwidth of 200 kHz. It is AC-coupled with a time constant much longer than the plasma duration. The output signals of the differential amplifiers are led to the control room via 40 m-long lines (50 Ω coaxial cables). Here the main amplifiers take care that the signals are in the proper voltage range for the transient recorders (0-1 V)

The 80 signals are sampled by separate transient recorders with a maximum sampling frequency of 1 MHz. Each module (composed of 8 transient recorders) has a memory of 4 Mbyte. This memory is large enough to store the signals for the complete RTP plasma shot, that lasts about 200 ms. The signals for all RTP diagnostics are stored in one single file. Since the space in the file is limited, it is impossible to store 40 Mbyte of information for x-ray tomography alone during each shot. Hence, data reduction will be necessary after each plasma shot. Therefore, a data reduction code will run in the local CPU available on each module in the near future. In this code, reduction of the sampling frequency will be performed for time slices where no or small activity is observed in x-ray signals. Eventually the tomography reconstruction procedure could also be performed in these CPU's.

Tomography Reconstruction

Each of the 80 channels measures the brightness $f(p,\phi)$, that is the integral of the local emissivity $g(r,\theta)$ of the plasma along its line of sight $L(p,\phi)$:

$$f(p,\phi) = \int_{L(p,\phi)} g(r,\theta) \qquad (1)$$

In order to reconstruct the local emissivity profile from the measured signal, a tomography reconstruction code will be employed. For our data we intend to use mainly the analytical method developed by Cormack in 1963 [6-7], and nowadays being extensively used in various tokamaks [8]. The method performs an expansion of both the emissivity and the brightness in a Fourier series. The simplicity and efficiency of this inversion method lies in the further expansion of the Fourier components of the emissivity in a series of orthogonal functions known as Zernicke polynomials. This last expansion leads to a simple solution, which can be efficiently implemented in a computer code. The main disadvantage of this method is the occurrence of artifacts in the reconstructed image near the boundary of the reconstruction region. This effect is due to the property that the Zernicke polynomials remain finite at the boundary. Since the expansion in a series of these polynomials has to be truncated at some maximum value, the resulting sum does not present a good behaviour near the edge.

In our case we expect to be able to resolve modes up to m=4 (sin mθ and cos mθ), and perhaps one components of m=5 mode. In the expansion of the Fourier components in terms of Zernicke polynomials, the maximum order of the polynomials will be limited to l=7-8.

Preliminary Results

Recently the first camera, located at 10°, has come into operation. First measurements with this camera have been performed on ECR heated plasmas with $n_e = (2\text{-}3)\times10^{19}$ m^{-3}, $I_p = 120$ kA, $B_T = 2.14$ T, and q_a=3.4. During this kind of discharges a very efficient heating of the electrons is observed [9]. Preliminary results for this kind of discharges show that with central ECR deposition sawtooth oscillations (Fig. 2) develop. In the first milliseconds after the onset of the ECR pulse (power = 200 kW) the q=1 surface seems to expand. This can be explained by the fact that the T_e-profile during ECRH is much more peaked than during the preceeding ohmic phase. The resulting j-redistribution leads to a $q_0<1$ whilst in the ohmic phase $q_0>1$.

Acknoledgement

This work was performed under the Euratom-FOM-association-agreement with financial support from NWO and Euratom.

References

[1] R. Décoste and P. Noël, Proc. SPIE Int. Soc. Opt. Eng. **661**, 50 (1986).
[2] C. Janicki, C. Déscoste, and C. Simm, Phys. Rev. Lett. **62**, (1989) 3038.
[3] D.F. da Cruz and A.J.H. Donné, Rev. Sci. Instrum. **61**, (1990) 3067.
[4] Hamamatsu Photonics Deutschland GmbH, Type No. S2313-16EL, Technical Data Sheet No. S-501.
[5] J. F. Camacho and R. S. Granetz, Rev. Sci. Instrum. **57**, 417 (1986).
[6] A. M. Cormack, J. Appl. Phys. **9**, 2722 (1963).
[7] A. M. Cormack, J. Appl. Phys. **10**, 2908 (1964).
[8] R. S. Granetz and P. Smeulders, Nucl. Fusion **28**, 457 (1988).
[9] F.C. Schüller, et al., This conference.

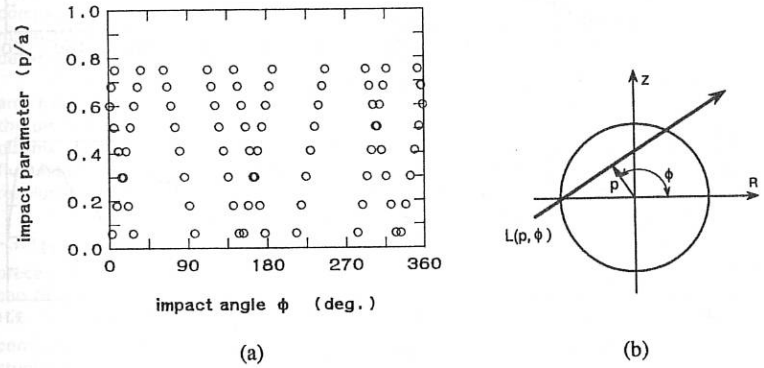

(a) (b)

Fig. 1- (a) The distribution of the observation chords in the (p,ϕ)-plane and (b) definition of the impact parameter, p, and impact angle, ϕ.

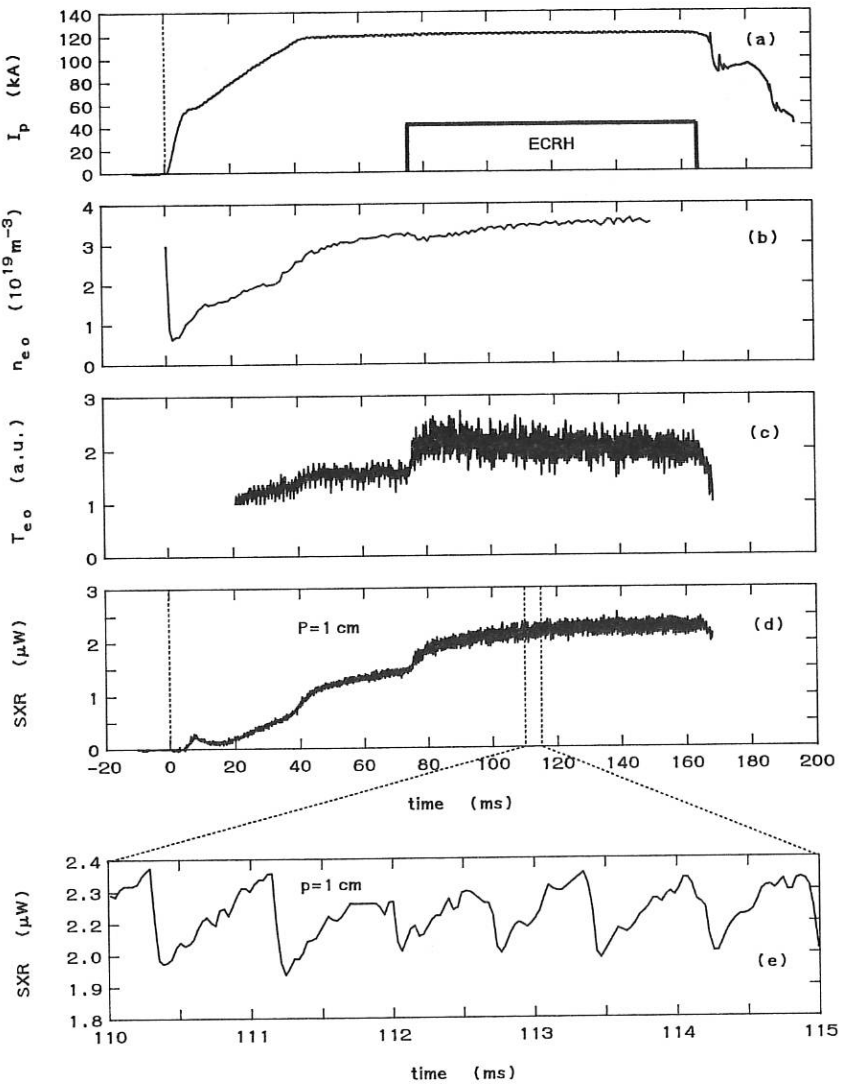

Fig. 2- Evolution of the plasma current (a), the central electron density measured with a FIR interferometer (b), the central temperature measured with heterodyne ECE (c) and the signal from the central chord from the soft x-ray tomography system (d). Sawtooth activity is observed during the ECRH pulse (e) (the sampling frequency was 50 μs).

STUDY OF q-PROFILE IN LHCD REGIMES WITH MICROWAVE REFLECTOMETRY

A. Silva+, M.E. Manso+, F.X. Söldner, H. Zohm, and F. Serra+

Max-Planck-Institut für Plasmaphysik, EURATOM Association , D-8046 Garching, FRG

+Instituto Superior Técnico, EURATOM Association , 1096 Lisboa Codex, Portugal

I - Introduction

The MHD activity of a tokamak discharge depends on the current profile. The confinement behaviour can be improved with optimized current density profiles; it is therefore very important to determine j(r). MHD modes can be destabilized at the rational surfaces, inducing density perturbations. We have studied those perturbations with broadband reflectometry, in LHCD discharges where significant modifications of the current distribution can occur /1/. The plasma profile is continuously probed, and it is possible to obtain the radial distribution of the MHD perturbations; so the q-profile and its temporal evolution could be estimated from single shot measurements. Results confirm that LH can strongly modify the plasma current density distribution.

II - Localization of MHD modes

Density perturbations affect the refractive index of the probing waves and the location of the plasma reflecting layers. Phase and amplitude modulations are produced as a result of large scale fluctuations, as it is the case for MHD modes. The effects are due mainly to perturbations located in the plasma reflecting region, and not in the propagation region, /2/, thereby allowing well resolved spatial measurements.

Fig.1 shows the results obtained in an LH discharge where a $m=2$ mode locked and led to a disruption. A density layer with constant density (fixed frequency reflectometry) was probed. The distribution of the frequency power spectrum before and at the disruption (t ~ 1.94 s) is shown in Fig.1(a). The slowing down of the mode is clearly resolved. The comparison between $m=2$ mode frequency obtained by reflectometry and the corresponding magnetic data given by Mirnov coils (Fig.1(b)), reveals that reflectometry can indeed detect density perturbations due to magnetic MHD modes.

In fixed frequency measurements only a limited number of plasma layers can be probed, and their locations must be obtained from independent data. With broadband measurements the plasma is continuously probed. By obtaining the average phase shift corresponding to the plasma profile and the component due to the fluctuations the radial distribution of the fluctuations can be determined from the same broadband raw data /3/. Typical spatial resolution of the measurements is 1 - 2.5 cm and the sensitivity is 1 - 2 mm.

In order to test this diagnostic technique two plasmas with different safety factors (q_a ~3.3 and 4.8) were studied, as shown in Fig.2. In both cases locked ($m=2,n=1$) modes precede the disruption. From the evaluated phase shift characteristics, $\Delta\Phi/\Delta F(r)$, phase jumps can be observed due to the flattening of the plasma profile (caused by the locked modes at $q=2$). Several perturbations are also seen at the expected location of other rational surfaces; the continuous increase of the phase shift due to the average profile is also observed. Numerical studies where a parabolic plasma profile was periodically disturbed, give further support to the interpretation of the experimental results. The electron density profiles obtained from the averaged phase shift data of Fig.2(a) are depicted in Fig.3; the flattening of the profile close to the expected locations of $q=2$ surfaces can be clearly seen. The locations of density perturbations for the two plasmas are presented in Fig.2(b); the q profiles for ohmic plasmas as

derived from the $T_e(r)$ profile, assuming neoclassical conductivity, are also shown for comparison.

Reflectometric measurements agree rather well with the expected q profiles for the two different plasmas. Differences from the expected ohmic values can be due not only to the LH waves, but also to the fact that the reflectometric data correspond to the outer radial positions where the density perturbations are first detected, leading to somewhat higher values for the position of the rational surfaces.

III - Changes in the q-profile during LHCD

LHCD discharges with different compound launched spectra were studied, where significant changes of the current density profile j(r) are expected to occur /1/. Fig. 4 refers to #29273, with $\Delta\varphi = 90° / 90° + 180°$ and $P_{LH} = 0.75MW / 0.75 + 0.3MW$. Fig. 4(a) shows a slow decrease in $(\beta_{equ} - \beta_p - l_i)/2$, for the second LH plateau, attributed to a decrease of the internal inductance l_i and therefore a broadening of j(r). The overshoot in the decrease of the U_{Loop} is an independent confirmation of this because it is caused by a decrease of the poloidal magnetic field energy due to the drop in l_i.

The local modification of j(r) can be inferred from the temporal evolution of the radial location of MHD modes as described above. The results obtained from several reflectometric samples during the plasma discharge, (for $20 \leq r \leq 40$cm) are presented in Fig. 4 (b). From the OH phase to the steady state phase of the first LH plateau (with $\Delta\varphi = 90°$), an outward radial shift of the radial position of the observed modes is found. For $t > 1.4$ s (second LH plateau, $\Delta\varphi = 90° + 180°$), a clear outward shift of the innermost detected surface (at $q \sim 3/2$) is seen; surfaces with higher q remain roughly at their position during this stage. The observed shifts are in agreement with Li beam measurements wich give the local j(r) profile /4/. For the case discussed here they predict a flattening of the current profile in the central region, and a steepening of the gradient of j in the region further out. The range of variation of the radial position of each mode from reflectometry measurements is depicted in Fig.5, where also the radial q-profile for the ohmic phase, as derived from $T_e(r)$ is plotted for comparison.

For another set of discharges with the same plasma parameters but different LH spectra ($\Delta\varphi = 90° + 150°$, $P_{LH} = 0.35 + 0.25MW$), the modification of j(r) was studied with reflectometry. Rational surfaces $q = 3$, 5/2 and 2 were identified both in OH and LH phases; an inward radial shift was measured in the $q = 2$ surface, corresponding to a flattening of the j(r) profile near $q = 2$. The results also agree qualitatively with local current density profiles obtained from Li-beam measurements.

IV - Concluding remarks

The study of the q-profiles in LHCD discharges with different wave spectra has been performed with broadband microwave reflectometry. Several MHD modes could be localized, namely modes located in the interior plasma, that cannot be easily detected from the external Mirnov coils. The radial shift of their locations indicates significant changes of j(r) during LHCD according to previous Li-beam measurements. From the experimental data, suppression and excitation of MHD modes due to LH could also be observed. The study shows the potential of this new reflectometric technique:(i) the temporal evolution of the q-profile can be estimated from single shot measurements, (ii) the correlation between local changes of the q and the n_e profiles, and the suppression or excitation of MHD modes can be investigated.

One of the limitations of this technique concerns the difficulties in identifying the resonant surfaces corresponding to the observed density perturbations, as the mode numbers cannnot be directly determined from reflectometry. The profile q(r) has to be estimated from another diagnostic at a reference time,and also a large number of reflectometric samples must be taken in order to follow the detailed temporal evolution of q(r).

References

/1/ F.X. Söldner et al., 13th Int. Conf. on Plasma Physics and Controlled Nuclear Fusion Research, Washington, IAEA-CN-53/E-1-1 (1990)

/2/ F. Simonet, PhD Thesis, Univ. Nancy (1985)

/3/ M.E. Manso et al., IPP Report, to be published

/4/ K. McCormick, Phys. Rev. Lett., 58, 491 (1987)

Figure Captions

Fig. 1: (a) Contour plot of the frequency power spectrum of density fluctuations for a probed density layer with $n_e = 0.7*10^{13} cm^{-3}$ during the time interval 1.75 to 2.0 s (#31070); (b) reflectometric raw signal for the time window (1.84 - 1.85) s prior to locking, showing the decrease in the rotation frequency of m=2 island, from ~1 kHz to ~0.5 kHz (1), and the signal from Mirnov coils (2).

Fig. 2: (a) Radial variation of the microwave phase shift $\Delta\Phi/\Delta F$ corresponding to 2 ms sweeps at t=1.75 s [#32206, q_a~3.3] and at t=1.88 s [#32207, q_a~4.8]. In both discharges $\bar{n}_e$~$1.3*10^{13}$ and LH [1.2;2.2] s; (b) q-profiles derived from $T_e(r)$ for the ohmic phases of shots in (a). The localization of the MHD modes obtained from the perturbations in the phase shift (a) is indicated.

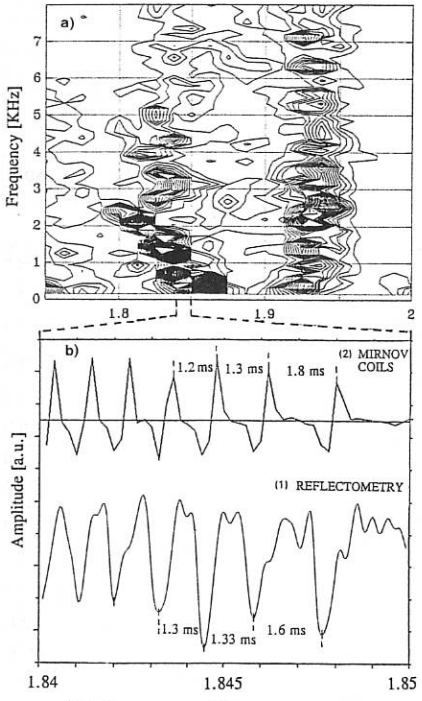

Fig. 1

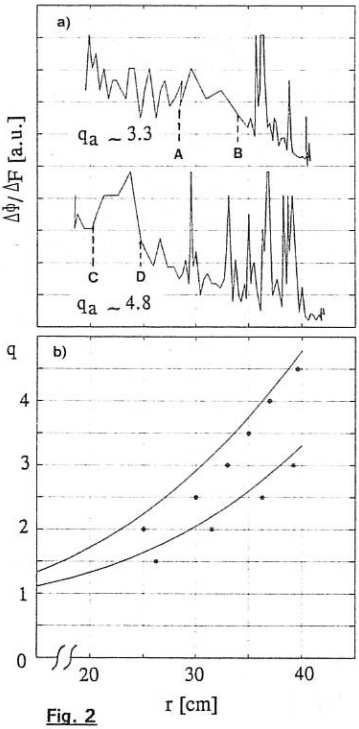

Fig. 2

Fig. 3: Density profiles obtained from the integration of the microwave phase shift information shown in Fig. 2(a).

Fig. 4: (a) The loop voltage and $(\beta_{equ}-\beta_p-l_i)/2$ are represented for the time interval (0.8 - 1.8 s), for #29273; (b) Temporal evolution of the location of the density perturbations on rational q-surfaces during OH and LHCD (LH [1.0; 1.8] s),

Fig. 5: Radial variation of the locations of density perturbations on q-surfaces during LHCD and the q-profile for the ohmic phase derived from the $T_e(r)$ profile.

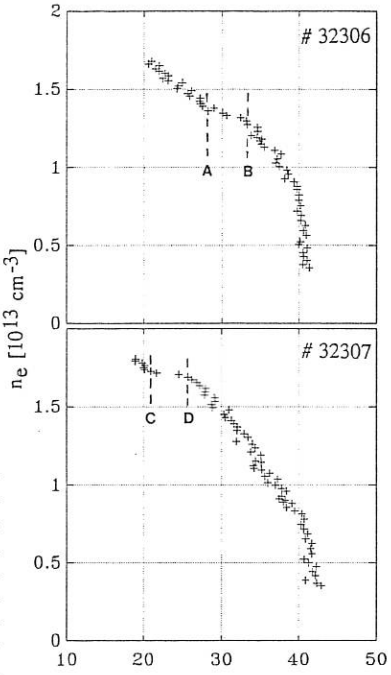

Fig. 3

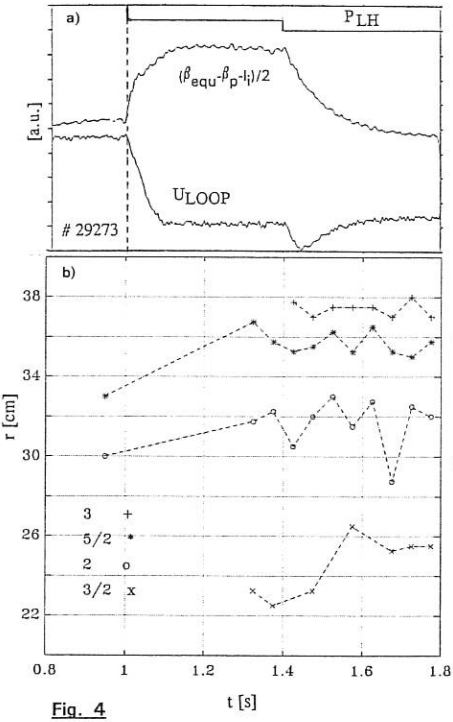

Fig. 4

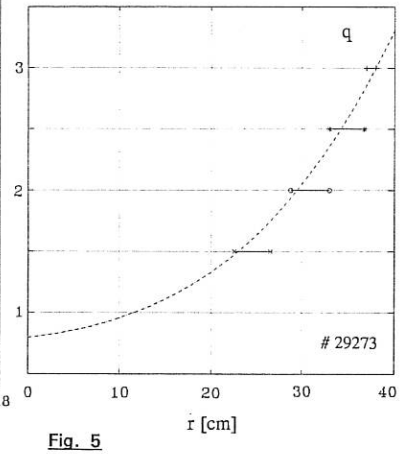

Fig. 5

DENSITY FLUCTUATION PROFILES ON TORE SUPRA

C. LAVIRON, X. GARBET, S.K. SAHA, P. DEVYNCK
Association EURATOM-CEA, CEN Cadarache (France)

and

A. TRUC, A. QUEMENEUR, P. HENNEQUIN, D. GRESILLON, F. GERVAIS
PMI - Ecole Polytechnique - Palaiseau (France)

1.INTRODUCTION

The ALTAIR experiment on TORE SUPRA for the analysis of plasma turbulence by CO_2 laser scattering includes some original features [1-2] : 2π rotation of analysed $\vec{k}$ wave vectors, heterodyne detection, and accessibility of 2 simultaneous and independent wave numbers.

Because of the very small scattering angle (~1mrad), such scattering experiments are usually considered as having no resolution along the beam. If we take into account the pitch angle $B_p(r)/B_t$ of the magnetic field lines ($\pm$ 7° around the magnetic axis along a vertical chord for q_a = 3.3) together with the fact that the fluctuation wave vectors are mainly perpendicular to these field lines, one can improve the spatial resolution along the chord of measurement.

We hereby present results, for measurements with k ranging from 3 to 15 cm^{-1}, showing this resolution. Using a suitable deconvolution method, density fluctuation profiles have been determined.

2.MEASUREMENTS

The CO_2 laser beam passes through the tokamak plasma along a vertical chord close to the plasma center. The analysed $\vec{k}$ vector is then horizontal and makes an angle α with the poloidal plane. Fluctuation measurements have been recorded with a rotation of the analysed $\vec{k}$ vector during stationary plasmas in ohmic regime (B_t=3T, I_p=1.2MA, R=2.39m, a=0.75m, q_{cyl}=3.3). The speed of rotation was 2°/s, covering a range of 12 to 15° during stationary conditions. Successive angles of $\vec{k}$ corresponded then to different positions of the analysed volume.

After proper filtering and amplification, the signal issued from the detector was then analysed by a spectrum analyser. A complete spectrum was recorded every 200ms, corresponding to a $\vec{k}$ rotation step of 0.4°. An example of two spectra for k= 12cm^{-1} is represented on fig.1 for α = -6° and +5°, corresponding respectively to the bottom and the top part of the plasma. The

frequency shift (respectevely negative and positive by ~300kHz) indicates a turbulence propagating in the ionic diamagnetic direction at 1.5 km/s in the laboratory frame. Integrating these spectra, a total fluctuation level was calculated, for a k value, as a function of α.

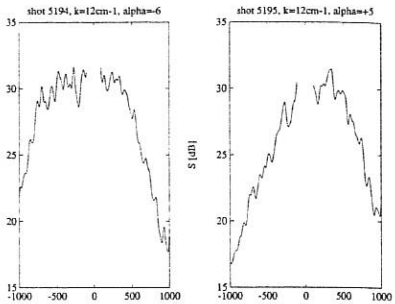

Fig.1 - Turbulence spectra S(f)

3.DECONVOLUTION METHOD

If the turbulence wave vector is assumed to be essentially perpendicular to the equilibrium magnetic field, the measured signal amplitude is proportional to the density fluctuation integrated along a vertical chord, i.e.,

$$I_{k,\omega}(\alpha) = \int_{-\infty}^{+\infty} dy\ \delta n_{k,\omega}(y)\ \exp -\left(\frac{\alpha-\xi(y)}{\delta\alpha_k}\right)^2$$

where k,ω are the turbulence wave number and frequency, α is the angle between a poloidal plane and the analysed wave vector k, $\xi(y)=B_p(y)/B_t$ is the pitch angle, y indicates the vertical direction abscissa ($y=\pm1$ corresponds to the last closed magnetic surface) and $\delta\alpha_k$ is the apparatus resolution ($\delta\alpha_k=\sqrt{2}\Delta k/k$, $\Delta k=2/w$ where w is the beam waist). The observed fluctuation $\delta n_{k,\omega}$ is related to the actual density fluctuation spectrum through a relation involving Δk.

The analysis has been achieved by studying $I_{k,\omega}(\alpha)$, the frequency integral of $\delta n_{k,\omega}$ for several values of k (the index ω will be dropped henceforth). The radial profile of δn_k is determined by investigating the best coefficients b, c and p so that $\delta n_k(y) = (b + c|y|^p)\ n(y)$, n(y) being the density profile. For such a δn_k profile, the signal $I_k(\alpha)$ is of the form $bI_0(\alpha) + cI_1(\alpha)$, where I_0 and I_1 correspond respectively to constant and $|y|^p$ profiles. The coefficients b and c are solution of a system of two linear equations. The inversion of this system gives the coefficients b and c for each value of p. The couple (b,c) which is finally kept is the one for which the fit $bI_0 + cI_1$ is the closest to the experimental profile I_k.

4.RESULTS

The measured fluctuation amplitude $I(\alpha)$, for $k=12cm^{-1}$, as a function

of α by superposition of results from 4 shots under identical plasma parameters, is compared on fig.2 with the calculated fluctuations after deconvolution. The corresponding absolute and relative fluctuations (δn and $\delta n/n$) are shown on fig.3. The $\delta n/n$ profile is very sharp: the result of the calculation for $\delta n/n = b + c|y|^p$ gives $b/c \cong 0.05$ and $p = 6$. For these parameters, the calculated and measured curves (fig.2) are in a good agreement.

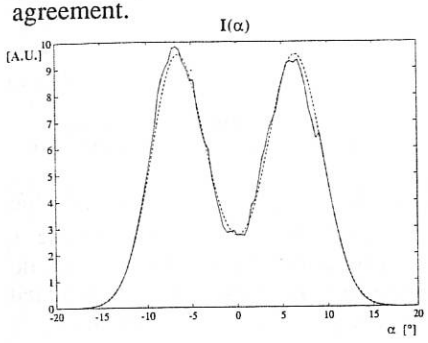

Fig.2 - Measured (—) and calculated (- -) fluctuation amplitude for k = 15cm-1

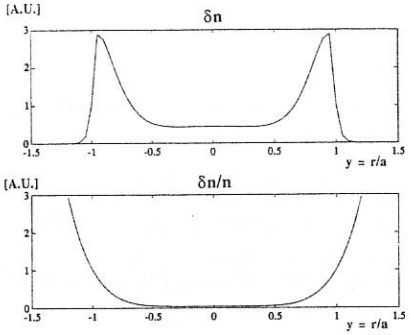

Fig.3 - δn and $\delta n/n$ profiles corresponding to the case of fig.2

The shape of the pitch angle curve with normalised minor radius for a typical shot is given on fig.4. Since this curve exhibit a maximum ξ_{max}, the wings of the signal $I_k(\alpha)$ should behave as

$$I_{max} \exp-\left(\frac{\alpha-\xi_{max}}{\delta\alpha_k}\right)^2$$

This property is verified from fig.2 and provides a check of the k and Δk value through an evaluation of $\delta\alpha_k$. Then, all the information on the δn_k profile is contained in the central hollow of the $I_k(\alpha)$ curve, which determines the accuracy of the method. The convergence is reached for sufficiently small values of $\delta\alpha_k$, i.e., for large values of k, typically $k \geq 9cm^{-1}$.

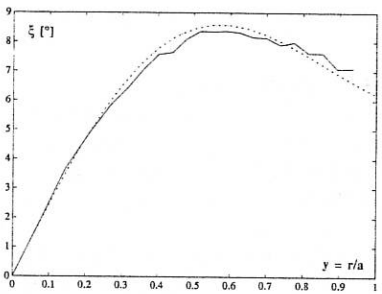

Fig.4 - Pitch angle profile $\xi(y)$, determined from magnetic probes

On fig.5, the results of the measurements with rotation of $\vec{k}$ are presented for k = 6, 9 12 and 15 cm^{-1}. When k increases, the central hollow is more pronounced, corresponding to a better spatial resolution. For all the

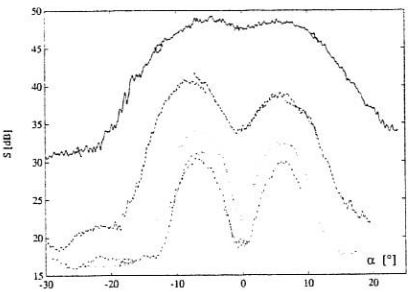

Fig.5 - Measured fluctuation for k = 6, 9, 12, 15cm^{-1}

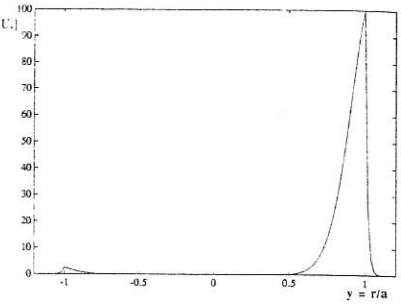

Fig.6 - Distribution of the measured density fluctuations as a function of y with $\delta n/n = y^6$

curves, the deconvolution gives a $\delta n/n$ profile, with p = 5 to 7. The ratio b/c decreases when k decreases, with $b/c \cong 0$ for $k < 9cm^{-1}$. So, the $\delta n/n$ profile is very sharp, meaning that the edge turbulence dominates the whole measurement. The quality of the fit between the observed and the calculated $I(\alpha)$ proves also that the turbulence is mainly perpendicular to the magnetic field lines.

Even at $6cm^{-1}$, some resolution exists, as shown by the central hollow in the $I(\alpha)$ curve. Simulations were made with all the parameters of these ohmic shots and for a turbulence profile taken as $\delta n/n = by^6$: as an example, fig.6 represents a distribution of the density fluctuations δn measured by the detector as a function of y, for $k = 6cm^{-1}$ and $\alpha = 6°$. We can see that all the measured turbulence originated from the upper part of the plasma, with $y > 0.5$.

5. CONCLUSION

It has been experimentally shown that the ALTAIR experiment gives a resolution along the measurement chord. This resolution is better for higher k and lower q_a. From it, we can then get fluctuation profiles showing a turbulence existing mostly near the periphery. This corresponds to a very weak turbulence inside the q=1 surface. It is therefore compatible with density profiles flatter in Tore Supra than on smaller machines where the b/c ratio is larger [3]. It also confirms the fact that the turbulence is locally perpendicular to the magnetic field lines.

References

1 - X. Garbet, C. Laviron, J. Olivain, F. Gervais, D. Grésillon, P. Hennequin, A. Quéméneur and A. Truc, Proceedings of the Cadarache Workshop on Electrostatic Turbulence, EUR-CEA-FC-1381 (1989), p. 121

2 - C. Laviron, X. Garbet, J. Olivain, A. Truc, A. Quéméneur, P. Hennequin, D. Grésillon and F. Gervais, Proceedings of 17th EPS Controlled Fusion and Plasma Heating, Amsterdam, Vol 14B, part IV (1990), p. 1588

3 - P. C. Liewer, Nuclear Fusion, Vol 25, N°5 (1985), p. 543

ELECTRON TEMPERATURE FLUCTUATIONS IN RTP

M. Verreck, M.J. van de Pol, A.J.H. Donné, C.A.J. Hugenholtz, A. Pauw and RTP-team.

FOM-Instituut voor Plasmafysica Rijnhuizen, Associatie EURATOM-FOM, Postbus 1207, 3430 BE Nieuwegein, The Netherlands.

Introduction

A 20-channel double-conversion superheterodyne mm-wave receiver has been installed at the RTP-tokamak experiment. Apart from the routine measurement of electron temperature profiles, this diagnostic wil be used for the study of fast electron temperature phenomena in ECRH heated plasmas. In this paper we describe the experimental set up and give first results obtained in ohmic and ECR heated tokamak discharges in RTP.

Experimental Set up

Second harmonic X-mode emission is measured by means of two antennas operating in the frequency bands 86-110 GHz and 110-146 GHz, respectively. The antennas are mounted inside the vacuum vessel to minimize the distance to the plasma. The viewing spot (i.e. the cross-section of the main antenna lobe and the resonance layer) is about 5 cm^2 in the plasma centre. A slight improvement of this spot size might be obtained with optical imaging techniques (lenses), but this is not envisaged for the experiment described below.

The waveguides from the tokamak to the ECE receiver system are mainly oversized straight sections, except for some parts that incorporate the DC/vacuum breaks, directional couplers, switches and bends. In this way a measurement of pure TE01-mode is maintained, corresponding with X-mode emission in the absence of non-toroidal magnetic field components.

The actual receiver consists of two frequency conversion stages and a demodulation part [2]. The first stage consists of 5 down-converters (broadband mixers + local Gunn oscillators), selecting 12 GHz wide parts from the incoming signal, which are then converted to a uniform IF band of 6-18 GHz. The second conversion stage consists of 4 mixers for each down-converter, with LO values: 7.5, 10.5, 13.5 and 16.5 GHz, selecting four 3 GHz wide parts from the 6 - 18 GHz band and converting them down to 1 - 1500 MHz by means of a double sideband mixing process. Note the effective reduction of the bandwidth by a factor 2

caused by the DSB-nature of the second mixing stage. A stepwise tunable low-pass filter is incorporated in the second IF stage. With this filter the full bandwidth of each channel can be varied from 400 - 2000 MHz, which corresponds with a variable spatial integration length along the line of sight of 1 - 18 mm, depending on the channel bandwidth and the radial position of the resonance layer. Eventually, the second IF band is demodulated for each of the 20 channels by square law detectors. The resulting signal is amplified, filtered and digitized with a maximum video bandwidth of 1 MHz.

T_e-resolution

The effective noise temperature of the system is low (few tenths of an eV). So the limit for T_e resolution is given by the effect of photon noise. In a square law detection system in absence of thermal noise, the signal to noise ratio is mainly determined by the product of bandwidth and sampling integration time [3]. Based on this assumption and on the fact that bandwidth is related to spatial resolution in ECE systems, one can deduce a minimal resolution product :

$$\left(\frac{\Delta T_e}{T_e}\right)^2 \left(\frac{\Delta R}{R}\right)(f\Delta t) > \frac{1}{2}$$

In this equation, ΔT_e, ΔR and Δt are the resolutions in the electron temperature, in the line of sight (integration length) and in the time, respectively. 'f' is the measuring frequency. Using a video bandwidth of 300 kHz and a radial resolution of 1 cm which are minimal values for measuring broadband fluctuations, we obtain a $\Delta T_e/T_e$ of about 10 %. To resolve broadband fluctuations, this value must be smaller than 1%. Regarding the additional deterioration of the spatial resolution caused by optical thickness effects and finite antenna pattern divergence, one can conclude that it is impossible to measure broadband fluctuations with standard ECE techniques.

For all T_e-fluctuations in the lower frequency range, such as sawteeth, MHD-modes, disruptions, additionally applied heat pulses by ECRH, this instrument is very well suited.

Experimental results

Although the double-superheterodyne ECE receiver is serving as a bulk temperature profile diagnostic since Februari 1991, we are still working on various calibration schemes. At present only a calibration against the single point Thomson scattering diagnostic is performed.

In ohmically heated plasmas, highly resolved measurements of sawtooth instabilities are used for local transport models, along with sawtooth measurements with a multi-channel interferometer and a set of chord averaged SXR emission measurements.

The main interest in the near future will go to measurements in ECRH heated plasmas. The results until now show on a number of occasions large temperature variations around the ECRH resonance layer during additional heating, whereas the off-centre temperature profile remains smooth. These phenomena are accompanied by a large shot-to-shot variation of the on-axis temperature measurement by Thomson scattering, while these measurements outside the the centre show good reproducibility. In Fig. 1 the time evolution of the electron temperatures at the resonance layer and 2 cm outward is shown. During ECRH shots without plasma, there is no coupling of the gyratron power (1st harmonic; 60 GHz) to the measurement system. The second harmonic content of the gyratron radiation causes a faint response only on the channel which measures at 120 GHz. This means that the measurements shown in fig. 1 are not disturbed by direct ECRH power detection.

Acknowledgements

This work was performed as part of the research programme of the association agreement of Euratom and the 'Stichting voor Fundamenteel Onderzoek der Materie' (FOM) with financial support from the 'Nederlandse Organisatie voor Wetenschappelijk onderzoek' (NWO) and Euratom.

References

[1] Liewer P.C., Nuclear Fusion 25, 543 (1985).

[2] Verreck M, Hugenholtz C.A.J., Proc. 7th Joint Workshop on ECE and ECRH (EC-7), Hefei, P.R. China (1989). p 322 - 327.

[3] Ziel, van der A., Noise: Sources, Characterization, Measurement, Prentice-Hall, N.J. (1970).

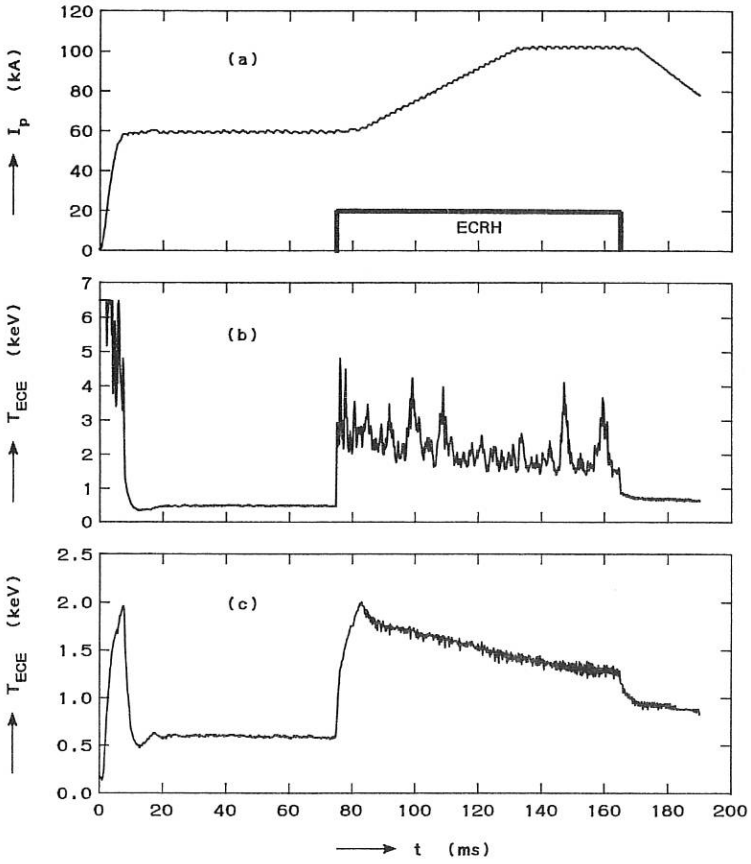

Fig 1. Time evolution of the plasma current (a). Strong variations are measured on the electron temperature during ECRH on the magnetic axis near the resonance layer (b). At 2 cm outward (c) the fluctuation level is much lower .

TORE-SUPRA X-RAY PULSE-HEIGHT ANALYZER DIAGNOSTIC

Y.PEYSSON, J.P. BIZARRO, G. T. HOANG, A. HUBBARD*, X. LITAUDON
D. MOREAU, C.POITOU–POCHEAU, J. M. RAX

DRFC/SPPF, Association EURATOM-CEA sur la Fusion Contrôlée
Centre d'Etudes Nucléaires de Cadarache B.P. n°1
13108 Saint-Paul-lez-Durance, France.
* Centre Canadien de Fusion Magnétique, Varennes, Québec, Canada J0L2P0

1. INTRODUCTION

A multichannel X-ray spectrometer has been installed on TORE-SUPRA in order to study photon emission between 30 and 700 keV, during lower hybrid experiments. This diagnostic is designed to observe the build-up of the momentum distribution of the fast electrons due to Landau damping on the RF waves [1], with both space and time resolution. In this paper, we describe the experimental set-up and present first results. For high density plasmas, well-defined spectra are observed up to 300-350 keV. The line-integrated emission profiles are peaked at low energy, and become hollow above 150 keV. This result is consistent with the accessibility of the RF waves inside the discharge. Low density plasmas exhibit a strongly peaked X-ray emission profile at all energies and, for the central chords, spectra extend up to 500 keV. In this case, it is shown that X rays scattered by the tokamak chamber become dominant below 200 keV, for the lines of sight at the edge of the plasma.

2. EXPERIMENTAL SET-UP

The high energy X-ray spectrometer probes the plasma along five chords in the same poloidal section as shown in Fig. 1. The lines of sight are labelled A, B, C, D, E, and their positions are respectively $r_p/a_p \approx +0.2, 0.0, -0.33, -0.52$ and -0.71 in a standard plasma centered inside the tokamak chamber ($a_p \approx 75$ cm). The two more peripheral lines of sight, D and E, cross the inner wall of the tokamak covered by 1 cm thick graphite tiles, whereas the three others face the upper port.

The versatile lead collimating system permits different apertures to be selected, to adjust the spatial resolution (2 - 15 cm). To prevent contamination of the signals by non-collimated X rays, all detectors are placed inside a lead box which has 10 cm thick sides. A special neutron shielding with light elements has been designed for the diagnostic, and will be installed in the near future.

Detection of the plasma bremsstrahlung emission at high energy in a flux of 2.5 MeV neutrons is a difficult task, even if detectors are protected by an efficient shielding. In order to reduce the noise induced by neutrons coming through the collimating apertures to an acceptable level during deuterium discharges, bismuth germanate ($Bi_4Ge_3O_{12}$ or BGO) scintillators have been chosen. Their high stopping efficiency compared to classical NaI(Tl) scintillators allows us to use less material (a factor 1/3) for similar performance. Thus, interactions with neutrons and secondary high energy γ rays produced in the vicinity of the detectors are expected to be reduced significantly, without a large degradation of the photofraction between 30 keV and 700 keV (see

Fig.2). With 23 mm thick BGO crystals, only 10-15% of the plasma emission is lost between 30keV and 400keV (Fig.2). Attenuation along the lines of sight is kept to a small level above 30 keV, by the use of a 1 mm thick aluminium vacuum window.

Luminescence properties of BGO under X-ray excitation are characterized by its extremely small afterglow (0.005 % after 3 ms), which enables a high counting rate (> 100 kHz) for time resolution. BGO has a disadvantage in that its scintillation conversion efficiency is only 10-15% of NaI(Tl). The fact that the BGO energy resolution is 50% lower than NaI(Tl), does not represent a serious handicap, as bremsstrahlung spectra are always very broad, (Fig.2).

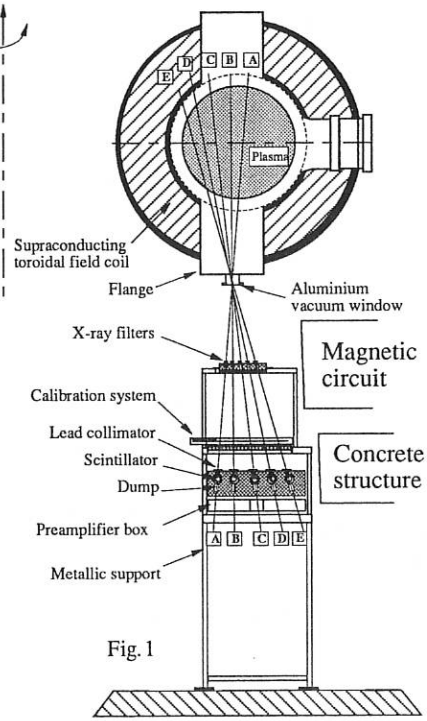

Fig. 1

3. RESULTS AND DISCUSSION

It is well known that LH current drive efficiency is a function of both the characteristics of the discharge (electron temperature and density) and the spectrum of the RF waves launched into the plasma. Optimization of the efficiency has been investigated at various densities : $n_e(0) \approx 1.5\text{-}5.0\ 10^{+19}\ m^{-3}$, for the TORE-SUPRA LH system by changing the phases between the waveguides of the launcher [2].

For the high density experiments, the duration of data acquisition is 1.0 s and helium plasma parameters are : $B_T \approx 3.9$ T, $I_p \approx 1.6$ MA, $T_e \approx 1.3$ keV and $Z_{eff} \approx 3.2$. The density profile is very flat (peaking factor 0.5). With $P_{HF} \approx 2.4$ MW, X-ray spectra extend up to 300-350 keV, and the slope of the power emitted per unit of energy dW/dk = k.dN/dk.dt decreases slightly from the center to the edge of the discharge (Fig. 3). The line integrated emission profile is hollow above 150 keV(Fig.4). It tends to fill in at lower photon energies, becoming peaked at 50 keV. No strong dependence of the profiles on the phase between the waveguides is noted. However, the emitted power ex-

Fig. 2

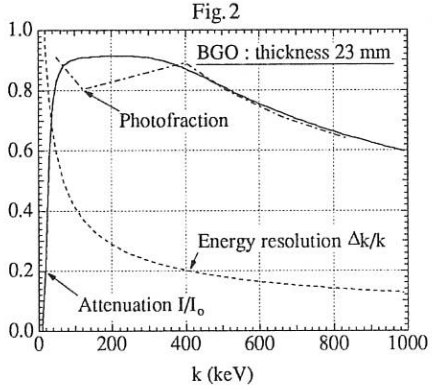

hibits a broad maximum centered for each line of sight at $\Delta\phi = 0°$, as observed for ECE emission and the current drive efficiency (Fig.5).

Fig.3

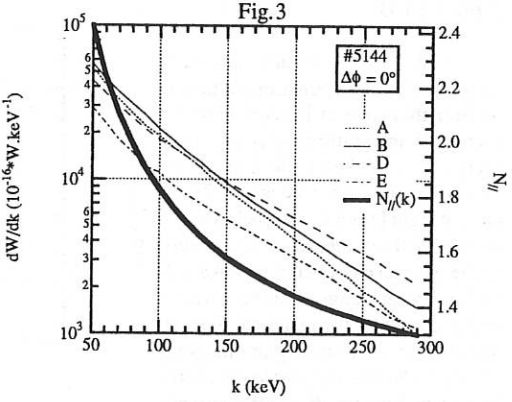

These results suggest that fast electrons (E > 150 keV) are mainly localized away from the center of the discharge. Resonant electrons of energy larger than 150 keV interact with RF waves having a refractive index $n_{//}$ lower than 1.6 (Fig.3), which are not accessible to the center of the discharge in these plasma conditions (Fig.4). Below 150 keV, waves of higher $n_{//}$ are concerned and, as they are accessible to the center of the discharge, the high energy X-ray emission becomes peaked.

The shape of the X-ray emission profile above 150 keV remains hollow over a long time (1.0 s) compared to the characteristic diffusion time of fast electrons, which is expected to be much shorter [3]. Therefore, this suggests that fast electrons are slowing down rapidly by multiple collisions as they are scattered towards the center of the discharge. This effect can also contribute to the peaking of the low energy part of the X-ray spectrum [4].

Variations of the X-ray emission with the phase between the wave-guides concern only the emitted power. The broad maximum at $\Delta\phi$=0° for k=50 keV, which has the same shape as the "$n_{//}$-weigthed antenna directivity" $\delta_{cd} = \langle 1/n_{//}^2 \rangle / (1/n^2_{//peak})$ [5], suggests that the high $n_{//}$ part of the RF spectrum in the plasma ($n_{//} \approx 2.4$) does not depend on the injected $n_{//peak}$ (Fig.5). Only the level of the RF power launched at $n_{//peak}$ is important in this case. On the other hand, the fact that dW/dk becomes clearly more sensitive to $\Delta\phi$ than δ_{cd} above 150 keV indicates that the amount of power at the lowest accessible $n_{//}$ in the plasma, corresponding to $n_{//} < 1.6$, is then slightly dependant on $n_{//peak}$. This is consistent with the small dissymetry observed between the positive and the negative side of $\Delta\phi$.

Fig.4

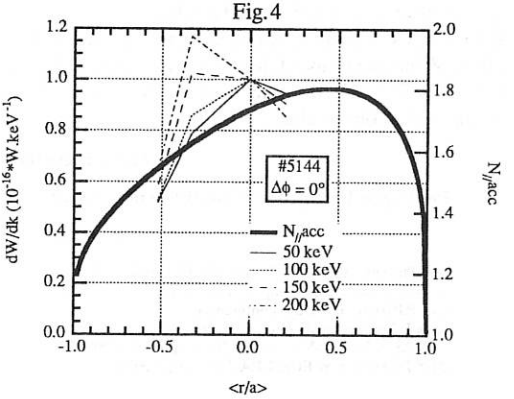

At low densities, X-ray emission extends up to 500 keV for central chords. In this case, the emission profile is strongly peaked at all photon energies. With $n_e(0) \approx 1.5\ 10^{+19}\ m^{-3}$ and $B_T = 3.9$ T, only the part of the wave spectrum corresponding to $n_{//} > 1.4$ is accessible to the center of the discharge. Thus, observation of radiation above 250 keV with lines of sight A,B and C suggests that the tail of the electron momentum distribution is modified by the remaining electric field

during LHCD.

The X-ray emission integrated above k ≈ 200 keV decreases continuously from the center to the edge of the discharge. If integration starts at lower energy (k ≈ 100 keV), the shape of the line-integrated profile becomes flat for lines of sight D and E. This behaviour is ascribed to the scattering of the radiation by the internal chamber of the tokamak. In this energy range, Compton scattering is dominant for materials like carbon or iron and, some photons going into the wall can emerge at lower energy back to the detector after a random walk.

Fig. 5

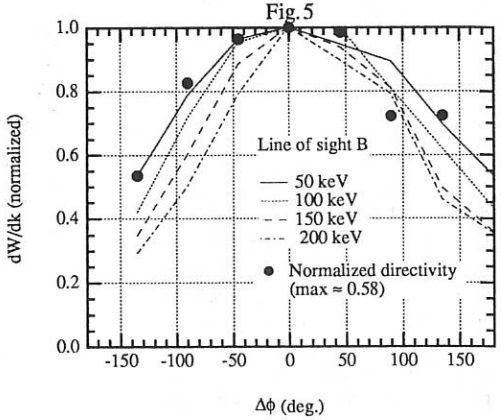

The radiation transport equation in steel covered by a 1 cm thick carbon layer has been solved by a Monte-Carlo method [6]. It is shown that the wall albedo increases from 0.15 for radiations with a normal incidence, to 0.40 when the incidence is nearly tangential. This result is quite independant of the photon energy from 50 to 500 keV, because of the high diffusion power of the carbon layer for photons energy below 150 keV.

Fig. 6

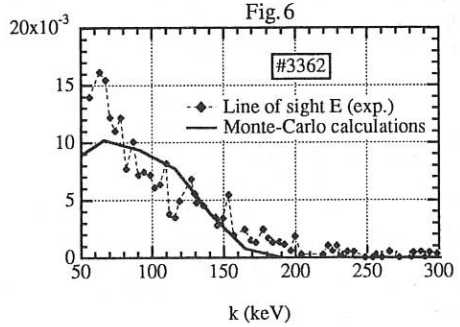

A simulation is presented, taking account of the toroidal geometry. We consider that the plasma X-ray spectrum is given by the central chords (which are free of scattered contribution as they are facing the upper port), and that the plasma contribution is nearly negligible for lines of sight D and E. It is then possible to reproduce fairly well the level of the line-integrated emission D and E near 100 keV, and the shape of the photon spectrum for the line of sight E (Fig.6). Moreover, we show that above 200 keV, the scattered contribution becomes negligible and, the direct plasma contribution is then observable.

Acknowledgements

The complete TORE-SUPRA Lower Hybrid group is greatly acknowledged for the RF operations.

References

[1] J.Stevens, et al., Nucl. Fusion, 25, 11 (1985) 1529
[2] G.Rey, et al., 15th Symp. on Fus. Techno. Utrecht, (1989) 514
[3] J.P.Bizarro, et al., this conferenece
[4] A.L.Pecquet, et al., this conference
[5] X.Litaudon, D.Moreau, Nucl. Fusion, 30, 3 (1990) 471
[6] Y.Peysson, Rep. EUR-CEA-FC-1410, (1990)

ACCELERATIION OF ELECTRONS DURING CURRENT INCREASE IN THE " TUMAN-3 " DEVICE.

V.I.Afanas'ev,E.R.Its,V.G.Kiptiliy,S.V.Krikunov,A.A.Korotkov,
A.N.Novochatskiy,K.A.Podushnikova,S.V.Petrov,
V.V.Rozhdestvenskiy,N.V.Sakharov,K.G.Shakhovets,
S.P.Yaroshevich

Ioffe Physico-Technical Institute,USSR,Leningrad.

Acceleration of electrons in the "Tuman-3" Ohmically heated helium plasma under B_t=5.2 kGs, J_p=45 kA, $\bar{N}=1.5\cdot10^{13}cm^{-3}$, $T_e(o)\simeq350$ eV Z_{ef}=3 has been studied.The density and temperature of elecrtons were determined from microwave multichord interferometery and Thomsom scattering measurements. J_p, U_p, ΔR and MHD-activity were measured by electromagnetic methods.

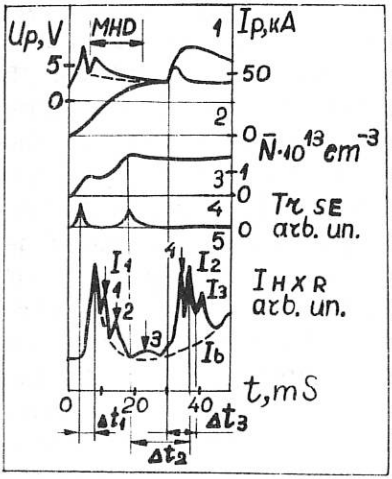

Fig.1 Oscillograms of the plasma current,(1),loop voltage,(2),mean electron density,(3),SE,(4),and HXR,(5) intensities.

Data on accelerated electrons were obtained from spectral measurements of the synchrotron emission,SE,in the frequency range including 4÷5 electron cyclotron harmonics and hard X-ray emission,HXR, with the quantum energy-(0.2÷4.0) MeV.Maximum, W_γ^m, and mean, W_γ, quantum energy values were obtained from HXR spectra.The full energy of electrons going out to the limiter and chamber walls was estimated according to the expression : $W_e=m_ec^2+W_\gamma^m$.The basic experimental data are presented in Fig.1÷3.

Fig.1 shows that under the J_p and U_p ramp up at the 2 ms,when $\bar{N}\approx4\cdot10^{12}cm^{-3}$, $T\sim10_e$ eV,the SE flash arises.With a some delay, Δt_1=3 ms,HXR appeares too.At the same time U_p goes down quickly from 5 V to 3 V.The HXR intensity becomes maximum relatively the SE flash wi-

th the delay, $\Delta t_1^m \simeq$ 6 ms. Then inspite of the $\bar{N}$ decrease and U_p growth because of the MHD-activity amplification under the J_p increase, l_{HXR} essentialy diminishes with the time constant $\tau_1 \approx 12$ ms. Peaks, 1÷3, on its slope are due to the MHD-mode, m=12÷6, exitation under appropriate resonanse sufaces going out in the prelimiter region. At the 15 ms, when $T_e(o) \simeq 300$ eV and $\bar{N} \leqslant 1 \cdot 10^{13} cm^{-3}$ one can see the second SE flash of lesser amplitude than the first one. Under the $\bar{N}$ increase SE disappeares. But the I_{HXR} increase with the peak, induced by the MHD-mode, m=5;4, exitation due to the second J_p ramp up begins after Δt_2 = 14 ms only, the drop with time constant τ_2 = 6 ms-after 21 ms. Under the second fast, for 4 ms, J_p ramp up from 48 kA to 78 kA at the 30 ms, when $T_e(o) \simeq 300$ eV, $\bar{N} \simeq 1.6 \cdot 10^{13} cm^{-3}$, SE is not arise, but during the second HXR flash drop the third one appeares. It's delay relatively the J_p ramp up beginning is of Δt_3=8 ms. The both flashes are summed with the background HXR which intensity, I_b, increases monotonically to the discharge end. The frequency spectra of SE arising at the 2 ms, (1), and the 15 ms, (2), are exibited in Fig 2. One can see that their shape is the same : the SE radiation temperature is small, but $T_r^1 \approx 2T_r^2$, and insignificantly goes down with the frequency growth. The such character of spectra is usual for SE of electrons having large energy in order of hundreds keV and witnesses about free acceleretion ofrunaways appearing during the discharge by the vortex electric field. In this case; $W_\parallel \gg W_\perp$, P_{SE} is small, EC harmonics can be overlapped. Fig. 3.1÷4 presents quantum energy spectra for three flashes and background HXR. Values of W_γ, W_γ^m and W_e are given here. It is seen that the energy of electrons born during various discharge stage may exceed $W_e \geqslant 1$ MeV. This is in accordance with energy esitmations for runaways appearing in the quasistationary stage near the plasma center, $r_c \simeq 0$, and goihg out to the limiter during the free acceleraton, [1]:

$(\gamma_\parallel^2 - 1)^{1/2} = \frac{2}{17} \cdot \frac{R}{a} \cdot J_p$; $W_\parallel = m_e c^2 \cdot (\gamma_\parallel - 1)$; $W_\parallel \simeq 6$ Mev. The life time of such

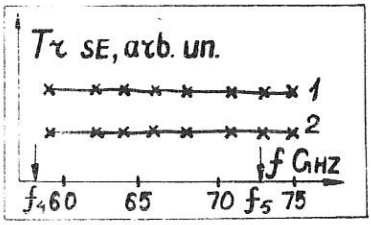

Fig. 2.

electrons: $\Delta t_m = 10^{-5} \cdot \frac{J_p}{U_p} \cdot \frac{R}{a}$; $\Delta t_m = 27$ ms; exceeds the experimentally observed one, $\Delta t_2 = 14$ ms. Therefore in our conditions runaways arise at the 15 ms in the plasma layer having $\frac{r_o}{a} \geq 1 \cdot \frac{\Delta t_{r_o}}{\Delta t_m}$; $r_o \geq 12$ cm where the vortex electric field, $E = \frac{U_p}{2\pi R}$, $E = 6 \cdot 10^{-3}$ V/cm, to critical value, $E_c = 4 \cdot 10^{-2} \frac{N}{T_e}$ seems to be 2-fold lager than in the central region, $E/E_c|_{r \geq r_o} \approx 0.034$, the runaway birth rate and relative density are appropriately $\Gamma \approx 6 \cdot 10^{-6}$, $N_r/N \approx 2 \cdot 10^{-2}$. As follows from the momentum conservation law: $(\gamma_{\parallel}^2 - 1)^{1/2} = \frac{e}{m_o c} \cdot E \cdot \Delta t$, such electrons can be accelereted for (3÷4) ms up to some hundreds keV. The expression: $W_c \approx T_e (1 + \frac{Z_{ef}}{2}) \cdot \frac{E_c}{E}$, allows us estimate $W_{\perp} \approx W_c \approx 10$ keV. This provides EC harmonic overlapping, small P_{SE}, Fig .2. P_{SE} drops quickly, Fig.1.4., because of the beam density decreased by the runaway birth rate diminishing with the plasma density growth, Fig.1.3, and losses of electrons going out to the limiter. The lesser amplitude of the second SE flash than of the first one and the SE absence during the second J_p ramp up, Fig.1.4, are due to the $\bar{N}$ growth also. Evaluatins show that the maximum energy of electrons going out to the limiter reaches $W_{\parallel}^m \sim 2.2$ MeV. At the same time as follows from the HXR spectrum. Fig.3.2, $W_e \approx 1.3$ MeV. Using the corrective coefficient: $K_e = \frac{W^m}{W_e}$; $K_e = 1.7$, one can estimate the energy of electrons appearing in the plasma periphery under the first and second J_p ramp

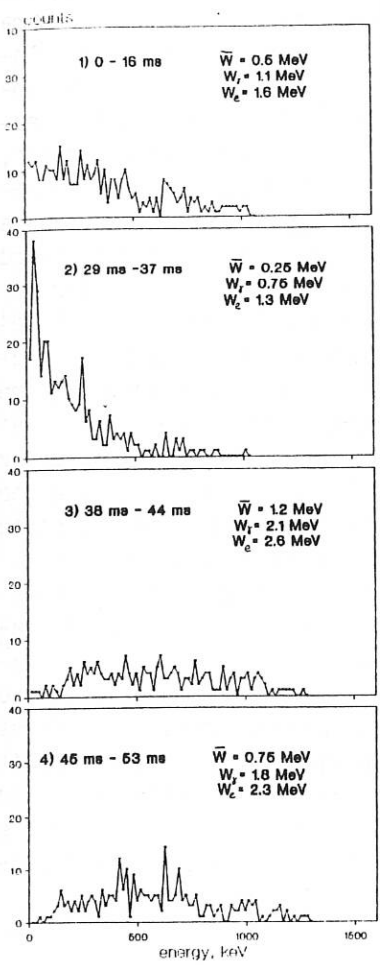

Fig. 3.

up: W_1^m=2.7 MeV, W_2^m=4.4 MeV, and initiating the background HXR, W_b^m=3.9 MeV. From known $W_{1,2}^m$, $\Delta t_{1,2}$ it is possible to determine the effective electric field accelerating runaways in the plasma periphery $E_1 \approx 3.4 \cdot 10^{-2}$ V/cm and $E_2 \approx 2 \cdot 10^{-2}$ V/cm. If peripheric plasma parameters are: T_{e1}=20eV, T_{e2}=50eV, $N_{1,2} \simeq 4 \cdot 10^{12}$ cm^{-3} one can obtain: E_1/E_c=0.04, E_2/E_c=0.06. In such conditions accelerated electrons can carry a remarkable part of the discharge current, [2,3]. This is supported by the observed, Fig.1,2, correlation between the U_p drop at the 5 ms and beam appearence in the plasma periphery. The beam prevents penetration of the current inward the plasma. The current appeares in the central region under growth of the MHD-activity pressing the beam inspite of the $\bar{N}$ decrease when the plasma conductivity becoms essentially less than neoclassical value. Electrons arising under the second J_p ramp up are accelerating up to lager energies than under the first one, though $E_1 \simeq E_2$, Fig.3.1,3, as they are confined with a larger current, $J_{p1} > J_{p2}$, Fig.1.1. In this reason electrons initiating the background HXR, Fig.3.2,4 are accelerated with the same electric field like ones arising at the 15 ms but up to lager energies.

Thus, in our conditions with relatively high N and Z_{ef} runaways appear during the whole discarge. They are freely accelerated before going out to the limiter. Together with runaways arising continuousely in the hot and dense plasma initiating the background HXR the group of runaways appeares during the first J_p ramp up, $\bar{N}$ growth, second J_p ramp up. When N is not too high it produces SE and HXR flashes. In this case on the relative delay of these flashes and maximum quantum energy for the appropriate HXR flash one can determine the effective electrical field producing and accelerating runaways in the plasma periphery.

1. V. V. Parail, O. P. Pogutze. Voprosi teorii plasmi Vip. 11 Pod red. M. A. Leontovich and B. B. Kadomtzev: Energoizdat, 1982, p. 5-55.

2. V. I. Afanas'ev, F. V. Chernyshev, V. E. Golant et al, 17th EPS Conf. on Contr. Fus. and Plasma Heatingh. Amsterdam, 25-29, June 1990, V14B, PartI, A-23, p 82-85.

3. S. E. Bender, J. N. Deshko, A. B. Izvozchikov et al. 15th Eur. Conf. on Contr. Fus. and Plasma Heating. Dubrovnic, 16-20, May, 1988, V12B, PartI, P3a120, p75-78.

ECE MEASUREMENTS USING DOPPLER-SHIFTED OBSERVATIONS

L. Rodriguez, N. Augé, G. Giruzzi, C. Javon, L. Laurent, M. Talvard

Association EURATOM-CEA sur la Fusion
DRFC - C.E.N. de Cadarache
13108 Saint Paul-lez-Durance (FRANCE)

1 Introduction.

Electron Cyclotron Emission (ECE) diagnostics are today routinely employed on various tokamaks to measure the electron temperature of thermal discharges because the plasma is optically thick at the second harmonic extraordinary mode. The frequency broadening arising from the magnetic field variation determines a direct relationship between plasma position and frequency.

ECE diagnostics are also used to study fast electrons. There is a strong interest focused on non thermal electron physics, correlated mainly with investigations of non inductive current driven by RF waves. When suprathermal electrons are present in the plasma the direct relation between frequency and position is lost. For standard ECE diagnostics with lines of sight in the mid-plane normal to the magnetic field, this is due to the relativistic shift. It is difficult to deduce directly the maximum energy of the electrons or their location (the power deposition profile) from the observed spectra. Therefore the interpretation of ECE spectra has to be done by appropriate simulation codes, in our case a 3-D Fokker-Planck code /1/ coupled to a radiation code /2/. However the result remains ambiguous.

More information can be obtained from several lines of sight, using both the relativistic shift and the Doppler effect. In the present paper, plasmas with both inductive and Lower Hybrid Current Drive are analysed with this technique.

2 Experimental set-up.

On Tore Supra, the plasma is observed simultaneously from the low field side along three horizontal chords located in the equatorial plane :

- The first one (M0) makes an angle $\theta = 90°$ with the magnetic field.
- The second one (BS) crosses the first one on the magnetic axis. It is slightly oblique: $\theta = 79°$ at the magnetic axis but because of the finite aspect ratio θ varies between θ_{min} on the low field side and θ_{max} on the the high field side in the plasma. $\theta_{min} = 74°$, $\theta_{max} = 82°$.
- The third one (RS) is symmetric. $\theta = 101°$, $\theta_{min} = 98°$, $\theta_{max} = 106°$.

The antenna angular acceptance is 2°. Radiation is analyzed by three Martin-Puplett type Michelson interferometers with InSb cryogenic detectors. Absolute *in situ* calibration has been performed independently for the three spectrometers. For each one, a spectrum is recorded every 22 ms. The frequency shift is given by:

$$\nu(R) = \nu_0(R)\frac{\sqrt{1-\beta^2}}{1-\beta_{//}\cos\theta} \qquad (1)$$

where ν_0 is the rest cyclotron frequency, R the major radius, and $\beta = v/c$. The factor in the numerator always shifts the frequency downwards while the effect of the denominator depends of the sign of $\beta_{//}\cos\theta$. For $\theta = 79°$, it can be shown that $\nu > \nu_0$ only if the electrons are located in velocity space in the ellipse shown in figure 1. This ellipse contains electrons flowing in the drift direction. For that reason we call the associated Michelson Blue Shift (BS). For $\theta = 101°$ (Red Shift) the same diagram is obtained with $v_{//}$ changed to $-v_{//}$. For $\theta = 90°$ ν is always smaller than ν_0. In the following the spectra for θ = 101°, 90°, 79° are represented respectively by dotted, heavy and dashed lines.

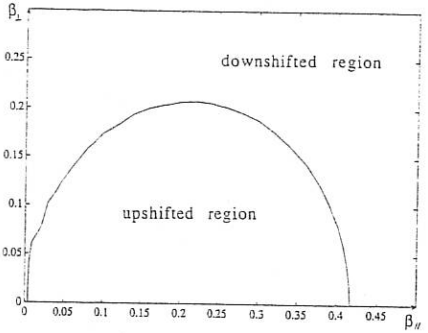

Figure 1

3 Ohmic discharges

Figure 2b shows the superposition of the three spectra recorded 3.0 s after plasma formation. The parameters are B = 3.85 T, I_p = 1.2 MA, $\langle n_e \rangle = 3\ 10^{19}\ m^{-3}$, V_{loop} = 1V. Figure 2a shows the cyclotron harmonics and cut-off frequencies as a function of minor radius. The most striking observation is that the BS spectrum is above the RS and M0 spectra in the 200 - 350 GHz range. This effect is systematic and cannot be attributed to calibration effects since it has been observed at different toroidal fields (2.6, 3., 3.5 and 4T). This is unexpected for thermal plasmas since only a small broadening (2.5-3. GHz) is expected because of Doppler effect. In other frequency domains like the second harmonic, low frequency (160-200 GHz) and third harmonic, high frequency (350-390 GHz) the amplitudes are identical for the three lines of sight.

The differences must be related to asymmetries in the distribution function in $v_{//}$. Similar non thermal features in EC and X-Rays during typical thermal shots have been observed in several machines /3-5/. However, the effect of the DC electric field cannot account for such asymmetries as checked by Fokker-Planck simulations. Two interpretations can be proposed :

a) Downshifted/upshifted second harmonic: The non thermal feature has been attributed to anomalous transport due to magnetic fluctuations, which cause a distortion of the distribution function /6/. Following this model the observation could be explained by the presence of a small number of moderate energy electrons slightly accelerated by the DC field (i.e. located in the ellipse of figure 1). Their second harmonic emission can be seen by BS line because, due to the upshift , they are resonant between the antenna and the optically thick thermal cyclotron layer). Conversely, they cannot be seen by RS or M0 because the downshift makes them resonant behind the thermal layer.

b) Downshifted third harmonic: Another possible interpretation is to introduce a small number of high energy electrons in the range 200 - 300 keV, in the inner plasma region. Their downshifted 3rd harmonic emission is seen by BS at 200 GHz and above. This determines the maximum energy of electrons. Nothing

is seen on RS and M0 because red shift due to the Doppler and/or relativistic effects makes these electrons radiate just below the optically thick 2nd harmonic.

4 RF assisted discharges

During lower hybrid current drive experiments or slide away discharges, two large peaks appear at the same frequencies in the three spectra (50-100 and 110-175 GHz as shown in Fig.2c). If the position and shape of the peaks were determined by equation (1) a significant difference between the three spectra would be observed: the peaks would move downwards in RS spectrum and upwards in BS spectrum. A better agreement is obtained assuming that electrons with a broad energy spectrum cause radiation between 50 and 175 GHz. The shape of the spectrum is rather determined by the cut-off and absorbing layers as can be seen by comparison of Fig 2a and 2c.

The existence of ECE at low frequency implies a substantial number of electrons with energies over 500 keV. Because of the accessibility condition, the lower-hybrid tail cannot extend so far. A possible explanation relies upon the combined effects of the lower hybrid power and of the residual Ohmic electric field, stretching the lower hybrid tail to higher energies. This was checked by means of the Fokker-Planck code; good agreement is found between the experimental and simulated spectra only when the dc field is included, i.e., very similar spectra for the three lines of sight. This interpretation needs confirmation in fully non-inductive long duration discharges.

A RF power scan between 0.1 to 3 MW has been made. The plasma current is kept constant, i.e., the loop voltage decreases for increasing RF power. The two peaks exihibit different behaviour. The amplitude of the highest frequency peak varies linearly with the power, because the number of the moderate energy electrons is mainly determined by their interaction with the lower hybrid wave. The amplitude of the low frequency peak shows a slower increase with RF power because the dynamics of high energy electrons is also governed by the electric field which decreases with RF power.

5 Conclusion

We have reported experimental evidence for asymmetries in ECE spectra measured along oblique lines of sight during Ohmic discharges. These could be attributed to small deviations from the Maxwellian distribution, due either to anomalous transport or to an energetic electron population. A clear interpretation of such asymmetries requires further experimental investigation.

During LHCD experiments, intense peaks appear in the optically thin low-frequency region of the ECE spectrum in windows between cut-off layers. The effects of the inductive electric field and RF power on ECE spectra have been investigated using a Fokker-Planck code. The interpretation is consistent with observations at different power levels.

/1/ R.L.Meyer, G. Giruzzi, V. Krivenski, Comp. Phys. Comm. **40** (1986) 153.
/2/ G. Giruzzi, Nucl. Fusion **28** (1988) 1413.
/3/ A.V. Gurevich et al., JETP Lett. **26** (1977) 569.
/4/ J.E. Rice et al., Phys. Rev. **A25** (1982) 1645.
/5/ G. Taylor et al., Plasma Phys. **31** (1989) 1957.
/6/ H.E. Mynik and J.D. Strachan Phys.Fluids **24**(4) 1981

Figure 2

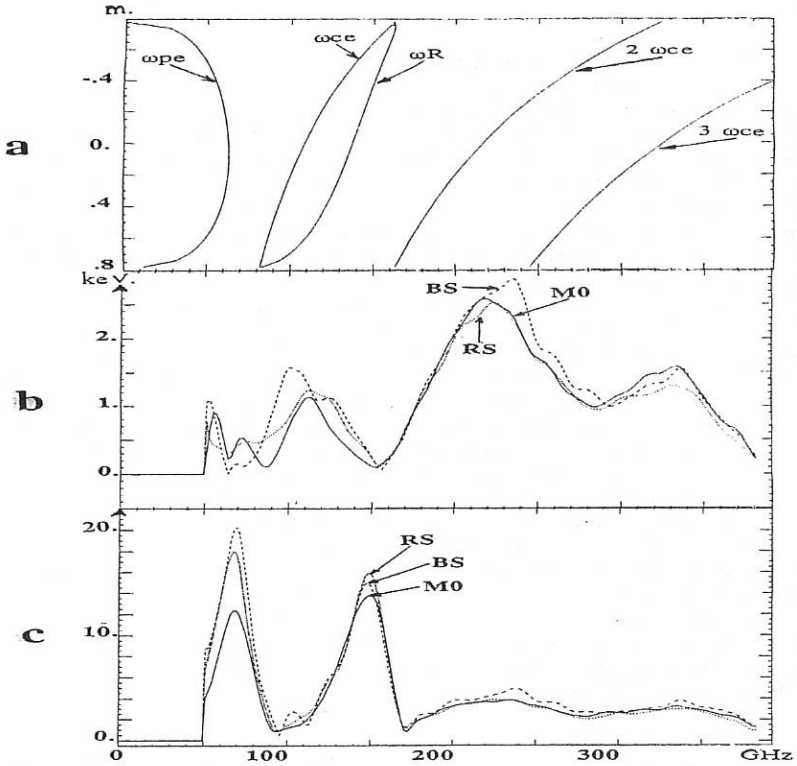

Figure 3

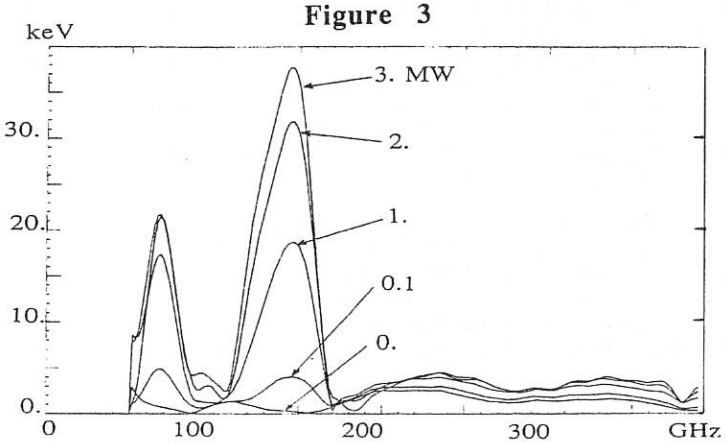

FIRST RESULTS WITH THE UPGRADED ECE HETERODYNE RADIOMETER ON JET

L Porte*, D V Bartlett, D J Campbell, A E Costley

JET Joint Undertaking, Abingdon, Oxon OX14 3EA, U K
*University of Strathclyde, Glasgow G4

1 Introduction

The capability of the JET ECE diagnostic has recently been extended by a major upgrading of the heterodyne radiometer [1]. In particular, the number of observation channels has been increased from 8 to 44, while the system's inherently high sensitivity, temporal resolution and spectral resolution have been maintained. The upgraded radiometer is capable of measurements in the first and second harmonics of the electron cyclotron frequency in both ordinary and extraordinary modes. While the advantages of the heterodyne system are particularly appropriate to edge measurements, the extended spectral range provides an improved spatial coverage of the electron temperature profile and permits a wide range of phenomena, including sawteeth and their associated heat pulses, elms and edge mhd activity, to be investigated.

2 The Multi–Channel Heterodyne Radiometer

ECE from JET is transmitted to the radiometer via the JET multichannel ECE waveguide system [2]. Each viewing channel consists of an internal antenna, wedged crystal quartz vacuum window and approximately 50m of oversized rectangular waveguide. At the entrance to the radiometer (figure 1), radiation is divided four ways by means of newly developed non–polarizing beamsplitters. Each of these consists of two orthogonal wire grids wound from 10μm tungsten wire and oriented at 45^{o} to the major axes of the rectangular waveguide. The ratio of transmitted to reflected signal in both modes of polarization is close to unity. A further polarizer is placed at the entrance to each of the heterodyne mixers to enable either the ordinary or the extraordinary polarization to be selected.

The radiometer itself contains four subsystems with frequency ranges: 73.1–78.9GHz, 79–91GHz, 91–103GHz and 115–127GHz. Each subsystem consists of a local oscillator (a Gunn diode generating ~20mW power), beam–lead GaAs Schottky–diode mixer, IF amplifier, power divider, band–pass filter, Schottky–diode detector and video–amplifier (figure 1). The first subsystem is divided into 8 channels, each with a bandwidth of 250MHz (corresponding to a spatial resolution of ~2cm), while the three other subsystems are divided into 12 channels each with a bandwidth of 500MHz (with a corresponding spatial resolution of ~4cm). This yields a total of 44 observation channels which span a significant fraction of the plasma, the precise range depending on the toroidal field. Note that the final spatial resolution of the system is influenced

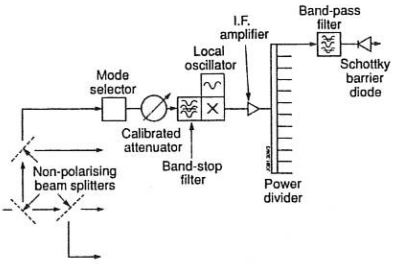

Fig 1 Schematic of one of the 12–channel subsystems of the heterodyne radiometer.

by the finite antenna pattern of the ECE system, which broadens the effective radial resolution.

Absolute calibration of the diagnostic is obtained by cross–calibration against an absolutely calibrated Michelson interferometer, while the relative calibration is enhanced by means of a technique which uses the plasma itself as a calibration source [3]. This method involves comparison of the relative responsivities of adjacent channels in the radiometer by sweeping the toroidal magnetic field while maintaining an approximately constant electron temperature profile. Previous analysis [3] suggests that in this way the relative calibration of the radiometer channels can be obtained to better than ±3%. The signal–to–noise ratio of the diagnostic may be determined either by intrinsic system noise or by fluctuations in the radiation field, depending on the regime in which the system is operated. For plasma observations it is more appropriate to characterize the noise performance of the system in terms of the minimum detectable temperature fluctuation, ΔT_e, which, for the heterodyne radiometer is of order 10eV for an electrical bandwidth of 3kHz.

3 ECE Measurements in the Plasma Edge

3.1 Limitations: The high sensitivity and good spatial resolution of the heterodyne radiometer permit accurate ECE measurements in the plasma edge [1] where low signal levels are usual and diagnosis by ECE is difficult. However, interpretation of the measurements in terms of electron temperature is complicated by several effects:

(i) *Harmonic overlap* between first harmonic emission from the small major radius side of the plasma and second harmonic emission from the outside edge in JET can cause systematic errors in the determination of the electron temperature when the optical depth of the second harmonic is $\lesssim 3$.

(ii) *Relativistically downshifted radiation* can cause an overestimate of the electron temperature. This effect arises when temperature gradients in the edge are very steep, as may occur during the H–mode, but the optical depth of the plasma at a given frequency is $\lesssim 3$. In such cases, emission at frequencies identified with the plasma edge

includes a contribution from relativistically downshifted emission from higher temperature regions deeper inside the plasma.

(iii) *Doppler shifted emission* can also degrade the quality of edge temperature measurements. Two effects have been identified. If the system antenna pattern is too wide, the Doppler shift due to the finite thermal velocity of electrons can introduce a contribution from higher temperature regions in a manner which is analogous to the relativistic downshifting effect and which occurs in similar conditions. An additional effect can occur [1] in which Doppler shifted first harmonic ordinary mode emission from the plasma core can appear in the the second harmonic at the edge due to polarization scrambling on reflection from the vessel walls.

(iv) *Non–thermal ECE* can be generated by large amplitude mhd phenomena in the plasma core. The mechanisms are not fully understood, but, since the core optical depth is very high, measurements in the core are generally unaffected by such non–thermal emission. However, the broadband nature of the emission can corrupt measurements in the plasma edge where the optical depth is lower.

All of these mechanisms can contribute to emission at frequencies corresponding to the plasma edge, so that care must be exercised in the interpretation of edge ECE measurements in terms of local electron temperatures. Analysis of ECE from the plasma edge must, therefore, be performed in conjunction with simulations of the ECE processes [4] which provide estimates of the relative magnitudes of such effects.

3.2 Edge Measurements in X–point Plasmas: The radiometer has been used to investigate the edge temperatures in the L and H–mode phases of JET plasmas. Figure 2a shows the time evolution of the H_α emission line, T_e close to the last closed flux surface (LCFS) and T_e close to the plasma centre during the L–to–H transition in a JET neutral beam heated discharge. During the phase marked 'L to H', which appears to be triggered by a sawtooth heat–pulse, rapid elms occur (which are not visible on the trace shown). Following a second sawtooth heat–pulse, a quiescent H–mode phase begins, with less–frequent elms, and the edge temperature continues to rise.

Figure 2b shows temperature profiles in the plasma edge at the four times indicated in figure 2a. Inside the LCFS, plasma parameters are such that the plasma is optically thick and simulations indicate that the measurements can be reliably interpreted in terms of local temperature. However, due to the steep temperature gradient close to the LCFS, the optical depth falls rapidly and the apparent rise in temperature outside the separatrix is the result of the effects outlined in section 3.1.

During elmy H–modes, rapid fluctuations can be observed in the edge electron temperature which are correlated with the H_α spikes. Figure 3a shows timetraces of H_α emission, edge T_e and near–central T_e during such an elmy phase. Note that part of the variation in amplitude of the H_α spikes is due to limitations in the sampling

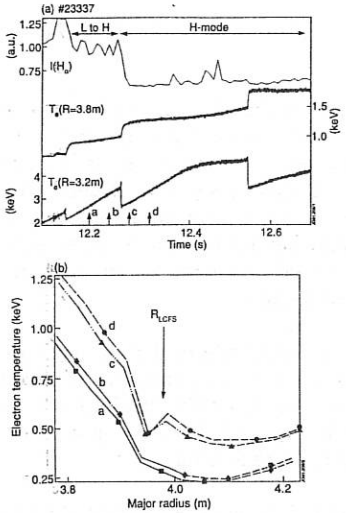

Fig 2 (a) T_e observations during the L–to–H transition. (b) Evolution of the edge T_e profile during the transition.

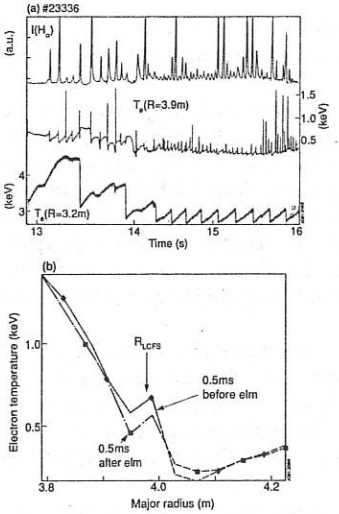

Fig 3 (a) T_e observations during an elmy H–mode. (b) Edge T_e profiles 0.5ms before and 0.5ms after an elm.

frequency. Each elm leads to a sawtooth–like modulation of the temperature trace inside the separatrix. In addition, in some cases, a very short, large amplitude, spike is observed in the temperature trace coincident with the H_α spike. The origin of such 'temperature' spikes is not yet understood and is the subject of further investigations.

Temperature profiles in the plasma edge 0.5ms before and 0.5ms after an elm are shown in figure 3b. The collapse time of the elm is much shorter than the observation period (perhaps $\sim 100\mu s$), indicating that the elm is a very rapidly growing instability. Note also that, in this case, the 'inversion radius' of the elm appears to be just outside the separatrix. However, the uncertainties in the relative position of the separatrix and T_e profile and the variation observed in the behaviour of the elms do not yet allow us to draw firm conclusions on the spatial localization of elms.

We would like to thank Dr G Kramer for many useful discussions and for the development of software for the analysis of the ECE data.

4 References

[1] N A Salmon, Ph D Thesis, University of London, November 1989.
[2] E A M Baker et al, EC–4 4th Int. Workshop on ECE and ECRH, Rome, March 1984, 11.
[3] K Uchino et al, EC–7 7th Int. Workshop on ECE and ECRH, Hefei, May 1989, 341.
[4] D V Bartlett, ibid [2], 27.

MEASUREMENT OF T_e-PROFILES IN THE BOUNDARY LAYER OF TEXTOR BY MEANS OF SPECTROSCOPICAL OBSERVATION OF A THERMAL HELIUM BEAM

B. Schweer, A. Pospieszczyk, G. Mank, U. Samm
Forschungszentrum Jülich GmbH, IPP, Association EURATOM-KFA, Germany
B. Brosda, B. Pohlmeyer
Ruhr-Universität Bochum, Institut für Experimentalphysik V, Germany

Introduction:

Profiles of the electron temperature ($T_e(r)$) and density ($n_e(r)$) in the plasma edge of a tokamak are important parameters for the description of the plasma wall interaction. Whereas the quasicontinuous determination of $n_e(r)$ by an atom beam in combination with a radial recording of its optical emission is now a well established and successful method in plasma boundary diagnostics /1/, an equivalent method for $T_e(r)$ is still missing. Elements are needed, which show ionization and excitation rates with a strong T_e-dependence up to about 100 eV. Especially helium is an excellent candidate as an atomic probe as it has a high ionization energy and can therefore penetrate relatively far into the boundary layer of a fusion plasma, and it can easily be applied (particularly as a thermal beam). Although numerous attempts have been made in the past, to use the intensities of neutral helium lines for measuring electron temperatures e.g./2//3//4//5/, the method is still not satisfactorily as several secondary processes (predominantly excitation transfer and cascading), which are also density and temperature dependent, introduce considerable interpretation difficulties. Recently however, there has been a collisional radiative models developed /6/, which have encouraged us to use spatially resolved optical spectroscopy of a thermal helium beam for the measurement of T_e-profiles in the boundary layer of TEXTOR.

Method:

For the measurement of T_e the ratio of singlet-to-triplet lines is used, which - for suitably chosen lines - is a function of the electron temperature. The choice of using line ratios is slightly different from the method described in /1/, where a single helium line emission profile was combined with the n_e-profile, determined by neutral lithium beam spectroscopy. Because helium has a much higher ionization energy (E_i=24.5eV), it penetrates deeper into the plasma than lithium (E_i=5.4eV), and the overlapping of both emission profiles, where T_e can be evaluated, is rather small.Using the line ratio method, beam attenuation and geometrical effects can be neglected except for the influence on the spatial resolution (see below). Thus line ratios during the whole time of a TEXTOR discharge can be well determined until several centimeters beyond the limiter up to electron densities of $\approx 10^{13}$ cm^{-3}. In order to convert the line ratios into electron temperatures, the experimental values were compared with model calculations. In this model the level population ($n \leq 4$) of a thermal helium beam is calculated for known electron temperatures and -densities, taking only electron collisions and radiation into account /6/. With the laser

ablation diagnostic n_e- and T_e-profiles which are covering the penetration depth of the He-beam are measured independently at one single point of time /7/. Using this n_e-profile and the corresponding line ratio profile in the model, $T_e(r)$ can be obtained, which can be compared with that one from the laser ablation. In principle for a complete modelling of $T_e(r)$ for the whole discharge the simultaneous knowledge of $n_e(r)$ is necessary, but the aim of the experiments described was also to find line ratios, which are nearly independent of n_e. This simplifies the evaluation procedure considerably and allow a fast quasicontinuous $T_e(r)$-determination of a TEXTOR discharge in the plasma boundary.

Experiment:

The injection of helium gas into the boundary layer of TEXTOR (I_p=340kA, B_t=2.25T, r_L=46cm) was performed through a collimator with 4 mm inner diameter, composed of thin channels (6 mm length, 50 μm diameter). This structure collimates the He-beam to about 11 cm FWHM at 15 cm distance. At TEXTOR a reservoir of 2 litre was filled with He up to a pressure of 20 mbar. Through a valve which is opened shortly before the start of the discharge the gas is flowing into the tube. The flux density at the collimator can be regulated by a needle valve. For the measurements in TEXTOR normally a relatively high total helium atom flux 5×10^{18}/s was determined from the pressure decay in the reservoir. As shown in fig.1 the He-beam is combined with the thermal Li-beam, measuring the n_e-profiles up to $5\times10^{12}cm^{-3}$. To avoid sputtering effects on the Li-oven the supporting system was retracted 10 cm behind the liner and so also the nozzle for the He-beam. The resulting broad distribution of the He-beam at the observation volume leads to a reduction of the radial resolution to about 3 mm. The He-density at a plasmaradius of r=45 cm decreases to $\approx 2\times10^{11}cm^{-3}$. The injected He flux was reduced by a factor of 10 in order detect possible changes in the plasma parameters during the gas injection. No significant changes in the emission profiles were observed. Therefore the system could be still improved concerning detection limit and spatial resolution by moving the nozzle further to the liner.

For the spatial recording of the emitted intensity profile $I_A(r)$ two 128 Si-diode array cameras /8/ were used in combination with interference filters for the selection of the appropriate wavelengths. Both cameras were aligned on the same observation volume. The image of the array in the plasma is 1.2 mm in radial and 12 mm in toroidal direction due to the rectangular size of each Si-element. The emission profiles could be recorded in a data acquisition system with a maximum repetition rate of 2 kHz.

Results and Discussion:

T_e- and n_e-profiles in the boundary layer of TEXTOR are shown in fig. 2a at t=1.5 s in the discharge measured with the laser ablation system. For the same time, integrated over 10 ms, the intensity profiles of the He singlet line at 728 nm (transition $3s^1S \rightarrow 2p^1P^o$) and the He triplet line at 706 nm ($3s^3S \rightarrow 2p^3P^o$) were recorded and plotted in fig. 2b. The signals are corrected for the transmission factors of the interference filters and for the sensitivities of the Si-diodes at the

selected wavelengths. No light from the background plasma was detected by using narrow bandwidth filters with 1nm FWHM. One should note that the emission from the thermal He-beam can be recorded as least as far as the temperature measurement by the laser ablation system is made.

For the discharges reported the electron density in the boundary layer of TEXTOR varies from $10^{12}cm^{-3}$ to $10^{13}cm^{-3}$ as can be seen in fig. 2a. For this density range the ratios of singlet to triplet line intensities I(λ=728nm/λ=706nm) and I(λ=502nm[transition: $3p^1P^o \rightarrow 2s^1S$]/$\lambda$=706nm) were modelled and the results are presented in fig. 3 and fig. 4. Comparing both figures, the ratio of the intensities at 728 nm and 706 nm must be favored since the density dependence is weaker (and between $5\times10^{12}cm^{-3}$ and $10^{13}cm^{-3}$ practically non-existing), whereas for the ratios at 502 nm and 706 nm the slope is steeper corresponding to a higher sensitivity to changes in the electron temperature.

In order to demonstrate these dependencies, T_e-profiles have been calculated using the measured n_e-profiles (for #45377 see fig.2b), and in addition those, which have been varied by ± 50%. For comparison the T_e-profiles obtained by the laser ablation diagnostic (fig.2a) are added in fig.5 and fig.6. Taking into account the uncertainty of these measurements the agreement of the T_e-profiles over the selected range is quite good in both cases. For I(λ=502nm/λ=706nm) the both T_e-profiles practically coincide for the exact $n_{e0}(r)$ from fig.2a. In case that the electron density profile is well known, I(λ=502nm/λ=706nm) should therefore be selected.

From the model calculations and our measurements we found that for the two reported singlet to triplet intensity ratios the method gives satisfactory results for the density range $1\times10^{13}cm^{-3} > n_e > 3\times10^{12}cm^{-3}$ (45cm< r <49 cm in fig. 5 an fig. 6). Outside these ranges strong deviations from the independently measured T_e-values are found. For electron densities above $1\times10^{13}cm^{-3}$ the triplet levels are obviously more populated than predicted. The reason for this might be the limitation to transitions $n\leq4$ in the model.

References:

/1/ Pospieszczyk, A., Aumayr, F., Bay, H.L., Hintz, E., Leismann, P.,Lie, Y.T., Ross, G.G., Rusbüldt, D., Schorn, R.P., Schweer, B.,Winter, H., J. Nucl. Mat. **162-164** (1989) 574-581

/2/ S.P.Cunningham, *Conference on Thermonuclear Reactions* (UCRL, Livermore, California, 1955); U.S. Atomic Energy Commission Report No. 279, p. 289

/3/ R.S.Sovie Phys.Fluids 7 (1964) 613

/4/ B.J.Eastlund, D.Spero, M.Johnson, P.Korn, C.B.Wharton, and E.R.Wilson J.Appl.Phys. **44** (1973) 4930

/5/ N.Brenning J.Quant.Spectrosc.Radiat.Tranfer **24** (1980) 293

/6/ B.Brosda and B.Pohlmeyer, HE-BEAM Internal Report Ruhr-Universität Bochum (July 1990)

/7/ Pospieszczyk, A., Ross, G.G. Rev. Sci. Instrum. **59** (1988) 1491-1493

/8/ Reticon array camera ,G128/10

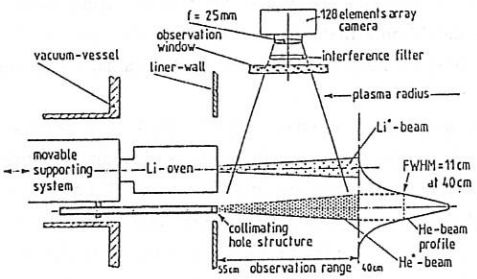

Fig. 1 Experimental set-up

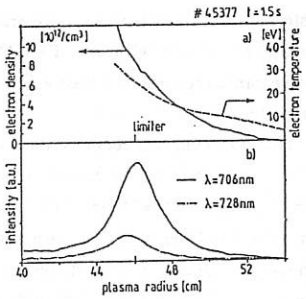

Fig. 2 a) n_e- and T_e-profiles from the laser ablation diagnostic, b) He-emission profiles

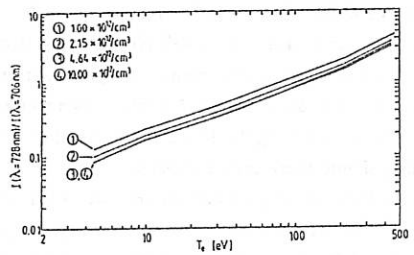

Fig. 3 Calculated line intensity ratio for singlet 728 nm to triplet 706 nm as a function of electron temperature

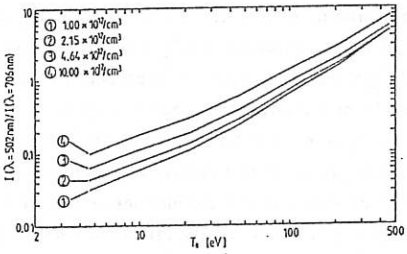

Fig. 4 Calculated line intensity ratio for singlet 502 nm to triplet 706 nm as a function of electron temperature

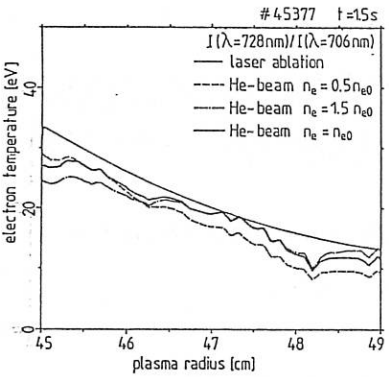

Fig. 5 Comparision of T_e-profiles measured with laser ablation and He-beam diagnostics (728 nm, 706 nm, ±50% n_e-profile variation

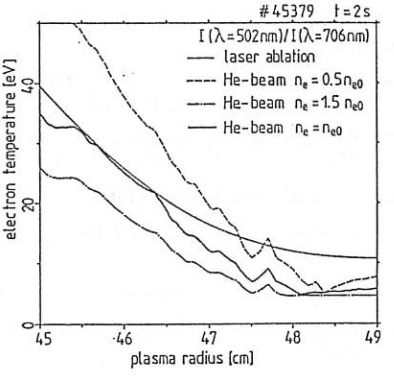

Fig. 6 Comparision of T_e-profiles measured with laser ablation and He-beam diagnostics (502 nm, 706nm, ±50% n_e-profile variation

MODEL CALCULATIONS FOR A 20 KEV NEUTRAL LITHIUM DIAGNOSTIC BEAM

E.Unterreiter, F. Aumayr, R.P. Schorn* and H. Winter

Institut für Allgemeine Physik, TU Wien, Wiedner Hauptstraße 8-10, A- 1040 Wien, Austria
*Institut für Plasmaphysik der KFA Jülich GmbH, Association EURATOM/KFA, Postfach 1913, W-5170 Jülich, Germany

Introduction

Electron density and impurity ion concentrations in the edge plasma of tokamak discharges can be determined with excellent spatial and temporal resolution by virtue of a neutral lithium diagnostic beam [1,2]. Spectroscopic observation of the LiI resonance line, mainly produced by electron collisions, and of characteristic impurity ion lines as induced by electron capture from injected fast Li atoms into excited ion states (Li-induced charge exchange spectroscopy - "Li - CXS"), delivers raw data from which the above information can be evaluated [3].

Model calculations

First of all, attenuation of the injected Li beam must be taken into account. Therefore we use an attenuation code which includes excitation, deexcitation, ionization and charge exchange with injected Li atoms via collisions with electrons and protons in the edge plasma environment. A system of coupled linear differential equations describes the time evolution of the Li atom beam composition, i.e. the densities n_i of its various atomic states i as seen by an observer moving with the injected Li atoms across the plasma edge [3].
Since the involved rate coefficients are only known for a few Li states, mainly the Li(2s) ground state, most of the needed values have to be estimated from different approximations. In order to decide which of the rate coefficients play an important role and should thus be known more precisely, test calculations have been carried out by excluding particular processes.
Fig. 1 shows a comparison of such calculated Li(2p) profiles with the result of a "complete" calculation. For this comparison we have regarded an ohmically heated TEXTOR plasma [3]. As can clearly be seen, the most important mechanisms for determining the Li(2p) population are charge exchange and electron impact excitation, since omission of the respective processes results in the relatively most pronounced deviations from the reference curve. Excluding other processes than charge exchange with protons and electron impact excitation yields profiles which are similar in both height and shape to the reference profile.
A critical proof for the accuracy of our model, in particular the reliability of the involved cross sections, is the agreement between radial profiles calculated for a given Li state and their corresponding measured line emission profiles. Experimental investigations are carried out for a number of excited Li ($n \geq 3$) states giving rise to visible emission lines.

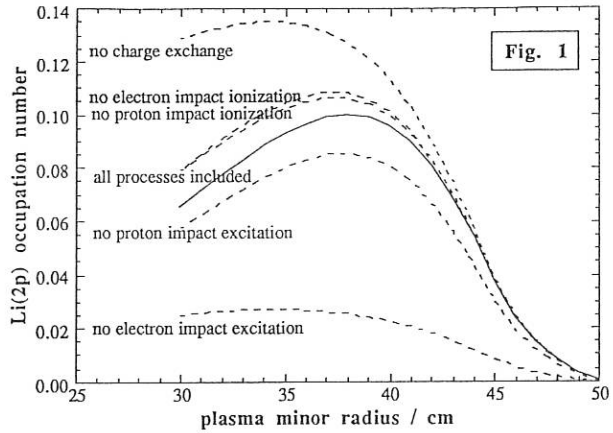

Consideration of ℓ-mixing

When applying Li-CXS for measuring impurity ion densities, the following problem is encountered. After population via electron capture from Li, various resulting excited impurity ion states may become mixed due to collisions with plasma particles before their radiative decay, in which case a correction of emission cross sections as originally derived from single collision experiments is needed to take into account the influence of these mixing processes. To study this in more detail, we have performed model calculations for occupation numbers in C^{3+} ions after electron capture into C^{4+}, as for this case especially careful ℓ-dependent capture measurements have been performed [4] in a binary collision experiment.

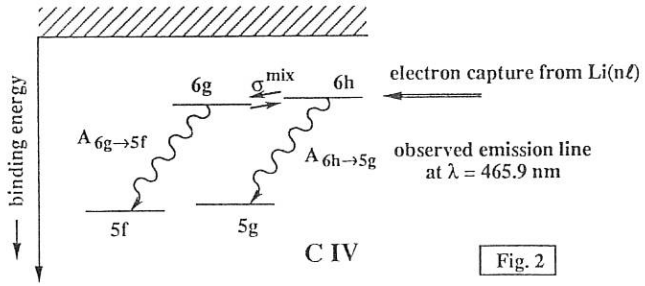

Fig.2 shows a scheme of the investigated states. A system of coupled differential equations taking into account mixing collisions and spontaneous radiative decay only leads to population numbers of the relevant states in dependence of the electron density and -temperature. As mixing cross section a quantum defect-dependent cross section for electron and proton impact excitation and deexcitation between neighbouring ℓ-levels from [5] has been used.

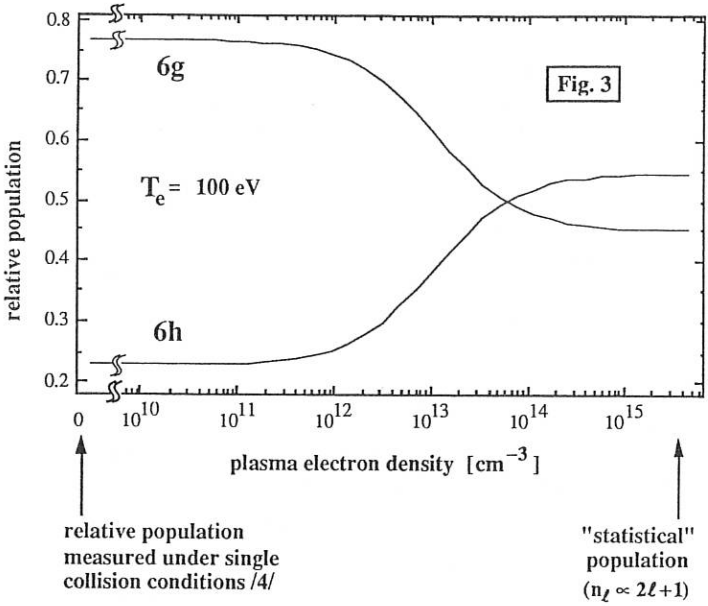

Fig. 3 shows the changing population of two C^{3+} 6ℓ substates with increasing electron density.
The initial occupation numbers (0.77 and 0.23 for 6g and 6h, respectively) change drastically towards higher electron density. At $n_e = 2 \times 10^{13}$ cm^{-3} the 6h occupation number has increased up to 0.42, which means an enhancement by nearly a factor of two for the observed emission line, which constitutes a clearly non-negligible effect.

Acknowledgement
This work has been supported by Kommission zur Koordination der Kernfusionsforschung at the Austrian Academy of Sciences.

References

1 F. Aumayr and H. Winter, Ann. Phys. **42** (1985) 228
2 K. McCormick and the ASDEX Team, Rev. Sci. Instrum. **56**, (1985) 1063
3 R.P. Schorn, E. Hintz, D. Rusbüldt, F. Aumayr, E. Unterreiter and H. Winter, Appl. Phys. B **52** (1991) 71
4 D. Dijkkamp, A. Brazuk, A.G. Drentje, F.J. de Heer and H. Winter, J.Phys.B: At.Mol.Phys. **17** (1984) 4371
5 I.L. Beigman and M.I. Syrkin, Proc. Lebedev Physical Institute (Moscow), Vol. **195** (1989) 121

ALT-II TOROIDAL BELT LIMITER BIASING EXPERIMENTS ON TEXTOR

R. Doerner, J. A. Boedo, D. S. Gray, R. W. Conn, R. A. Moyer, UCLA,
W. Y. Baek, K. H. Dippel, K. H. Finken, A. Pospieszczyk,
B. Schweer, the TEXTOR Team, the NBI Team, KFA Jülich,
D. Hillis, J. Hogan, ORNL, M. Ciotti, ENEA Frascati.

Edge electric fields have been related to H-mode-like behaviour (1,2). The experiments reported here are an attempt to control the SOL profiles by electrostatic biasing of the full toroidal-belt limiter ALT-II. The specific goals are: influencing the edge particle flows, particle removal, power deposition and the global confinement.

The ALT-II pump limiter (3,4) is a full toroidal belt located at 45° below the outer midplane and consisting of eight graphite covered blades which can be independently biased. Particle scoops located behind the limiter neutralize and direct the incoming plasma into the pumping ducts.

Voltages up to 900V and currents up to 600A have been obtained using a 1 MW power supply. Experiments reported here have been performed with levels of biasing power of up to 180 KW and in discharges characterized by B_t=2.25 T, I_p=340KA and $\langle n_e \rangle = 2.5\text{-}3.0 \times 10^{13}$ cm^{-3}. The typical time sequence consists of an initial ohmic phase followed by a biasing phase from 1.0 to 2.0 sec. and an overlapping neutral beam injection (NBI) phase from 1.5 to 2.5 sec. The gas feed is switched off at 0.8 sec. For the data shown here, a helium puff lasting 15 msec was injected at 0.8 sec.

The biasing voltage is referenced to the liner. Two biasing configurations are examined; 1) biasing ALT-II with the plasma positioned on ALT-II and 2) biasing ALT-II with the plasma positioned to contact both the inner-bumper limiter (at liner potential) and ALT-II (creating enhanced poloidal electric fields). Comparisons are made for both bias polarities with co-NBI, counter-NBI and ohmic discharges. Radial profiles of floating potential (V_f), poloidal field (E_{pol}), n_e and T_e are obtained using a fast-reciprocating probe.

Configuration I Operation

During this mode of operation, the central density increases (10-15%), and the profiles steepen in the bulk for either polarity

of bias. No impurity release into the discharge is observed. The D-alpha monitors indicate a modest increase in intensity pointing to augmented recycling. During negative biasing, flux probes located inside the limiter scoops show a drop of as much as 90% in the collected flux (Fig. 1) on the electron drift side and 20% on the ion drift side; the positive biasing case shows little effect.

The n_e profiles at the scrape-off layer (SOL) measured by the scanning probe and spectroscopic techniques (Li laser ablation) show a moderate steepening during the OH phase, in contrast with significant changes in the shape and an increase in the decay length of such profiles during the NBI phase. The T_e profiles develop "bumps" between the radius of the limiter scoops and the liner. These features disappear during the NBI phase.

The V_f profiles (Fig. 2) are flat across the radial extent of the limiter (3.5 cm) and show a rapid decrease afterwards, more so in the negative bias case. The NBI causes a sharp negative offset on V_f of about -100V in either polarity.

Modelling of these discharges using the TRANSP code (5) finds that the particle confinement time changes are small. The input for modelling consists of the electron density and temperature profiles, D-alpha radiation measured at different locations on the various limiters and walls and the fueling rate. The results are consistent with the moderate increase seen in D-alpha.

Configuration II Operation.

On this configuration, large currents are drawn from the biasing power supply and all the effects observed in the configuration I are enhanced. The central line-averaged density (Fig. 3) shows a larger increase (30%) and the flux probes indicate a reduced particle collection even during positive biasing. The D-alpha monitors show a similar behaviour as in configuration I.

The fast reciprocating probe and laser ablation measurements indicate larger changes in the SOL profiles of n_e and T_e even during the ohmic phase. The n_e decay length decreases by 30% during negative biasing in the OH phase and even further during the NBI phase.

The flat section of the V_f profile (Fig. 2) now extends over 5 cm in the positive bias case and 1 cm during negative bias. Large gradients in the radial electric field are created. An offset of -100V is produced by NBI here as well.

By contrast with the configuration I, the poloidal field shows changes of up to 4V/cm (30%) depending on the biasing polarity. Helium was injected in these discharges to get information on tau-He for the different biasing polarities. The changes observed (from 60ms to 80ms) are within the error limits of the diagnostics. This is being investigated further.

Summary

Existing results show a small increase in the particle and energy confinement times. The stored energy increases during the biasing also, but the question of how much of the biasing power is deposited in the plasma is still open.

Large reductions in the particle flux into the limiter scoops are observed. These changes can not be explained by the observed modifications in the decay lenghts of the profiles, but could be consistent with flows in the SOL induced by the electric fields. Shifts of the plasma colum is discarded as being the source of these effects.

Significant modifications have been induced in the electric fields, density and temperature profiles in the SOL. The power deposition in the blades has also been monitored and the results are not conclusive. Experiments are continuing in order to answer the questions raised.

1-R. J. Groebner, *et al,* Proceedings of the 16th European Conference on Controlled Fusion and Plasma Physics, Venice, 13B, part I, (1989) 245.
2-R. J. Taylor, *et al,* Physical review Letters 63 (1989) 2369 .
3-D. Goebel, *et al,* J. Nuc. Mater., 115 (1989) 162-164.
4-R. W. Conn, *et al,* Fusion Engrg. Des. 13 (1990) 251.
5-R. J. Goldston, J. Computat. Phys., 43 (1981) 61.

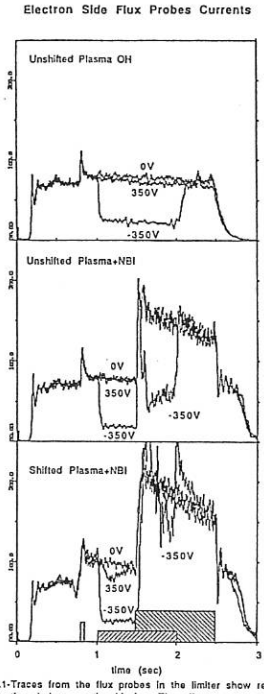

Fig.1-Traces from the flux probes in the limiter show reduced particle collection during negative biasing. The effects are more significant for shifted plasmas.

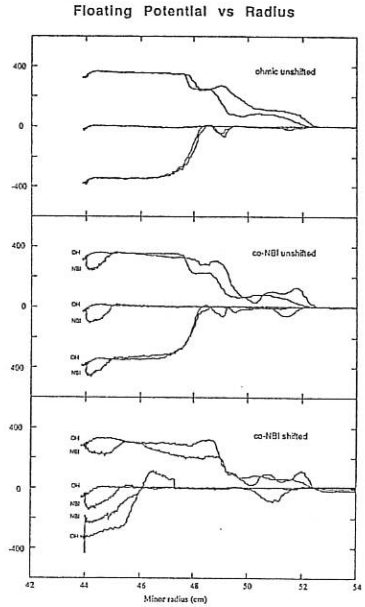

Fig.2-The floating potential measured by the scanning probe is shown as a function of radius for biasing discharges. Measurements taken during OH, NBI and shifted plasma+NBI are displayed. The double traces correspond to discharges where the NBI was turned on while the probe sampled the plasma. Notice the drop of 100V in the floating potential.

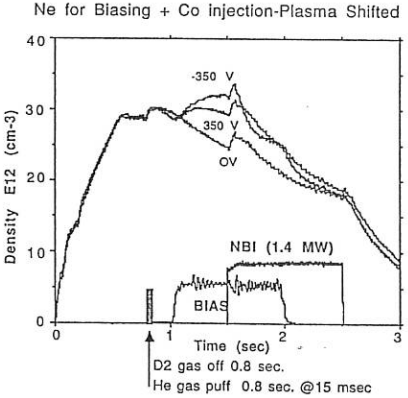

Fig. 3-The central line-averaged density increases significantly during the biasing. the most pronounced effect occurs for negative polarity.

FUSION ALPHA PARTICLE TRANSPORT STUDIES USING ENERGY DEPENDENT DIFFUSION COEFFICIENTS

G. Kamelander
Austrian Research Center Seibersdorf
A-2444 Seibersdorf

ABSTRACT
Predictive codes simulating the plasma dynamics of next generation TOKAMAKs must be equipped with alpha particle routines to calculate the deposition rates and to investigate the possibilities of instabilities triggered by thermonuclear alphas. The α-particle transport has been investigated recently by a special kinetic equation including the transport losses represented by energy integrated heat- and particle fluxes into the source term. In the present paper this method is extended to energy dependent transport coefficients and included into a transport code. As an example the slowing down tail enhanced neoclassical α-transport is given.

INTRODUCTION

A special kinetic equation published by Ref. [1] and improved by Ref. [2] is appropriate to calculate the α-particle distribution function if the particle fluxes and heat fluxes, i.e. the transport coefficients, are known. This FOKKER-PLANCK-typ kinetic equation for the α-distribution function F_α is given by

$$\frac{\partial F_\alpha}{\partial t} + \frac{\partial}{\partial E}(LF_\alpha) - \frac{\partial^2}{\partial E^2}(DF_\alpha) = Q_{ex}(\rho,E) + Q_{in}(\rho,E) \qquad (1)$$

L and D are the FP coefficients, Q_{ex} is the thermonuclear source and Q_{in} represents the transport source depending on energy independent transport coefficients. Q_{in} is constructed such that conservation of particle number and energy is satisfied. This theory has beeen successfully applied to a special anomalous transport model [2] and to ripple transport [3].

THE MODIFIED KINETIC EQUATION

If more realistic transport problems are studied energy dependent transport coefficients must be considered. For this reason we construct a new transport source

$$Q_{in}(\rho,E) = -f_\alpha(\rho,E)\nabla\Gamma - \gamma(\rho,E)\frac{(\gamma_1(\rho)-E)}{\gamma^2{}_1-\gamma_2}.\Gamma.\nabla E - g(\rho,E)\frac{(g_1(\rho)-E)}{g^2{}_1-g_2}\nabla q_\alpha \qquad (2)$$

conserving particle number and energy. $f_\alpha(r,E,T)$, $\gamma(r,E,t)$ and $g(r,E,t)$ mean distribution function, particle flux and heat flux normalized to one. Γ_α and q_α represent the energy integrated fluxes and the i-th moments of γ and g are referred to as γ_i and g_i. $E(\rho)$ is the first energy moment of f_α. Eq.(1) can be solved by iterations.

EXAMPLES FOR ENERGY DEPENDENT TRANSPORT COEFFICIENTS

As a first step the computer code has beeen tested by a synthetic diffusion coefficient

$$D(E) = D_o + w.(E-E_{min})^p.(n_e(\rho)/n_e(o))^q \quad (3)$$

The coefficients D_o, w, p, q are arbitrary constants to be prescribed. As a more realistic case the tail alpha neoclassical transport coefficients retaining both electron and ion drag and pitch angle scattering by the background ions [4] has been investigated. We use the particle fluxes

$$\Gamma_\alpha(\rho,v) = -\frac{4\pi}{3\tau_s}\left(\frac{m_\alpha c I}{z_\alpha e}\right)^2 \langle B^{-2}\rangle (1-Y).v[(v^3{}_c+v^3)+v^3{}_b](R_o B_p)^{-1}\frac{\partial F_\alpha}{\partial \rho} \quad (4)$$

and a corresponding expression for the heat flux. Y is approximated by

$$Y(\varepsilon) = \langle (R/R_o)^2\rangle (1 - 1.46\varepsilon^{1/2} - 0.1\varepsilon + 0.56\varepsilon^{3/2}). \quad (5)$$

The symbols in (4) and (5) are standard.

RESULTS AND CONCLUSIONS

We consider a NET-type plasma. R_o = 630 cm, a = 205 cm, κ = 2.2, B_o = 6T, I = 25A. The electron and ion densities decrease from $1.33.10^{14}$ in the center to $10^{13}/cm^3$ at the edge. The temperature varies from 10 kev to 1 kev. Isolating the alpha particle effects the plasma temperature kept constant.

Fig. 1 shows the energy integrated diffusion coefficient

$D(\rho)=\int \dot{f}_\alpha(E)d(E)dE$ as a function of the effective radius, where D(E) is derived from eq.(4). This figure confirms the results of CATTO [4] that the neoclassical tail diffusion is considerably higher than ash diffusion. Fig. 2 gives the energy dependence of the diffusion coefficient at ρ = 50 cm. The diffusion coefficient is increasing with the energy as it is clear from eq. (4). Both Fig. 1 and Fig. 2 have been evaluated for an equilibrium where d/dt = 0 in eq. (1). Fig. 3 gives the time evolution of the distribution function near the center at three times after switching on the alpha source. t = 0,6 sec is equal to the equilibrium results. We conclude that this transport is not sufficient for the inversion of the distribution function. Fig. 4 contains the particle flux as a function of the effective radius. Fig. 5 shows a comparison of the equilibrium distribution function without (a) and with (b) α-transport according eq. (4) at ρ = 50 cm. In Fig. 7 the equilibrium α-particle density has been drawn as a function of the effective radius (a) neglecting and (b) considering α-transport. Finally we give a comparison of the equilibrium power deposition rates. We conclude that even the lower limit of α-transport given by eq. (4) leads to a noticable reduction of the deposition rate. The effects on the energy balance should be investigated.

REFERENCES

[1] D.F.DÜCHS, D.PFIRSCH, IAEA-CN-33/A 17-1
[2] G.KAMELANDER, Fusion Technology, Vol.18, No.3, 1990
[3] G.KAMELANDER et al., IAEA-CN-53/6-2-1, 1990
[4] P.CATTO, SAIC-87/1826, PRI-116, UC-20 g, Oct. 1987

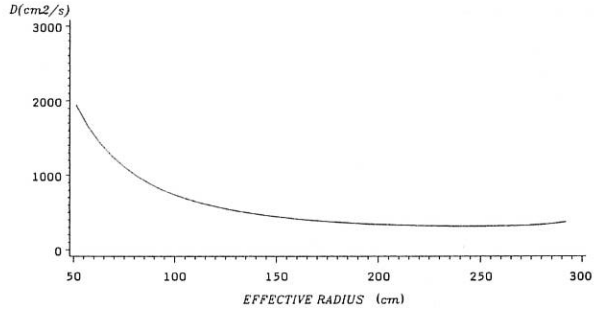

Figure 1: energy averaged diffusion cross section as a function of the effective radius

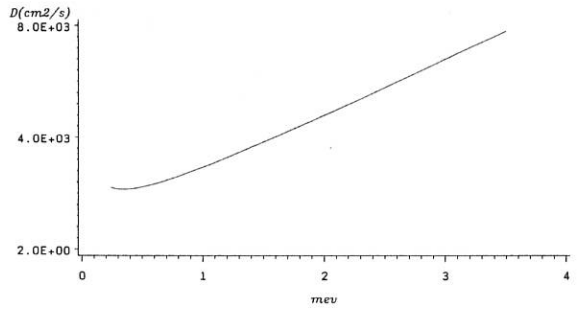

Figure 2: Energy dependent diffusion coefficient at ϱ = 50 cm

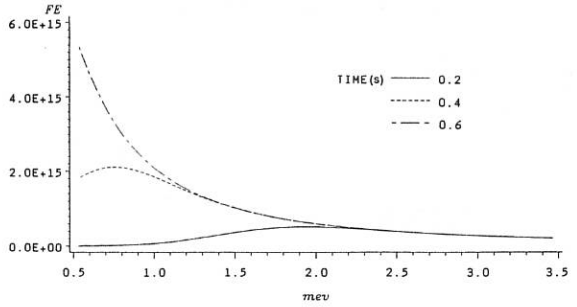

Figure 3: Time evolution of the alpha particle distribution at ϱ = 50 cm

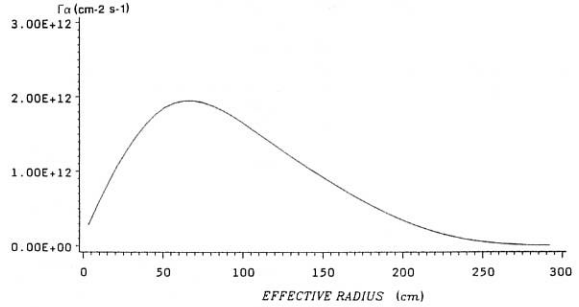

Figure 4: Alpha particle flux as a function of the effective radius

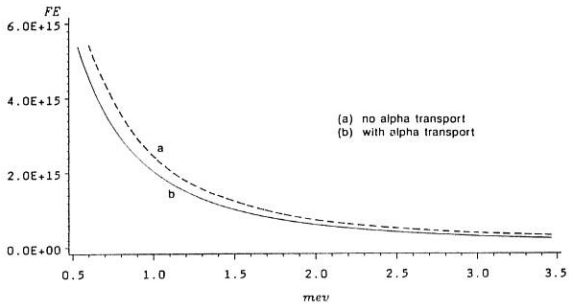

Figure 5: Equilibrium alpha particle distribution function at ϱ = 50 cm

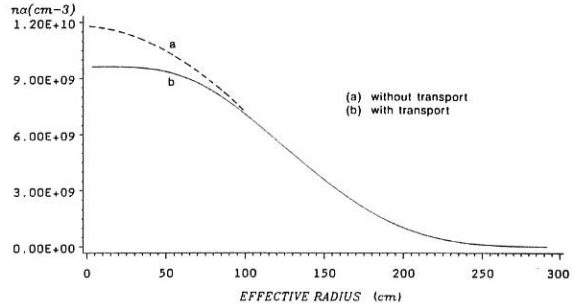

Figure 6: Equilibrium alpha particle density

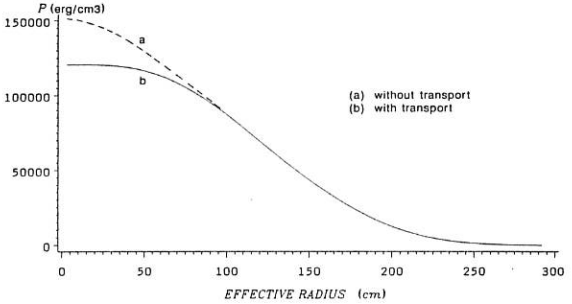

Figure 7: Alpha power deposited to the plasma

INDEX OF AUTHORS